Stochastic processes in the interstellar medium

Emeric Bron

Université Paris Diderot (Paris 7)
Sorbonne Paris Cité

École Doctorale 127
Astronomie et Astrophysique d'Île-de-France

Doctorat :
Astronomie et astrophysique

Emeric Bron

STOCHASTIC PROCESSES IN THE INTERSTELLAR MEDIUM

Processus stochastiques dans le milieu interstellaire

SECONDE PARTIE

Thèse dirigée par :
Jacques Le Bourlot
et
Franck Le Petit

Soutenue le jeudi 13 novembre 2014

Jury :
M. Stéphane Corbel, président
M. Pierre Hily-Blant, rapporteur
Mme Herma Cuppen, rapportrice
Mme Christine Joblin, examinatrice
M. Laurent Verstraete, examinateur
M. Franck Le Petit, directeur de thèse

STOCHASTIC PROCESSES IN THE INTERSTELLAR MEDIUM

EMERIC BRON

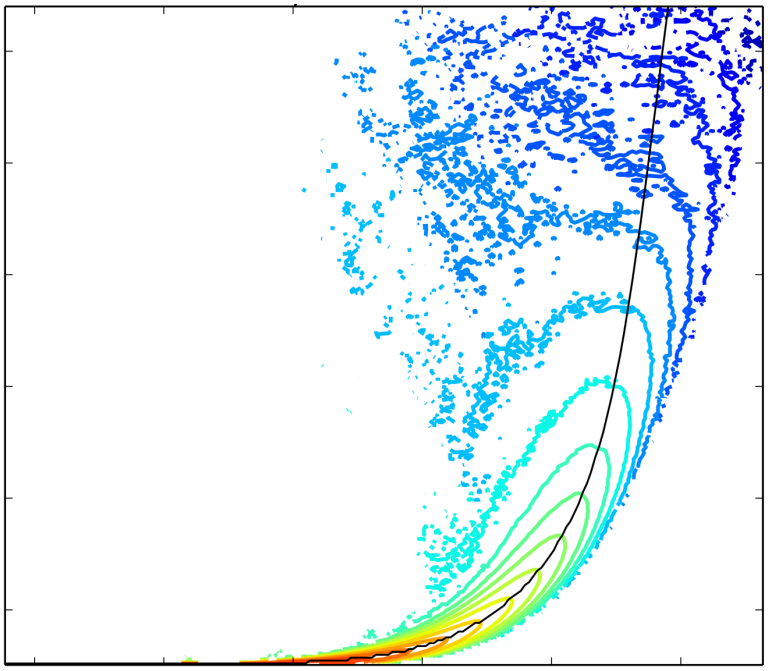

Application to Surface Chemistry and Turbulent Chemistry

Université Paris Diderot
29 Janvier 2015 – version 1.5a

CONTENTS

REMERCIEMENTS

Je remercie tout d'abord mes deux directeurs de thèse, Jacques Le Bourlot et Franck Le Petit, pour leurs conseils, leur soutien et tout ce qu'il m'ont appris au cours de ces trois années. Je leur suis particulièrement reconnaissant pour la grande liberté qu'ils m'ont laissé dans mon travail, liberté qui m'a permis d'explorer des domaines lointains pour y trouver les outils qui m'ont semblé utiles (au risque de m'être dispersé parfois). Je remercie en particulier Jacques pour avoir été à l'origine du sujet de cette thèse et Franck pour son précieux soutien durant les derniers mois de rédaction.

Je remercie également Pierre Hily-Blant et Herma Cuppen d'avoir accepté d'être les rapporteurs de cette thèse et de m'avoir, par leurs corrections et commentaires, aidé à améliorer ce manuscrit et à prendre du recul sur mon travail. Je remercie Christine Joblin et Laurent Verstraete d'avoir pris part à mon jury de thèse et d'avoir aidé à corriger les dernières erreurs par une relecture attentive, et Stéphane Corbel d'avoir accepté de présider ce jury.

J'ai également pu profiter au cours de cette thèse de l'aide du reste de l'équipe MIS de Meudon. Je remercie Benjamin Godard, qui a partagé mon bureau pendant cette dernière année, pour les nombreuses discussions fort enrichissantes que j'ai pu avoir avec lui, et pour l'atmosphère tropicale qu'il a apportée à ce bureau. Je remercie Evelyne Roueff de m'avoir fait profiter, par ses réponses et conseils avisés, de sa grande érudition sur le milieu interstellaire. Je remercie David Languignon pour nos discussions sur Python, la programmation, et le Machine Learning.

Certaines parties de cette thèse résultent de collaborations : la section 6.5 résulte d'une collaboration avec Benjamin Godard, et la partie iv d'une collaboration avec Christine Joblin et Cecilia Pinto. Je les en remercie. J'ai grandement bénéficié des discussions que j'ai pu avoir avec (entre autres) Christine Joblin, Laurent Verstraete, Maryvone Gerin, Edith Falgarone et Pierre Lesaffre.

Je voudrais aussi remercier ici quelques enseignants particulièrement marquants qui ont significativement contribué à forger mon esprit scientifique : Mme Maurice au lycée A. Renoir d'Asnières, M. Bertrand, M. Barnier et M. More au lycée Condorcet, Jean-Michel Raymond et Werner Krauth à l'ENS, et Didier Pelat à l'Observatoire de Paris.

Pour finir, je remercie tout ceux qui m'ont soutenu tout au long de cette thèse, m'ont permis de me changer les idées de temps en temps et de garder un minimum de vie sociale. Entre autres, je remercie mes amis de toujours : André, Anouche, Gabriel, Olivier, Payam, Wilson, avec des remerciements particuliers à Anouche et Gabriel qui ont eu le courage de venir voir ma soutenance en anglais ; mes amis du master : Adrien, Elise, Jonathan, Julien, Lapo,

Lucky, Maïca, Uddhab ; et mes compagnons d'escalade : Alexandre, Anouche, Diane, Hadrien. Je remercie mes parents, qui m'ont soutenu moralement et logistiquement, et qui ont préparé le pot de thèse. Et bien sûr, je remercie Hayley pour sa compagnie toujours riante et douce, même quand nous étions tous les deux dans les plus durs moments de la rédaction.

ABSTRACT

In this thesis, I have tackled two seemingly unrelated problems in the modeling of the neutral interstellar medium (ISM).

The first is the description of H_2 formation on interstellar dust grains under realistic conditions. The precise determination of the H_2 formation rate and abundance is crucial, as it controls most of the subsequent development of the chemical complexity in the ISM, as well as part of its physics. The temperature of small grains ($\lesssim 10\,\mathrm{nm}$) fluctuates constantly as those grains are sensitive to the energy of individual UV photons, and the surface mechanisms of H_2 formation, which are sensitive to the grain temperature, are kept out of equilibrium by the fluctuations. I have developed an exact resolution formalism for the statistical equilibrium of this system, and implemented its numerical resolution. Among other results, taking the fluctuations into account leads to large differences for the Langmuir-Hinshelwood mechanism, whose efficiency is increased in atomic gas and decreased inside molecular gas.

The second problem is related to the ubiquitous presence of molecules such as CH^+, whose formation is highly endothermic, in the diffuse ISM where the observed gas temperature ($< 100\,\mathrm{K}$) is insufficient to trigger their formation. It has been proposed that the intermittent dissipation of turbulence could inject the necessary energy, creating hot spots, which could also explain the observed rotational excitation of H_2 in such regions. At small scales, the gas is thus perturbed by strong fluctuations of the energy injection rate. I propose a model for the Lagrangian evolution of the local physico-chemical state of the gas based on stochastic processes, and apply it to derive the distribution of the gas temperature in the diffuse atomic medium, and the average excitation of H_2 in the diffuse molecular gas.

Both problems are thus similar and can be described in a more abstract way as systems whose state is perturbed by strong fluctuations of their environment. In order to derive the statistical equilibrium of the system in our two cases, similar methods are used based on the framework of (markovian) stochastic processes. The results obtained here demonstrate the usefulness of this approach, and possible developments for other applications are discussed.

Finally, I also present the modeling of the PDR NGC7023 Northwest with the Meudon PDR Code in comparison to Hershel observations, showing the excellent capacity of the Meudon PDR Code to reproduce the observables in dense and intense PDRs.

RÉSUMÉ

Mon travail de thèse a porté sur la modélisation du milieu interstellaire (MIS), et plus particulièrement sur deux problèmes qui peuvent sembler sans lien au premier abord.

Le premier concerne la formation de H_2 sur les grains de poussière interstellaires. Il est en effet crucial de comprendre précisément le taux de formation de H_2 et son abondance, dont dépend tout développement d'une chimie plus complexe, et qui contrôlent également une partie de la physique du gaz interstellaire. Mais les petits grains ($\lesssim 10\,\mathrm{nm}$) sont sensibles à l'énergie des photons UV individuels et leur température fluctue donc constamment. Les processus de surface qui forment H_2, étant sensibles à la température de la surface, sont alors maintenus hors d'équilibre par ces fluctuations, un effet très peu étudié jusqu'à présent.

Le second problème est lié à l'omniprésence observée de molécules telles que CH^+, dont la formation est très endothermique (quelques $10^3\,\mathrm{K}$), dans le MIS diffus ($n_\mathrm{H} \sim 10 - 100\,\mathrm{cm}^{-3}$) où les températures observées ($\lesssim 100\,\mathrm{K}$) sont insuffisantes pour permettre leur formation. Il a été proposé que l'énergie nécessaire à leur formation puisse provenir de la dissipation intermittente de la turbulence, créant des points chauds dans le gaz qui pourraient aussi expliquer l'excitation rotationnelle de H_2 observée dans ces régions. Aux plus petites échelles de la cascade turbulente, le gaz est donc soumis à une injection d'énergie dont le taux fluctue fortement, et qui perturbe la chimie de façon aléatoire.

Ces deux problèmes sont donc similaires à un niveau plus abstrait en ce qu'ils portent sur des systèmes dont l'état est perturbé par de grandes fluctuations de leur environnement. Afin de calculer l'équilibre statistique dans nos deux cas, j'ai développé des méthodes similaires, basées sur le formalisme des processus aléatoires (markoviens). Les résultats obtenus ici démontrent l'intérêt de la méthode, et des développements en vue d'autres applications sont discutés.

Pour le problème de la chimie de surface sur des grains dont la température fluctue, un formalisme basé sur les processus stochastiques (à sauts discontinus) et sur l'équation maîtresse associée a été développé, sous une forme complètement indépendante de toute procédure de discrétisation.

Dans ce cadre, j'ai pu revisiter les statistiques des fluctuations de température et comparer les résultats obtenus aux travaux publiés sur le sujet. J'ai également obtenu une approximation analytique de la PDF[1] dans la limite

1 PDF (*Probability Density Function*) : densité de probabilité.

des gros grains, et une deuxième approximation plus physique permettant de calculer très rapidement l'émissivité des grains en tenant compte des fluctuations. Cette seconde approximation a été implémentée dans le code PDR de Meudon.

Plus généralement, ce formalisme peut être appliqué à n'importe quelle réaction de surface sur des grains dont la température fluctue, dans la limite des capacités de calcul.

J'ai en particulier considéré deux mécanismes de formation de H_2 à la surface des grains : le mécanisme de Langmuir-Hinshelwood (réaction entre atomes adsorbés) sur des sites de physisorption, et le mécanisme d'Eley-Rideal (réaction entre un atome adsorbé et un atome du gaz) sur des sites de chemisorption. Une simplification analytique de l'équation maîtresse a été obtenue dans le cas de réactions linéaires comme dans le mécanisme d'Eley-Rideal. Pour les deux mécanismes, une méthode de résolution numérique est proposée, basée sur les propriétés des valeurs propres des opérateurs intégraux qui apparaissent dans les équations.

Le résultat le plus surprenant de ces calculs est que le mécanisme de Langmuir-Hinshelwood peut fonctionner efficacement dans du gaz qui n'est pas protégé du rayonnement UV, pour des champs d'intensité G_0[2] jusqu'à quelques centaines. Ce résultat apporte un éclairage nouveau sur le paradoxe entre les expériences (par exemple Katz et al. 1999) qui montrent que ce mécanisme n'est efficace que dans une gamme limitée de températures de surface ($T < 20\,\mathrm{K}$), et les observations (par exemple Habart et al. 2011) qui indiquent une formation efficace de H_2 dans des régions (PDRs[3]) où les grains sont plus chauds que 20 K. Durant les fluctuations de la température, la majeure partie de l'énergie absorbée est ré-émise durant des pics de température très courts, et la majeure partie du temps est en fait passée à basse température, ce qui permet de former H_2 efficacement. Seuls les petits grains sont suffisamment affectés par les fluctuations pour observer cet effet, et l'efficacité du mécanisme de Langmuir-Hinshelwood est ici grandement augmentée pour des grains de tailles allant jusqu'à 20 nm. En conséquence, ce mécanisme devient efficace dans une large gamme de conditions astrophysiques, incluant les PDRs modérées ($G_0 \lesssim 200$).

Le mécanisme d'Eley-Rideal n'est que faiblement affecté par les fluctuations. Son efficacité est légèrement réduite, les plus petits grains n'ayant pas le temps de reconstituer leur population de surface entre deux fluctuations qui l'évaporent. Cet effet résulte donc d'une compétition entre le temps caractéristique de récurrence des fluctuations, et le temps caractéristique de ré-adsorption des atomes depuis le gaz.

2 Le paramètre G_0 mesure l'intensité du champs de rayonement dans la gamme $912 - 2400$Å. Une valeur de 1 correspond au champs interstellaire standard de Habing [1968].

3 PDR (*Photon-Dominated Region*) : région où la chimie est dominée par les réactions de photodissociation.

Ce même effet de compétition devient également important pour le mécanisme de Langmuir-Hinshelwood plus profondément à l'intérieur des nuages, après la transition H/H_2. En effet, dans un gaz moléculaire, l'abondance d'hydrogène atomique est très faible et le temps caractéristiques d'adsorption des atomes est donc long, ce qui rend les petites fluctuations causées par les photons infrarouges à ces profondeurs capables de maintenir la chimie de surface hors d'équilibre et donc de réduire l'efficacité de formation. Il y a donc un mécanisme d'auto-limitation de la formation de H_2 : le gaz ne peut devenir complètement moléculaire puisque quand la fraction atomique décroit, les fluctuations causent une diminution de l'efficacité de formation. Dans les nuages moléculaires denses, ces fluctuations pourraient être causées par les photons UV secondaires et par les rayons cosmiques, tandis que les photons du proche infrarouge seraient suffisant dans les nuages diffus (les grains y sont plus petits). Ce mécanisme de limitation pourrait être pertinent pour expliquer la fraction atomique dans les nuages sombres, ou la fraction moléculaire dans le gaz diffus.

Pour traiter le problème de la chimie turbulente dans le milieu interstellaire, je propose ici une adaptation des méthodes PDF qui ont été développées dans le domaine de la combustion turbulente (par exemple, Pope 1985). Le principe de ces méthodes est d'utiliser l'équation de transport de la PDF à un point, avec comme approximation de fermeture des modèles stochastiques lagrangiens pour les termes problématiques. La simulation Monte-Carlo du processus stochastique permet ensuite de calculer la PDF.

Dans le cas de la turbulence homogène et stationnaire, cette approche revient simplement à modéliser l'évolution lagrangienne du taux instantané de dissipation vu par un élément de fluide par un processus aléatoire ayant les bonnes propriétés statistiques, et à coupler l'évolution dynamique de l'état thermo-chimique du gaz à ce processus stochastique de chauffage. Un modèle simple du processus stochastique de dissipation est proposé ici, basé sur le modèle log-normal de l'intermittence.

Ce formalisme est ici appliqué au milieu neutre diffus. Dans cette version préliminaire, l'évolution chimique n'est pas calculée, et seul l'état thermique du gaz est suivi. Le gaz est la plupart du temps chauffé par l'effet photoélectrique, sauf pendant les pics de dissipation turbulente où le chauffage est dominé par la turbulence pendant de courtes phases très intenses. Le refroidissement est dominé par l'émission de C^+ et O dans le gaz atomique, tandis que dans le gaz moléculaire, H_2 peut devenir le refroidisseur principal pendant les phases chaudes. Les PDFs de température calculées montrent que le chauffage intermittent par la turbulence crée une fraction significative de gaz chaud (entre quelques centaines et quelques milliers de K), avec une grande variation selon l'efficacité des refroidisseurs. Cette fraction de gaz chaud contribue à peupler les niveaux rotationnels excité de H_2, et l'excitation moyenne calculée est en bon accord avec les observations de H_2 en

absorption par FUSE.

Enfin, je présente également la modélisation à l'aide du code PDR de Meudon de la PDR NGC7023 Nord-Ouest. Le grand nombre de contraintes observationnelles disponibles pour cette PDR (observations Herschel, complétées par des observations plus anciennes) permet de tester de façon poussée les capacités du code PDR de Meudon à reproduire les observations dans des PDRs intenses comme NGC7023. Les traceurs du bord de la PDR sont extrêmement bien reproduits par un modèle isobare, tandis que les raies provenant de régions plus en profondeur montrent des écarts aux modèles plus importants, dont une partie peut être expliquée par des effets d'écrantage mutuels entre H_2, CO et ses isotopes.

Part I

INTRODUCTION

FOREWORD

The interstellar medium is the theater of a wide variety of physical and chemical processes, taking place on a large range of length-scales and at very diverse energies. A rich chemistry can develop, interacting with the other physical processes, and the molecules that it creates can in return contribute to the physics of this interstellar matter. This complex physico-chemical system gives birth to new stars, and controls the evolution of galaxies. A precise understanding of its dynamics is thus necessary.

This thesis focuses on a specific kind of problem that arises in such complex interlinked systems, in which a chemical system is kept out of equilibrium by large fluctuations of its environment. If those fluctuations have stationary statistics, a statistical equilibrium of the chemical system can be expected, and we will show how this equilibrium can be described in terms of probability density functions (PDFs) and computed in the framework of stochastic processes.

This idea will be developed on two specific problems in the modeling of the neutral interstellar medium.

The first is the formation of H_2 on dust grains. H_2 is the first step of most of the interstellar chemistry, and understanding quantitatively its formation process is crucial for all modeling of molecular clouds, and of star formation inside these clouds. As the temperature of the dust grains on the surface of which H_2 forms fluctuates constantly because they are sensitive to the energy of individual UV photons, the question arises of how to compute the average formation rate in such a situation. Spitzer observations of H_2 show that H_2 formation is still not precisely understood, and the impact of the temperature fluctuations on H_2 remains largely unexplored. This fluctuation problem is naturally formalized in the framework of (pure jump) stochastic processes, and we develop here a full resolution method.

The second problem comes from an hypothesis to explain the presence in the cold ($< 100\,\mathrm{K}$) diffuse interstellar medium of molecules (e.g. CH^+, SH^+, ...) that are highly endothermic, and can thus only be formed by crossing a high energy barrier. The hypothesis is that the energy necessary to trigger the formation of those molecules comes from the dissipation of the turbulent motions of the interstellar gas. This turbulence could thus play a role in the unexpected molecular richness of the diffuse ISM. In turbulence, the large scale motions are indeed unstable and disintegrate into smaller and smaller eddies, until reaching a scale where the kinetic energy is efficiently dissipated into thermal energy. This dissipation process occurs at small scales in a very intermittent way, with strong bursts of dissipation in small localized regions

in which most of the energy is dissipated. The chemistry in such gas is thus perturbed by a strongly fluctuating input of energy. The problem of computing the average chemical abundances in this situation is a more complex form of the problem encountered for H_2 formation, which suggests an approach using similar (albeit more complex) tools. This possible influence of turbulence on the chemistry has been investigated before with detailed models of individual dissipative structures, while using simplistic statistics for the occurrence of these dissipation events. To go further, we adopt an empirical approach to turbulence by using a stochastic process reproducing the statistics predicted by the few theoretical models of intermittency, or observed in numerical and laboratory experiments.

The ideas and tools developed for these problems could be relevant for a variety of other astrophysical problems, where a cloud, or a smaller element of gas, is subject to a forcing that fluctuates on a short timescale with statistics evolving on a much longer timescale. In these situations, a statistical equilibrium can be defined. For instance, we could think about the cycling of interstellar matter between the different phases of the ISM (especially between CNM and WNM), where the cycling is fast compared to the slow evolution of the galactic environment.

In this first part, we introduce the astrophysical context of these two problems, starting with a general overview of the physico-chemistry of the interstellar medium in our galaxy in Chap. 1, followed by a description of the physics of interstellar dust grains, on which H_2 formation takes place, in Chap. 2, and a presentation of the phenomenon of intermittency in turbulence and its importance in the interstellar medium in Chap. 3. This part ends in Chap. 4 with an introduction to the mathematical framework of stochastic processes that will be used to tackle our two problems, in which the central equations describing the statistics of such processes are presented.

The problem of the modeling of H_2 formation on the surface of grains whose temperature fluctuates is treated in Part ii of this thesis. The microphysical model of H_2 formation on dust and of the dust temperature fluctuations is described in Chap. 5, and results when ignoring the fluctuations are derived for comparison. Chap. 6 then describes the statistics of dust temperature fluctuations in terms of stochastic processes, and several approximations are discussed, one of which allows a fast computation of the dust emissivity. The framework is then enlarged in Chap. 7 to include the formation of H_2 on the surface of the grain, and the resolution method is described and tested. The results of this computation are presented in Chap. 8 which reproduces the article published in Astronomy & Astrophysics on this subject.

Part iii presents a stochastic process approach to the problem of turbulence-driven chemistry. The general description of turbulence in terms of PDFs is described in Chap. 9, as well as the use of stochastic processes as closure models. A specific stochastic model for our purpose is presented, based on the log-

normal model of intermittency. This model is then applied in Chap. 10 to two simple astronomical models as preliminary demonstrations of the method : the question of the distribution of the gas temperature in the diffuse atomic ISM, and the question of the excitation of H_2 in a turbulent diffuse molecular gas.

Part iv presents a side project on the modeling of the PDR NGC 7023 Northwest for the interpretation of Herschel observations. Finally, Part v summarizes our conclusions, and presents perspectives on the future developments of this work.

1

THE INTERSTELLAR MEDIUM

The space between stars is not empty, and Hubble's beautiful images have made famous the gigantic interstellar clouds that float among the stars (for instance Fig. 1). The medium that occupies this space is called the *interstellar medium* (commonly abbreviated as ISM). Most of it is dark and only noticeable as it obscures the light of the stars behind it, and the bright and dramatic views offered by Hubble only result from the conjunction of denser concentrations of gas and close-by bright stars that illuminate the cloud.

Mostly constituted of gaseous material with the addition of very small (with sub-micron sizes) solid particles called *interstellar dust grains*, the ISM is less dense (on average ~ 1 atom/molecule/ion per cubic centimeter in the plane of our galaxy) than the best vacuums created on earth (such as the vacuum in the beam pipes of the LHC, $100 - 1000$ atoms per cubic centimeters). However, it is distributed very in-homogeneously, with extremely diffuse regions (0.006 particle per cubic centimeter) and denser clouds (up to 10^6 cm^{-3} in the molecular parts). We describe in more details these different phases of the ISM in Sect. 1.2.2.

This extremely tenuous component of the Milky Way nevertheless plays a very important role in the evolution and structure of the galaxy. This role is discussed in Sect. 1.1 and 1.2.2.

We do not have direct access to the ISM, as the whole solar system is dominated by the influence of the Sun through its magnetic field and wind. We must thus rely on observational methods to deduce the physicochemical conditions of the ISM (such as its density, temperature, chemical composition, ...). Those methods are discussed in Sect. 1.3.2. Especially important are the molecular lines that give detailed informations in dense and cold gas. The ISM indeed presents a surprising molecular richness, which we discuss in Sect. 1.3.

As the work of this thesis is mainly concerned with molecular or at least neutral atomic gas, this presentation is voluntarily biased towards the dense components of the ISM. See Ferrière [2001] and Cox [2005] for a more balanced presentation.

1.1 THE LIFE CYCLE OF GALACTIC MATTER

Stars do not live forever. After running out of their nuclear fuel—which they burn quicker the more massive they are—, they die a more or less tumultuous death depending on their mass. Very massive stars live a very short life,

Figure 1: Infrared composite image of the Monkey Head Nebula (NGC2174) obtained by the Hubble Space Telescope. Credits: NASA, ESA, and the Hubble Heritage Team (STScI/AURA).

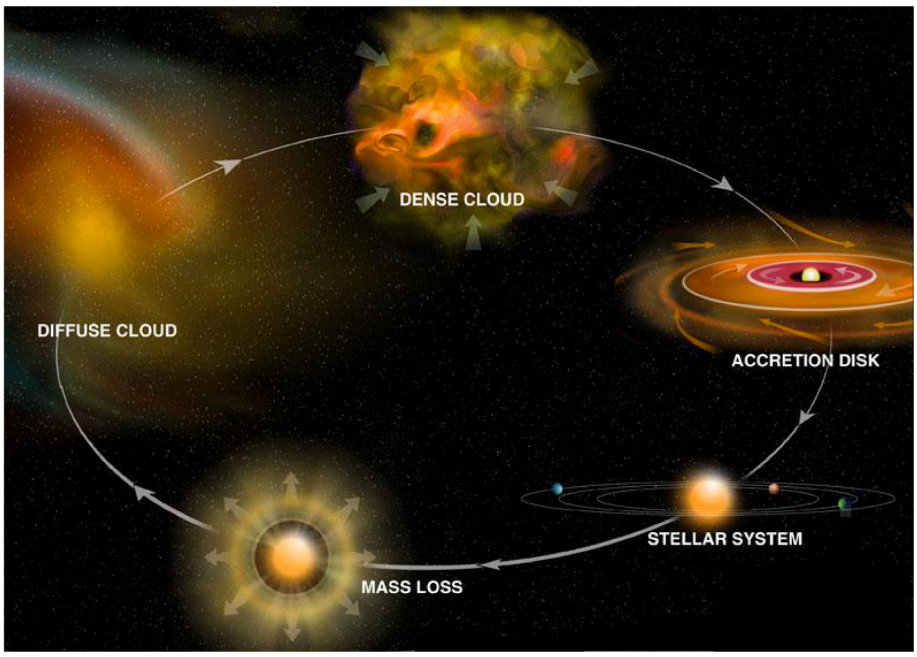

Figure 2: The life cycle of galactic matter. Credits: Bill Saxton, NRAO/AUI/NSF.

during which they expel large amounts of matter in strong winds, and die in powerful explosions known as *supernovae* during which more matter is injected into the ISM. Smaller stars only expel their outer layers at the end of a longer life. As result a significant fraction of the matter that constitutes stars is returned to the interstellar medium when the star dies.

During the life of the star, light elements (hydrogen, helium) are transformed into heavier elements (carbon, oxygen, and heavier elements, the heaviest elements being formed during supernova explosions), a process called *stellar nucleosynthesis* (see Nomoto et al. [2013] for a recent review). The material that is returned to the ISM is thus enriched in heavy elements compared to its state at the birth of the star.

In the tenuous ISM, which is continuously replenished this way, various dynamical processes (for instance the shock waves generated by supernovae) can then create local concentrations of matter, denser clouds that become subject to self-gravity and collapse. They become denser and denser as radiative cooling processes (discussed below) carry away the thermal energy and reduce the thermal pressure that may counteract gravity. At the end of this collapse, the gas becomes sufficiently dense and hot to trigger nuclear fusion reactions and a new star lights up.

The galactic matter thus undergoes a cycle which is depicted in Fig. 2. As successive generations of stars pass, the galactic matter is progressively enriched in heavy elements, with the observable consequence that younger stars have a higher content in heavy elements than older stars (elements heavier than hydrogen and helium are usually called *metals* in the astronomical

element	abundance ratio	reference
He/H	0.1	(1)
C/H	1.3×10^{-4}	(2)
N/H	7.5×10^{-5}	(3)
O/H	3.2×10^{-4}	(4)
S/H	1.9×10^{-9}	(2)

Table 1: Abundance ratios in the ISM for the heavier elements. References: (1) Stahler and Palla [2005],(2) Savage and Sembach [1996],(3) Meyer et al. [1997], (4) Meyer et al. [1998].

context). A comprehensive review of the star formation process starting from the formation of giant molecular clouds can be found in McKee and Ostriker [2007].

1.2 CONSTITUENTS AND ORGANIZATION

1.2.1 *Constituents*

The interstellar matter composition today is the product of this galactic evolution. Our Galaxy contains 70.4% of hydrogen (in mass), 28.1% of helium and 1.5% of heavier elements (the proportions of the most important elements are given in Table 1). The mass of the interstellar matter represents roughly $10 - 15\%$ of the galactic disk.

The ISM can be decomposed into 5 components interacting with each other:

- The gas,
- small dust grains,
- cosmic ray particles traveling at relativistic speeds,
- a bath of photons originating in the stars of the galaxy,
- and a magnetic field that permeates and strongly influence the other material components.

THE INTERSTELLAR GAS: The gas is mostly concentrated in the galactic disk. It fills the space between the stars in an extremely inhomogeneous way. Indeed, roughly half of the total gas mass occupies only $1 - 2\%$ of the volume, concentrated in dense regions that are called *clouds*.

The gas in clouds is usually mostly neutral, in the sense that the hydrogen is in neutral form. They are indeed dense enough so that the photons able to ionize hydrogen (the main constituent) cannot penetrate inside them past a

thin surface layer (all other elements that have ionization energy lower than that of H can be ionized as the corresponding photons penetrate deeper, resulting in a ionization fraction of at most $\sim 10^{-4}$ when C is ionized). Clouds are then classified depending on whether the main elements are in atomic or molecular form. The remainder of the gas constitutes a more tenuous inter-cloud medium which can be in neutral atomic or ionized form. The different classifications of the ISM phases are discussed in more details in Sect. 1.2.2 below.

Finally, this gas is animated with large and complex dynamical motions. The velocity differences between cold clouds are typically supersonic, and large velocity dispersions are also observed inside individual clouds. The clouds have a typical lifetime of the order of 10 million years. Large scale flows in the gas are created by the stars through supernova explosions and stellar winds, and by the galactic differential rotation, and those flows feed a turbulent cascade of motions down to the smallest scale where it is dissipated (interstellar turbulence is discussed in detail in Chapter 3).

INTERSTELLAR DUST GRAINS: The interstellar dust grains are small solid particles with sizes going from the micron down to the size of large molecules (a fraction of nm). They are mixed with the gas and follow its distribution, the quantity of dust material being roughly proportional to the gas density. However, the relative amounts of the different grain sizes vary with the gas conditions, with typically bigger grains in dense clouds. It is also from this dust material that planets form (or at least their solid core for gaseous planets) in the protoplanetary disk surrounding the protostar following the collapse of an interstellar cloud.

Dust grains absorb and scatter the light from stars, causing a progressive extinction of starlight as it travels through the ISM. This extinction is more efficient for short wavelengths (e.g., blue light, UV light) than for longer wavelengths (e.g., red light, IR light), and, as a result, stars that are seen through large quantities of dust appear redder than they really are. This effect is called *reddening*, and it is the observation that stars seem to be redder the more distant they are that led, among other things, to the realization that the interstellar space is filled by an ubiquitous material medium (see for instance Trumpler 1930a). The precise dependence of this extinction on wavelength gives information on the composition and size of dust grains.

Observations of the interstellar gas show that the abundances of many heavy elements (such as C and Si) in the gas are much lower than what can be measured in the Sun. The missing part is what constitutes the solid dust particles, and precisely measuring those differences, which are called the *elemental depletions*, gives more information on the composition of the dust grains.

We will discuss in more details the current knowledge on dust grains and their role in the ISM in Chapter 2.

THE MAGNETIC FIELD: The ISM is also permeated by a magnetic field, which is highly irregular but overall mostly directed parallel to the galactic plane. Its average strength in the galactic plane is of the order of $1\,\mu$G, while the amplitude of the fluctuations is of the order of $5\,\mu$G. It is much less than the magnetic field on the surface of Earth, but has nevertheless—due to the large timescales and length scales involved—a very important influence on the dynamics and structure of the ISM. All charged particles are constrained in their movement by the local magnetic field. It thus controls the propagation of cosmic rays, and is an important force that shapes the ionized gas and to a lesser extent the neutral gas due to the ionization of C.

The origin of this magnetic field is not completely understood, but it is thought to be maintained by a turbulent dynamo process where the turbulent motions of ionized (or partially ionized) gas transfer part of their kinetic energy to the magnetic field (similarly to the turbulent dynamo in Earth liquid core that creates the terrestrial magnetic field). As this dynamo process can only work if a magnetic field is initially present (then amplifying it and maintaining it at some saturation level), it has been proposed that the seed magnetic field could be a remnant of stellar magnetic fields partly ejected at the death of the first stars, or could be an extragalactic magnetic field already present when the galaxy formed (see Widrow et al. [2012] for a review of the possible origins of the seed magnetic field, and Durrer and Neronov [2013] for more details on the possible formation processes of a cosmological magnetic field).

COSMIC RAY PARTICLES: Cosmic rays are a variety of matter particles traveling at nearly light speed. Measurements from Earth find them to be mostly protons, with $\sim$ 10% helium nuclei, $\sim$ 2% electrons and 1% heavier nuclei (plus trace amounts of positrons and antiprotons). However, direct measurements made on Earth are highly influenced by the proximity of the Sun, and actually almost all low energy cosmic rays ($\lesssim 1\,$GeV particles) that we receive are produced by the Sun, while higher energy particles come from outside of the solar system. Moreover, the observed energy spectrum of the cosmic rays is strongly affected by the magnetic field of the solar wind, making it difficult to estimate the cosmic ray spectrum in the ISM. Here again, the high energy part of the spectrum is less affected and better known. The energy density of the cosmic rays outside of the solar system has been estimated to be $1.8\,\mathrm{eV.cm^{-3}}$ (Webber 1998).

In addition to direct observations, cosmic rays can be studied from their interactions with interstellar matter. First, their interaction with matter and photons in the ISM produces γ-rays, which can then be observed. Cosmic rays also ionize molecules in clouds (the ionization of H_2 is of special importance in the chemical network as will be discussed below). Observations of molecular ions (e.g., H_3^+) thus give additional informations on the cosmic ray spectrum (mostly on the low energy part of the spectrum which is more

efficient at ionizing molecules). A review of those different methods of study and of their results can be found in Wiedenbeck [2013].

Cosmic rays are probably initially produced by different types of stars at different stages of their lives before being accelerated in the ISM to nearly light speed. The acceleration is caused by multiple scattering by the irregularities of the interstellar magnetic fields, either in supernova shock waves, or in the fluctuating magnetic field of the magnetohydrodynamic turbulence of the ISM. Blasi [2013] gives a review of the theory of the origins of cosmic rays.

THE RADIATION FIELD: The last component is the light that pervades the ISM. This radiation field covers the full electromagnetic spectrum, and different wavelength ranges are dominated by different types of sources. In the domain of microwave radiations, the interstellar radiation field is dominated by the cosmic microwave background (CMB) emitted at the recombination era, and redshifted to the microwave domain by the expansion of the Universe. The CMB follows very closely a black-body law at 2.73 K. The far- and mid-infrared domain is dominated by the thermal emission of the dust grains. Finally, the near-IR, visible and UV domains are dominated by the light of stars, with more massive stars contributing to lower wavelengths. These different wavelength domains contain energy densities of roughly the same order of magnitude.

The part of the radiation field that has the strongest influence on the ISM gas is the UV radiation field, whose interaction with matter is very destructive. High energy UV photons tend to eject electrons from atoms, a process called *photoionization*. Each atom requires a different energy to be ionized, with the first ionization of hydrogen requiring photons with wavelengths lower than 912 Å. As the photoionization process causes the absorption of the photon, photons below this limit (called the Lyman limit) tend to be quickly absorbed in the ISM. The regions where hydrogen is mostly neutral thus have very few photons below this limit[1]. As a result, only atoms with ionizations energies that are lower than that of hydrogen can be ionized in the neutral medium. The most abundant of these atoms is carbon, which is thus the main contributor of electrons in the neutral medium and can give a ionization fraction of at most 10^{-4} (the relative abundance of carbon). In addition, such UV photons can also eject electrons from dust grains, a process called *photoelectric effect*. The electrons ejected by photoionization or photoelectric effect receive a part of the surplus energy from the photon as kinetic energy, which they then give to the gas by collision. As a result, UV photons are often a dominant heating process of the gas, either from the ionization of gas atoms in ionized regions, or from the photoelectric effect on dust grains in neutral regions.

1 A few secondary photons may be created in situ.

Phase	T [K]	n_H [cm^{-3}]	Volume filling factor
Molecular	$10 - 20$	$10^2 - 10^6$	1%
CNM (atomic)	$50 - 100$	$20 - 50$	4%
WNM	$6000 - 10000$	$0.2 - 0.5$	30%
WIM	~ 8000	$0.2 - 0.5$	15%
HIM	$\sim 10^6$	~ 0.0065	50%

Table 2: Physical conditions of the five phases of the ISM. See text for a description. Values of the densities and temperatures from Ferrière [2001], volume filling factors taken from Stahler and Palla [2005].

Lower energy UV photons can also dissociate molecules. As a result, only regions in which UV photons do not penetrate can be molecular. The UV photons that could dissociate a molecule can either be absorbed by dust grains, or by similar molecules being dissociated in the outer layer of the cloud. As a result, molecular gas tends to be located at the center of clouds, protected by the external layers which remain atomic. The structure of neutral clouds will be described more precisely in Sect. 1.2.2.

1.2.2 *The phases of the ISM*

Observations show that the ISM presents a wide variety of local properties, which are usually grouped in five phases based mostly on the ionization state of the gas and on its temperature (Ferrière 2001). The physical conditions of each phase are given in Table 2. From the densest to the most tenuous, those phases are:

- The *molecular gas*: neutral gas in which hydrogen is mainly in the form of dihydrogen molecules (H_2). It usually lies in the inner part of clouds. This phase is actually rather a sub-phase of the cold neutral medium (next in the list) with roughly the same order of temperatures and higher densities, but is usually included in the five-phases description of the ISM. Most of the work of this thesis concerns this phase of the ISM. Dense molecular cores are often subject to self-gravity, contrary to the other phases.

- The *cold neutral medium* (CNM): dense and cold neutral gas. Interstellar clouds are regions where the ISM is in this phase (or in the molecular phase). If the molecular gas is distinguished, then this phase refers to the cold atomic medium only. It is usually less dense than the molecular gas, as a dense gas quickly absorbs the dissociative UV photons and becomes molecular. When molecular gas is present, it is always surrounded by a layer of atomic medium. But clouds can be entirely

atomic if they are not large or dense enough to protect their core from UV photons, in which case they are usually called diffuse clouds.

- The *warm neutral medium* (WNM): neutral gas is also found in a state of much lower density with high temperature, in rough pressure equilibrium with the CNM. The origin of this coexistence of two phases in the same pressure range and conditions is explained below. This phase usually surrounds an ensemble of clouds, forming giant cloud complexes.

- The *warm ionized medium* (WIM): the gas surrounding stars is usually ionized by the stellar radiation, forming a roughly spherical region of ionized gas called an H_{II} *region*. But these localized structures are not the only ionized parts of the ISM. It was more recently recognized that the UV radiations of bright O stars of the galaxy somehow manage to escape their immediate vicinity and collectively create extremely extended regions of ionized gas (with physical conditions similar to the WNM), mainly located in the halo of the galaxy. For a very detailed discussion of this phase, see the review by Haffner et al. [2009].

- The *hot inter-cloud medium* (HIM): Finally, supernova explosions create bubbles (or super-bubbles when several supernovae successively explode in the same region) of extremely low density and extremely high temperatures. These expanding bubbles often connect to each other and to the galactic halo, creating tunnels. It is probably this network of almost empty tunnels which allows the UV radiation of O stars to travel far across the galaxy and out of the disk, and to ionize large portions of gas, creating the WIM phase.

As we are more interested in the dense parts of the ISM, we now discuss in more details the neutral phases (CNM and WNM). We first discuss the mechanism that causes the coexistence of two different phases in the same pressure conditions, before giving a finer classification for the different types of CNM regions.

The cold atomic gas of the ISM has been shown to be thermally unstable. For a given gas density, the temperature corresponding to thermal balance between the heating terms (the photoelectric effect largely dominates the heating in the neutral medium) and the cooling terms (radiative cooling mostly caused by C^+ and O) can be computed, and the corresponding pressure derived. The result is an equilibrium curve as shown on Fig. 3 (taken from a recent version of this analysis: Wolfire et al. 2003). The parts where pressure increases with density are stable (the gas "resists" when it is compressed by external forces), while the region where pressure decreases when density increases is unstable and tends to collapse to the high density stable branch. As the average density of the neutral medium (slightly higher than $1\,\mathrm{cm}^{-3}$ at the radius where the Sun is located) falls into the unstable regime, we expect

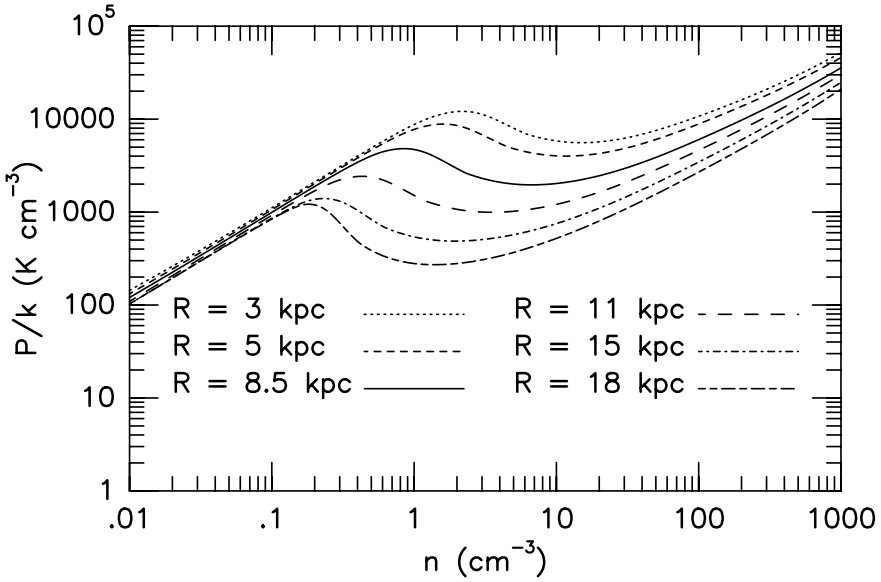

Figure 3: Equilibrium curves for the atomic neutral medium at different radial positions in the galaxy, showing the thermal instability of the neutral ISM. Graph from Wolfire et al. [2003].

a dense cold phase and a more diffuse warmer phase to coexist in pressure equilibrium.

However, several aspects of this picture are problematic, as discussed in the review by Cox [2005]. Relying on pressure equilibrium is somewhat simplistic in the highly turbulent ISM, especially as thermal pressure is often not the dominant contribution to the total pressure (with magnetic pressure, cosmic ray pressure and dynamical pressure being the main contributors). In addition, the observed uniformity of pressure is not a strong evidence that the phases of the ISM are indeed formed by segregation under pressure equilibrium. Indeed, even if there is no pressure equilibrium and no phase segregation because of other factors or of the gas being kept in the unstable regime by dynamical events, the shape of the curve (a range of almost 3 orders of magnitude in density corresponds to no more than a factor of 3 variation in pressure) ensures that a roughly uniform pressure will be observed. Moreover, the timescale of transition between the phases are often found to be longer that the timescale of external dynamical perturbations. As a result, the effect of this bistability is significantly complicated in the turbulent magnetized ISM. Vázquez-Semadeni et al. [2003] devote a full review article to the more complete picture of thermal instability in a turbulent ISM with a strong magnetic field.

It is mainly in the CNM that a significant chemistry can occur. In this thesis, we will thus restrict ourselves to the CNM phase of the ISM. Two ways of further classifying the state of the gas in the CNM exist, depending on wether we adopt an observational point of view, or a physical modeling point of view.

From a modeling point of view, the main distinction is based on which energy source dominates the chemistry. There are two most common sources.

In a gas that is not completely shielded from the UV radiation field, chemistry is dominated by photodissociation reactions and by the high ionization fraction that comes from the photoionization of carbon (as electrons efficiently destroy molecular ions through dissociative recombination). These regions go from diffuse clouds where the gas is not dense enough to significantly extinct the UV field over the size of the cloud, to the external layers of denser cloud where the UV field has not yet been completely absorbed. They are called *photodissociation regions* or *photon-dominated regions*, which both give the acronym *PDR*, as the dominant energy input for the chemistry is the radiation field. Note that this general definition is not restricted to dense regions close to bright stars, forming bright emission nebulae, but also describes a large fraction of the diffuse CNM.

In denser and more central regions of clouds, where the UV field has been completely absorbed, the dominant energy source becomes cosmic rays, which ionize the gas. Most importantly, they ionize H_2 molecules into H_2^+, which then reacts with H_2 to form $H_3{}^+$ and starts a chain of ion-neutral reactions (ion-neutral reactions tend to have much higher rates than neutral-neutral) leading to the great variety of molecules found in dense clouds. These regions are usually simply designated as dense clouds or dense core, but could also be named cosmic-rays dominated regions.

Finally, the dynamics of the gas can also be important and the dissipation of its kinetic energy can become the dominant influence on the chemistry. It is the case in shocks, and possibly in the localized and intermittent regions where the turbulence is dissipated (this process is discussed in Chapter 3).

On the other hand, a more observational classification (proposed by Snow and McCall 2006) is based on the state of hydrogen and carbon in the gas. In the CNM, H is not ionized, but it can be either mostly in atomic or molecular form (H_2). Carbon can be either ionized, atomic or in molecular form (as carbon monoxide CO). This classification mostly follows the progressive extinction of the UV radiation field, and is thus more adapted to PDR regions or cosmic-ray dominated regions. The four categories are :

- The *diffuse atomic gas*: defined as the regions where the molecular fraction of hydrogen is less than 10%. This corresponds to regions where the UV radiation field is strong enough to quickly dissociate molecular hydrogen. Carbon is ionized and the electron abundance is thus relatively high. As most molecules are quickly destroyed, these regions are usually poor in molecules. Clouds entirely made of diffuse atomic gas usually have densities in the range $10 - 100\,\mathrm{cm}^{-3}$ and temperatures in the range $30 - 100\,\mathrm{K}$, but this type of gas can also be found in the most external layers of denser clouds, having then higher densities. When

dense clouds are found close to bright star, the external layer of atomic gas can have much higher temperatures (a few 1000 K).

- The *diffuse molecular gas*: defined as the regions where the molecular fraction of hydrogen is more than 10%, but the fraction of ionized carbon is still more than 50%. The UV field is sufficiently damped for the hydrogen to be molecular, and the formation of a few other molecules becomes possible (small amounts of CH^+, HCO^+, CO...). But the UV radiations remain sufficient to keep the carbon mostly in its ionized form C^+. For this to occur, diffuse molecular gas must be surrounded by enough diffuse atomic gas for the radiation field to be sufficiently absorbed. As for diffuse atomic medium, this gas can be found either in low density clouds made only of diffuse molecular and atomic gas, or as the external layer of denser clouds. In the first case, it usually has densities of $100 - 500\,\mathrm{cm}^{-3}$ and temperatures of $30 - 100\,\mathrm{K}$.

- The *translucent gas*: defined as the regions where the fraction of C^+ is less than 50%, but the fraction of carbon in the form of CO is still less than 90%. As the radiation field is not strong enough anymore to keep the carbon ionized, the electron fraction is decreased, changing the chemistry. But some UV photons are still present to dissociate CO. This phase is more uncertain because no observation has found this type of gas, and because its importance strongly varies in different models of the ISM, with sometimes a region where atomic carbon dominates and sometimes a direct transition from C^+ to CO.

- The *dense molecular gas*: defined as the regions where the fraction of carbon in the form of CO is more than 90%.This corresponds to regions where the UV radiation field has been completely absorbed and does not play any role. It is thus usually equivalent to cosmic-rays dominated regions. To exist, such regions must be surrounded by layers of the previous types that protect it from the interstellar UV field. This type of gas is always dense (densities of $10^4\,\mathrm{cm}^{-3}$ or more) and cold (a few 10 K). Those parts are the most rich in molecules, and a significant part of the chemistry occurs in the ice layer that covers dust grains in these regions.

We see that this classification mostly follows the progressive evolution of the gas in PDRs as the radiation field is progressively absorbed. This structure is illustrated on Fig. 4 by the results of a PDR model. Two processes contribute to this shielding from the UV field. First, dust grains efficiently absorb the UV radiation at all wavelengths (with an efficiency that increases when the wavelength decreases). Second, H_2 and CO photodissociation occurs indirectly, with photonz causing a transition of the molecule to an excited electronic state which can then dissociates. As a result, the photons

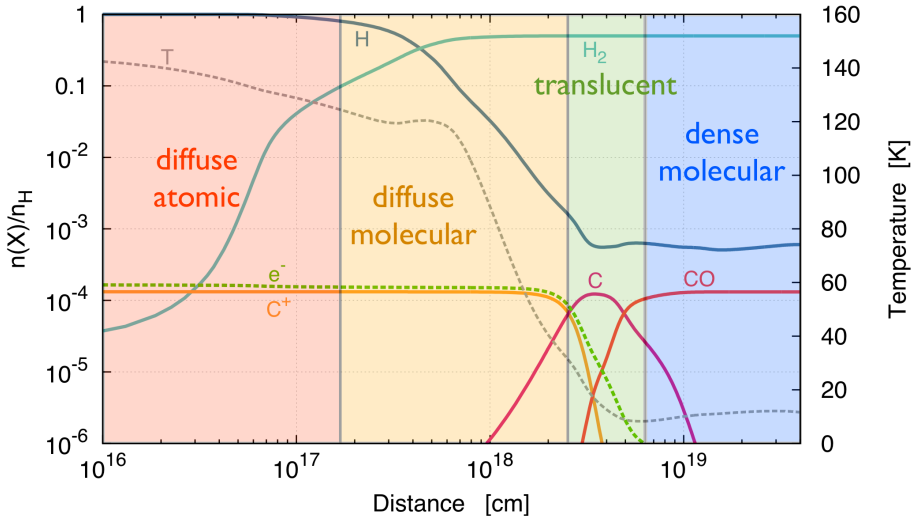

Figure 4: Illustration of the different phases in a PDR according to the classification of Snow and McCall [2006]. This results from a PDR model with the radiation field entering from the left.

that cause dissociation are at specific wavelengths. As each dissociation absorbs one photon, this process causes line absorption at the corresponding wavelength, which is thus damped faster than the continuum. This is called self-shielding as the molecule deeper in the cloud is protected by identical molecules which are dissociated at the edge of the cloud. It is usually the dominant shielding process for H_2 except in low density gas. Note that the chemical timescales at the outer edge of this structure (dominated by photodissociation, of the order of a few 100 yr), and inside the dense molecular part (dominated by cosmic ray ionizations, of the order of a few 100 Myr), are extremely different.

This classification thus describes the transition from PDRs to cosmic-rays dominated regions. Dynamics-dominated region can occur in any of these regions and do not always affect for instance the state of hydrogen, but have other chemical signatures.

1.2.3 *The ISM structure*

When combining the observed densities of these different components, one can estimate how the interstellar hydrogen is distributed in the galaxy. Such an estimate is made in Cox [2005] and shown on Fig. 5. As is well known, in spiral galaxies, matter is concentrated in a disk. We see it as a ~ 100 pc-thin disk where most of the CNM and molecular gas is found. However, we also see that the density falls off quite slowly above the disk, mostly because of the diffuse component. The galactic disk is thus actually quite thick.

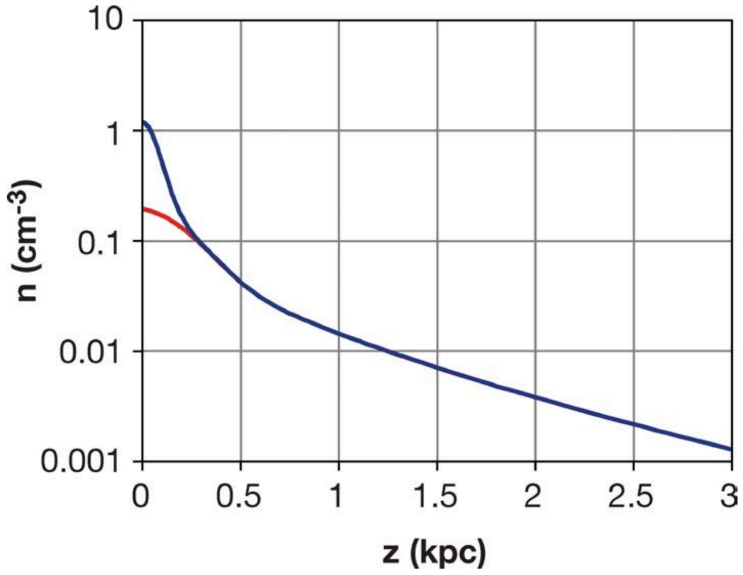

Figure 5: Average interstellar hydrogen density in the galaxy as a function of height above the galactic plane. The total density is shown in blue, while the contribution of the warm diffuse components (WNM+WIM) is shown in red. The HIM is not included. Figure taken from Cox [2005].

Knowing this vertical distribution of density, one can compute both the weight felt by the interstellar matter at each height, and the thermal pressure (using temperature estimates from Table 2). For the vertical density distribution to be stable, the vertical pressure gradient must compensate the weight distribution. This allows to estimate the total pressure (including magnetic, cosmic-ray, dynamical and radiative pressures). Such a computation yields a total pressure ten times larger than the thermal pressure in the mid-plane (and the factor is larger going away from the disk). Thermal pressure is thus not a dominant force in the ISM, at least in a large scale picture. Assuming equipartition between magnetic, cosmic-ray and dynamical pressure to account for the missing pressure seems to be in good agreement with observations (e.g., it gives a magnetic field strength in the mid-plane of $\sim 5\,\mu$G, compatible with observations). See Cox [2005] for a discussion of the remaining problematic points.

Moreover, rough estimates of the volume filling factors of the different phases in the mid-plane show that the first four phases (molecular + CNM + WNM + WIM) only account for roughly half of the volume. The remaining part must be filled with a very low density component (the HIM). Superbubbles created around OB association by the winds and supernovae could account for 20% of the volume (Ferrière 1998). But many observations seem to point to many smaller and colder bubbles connected by tunnels, such as the Local Bubble or the MonoGem Ring. Such regions have densities of the order of a few $10^{-3}\,\mathrm{cm}^{-3}$. Some regions seem to have seen supernova explosions

in an already extremely tenuous but cold medium (see the discussion in Cox 2005).

The complete picture of the structure of the ISM in the galaxy is thus complex, and far from being fully understood. Cox [2005] advocates a view where the magnetic field plays a dominant role in structuring the ISM, sustaining its mass distribution and containing the cosmic rays, and where it is only overcome by the strongest dynamical events (supernova, winds from OB associations,...).

1.3 MOLECULES IN THE ISM

1.3.1 *Molecular richness*

A great molecular richness has been observed in the ISM, with more than a hundred species detected, ranging from simple diatomics such as H_2 to large molecules such as fullerenes (C_{60}) or polycyclic aromatic hydrocarbons (PAHs). Mainly two separate range of sizes are detected in the ISM : "small" molecules (up to $12-13$ atoms) and very large molecules (several tens of atoms).

In the first group, we find a large number of diatomics, from the first detected molecules (CN, CH, CH^+, see for instance McKellar 1940, Douglas and Herzberg 1941, Adams 1941), to the central molecules H_2 and CO (who, when present, are the dominant reservoirs of H and C respectively). Those five molecules are the most abundant molecules in the ISM, and the other molecules have much lower abundance levels. Other diatomics such as C_2, OH, NH or N_2 are observed. Detected triatomics include H_3^+, C_3, HCO^+, HCN, and larger molecules such as H_2CO or C_3H_2 are also observed. See Snow and McCall [2006] for a review of the diffuse CNM and of the observed molecules.

In addition to those relatively small molecules, a large body of evidences points to the existence of one or several families of very large molecules in the ISM. Polycyclic aromatic hydrocarbons (PAHs) are the widely accepted hypothesis to explain the infrared emission features in the $3-13\,\mu$m range. Large carbon-based molecules such as C_{60} have been identified, and the diffuse interstellar bands (DIB, a set of unidentified visible absorption bands) are thought to be caused by large organic molecules (which might also be PAHs).

Molecules are mostly observed in the CNM. They are usually quickly destroyed by the UV field if it is not yet completely absorbed. Thus in all regions of the CNM (from the classification of Snow and McCall 2006) except dense molecular gas, the observed presence of molecules indicates that their formation mechanism must be efficient enough to balance their fast destruction. While the formation of the first group of molecules can be expected

even in diffuse clouds, the second group (PAHs and other large molecules) are likely not formed by chemistry in situ. They could either be preexisting (for instance formed in the atmosphere of red giants and injected into the ISM), or result from the processing and destruction of dust grains (e.g. by the UV radiation field).

The other molecules result from interstellar chemistry. Part of it occurs in the gas phase, and is often based on fast ion-neutral reactions or radical-neutral reactions, and slower radiative association reactions for formation, and photodissociation and dissociative recombination with electrons for destruction. In diffuse gas, all molecules except H_2 are formed in the gas phase. The gas phase formation of H_2 is extremely inefficient and H_2 forms on the surface of dust grains. H atoms are adsorbed on the surface of dust grains, they wander on the surface by thermal hopping or tunneling and react with each other. In denser clouds, chemistry on the surface of dust grains becomes more important, and could be the origin of several large molecules. Surface chemistry on dust grains is discussed in Chapter 2.

1.3.2 *Observational diagnostics*

These molecules provide very important informations on the physical conditions of the ISM, which can complement the information given by dust and atomic ions in atomic gas. Indeed, molecules possess, in addition to their electronic levels, a spectrum of rotational and vibrational levels whose energies lie much lower. These levels are more easily excited at the low temperatures of the CNM, allowing us to see the gas in emission. Transitions involving rotational levels usually lie in the radio/microwave domain, those involving vibrational states in the infrared, and those between electronic levels in the visible/UV part of the spectrum, with some exceptions. As long wavelengths are less absorbed by interstellar dust, molecules also give us access to denser gas, both in absorption as the background source can penetrate deeper through the cloud in the IR and radio than in the visible and UV, and in emission as rotational levels lie low enough to be excited in the cold of dark clouds.

As molecules are excited by both collisions in the gas and photons from the radiation field, they can give us informations on both, depending on the properties of the molecules and the respective strengths of the two excitation mechanisms. If only collisional transitions were to be taken into account, the excitation of the molecule would be at thermal equilibrium with the gas and follow a Boltzmann distribution at the gas temperature. Consequently, the temperature derived from the Boltzmann fit of the observed excitation is called the excitation temperature. If the molecule does not actually follow such a distribution, this temperature can be ill defined and people sometimes give several excitation temperatures corresponding to different group of level.

Those temperatures are usually "best fit" results, and do not describe completely the excitation. On the other hand, the excitation temperature between two levels is always uniquely defined and characterizes the ratio of the populations in the two levels.

The question of knowing whether those excitation temperatures have any relationship with a physical temperature depends on the specific case. Even in the absence of any external radiation field, molecules can still de-excite radiatively, and as a result their excitation distribution can diverge from the Boltzmann law if this process is sufficiently efficient. As higher energy levels tend to have faster radiative de-excitation, only the first few levels, if any, can follow a Boltzmann distribution at the gas kinetic temperature. As the dominant mechanism depends on the collision rate, which depends on the gas density, one usually define for each level a critical density at which the two de-excitation processes contribute equally and above which the Boltzmann distribution is valid, at least up to the level under consideration. When the gas is above the critical density, the excitation temperature is thus the gas kinetic temperature. Note that as long as radiative excitation is still absent or negligible, the gas temperature can in principle always be derived from the excitation of the molecule independently of the critical density, although not by a simple excitation temperature computation. The statistical equilibrium distribution might differ from the Boltzmann law and have to be computed from the properties of the levels, but is still completely determined by the gas temperature.

When the radiation field becomes strong enough to be the dominant excitation mechanism—and it always does above some level as collisions energies are restricted to a low range of values and cannot excite high energy levels—, the picture is changed. If the radiative processes completely dominate and if the radiation field can be approximated by a black body law—at least in the range of wavelengths where the transitions occur—, the distribution of the excitation follows again a Boltzmann law this time at the temperature of the radiation field. But cascade mechanisms (photons excite high-lying levels, and radiative de-excitation from these levels becomes the dominant population mechanism for some lower levels), chemical excitation (in exothermic reactions, the molecules are usually formed in excited states), and line of sight effects (the gas experiences different physical conditions at different positions of the line of sight, and all contributions are mixed in the observation) can significantly complicate the picture.

As a result, different molecules give different kind of informations. For instance, the high dipole moment of CN makes it completely dominated by the radiation field, which, at the wavelength of the rotational transitions, is essentially the cosmic microwave background (CMB). As a result, the excitation temperature of CN is that of the CMB, and it gave a first measure of this temperature before the existence of the CMB was even known (McKellar [1941], Thaddeus and Clauser [1966]). At the opposite, homonuclear molecules such

as H_2 or C_2 can only have quadrupolar radiative (ro-vibrational) transitions. Consequently, their rotational levels are very weakly coupled to the radiation field, and the lowest few levels follow very closely the gas temperature (if they have time to reach equilibrium, as $J = 1 - J = 0$ conversion is very slow for H_2). The downside is that the emission rates are very low, making the emission of those molecules harder to detect (but they remain more easily observable in absorption). A molecule with a small dipole moment such as CO has an intermediate behavior. Both collisions and the radiation field contributes to the lower rotational levels, so that informations on the gas conditions can still be retrieved. In addition, its more efficient radiative transitions and its high abundance make its emission much easier to observe.

But molecules do not only give informations through their excitation, their mere presence and abundance is informative. As explained above, their abundance results from the equilibrium between formation and destruction. In PDRs, destruction processes are usually controlled by the radiation field, while formation occurs most often by gas phase reactions. Their abundance thus contains information relative to the radiation field, to the gas density and to the gas temperature for reactions with an activation barrier. This analysis requires detailed modeling of the chemical network, thermal balance and radiative transfer. For instance, the Meudon PDR Code is a numerical code tailored for such an analysis of the chemical abundances in PDRs, and is presented in details in Chap. B.

Among the processes of the ISM, the first part of this thesis focuses on the formation of H_2 on the surface of dust grains. We thus devote the next Chapter to a more detailed discussion of interstellar dust grains and surface chemistry. As the second part of the thesis tries to tackle the problem of interstellar chemistry in a turbulent ISM (and especially the modeling of a dissipation-driven chemistry), Chapter 3 presents interstellar turbulence.

2

DUST AND SURFACE CHEMISTRY

The presence of small solid particles in the ISM was discovered almost simultaneously to the existence of the ISM itself as an all-pervasive material medium (and not only localized concentrations of matter around stars). While interstellar matter was long known in localized concentrations such as reflexion nebulae, one of the first evidences of its presence everywhere between stars came from the observation of an extinction of starlight proportional to the star's distance, suggesting a roughly homogeneous (at least in a statistical sense) intervening material medium. In a series of articles, Trumpler [1930a,b,c] demonstrated the presence of such an extinction (by comparing the apparent diameter of globular clusters to their luminosity), but also established the existence of a reddening effect through selective absorption (stronger absorption for shorter wavelength, by comparing the actual color index of stars to what should be expected from their spectral type), and finally measured this wavelength-dependence of the extinction, giving the first measurement of the interstellar extinction curve (in the visible) by the pair method (comparing two stars of similar spectral types but different distances). He concluded that small solid particles must be the cause, and suggested that micron-sized particles might be compatible with the observations.

Since then, many more observational evidences have been gathered, while a variety of possible dust materials have been studied in the laboratory. As a result, possible models of the dust population in the ISM have been proposed, reproducing with some success most of the observables while relying in large part on experimental data for the optical properties of the different materials. However, problems remain: some discrepancies with the observations are still present, the optical properties often have to be tweaked and sometimes empirically taken from astronomical observations, and the observational constraints are such that several different models can perform equally well. In this chapter, we first review the observational constraints and the current dust models. We then describe the role of dust grains in the physico-chemistry of the ISM, before giving a short discussion of the formation and evolution of dust in the ISM.

2.1 OBSERVATIONAL EVIDENCES

Most of the observational constraints at our disposal come from the interaction of dust with starlight, either directly by absorbing, scattering or polariz-

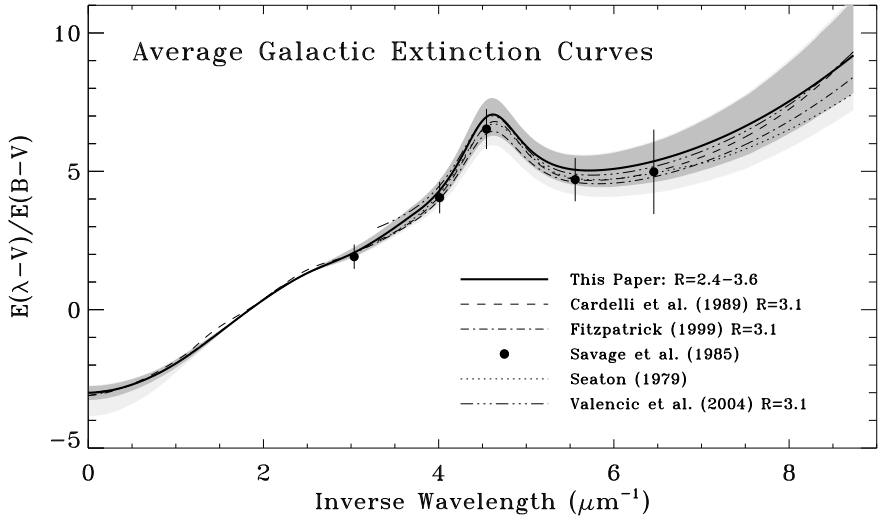

Figure 6: Average Galactic extinction curve for the diffuse ISM (lines of sight with $R_V = 2.4 - 3.6$ only) determined by Fitzpatrick and Massa [2007] with the variance shown as the dark grey shaded area. Figure taken from Fitzpatrick and Massa [2007].

ing it, or indirectly by absorbing starlight photons before radiating the energy away thermally or as a photoluminescence process.

When trying to infer the composition of dust, we must make sure that it is compatible with what we know of the relative abundances of the elements, and with the fraction of those abundances that are already accounted for by the gas phase. This gives us a second family of constraints.

2.1.1 *Extinction of light*

Dust grains absorb light or scatter it away from its initial travel direction. Both result in a progressive attenuation of the light traveling along a given direction, and the combined effect is called extinction. For large solid bodies (large compared to the wavelength under consideration), this extinction is independent of the wavelength and results directly from the geometrical cross-section of the body. For small particles (much smaller than the wavelength), we are in the Rayleigh regime with an extinction $\propto 1/\lambda$ (dominated by absorption). For sizes comparable with the wavelength, the precise shape depends on the material but an overall decrease with wavelength remains.

In addition to the continuum extinction, localized (in wavelength) absorption bands (or features) can also be caused by electronic transitions (for instance the 2175 Å absorption bump thought to be caused by $\pi \rightarrow \pi^*$ electronic transitions in hexagonal carbon rings), or vibrational excitation of specific bonds (e.g., the 9.7 μm feature probably due to the $Si - O$ stretching mode in silicates). Those features and their precise shape yield important informations on the material dust grains are made of.

The extinction $A(\lambda)$ at some wavelength λ is defined as the difference in the apparent magnitude of a star caused by the intervening medium. The difference between the apparent magnitude m and the absolute magnitude M (the brightness of the object if placed at 10 parsecs from the observer) is thus the combination of the geometrical dilution due to distance and the extinction:

$$m - M = 5\log_{10}(d) - 5 + A \tag{1}$$

with d in parsecs.

The extinction is often given for a photometric band such as the V band (centered at 551 nm with bandwidth of 88 nm), and is then written as A_V. One usually measures the reddening effect using the selective absorption $E(B-V) = A_B - A_V$. One can similarly define $E(\lambda - V) = A(\lambda) - A(V)$. As the pair method (comparing two stars of same spectral types) only yields a non-normalized measure of the extinction curve, the extinction curve is usually given in a normalized way either as $\frac{E(\lambda - V)}{E(B-V)}$ or as $\frac{A(\lambda)}{A_V}$ (the normalization is often taken at some other reference wavelength instead of the V band).

The extinction curves derived from the observations have been studied in great details in a series of papers by Fitzpatrick and Massa [1986, 1988, 1990, 2005, 2007, 2009], from the infrared to the far ultraviolet. First using the pair method in the first three papers (Fitzpatrick and Massa 1986, 1988, 1990), the authors proposed a fitting formula able to reproduce all observed extinction curves. They revisited and extended this study more recently (Fitzpatrick and Massa 2005, 2007, 2009), this time by fitting simultaneously the extinction curve and a stellar model, thus avoiding the pair method and greatly increasing the accuracy of the derived extinction curves. In addition to providing the functional form fitting all observed extinction curves, cataloguing the resulting fit parameters for several hundred of lines of sight, and determining the average galactic extinction curve, they also explore in details the variability and statistics of the extinction curves and study the correlations (or absence thereof) between different properties of the extinction curves. These correlations or decorrelations provide useful constraints on the dust composition (parts of the extinction curve that are not correlated are probably not caused by the same dust component), which are overlooked in most dust models that only try to reproduce the average extinction curve.

The average extinction curve is shown in Fig. 6, while the full sample of Fitzpatrick and Massa [2007] is shown in Fig. 7, displaying the large variability in observed extinction curves.

The reddening effect is often measured using the ratio of total to selective absorption $R_V = \frac{A_V}{E(B-V)}$. Most parameters of the fits appear to be strongly correlated with R_V, so that the extinction curves are sometimes parametrized by R_V only (Cardelli et al. 1989), which, in the absence of a complete measurement, gives a good approximation of the visible-UV part.

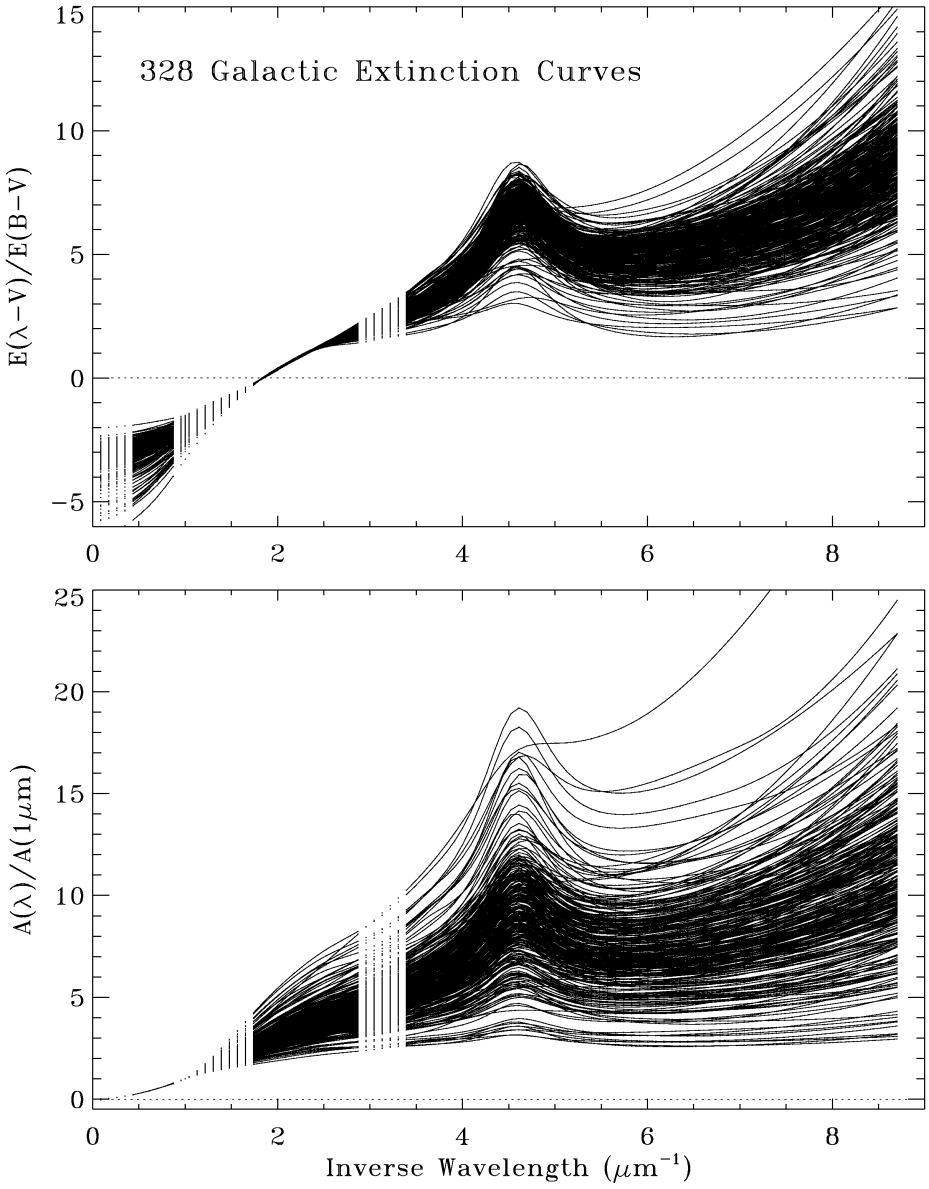

Figure 7: Sample of extinction curves measured by Fitzpatrick and Massa [2007]. Figure taken from Fitzpatrick and Massa [2007].

In addition to the 2175 Å UV bump clearly visible on Fig. 6 and 7, the most prominent extinction features are the 9.7 μm and 18 μm silicate features, and the 3.4 μm feature attributed to the C − H stretching mode in aliphatic hydrocarbons. Numerous other absorption band in the visible remain a mystery (despite numerous hypothesis, see Krelowski 2002, Snow and Destree 2011) and are called the "diffuse interstellar bands" (DIB).

2.1.2 *Scattering*

In addition to its contribution to extinction, the scattering of light can be directly measured in some situations, such as reflection nebulae (concentrations of interstellar matter in the neighborhood of some stars, that reflect their light), dark clouds, or the diffuse galactic light.

The scattering efficiency is usually parametrized as an overall albedo a giving the fraction of the light reaching the surface that is scattered, and a phase function $\Phi(\alpha)$ giving the efficiency as a function of the scattering angle α. This phase function is usually fitted by the single-parameter Henyey-Greenstein function (Henyey and Greenstein 1941):

$$\Phi_{HG}(\alpha) = \frac{1 - g^2}{4\pi(1 + g^2 - 2g\cos(\alpha))} \tag{2}$$

where $g = \langle \cos\alpha \rangle$ is a measure of the asymmetry between backward and forward scattering. The scattering properties are thus usually given as the two functions $a(\lambda)$ and $g(\lambda)$. The Henyey-Greenstein function is mostly used for practical reasons and is not a really good fit for realistic grains.

Gordon [2004] gives a review of the most recent observations of scattering from the infrared to the ultraviolet. Draine [2003a] also reviews the physics of scattering along with the observations, and propose an improved fit to the phase function. The compilation of observational data given by Gordon [2004] is shown on Fig. 8.

Dust also scatters light in the X-ray domain with small scattering angles, creating halos around X-ray sources. This phenomenon is discussed in Draine [2003b], where predictions are made from dust models and compared to the observations. The use of small angle X-ray scattering as a constraint for dust models is also reviewed in Dwek et al. [2004].

2.1.3 *Polarization*

Starlight that has been extinguished by the ISM (as evidenced by its reddening) also appears to be linearly polarized at a few percents (Hall 1949). This is usually interpreted as selective extinction by asymmetrical grains (i.e., elongated) that are all aligned in the same direction. While the alignment of dust grains seems to be an established observational fact, the mechanisms causing

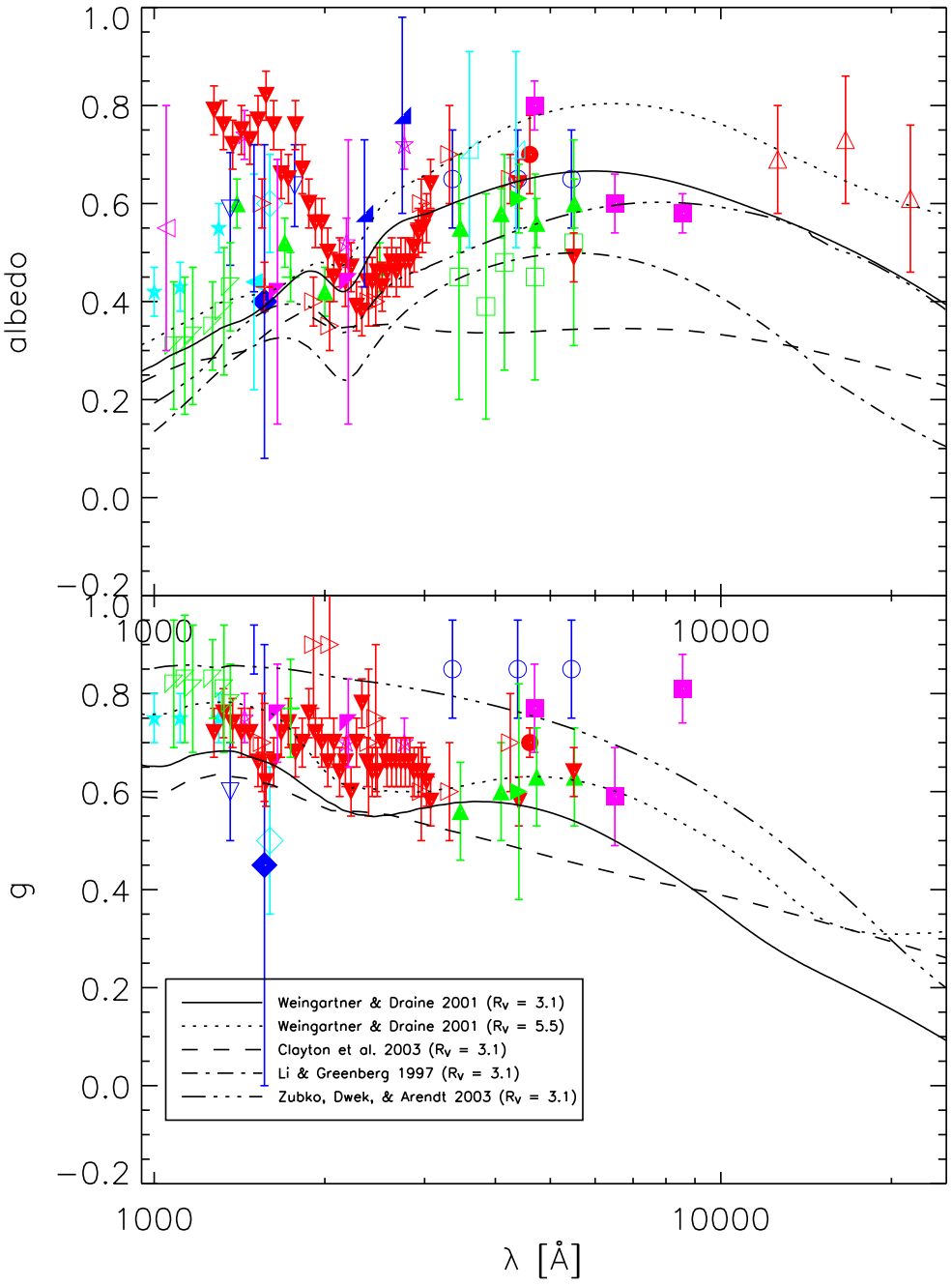

Figure 8: Observations of the scattering of light by dust. Data selected and compiled by Gordon [2004]. Figure taken from Gordon [2004].

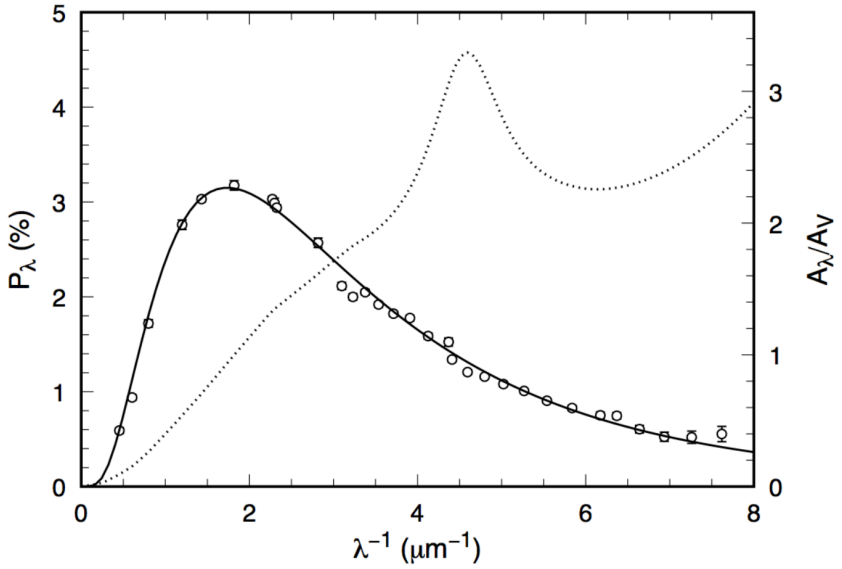

Figure 9: Polarization curve (solid line) compared to the extinction curve (dashed line) for the star HD 99872. Figure taken from Whittet 2004 (data points from Martin et al. 1999).

it remain under discussion. The alignment is usually observed to trace the magnetic field, so that the grains are aligned with respect to the magnetic field (but the alignment can be parallel or perpendicular depending on the alignment mechanism and the conditions).

Lazarian [2003] and Roberge [2004] give reviews of the modern theory of grain alignment. Alignment with the magnetic field occurs as a two-stage process: alignment of the rotation axis with the principal axis of the body (fast thanks to internal dissipation mainly by nuclear spin alignment causing magnetic dissipation), and alignment of the rotation axis with the magnetic field. Several processes have been proposed, with rotation being caused by inhomogeneously distributed H_2 formation on the surface or by radiative torques (which, even in an isotropic radiation field, can spin up irregularly shaped grains). Radiative torques seem to be the most consistent with observations.

The observations of starlight polarization by dust are reviewed in Whittet [2004]. The comparison with the extinction curve shows that some absorption features are polarized, while other are not, suggesting that only some components of the dust population are aligned. For instance, the 2175 Å absorption bump is not polarized (see Fig. 9) and the grains carrying the aromatic carbon component are thus most likely not subject to alignment, while the silicate features (10 and 19 μm) seem to be polarized. The 3.4 μm aliphatic carbon feature also seems to be non-polarized. This rules out models in which silicates and carbon are mixed in the same grains. The diffuse interstellar bands are also non-polarized. Moreover, the fact that the UV extinction rise is not po-

larized indicates that only big grains polarize starlight, either because small grains have more symmetrical shapes or because they are less affected by the alignment mechanisms.

2.1.4 *Dust emission*

Grains are heated by the light they absorb. They also radiate energy away by emitting photons, and this emission carries precious information about the dust population. Big grains ($\sim 100\,\mathrm{nm}$) emit thermally in the far-infrared with a modified black-body law, and their temperature can be directly deduced from this emission. For very small grains ($\lesssim 10\,\mathrm{nm}$), the picture is more complex. As small grains have small heat capacities, they are sensitive to the energy of the individual UV photons, which cause spikes in the grain temperature. Small grains thus have constantly fluctuating temperatures, and their emission is dominated by the transient high-temperature phases, resulting in near-infrared emission. This effect is discussed and modeled in details in Chap. 5 and 6. This emission in the near- and mid-infrared is mainly constituted of emission bands. The smallest grains are thought to be large molecules of the PAH family (see Tielens 2008 for a review), and the emission bands correspond to $\mathrm{C}-\mathrm{C}$ stretching ($6.2\,\mu\mathrm{m}$ and $7.7\,\mu\mathrm{m}$), $\mathrm{C}-\mathrm{H}$ stretching ($3.3\,\mu\mathrm{m}$) and bending (8.6 and $11.3\,\mu\mathrm{m}$) modes in these molecules. A typical dust emission spectrum for the diffuse intergalactic medium is shown on Fig. 10.

The mechanism of stochastic heating of very small grains and PAHs that gives rise to the near- and mid-infrared spectrum is discussed and modeled in detail in Draine and Li [2001]. Li [2004] also gives a discussion of the transient excitation and re-emission of large molecules such as PAHs following the absorption of an UV photon.

Dust is also observed to emit in the microwave domain (see Lazarian and Finkbeiner [2003] for a review), in excess to the predictions from thermal (vibrational) emission. This could be due to rotational emission from very small asymmetrical grains, or to magnetic dipole emission from magnetic grains. Recent works favor the hypothesis of rotating very small grains (e.g. Ysard et al. 2010).

2.1.5 *Elemental depletions and abundance constraints*

Dust models trying to fit the observational constraints discussed above will make hypotheses about the composition of dust grains. As a result, they require some amounts of the heavy elements (C, Si, Mg, Fe, etc.) to be locked up in the dust grains. For a model to be realistic, these amounts must be available in the ISM.

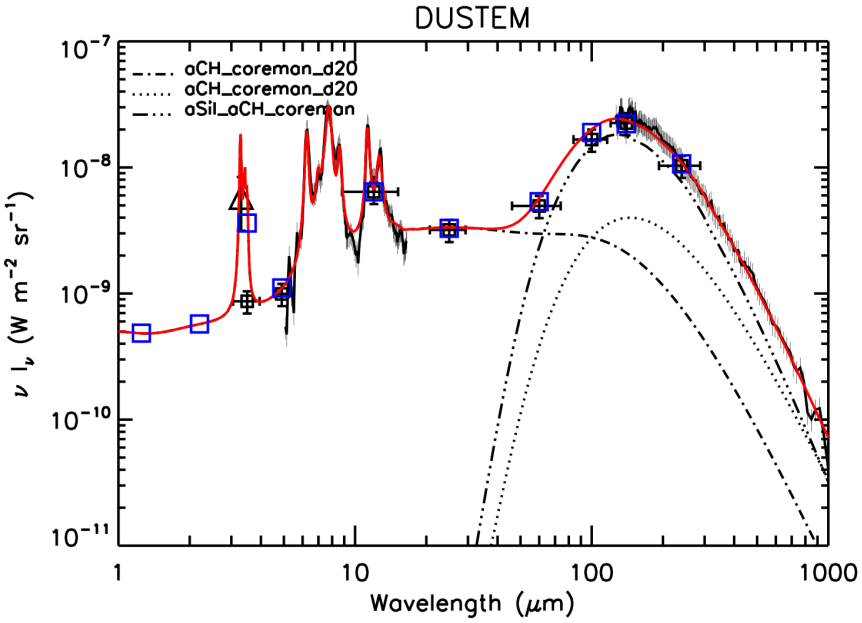

Figure 10: Dust emission spectrum, with observational data compared to a dust model. The observations includes: the $5 - 15\,\mu$m ISOCAM/CVF ISO spectrum (black line with error bars), the $100 - 1000\,\mu$m FIRAS/COBE spectrum (black line with error bars), the $3.3\,\mu$m AROME narrow band measurement (black triangle), and DIRBE/COBE photometry (black squares). Figure taken from Jones et al. [2013].

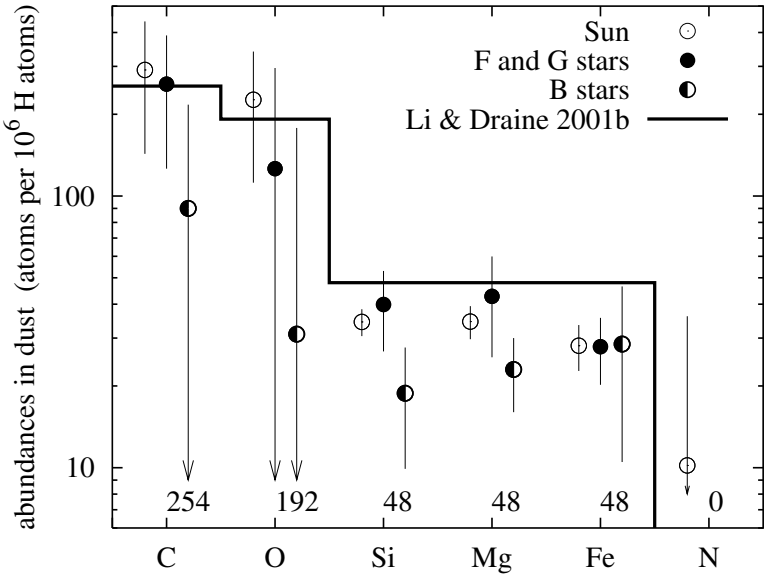

Figure 11: Estimated abundances of heavy elements in dust, with comparison to the Li and Draine 2001 dust model. Figure from Zubko et al. [2004] using data from Holweger [2001] for solar abundances and from Sofia and Meyer [2001] for stellar abundances.

The elemental abundances in the ISM are not directly measurable, and we have to extrapolate from solar and stellar abundances. Once some hypothesis is made about the ISM abundances, the gas phase abundances can be measured, and the difference constitutes the available material for dust.

The interstellar abundances are usually inferred from either the solar (Holweger 2001) or stellar abundances for either B stars or F and G stars (Sofia and Meyer 2001). Observations suggest that the interstellar abundances cannot be substantially lower than the solar or F and G stellar abundances. As discussed by Draine [2004a], possible processes of segregation between gas and dust during star formation probably induce differences between ISM and stellar abundances, possibly resulting in lower abundances of grain constituents in stars.

The gas phase abundances are reviewed by Jenkins [2009] over a large number of lines of sight. The observed depletion of oxygen in the gas phase seems to be problematic, as the missing quantity is much more than what is accounted for by current dust models (see Whittet [2010]). This could suggest that an additional oxygen-rich dust component is present.

The constraints given by the elemental abundances are shown on Fig. 11.

2.2 DUST MODELS

As the observations described in the previous section result from the combined effects of all grain types and sizes, with the dust possibly experiencing a variety of environments along the line of sight, neither the composition and size distribution of dust grains nor the number of distinct dust components can be directly deduced from the data. Nevertheless, the wealth of observational evidence gives tight constraints on hypothetical dust models that can be proposed.

A dust model consists in specifying the different dust components (types of grains), their composition, their size-dependent optical and thermal properties (absorption coefficient, albedo, scattering g parameter, heat capacity, *etc.*), and a size distribution for each component.

Several aspects of the observations hint at possible compositions and dust components, so that models are not built on pure speculations. Absorption features are often signatures of specific families of materials. For instance, the 9.7 and 18 μm features are characteristic of silicates. Moreover, the lack of structure in those absorption features mostly rules out crystalline silicates. In a similar way, the near- and mid-infrared emission features are quite strongly similar to PAH spectra that are theoretically predicted or measured in the laboratory. In addition, theories of dust formation and processing can provide hypothetical compositions.

As a result, most dust models agree on broad categories of grains (see for instance the review by Draine 2003c):

- a silicate family, mostly amorphous, which might be of composition close to olivine $MgFeSiO_4$ (Sofia and Meyer 2001).

- a carbonaceous family, with an appreciable fraction of aromatic carbon (from the 2175 Å absorption bump), and some aliphatic carbon (to explain the 3.4 μm extinction feature). This might be graphite, hydrogenated amorphous carbon, PAHs and PAH clusters.

The precise composition and number of distinct components depend on the specific grain model, but those two categories most likely constitute two distinct components (as silicate features are polarized, while carbon features seem not to be).

Dust models then have to be compared to the observational constraints as discussed in Draine 2004a.

2.2.1 *The Mathis, Rumpl, and Nordsieck 1977 (MRN) model*

Mathis et al. [1977] gave one of the first attempt to solve the inversion problem of deducing the dust size distribution from the observations. They considered only the extinction curve and the abundance constraints, and tried to find the best fitting size distributions for various combination of components (without using a prescribed functional form for the size distributions). They find that the choice of the components is not settled by the comparison: in addition to the fact that only a limited number of hypotheses were tested, several combinations gave a similar quality of fit. All involved graphite (which was the only carbon component tested) supplemented by silicates (olivine and enstatite gave similar results). For reasons that have been discussed much later by Zubko et al. [2004] (and inherent to the mathematical inversion problem), the resulting size distributions are discontinuous (with an alternation of peak bins and zero bins). However, once those discontinuities are smoothed out , a clear power-law shape emerges for all components with exponent $\alpha \simeq -3.5$, extending between $a = 5\,\mathrm{nm}$ and 250 nm for the graphite component, and between 25 and 250 nm for the silicate component (olivine and enstatite give similar results). The authors note that the lower limit of the graphite distribution is not well constrained as for the range of wavelength used (0.11 to 1 μm), 5 nm grains are in the Rayleigh regime which is not sensitive to size. The biggest grains also approach the grey extinction regime, but abundance constraints limit the maximum size.

2.2.2 *The Draine model*

One of the currently most used models has been built and refined by Bruce Draine and collaborators in a series of papers (Weingartner and Draine 2001a, Draine and Li 2001, Li and Draine 2001, 2002, Draine and Li 2007). This

model follows the MRN model by taking a carbonaceous (graphite) component and a (amorphous) silicate component, but extends the carbon component to down to molecular sizes by using a continuous transition to PAH properties for small sizes (below 5 nm) in order to reproduce the near-infrared emission caused by the stochastic heating of very small grains (this mechanism is modeled in Draine and Li [2001]). Noting that the size distribution of the very small grains necessary for the emission has little effect on the extinction, they separately adjust the very small grain part and the bigger grains. The size distribution of the large graphite and silicate components are fitted to the extinction curves (using the parametrization of Fitzpatrick 1999 as a function of R_V) and to the abundance constraints simultaneously in Weingartner and Draine [2001a] by assuming a given functional form (modified power laws with additional curvature and exponential cut-off), while the size distribution of very small carbonaceous grains is composed of two manually adjusted lognormal distributions that fit the emission spectrum (Li and Draine 2001). This model is revisited in Draine and Li [2007], with updated PAH properties and the new emission data provided by *Spitzer.*

The resulting distribution is described in Chap. 5 (Sect. 5.3.3). This model fits most of the observational constraints very well, but requires too much heavy elements (especially twice the solar abundance of Fe)

2.2.3 *The Zubko et al. 2004 models*

Zubko et al. [2004] took an in depth look at the inversion problem consisting in deducing the size distribution directly from the observational constraints (given a set of predefined dust components with given properties). They show that this problem leads to a Fredholm integral equation of the first kind, an ill-posed problem. However, with the addition of a few assumptions on the smoothness of the size distribution, a regularization method can be used to find the solution.

The problem is solved under the simultaneous constraints of the extinction curve, the infrared emission spectrum, and the heavy element abundances (using the average observations of the diffuse ISM). As possible dust components, they consider: PAHs, graphite, amorphous carbon, silicates ($MgFeSiO_4$) and composite grains made of a mix of silicates, organic refractory material, water ice and voids. They apply their solution method to different combinations of these components, and show that good fits can be obtained for all of the proposed dust models:

- PAH - graphite - silicate, same components as the Draine model, for which a better fit is obtained, which verifies the abundance constraints
- PAH - amorphous carbon - silicates, amorphous carbon being a more realistic interstellar material as graphite is unlikely to form and survive in the ISM.

- PAH - graphite - silicate - composites
- PAH - amorphous carbon - silicates - composites
- PAH - silicates - composites for a low carbon model in the hypothesis of the ISM abundances being the B stars abundances

Their results seem to favor slightly the models with composite grains, which are also found to match the albedo and g constraints (which were not included in the resolution procedure). But Dwek et al. [2004] further compared the models to small-angle X-ray scattering data and found them to favor models without composites.

2.2.4 *The Compiègne et al. 2011 model*

Compiègne et al. [2011] proposed a model matching the extinction and emission properties of the diffuse ISM at high galactic latitudes. The model is quite similar to the Draine model, but graphite has been replaced by amorphous carbon. As said before, amorphous carbon is a more likely material in the ISM harsh conditions. Moreover, shocks observations show that carbon grains are almost completely destroyed (see for instance Slavin 2009, Welty et al. 2002), a fact that favors amorphous carbon as it is more easily destroyed in shocks (see Serra Díaz-Cano and Jones 2008).

As a result, a larger fraction of PAHs than in the Draine model (7.7% in mass versus 4.6%) is required to explain the 2175 Å absorption bump. The size distributions of the different components are described in Chap. 5 (Sect. 5.3.3).

2.2.5 *The Jones et al. 2013 model*

Jones et al. [2013] propose a model based on the carefully derived (Jones 2012a,b,c) size-dependent properties of hydrogenated amorphous carbon grains (HAC), including the effect of photo-processing converting H-rich aliphatic carbon into H-poor aromatic carbon up to a depth of 20 nm. As a result a single carbonaceous population can exhibit PAH-like feature due to very small mostly aromatic grains, and aliphatic features from the big grains. They add a silicate component coated with a 5 nm layer of aromatic carbon.

A standard model is adjusted to the observations, and the complete set of data makes it possible to study the evolution of the observable properties as photo-processing, accretion and coagulation occur. It is thus the first model to take into account an hypothetical formation and evolution scenario.

However, the HAC optical properties had to be adjusted to the observations, in particular to reduce the strength of the 2175 Å absorption bump.

2.3 PHYSICAL PROCESSES

The physical state of the grain varies depending on the external conditions. Usually followed in models are the grain temperature and charge state.

2.3.1 *Energy balance*

Dust grains interact simultaneously with the radiation field and with the gas through collisions. In most ISM environments, the energy exchanges with the radiation field dominates over the exchanges by collision with the gas, and the grain temperature results from the balance between emitted and absorbed radiation. For very small grains, the discrete nature of photons becomes apparent (each individual photon causes a significant spike in the temperature), and the balance becomes only statistical, with the temperature constantly fluctuating but the average radiated and absorbed powers compensating each other. The details of this process are discussed in great details in Chap. 5 and 6.

In high density environments ($n_{\mathrm{H}} \gtrsim 10^5\,\mathrm{cm}^{-3}$), collisions can become an important exchange of energy between the grain and the gas (Burke and Hollenbach 1983). Depending on the situation, the gas can transfer energy to the grains that then radiate it away, becoming the dominant cooling channel. The opposite is also possible, with the grains heating the gas, for instance deep inside dense clouds where only infrared radiation penetrates, heating the dust grains. In most cases, those transfers are more important for the gas energy balance than for the grains, which mostly cool radiatively. The strong coupling between gas and dust in high-density environments often leads to models assuming equal temperatures for gas and grains.

2.3.2 *Charge balance*

Several different processes contribute to the charge balance of grains. The two most important are the ejection of electrons by energetic photons, and accretion of electrons from the gas. The ejection process is called *photoelectric effect* if an electron from the valence band is ejected, and *photo-detachment* if an excess electron is ejected from a negatively charged grain. Similarly, the accretion process is called *attachment* for a neutral or negatively charged grain, and *recombination* for a positively charged grain. Positive ions can also recombine with electrons from the grain.

The physics of those processes and of grain charge balance is discussed in Weingartner and Draine [2001b], with further discussion of ion recombination in Weingartner and Draine [2001c], and an extension to higher energy photons (EUV and X-rays) in Weingartner et al. [2006].

The electrons ejected by energetic photons take away the energy difference between the photon energy and the ionization or detachment threshold as kinetic energy. The typical energy is of a few eV, and is progressively lost by collisions with gas particles, resulting in gas heating. This is the dominant heating mechanism in the diffuse CNM and at the edge of denser clouds (PDRs), and even in some HII regions. The smallest grains ($a < 100\,\text{Å}$) completely dominate the photoelectric heating (larger total surface and higher efficiency). Recombination of ions on dust grains also has a significant impact on the ionization fraction of the gas in the CNM.

The resulting charge state of the grain can affect its optical properties as is the case for PAHs, for which the ratio of the 6.2 μm and 11.2 μm emission features varies with the ionization degree, and can be used to measure it (Tielens 2008).

2.4 SURFACE CHEMISTRY

The interactions between dust and gas are not limited to energy and charge exchange. Atoms and molecules can adsorb on the surface, and reactions between adsorbed species can then occur. This allows some reactions that would be impossible or too slow in the gas phase. The most important of them is the formation of H_2. Those processes are very sensitive to the dust temperature, which controls the evaporation of the surface species, but also their diffusivity on the surface. As said previously, small grains represent most of the total dust surface on which reactions can occur, and are subject to fluctuations of their temperatures. Temperature fluctuations can thus have an important effect on surface chemistry and have to be included in the models in at least some situations. The development of a computation method to take this effect into account was one of the objectives of this thesis, and has been carried out for H_2 formation (see Part. 7).

2.4.1 H_2 *formation*

H_2 is destroyed by UV radiation, and gas phase formation is too slow to explain the observed abundances. It was thus soon proposed that H_2 forms on dust surface, where dust acts as a catalyst (Gould and Salpeter 1963, Hollenbach and Salpeter 1971). Hydrogen atoms adsorb on the grain surface, where they can migrate depending on the binding mechanism. When they meet each other, or meet atoms from the gas phase, they react and form a H_2 molecule, which is stabilized by the possibility to exchange energy with the grain. The detailed H_2 formation mechanisms are described in Chap.5, and the treatment of H_2 formation on dust grains undergoing temperature fluctuations in Chap. 7 and 8.

2.4.2 *Other reactions and ice formation*

H_2 formation is not the only reaction to occur on the surface of dust grains. Deeper inside clouds, where the external radiation field cannot reach and the dust is colder, a larger network of surface reactions involving mainly H, O, C and N becomes possible as the low dust temperatures allow these atoms and the molecules to which they belong (e.g., CO) to adsorb on the surface without being immediately evaporated. This leads to the progressive covering of the grain surface by an ice mantle containing mainly H_2O, CO and CO_2 (see Gibb et al. 2004 for an overview of ices in the ISM, and Garrod and Pauly 2011 for recent models of ice formation).

During this phase, more complex molecules start to form on the surface by successive hydrogenation (e.g., leading from CO to methanol CH_3OH). Complex molecules are indeed observed in dense objects at the initial stages of star formation, such as hot cores (see Herbst and van Dishoeck 2009 for a review of complex organic molecules in the ISM). As gas phase pathways to these molecules are lacking (blocked by reaction barriers), it is thought that complex molecules are formed on dust surfaces and in the ice mantle during the cold stages of the contraction, and released to the gas during the later warm-up. Various models have tried to retrace this process with relative success (e.g., Garrod et al. 2008, Vasyunin and Herbst 2013). The chemical evolution may lead to complex organic molecules that play a central role in terrestrial life, as exemplified by the model of Garrod [2013] predicting the formation of glycine, the simplest amino-acid.

2.5 FORMATION AND EVOLUTION

2.5.1 *Formation processes*

Dust formation is thought to occur in the envelopes of stars during late life stages, such as AGB stars which are thought to be the most efficient production sources. In those expanding envelopes, the density and temperature conditions allow the condensation of solid particles. Silicate dust formation is thought to occur by nucleation of SiO or SiC depending on the abundances of the star (see for instance Gail et al. 2013), while carbon dust may start from condensation of C_2H_2 into solid carbon. Ferrarotti and Gail [2006] give complete models of dust formation for different types of stars, providing estimates of the formation rates of the different dust components. The grains formed during this phase probably grow further by accretion later in the cycle. Processing and accretion progressively transform this stardust into the interstellar dust described in this chapter.

2.5.2 *Processing and destruction*

Dust experiences harsh conditions in the ISM. It is submitted to a bombardment of UV photons and cosmic rays, violently collides with other grains in shocks, and its temperature varies in a wide range. Those conditions can destroy grains, and this destruction rate must be balanced overall by the formation process. The conclusion of such a comparison (see Jones and Nuth 2011) seems to be that formation by stars is sufficient for the more resistant silicate grains, but that carbon grains are destroyed faster and need to be reformed in the ISM. The process could be grain growth by accretion of gas material in molecular clouds, followed by collisions breaking the grains into smaller particles, and final destruction occurring at the smallest sizes. We would thus have a cascade of destruction during some phases of the dust life cycle (shocks, PDR), balanced by growth of the grains during quieter phases (dense molecular clouds).

In addition, irradiation by UV photons and energetic particles can modify the atomic structure of the material. For instance, Jones et al. 2013 propose that carbon dust is initially hydrogen-rich aliphatic carbon, but is progressively turned into hydrogen-poor aromatic carbon by UV processing. As UV photons cannot penetrate very deep inside the grain, the processing effect changes with grain size: small grains are completely aromatized, while bigger grains only have a thin processed layer on their surface.

Finally, low velocity collisions can stick grains together, producing agglomerates of different materials. This process is called coagulation, and most likely takes place in dense molecular clouds, where observations show a growth of the grain sizes (through a change in R_V and the extinction curve).

3

TURBULENCE

Turbulence has long been ignored in the theory of the interstellar medium, before gradually acquiring its current acceptance as a central structuring force in the ISM. In this chapter, we review the basic properties of turbulence, before discussing interstellar turbulence, its observational evidences, its causes and the multiple roles it plays in the dynamics of the ISM. Finally, we give a more detailed discussion of its possible role as suprathermal source of energy for endothermic reactions through its intermittent dissipation at small scales.

The second part of the work of this thesis is indeed devoted to the proposition of a modeling framework for the problem of turbulent chemistry in the ISM, and more specifically the case of turbulence-driven chemistry in which parts of the chemical network are opened thanks to the energy dissipated by turbulence triggering endothermic reactions. Such a mechanism as been proposed to explain the long-known presence of CH^+ in the diffuse ISM, despite a highly endothermic formation (4640 K), as is discussed in the last section of this chapter.

3.1 TURBULENCE

Turbulence is a long-standing unsolved problem of classical physics. Despite the equations governing the dynamics of a fluid being established since the mid-eighteenth century for the idealized inviscid case (Euler's equation) and the mid-nineteenth century for the general viscous case (the Navier-Stokes equation), a general theory of turbulence is still missing, and several fundamental problems remain open, both from a physical and mathematical point of view (making the existence and smoothness of solutions of the Navier-Stokes equation one of the seven Millennium Prize Problems stated by the Clay Mathematics Institute).

We give here a quick overview of the most useful results on turbulence, with a bias towards the properties of the energy dissipation. General presentations of the theory of turbulence can be found in the books by Monin and Yaglom [1971, 1975], Frisch [1995], Pope [2000], Davidson [2004]. We will mainly discuss results concerning incompressible hydrodynamical turbulence. The dynamics of such a flow in the absence of body forces is governed by the two equations

$$\frac{\partial u_i}{\partial t} + u_j \partial_j u_i = -\frac{1}{\rho}\partial_i p + \nu \partial_j \partial_j u_i \tag{3}$$

which is the Navier-Stokes equation expressing momentum conservation, and where $\overrightarrow{u}$ is the velocity field, ρ the density, p the pressure and ν the kinematic viscosity, and

$$\frac{\partial \rho}{\partial t} + u_j \partial_j \rho = 0 \tag{4}$$

which expresses mass conservation.

These seemingly simple equations contain the complexity of turbulent flows. The non-linear advection terms are the important terms causing distortions of the flow structure. One way to picture their action is to notice that they create coupling between different wave numbers in Fourier space.

3.1.1 *Definition*

No formal definition of turbulence exists, but several defining characteristics are usually invoked. At a very informal level, turbulence is a state of a flow where very complex and irregular motions make the evolution unpredictable, as opposed to smooth laminar flows. More precisely, an experimental characteristic of turbulence is the non-reproducibility of the flow. This is a consequence of the chaotic nature of turbulent flows, in which unavoidable uncertainties on the initial conditions result in complete unpredictability after some time. Note that being chaotic is not in itself sufficient to make a flow turbulent. This property has for consequence that the study of turbulence is necessarily statistical, as only the statistical properties of the flow are reproducible and predictable.

An additional characteristic of turbulence is the idea of a cascade of destabilizations of flow structures into smaller and smaller structures. This idea was concisely expressed by Richardson in the verse:

> *Big whirls have little whirls that feed on their velocity,*
> *and little whirls have lesser whirls and so on to viscosity.*

While whirl motions might not be universally a defining trait of turbulence (it is at least of incompressible hydrodynamical turbulence), the idea of a cascade of flow structures of decreasing sizes with transfer of energy from the large structures to smaller structures over some range of scales is quite universal (in some particular cases, an inverse cascade can transfer energy towards larger scales in some domain of scales, such as in two-dimensional turbulence). Some aspect of self-similarity is also usually found in this cascade, with the small structures being in some way scaled down versions of the bigger structures. This leads naturally to try to characterize the properties of the flow in terms of the scale of the structure under consideration, and to try to express scaling laws relating the quantities at a given scale, as we will see in the next subsection. This has also led to the wide use of the Fourier transform as a way to transform the position-dependent quantities

into scale-dependent quantities. However, the relevance of a decomposition into planar waves for a turbulence often characterized by whirling motions is questionable as discussed by Davidson [2004].

Finally, one of the surprising characteristics of turbulence is the fact that the energy dissipation rate does not go to zero as the viscosity (or the corresponding dissipation parameter for other mechanisms) goes to zero, contrary to laminar flows. When the viscosity is decreased, the cascade just extends to smaller scales where energy can be dissipated at the required rate. In the limit of zero viscosity, we can thus expect an infinite cascade and a strongly singular velocity field.

The transition from smooth laminar flows to irregular turbulent flows can be related to a dimensionless parameter called the Reynolds number:

$$\mathrm{Re} = \frac{U\,L}{\nu} \tag{5}$$

where ν is the kinematic viscosity, U is the characteristic velocity difference in the largest structures of the flow, and L the characteristic scale of the largest structures. This number compares the importances of the non-linear advection term $u_j \partial_j u_i$ which scales as $U^2 L^{-1}$ and the viscous dissipation term $\nu \partial_j \partial_j u_i$ which scales as $\nu U L^{-2}$ in the Navier-Stokes equation. Thus when this number is small, viscosity dominates and smoothes out any distortion of the flow that the non-linear advection term would tend to create. On the contrary, when it is large, the distortions can develop and destabilize the main flow structure into smaller structures. These new smaller structures have smaller length scale and velocity. If the new Reynolds number of these structures is still large, they will also be disrupted and give birth to smaller structures, initiating the turbulent cascade. Experimentally, fully developed turbulence generally occur for $\mathrm{Re} \gtrsim 2000 - 3000$, but is highly dependent on the precise setting of the flow. For flows around a solid object, a carefully studied shape (such as planes) can delay the transition to turbulence to $\mathrm{Re} \sim 10^6$.

3.1.2 *Kolmogorov theory and scalings*

The theory developed by the Russian mathematician A. N. Kolmogorov (who is also one of the founding fathers of modern probability theory and stochastic process theory) in 1941 remains one of the most important advances in the understanding of turbulence so far. This theory develops the idea of the energy cascade proposed by Richardson, where large flow structures (historically called eddies, without a proper definition) transfer energy to smaller structures, in a cascade that continues as long as the Reynolds number at the scale of these structures is large enough, and ends in structures that have $\mathrm{Re} \sim 1$ where viscosity becomes dominant and dissipates the energy.

The idea of the theory of Kolmogorov is to make the hypothesis that once a scale small enough compared to the scale of the largest motions of the flow

has been reached, the statistical properties of the cascade lose the information about the geometry of the flow, and become locally isotropic and universal. The range of scales in which this hypothesis is valid is called the universal range. Thus, these properties can only depend on the rate at which energy is injected in the cascade, that we note ϵ for reasons that will become clear soon, and on the viscosity ν.

From dimensional reasoning, the cascade possesses unique characteristic length scale, timescale and velocity:

$$\eta \propto \left(\frac{\nu^3}{\epsilon}\right)^{\frac{1}{4}} \tag{6}$$

$$\tau_\eta \propto \left(\frac{\nu}{\epsilon}\right)^{\frac{1}{2}} \tag{7}$$

$$u_\eta \propto (\epsilon\nu)^{\frac{1}{4}} \tag{8}$$

which are called the Kolmogorov length scale, timescale and velocity. From these relations, it is obvious that the corresponding Reynolds number is of order unity, so that those values characterize the scale at which the cascade ends and the energy is dissipated. Moreover, the viscous energy dissipation rate for eddies with those characteristics can be dimensionally estimated as $\nu(u_\eta/\eta)^2 = \epsilon$, which is consistent with overall energy conservation in the cascade: energy is injected at rate ϵ at the beginning of the cascade, is transferred without loss from scale to scale as long as viscosity is negligible, and thus dissipated at rate ϵ at the Kolmogorov scale.

The universality of the cascade is then apparent as the statistics of the dimensionless variables $\overrightarrow{y} = \left(\overrightarrow{x} - \overrightarrow{x_0}\right)/\eta$ and $\overrightarrow{w} = \left(\overrightarrow{u}\left(\overrightarrow{x}\right) - \overrightarrow{u}\left(\overrightarrow{x_0}\right)\right)/u_\eta$ cannot depend on any parameter of the flow (no dimensionless quantity can be formed from ϵ and ν only), for scales small enough for the previous hypothesis to hold.

The second hypothesis made by Kolmogorov is that for scales large enough compared to η, the effect of viscosity becomes negligible, and the statistical properties of the cascade can thus only depend on ϵ. As the dominating term is then the inertial advection term, the range in which this hypothesis is valid is called the inertial range, which is included in the universal range. As no length scale, timescale or velocity can be built from ϵ alone, this regime of the cascade is scale-less and thus self-similar. At each scale l, the flow structures must have velocity $u_l \propto (\epsilon l)^{\frac{1}{3}}$ and timescale $\tau_l \propto \left(l^2/\epsilon\right)^{\frac{1}{3}}$. Again, we see that, as expected, the rate at which the structures of scale l lose their kinetic energy must be of order ϵ. Many useful results can be derived from these ideas, and we now summarize a few useful ones.

Theoretical studies usually consider homogeneous turbulence. In this situation, statistical functions of the position only are uninteresting (they are constant across space), and statistical functions that depend on some measure of the scale must be used. Two equivalent ways to do so are:

- the use of the velocity autocorrelation tensor

$$R_{ij}(\overrightarrow{r}) = \langle u_i(\overrightarrow{x}) u_j(\overrightarrow{x} + \overrightarrow{r}) \rangle \tag{9}$$

which is independent of $\overrightarrow{x}$ for homogeneous turbulence, and depends only on $||\overrightarrow{r}||$ for isotropic turbulence. Note that in the usual statistical terminology, it is actually an autocovariance function. This autocorrelation function gives statistical informations about the structure of the flow at different scales $\overrightarrow{r}$.

- the use of the Fourier transform of the velocity field

$$\widehat{u}_i(\overrightarrow{k}) = \iiint d\overrightarrow{x}\, e^{-i\overrightarrow{k}.\overrightarrow{x}} u_i(\overrightarrow{x}), \tag{10}$$

we then define the velocity spectrum tensor as

$$\Phi_{ij}(\overrightarrow{k}) = \left\langle \widehat{u}_i(\overrightarrow{k}) \widehat{u}_j(\overrightarrow{k}) \right\rangle. \tag{11}$$

The power spectrum is then

$$P(\overrightarrow{k}) = \frac{1}{2}\Phi_{ii}(\overrightarrow{k}) \tag{12}$$

and the energy spectrum is

$$E(k) = \iint_{|\overrightarrow{k}|=k} d\overrightarrow{k}\, P(\overrightarrow{k}) \tag{13}$$

This energy spectrum approximately gives the energy contained in the structures of scale $\frac{2\pi}{k}$.

Those two approaches are related by the Wiener-Khinchin theorem, according to which

$$\Phi_{ij}(\overrightarrow{k}) = \frac{1}{(2\pi)^3} \iiint d\overrightarrow{r}\, e^{-i\overrightarrow{k}.\overrightarrow{r}} R_{ij}(\overrightarrow{r}). \tag{14}$$

For k corresponding to the inertial range ($\frac{2\pi}{k}$ small compared to the injection scale and large compared to the Kolmogorov scale), the Kolmogorov theory applied to these quantities then gives the classical scaling laws

$$E(k) = C_K \epsilon^{\frac{2}{3}} k^{-\frac{5}{3}} \tag{15}$$

and

$$P(k) = \frac{C_K}{4\pi} \epsilon^{\frac{2}{3}} k^{-\frac{11}{3}} \tag{16}$$

(where we use the isotropy of turbulence to have a dependance on $k = \left\| \overrightarrow{k} \right\|$ only). C_K is the Kolmogorov constant, supposed universal. Experiments

have shown good agreement of the measures with those scaling laws, with $C_K = 1.62$.

A group of more general statistics that are commonly used are the structure functions. The structure function of order p is defined as

$$S_p(l) = \left\langle \left[\left(\vec{u}(\vec{x} + \vec{l}) - \vec{u}(\vec{x}) \right) \cdot \frac{\vec{l}}{l} \right]^p \right\rangle \tag{17}$$

The second order structure function is directly related to the autocorrelation function and is thus equivalent to the previous approaches. Kolmogorov theory gives

$$S_p(l) = C_p \epsilon^{\frac{p}{3}} l^{\frac{p}{3}} \tag{18}$$

where C_p are constants that are expected to be universal.

Note that all those results come from Kolmogorov's hypotheses and dimensional arguments only, and are not rigorously proved from the Navier-Stokes equation.

An exact approach has been attempted by deriving an evolution equation for the autocorrelation function from the Navier-Stokes equation. This leads to the Karman-Howarth equation, or equivalently to the Kolmogorov equation for the second order structure function. Both are unclosed as an additional unknown function appears (in the Kolmogorov equation, it is the third order structure function). Despite this closure problem (which leads to an infinite hierarchy of coupled evolution equations for the structure functions), in the case of locally isotropic turbulence and in the inertial range, the Kolmogorov equation simplifies to give one of the only exact results in turbulence theory:

$$S_3(l) = -\frac{4}{5}\epsilon l \tag{19}$$

The Karman-Howarth equation also shows that it is the non-gaussianity of the velocity field that allows the energy transfer in the inertial range.

3.1.3 *Intermittency*

Comparisons of these predictions to experimental results have shown that despite a good agreement for the low order statistics (energy spectrum, second order structure function,...), higher order statistics significantly deviate from the predictions. This is attributed to the phenomenon of intermittency in the turbulent cascade. The idea is that the transfer of energy from scale to scale is not homogeneous in space but is subject to fluctuations: one structure may, when destabilizing, give more energy to the substructures in one part of its original region, and less to the other parts. Those fluctuations are then naturally amplified by the cascade, and this leads to very large fluctuations at the smallest scales. This is in contradiction with the idea of Kolmogorov theory that a given scale sees the average dissipation rate ϵ.

To be more precise, let us call ϵ the energy injection rate and average dissipation rate, which is also the average energy transfer rate in the cascade. Let us call ϵ_0 the true local dissipation rate (which is a function of space and time). If we consider a given flow structure of size r, at position $\overrightarrow{x}$, it is natural to think that the quantity to which it is sensitive is not the average dissipation rate, but the local average

$$\epsilon_r(\overrightarrow{x}, t) = \frac{3}{4\pi r^3} \iiint_{\|\overrightarrow{r}\|<r} \epsilon_0(\overrightarrow{x} + \overrightarrow{r}, t)\, d^3\overrightarrow{r} \tag{20}$$

which is subject to fluctuations according to the mechanism described above.

This led Kolmogorov to refine his hypotheses (Kolmogorov 1962, Obukhov 1962). It is only the statistical properties conditional on the local value of ϵ_r that are universal for scales small compared to the injection scale, and they depend on ϵ_r and ν only. In the inertial range, they depend only on ϵ_r. This leads to the new prediction for the conditional structure functions:

$$\left\langle (\Delta_r u)^p \,|\epsilon_r = \varepsilon \right\rangle = C_p\, \varepsilon^{\frac{p}{3}}\, r^{\frac{p}{3}} \tag{21}$$

The unconditional structure functions are then

$$S_p(r) = \left\langle \left\langle (\Delta_r u)^p \,|\epsilon_r = \varepsilon \right\rangle \right\rangle = C_p \left\langle \epsilon_r^{\frac{p}{3}} \right\rangle r^{\frac{p}{3}} \tag{22}$$

For $p = 3$, we still recover the exact result $S_3(r) \propto \epsilon\, r$.

Due to the successive amplifications of the fluctuations of ϵ_r during the cascade, Kolmogorov conjectured that the mean-square dissipation fluctuation scales as

$$\frac{\langle \epsilon_r^2 \rangle}{\epsilon^2} \propto \left(\frac{L}{r}\right)^{\mu} \tag{23}$$

where μ is called the intermittency exponent. Experiments suggest $\mu \simeq \frac{1}{4}$. This allows to compute

$$S_6(r) \propto \epsilon^2 L^{\frac{1}{4}} r^{\frac{7}{4}} \tag{24}$$

More generally, if we define the scaling exponent ζ_p as the exponent of r in the structure function of order p, Kolmogorov assumed a log-normal distribution for ϵ_r and derived the general expression for the scaling exponents:

$$\zeta_p = \frac{1}{3} p \left[1 - \frac{1}{6}\mu(p-3)\right] \tag{25}$$

For $\mu = 1/4$, this gives

$$\zeta_p = \frac{1}{3} p \left[1 - \frac{1}{24}(p-3)\right] \tag{26}$$

The corrections to the second order statistics are negligible (the correction to the $\frac{5}{3}$ exponent of the energy spectrum is only $\frac{1}{36}$), but the higher order

structure function exponents are significantly modified, and give a very good agreement with the experimental data for $p \lesssim 10 - 12$. Discrepancies start growing again for higher p, a problem which has been traced to the use of a log-normal distribution for ϵ_r.

A fractal approach has also been developed. The idea of a fractal model is that a given structure in the cascade, when destabilizing and transmitting its energy to a lower scale, does so to only a fraction of its volume. The resulting active volume becomes a fractal object with a dimension depending on the fraction of active volume at each scale. The naive application of this idea with a constant volume fraction β (called the β model) does not fare well in comparison to the observations, as it also predicts a linear dependency of ζ_p on p, and more complex multi-fractal models are required to produce the required curvature.

The most successful model so far is the log-Poisson model (She and Leveque 1994, Dubrulle 1994, She and Waymire 1995), which is based on a multiplicative cascade with defects occurring with a Poisson distribution. It predicts that

$$\zeta_p = \frac{p}{9} + 2\left[1 - \left(\frac{2}{3}\right)^{\frac{p}{3}}\right] \tag{27}$$

Very recently, David Ruelle (Ruelle 2012, 2014) proposed a statistical mechanical approach to this problem of the fluctuations of the local dissipation rate, and derived new expressions for the structure exponents that seem to agree with the experiments.

3.1.4 *Compressible turbulence and MHD turbulence*

The understanding of turbulence is greatly complicated when adding additional features to the flow, such as compressibility or considering a magnetized fluid. However, compressible and magneto-hydrodynamic turbulence is more realistic for the interstellar medium with partially ionized gas and observed magnetic fields, and supersonic velocity dispersions.

Little is known about classical turbulence, but even less about compressible and MHD turbulence. We summarize here some relevant questions and results.

For MHD turbulence, the fact that the large scale magnetic field affects all scales breaks the hypothesis of local isotropy of the small scales in Kolmogorov theory, and complicates the situations. Moreover, numerical results seem to indicate that part of the energy can be transferred between the magnetic field and the velocity field directly from the large scales to the small scales in parallel to the cascade (Alexakis et al. 2005). Energy can also in some cases be transferred from the small scales to the large scale magnetic field resulting in a dynamo effect. This greatly complicates the classical picture of the turbulent cascade.

Scaling laws have been proposed for MHD turbulence (Kraichnan 1965, Goldreich and Sridhar 1997). A general presentation of MHD turbulence can be found in the book by Biskamp 2003.

Compressibility brings the complication that kinetic energy is not conserved anymore even at scales where viscosity is negligible, as kinetic energy can be converted into thermal energy by compression and vice-versa. A compressible flow can be decomposed into a solenoidal (incompressible-like) component, and an irrotationnal (compressible) component. The compressible component creates shocks, while the solenoidal component tends to follow the usual cascade of eddies, but the two components can exchange energy in both directions. Some numerical results (Porter et al. [2002]) tend to show that in decaying turbulence the compressible component quickly decays and transmits its energy to the solenoidal component, so that after the initial phase, more than 70% of the energy is contained in the solenoidal modes. Moreover, they show that the structure exponents seem to be identical to incompressible turbulence, which may indicate that the small scales behave as an incompressible turbulent cascade and that compressibility only affects the large scales.

3.2 INTERSTELLAR TURBULENCE

After a few early propositions that did not catch on (von Weizsäcker 1951), the omnipresence of turbulence in the interstellar medium has been slowly recognized starting from the 80's. Its role is still a subject of debates today, but its presence and importance is now clearly established.

We now give a quick overview of the observational evidences of turbulence in the ISM, of the probable sources of kinetic energy initiating the turbulent cascade, and of the various roles that turbulence can play in different environments.

3.2.1 *Observational evidences*

The first argument in favor of a turbulent ISM comes from estimates of the Reynolds number based on the observed velocity dispersion of clouds. The resulting Reynolds number are of the order of 10^7. In addition, the velocity dispersions are actually supersonic, so that interstellar turbulence is probably highly compressible. As the gas in the CNM is also partially ionized and permeated by a magnetic field of a few micro-gauss, non-ideal MHD processes are most likely also at play, so that several dissipation processes work in parallel (shocks, viscous shear, resistivity and ambipolar diffusion).

Observations of scaling laws between the velocity dispersion and the cloud size on one hand, and between the cloud mass and the cloud size on the other hand (Larson [1981]), reminiscent of those found in Kolmogorov theory, have

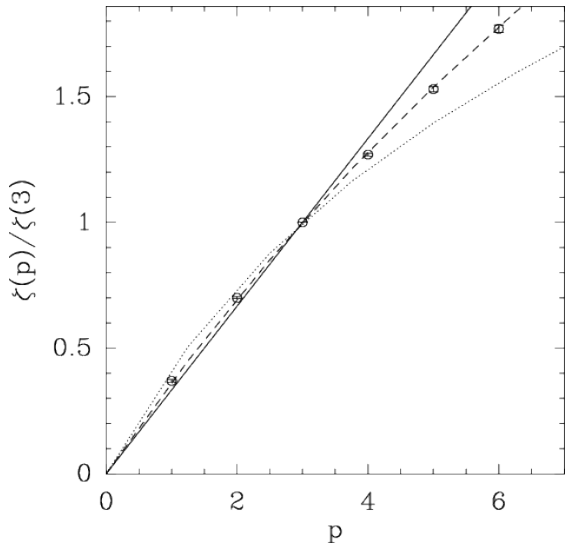

Figure 12: Structure function exponents for ^{12}CO observations of Polaris (Hily-Blant et al. 2008). Solid line: predictions of the Kolmogorov theory of 1941 (no intermittency), dashed line: log-Poisson model of She and Leveque [1994] for incompressible turbulence, dotted line: predictions of Boldyrev et al. [2002] for supersonic turbulence. Figure taken from Hily-Blant et al. [2008].

been interpreted as evidences of turbulence. Those scaling laws have been confirmed and extended by later studies (e.g. Heyer and Brunt 2004).

Power spectra have also been derived from observations, and show a power law behavior over a large range of scales, with exponents comparable to the predictions of the Kolmogorov theory. Such spectra have been determined from a variety of observations: HI emission (Miville-Deschênes et al. 2003), HI absorption (Deshpande et al. 2000), dust emission (Miville-Deschênes et al. 2010), the electronic density measured from interstellar scintillation (Armstrong et al. 1995), and ^{12}CO and ^{13}CO emission (Bensch et al. 2001). The interpretation of these exponents remains difficult as the observables do not trace the velocity fields directly. A particularly striking evidence of turbulence is the transition in slopes found by Elmegreen et al. [2001] in the HI spectrum of the large Magellanic Cloud when reaching scales comparable to the thickness of the HI layer, as expected for the transition from 3D to 2D turbulence.

Finally, a third type of evidence of turbulence in the ISM comes from the measurement of the velocity increment statistics, inferred from the centroid velocity of line profiles (e.g, Hily-Blant et al. 2008, Hily-Blant and Falgarone 2009). These reveal the non-gaussianity expected from the intermittency of the turbulence cascade (see Sect. 3.1.3), and the structure exponent derived from those PDF are surprisingly close to the the predictions of She and Leveque [1994] for incompressible turbulence, as shown on Fig. 12. Moreover, the extreme values forming the non-gaussian wings of the PDF correspond to

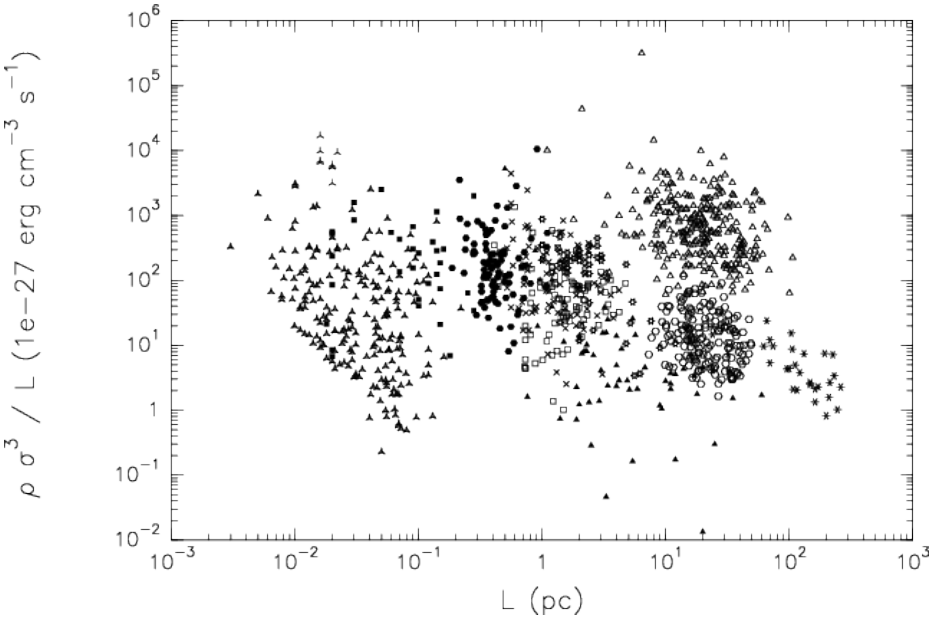

Figure 13: Compilation of estimations of the energy transfer rate in the turbulent cascade, from observations of molecular clouds. Figure taken from Hennebelle and Falgarone [2012].

coherent elongated structures with high shear, resembling vortices or shear layers (Falgarone et al. [2009]).

More evidences are compiled in the reviews by Elmegreen and Scalo [2004] and Hennebelle and Falgarone [2012]. A recurrent surprise from those evidences is that many results seem to agree well with the prediction for classical incompressible turbulence despite the MHD and incompressible nature expected for interstellar turbulence.

3.2.2 *Energy sources*

The energy transfer rate derived from the observed velocity dispersion in molecular clouds is shown on Fig. 13. The scatter is very large (two orders of magnitude), but no global trend appears for the energy transfer rate for scales from 10^2 to 10^{-2} pc, and the average value is also consistent with the one observed in HI gas (2×10^{-25} erg.cm^{-3}.s^{-1}). This might indicate one large uninterrupted turbulent cascade joining the different phases of the neutral ISM.

As the turbulent motions decay typically in one turnover time (1 Myr for a $\sim$ pc sized cloud and a $\sim$ km.s^{-1} velocity dispersion), this energy has to be continuously replenished. The question of the origin of this energy remains open. Several injection mechanisms have been identified, but their relative importance remains debated.

They can be grouped into stellar sources (supernovae, protostellar wind, O star winds, super-bubbles expansion), galactic rotation (spiral shock, instabilities due to the differential rotation), and cloud accretion. The uniformity of the dissipation rates across molecular clouds and the absence of characteristic scale in their spectrum could point to an external source of energy at scales larger than the clouds.

It is usually estimated that supernovae and super-bubble expansion are the dominant energy sources, but other sources could also provide the required energy more locally (e.g., accretion onto a cloud, Klessen and Hennebelle [2010]).

An important question is the type of forcing that those sources create, in term of compressible or solenoidal modes. Indeed, compressible modes tend to dissipate in large shocks, while solenoidal energy is more prone to undergo a turbulent cascade.

A more detailed discussion of the energy sources of turbulence can be found in Elmegreen and Scalo [2004] and Hennebelle and Falgarone [2012].

3.2.3 *Roles*

Turbulence has been proposed to play a major role in several aspects of the ISM. For more details see the reviews by Elmegreen et al. [2001] and Scalo and Elmegreen [2004].

One of the first proposed effects of turbulence is to shape and support the structure of the ISM. The hierarchical structure of the ISM is interpreted as a result of compressible turbulence, while the vertical density profile of the galactic disk requires a dynamical pressure much larger than the thermal pressure. Turbulent pressure has also been proposed as a support mechanism for clouds that could slow down the collapse, but numerical studies show that turbulence tends to disrupt and fragment clouds more than to support them statically. This turbulent fragmentation process is of great potential importance for star formation.

One well studied effect of turbulence is to enhance the diffusion of passive contaminants in the flow. In the ISM, this effect has been invoked for several distinct problems. One is the observed homogeneity of metals in the galaxy. Estimates comparing the timescales of supernova ejection of metals and of reincorporation of metals into new generations of stars show that in the absence of an enhanced mixing mechanism, the distribution of metals should be very spotty. Turbulent transport allows faster mixing and homogenization of the heavy elements in the ISM, as required by the observations.

Turbulent mixing has also been advocated to explain some aspects of the chemical composition of the CNM, such as the presence of CO in diffuse gas insufficiently shielded from radiation, or the presence of atomic hydrogen inside molecular clouds. However, other mechanisms could explain these ob-

servations. Moreover, the estimation of the efficiency of turbulent mixing for species whose chemistry is controlled by photodissociation is not straightforward. Usual mixing length theory does not apply without adaptation in this case, as it assumes that a fluid element conserves its chemical composition while being transported until it reaches the smallest scales of the turbulent cascade where molecular mixing can take place. Photodissociation will of course quickly change the composition of the fluid element as soon as its position is modified.

Turbulence also plays a role in the scattering and acceleration of cosmic rays. Finally, one last category of possible effects will be discussed in the last section of this chapter.

3.3 TURBULENT CHEMISTRY

The energy contained in the interstellar turbulence is dissipated at the end of the cascade. The absence of cut-off in the observed power spectra shows that the dissipative scales are not resolved by modern instruments, as expected from simple estimates (the dissipative scale is of the order of a few AU for typical diffuse medium conditions; see the estimation at the beginning of Chap. 10). As this dissipation is extremely intermittent, it is expected to create localized and temporary hot spots in which endothermic chemistry can be activated by the dissipated energy. We discuss here observational evidences of this mechanism and the models that have been developed to account for this effect.

3.3.1 CH^+, SH^+ *and* H_2 *in the diffuse ISM*

CH^+ is one of the first interstellar molecules to have been observed in absorption. Yet, conditions in the diffuse CNM in which it is ubiquitously observed are too cold for the very endothermic reaction $C^+ + H_2 \rightarrow CH^+ + H$ (4640 K). More recently detected, SH^+ is similarly problematic. These observations have been confirmed and improved many times since the first detection of these molecules (e.g., Godard et al. [2012]), and still contradict the predictions of usual PDR-type models, where the chemical dynamics is driven by the UV radiation field. As the discrepancy mainly concerns molecules with very endothermic formation, this points towards another energy source acting in a small fraction of the volume, so that the other observables are dominated by the contribution of the large inactive volume and conform to the predictions of the PDR models. Thus, the origin of those molecules could be explained by the intermittent dissipation of energy that occurs at small scales.

Another evidence of this mechanism is the observation by FUSE of significant amounts of rotationally excited H_2 on diffuse lines of sight (e.g., Gry et al. [2002], Lacour et al. [2005]). This excited H_2 in the diffuse ISM has

also been observed in emission by Falgarone et al. [2005]. The radiation field is too weak in these region to cause such levels of excitation by pumping and cascades, and the gas temperature inferred from the first levels of H_2 is too low to explain the observed populations of the $J > 2$ levels. This again points towards the presence on the line of sight of a small fraction of high temperature gas, in which those levels can be collisionaly excited.

Finally, the observed CO abundances on diffuse lines of sight remain one order of magnitude above the predictions of PDR models (Levrier et al. 2012). As CO can be formed through the reaction chain CH^+– CH_2^+– CH_3^+– HCO^+– CO initiated by the endothermic formation of CH^+, the mechanism described above to explain the abundance of CH^+ could also explain the abundance of CO.

3.3.2 *Modeling the interstellar turbulent chemistry*

The first tentative to explain the abundance of CH^+ by a localized dissipation event was published by Elitzur and Watson [1978], in the form of a shock originating from the HII region surrounding the observed star. Their model reproduced the observations of the time, by reaching a sufficiently high gas temperature to trigger the endothermic reactions.

In a series of paper (Draine and Katz 1986a,b, Draine 1986), Bruce Draine proposed that the magnetic continuous shocks which he had presented earlier (Draine 1980) could activate the endothermic reaction due to suprathermal collisions caused by ion-neutral drift in the magnetic precursor. A lower gas temperature was thus required, which could avoid the overproduction of OH compared to previous models.

This kind of models was later further developed by Flower and Pineau des Forets [1998]. The ubiquitous presence of CH^+ raised the question of the likelihood of the presence of a single strong shock on every line of sight. This led Gredel et al. [2002] to propose a model in which a distribution of low velocity shocks could explain the observations.

In parallel, another kind of dissipative structure was proposed by Joulain et al. [1998]. In this model, a MHD vortex was proposed to represent the small scale dissipative structures of MHD turbulence, and the endothermic formation of CH^+ was triggered by the ion-neutral drift, similarly to the shock models. This model was later further developed by Godard et al. [2009], in which the importance of the cooling phase following the dissipation event was demonstrated, and the contributions of the dissipative structures, the cooling gas and the quiescent gas were mixed to model the observation of a line of sight. The model was shown to reproduce the observations of CH^+, SH^+, CO and H_2 (and several other tracers).

While these models reproduce in great detail one dissipative structure, the statistical treatment remains rudimentary. The intermittency of the dissipa-

tion is reduced to a binary vision (quiescent gas, and dissipative structures with a single intensity), and the statistics of the Lagrangian history of a fluid element is not investigated. For instance, does a particle that just experienced a dissipative structure has the time to return to the quiescent state before experiencing another dissipation event ? As a wide range of intensities of dissipation events exists with different occurrence timescales, this question requires detailed models of the statistical Lagrangian evolution of the fluid elements.

The work presented in the second part of this thesis (Chap. 9 and 10) proposes a modeling framework to tackle this problem with a flexibility that allows to consider different kinds of dissipative events (shocks, vortices,...). It could also be extended to study the effect of turbulent mixing on the chemical transition front (H/H_2, $C+/CO$).

4

STOCHASTIC PROCESSES

The usual task of physical modeling is to build a description of the dynamical evolution of some physical system. The system is described by a collection of physical variables, and the dynamical evolution of the system is prescribed as functions of time describing the evolution of the variables. The prescription is done through laws taking most often the form of differential equations. But this deterministic approach, despite its numerous successes in the history of Science, only allows to address a limited class of problems.

Many interesting problems involve systems in which all the information cannot be known, either because of some inherent probabilistic nature of the process (as in quantum mechanics), or because the system under consideration is perturbed by an environment that we can't or don't want to model, or because including a full description of the system would require an intractable amount of information in term of number of variables (for instance following all particles positions in a gas) or in term of the precision required on each variable (as in chaotic systems). For these problems, a probabilistic approach has proved very powerful and produced the well known successes of Statistical Physics.

In a probabilistic view, a stochastic process is the natural counterpart to the usual deterministic dynamical system, with the Markov property replacing the usual absence of memory in differential equations (usual differential equations relate quantities and their derivatives at the same instant t), and stochastic differential equations replacing the differential equations in some cases.

This chapter gives an informal introduction to stochastic processes and the associated concepts and tools that have been used in this thesis. As this chapter uses heavily the concepts of probability theory, a quick summary of probability theory is given in Appendix A. For simplicity, all measure-theoretic concepts are avoided in this presentation. The results presented here can be found in the usual textbooks about stochastic processes such as Gardiner [2004] or Gillespie [1992].

4.1 GENERAL DEFINITIONS

4.1.1 *Stochastic processes*

Informally, a stochastic process is simply a random function of time. But to characterize it, we will need a more formal definition :

A stochastic process is a collection $(X_t)_{t\in\mathcal{T}}$ of random variables (with values in some set $\mathcal{S}$), indexed by a set $\mathcal{T}$. The most abstract definition only requires $\mathcal{T}$ to be any totally ordered set, but in all physical applications $\mathcal{T}$ will represent time and be constituted of numbers. It will usually be either $\mathbb{R}$ (or some interval of $\mathbb{R}$), or a discrete set of times if the evolution is only modeled through discrete time-steps.

The set $\mathcal{T}$ will thus be called the *time set*, while $\mathcal{S}$ will be called the *state set*. Note that the stochastic process can have vector values, so that if the system is to be described by several physical variables, its evolution can indifferently be modeled as several coupled stochastic processes or one single vector-valued stochastic process.

Fully characterizing one general stochastic process is not simple. If we consider one specific time s, X_s is a random variable and is characterized by its PDF $f_{X_s}(x)$. But if we consider two times s and t, we need the joint PDF $f_{X_sX_t}(x,y)$ of X_s and X_t to take into account possible correlations between the two variables. To simplify the notations, for any finite family of times $(t_0,t_1,\dots,t_n)$ (not necessarily ordered here), it is usual to note the joint PDF of the values of the process at those times as $f(x_0,t_0;x_1,t_1;\dots;x_n,t_n)$. Thus, f will actually refer to a different function depending on the number of its arguments. Similarly, the conditional PDF of the process at times $(t_1,\dots,t_k)$ knowing its values at times $(t_{k+1},\dots,t_n)$ will be noted

$$f\left(x_1,t_1;\dots;x_k,t_k\,|x_{k+1},t_{k+1};\dots;x_n,t_n\right)$$

.

We can of course relate any multi-times PDF $f(x_0,t_0;x_1,t_1;\dots;x_n,t_n)$, to the PDF of the values at $n-1$ of those times through:

$$f(x_0,t_0;x_1,t_1;\dots;x_{n-1},t_{n-1}) = \int dx_n\, f(x_0,t_0;x_1,t_1;\dots;x_n,t_n) \tag{28}$$

but adding more time points always brings potentially more information about the process. Completely characterizing the process would thus require knowing an infinite family of such multi-times joint PDFs. This makes the use of general stochastic processes very difficult in practice, and explains why most applications use specific sub-classes of stochastic processes, such as Markov processes, which we will define very soon.

One class of processes worth mentioning here is that of *gaussian processes*, for which all joint PDFs for finite families of times $f(x_0,t_0;x_1,t_1;\dots;x_n,t_n)$ are joint gaussian. One can show that such processes are uniquely defined by their mean function $m(t) = \langle X_t\rangle$ and their covariance function $K(t,t') = \langle X_tX_{t'}\rangle$, making them practically usable.

4.1.2 *The several meanings of "continuous"*

The word "continuous" can be used to denote different properties of a stochastic process.

First, the time set can be continuous, corresponding to a continuous description of time. In this case, we will call the process a *continuous-time* stochastic process, as opposed to *discrete-time* stochastic processes. One well known example of discrete-time stochastic processes are Markov chains (used for instance in Markov Chain Monte Carlo algorithms).

The state set can also be continuous or discrete, defining *continuous-state* stochastic processes and *discrete-state* stochastic processes.

In the work of this thesis, we will only consider continuous-time stochastic processes. The remaining of this chapter will thus only consider such processes.

The last and most important meaning of "continuous" concerns the trajectories, or sample paths, that the process can take. Different definition of continuity exists, corresponding to the different concepts of stochastic limit (limit in distribution, mean square limit, stochastic limit and almost certain limit). For simplicity, we will only use the almost certain continuity or sample continuity, and say that a process is continuous if its sample paths are continuous in almost all realizations (i.e. the probability of the sample path of one realization being a continuous function of time is 1).

Continuity is often an expected property of the evolution of physical variables, but some systems can exhibit a discontinuous behavior (e.g. when absorbing a photon).

4.1.3 *Markov processes*

A natural assumption about physical systems is that the future evolution is fully determined by only the present state of the system and not directly by its past. A simplified model could exhibit some kind of memory effect because it doesn't fully describe the present state of the system, but a sufficiently exhaustive description of the state should always lead to an evolution fully determined by the present state.

In a stochastic evolution, this principle takes another form. The present state doesn't determine the future evolution as this evolution is stochastic. But we expect that knowing the past doesn't bring any information about the future if the present state is already known. This is expressed using conditional probabilities by saying that for any family of times $(t_0, t_1, \ldots, t_n)$ (assumed ordered : $t_0 < t_1 < ... < t_n$):

$$f(x_n, t_n; \ldots; x_{k+1}, t_{k+1} \,|x_k, t_k; \ldots; x_0, t_0) = f(x_n, t_n; \ldots; x_{k+1}, t_{k+1} \,|x_k, t_k) \quad (29)$$

This property is called the *Markov property*, and the stochastic processes possessing it are called *Markov processes*.

The power of this assumption comes from the fact that all multi-times PDF $f(x_n, t_n; \dots; x_0, t_0)$ can now be determined by knowing only the two-times conditional PDF $f(x, t\,|y, s\,)$, and the one-time PDF $f(x, t)$. For instance:

$$\begin{aligned} f(x_3, t_3; x_2, t_2; x_1, t_1) =& f(x_3, t_3; x_2, t_2\,|x_1, t_1\,) f(x_1, t_1) \\ =& f(x_3, t_3\,|x_2, t_2; x_1, t_1\,) f(x_2, t_2\,|x_1, t_1\,) f(x_1, t_1) \\ =& f(x_3, t_3\,|x_2, t_2\,) f(x_2, t_2\,|x_1, t_1\,) f(x_1, t_1) \end{aligned}$$

where the first two equalities simply come from the definition of conditional PDFs, while the last comes from the application of the Markov property (29). More generally, we can easily show by recurrence that any multi-times PDF can be decomposed in the same fashion:

$$f(x_n, t_n; \dots; x_0, t_0) = f(x_n, t_n\,|x_{n-1}, t_{n-1}\,) \dots f(x_1, t_1\,|x_0, t_0) f(x_0, t_0\,) \tag{30}$$

We will now derive equations governing this conditional PDF $f(x, t\,|y, s\,)$.

4.2 THE CHAPMAN-KOLMOGOROV EQUATION AND ITS DIFFERENTIAL FORMS

4.2.1 *The Chapman-Kolmogorov equation*

From the definition of conditional PDFs, we have:

$$\begin{aligned} f(x, t) &= \int dy\, f(x, t; y, s) \\ &= \int dy\, f(x, t\,|y, s\,) f(y, s) \end{aligned} \tag{31}$$

which relates the two-times conditional PDF $f(x, t\,|y, s\,)$ to the one-time PDF $f(x, t)$, which is the useful quantity for most practical problems (it allows for instance to compute all the moments of the variables).

Similarly, we have for any time $u \in [s, t]$:

$$\begin{aligned} f(x, t\,|y, s\,) &= \int dz\, f(x, t; z, u\,|y, s\,) \\ &= \int dz\, f(x, t\,|z, u; y, s\,) f(z, u\,|y, s\,) \end{aligned} \tag{32}$$

This is the most general expression for any stochastic process, and similar relations can be written for 3- and multi-times conditional PDFs. But making use of the Markov properties, we now find that for Markov processes:

$$\boxed{f(x, t\,|y, s\,) = \int dz\, f(x, t\,|z, u\,) f(z, u\,|y, s\,)} \tag{33}$$

This equation is called the Chapman-Kolmogorov equation.

4.2.2 *General differential form of the Chapman-Kolmogorov equation*

For practical applications, we can think of the two-times conditional PDF as giving the PDF of the present state at current time t, conditional on the initial condition. To reflect this, we will use more the explicit notations $f(x, t\,|x_0, t_0)$. It would be natural to want a differential equation governing the evolution with t of this conditional PDF. To be able to derive such an equation, we need to restrict slightly the class of processes that we consider by requiring some regularity conditions. We will follow here the derivation of Gardiner [2004] which, despite somewhat more obscure conditions and a slightly heavier derivation, allows to derive a general equation including processes with jump, and of which the Fokker-Planck equation and the Master Equation are special cases. A simpler derivation leading directly to the Fokker-Planck equation but excluding jump processes can be found in Gillespie [1992].

We will consider here the state space to be some finite-dimensional vector space, and note vectors in bold fonts. For any $\epsilon > 0$ (which will later go to zero), we require the following conditions:

1. for any $|\mathbf{x} - \mathbf{z}| \geq \epsilon$, the limit

$$\lim_{\Delta t \to 0} \frac{1}{\Delta t} f(\mathbf{x}, t + \Delta t\,|\mathbf{z}, t) = W(\mathbf{x}\,|\mathbf{z}\,; t) \tag{34}$$

   exists and is finite. $W(\mathbf{x}\,|\mathbf{z}\,; t)$ represents the transition probability per unit of time corresponding to discontinuous jumps from $\mathbf{z}$ to $\mathbf{x}$. This limit must be zero for continuous processes, and requiring it to exist and be finite simply excludes pathological and non-physical cases. We will call $W(\mathbf{x}\,|\mathbf{z}\,; t)$ the jump transition rate.

2. The limit

$$\lim_{\Delta t \to 0} \frac{1}{\Delta t} \int_{|\mathbf{x}-\mathbf{z}|<\epsilon} d\mathbf{x}\,(x_i - z_i)\, f(\mathbf{x}, t + \Delta t\,|\mathbf{z}, t) = A_i(\mathbf{z}, t) + O(\epsilon) \tag{35}$$

   exists and is finite. We see that $\mathbf{A}(\mathbf{z}, t)$ represents the contribution from continuous movement to some kind of average speed. If no continuous movement is present, this limit will simply be $O(\epsilon)$ and go to zero when $\epsilon \to 0$. But it can also be zero when a continuous movement is present but its average is null (e.g. movement in both directions with equal probabilities). We will thus call it the drift coefficient.

3. The limit

$$\lim_{\Delta t \to 0} \frac{1}{\Delta t} \int_{|\mathbf{x}-\mathbf{z}|<\epsilon} d\mathbf{x}\,(x_i - z_i)(x_j - z_j)\, f(\mathbf{x}, t + \Delta t\,\big|\mathbf{z}, t) = B_{ij}(\mathbf{z}, t) + O(\epsilon) \tag{36}$$

exists and is finite. This again describes the continuous part of the evolution, but characterize its second moment, thus representing a continuous diffusion movement of the process. We will thus call $B_{ij}(\mathbf{z}, t)$ the diffusion coefficient

It is possible to show that under such conditions, all limits similar to Eq. (36) for higher order moments are zero (see Gardiner [2004]).

We next consider the expectation of some function $G(\mathbf{z})$ (twice differentiable):

$$\langle G(\mathbf{X}(t)) \,|\mathbf{X}(t_0) = \mathbf{x_0} \rangle = \int d\mathbf{x}\, G(\mathbf{x})\, f(\mathbf{x}, t \,|\mathbf{x_0}, t_0)$$

and write its derivative with respect to t:

$$\begin{aligned}
&\frac{\partial}{\partial t} \langle G(\mathbf{X}(t)) \,|\mathbf{X}(t_0) = \mathbf{x_0} \rangle \\
&\quad = \lim_{\Delta t \to 0} \frac{1}{\Delta t} \left[\int d\mathbf{x}\, G(\mathbf{x})\, f(\mathbf{x}, t + \Delta t \,|\mathbf{x_0}, t_0) - \int d\mathbf{x}\, G(\mathbf{x})\, f(\mathbf{x}, t \,|\mathbf{x_0}, t_0) \right] \\
&\qquad = \lim_{\Delta t \to 0} \frac{1}{\Delta t} \left[\int d\mathbf{x} \int d\mathbf{z}\, G(\mathbf{x})\, f(\mathbf{x}, t + \Delta t \,|\mathbf{z}, t) f(\mathbf{z}, t \,|\mathbf{x_0}, t_0) \right. \\
&\qquad\qquad \left. - \int d\mathbf{x}\, G(\mathbf{x})\, f(\mathbf{x}, t \,|\mathbf{x_0}, t_0) \right] \qquad (37)
\end{aligned}$$

where we have used the Chapman-Kolmogorov equation (Eq. (33)) to expand the first term of the second line.

The first term can be seen as a path integral, summing over all possible positions $\mathbf{z}$ at time t for a path that goes from $\mathbf{x_0}$ at t_0 to $\mathbf{x}$ at $t + \Delta t$. As t and $t + \Delta t$ are infinitesimally close, we expect that continuous movement will only contribute to values of $\mathbf{z}$ infinitesimally close to $\mathbf{x}$, while farther values will be contributed by discontinuous jump movement. We will thus split this integral into the parts corresponding to $|\mathbf{x} - \mathbf{z}| < \epsilon$ and $|\mathbf{x} - \mathbf{z}| \geq \epsilon$, in order to make the coefficient defined in Eq. (34), (35) and (36) appear:

$$\begin{aligned}
\frac{\partial}{\partial t} \langle G(\mathbf{X}(t)) \,|\mathbf{X}(t_0) = \mathbf{x_0} \rangle = \lim_{\Delta t \to 0} \frac{1}{\Delta t} \Bigg[& \\
& \iint_{|\mathbf{x}-\mathbf{z}|<\epsilon} d\mathbf{x} d\mathbf{z}\, G(\mathbf{x})\, f(\mathbf{x}, t + \Delta t \,|\mathbf{z}, t) f(\mathbf{z}, t \,|\mathbf{x_0}, t_0) \\
& + \iint_{|\mathbf{x}-\mathbf{z}|\geq\epsilon} d\mathbf{x} d\mathbf{z}\, G(\mathbf{x})\, f(\mathbf{x}, t + \Delta t \,|\mathbf{z}, t) f(\mathbf{z}, t \,|\mathbf{x_0}, t_0) \\
& - \iint d\mathbf{x} d\mathbf{z}\, G(\mathbf{z})\, f(\mathbf{x}, t + \Delta t \,|\mathbf{z}, t) f(\mathbf{z}, t \,|\mathbf{x_0}, t_0) \Bigg] \qquad (38)
\end{aligned}$$

where in the last line we have made $f(\mathbf{x}, t + \Delta t \,|\mathbf{z}, t)$ to appear artificially (note that the integration over $\mathbf{x}$ is simply one, and gives back the last term of Eq. (37) up to a renaming of the variable of integration).

In the first term ($|\mathbf{x}-\mathbf{z}| < \epsilon$), we will now expand $G(\mathbf{x})$ around $\mathbf{z}$ to the second order (we took G to be twice differentiable):

$$G(\mathbf{x}) = G(\mathbf{z}) + (x_i - z_i)\frac{\partial G(\mathbf{z})}{\partial z_i} + \frac{1}{2}(x_i - z_i)(x_j - z_j)\frac{\partial^2 G(\mathbf{z})}{\partial z_i \partial z_j} + |\mathbf{x}-\mathbf{z}|^2 R(\mathbf{x},\mathbf{z})$$

where $R(\mathbf{x},\mathbf{z})$ is a remainder term that goes to zero when $|\mathbf{x}-\mathbf{z}| \to 0$.

The first term of the right-hand side of Eq. (38) can thus be expanded as:

$$\begin{aligned}
&\iint_{|\mathbf{x}-\mathbf{z}|<\epsilon} d\mathbf{x}d\mathbf{z}\, G(\mathbf{z})\, f(\mathbf{x}, t+\Delta t\,|\mathbf{z}, t)f(\mathbf{z}, t\,|\mathbf{x_0}, t_0) \\
&\quad + \iint_{|\mathbf{x}-\mathbf{z}|<\epsilon} d\mathbf{x}d\mathbf{z} \left[(x_i - z_i)\frac{\partial G(\mathbf{z})}{\partial z_i}\right] f(\mathbf{x}, t+\Delta t\,|\mathbf{z}, t)f(\mathbf{z}, t\,|\mathbf{x_0}, t_0) \\
&+ \iint_{|\mathbf{x}-\mathbf{z}|<\epsilon} d\mathbf{x}d\mathbf{z} \left[\frac{1}{2}(x_i - z_i)(x_j - z_j)\frac{\partial^2 G(\mathbf{z})}{\partial z_i \partial z_j}\right] f(\mathbf{x}, t+\Delta t\,|\mathbf{z}, t)f(\mathbf{z}, t\,|\mathbf{x_0}, t_0) \\
&\quad + \iint_{|\mathbf{x}-\mathbf{z}|<\epsilon} d\mathbf{x}d\mathbf{z}\, |\mathbf{x}-\mathbf{z}|^2 R(\mathbf{x},\mathbf{z})\, f(\mathbf{x}, t+\Delta t\,|\mathbf{z}, t)f(\mathbf{z}, t\,|\mathbf{x_0}, t_0)
\end{aligned}$$

The first term can be grouped with the last term of Eq. (38) to give

$$-\iint_{|\mathbf{x}-\mathbf{z}|\geq\epsilon} d\mathbf{x}d\mathbf{z}\, G(\mathbf{z})\, f(\mathbf{x}, t+\Delta t\,|\mathbf{z}, t)f(\mathbf{z}, t\,|\mathbf{x_0}, t_0).$$

The last term will go to zero when $\epsilon \to 0$, therefore we stop writing it in the following expressions. We can now rewrite Eq. (38):

$$\begin{aligned}
\frac{\partial}{\partial t}\langle G(\mathbf{X}(t))\,|\mathbf{X}(t_0) = \mathbf{x_0}\rangle = \lim_{\Delta t\to 0}\frac{1}{\Delta t}\Bigg[\\
&+ \iint_{|\mathbf{x}-\mathbf{z}|<\epsilon} d\mathbf{x}d\mathbf{z}\, \frac{\partial G(\mathbf{z})}{\partial z_i}(x_i - z_i)\, f(\mathbf{x}, t+\Delta t\,|\mathbf{z}, t)f(\mathbf{z}, t\,|\mathbf{x_0}, t_0) \\
&+ \iint_{|\mathbf{x}-\mathbf{z}|<\epsilon} d\mathbf{x}d\mathbf{z}\, \frac{1}{2}\frac{\partial^2 G(\mathbf{z})}{\partial z_i \partial z_j}(x_i - z_i)(x_j - z_j)\, f(\mathbf{x}, t+\Delta t\,|\mathbf{z}, t)f(\mathbf{z}, t\,|\mathbf{x_0}, t_0) \\
&+ \iint_{|\mathbf{x}-\mathbf{z}|\geq\epsilon} d\mathbf{x}d\mathbf{z}\, G(\mathbf{z})\, f(\mathbf{z}, t+\Delta t\,|\mathbf{x}, t)f(\mathbf{x}, t\,|\mathbf{x_0}, t_0) \\
&- \iint_{|\mathbf{x}-\mathbf{z}|\geq\epsilon} d\mathbf{x}d\mathbf{z}\, G(\mathbf{z})\, f(\mathbf{x}, t+\Delta t\,|\mathbf{z}, t)f(\mathbf{z}, t\,|\mathbf{x_0}, t_0)\Bigg] \qquad (39)
\end{aligned}$$

(note that in the third term the names of the integration variables have been permuted for later simplification).

Taking the limit inside the $\mathbf{z}$ integral and performing the integration over $\mathbf{x}$ in the first two terms, we fall back on the definitions of the drift and diffusion coefficients (Eq. (35) and (36)) and get:

$$\int d\mathbf{z}\left[A_i(\mathbf{z}, t)\frac{\partial G(\mathbf{z})}{\partial z_i} + \frac{1}{2}B_{ij}(\mathbf{z}, t)\frac{\partial^2 G(\mathbf{z})}{\partial z_i \partial z_j}\right] f(\mathbf{z}, t\,|\mathbf{x_0}, t_0) + O(\epsilon)$$

Taking the limit inside the integrals of the last two terms makes the transition rate appear:

$$\iint_{|\mathbf{x}-\mathbf{z}|\geq\epsilon} d\mathbf{x}d\mathbf{z}\, G(\mathbf{z})\ [W(\mathbf{z}\,|\mathbf{x};t)f(\mathbf{x},t\,|\mathbf{x_0},t_0)-W(\mathbf{x}\,|\mathbf{z};t)f(\mathbf{z},t\,|\mathbf{x_0},t_0)]$$

and we finally get

$$\begin{aligned}\frac{\partial}{\partial t}\left\langle G(\mathbf{X}(t))\,|\mathbf{X}(t_0)=\mathbf{x_0}\right\rangle &= \\ \int d\mathbf{z}\ \left[A_i(\mathbf{z},t)\,\frac{\partial G(\mathbf{z})}{\partial z_i}+\frac{1}{2}B_{ij}(\mathbf{z},t)\frac{\partial^2 G(\mathbf{z})}{\partial z_i\partial z_j}\right] f(\mathbf{z},t\,|\mathbf{x_0},t_0)+O(\epsilon)& \\ +\iint_{|\mathbf{x}-\mathbf{z}|\geq\epsilon} d\mathbf{x}d\mathbf{z}\, G(\mathbf{z})\ [W(\mathbf{z}\,|\mathbf{x};t)f(\mathbf{x},t\,|\mathbf{x_0},t_0)-W(\mathbf{x}\,|\mathbf{z};t)f(\mathbf{z},t\,|\mathbf{x_0},t_0)] &\quad (40)\end{aligned}$$

We see that the parts corresponding to $|\mathbf{x}-\mathbf{z}|<\epsilon$ indeed led to the drift and diffusion term, while the parts with $|\mathbf{x}-\mathbf{z}|\geq\epsilon$ led to the jump term.

We now take the limit $\epsilon\to 0$:

$$\begin{aligned}\frac{\partial}{\partial t}\left\langle G(\mathbf{X}(t))\,|\mathbf{X}(t_0)=\mathbf{x_0}\right\rangle &= \\ \int d\mathbf{z}\ \left[A_i(\mathbf{z},t)\,\frac{\partial G(\mathbf{z})}{\partial z_i}+\frac{1}{2}B_{ij}(\mathbf{z},t)\frac{\partial^2 G(\mathbf{z})}{\partial z_i\partial z_j}\right] f(\mathbf{z},t\,|\mathbf{x_0},t_0)& \\ +\int d\mathbf{z}\, G(\mathbf{z})\int d\mathbf{x}\ [W(\mathbf{z}\,|\mathbf{x};t)f(\mathbf{x},t\,|\mathbf{x_0},t_0)-W(\mathbf{x}\,|\mathbf{z};t)f(\mathbf{z},t\,|\mathbf{x_0},t_0)] &\quad (41)\end{aligned}$$

where in pathological cases, the second term is actually the Cauchy principal value of the integral (as we haven't actually defined $W(\mathbf{x}\,|\mathbf{z};t)$ when $\mathbf{x}=\mathbf{z}$).

We will now integrate the first term by part, and must specify the boundary conditions. Those conditions depend on the domain of possible values of the process. For a $\mathbb{R}^n$-valued process, the conditions are usually that $f(\mathbf{z},t\,|\mathbf{x_0},t_0)$ and its derivatives go to zero when $|\mathbf{z}|\to+\infty$. We will assume that it is the case, but the surface term can also be shown to cancel for other cases. Integrating by parts the first term, we get:

$$\int d\mathbf{z}\, G(\mathbf{z})\left[-\frac{\partial}{\partial z_i}\left(A_i(\mathbf{z},t)\,f(\mathbf{z},t\,|\mathbf{x_0},t_0)\right)+\frac{1}{2}\frac{\partial^2}{\partial z_i\partial z_j}\left(B_{ij}(\mathbf{z},t)\,f(\mathbf{z},t\,|\mathbf{x_0},t_0)\right)\right]$$

as the surface terms cancel. Plugging this result into Eq. (41), and expressing the left-hand side according to its definition (plus taking the time derivative inside the integral) finally gives:

$$\begin{aligned}\int d\mathbf{z}\, G(\mathbf{z})\,\frac{\partial f(\mathbf{z},t\,|\mathbf{x_0},t_0)}{\partial t} &= \\ \int d\mathbf{z}\, G(\mathbf{z})\left[-\frac{\partial}{\partial z_i}\left(A_i(\mathbf{z},t)\,f(\mathbf{z},t\,|\mathbf{x_0},t_0)\right)+\frac{1}{2}\frac{\partial^2}{\partial z_i\partial z_j}\left(B_{ij}(\mathbf{z},t)\,f(\mathbf{z},t\,|\mathbf{x_0},t_0)\right)\right]& \\ +\int d\mathbf{z}\, G(\mathbf{z})\int d\mathbf{x}\ [W(\mathbf{z}\,|\mathbf{x};t)f(\mathbf{x},t\,|\mathbf{x_0},t_0)-W(\mathbf{x}\,|\mathbf{z};t)f(\mathbf{z},t\,|\mathbf{x_0},t_0)] &\quad (42)\end{aligned}$$

and as this equation holds for any (twice-differentiable) function G, the integrands are also equal:

$$\boxed{\begin{aligned}\frac{\partial f(\mathbf{z},t\,|\mathbf{x_0},t_0)}{\partial t} &= \int d\mathbf{x}\,\left[W(\mathbf{z}\,|\mathbf{x};t)f(\mathbf{x},t\,|\mathbf{x_0},t_0) - W(\mathbf{x}\,|\mathbf{z};t)f(\mathbf{z},t\,|\mathbf{x_0},t_0)\right] \\ &-\frac{\partial}{\partial z_i}\left(A_i(\mathbf{z},t)\,f(\mathbf{z},t\,|\mathbf{x_0},t_0)\right) + \frac{1}{2}\frac{\partial^2}{\partial z_i \partial z_j}\left(B_{ij}(\mathbf{z},t)\,f(\mathbf{z},t\,|\mathbf{x_0},t_0)\right)\end{aligned}} \tag{43}$$

This equation is called the differential Chapman-Kolmogorov equation, and it shows that we can define the process by giving its jump transition rate (first integral term) and its drift and diffusion coefficients (respectively second and third terms). The two times conditional PDF can then be computed from this differential equation, using the fact that $f(\mathbf{z},t_0\,|\mathbf{x},t_0) = \delta(\mathbf{z}-\mathbf{x})$ as the initial condition.

We will now detail the most important special cases. We first consider continuous processes (for which the jump transition rate $W(\mathbf{z}\,|\mathbf{x},t)$ must be zero), and then pure jump processes.

4.2.3 *The Liouville equation*

We first consider a continuous process ($W(\mathbf{z}\,|\mathbf{x},t) = 0$) for which the diffusion coefficient $B_{ij}(\mathbf{z},t)$ is zero. Eq. (43) then reduces to:

$$\frac{\partial f(\mathbf{z},t\,|\mathbf{x_0},t_0)}{\partial t} = -\frac{\partial}{\partial z_i}\left(A_i(\mathbf{z},t)\,f(\mathbf{z},t\,|\mathbf{x_0},t_0)\right) \tag{44}$$

in which we recognize the Liouville equation for the PDF of a deterministic system obeying the differential equation:

$$\frac{d\mathbf{z}}{dt} = \mathbf{A}(\mathbf{z},t) \quad ; \quad \mathbf{z}(t_0) = \mathbf{x_0}$$

The drift coefficients represents the deterministic part of the movement, and a stochastic process where only the drift coefficient is non-zero is simply a deterministic process. The framework of stochastic processes thus includes and extends all usual deterministic dynamical systems.

4.2.4 *The Fokker-Planck equation*

Let us now consider a more general continuous process. Eq. (43) becomes:

$$\boxed{\frac{\partial f(\mathbf{z},t\,|\mathbf{x_0},t_0)}{\partial t} = -\frac{\partial}{\partial z_i}\left(A_i(\mathbf{z},t)\,f(\mathbf{z},t\,|\mathbf{x_0},t_0)\right) + \frac{1}{2}\frac{\partial^2}{\partial z_i \partial z_j}\left(B_{ij}(\mathbf{z},t)\,f(\mathbf{z},t\,|\mathbf{x_0},t_0)\right)} \tag{45}$$

which is known as the Fokker-Planck equation (or forward-Kolmogorov equation). While the first term tends to conserve the volume occupied in state space (phase space) during time evolution according to the Liouville theorem, the second term tends to spread it, justifying its name of *diffusion* coefficient. A continuous Markov process is called a *diffusion process*.

In this case, the definitions of $\mathbf{A}$ and $\mathbf{B}$ (Eq. 35 and 36) can be simplified as:

$$A_i(\mathbf{z},t) = \lim_{\Delta t\to 0}\frac{1}{\Delta t}\int d\mathbf{x}\,(x_i - z_i)\,f(\mathbf{x},t+\Delta t\,|\mathbf{z},t) \tag{46}$$

$$B_{ij}(\mathbf{z},t) = \lim_{\Delta t\to 0}\frac{1}{\Delta t}\int d\mathbf{x}\,(x_i - z_i)(x_j - z_j)\,f(\mathbf{x},t+\Delta t\,|\mathbf{z},t) \tag{47}$$

4.2.5 *The Master equation*

A process for which $\mathbf{A}(\mathbf{z},t) = 0$, $\mathbf{B}(\mathbf{z},t) = 0$ and $W(\mathbf{z}\,|\mathbf{x},t) \neq 0$ is called a pure jump process. Its evolution is constituted of discontinuous jumps separated by constant phases. Eq. (43) takes the form:

$$\boxed{\frac{\partial f(\mathbf{z},t\,|\mathbf{x_0},t_0)}{\partial t} = \int d\mathbf{x}\,W(\mathbf{z}\,|\mathbf{x};t)f(\mathbf{x},t\,|\mathbf{x_0},t_0) - f(\mathbf{z},t\,|\mathbf{x_0},t_0)\int d\mathbf{x}\,W(\mathbf{x}\,|\mathbf{z};t)} \tag{48}$$

It is then called the Master Equation.

It is often used in cases where the state space is discrete (e.g. number of molecules in a chemical system), for which it takes the form:

$$\frac{\partial f(n,t\,|n_0,t_0)}{\partial t} = \sum_m W(n\,|m;t)f(m,t\,|n_0,t_0) - f(n,t\,|n_0,t_0)\sum_m W(m\,|n;t) \tag{49}$$

4.2.6 *Important examples*

4.2.6.1 *The Wiener process*

The simplest case of non-deterministic diffusion process is given by $A(z,t) = 0$, and $B(z,t) = 1$ (we consider here a one-dimensional process). Such a process W_t is called the Wiener process. It obeys the Fokker-Planck equation:

$$\frac{\partial f(z,t\,|x_0,t_0)}{\partial t} = \frac{1}{2}\frac{\partial^2 f(z,t\,|x_0,t_0)}{\partial z^2} \tag{50}$$

which is a diffusion equation with the well known solution (easily derived by use of the characteristic function/Fourier transform):

$$f(x,t\,|x_0,t_0) = \frac{1}{\sqrt{2\pi(t-t_0)}}\,e^{-\frac{(x-x_0)^2}{2(t-t_0)}} \tag{51}$$

(where we have used the natural initial condition $f(x, t_0 \,|x_0, t_0) = \delta(x - x_0)$). Using this expression in the general expansions of multi-times PDF for Markov processes (30), we see that the Wiener process is also a gaussian process. From this expression, one can also easily prove that at any time, the path is almost certainly non differentiable, despite being continuous. Sample path are thus extremely irregulars.

From Eq. 51, we can deduce the first moments of the Wiener process:

$$\langle W_t \,| W_{t_0} = x_0 \rangle = x_0 \tag{52}$$

$$\left\langle (W_t - x_0)^2 \,| W_{t_0} = x_0 \right\rangle = t - t_0 \tag{53}$$

$$\langle X_t X_s \,| W_{t_0} = x_0 \rangle = \min(t - t_0, s - t_0) + w_0^2 \tag{54}$$

One very important property of the Wiener process is the independence (and stationarity) of its increment. Consider a finite family of (ordered) times $(t_0, t_1, \ldots, t_n)$. As for any Markov process, the joint PDF of the values of the Wiener process at those times can be expressed as (Eq. (30)):

$$f(x_n, t_n; x_{n-1}, t_{n-1}; \ldots; x_0, t_0) = \prod_{i=0}^{n-1} f(x_{i+1}, t_{i+1} \,| x_i, t_i) f(x_0, t_0)$$

and using the expression of the conditional PDF (51):

$$f(x_n, t_n; x_{n-1}, t_{n-1}; \ldots; x_0, t_0) = \prod_{i=0}^{n-1} \frac{1}{\sqrt{2\pi(t_{i+1} - t_i)}} e^{-\frac{(x_{i+1} - x_i)^2}{2(t_{i+1} - t_i)}} f(x_0, t_0)$$

If we now define the increments of the Wiener process as $\Delta W_i = W_{t_i} - W_{t_{i-1}}$, and $\Delta t_i = t_i - t_{i-1}$, we can deduce the joint PDF for the increments and the initial value of the process:

$$f_{\Delta W_n \ldots \Delta W_1 \, W_0}(\Delta x_n; \Delta x_{n-1}; \ldots; \Delta x_1; x_0) = \prod_{i=1}^{n} \frac{1}{\sqrt{2\pi \Delta t_i}} e^{-\frac{\Delta x_i^2}{2\Delta t_i}} f(x_0, t_0)$$

which shows that the increments of the Wiener process are independent of each other and of the initial value W_{t_0} (and that they are stationary as their PDFs only depend on the Δt_i). This property will be extremely useful to define stochastic integration and Itō stochastic differential equations, but also for numerical simulations of diffusion processes.

It is however obvious from expression (51) that the Wiener process has no stationary distribution. The Wiener process is always spreading further and further from its starting point (Eq. (53)).

4.2.6.2 *The Ornstein-Uhlenbeck process*

The simplest diffusion process which possesses a stationary distribution is the Ornstein-Uhlenbeck process (abbreviated as OU process). It is defined as (once again we consider a one-dimensional process, but a multidimensional OU process can be defined similarly) $A(x,t) = -k(x-\mu)$ and $B(x,t) = D$. It is similar to the Wiener process, but with a linear restoring drift term. It obeys the Fokker-Planck equation:

$$\frac{\partial f(z,t\,|x_0,t_0)}{\partial t} = \frac{\partial}{\partial z}\left(k(x-\mu)f(z,t\,|x_0,t_0)\right) + \frac{1}{2}D\frac{\partial^2 f(z,t\,|x_0,t_0)}{\partial z^2} \tag{55}$$

of which the solution is:

$$f(x,t\,|x_0,t_0) = \frac{1}{\sqrt{\pi\frac{D}{k}(1-e^{-2kt})}} e^{-\frac{(x-\mu-(x_0-\mu)e^{-kt})^2}{\frac{D}{k}(1-e^{-2kt})}} \tag{56}$$

which converges towards the stationary PDF:

$$f_s(x) = \sqrt{\frac{k}{\pi\, D}}\,\exp\left(-\frac{k\,(x-\mu)^2}{D}\right) \tag{57}$$

4.3 STOCHASTIC DIFFERENTIAL EQUATIONS

4.3.1 *Langevin equations and definition problems*

Very often, we wish to start from a deterministic model, and add a stochastic component to build a more complete stochastic model. It is thus natural to look for a way to generalize the formalism of differential equations to stochastic process. This leads to what are called in physics Langevin equations, for instance:

$$\frac{dy}{dt} = a(y,t) + b(y,t)\,\xi(t) \tag{58}$$

where $\xi(t)$ is a random fluctuating function of time. Most often, the fluctuation timescale is supposed to be much shorter than the "average" dynamics of the equation, and ξ is thus idealized as a completely uncorrelated noise called *white noise*, that is verifying $\langle\xi(t)\xi(s)\rangle = \delta(t-s)$ and $\langle\xi(t)\rangle = 0$ (we can normalize it by including any mean and scaling in a and b). However, the definition of such an equation is somewhat problematic. Let us first try to properly define what kind of stochastic process $\xi(t)$ is.

By writing Eq. 58, we usually assume that it is integrable, and that an integral such as $\int_0^t \xi(s)\,ds$ exists. Another expectation is the continuity of the solution, so that we might expect the process $X_t = \int_0^t \xi(s)\,ds$ to be continuous. This implies then that X_t is a Markov process. We can indeed split the integral into two statistically independent term: $\int_0^t \xi(s)\,ds = \int_0^{t'} \xi(s)\,ds + \int_{t'}^t \xi(s)\,ds =$

$\lim_{\epsilon\to 0}\left(\int_0^{t'-\epsilon}\xi(s)\,ds\right)+\int_{t'}^{t}\xi(s)\,ds$, thus showing that the increment $X_t - X_{t'}$ is independent of $X_{t'}$ and of X_s for any $s < t'$. It is thus a diffusion process, and we can compute its drift and diffusion coefficients from Eq. 46 and 47:

$$A(x,t) = \lim_{\Delta t\to 0}\langle X_{t+\Delta t} - X_t \,|X_t = x\rangle = 0$$
$$B(x,t) = \lim_{\Delta t\to 0}\left\langle (X_{t+\Delta t} - X_t)^2 \,|X_t = x\right\rangle = 1$$

$\int_0^t \xi(s)\,ds$ is thus simply the Wiener process. It is then not differentiable (at any point), which conflicts with its definition as an integral. The Langevin equation (Eq. 58) is thus not properly defined in this differential form. However, we might want to replace $\xi(s)\,ds$ with $dW(s)$ the infinitesimal increment of the Wiener process and write it in integral form as:

$$\int_0^T dy(t) = \int_0^T a(y,t)\,dt + \int_0^T b(y,t)\,dW(t) \tag{59}$$

The last integral is a kind of Riemann-Stieltjes integral with respect to the random function $W(t)$ but remains to be properly defined.

4.3.2 *Itō integral and Itō stochastic differential equations*

We can try to define the stochastic integral $\int_0^T G(t)\,dW(t)$ as a Riemann-Stieltjes integral:

$$\int_0^T G(t)\,dW(t) = \lim_{N\to+\infty}\sum_{i=0}^{N-1} G(\tau_i)\,(W(t_{i+1}) - W(t_i))$$

with $t_i = i\frac{T}{N}$ and $\tau_i \in [t_i, t_{i+1}]$. For usual Riemann-Stieltjes integrals $\int_0^T G(t)\,df(t)$ where $f(t)$ is a deterministic function, the choice of the τ_i does not matter in the definition of the integral. But when integrating with respect to a stochastic process, it does. To see it, let us compute $\int_0^T W(t)dW(t)$. It is itself a random variable, and we are interested in its mean. Let us call:

$$S_n = \sum_{i=0}^{N-1} W(\tau_i)\,(W(t_{i+1}) - W(t_i))$$

Then:

$$\begin{aligned}\langle S_n\rangle &= \sum_{i=0}^{N-1}\langle W(\tau_i)W(t_{i+1})\rangle - \langle W(\tau_i)W(t_i)\rangle \\ &= \sum_{i=0}^{N-1}\min(\tau_i, t_{i+1}) - \min(\tau_i, t_i) \quad \text{(from Eq 54)} \\ &= \sum_{i=0}^{N-1} t_{i+1} - \tau_i\end{aligned}$$

if we chose $\tau_i = \alpha t_i + (1-\alpha)t_{i+1}$ for some $\alpha \in [0,1]$:

$$\langle S_n \rangle = \sum_{i=0}^{N-1} \alpha(t_{i+1} - t_i) = \alpha T$$

The mean value of the integral thus depends on the choice of α, leading to several possible definitions of stochastic integrals.

The Itō integral corresponds to the choice $\tau_i = t_i$, and is defined as:

$$\int_0^T G(t)dW(t) = \lim_{N\to+\infty} \sum_{i=0}^{N-1} G(t_i)\left(W(t_{i+1}) - W(t_i)\right) \tag{60}$$

(where the limit is a mean-square limit).

An Itō stochastic differential equation (or Itō SDE) is an equation of the form of Eq. 59 where the stochastic integral is interpreted as an Itō integral. It is often written using a short-hand differential notation:

$$dY = a(Y,t)\,dt + b(Y,t)\,dW(t) \tag{61}$$

In the context of stochastic differential equations, only integrals of what are called *non-anticipating functions* will occur. A non-anticipating function with respect to a Wiener process W is a function (possibly random), whose value at any time t is independent of the future increments of the Wiener process $W(s) - W(t)$ for $s > t$. Simply put, it is a (random) function whose value at time t is only influenced by the past. All solutions to Itō stochastic differential equations (Itō SDE) are non-anticipating. The Itō integral is particularly adapted to such functions, as the sum in its definition (Eq. 60) then only includes product of independent variables ($G(t_i)$ and $(W(t_{i+1}) - W(t_i))$ are independent).

Important properties of the Itō integral for non-anticipating integrand are:

$$\left\langle \int_0^T G(t)dW(t) \right\rangle = 0 \tag{62}$$

which comes directly from the independence of the terms in the defining sum and the fact that the increments of the Wiener process have a zero mean, and:

$$\left\langle \int_0^T G(t)dW(t) \int_0^T H(t)dW(t) \right\rangle = \int_0^T \langle G(t)H(t)\rangle\, dt \tag{63}$$

which can be similarly proven by using the same independence argument and rearranging the sums.

4.3.3 *Itō's lemma for variable changes*

This last equation (Eq. 63), added to the fact that $\langle dW^2 \rangle = dt$ (Eq. 53), hints at the fact that dW behave as some kind of infinitesimal of order $1/2$ compared

to dt. As dW is not formally defined outside of an integral, this idea can be proven by showing that:

$$\int_0^T G(t)\,[dW(t)]^2 = \int_0^T G(t)dt \tag{64}$$

Using the definition in term of mean-square limit, we thus want to compute:

$$\lim_{N\to+\infty}\left\langle\left[\sum_i G_{i-1}(\Delta W_i^2-\Delta t_i)\right]^2\right\rangle = \lim_{N\to+\infty}\sum_i\left\langle G_{i-1}^2(\Delta W_i^2-\Delta t_i)^2\right\rangle + 2\lim_{N\to+\infty}\sum_{\substack{i,j\\ i>j}}\left\langle G_{i-1}G_{j-1}(\Delta W_j^2-\Delta t_j)(\Delta W_i^2-\Delta t_i)\right\rangle$$

where $\Delta W_i = W(t_{i+1}) - W(t_i)$ and $\Delta t_i = t_{i+1} - t_i$. Using the independence property of non-anticipating functions, we can split the average products:

$$\lim_{N\to+\infty}\left\langle\left[\sum_i G_{i-1}(\Delta W_i^2-\Delta t_i)\right]^2\right\rangle = \lim_{N\to+\infty}\sum_i\left\langle G_{i-1}^2\right\rangle\left(\left\langle\Delta W_i^4\right\rangle - 2\left\langle\Delta W_i^2\right\rangle\Delta t_i + \Delta t_i^2\right) + 2\lim_{N\to+\infty}\sum_{\substack{i,j\\ i>j}}\left\langle G_{i-1}G_{j-1}(\Delta W_j^2-\Delta t_j)\right\rangle\left(\left\langle\Delta W_i^2\right\rangle - \Delta t_i\right)$$

The second term is clearly zero as $\left\langle\Delta W_i^2\right\rangle = \Delta t_i$. Moreover, knowing that $\Delta W_i \sim \mathcal{N}\left(0, \sqrt{\Delta t_i}\right)$, we have $\left\langle\Delta W_i^4\right\rangle = 3\Delta t_i^2$, so that:

$$\lim_{N\to+\infty}\left\langle\left[\sum_i G_{i-1}(\Delta W_i^2-\Delta t_i)\right]^2\right\rangle = 2\lim_{N\to+\infty}\sum_i\left\langle G_{i-1}^2\right\rangle\Delta t_i^2 = 0$$

which proves Eq. 64. Similar demonstrations show that higher order terms (dW^3, $dtdW$, ...) vanish.

The result is that in all practical manipulations of Itō SDE, we can use the formal rule $dW^2 = dt$. The most important result is that the usual chain rule for variable change is modified. Suppose we have a stochastic diffusion process X_t obeying the Itō SDE $dX_t = a(X_t,t)dt + b(X_t,t)dW_t$, and consider a (deterministic) function $f(x,t)$. We are interested in the process $Y_t = f(X_t,t)$. Keeping in mind that only terms in dt, dW and dW^2 survive in the integrals, we can expand:

$$\begin{aligned} dY_t &= \frac{\partial f}{\partial t}dt + \frac{\partial f}{\partial x}dX_t + \frac{1}{2}\frac{\partial^2 f}{\partial x^2}dX_t^2 \\ &= \frac{\partial f}{\partial t}dt + \frac{\partial f}{\partial x}\left(a(X_t,t)dt + b(X_t,t)dW_t\right) + \frac{1}{2}\frac{\partial^2 f}{\partial x^2}b^2(X_t,t)dW_t^2 \end{aligned}$$

which finally gives the SDE for Y_t:

$$\boxed{dY_t = \left[\frac{\partial f}{\partial t} + \frac{\partial f}{\partial x}a(X_t,t) + \frac{1}{2}\frac{\partial^2 f}{\partial x^2}b^2(X_t,t)\right]dt + \frac{\partial f}{\partial x}b(X_t,t)dW_t} \tag{65}$$

This result is known as Itō's lemma, where we notice the additional term $\frac{1}{2}\frac{\partial^2 f}{\partial x^2}b^2(X_t,t)\,dt$ compared to the usual chain rule.

4.3.4 *Stochastic differential equations and their corresponding Fokker-Planck equations*

This important result allows us to now relate the coefficients of the SDE (Eq. 61) to the coefficients in the Fokker-Planck equation for the diffusion process. Using Itō's lemma (Eq. 65) for a function G depending on x only, we find that:

$$\frac{d}{dt}\langle G(X_t)\rangle = \left\langle \frac{\partial G}{\partial x}a(X_t,t)\right\rangle + \frac{1}{2}\left\langle \frac{\partial^2 G}{\partial x^2}b^2(X_t,t)\right\rangle$$

We can now express the averages using the PDF $f(x,t\,|x_0,t_0)$:

$$\frac{d}{dt}\int dx\, G(x)\, f(x,t\,|x_0,t_0) = \int dx\, \left[\frac{\partial G(x)}{\partial x}a(x,t) + \frac{1}{2}\frac{\partial^2 G(x)}{\partial x^2}b^2(x,t)\right] f(x,t\,|x_0,t_0)$$

Finally, performing integration by part (we suppose again here that the surface terms cancel due e.g. to natural boundary conditions), we obtain:

$$\int dx\, G(x)\frac{df}{dt}(x,t\,|x_0,t_0) = \int dx\, \left(-G(x)\frac{\partial}{\partial x}\left[a(x,t)\, f(x,t\,|x_0,t_0)\right] + G(x)\frac{1}{2}\frac{\partial^2}{\partial x^2}\left[b^2(x,t)\, f(x,t\,|x_0,t_0)\right]\right)$$

And finally:

$$\frac{df(x,t\,|x_0,t_0)}{dt} = -\frac{\partial}{\partial x}\left[a(x,t)\, f(x,t\,|x_0,t_0)\right] + \frac{1}{2}\frac{\partial^2}{\partial x^2}\left[b^2(x,t)\, f(x,t\,|x_0,t_0)\right] \tag{66}$$

Which is the Fokker-Planck equation (Eq. 45), and we see that the coefficients defined for general Markov processes (Eq. 35 and 36) are simply related to those of the Itō SDE (Eq. 61) by $A(x,t) = a(x,t)$ and $B(x,t) = b^2(x,t)$.

Part II

DUST : TEMPERATURE FLUCTUATIONS AND SURFACE CHEMISTRY

5

A SIMPLE DUST MODEL

As said in Sect. 2, small grains have fluctuating temperatures due to single UV-photon absorptions. This is likely to affect the chemistry occurring on their surface, by causing massive desorption during the temperature spikes and keeping the chemical reactions out of equilibrium, as will be seen in the following chapters. We solve this problem for the case of H_2 formation on dust, as it occurs in UV-rich environments such as dense PDRs, or diffuse clouds, where the formation efficiency of H_2 determines the atomic-to-molecular transition. More complex surface chemistry is restricted to the inner parts of dense clouds where most of the UV radiation has been extinguished and where the dust grains are also probably bigger, and dust temperature fluctuations are thus less important in these regions (but the effect of secondary UV photons or cosmic rays may be worth investigating in terms of fluctuations).

This chapter presents the physical model that we use to tackle this problem. It is kept simple on purpose in order to allow for a solution, but all major physical processes are included. The neglected aspects will be noted along the description of the model. In particular, the physisorption- and chemisorption-based mechanisms are kept independant for simplicity. Cazaux and Tielens [2004] have shown that taking into account the interactions bewteen physisorbed and chemisorbed atoms could lead to a higher H_2 formation efficiency on warm grains. The formalism that we develop in the next three chapters could be adapted to a more complete microphysical model in future developments of this work.

Our focus is on the physics governing the grain temperature, and on the chemistry occurring on its surface, especially H_2 formation. Processes related to the destruction or processing of the dust grain itself by its environment are left aside. The dust grain is thus taken as an inert substrate on which chemistry between adsorbed species occur, and only its thermal state is dynamically followed. Because of our focus on H_2 formation in PDR regions, we consider neither the possible ice coating of the grain, nor ice chemistry and processing occurring inside the ice layer. Chemistry is supposed to occur only at the grain surface.

All dust data in this model come from the `DustEM` code, and are described in Compiègne et al. [2011]. They are gathered from various references which are given along the description of the model.

5.1 DUST-RADIATION INTERACTIONS

Dust is mostly known for its interaction with radiation, causing extinction, reddening and scattering. In addition to its observational effects for background objects, this interaction with light also controls in most situations the temperature of dust grains, which are heated by photon absorptions, and cool by emitting (mostly IR) photons. In our model, we assume that thermal balance of dust grains is completely controlled by radiative processes. One must keep in mind that in dark and very dense clouds, the collisional interactions with the gas can dominate over the heating by the radiation field, in which case the temperatures of the grains tend to equal the gas temperature. This specific regime will not be described by our model.

5.1.1 *Heat capacity*

The ability of the grain material to store thermal energy is described by its heat capacity, which relates its thermal energy to its temperature. To accurately describe the grain behavior, we take into account the temperature dependance of heat capacities, corresponding to the opening of new internal modes at higher temperatures. The thermal energy E of the grain is thus related to its temperature T by:

$$E(T) = \int_0^T C(T')\, dT' \tag{67}$$

where $C(T)$ is the total heat capacity of the grain. We will repeatedly use notations such as $E(T)$ to denote the thermal energy corresponding to temperature T, and $T(E)$ to denote the temperature corresponding to thermal energy E. Note that we exclude any zero point energy[1] from the definition of our thermal energy so that $E(0) = 0$.

For carbonaceous grains, we use graphite properties for both graphite grains and amorphous carbon grains (taking a mass density $\rho = 1.81\,\mathrm{g.cm^{-3}}$ for amorphous carbon, and $\rho = 2.24\,\mathrm{g.cm^{-3}}$ for graphite, following Compiègne et al. [2011]). The graphite heat capacity is taken from Draine and Li [2001]. For silicate grains, the heat capacity is also from Draine and Li [2001], obtained by fitting a Debye model to experimental data from Leger et al. [1985] (with a mass density of $\rho = 3.5\,\mathrm{g.cm^{-3}}$). The case of PAHs will be discussed in Sect. 5.1.5. The resulting heat capacity per unit mass for amorphous carbon and silicate materials is shown in Fig. 14.

1 We also neglect discretization of the lowest energy states.

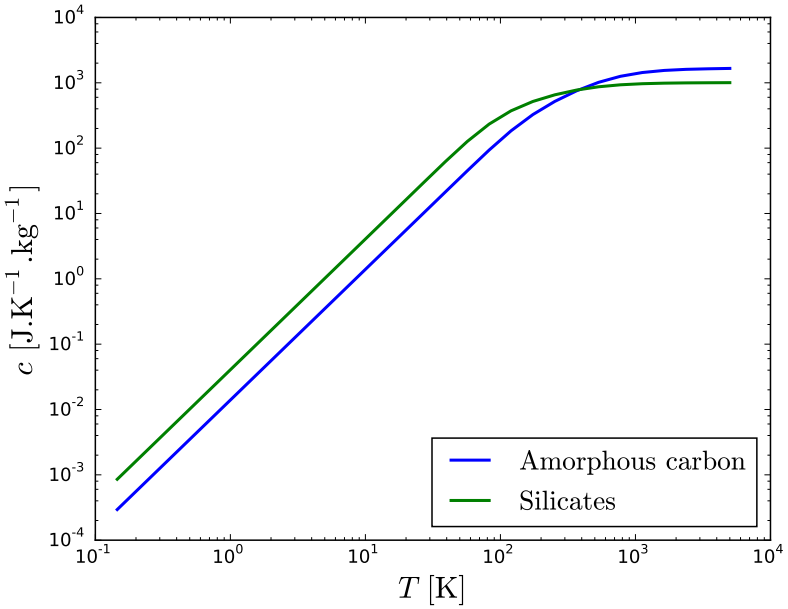

Figure 14: Massic heat capacity for amorphous carbon grains and for silicate grains, as functions of the grain temperature. See the text for references.

5.1.2 *Radiative processes for a spherical dust grain*

Real grains are of course of complex shapes. Growth of the grains by sticking collisions should lead to complex quasi-fractal shapes as illustrated by interplanetary dust grains found in the Solar System (Fig. 15), while processing by energetic events (photons, cosmic rays, collisions) tends to make the grains more compact. Moreover, the asymmetry of the grains shape is apparent through the polarization of starlight discovered long ago (Hall [1949]), and due to grains alignment by a complex combination of mechanisms (see Draine [2004b] for an introduction).

For our purpose, considering simplified spherical grains is sufficient. We characterize the size of a grain by its radius a. Due to its small size, a grain absorbs photons with an efficiency that varies with wavelength (or photon energy). This absorption efficiency is characterized for each grain by its *absorption cross section*, $\sigma_{\text{abs}}(U)$ defined as a function of the photon energy U (in all the following, we use photon energy rather than wavelength or frequency as it makes the expression of the grain energy balance simpler and clearer). The absorption cross section is defined so that if a unidirectional radiation field of flux $F_U(U)$ (in S.I. units W.m^{-2}.J^{-1}) irradiates the grain, the total power absorbed by the grain is $\int dU\, \sigma_{\text{abs}}(U) F_U(U)$.

The absorption cross-section depends on the size a and the composition of the grain. However, in the macroscopic limit $a \gg \lambda$, the absorption cross-section tends toward the geometrical cross-section of the grain πa^2. It is

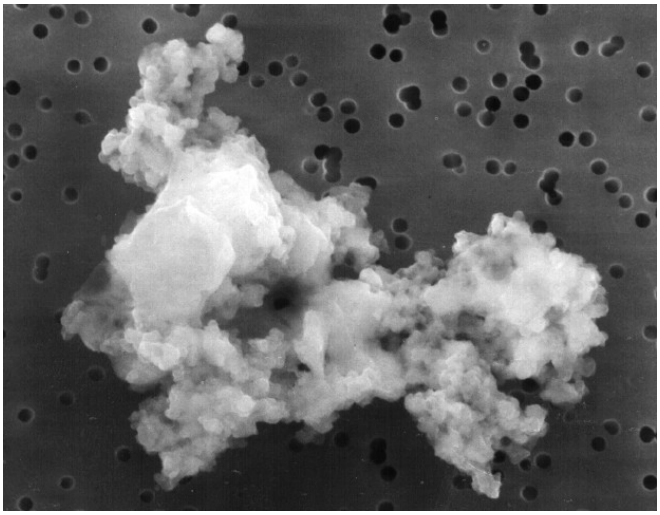

Figure 15: Interplanetary dust particle (10 μm) collected in the stratosphere by a U2 aircraft (NASA).

thus natural to characterize the grain absorption property by a dimensionless *absorption coefficient* defined as:

$$Q_{\rm abs}(U) = \frac{\sigma_{\rm abs(U)}}{\pi a^2} \tag{68}$$

As described in Compiègne et al. [2011], the optical properties for amorphous carbon grains are taken from Colangeli et al. [1995], they corresponds to a sp^2-rich hydrogenated amorphous carbon material believed to be more representative of carbonaceous interstellar dust material than the graphite used in the model of Draine and Li [2007], and the absorption cross sections are computed from these properties using Mie calculations. For silicate grains, the optical properties are taken from Draine [2003a]. PAHs are discussed in Sect. 5.1.5. The absorption coefficients for amorphous carbon grains and silicate grains are displayed on Fig. 16 and 17.

For a grain submitted to a general radiation field of intensity $I_U(U,\theta,\phi)$ (in S.I. units W.m^{-2}.J^{-1}.sr^{-1}, the angles θ and ϕ giving the direction), and assuming spherical symmetry for the grain (the absorption properties are the same for every part of the surface), the absorbed power at photon energy U (per unit photon energy) can be simply expressed as:

$$\begin{aligned} P_U^{\rm abs}(U) &= \int_0^{\pi} d\theta \int_0^{2\pi} d\phi\, a^2\, \pi\, J(U)\, Q_{\rm abs}(U) \\ &= 4\pi^2 a^2 Q_{\rm abs}(U)\, J(U) \end{aligned} \tag{69}$$

where $J(U) = \frac{1}{4\pi} \int_\Omega I_U\, d\Omega$ is the mean intensity, i.e. the average of $I_U(U,\theta,\phi)$ over all directions. This simplified expression is not valid if the absorption properties of the grain are not spherically symmetric, and explicit integration over all directions seen by all points of the surface must then be performed.

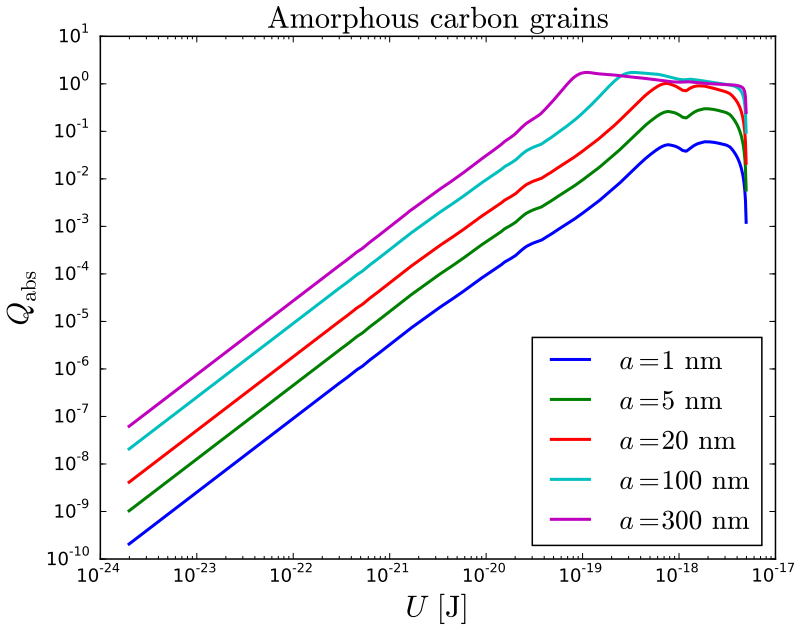

Figure 16: Absorption coefficients as functions of the photon energy for amorphous carbon grains. See the text for references.

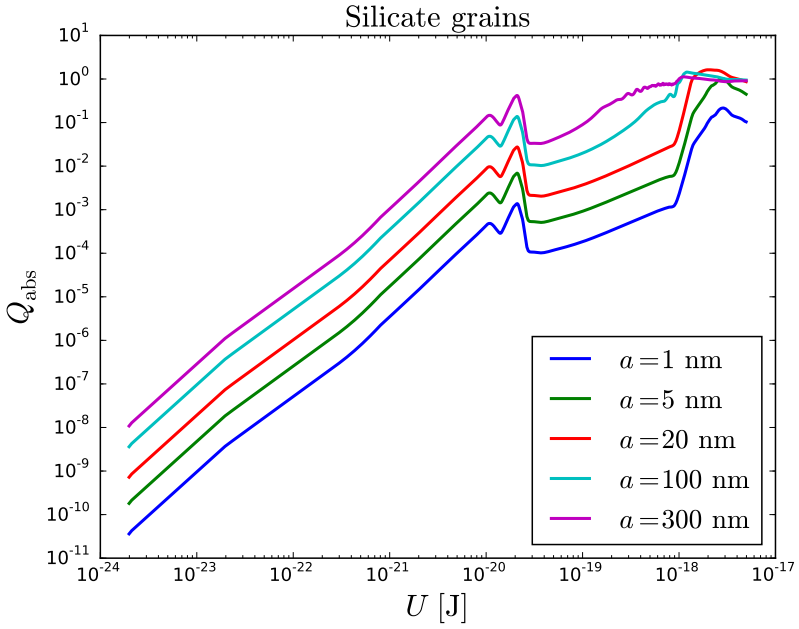

Figure 17: Absorption coefficients as functions of the photon energy for silicate grains. See the text for references.

The simplification can be seen from the fact that a spherically symmetric grain is insensitive to the anisotropies of the radiation field (for the absorbed power which is not a directed quantity; it would be different if we were considering the transfer of momentum).

The total absorbed power is then:

$$P_{\rm abs} = 4\pi^2 a^2 \int_0^{+\infty} dU\, Q_{\rm abs}(U)\, J(U) \tag{70}$$

In the following, the discrete nature of photons will be of central importance, as it will be the cause of the fluctuations of grain temperatures. We are thus not only interested in the average power absorbed by the grain, but also by the rate $R_{\rm abs}(U)$ of absorption of photons of energy U (per unit photon energy):

$$R_{\rm abs}(U) = 4\pi^2 a^2 Q_{\rm abs}(U)\, \frac{J(U)}{U} \tag{71}$$

The random process of the absorption of photons by the grain can be described by a Poisson process of rate $R_{\rm abs}(U)$.

Grains also emit thermally. We use the usual grey body approximation : by consideration of a situation where the grain would be at thermal equilibrium with the radiation field, we can see that a grain at temperature T must emit with a surfacic intensity $Q_{\rm abs}(U)\, B_U(U,T)$, where

$$B_U(U,T) = \frac{2}{h^3 c^2} \frac{U^3}{e^{\frac{U}{k_{\rm B}T}} - 1} \tag{72}$$

is the black body intensity at temperature T. The total power emitted by the grain at photon energy U (per unit photon energy) is thus:

$$P_U^{\rm em}(U,T) = 4\pi^2 a^2 Q_{\rm abs}(U)\, B_U(U,T) \tag{73}$$

Due to the small size of the grain, we have to take into account one physical restriction for this emitted power. As small grains have very small heat capacities, their total thermal energy can be of the same order as the energy of an infrared photon. As a grain cannot emit a photon that would take away more energy than its thermal energy content, the emission spectrum stops at this energy. Consequently, the total emitted power is:

$$P_{\rm em}(T) = 4\pi^2 a^2 \int_0^{E(T)} dU\, Q_{\rm abs}(U)\, B_U(U,T), \tag{74}$$

and the rate of photon emission at photon energy U (per unit photon energy) is:

$$R_{\rm em}(U,T) = 4\pi^2 a^2 Q_{\rm abs}(U)\, \frac{B_U(U,T)}{U} \tag{75}$$

The photon emission process is also a Poisson process, with rate $R_{\rm em}(U,T)$.

Scattering will not play any role in our model as it does not affect the state of the grain. As said previously, we also neglect photoprocessing of the dust (which can lead to a modification of the size and shape of the grain).

5.1.3 *External radiation field*

The radiation field that we use to illuminate the grains is a standard interstellar radiation field, whose UV component is scaled by a factor χ to represent the possible presence of close stars. This radiation field is the same as the incident radiation field of the `Meudon PDR Code`. It is based on the standard interstellar radiation field described in Mathis et al. [1983], with the following modifications :

- the fit of the near-IR and visible components has been redone using DIRBE data
- a more detailed contribution to the IR from dust emission of the surrounding environment has been added, computed by `DustEM` (Compiègne et al. [2011])

Only the UV component is scaled by the factor χ, to represent the possible proximity of bright stars.

The resulting radiation field for different values of χ is shown on Fig. 18. This field is used to irradiate the grains in all the models that we will present, unless specified otherwise.

The intensity of the UV field is usually quantified using:

$$G_0 = \frac{1}{u_{\text{Habing}}} \int_{912\,\mathring{A}}^{2400\,\mathring{A}} u_\lambda(\lambda)\, d\lambda \tag{76}$$

where u_λ is the energy density of the radiation field, and $u_{\text{Habing}} = 5.3 \times 10^{-14}\,\text{erg.cm}^{-3}$ is the integral between 912 Å and 2400 Å of the standard radiation of Habing [1968]. We will usually give the intensity of the radiation field in terms of G_0 rather than χ.

5.1.4 *Equilibrium temperature*

If the discrete nature of photons is neglected, the grain reaches an equilibrium state where the absorbed and emitted power balance each other. This equilibrium defines a characteristic temperature that is usually called the *equilibrium temperature* of the grain T_{eq}:

$$P_{\text{em}}(T_{\text{eq}}) = P_{\text{abs}} \tag{77}$$

where P_{abs} and $P_{\text{em}}(T)$ are defined respectively in Eq. 70 and 74. The resulting equilibrium temperature is shown on Fig. 19 for amorphous carbon grains and on Fig. 20 for silicate grains.

When taking into account discrete photon absorption and emission events, no such equilibrium exists and the temperature fluctuates in time. However, if the radiation field is stationary, a statistical equilibrium exists (where the

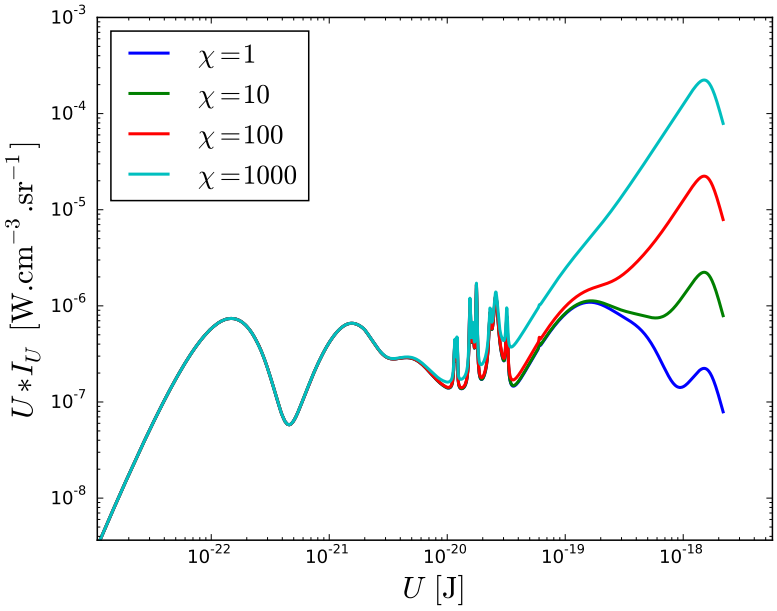

Figure 18: Interstellar radiation field as a function of photon energy for different values of the scaling factor χ. The field stops at the Lyman limit ($U_{\text{Lyman}} = 2.18 \times 10^{-18}$ J) and is zero above it.

statistical properties of the temperature are constant), as is described in Chapter 6.

If the grain is big enough so that its internal energy is large compared to the energy of individual photons, fluctuations become negligible and the equilibrium temperature T_{eq} is a good approximation of the temperature of the grain. One way to define a frontier to this continuous regime is to compare the thermal energy that the grain would have at the equilibrium temperature to the maximum photon energy. In the situations of interest to us (neutral gas), a natural cut is present in the radiation field at the Lyman limit $U_{\text{Lyman}} = 2.178655 \times 10^{-18}$ J. The equilibrium temperature is thus expected to become a good approximation when:

$$E(T_{\text{eq}}) \gg U_{\text{Lyman}} \tag{78}$$

The corresponding frontier is displayed on Fig. 19 and 20. The equilibrium temperature approximation is thus valid only for the biggest grain sizes under an unshielded radiation field. Note that if we consider grains deeper inside a cloud where the UV radiation field has been extinguished by dust and H_2 absorption, the effective maximal photon energy is much reduced and the equilibrium temperature is valid for a larger range of grain sizes. Yet, as will be shown later, small grains still undergo temperature fluctuations caused by near-IR photons (emitted by the dust at the edge of the cloud).

A more precise determination of the frontier should more carefully define the maximal photon energy as the maximal photon energy where significant

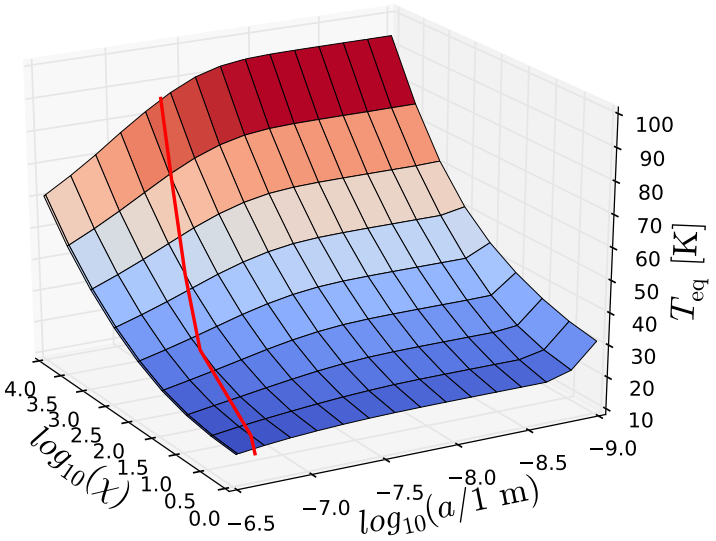

Figure 19: Equilibrium temperature T_{eq} of an amorphous carbon grain as a function of its size a and of the radiation field scaling factor χ. The red line marks the frontier where $E(T_{eq}) = 10 \times U_{Lyman}$, so that the equilibrium temperature is meaningful to the left of this frontier. The grain sizes go from 300 nm down to 1 nm.

power is transmitted to the grain. If high energy photons are present but do not carry a significant part of the power, they will cause temperature fluctuations but those will be too rare to affect the average temperature of the grain, for which the equilibrium temperature will then be a precise approximation.

5.1.5 *PAHs*

PAHs are not directly compatible with the picture described above in two ways.

First, they are single molecules, with a discrete spectrum of vibrational modes, and the definition of a temperature and of a continuous heat capacity at low energy is an oversimplification. Given a discrete set of energy states $\{E_i\}$, the statistical equilibrium corresponding to temperature T is given by a Boltzmann distribution of the level probabilities:

$$p_i = \frac{e^{-\frac{E_i}{kT}}}{\sum_j e^{-\frac{E_j}{kT}}} \tag{79}$$

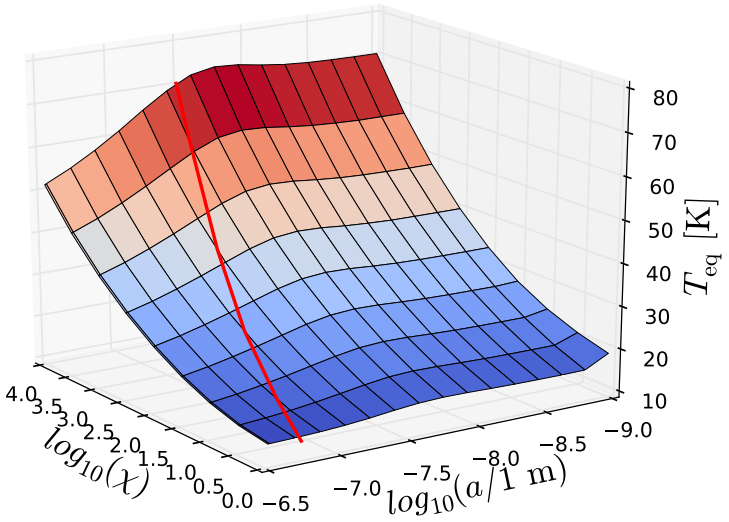

Figure 20: Same as Fig. 19 for silicate grains.

For any energy E, one can thus define a corresponding temperature as the temperature T at which the expected energy for the statistical equilibrium is equal to E:

$$E = \overline{E}(T) = \frac{\sum_i E_i \, e^{-\frac{E_i}{kT}}}{\sum_i e^{-\frac{E_i}{kT}}} \tag{80}$$

The heat capacity can then be defined as

$$C(T) = \frac{d\overline{E}(T)}{dT} \tag{81}$$

Such a detailed model of PAHs is constructed in Draine and Li [2001], using a Debye model for the vibrational modes of the carbon skeleton, and additional modes at the known frequencies for C-H bending and stretching modes. They perform both a detailed calculation of PAH excitation with the full discrete spectrum, and an approximate "thermal" model of the temperature fluctuations using the heat capacity defined as Eq. 81 from the detailed excitation model. They show that the results are in very good agreement. We will thus neglect the discrete excitation spectrum of PAHs, and treat them as solid grains using the heat capacity from Draine and Li [2001]. The absorption coefficients are those from Draine and Li [2007] with additional modifications described in Compiègne et al. [2011].

The second difference is that they cannot be considered spherical. Single PAHs are disk-like flat structures. For bigger sizes a structural change is

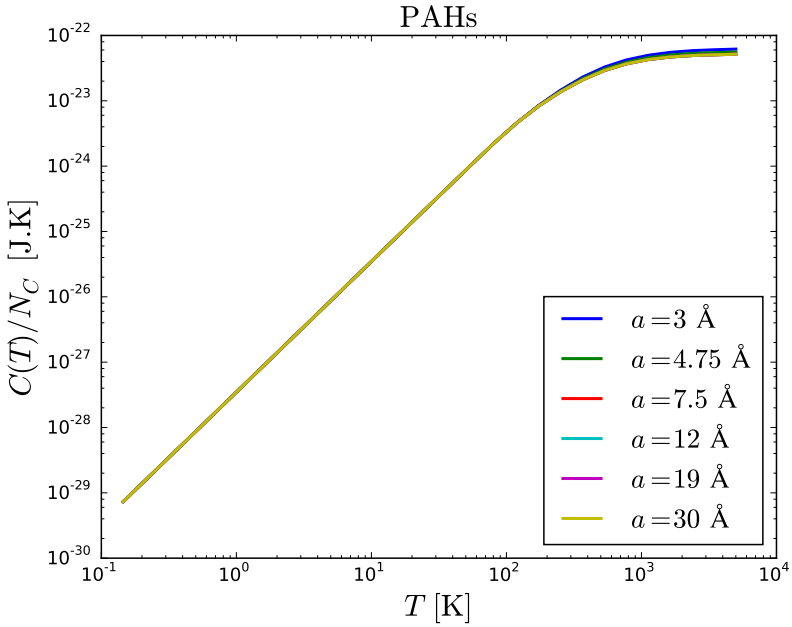

Figure 21: Heat capacities per C atom for PAHs, as functions of the grain temperature (data from Draine and Li 2001). The sizes are given by the equivalent radius a defined by Eq. 82.

expected from 2D to 3D (single PAH to PAH clusters), leading to more spherical shapes. This structural change is taken into account in the data of Draine and Li [2001, 2007], and an equivalent size is defined as the radius of a sphere with the same number of atoms:

$$a = 10\,\mathring{A}\,\left(\frac{N_C}{468}\right)^{\frac{1}{3}} \tag{82}$$

where N_C is the number of carbon atoms in the PAH. We will always use this equivalent size even when referring to single PAHs, so that for coronene ($C_{24}H_{12}$), $a = 1.71$ Å.

Fig. 21 shows the corresponding heat capacity per C atom. We see size dependance only for the smallest sizes because the transition from a planar to a spherical geometry occurs between $N_C = 54$ ($a = 4.9$ Å) and $N_C = 102$ ($a = 6$ Å) (see Draine and Li [2001]). Fig. 22 shows the absorption coefficients for PAHs (Compiègne et al. 2011), with the infrared features clearly visible.

The resulting equilibrium temperatures are shown on Fig. 23. Of course, the condition defined by Eq. 78 is never verified in the parameter domain of this plot, and PAH temperatures cannot be approximated by the equilibrium temperature. It is shown here for comparison with the average temperatures computed in Chapter 6. The sharp rise for the smallest sizes is the effect of the emission cutoff (see Eq. 74), which makes the cooling of very small PAHs less efficient.

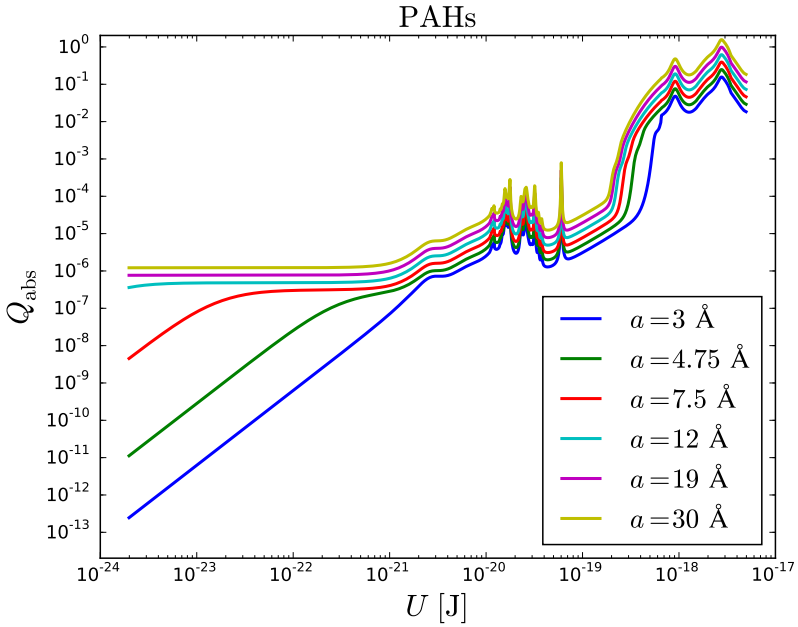

Figure 22: Absorption coefficients for PAHs, as functions of the photon energy (data from Compiègne et al. 2011). The sizes are the equivalent radius defined by Eq. 82.

5.2 H_2 FORMATION ON DUST GRAINS

As explained in Chapter 2, H_2 formation in the interstellar medium occurs predominantly on the surface of dust grains and involves reactions between hydrogen atoms adsorbed on the surface, or between adsorbed atoms and gas atoms. Several mechanisms have been proposed to explain this formation in different astrophysical situations. In our models, we will take into account two of these mechanisms : the physisorption-based Langmuir-Hinshelwood mechanism (LH mechanism), and the chemisorption-based Eley-Rideal mechanism (ER mechanism). For simplicity, we will consider those two mechanisms as independent, i.e. chemisorbed atoms and physisorbed atoms do not see each other.

5.2.1 *Binding sites*

The potential energy landscape for the interaction between a hydrogen atom and the surface of a grain shows two kinds of potential wells at different distances from the surfaces and different binding energies. This has been theoretically established for perfect surfaces such as graphite and graphene (see for instance Jeloaica and Sidis 1999), and similar properties have been found experimentally for various kind of surfaces (e.g. Pirronello et al. 1997b, Zecho et al. 2002). A typical potential energy curve is shown on Fig. 24.

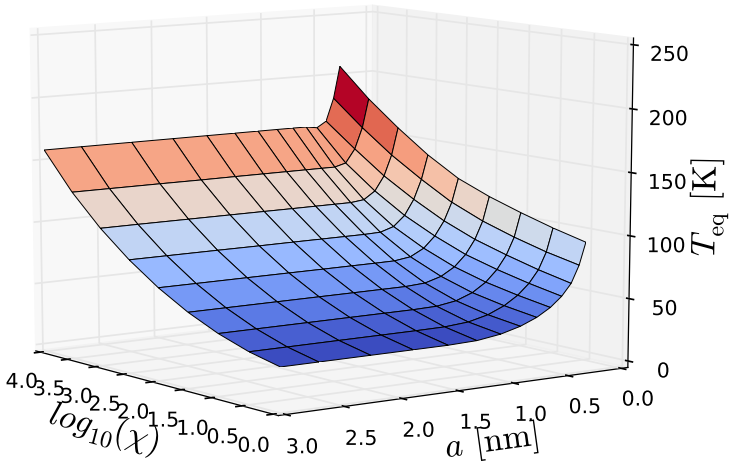

Figure 23: Equilibrium temperature for PAHs as a function of size (equivalent radius) and radiation field intensity. The sizes go from 3 Å to 30 Å. This equilibrium temperature approximation is never valid for PAHs and is only shown here for comparison.

We detail here these two kinds of binding.

PHYSISORPTION : The first potential well when the atom approaches the surface corresponds to Van der Waals interactions. The depth of the well has been estimated both from experiments and theoretical computations.

Density Functional Theory (DFT) calculations (Jeloaica and Sidis 1999, Ferro et al. 2002, Sha and Jackson 2002) usually agree on a physisorption well of very low binding energy ($\sim$ 8 meV) situated at $\sim$ 4 Å of the surface, and almost completely site-independent, meaning that the atoms are not restricted in their motion parallel to the surface and can migrate freely. However, the accuracy of DFT calculations for such large H-surface distances is questionable. The qualitative aspects of the results (large distance from the surface, free motion parallel to the surface) are more reliable.

On the other hand, numerous experimental studies of physisorption of atomic hydrogen (or deuterium) on various surfaces have been performed. Most of these studies measure HD formation and fit the results with a rate equation model, yielding best estimates for the binding energies, and barrier energies for migration. Such studies have been performed for silicate surfaces (Pirronello et al. 1997a,b and interpretation by Biham et al. 1998, Katz et al. 1999 for olivine surfaces, Perets et al. 2007 for polycrystalline and amorphous

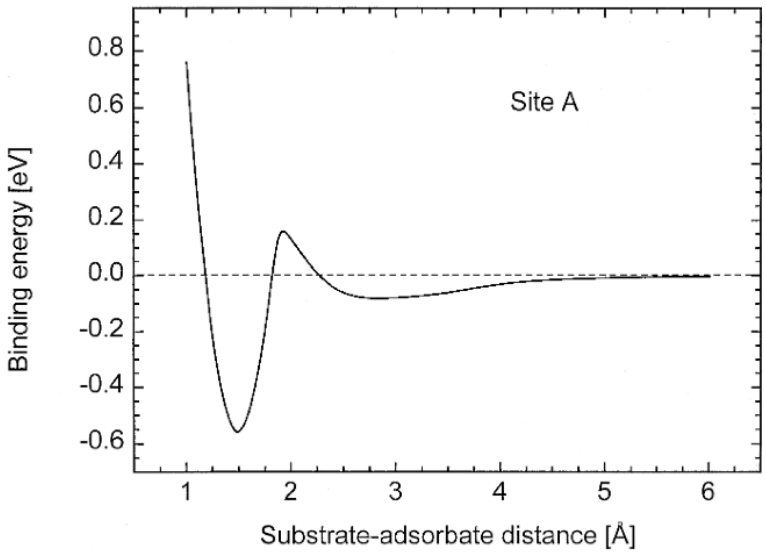

Figure 24: Interaction of an hydrogen atom with a graphite surface (on top of a C atom) obtained by a Density Functional Theory calculation, and taking into account surface relaxation (puckering of the C atom). From Jeloaica and Sidis 1999. The shallowest well corresponds to physisorption and the deepest one to chemisorption. Note the barrier separating the chemisorption well from the physisorption well.

silicate surfaces), carbonaceous surfaces (Pirronello et al. 1999 and interpretation by Katz et al. 1999 for amorphous carbon grains) and ice surfaces (Perets et al. 2005 for low and high density water ices). Note that contrary to the DFT models, the physisorption sites in the interpretation of those experiments are supposed to be localized and separated by inter-site barriers which have to be overcome thermally or by tunneling for migration to occur. We will thus adopt this representation in our models, as these experimental results are at the present time more reliable than DFT calculations for physisorption. The resulting binding and barrier energies are given in Table 3.

In the models presented here, we mostly use the values corresponding to amorphous carbon. Amorphous silicates and ices can be seen to have similar values.

CHEMISORPTION: The second potential well corresponds to a covalent bond. It has mostly been studied theoretically through DFT calculations. Numerous calculations of the binding energy on graphitic surfaces or graphene have been performed (Sha and Jackson 2002, Ferro et al. 2003, Duplock et al. 2004, Lehtinen et al. 2004, Hornekær et al. 2006, Chen et al. 2007, Roman et al. 2007, Kerwin and Jackson 2008, Casolo et al. 2009) giving values in the range $E_{\text{chem}} = 0.67 - 0.87\,\text{eV}$. Computations on PAHs have also been performed (Bonfanti et al. 2011) showing a stronger binding energy for edge

Surface type	Binding energy E_{phys} [meV]	Migration barrier E_{migr} [meV]	Ref.
Olivine	32.1	24.7	(1)
Polycrystalline silicate	32	25	(2)
Amorphous silicate	44	35	(2)
Amorphous carbon	56.7	44.0	(1)
Ice (water, high density)	62	55	(3)
Ice (water, low density)	52.3	44.5	(3)

References : (1) Katz et al. 1999, (2) Perets et al. 2007, (3) Perets et al. 2005

Table 3: Physisorption binding energies for atomic hydrogen, and energy barriers for migration, obtained from experimental studies.

sites ($1-3\,$eV) than for non-edge sites ($0.5-1\,$eV). As will be seen in Sect. 5.2.3 this binding energy has no influence when neglecting temperature fluctuations as grain temperatures are too low to trigger desorption. When we consider fluctuations (Chapter 6), the choice of this value will however be important. Unless specified otherwise, we will use a low value of 0.6 eV (7000 K) to estimate an upper limit of the effect of temperature fluctuations on H_2 formation through the chemisorption-based Eley-Rideal mechanism.

As seen on Fig. 24, an energy barrier separates the bound state from the free state. This makes chemisorption a thermally activated process, and thus requires the gas to be sufficiently hot for adsorption to occur. On perfect graphitic surfaces, theoretical estimations of this barrier give values of $E_{barr} = 0.15-0.2\,$eV (Sha and Jackson 2002, Kerwin and Jackson 2008). However, the surfaces of interstellar grains are more likely to be rough surfaces with many surface defects. Such defects have been shown to allow almost barrierless chemisorption (Ivanovskaya et al. 2010, Casolo et al. 2013). The barrier is also strongly reduced for edge sites on PAHs (Bonfanti et al. 2011). Based on those uncertainties, an inverse approach has been taken in Le Bourlot et al. [2012], were the effective value of the barrier has been chosen so as to yield adequate H_2 formation in PDR conditions (where physisorption-based LH formation is expected to be inefficient). The necessary barrier height is then $E_{barr} = 26\,$meV. We follow this prescription in the models presented here, and further discuss this choice later (Chapter 8) after presenting our models of H_2 formation on fluctuating grains.

More detailed models of chemisorption have shown that the adsorption of one hydrogen atom modifies the properties of the neighboring sites (Hornekær et al. 2006), making chemisorption of a second atom almost barrier-less in a para-dimer configuration (the two atoms are on top of opposite C atoms of

the hexagonal ring). We do not consider such details here, in order to keep the model simple.

5.2.2 *Surface processes*

We do not follow the individual positions of each adsorbed atom, but only the total number of adsorbed atoms. We thus neglect any inhomogeneous repartition of the atoms. We note that because of the quadratic term in the LH reaction rate for physisorbed atoms (detailed later, see Eq. 94), any such inhomogeneity would result in faster overall formation.

We now detail the possible events for individual atoms (physisorbed or chemisorbed).

STICKING : Hydrogen atoms from the gas collide with the grain with rate:

$$k_{\text{coll}} = \pi a^2 \, n(\text{H}) \sqrt{\frac{8 k_{\text{B}} T_{\text{gas}}}{\pi m_{\text{H}}}} \tag{83}$$

When there is a collision, the atom can stick to the surface and become adsorbed, or bounce back to the gas. The probability that a colliding atom sticks to the grain is called the *sticking coefficient*. It might depend on the velocity of the atom, its angle with the surface and the specific location of the impact on the surface. For a gas at temperature T, it will thus depend on this gas temperature, and on the effective cross section of the site.

For physisorption, the potential well is barrier-less, and the main restriction to sticking is the necessity for the atom to dissipate its kinetic energy before bouncing back from the surface. The interactions between the atom and the surface must thus allow sufficiently rapid redistribution of the energy compared to the residence time of the atom in the neighboring of the surface. We use the very simple model of this process described in Le Bourlot et al. [2012], yielding:

$$s(T_{\text{gas}}) = \frac{1}{1 + \left(\frac{T_{\text{gas}}}{T_2}\right)^{\beta}} \tag{84}$$

with $T_2 = 464\,\text{K}$ and $\beta = 1.5$. This gives a sticking coefficient of 1 in the low temperature limit, and decreasing as $T_{\text{gas}}^{1.5}$ for high temperatures as the atoms are then too energetic to have enough time to thermalize with the grain.

For chemisorption, the atom must in addition overcome the adsorption barrier, and we use:

$$s(T_{\text{gas}}) = \frac{e^{-\frac{E_{\text{barr}}}{k_B T_{\text{gas}}}}}{1 + \left(\frac{T_{\text{gas}}}{T_2}\right)^{\beta}} \tag{85}$$

with the same values of T_2 and β as for physisorption ($T_2 = 464\,\text{K}$ and $\beta = 1.5$). As explained in Sect. 5.2.1 we take $E_{\text{barr}}/k_{\text{B}} = 300\,\text{K}$.

THERMAL DESORPTION : Adsorbed atoms are supposed thermalized at the grain temperature. They can thus escape the potential well with rate:

$$k_{\rm des}(T) = \nu_0 \, e^{-\frac{T_{\rm binding}}{T}} \tag{86}$$

with ν_0 being a characteristic frequency of the oscillations of the atom inside the well:

$$\nu_0 = \frac{1}{\pi}\sqrt{\frac{2\,E_{\rm binding}}{d_0^2\,m_{\rm H}}} \tag{87}$$

as described in Hasegawa et al. [1992], where $E_{\rm binding}$ (and $T_{\rm binding} = E_{\rm binding}/k_{\rm B}$) is the binding energy (corresponding to physisorption or chemisorption) and d_0 is a characteristic width of the potential well taken as $d_0 = 1\,$Å.

THERMAL MIGRATION : For physisorption, we recall that the potential energy surface allows for easy motions from one site to the next. The atom can thermally overcome the barrier separating its adsorption site from the neighboring site, the migration rate is then:

$$k_{\rm migr}^{\rm (thermal)}(T) = \nu_0 \, e^{-\frac{T_{\rm migr}}{T}} \tag{88}$$

where $T_{\rm migr} = E_{\rm migr}/k_{\rm B}$ with $E_{\rm migr}$ the energy height of the barrier between neighboring physisorption sites, and ν_0 is defined by Eq. 87.

We do not allow any migration for chemisorbed atoms.

TUNNELING : Alternatively, a physisorbed atom can jump from one site to its neighbor through quantum tunneling. We use the expression from Le Bourlot et al. [2012]:

$$k_{\rm migr}^{\rm (tunnel)}(T) = \frac{\nu_0}{1 + \frac{T_{\rm migr}^2 \, \sinh^2\left(d_{\rm s}\,\hbar^{-1}\sqrt{2 m_{\rm H}\,k_{\rm B}\,(T_{\rm migr}-T)}\right)}{4T\,(T_{\rm migr}-T)}} \tag{89}$$

LANGMUIR-HINSHELWOOD REACTION : Langmuir-Hinshelwood reaction (for physisorbed atoms only) occurs when two adsorbed atoms meet on the surface. No activation barrier is present for this reaction. We assume that the energy released by the formation reaction of H_2 (4.5 eV) allows the newly formed molecule to be immediately released into the gas.

ELEY-RIDEAL REACTION : Eley-Rideal reaction occurs when a gas atom falls onto an already occupied site. We take this process into account for both physisorbed and chemisorbed atom. For simplicity and because it has become customary to associate Langmuir-Hinshelwood with physisorption and Eley-Rideal with chemisorption, we will keep calling Eley-Rideal the chemisorption-based mechanism (involving Eley-Rideal reaction only), and Langmuir-Hinshelwood the physisorption-based mechanism (involving both

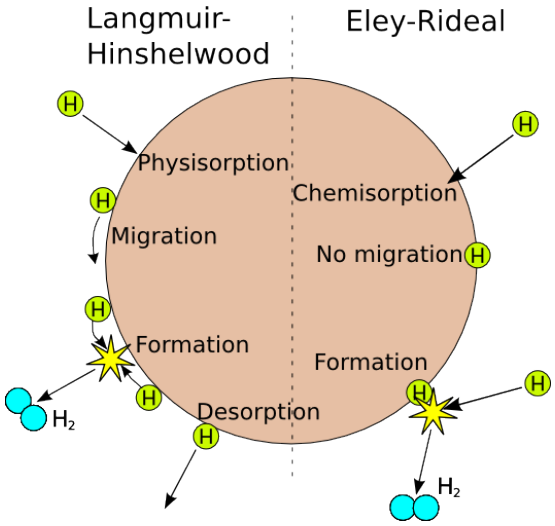

Figure 25: Graphical summary of the two formation mechanisms, detailing the different processes.

Langmuir-Hinshelwood reaction, and a small contribution from Eley-Rideal reactions as will be seen in Sect. 5.2.3).

The possibility of this Eley-Rideal reaction process for physisorbed atoms is expected from theoretical models (Martinazzo and Tantardini [2006]), although it cannot contribute to most experimental setups where the surface is irradiated with atoms in a first phase, and then slowly heated up in a second phase during which the rate of molecules coming out is measured. No activation barrier has yet been evidenced.

For chemisorbed atoms, there has been some discussion about an activation barrier, found in early studies (Morisset et al. [2004]), but debated by later work (Rougeau et al. [2011]). We do not take this barrier into account. Here again, we assume the new molecule to be released into the gas upon formation.

5.2.3 *Langmuir-Hinshelwood mechanism*

We now put all these processes together for physisorbed atoms in our model of Langmuir-Hinshelwood H_2 formation. The global picture of this formation mechanism is presented on the left part of Fig. 25.

We note n the number of physisorbed atoms on the surface, and N_s the total number of physisorption sites. We assume the sites to be separated by a typical distance of $d_s = 2.6\,\text{Å}$ (as in Le Bourlot et al. 2012), so that:

$$N_s = \frac{4\pi\, a^2}{d_s^2} \simeq 1.86 \times 10^2 \left(\frac{a}{1\,\text{nm}}\right) \tag{90}$$

The rate of adsorption of new atoms from the gas is governed by the collision rate, the sticking probability, and the probability to fall on an unoccupied site:

$$R_{\rm ads} = k_{\rm coll}\, s(T_{\rm gas}) \left(1 - \frac{n}{N_{\rm s}}\right) \tag{91}$$

where $k_{\rm coll}$ is defined by Eq. 83 and $s(T_{\rm gas})$ by Eq. 84.

When gas atoms fall on an occupied site, direct Eley-Rideal reaction occurs. The total rate of such reactions on the grain is simply:

$$R_{\rm form}^{\rm (ER)} = k_{\rm coll}\, \frac{n}{N_{\rm s}} \tag{92}$$

Each atom desorbs with a rate given by Eq. 86, so that the total desorption rate for the grain is:

$$R_{\rm des} = n\, k_{\rm des}(T) \tag{93}$$

with $k_{\rm des}(T)$ defined by Eq. 86 for $E_{\rm binding} = E_{\rm phys}$.

Finally, atoms migrate on the surface, and sometime meet another atom. Assuming an homogeneous repartition of the atoms on the surface, a simple approximation is to consider that when an atom jumps to another site, there is a probability $\frac{n-1}{N_{\rm s}}$ that this site is occupied, so that the total LH formation rate on the grain is:

$$R_{\rm form}^{\rm (LH)} = k_{\rm migr}(T)\, \frac{n(n-1)}{N_{\rm s}} \tag{94}$$

where $k_{\rm migr}(T) = k_{\rm migr}^{\rm (thermal)}(T) + k_{\rm migr}^{\rm (tunnel)}(T)$ with $k_{\rm migr}^{\rm (thermal)}(T)$ defined by Eq. 88 and $k_{\rm migr}^{\rm (tunnel)}(T)$ by Eq. 89. A more detailed treatment of this rate, by computing the meeting probability of random walkers on a spherical surface, has been developed by Lohmar and Krug [2006], Lohmar et al. [2009].

The usual rate equation approximation consists in approximating n as a continuous variable, and writing a differential equation for its evolution. We then obtain:

$$\frac{dn}{dt} = R_{\rm ads} - R_{\rm des} - R_{\rm form}^{\rm (ER)} - 2R_{\rm form}^{\rm (LH)} \tag{95}$$

as one LH reaction event removes two hydrogen atoms from the surface. Of course, this approximation is only meaningful if n is large. In such a case, $n(n-1)$ can be replaced by n^2, and by writing all the terms explicitly we get:

$$\frac{dn}{dt} = k_{\rm coll}\, s \left(1 - \frac{n}{N_{\rm s}}\right) - n\, k_{\rm des}(T) - k_{\rm coll}\, \frac{n}{N_{\rm s}} - 2k_{\rm migr}(T)\, \frac{n^2}{N_{\rm s}} \tag{96}$$

where we have written s instead of $s(T_{\rm gas})$ to simplify the expressions.

If the temperature T of the dust grain is assumed to be constant, then there is an equilibrium population n_{eq} given by:

$$n_{\mathrm{eq}}(T) = \frac{(1+s)\,k_{\mathrm{coll}}}{4k_{\mathrm{migr}}(T)} \left(1 + \frac{N_{\mathrm{s}}\,k_{\mathrm{des}}(T)}{(1+s)\,k_{\mathrm{coll}}}\right) \times \left[\sqrt{1 + \frac{8N_{\mathrm{s}}\,s\,k_{\mathrm{mig}}(T)}{(1+s)^2\,k_{\mathrm{coll}}} \frac{1}{\left(1+\frac{N_{\mathrm{s}}\,k_{\mathrm{des}}(T)}{(1+s)\,k_{\mathrm{coll}}}\right)^2}} - 1\right] \quad (97)$$

The resulting rate of formation of H_2 (taking into account both LH and ER reaction) at this equilibrium is then:

$$r_{\mathrm{H_2}}^{(\mathrm{eq})}(T) = k_{\mathrm{migr}}(T)\,\frac{\left[n_{\mathrm{eq}}(T)\right]^2}{N_{\mathrm{s}}} + k_{\mathrm{coll}}\,\frac{n_{\mathrm{eq}}(T)}{N_{\mathrm{s}}} \quad (98)$$

It can easily be seen from the expressions that $n_{\mathrm{eq}}(T)$ and $r_{\mathrm{H_2}}^{(\mathrm{eq})}(T)$ are proportional to the grain surface. It is thus usual to consider the formation efficiency η, defined as:

$$\eta = \frac{2r_{\mathrm{H_2}}(T)}{k_{\mathrm{coll}}} \quad (99)$$

which gives the fraction of colliding H atoms that are turned into H_2. This quantity is independent of the grain size, except for the dependency of the grain temperature on the grain size. The efficiency of the Langmuir-Hinshelwood mechanism for an amorphous carbon surface (see binding and barrier energy values in Table 3) is shown on Fig. 26, as a function of the grain temperature and the density of atomic hydrogen in the gas. The gas temperature has two effects (not shown on this figure), one through the collision rate, which is thus equivalent to the effect of changing $n(\mathrm{H})$, and one through the sticking coefficient, resulting in an overall decrease of the efficiency when $T_{\mathrm{gas}} \gtrsim 450\,\mathrm{K}$ (the high efficiency plateau then becomes significantly lower than 1).

One has to keep in mind that the rate equation (Eq. 96) yielding these results stands on two strong assumptions :

- By assuming n to be a continuous variable, it implicitly assumes that n is large so that the intrinsic fluctuations of n caused by the random nature of the chemical processes are negligible. An exact treatment requires writing the Master Equation (see Eq. 49) for this process using the transition rates defined in the present section. This has been done and solved analytically by Biham and Lipshtat [2002] (and Lipshtat and Biham 2003 proposed an approximated resolution method). Garrod 2008 also proposed a correction to the rate equation by using an approximation of the low population limit of the Master Equation, yielding a corrected expression for the formation rate (Eq. 94) when n is small.

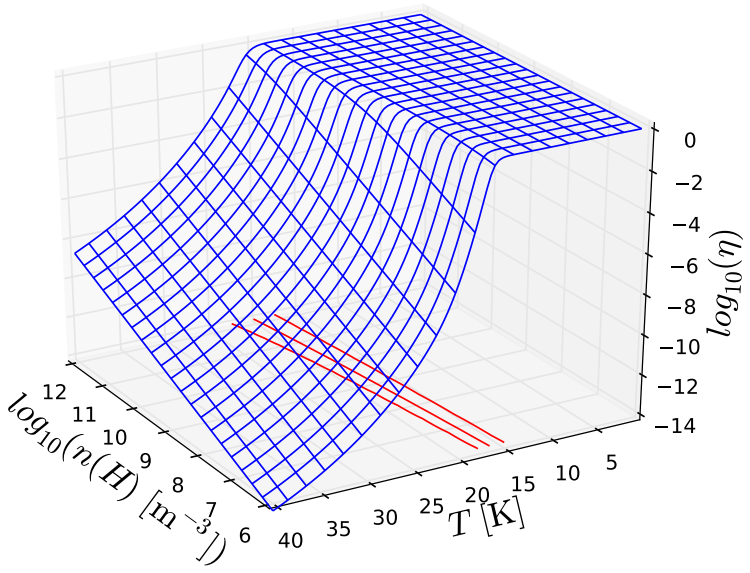

Figure 26: H_2 formation efficiency by the Langmuir-Hinshelwood mechanism as a function of the grain temperature T and the density of atomic hydrogen in the gas $n(H)$, for an amorphous carbon surface, in a 100 K gas. The three red contour lines projected on the base plane show respectively the 90%, 50% and 1% efficiency levels.

- The equilibrium that we computed assumes that the grain temperature stays constant. As said before (and as will be studied in details in Chapter 6), the temperature of small dust grains fluctuates. A method to compute the average formation rate when the grain temperature fluctuates due to photon absorptions will be constructed in Chap. 7.

In the astrophysical context, the results of this approximation are problematic as we see that the formation is only efficient below $15 - 20$ K while the equilibrium temperatures are all above ~ 20 K in unshielded conditions such as PDRs or the diffuse medium.

5.2.4 *Eley-Rideal mechanism*

For the chemisorption-based Eley-Rideal mechanism, the list of processes is reduced as we do not allow any migration. An overview of this mechanism is depicted in the right part of Fig. 25 . In this case, n is the number of chemisorbed atoms on the grain surface.

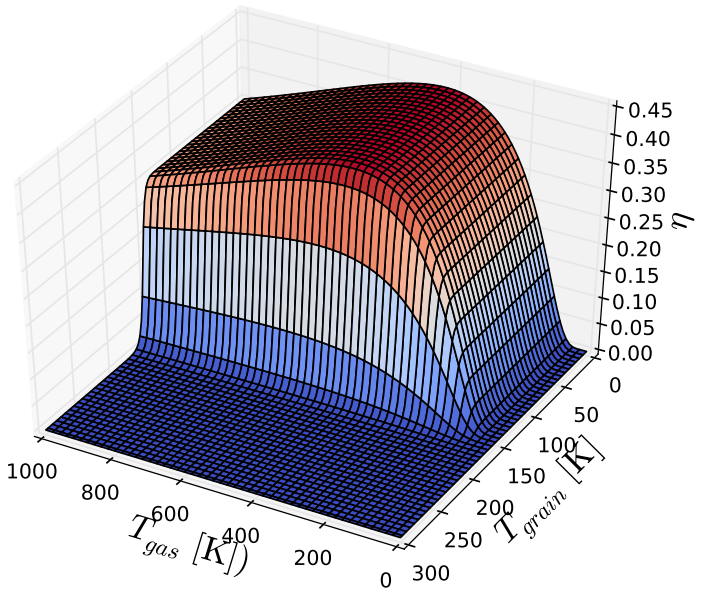

Figure 27: H_2 formation efficiency by the Eley-Rideal mechanism as a function of grain temperature and gas temperature, for an amorphous carbon grain in a gas with $n(\mathrm{H}) = 10^4\,\mathrm{cm}^{-3}$.

As for the LH mechanism, the total adsorption rate for the grain is:

$$R_{\mathrm{ads}} = k_{\mathrm{coll}}\, s(T_{\mathrm{gas}}) \left(1 - \frac{n}{N_{\mathrm{s}}}\right) \tag{100}$$

with k_{coll} defined by Eq. 83, and $s(T_{\mathrm{gas}})$ defined this time by Eq. 85.

The total desorption rate is:

$$R_{\mathrm{des}} = n\, k_{\mathrm{des}}(T) \tag{101}$$

with $k_{\mathrm{des}}(T)$ defined by Eq. 86 for $E_{\mathrm{binding}} = E_{\mathrm{chem}}$.

Finally, the formation rate by direct Eley-Rideal reaction is:

$$R_{\mathrm{form}} = k_{\mathrm{coll}}\, \frac{n}{N_{\mathrm{s}}} \tag{102}$$

In the rate equation approximation, we can similarly to the LH case write the evolution equation:

$$\frac{dn}{dt} = k_{\mathrm{coll}}\, s \left(1 - \frac{n}{N_{\mathrm{s}}}\right) - n\, k_{\mathrm{des}}(T) - k_{\mathrm{coll}}\, \frac{n}{N_{\mathrm{s}}} \tag{103}$$

where we noted s instead of $s(T_{\mathrm{gas}})$ for simplicity.

Again, if the temperature of the grain is assumed to be constant, then an equilibrium population $n_{\mathrm{eq}}(T)$ exists and is:

$$n_{\mathrm{eq}}(T) = N_{\mathrm{s}} \frac{s}{(1+s) + \frac{N_{\mathrm{s}} k_{\mathrm{des}}(T)}{k_{\mathrm{coll}}}} \tag{104}$$

and the equilibrium formation rate is:

$$r_{\mathrm{H_2}}^{(\mathrm{eq})}(T) = k_{\mathrm{coll}} \frac{n_{\mathrm{eq}}(T)}{N_{\mathrm{s}}} \tag{105}$$

Here again, we define the formation efficiency η by Eq. 99. This quantity is again independent of the grain size if the grain temperature is kept fixed. The resulting efficiency is shown on Fig. 27 as a function of grain temperature and gas temperature. The Eley-Rideal mechanism is thus independent of the grain temperature up to 150 K, which is higher than the range of the equilibrium temperatures determined previously (see Fig. 19, 20 and 23). However, the efficiency of this mechanism requires a gas temperature greater than ~ 100 K due to the sticking barrier.

Again, these are the results of the equilibrium rate equation approximation. In this case however, the intrinsic population fluctuations are not a problem, as it is easy to see that because of the linearity in n of all the rates, the rate equation is the exact evolution equation for the average population. The assumption of a constant grain temperature is still problematic as grain temperature fluctuations caused by UV photons bring the grain temperature above 150 K, triggering desorption of its population. The exact treatment of this problem will be presented in Chap. 7.

5.3 DUST COMPONENTS AND SIZE DISTRIBUTION

Elemental depletions (the reductions of the observed relative abundances of elements in the gas compared to the solar abundances), extinction curves and pre-solar grains in meteorites give us clues about the composition and size of dust grains in the interstellar medium (see Chap. 2 for a detailed discussion). Various models of the interstellar dust population have been published (Mathis et al. 1977, Draine and Li 2007, Compiègne et al. 2011). They usually consist of two main components with sizes distributed over a wide range (nm to μm scale) : a carbonaceous component, either of graphitic type, or of amorphous carbon type, and a silicate component (recent models favor amorphous silicates over crystalline silicates). In addition, a PAH component is added with a narrow size range (~ 0.5 nm to ~ 1 nm). The overall size distributions favor small grains over big grains in numbers. They are also such that the total dust surface is dominated by the small grains, while the dust mass is dominated by the biggest sizes.

In our models, we use very simplified dust models to highlight the effects of dust temperature fluctuations on the total H_2 formation rate on a full

distribution of grain sizes. We present them here and compare them to the most recent detailed dust models.

5.3.1 *A simplistic model*

When presenting our results on H_2 formation with grain temperature fluctuations, we show that the effects are strongly dependent on grain size. To evaluate the overall effect on formation in interstellar conditions, we use a very simplified dust population model retaining only the main features of the more detailed models : a size distribution obeying roughly a -3.5 power law (similar to the *MRN* distribution, Mathis et al. 1977), and extending down to nm sized grains.

We thus consider a single component distribution comprising only amorphous carbon grains and extending from 1 nm grains to 300 nm (the large grain end of the distribution is unimportant for our results as it contributes a very small fraction of the available dust surface), and obeying a power law:

$$\frac{dn_g(a)}{da} = A_{gr}\, a^{-3.5} \tag{106}$$

where $dn_g(a)$ is the number of grain of size in $[a, a+da]$ per unit volume of gas, and A_{gr} is a normalization constant. This constant is directly related to the dust-to-gas mass ratio, taken at the usual value of $G = 0.01$. Indeed, the total mass of grains per unit volume of gas can be computed from Eq. 106:

$$\begin{aligned} M &= \int_{a_{min}}^{a_{max}} da\, \frac{4}{3}\pi a^3\, \rho_{grain}\, A_{gr}\, a^{-3.5} \\ &= \frac{8}{3}\pi\, \rho_{grain}\, A_{gr}\, \left(\sqrt{a_{max}} - \sqrt{a_{min}}\right) \end{aligned} \tag{107}$$

where ρ_{grain} is the mass density of the grain material (we take $\rho_{grain} = 1.81\,\mathrm{g.cm^{-3}}$ for amorphous carbon as said in Sect. 5.1.1) and the mass of gas per unit volume is $1.4\, n_H\, m_H$ where n_H is the density of hydrogen atoms (regardless of their molecular or atomic form) and the factor 1.4 accounts for the presence of helium, so that we can express the normalization factor as:

$$A_{gr} = \frac{3}{8}\, \frac{1.4\, n_H\, m_H\, G}{\pi \rho_{grain}\, \left(\sqrt{a_{max}} - \sqrt{a_{min}}\right)} \tag{108}$$

5.3.2 *The dust model of the Meudon PDR Code*

When coupling the H_2 formation models to the `Meudon PDR Code`, we use the standard dust distribution of this code. As described in Sect. B, it has the power law size distribution given by Eq. 106, with grain sizes going from 1 nm to 300 nm, but uses hybrid grain properties (absorption coefficients

and heat capacities) corresponding to a weighted average between graphite and silicate properties (70%-30%). The mass density is similarly a 70%-30% weighted average of the mass densities of graphite and silicates, thus giving $\rho_{\text{grain}} = 2.618\,\text{g.cm}^{-3}$.

5.3.3 *Comparison with more complete dust models*

THE DRAINE DUST MODEL This model is described in a series of paper by Draine and Li (Draine and Li 2001, Li and Draine 2001, 2002, Draine and Li 2007). We take here the model with $q_{PAH} = 4.6\%$. The dust population is constituted of:

- a PAH component. Its size distribution is built from two log-normal distributions:

$$\frac{dn_{PAH}}{da} = \frac{n_1}{a}\, e^{-\left(\frac{\ln(a/a_{01})}{\sqrt{2}\sigma_1}\right)^2} + \frac{n_2}{a}\, e^{-\left(\frac{\ln(a/a_{02})}{\sqrt{2}\sigma_2}\right)^2} \tag{109}$$

  with $a_{01} = 4\,\text{Å}$, $a_{02} = 20\,\text{Å}$, $\sigma_1 = 0.4$, $\sigma_2 = 0.55$, and n_1 and n_2 are normalization factors such that 4.6 % of the total dust mass is in the PAH component, and 75% of this fraction is in the first lognormal while 25% is in the second.

- A graphite component, following the size distribution (Weingartner and Draine 2001a):

$$\frac{dn_{gr}}{da} = \frac{n_{\text{H}} C}{a} \left(\frac{a}{a_t}\right)^{\alpha} \frac{1}{1+\beta\,\frac{a}{a_t}} \times \begin{cases} 1 & \text{if} \quad a < a_t \\ \exp\left(-\left[\frac{a-a_t}{a_c}\right]^3\right) & \text{if} \quad a > a_t \end{cases} \tag{110}$$

  with $\alpha = -1.54$, $\beta = 0.165$, $a_t = 10.7\,\text{nm}$, $a_c = 428\,\text{nm}$ and $C = 9.99 \times 10^{-12}$.

- A silicate component, following a similar size distribution (Weingartner and Draine 2001a):

$$\frac{dn_s}{da} = \frac{n_{\text{H}} C}{a} \left(\frac{a}{a_t}\right)^{\alpha} \left(1+\beta\,\frac{a}{a_t}\right) \times \begin{cases} 1 & \text{if} \quad a < a_t \\ \exp\left(-\left[\frac{a-a_t}{a_c}\right]^3\right) & \text{if} \quad a > a_t \end{cases} \tag{111}$$

  with $\alpha = -2.21$, $\beta = 0.3$, $a_t = 164\,\text{nm}$, $a_c = 100\,\text{nm}$ and $C = 10^{-13}$.

These values are taken for $R_V = 3.1$. See Weingartner and Draine 2001a (Table 1) for values corresponding to other choices of R_V.

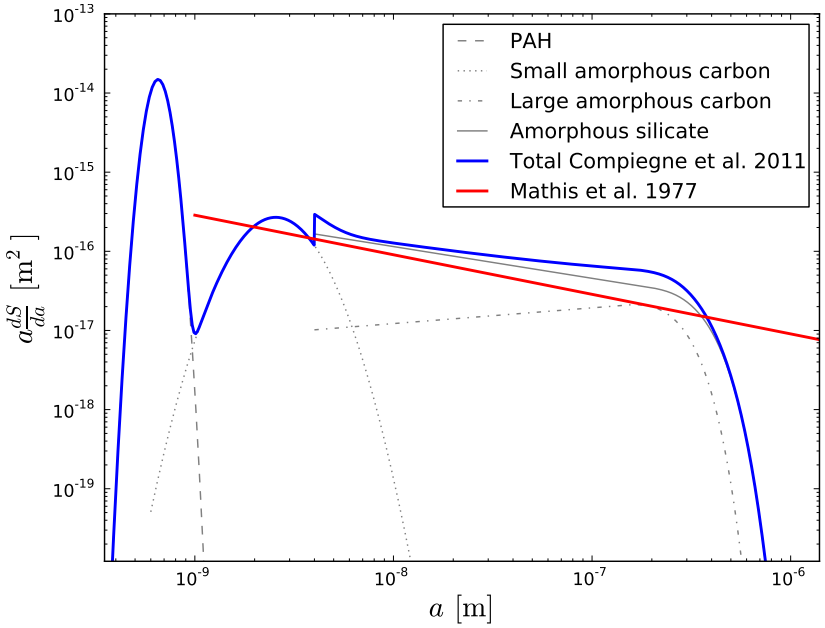

Figure 28: Comparison of a simplified MRN-like power law with the `DustEM` dust model. Distribution of the total dust surface across grain sizes.

THE DUSTEM DUST MODEL This model is described in Compiègne et al. 2011. It is built from 4 components :

- a PAH component with a lognormal size distribution:

$$\frac{dn_{\rm PAH}}{da} = \frac{A_{PAH}}{a}\, e^{-\left(\frac{\ln(a/a_0)}{\sqrt{2}\sigma}\right)^2} \tag{112}$$

  with $a_0 = 6.4\,$Å, $\sigma = 0.1$ and $A_{\rm PAH}$ a normalization factor so that 7.7% of the total dust mass is in this component.

- a small amorphous carbon grain component, also with a log-normal distribution:

$$\frac{dn_{SamC}}{da} = \frac{A_{SamC}}{a}\, e^{-\left(\frac{\ln(a/a_0)}{\sqrt{2}\sigma}\right)^2} \tag{113}$$

  with $a_0 = 20\,$Å, $\sigma = 0.35$ and $A_{\rm SamC}$ a normalization factor so that 1.6% of the total dust mass is in this component.

- a large amorphous carbon grain component, with power law size distribution with exponential cut-off at large sizes:

$$\frac{dn_{\rm LamC}}{da} = A_{\rm LamC}\, a^{-\alpha} \times \begin{cases} 1 & \text{if} \quad a < a_t \\ e^{-\left(\frac{a-a_t}{a_c}\right)^\gamma} & \text{if} \quad a > a_t \end{cases} \tag{114}$$

with $\alpha = 2.8$, $a_t = 150\,\mathrm{nm}$, $a_c = 150\,\mathrm{nm}$, $\gamma = 2$, and A_{LamC} is a normalization factor so that 14.2% of the total dust mass is in this component. This component starts at $a_{min} = 4\,\mathrm{nm}$.

- a silicate grain component, with a similar size distribution:

$$\frac{dn_{\mathrm{Sil}}}{da} = A_{\mathrm{Sil}}\, a^{-\alpha} \times \begin{cases} 1 & \text{if} \quad a < a_t \\ e^{-\left(\frac{a-a_t}{a_c}\right)^{\gamma}} & \text{if} \quad a > a_t \end{cases} \tag{115}$$

with $\alpha = 3.4$, $a_t = 200\,\mathrm{nm}$, $a_c = 200\,\mathrm{nm}$, $\gamma = 2$, and A_{Sil} is a normalization factor so that 76.5% of the total dust mass is in this component. This component starts at $a_{min} = 4\,\mathrm{nm}$.

Fig. 28 shows a comparison of the surface distribution between the `DustEM` dust model and our simplified MRN-like power law model.

6

DUST TEMPERATURE FLUCTUATIONS AND DUST EMISSIVITY

The approach presented in the previous chapter, characterizing the dust temperature using the equilibrium temperature (Eq. 77), and computing the formation rate from the rate equation (Eq.96 or Eq. 103), makes several problematic assumptions as discussed earlier. By approximating the population of surface atoms by a continuous variable, it neglects its discrete nature, which is especially problematic when this population is of order unity as each adsorption, desorption or reaction then constitutes a strong fluctuation in the surface population. This is what we could call the intrinsic fluctuations of the surface population due to its integer nature, and already requires a statistical treatment which has been done by Biham and Lipshtat [2002]. This effect is important for small grains (< 100 adsorption sites), especially in low density environments as the adsorption rate is lower compared to the other processes.

In addition, we noted that the equilibrium temperature is a poor approximation for small grains unshielded from the UV radiation field. Each individual photon indeed causes a strong fluctuation of the grain temperature. This problem has been studied for the purpose of computing dust emissivity, and especially the component emitted by small grains and PAHs. See for instance Draine and Li [2001], Li and Draine [2001], or Desert et al. [1986], Compiègne et al. [2011] for the `DustEM` code. These temperature fluctuations significatively affect the emissivity of the small grains ($\lesssim 10\,\mathrm{nm}$), and an estimation of the domain of validity of the equilibrium temperature approximation as been given in the previous chapter (see Fig. 19 and 20).

For the purpose of modeling the surface chemistry on grains with temperature fluctuations, we need to generalize those approaches to compute not only the statistical properties of the intrinsic population fluctuations and of the temperature fluctuations, but also the coupled statistics of the temperature fluctuations and the induced fluctuations of the surface population. This is done in the next Chapter. In the present Chapter, we present as an introduction the full treatment of the dust temperature fluctuations in the framework of the Master Equation.

We will thus revisit results on the dust temperature distributions and dust emissivities, discuss different limits and approximations, and especially describe a fast method that I developed for computing the dust emissivity, centered on a single-photon approximation for small grains, and describe its implementation in the Meudon PDR Code.

6.1 A MASTER EQUATION APPROACH

The processes of heating and cooling of the grain by individual photons cause jumps in its temperature. The time evolution of the grain temperature can be modeled as a pure jump Markov process (see Chapter 4, and especially Sect. 48), with the transition rates defined by Eq. 71 for upward jumps, and Eq. 75 for downward jumps.

6.1.1 *Master Equation*

As the transitions in the thermal state of the grain (due to photons) are more easily expressed in terms of energy jumps, we will describe the grain state by its thermal energy E rather than by its temperature T. E thus follows a pure jump Markov process. We note $f(E,t\,|E_0,t_0)$ its two-times conditional PDF. From the Markov property, we know that this quantity fully describes the stochastic process (Sect. 4.1.3). As demonstrated in Chapter 4, $f(E,t\,|E_0,t_0)$ obeys the Master Equation:

$$\frac{\partial f(E,t\,|E_0,t_0)}{\partial t} = \int_0^{+\infty} dE'\, W(E\,|E';t) f(E',t\,|E_0,t_0) - f(E,t\,|E,t_0) \int_0^{+\infty} dE'\, W(E'\,|E;t) \quad (116)$$

with the natural initial condition $f(E,t\,|E_0,t_0) = \delta(E-E_0)$, and the transition rate is:

$$W(E'\,|E,t) = \begin{cases} R_{\rm abs}(E'-E) & \text{if} \quad E' > E \\ R_{\rm em}(E-E',T(E)) & \text{if} \quad 0 < E' < E \\ 0 & \text{if} \quad E' < 0 \end{cases} \quad (117)$$

The transition rate is thus independent of time, so that we can write it $W(E'\,|E)$ in the following. In addition, we note that as $Q_{\rm abs}(U)$ behave as U^2 at small U, and the black body law (which is also the shape of the external radiation field at small U) also behave as U^2, both $R_{\rm abs}(U)$, and $R_{\rm em}(U)$ behave as U^3 at small U (U is the photon energy as before). Our transition rate is thus a $\mathcal{C}^2$ function of $E'-E$.

We can easily transform this equation into an equivalent equation for the one-time PDF $f(E,t)$ by multiplying the equation by the initial PDF at t_0, $f_0(E_0)$, and integrating over E_0:

$$\frac{\partial f(E,t)}{\partial t} = \int_0^{+\infty} dE'\, W(E\,|E') f(E',t) - f(E,t) \int_0^{+\infty} dE'\, W(E'\,|E) \quad (118)$$

with as initial condition the initial PDF $f(E,t_0) = f_0(E)$.

We are interested in the situation where this PDF is stationary. If such a stationary state exists, we note the stationary one-time PDF $f_E(E)$. It then obeys:

$$\int_0^{+\infty} dE'\, W(E\,|E')f_E(E') - f_E(E)\int_0^{+\infty} dE'\, W(E'\,|E) = 0 \tag{119}$$

which we can rewrite as:

$$\int_0^{+\infty} dE'\, \frac{W(E\,|E')}{L(E)} f_E(E') = f_E(E) \tag{120}$$

where we have defined the loss rate $L(E)$ as:

$$L(E) = \int_0^{+\infty} dE'\, W(E'\,|E) \tag{121}$$

Eq. 120 shows that a stationary distribution exists if and only if:

- the integral operator defined by the left-hand side has 1 as an eigenvalue
- there exists an eigenfunction for this eigenvalue with constant sign (so that with proper normalization it can be interpreted as a PDF).

The problem of computing the stationary distribution of the temperature of dust grains thus reduces to diagonalizing an integral operator. Before proceeding with the study of the properties of this operator, we give the explicit expression of Eq. 120 in terms of $R_{\text{abs}}(U)$ and $R_{\text{em}}(U, T(E))$:

$$\frac{\int_0^E dU\, R_{\text{abs}}(U) f_E(E-U) + \int_0^{+\infty} dU\, R_{\text{em}}(U, T(E+U)) f_E(E+U)}{\int_0^E dU\, R_{\text{em}}(U, T(E)) + \int_0^{+\infty} dU\, R_{\text{abs}}(U)} = f_E(E) \tag{122}$$

where we have also made the variable change to photon energy U in the integrals.

We have here written the equation for the thermal energy PDF f_E, but the temperature PDF f_T can easily be computed from this result using the usual variable change rule for PDF:

$$f_T(T) = f_E(E(T))\, C(T) \tag{123}$$

6.1.2 *Properties of the eigenvalues*

We now investigate the properties of the operator defined by Eq. 122, and propose a tentative demonstration of the existence and unicity of a stationary distribution.

Let us define the operator $\mathcal{L}$ as:

$$\mathcal{L}[f](E) = \int_0^{+\infty} dE' \, \frac{W(E\,|E')}{L(E)} f(E') \tag{124}$$

We consider the usual scalar product between real functions:

$$\langle f, g \rangle = \int dx \, f(x) \, g(x)$$

The adjoint operator of the operator $\mathcal{L}$ is then $\mathcal{L}^*$ defined by:

$$\mathcal{L}^*[f](E) = \int_0^{+\infty} dE' \, \frac{W(E'\,|E)}{L(E')} f(E') \tag{125}$$

It is easy to see that 1 is an eigenvalue of the operator $\mathcal{L}^*$ as:

$$\begin{aligned} \mathcal{L}^*[L](E) &= \int_0^{+\infty} dE' \, \frac{W(E'\,|E)}{L(E')} L(E') \\ &= \int_0^{+\infty} dE' \, W(E'\,|E) \\ &= L(E) \end{aligned} \tag{126}$$

Thus, 1 is also in the spectrum of $\mathcal{L}$. However, as we are in infinite dimension, this does not prove that 1 is an eigenvalue of $\mathcal{L}$.

It can be checked from the expressions of R_{abs} and R_{em} that $\frac{W(E|E')}{L(E)}$ is square integrable, so that $\mathcal{L}$ is a Hilbert-Schmidt integral operator and is thus continuous and compact. Then, we can use the fact that for compact operators, any non-zero value in the spectrum of $\mathcal{L}$ is an eigenvalue, so that 1 is indeed an eigenvalue of $\mathcal{L}$.

This still does not prove the existence of a stationary distribution, as the eigenfunction must be of constant sign so that it can become a proper PDF after normalization.

For this, we use the Krein-Rutman theorem (Du 2006). We restrict ourselves to continuous functions, and assume that the radiation field remains non-zero after the Lyman cut (although arbitrarily small) so that the image of any non-negative (and non strictly zero) function by $\mathcal{L}$ (and by $\mathcal{L}^*$) is a strictly positive function. $\mathcal{L}$ (and $\mathcal{L}^*$) then verifies the stronger form of the Krein-Rutman theorem so that their spectral radius is a simple eigenvalue with a strictly positive eigenfunction, and this eigenfunction is the only positive eigenfunction. As we have seen that $L(E)$ (which is a positive function) is an eigenfunction of $\mathcal{L}^*$ for the eigenvalue 1, this means that 1 is the spectral radius of $\mathcal{L}^*$ and $\mathcal{L}$, and thus that 1 is a simple eigenvalue of $\mathcal{L}$ with a positive eigenfunction.

This proves the existence and the unicity of a stationary PDF for our problem.

6.1.3 *Resolution method*

We will solve this problem numerically by discretizing the problem, i.e. reducing the problem to a finite-dimensional function space, such as piecewise linear functions on a fixed grid. The most obvious way to solve the problem is then to diagonalize the matrix corresponding to the operator $\mathcal{L}$. If the discretization has been done with sufficient precision, one of the eigenvalues should be very close to 1. The solution is then the associated eigenvector, normalized so that:

$$\int_0^{+\infty} dE\, f_E(E) = 1 \tag{127}$$

Another resolution method is suggested by the Krein-Rutman theorem. As 1 is the spectral radius, all other eigenvalues have their modulus strictly inferior to 1, and we can thus expect that:

$$\lim_{n \to +\infty} \mathcal{L}^n[g] = f_E \tag{128}$$

i.e. iterating the application of the operator $\mathcal{L}$ to any strictly positive initial guess should converge towards the eigenfunction associated with the eigenvalue 1. This suggests an iterative method which might, depending on the number of iterations necessary to converge, be faster than diagonalization.

The facts that those properties are still valid after discretization is ensured by the Perron-Frobenius theorem (of which the Krein-Rutman theorem is a generalization to infinite dimension), which states that for a square matrix with strictly positive coefficients, its spectral radius is a simple eigenvalue called the leading eigenvalue with a real eigenvector with all coefficients positive, and that all other eigenvalues have strictly smaller modulus and have eigenvectors with at least one negative or imaginary coefficient. The operation described by Eq. 128 is then called the Perron projection, and is the projection on the eigenspace corresponding to this leading eigenvalue.

Finally, we note one last point on the equilibrium equation (Eq. 122). From the equation, it is easy to see that $f_E(E)$ goes to a finite value as $E \to 0$:

$$f_E(0) = \frac{\int_0^{+\infty} dU\, R_{\text{em}}(U, T(U)) f_E(U)}{\int_0^{+\infty} dU\, R_{\text{abs}}(U)} > 0 \tag{129}$$

6.2 NUMERICAL RESOLUTION

6.2.1 *Discretization of the problem*

The first approximation we need to do in order to solve the problem numerically is to choose an upper limit E_{max} for the energy domain, and assign the PDF to be zero above this limit. As the heating from the radiation field is mainly contributed by a finite wavelength range (e.g. no photon above the

Lyman limit), and the cooling increase with the grain thermal energy, it is natural to assume that the equilibrium PDF will become negligible above a certain limit.

We discretize the problem by considering only piecewise linear functions. Defining a grid of N energy points spanning the energy domain $\{E_i\}_{i\in[1..N]}$, we only consider functions that are affine on each of the segments $[E_i, E_{i+1}]$. As seen in the previous section (Eq. 129), the PDF does not go to zero when $E \to 0$, thus our grid should start with $E_1 = 0$. However, we will see in Sect. 6.2.3, that this finite value of the PDF at zero becomes negligible compared to the bulk of the PDF for big grains. For big grains, we thus use a grid which starts at some non-zero initial value E_{min}, and assume the PDF to be zero below this value.

We use a logarithmically distributed grid. When 0 is included in the grid:

$$\begin{cases} E_1 = 0 \\ E_i = E_{\text{min}} \left(\frac{E_{\text{max}}}{E_{\text{min}}}\right)^{\frac{i-2}{N-2}} \quad \text{if} \quad 2 \leq i \leq N \end{cases} \tag{130}$$

and when 0 is not included:

$$E_i = E_{\text{min}} \left(\frac{E_{\text{max}}}{E_{\text{min}}}\right)^{\frac{i-1}{N-1}} \quad \text{for} \quad 1 \leq i \leq N \tag{131}$$

The choice between those to cases, and the choice of E_{min} is done after a first estimation of the equilibrium temperature using an empirical formula yielding adapted bounds for the relevant range of grain sizes and radiation fields.

For piecewise linear functions on this grid, the Master Equation (Eq. 120) can be written as:

$$\sum_{j=1}^{N-1} \int_{E_j}^{E_{j+1}} dE' \, \frac{W(E_i \,|E')}{L(E_i)} \left(\frac{E' - E_j}{E_{j+1} - E_j} f_E(E_{j+1}) + \frac{E_{j+1} - E'}{E_{j+1} - E_j} f_E(E_j) \right) = f_E(E_i) \tag{132}$$

for each $i \in [1..N]$. We can then group the terms involving each $f_E(E_j)$ in the left-hand side, resulting in an equation of the form:

$$\sum_{j=1}^{N} \frac{M_{ij}}{L(E_i)} f_E(E_j) = f_E(E_i) \tag{133}$$

with:

$$M_{ij} = \int_{E_j}^{E_{j+1}} dE' \, W(E_i \,|E') \frac{E_{j+1} - E'}{E_{j+1} - E_j} + \int_{E_{j-1}}^{E_j} dE' \, W(E_i \,|E') \frac{E' - E_{j-1}}{E_j - E_{j-1}} \tag{134}$$

for $j \in [2..N-1]$, and:

$$M_{i1} = \int_{E_1}^{E_2} dE' \, W(E_i \,|E') \frac{E_2 - E'}{E_2 - E_1} \tag{135}$$

and:

$$M_{iN} = \int_{E_{N-1}}^{E_N} dE' \, W(E_i \,|E') \frac{E' - E_{N-1}}{E_N - E_{N-1}} \tag{136}$$

$M_{ij}/L(E_i)$ is thus the matrix representing the discretized version of the integral operator $\mathcal{L}$. We have thus transformed our problem into a usual finite-dimensional linear algebra problem.

The grid $\{E_i\}$ is chosen to give a compromise between the precision of the final f_E that we compute and the computation time. The result is that successive points E_j and E_{j+1} can be separated by a distance larger than the characteristic dimension over which the transition rate varies. For instance, the Q_{abs} of PAHs show strong variations on a small interval around $10\,\mu$m where the characteristic PAH features are located (Fig. 22). Some care must thus be taken when computing the integral pieces defined by Eq. 134, 135 and 136. To keep all the precision available in the data, we build a grid of photon energies containing all the values present in the data grids for the absorption coefficient of the grain $Q_{\text{abs}}(U)$ and the incident radiation field $J_U(U)$. Missing values are interpolated from the known values if there are inside the bounds of the data grids. Otherwise we use the known power-law behaviors of those quantities at low photon energies to extrapolate. The numerical integration of the integrals Eq. 134, 135 and 136 to compute the coefficients of the matrix M_{ij} is done on this fine-grained grid.

As discussed in the previous Section, we have two resolution methods:

- We can diagonalize the matrix $M_{ij}/L(E_i)$, select the real eigenvalue that is closest to 1, and take as our solution f_E the corresponding eigenvector after normalization (Eq. 127).
- We can iterate the multiplication by $M_{ij}/L(E_i)$ from an initial guess (which must be a positive function to ensure that it is not orthogonal to the true solution), thus approximating the Perron projection. We take a constant function as our initial function, and monitor the convergence of the process by measuring the distance of the displacement of the function at each step (the ratio of the L_2 norm of the displacement to the L_2 norm of the initial function). We stop the iteration when the result moves less than a fixed precision threshold.

Both methods are implemented, and their comparative advantages are discussed in the next Section.

6.2.2 *Numerical tests*

We start by investigating the precision of the diagonalization method. We thus diagonalize the matrix $M_{ij}/L(E_i)$ obtained with different grid resolutions, and compare the eigenvalue found to 1, which is the expected eigenvalue. Fig. 29 shows the difference between this numerical eigenvalue and

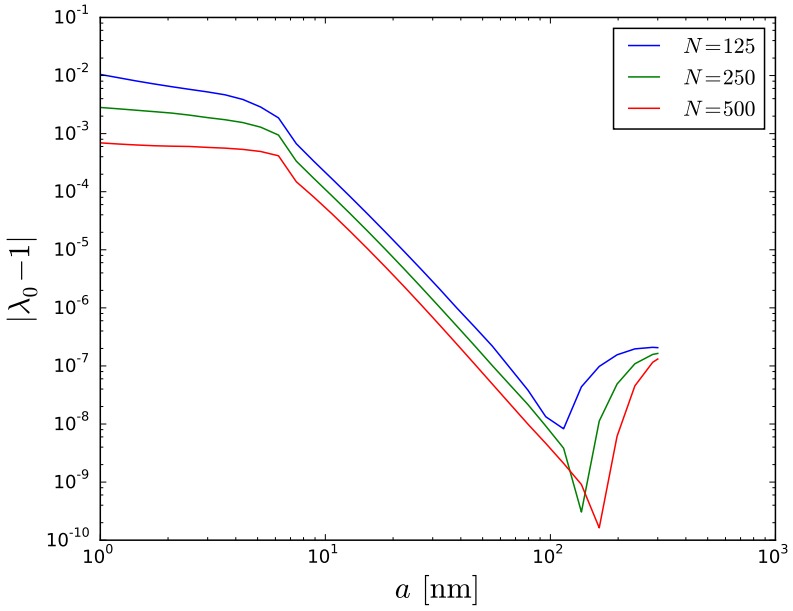

Figure 29: Relative error of the leading eigenvalue of the discretized matrix $M_{ij}/L(E_i)$ compared to the true eigenvalue 1 of the operator $\mathcal{L}$, as a function of grain size a and for different numerical resolutions N.

the expected value of 1. We see that as expected, the matrix $M_{ij}/L(E_i)$ possesses an eigenvalue very close to 1, and that this eigenvalue remains present when we reduce the numerical resolution.

However, the precision of this eigenvalue is not the only way to assess the numerical precision of our computation. On Fig. 30, we look at the numerical convergence of the resulting eigenfunction. The thermal energy PDF is plotted for increasing grain sizes, each time showing the results of different numerical resolutions. While for the small grains, the result seems already converged at the lowest resolution shown, for bigger grains the convergence is much slower. For the largest grain shown, it is still not converged at the highest resolution shown. Thus, the error of the eigenvalue compared to 1 is not a good measure of the precision of the numerical scheme. Indeed, we see that while the error on the eigenvalue is smaller for bigger grains (Fig. 29), the accuracy on the eigenfunction is actually better for small grains.

However, this slow convergence for the biggest grains is not problematic, as the distribution is strongly peaked (see the width on Fig. 30). Fluctuations are thus negligible for those grains, and unlikely to affect any physical or chemical process on the grain. For instance, if we look at the average grain temperature $\langle T \rangle = \int_0^{+\infty} dT\, T\, f_T(T)$, displayed on Fig. 31, we see that the result for big grains is accurately estimated at low resolution, and the most problematic case is for intermediate grain sizes. In all cases, the relative precision reaches the percent level for a resolution of at most 300 grid points.

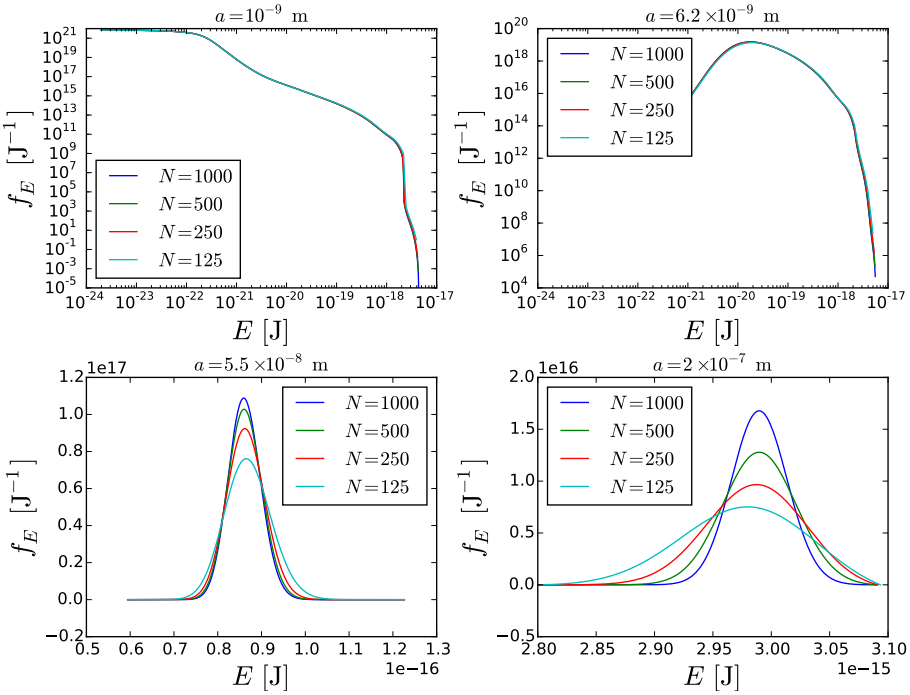

Figure 30: Numerical convergence of the thermal energy PDF as the number of grid points is increased, for four different grain sizes. The top plots are in logarithmic scales, while the bottom plots (for bigger grains) are in linear scales.

For big grains, the equilibrium temperature described in Sect. 5.1.4 is a good approximation for most purposes. It neglects completely the fluctuations, and assumes a constant temperature for the grain. If one need the full PDF of the fluctuations, an analytical approximation of the temperature PDF of big grains will be derived in Sect. 6.3.1.

The iterative method described in Sect. 6.1.3 is another way to compute the solution. In this case, we use the relative distance between the result of iteration i and the result of iteration $i+1$ (using L_2 distance and norm) to assess the stationarity of the solution. We choose a threshold of 10^{-7} in the following.

Fig. 32 (solid lines) shows the number of iterations necessary to reach this convergence threshold as a function of grain size and for different resolutions. This number of iterations appears to be independent of the numerical resolution, which confirms that this method is asymptotically $O(N^2)$ (because of matrix multiplications) while the diagonalization is in $O(N^3)$. However, we also see that this number quickly increases with grain size (roughly as a power law), and reaches very high numbers (several millions of iterations) for big grains. In practice, this results in the iterative method being faster for small grains, and the diagonalization method being faster for big grains.

We can speed up the iterative method by using the fact that we expect the solution to evolve continuously when the grain size increases. Thus, instead

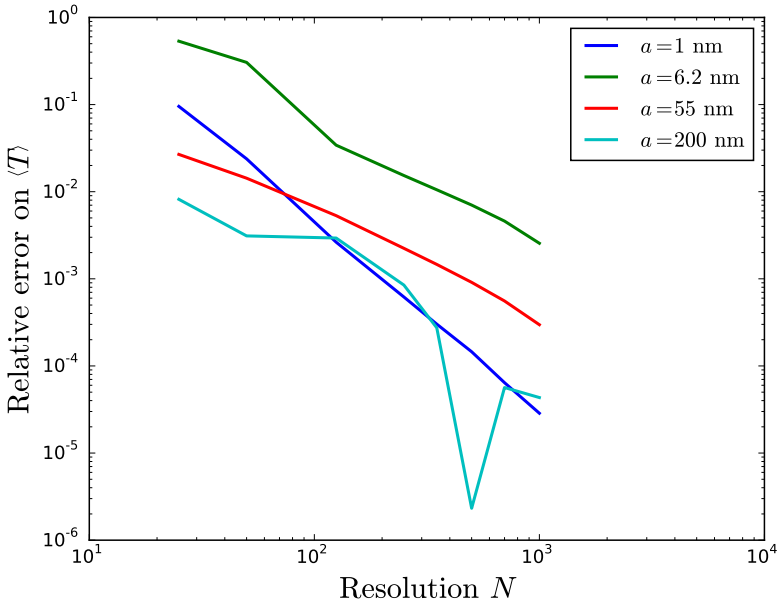

Figure 31: Relative error on the computed average grain temperature $\langle T \rangle$ as a function of the number of grid points N. The "true" average temperature for each grain is taken as the result at $N = 2000$.

of always starting from a constant initial guess, we can compute sequentially the different sizes and use the result obtained for one size as the initial guess for the next one. The improvement is shown on Fig. 32 (dashed lines). It results in a reduction of the number of iterations by a factor of roughly 3 on average.

We will thus use this improved iterative procedure for small grains, and automatically switch to the diagonalization procedure when it becomes faster. However, the diagonalization method tends to leave numerical noise on the low probability part of the PDF, as shown on Fig. 33, while the results of the iterative method show no such problem. This noise only concerns a region of the PDF which has no physical importance, so that it can be ignored for most uses. However, when using this temperature PDF to compute the average H_2 formation rate on the grain (described in Chapter 7), the numerical procedure that we then use proved to be very sensitive to this kind of noise. To get rid of this noise without paying the large computational cost of the iterative method for big grains, we apply the iterative method for a limited number of iterations starting from the result of the diagonalization method. We use 1000 operations, which proved to be enough to reduce the noise sufficiently.

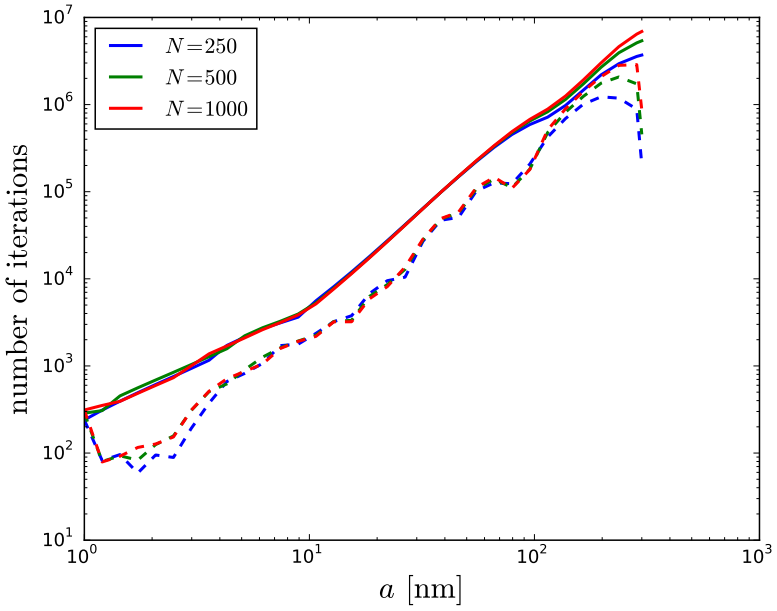

Figure 32: Number of iterations necessary to converge with the iterative resolution method, as a function of grain size, and for different resolutions. Two initialization methods are shown: starting from a constant function each time (solid lines), or restarting from the result of the previous grain size (dashed line).

6.2.3 *Results*

We now analyze the physical results obtained by this numerical solution. As explained in Sect. 6.1.1, we first compute the PDF in terms of thermal energy of the grain (f_E), before converting it into the temperature PDF f_T. Fig. 34 shows the thermal energy PDFs of amorphous carbon grains under a radiation field $\chi = 100$, for increasing grain sizes. The shape of the PDF changes continuously from the complete asymmetry for small grains, with most probability in the lowest energies and a very extended tail towards high energies, to the extremely narrow PDF of big grains.

As expected from our remark of Sect. 6.1.3, we observe for small grains that the PDF presents a plateau at low energies. For the smallest sizes, this plateau is the maximum of the PDF, which is a strictly decreasing function of the thermal energy. For slightly bigger grains, it starts loosing its importance and the PDF presents a peak at a non-zero energy. It then becomes more and more negligible, and does not appear anymore on the curves as our automatic bounds-finding method cuts out this part of the PDF.

Another noteworthy feature that appears on the PDF of small grains is a sharp cut at 2.18×10^{-18} J. This corresponds to the Lyman limit present in the external radiation field. No photon of higher energy than this limit is present. For small grains, the bulk of the probability is in the lower energies,

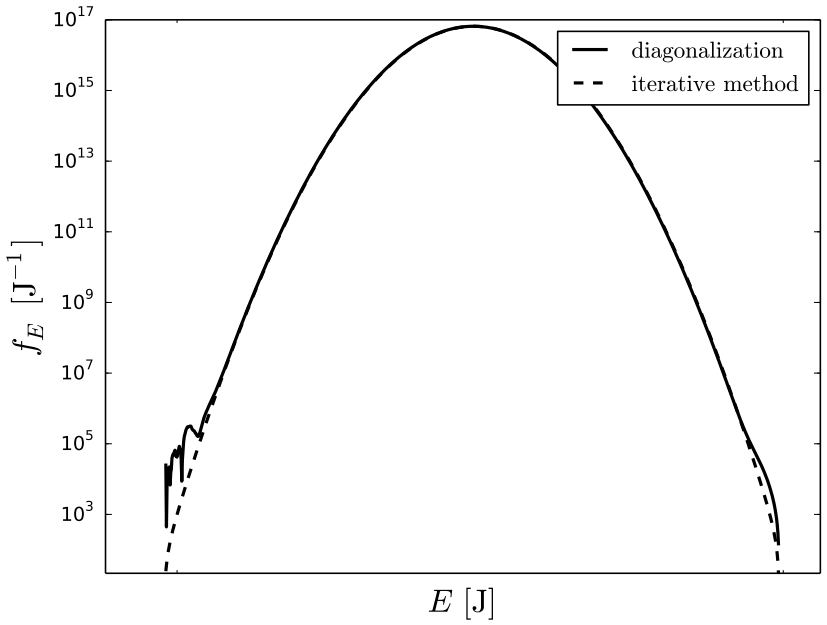

Figure 33: Thermal energy PDF for a 80 nm grain computed by diagonalization (solid line), or by the iterative method (dashed line) at the same resolution (N=500).

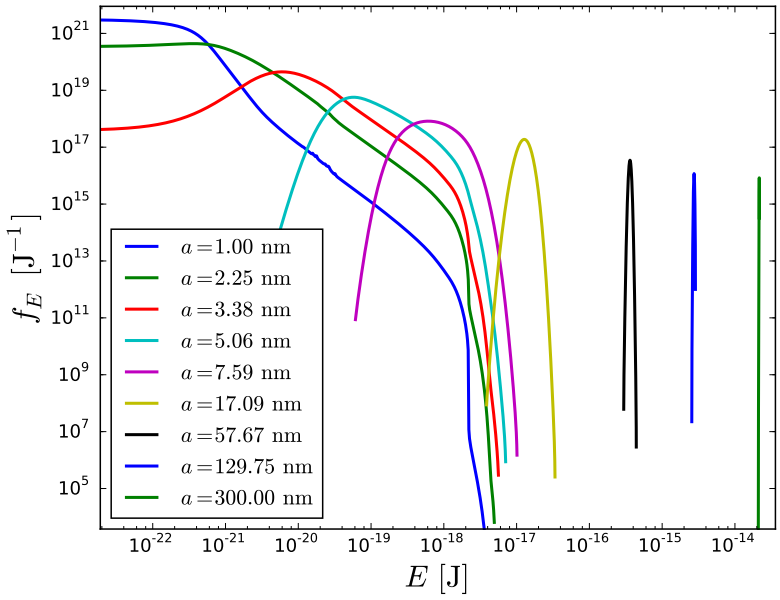

Figure 34: Thermal energy PDF f_E for amorphous carbon grains of different sizes, under a radiation field strength $\chi = 100$.

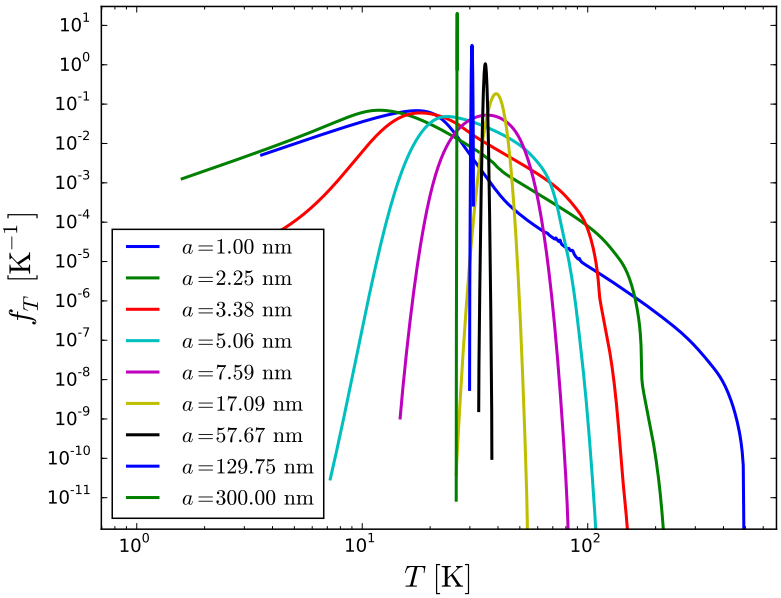

Figure 35: Temperature PDF f_T of amorphous carbon grains for the same conditions as in Fig. 34.

and a grain absorbing one photon from its most probable state thus cannot go significantly above the Lyman limit. As for such small grains these energies correspond to very high temperatures (see below the temperature PDFs), they cool extremely fast after the first photon, and absorbing a second photon before significant cooling is extremely rare. This appears in the very low probability part of the PDF located above the Lyman limit.

When the grain size grows, this cut loses its sharpness and slowly disappears. Bigger grains reach only lower temperatures after absorption, and thus cool slower. Moreover, their higher cross section makes them absorb photons more often. As a result, multi-photon absorptions become more likely as the grain size grows, until the effect of the Lyman limit completely disappears from the PDF.

As photon absorptions become more and more frequent and the cooling less and less efficient when the grain size grows, the PDF shifts to higher energies and its relative width decreases. The asymmetry of the PDF is also reduced, and the PDF approaches a rough log-normal shape for big grains (see Sect. 6.3.1 for a detailed discussion of the limit shape of the PDF for big grains). Of course, this shift simply translates the increase of the total heat capacity as the grain size grows. It is thus more meaningful to analyze this evolution for the temperature PDF of the grain f_T.

Fig. 35 shows the temperature PDFs of the same grains in the same conditions. The low energy plateau becomes a power law behavior at low temperatures because of the power law shape of the heat capacities (see Fig. 14 in the previous chapter). We can now observe that the extension of the high

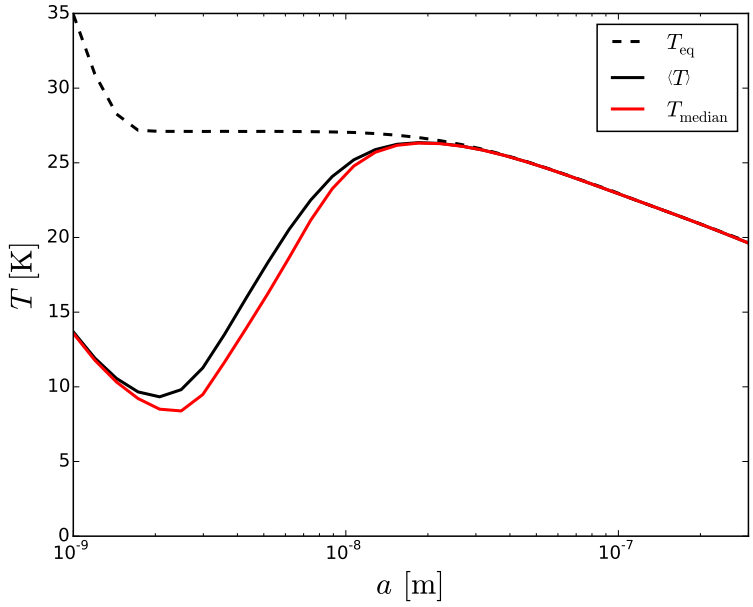

Figure 36: Comparison of the equilibrium temperature $T_{\rm eq}$ (dashed line, see Sect. 5.1.4 for definition), the true average temperature $\langle T \rangle$ (black solid line), and the median temperature $T_{\rm median}$ (red line) derived from the temperature PDF, as functions of the grain size, for amorphous carbon grains under a radiation field with $\chi = 10$.

temperature tail of the PDF decreases when the grain size increases, translating the reduced importance of the energy of a single photon for bigger grains. A 1 nm grain (amorphous carbon) can thus reach 500 K, while a 5 nm grain reaches only 100 K.

We also see that this reduction of the high temperature tail goes with an increase of the peak temperature of the PDF (except for the biggest grains). This can be understood in term of the average energy balance of the grain. Despite the fluctuations, the average emitted power must balance the received power. Despite its low probability, the high temperature tail contributes very significantly to the emitted power (because of the black body power $\propto T^4$). The high probability (low temperature) part then does not have to radiate as much energy and can be at lower temperatures. In other words, a few hot grains radiate away most of the incoming energy, while most of the grains lie at low temperatures. When the high temperature tail is reduced, the bulk of the PDF thus needs to become warmer to maintain the average energy balance.

This effect results in large differences between the equilibrium temperature (see Sect. 5.1.4 for definition) and the true average temperature of the grain. This comparison is shown on Fig. 36 for amorphous carbon grains receiving an external radiation field with $\chi = 10$. In the domain where the fluctuations are important, the average temperature is strongly reduced compared to the

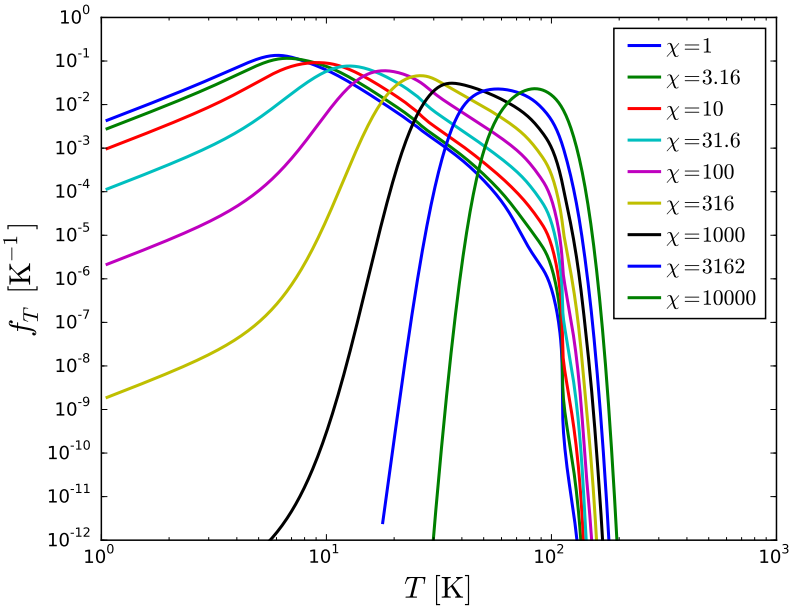

Figure 37: Temperature PDF f_T of a 3.38 nm amorphous carbon grain for increasing radiation field strengths.

equilibrium temperature. This is due to the effect described in the previous paragraph. The computation of the equilibrium temperature assigns a single constant temperature to the grains, the energy balance then requires this temperature to be high enough so that the received power is balanced by the emitted power. When allowing the temperature to fluctuate, the grains can spend a very small fraction of their time at high temperatures where they radiate away most of the absorbed energy, and spend most of their time at a much lower temperature. The average temperature is then dominated by the large fraction of the time spent at low temperatures and is much lower than the equilibrium temperature. The median temperature is also shown. Due to the PDF skewness towards the high temperature, the median temperature is lower than the average. Grains thus spend more than half of their time below their average temperature. This will be of great importance when studying H_2 formation on dust grains (Chapter 7). For big grains, fluctuations become negligible because the energy of individual photons becomes negligible compared to the average energy of the grain. As a result, the three temperatures converge for big grains. In addition we observe that both the average temperature and the equilibrium temperature increase again when going to very low sizes. This is caused by the limited cooling capacity of very small cold grains noted in Sect. 5.1.2 (a grain cannot emit a photon containing more energy than it possesses, the frequency domain in which small cold grains can emit is thus limited).

Fig. 37 shows the evolution of the temperature PDF of a 3.38 nm amorphous carbon grain when the radiation field strength is increased. As the

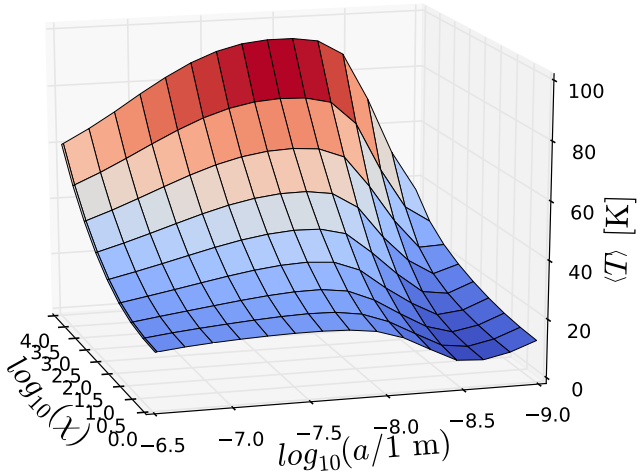

Figure 38: Average grain temperature as a function of grain size a and radiation field intensity χ for amorphous carbon grains.

high energy photons become more and more frequent, the grain has less time to cool between absorptions. The peak of its PDF is thus shifted to a higher temperature. As this means that its average thermal energy becomes greater, the energy of individual photons becomes less and less significant, resulting in weaker fluctuations and in a narrower PDF. We thus have a similar evolution when increasing the radiation field strength for a given size as when increasing size for a given radiation field, except that the average temperature shifts to higher temperatures as the grain heat capacity remains fixed.

Finally, we show the average temperatures of grains as a function of both grain size and radiation field intensity for amorphous carbon grains on Fig. 38, for silicate grains on Fig. 39 and for PAHs on Fig. 40. These graphs can be compared to the corresponding graphs for equilibrium temperatures (Fig. 19, 20 and 23). The domain of validity of the equilibrium temperature derived in the previous chapter proves to be quite accurate in delimiting the domain not affected by fluctuations. We see that contrary to what one might expect, a stronger radiation field results in slightly less important fluctuations. When UV photons become more frequent, grains have indeed less time to cool between photon absorptions and thus fluctuate in a narrower (and shifted towards high values) range of temperatures.

Of course, as most physical and chemical processes on dust grains depend non-linearly on the temperature, knowing the average temperature is not sufficient. The computation of dust emissivity, for which the knowledge of

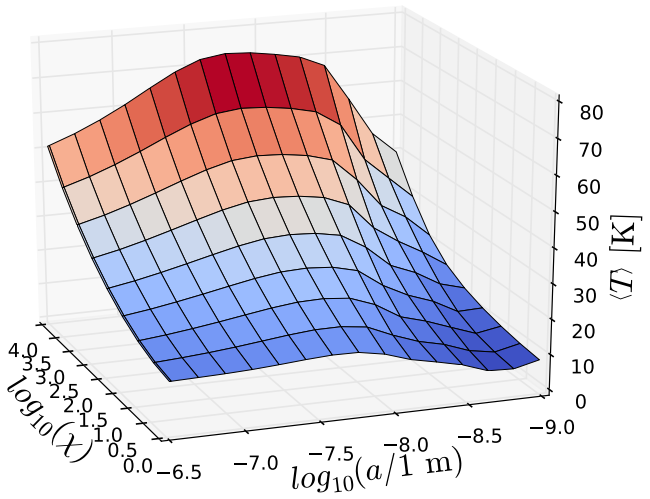

Figure 39: Average grain temperature as a function of grain size a and radiation field intensity χ for silicate grains.

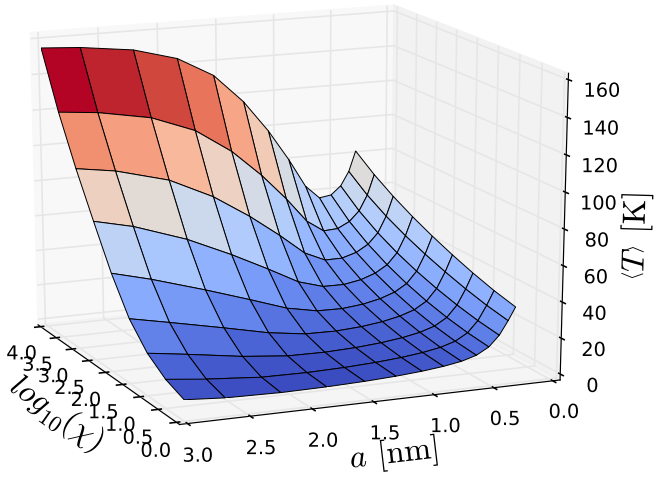

Figure 40: Average grain temperature as a function of grain size a and radiation field intensity χ for PAHs.

the temperature PDF is sufficient, will be described in Sect. 6.4. For the modeling of surface chemistry, a more detailed statistical treatment is needed. It will be described in Chapter 7.

6.3 LIMIT CASES

Before discussing applications of this computation of the temperature PDF of dust grains to the computation of their emissivity, we discuss here the asymptotic behavior of the PDF in different limits, and different approximations that can be used. We first discuss the Kramers-Moyal expansion, considering the asymptotic behavior for small jumps (and thus for big grains). We then discuss the less rigorous continuous cooling approximation, which neglect the discrete nature of photon emission while still taking into account the discrete nature of photon absorption.

6.3.1 *Kramers-Moyal expansion in the big grain limit*

For big grains, the jumps caused by photon absorptions become negligibly small and extremely frequent, so that the variation of the grain thermal energy could be approximated by a continuous evolution. This means that if the jumps are sufficiently small and frequent, we can approximate the pure jump stochastic process by a continuous diffusion process governed by a Fokker-Planck equation. The simplest way to derive such an approximation is called the Kramers-Moyal expansion (Kramers 1940, Moyal 1949), but its implicit use goes back to Einstein 1905, where Einstein models the brownian motion as a pure jump process before using this expansion to derive the diffusion equation.

We consider a general Master Equation (we assume the transition rate to be time independent to simplify the notations):

$$\frac{\partial f(x)}{\partial t} = \int dx' \, W(x \,|x') \, f(x') - \int dx' \, W(x' \,|x) \, f(x) \tag{137}$$

where $W(x' \,|x)$ is the transition rate from x to x'. We define $y = x' - x$ the distance of the jump, and reparameterize the transition rate as a function of the initial state x and the jump distance y:

$$t(x, y) = W(x + y \,|x) \tag{138}$$

We can then rewrite Eq. 137 as:

$$\frac{\partial f(x)}{\partial t} = \int dy \, t(x - y, y) \, f(x - y) - \int dy \, t(x, y) \, f(x) \tag{139}$$

As we expect the transitions to be mainly small jumps compared to the initial position x, we will use the series expansion of $t(x-y,y)\,f(x-y)$ around x:

$$t(x-y,y)\,f(x-y) = \sum_{k=0}^{+\infty} \frac{(-y)^k}{k!} \frac{d^k}{dx^k} \left[t(x,y)\,f(x)\right] \tag{140}$$

We now inject this expansion into Eq. 139:

$$\frac{\partial f(x)}{\partial t} = \int dy \sum_{k=1}^{+\infty} \frac{(-y)^k}{k!} \frac{d^k}{dx^k} \left[t(x,y)\,f(x)\right] \tag{141}$$

We permute the sum and the integral:

$$\frac{\partial f(x)}{\partial t} = \sum_{k=1}^{+\infty} \frac{(-1)^k}{k!} \frac{d^k}{dx^k} \left[f(x) \int dy\, y^k\, t(x,y)\right] \tag{142}$$

This is the Kramers-Moyal expansion. Truncating the series to keep only the first two terms yields:

$$\frac{\partial f(x)}{\partial t} = -\frac{d}{dx}\left[f(x) \int dy\, y\, t(x,y)\right] + \frac{1}{2}\frac{d^2}{dx^2}\left[f(x) \int dy\, y^2\, t(x,y)\right] \tag{143}$$

We recognize a Fokker-Planck equation corresponding to a continuous diffusion process with coefficients (see Chapter 4, and more precisely Sect. 4.2.4):

$$\begin{aligned} A(x) &= \int dy\, y\, t(x,y) \\ B(x) &= \int dy\, y^2\, t(x,y) \end{aligned} \tag{144}$$

We can rewrite these coefficients in terms of the initial transition rate $W(x'|x)$:

$$\begin{aligned} A(x) &= \int dx'\,(x'-x)\,W(x'|x) \\ B(x) &= \int dx'\,(x'-x)^2\,W(x'|x) \end{aligned} \tag{145}$$

We now apply this approximation to the Master Equation governing the thermal energy E of dust grains. Let us first derive the explicit expressions of the coefficients $A(E)$ and $B(E)$, using the expression of $W(E'|E)$ given in Eq. 117. For $A(E)$, we have:

$$\begin{aligned} A(E) &= \int_0^E dE'\,(E'-E)\,R_{\rm em}(E-E',T(E)) + \int_E^{+\infty} dE'\,(E'-E)\,R_{\rm abs}(E'-E) \\ &= -\int_0^E dU\,U\,R_{\rm em}(U,T(E)) + \int_0^{+\infty} dU\,U\,R_{\rm abs}(U) \end{aligned} \tag{146}$$

We recognize the total emitted power $P_{\rm em}(T)$ (Eq. 74) and total absorbed power $P_{\rm abs}$ (Eq. 70), so that:

$$A(E) = -P_{\rm em}(T(E)) + P_{\rm abs} \tag{147}$$

Similarly, we have for $B(E)$:

$$B(E) = \int_0^E dE' \, (E' - E)^2 \, R_{\rm em}(E - E', T(E)) + \int_E^{+\infty} dE' \, (E' - E)^2 \, R_{\rm abs}(E' - E) \tag{148}$$

so that:

$$B(E) = \int_0^E dU \, U^2 \, R_{\rm em}(U, T(E)) + \int_0^{+\infty} dU \, U^2 \, R_{\rm abs}(U) \tag{149}$$

Note that if we only keep the first term of the Kramers-Moyal expansion, Eq. 143 becomes:

$$\frac{\partial f(E)}{\partial t} = -\frac{d}{dx} \left[f(E) \left(-P_{\rm em}(T(E)) + P_{\rm abs} \right) \right] \tag{150}$$

which is the Liouville equation corresponding to the deterministic dynamical system:

$$\frac{dE}{dt} = -P_{\rm em}(T(E)) + P_{\rm abs} \tag{151}$$

We thus find back at the first order the continuous treatment of radiation, which at equilibrium gives the equilibrium temperature (Eq. 77).

As we are interested in the asymptotic shape of the PDF for big grains, we will consider the second order truncation given by Eq. 143 (the first order gives a Dirac). We are looking for the statistical equilibrium, so that our equation becomes:

$$0 = -\frac{d}{dE} \left[f_E(E) \, A(E) \right] + \frac{1}{2} \frac{d^2}{dE^2} \left[f_E(E) \, B(E) \right] \tag{152}$$

A first integration gives:

$$\frac{d}{dE} \left[f_E(E) \, B(E) \right] = 2 \, f_E(E) \, A(E) \tag{153}$$

The integration constant is zero, as the boundary condition is:

$$\lim_{E \to +\infty} f_E(E) = 0 \tag{154}$$

and we can assume that it goes to zero faster than the power law divergence of $A(E)$ and $B(E)$ at high dust temperature (for instance because the radiation field is cut at the Lyman limit). A second integration then gives:

$$f(E) = \frac{K}{B(E)} e^{2 \int_0^E \frac{A(E')}{B(E')} dE'} \tag{155}$$

The constant K can be determined from the normalization condition :

$$\int dE \, f(E) = 1 \tag{156}$$

This solution can thus be easily computed numerically from the knowledge of the photon absorption and emission rates (Eqs. 71 and 75). This computation is much faster than the numerical resolution of the Master Equation. It takes a time in $O(NM)$ where N is the numerical resolution of the thermal energy grid, and M is the numerical resolution of the photon energy grid on which the data (Q_{abs}, J) are given.

We show the comparison of this approximation with the exact results obtained before on Fig. 41. The approximation provided by the Kramers-Moyal expansion starts being accurate at $a = 38\,\text{nm}$. It perfectly reproduces the exact shape of the PDF for bigger grains. For the biggest sizes, we start seeing discrepancies again, but those actually come from the very slow convergence of the numerical resolution of the Master Equation for big grains (noted in Sect. 6.2.2). Despite the high resolution used here ($N = 4000$), the PDF for the last two sizes is still not converged. However, the results for increasing numerical resolutions clearly show a convergence toward the Kramers-Moyal result.

We have thus derived a precise approximation for grains bigger than $\sim 40\,\text{nm}$, which can be computed much faster than the exact solution. We did not use it in the following parts, but it could be used as the initial guess for our iterative procedure. The convergence would then be extremely fast for big grains (the initial guess is very close to the true solution), which were previously the slowest to converge. For small grains, the convergence would also be faster than starting from a constant function.

6.3.2 *Continuous cooling approximation*

An approximation often used for the computation of dust emissivity is the continuous cooling approximation (Desert et al. 1986, Draine and Li 2001). This idea is to consider the cooling of the grain as a continuous deterministic process, while the heating is still treated as a discrete jump process. This is based on the observation that the temperature fluctuations are mainly caused by UV photons, while the cooling takes the form of IR photons of much lower energies. However, we note that for a cold small grain, the energy of an IR photon is not negligible compared to the thermal energy of the grain, so that we expect this approximation to be inaccurate in the low temperature part of the PDF.

Considering a Markovian stochastic process with jumps caused by absorption (with rate $R_{\text{abs}}(U)$, see Eq. 71), and a drift $-P_{\text{em}}(T)$ caused by emission,

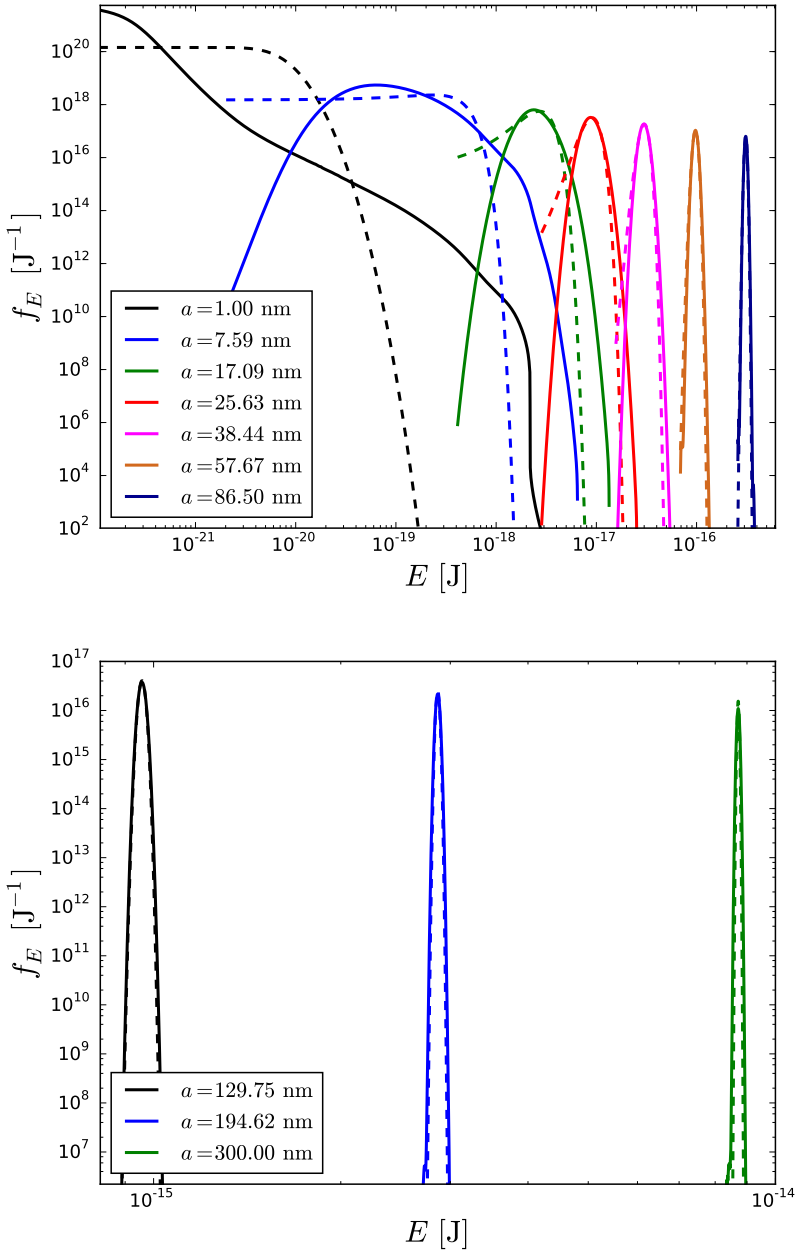

Figure 41: Comparison of the exact thermal energy PDF f_E (solid lines) and the approximate result of the Kramers-Moyal expansion (dashed lines). The grains are amorphous carbon grains exposed to a radiation field with $\chi = 1$.

the PDF obeys the general differential Chapman-Kolmogorov equation (Sect. 4.2.2, Eq. 43):

$$\frac{df(E)}{dt} = \int_0^E dU\, R_{\text{abs}}(U)\, f(E-U) \; - f(E) \int_0^{+\infty} dU\, R_{\text{abs}}(U) + \frac{d}{dE}\left(P_{\text{em}}(T(E))\, f(E)\right) \quad (157)$$

We are of course interested in the stationary PDF, which obeys the integro-differential equation:

$$f(E) \int_0^{+\infty} dU\, R_{\text{abs}}(U) - \frac{d}{dE}\left(P_{\text{em}}(T(E))\, f(E)\right) = \int_0^E dU\, R_{\text{abs}}(U)\, f(E-U) \quad (158)$$

Noting $L = \int_0^{+\infty} dU\, R_{\text{abs}}(U)$, which is a constant once the external radiation field is fixed (it represents the total rate of photon absorptions, regardless of frequencies), we can rewrite this equation as:

$$\frac{d}{dE}\left(f(E)\, P_{\text{em}}(T(E))\, e^{-\int_0^E dE' \frac{L}{P_{\text{em}}(T(E'))}}\right) = - e^{-\int_0^E dE' \frac{L}{P_{\text{em}}(T(E))}} \int_0^E dU\, R_{\text{abs}}(U)\, f(E-U) \quad (159)$$

Integrating over E once (and using the fact that $f(E)$ goes to zero fast enough when $E \to +\infty$ to set the integration constant to zero), we get:

$$f(E)\, P_{\text{em}}(T(E))\, e^{-\int_0^E dE' \frac{L}{P_{\text{em}}(T(E'))}} = \int_E^{+\infty} dE'\, e^{-\int_0^{E'} dE'' \frac{L}{P_{\text{em}}(T(E''))}} \int_0^{E'} dU\, R_{\text{abs}}(U)\, f(E'-U) \quad (160)$$

We can reorganize the terms:

$$f(E) = \int_E^{+\infty} dE' \frac{e^{-\int_E^{E'} de \frac{L}{P_{\text{em}}(T(e))}}}{P_{\text{em}}(T(E))} \int_0^{E'} dU\, R_{\text{abs}}(U)\, f(E'-U) \quad (161)$$

We make the variable change $E'' = E' - U$:

$$f(E) = \int_E^{+\infty} dE' \frac{e^{-\int_E^{E'} de \frac{L}{P_{\text{em}}(T(e))}}}{P_{\text{em}}(T(E))} \int_0^{E'} dE''\, R_{\text{abs}}(E-E'')\, f(E'') \quad (162)$$

We permute the integrals:

$$f(E) = \int_0^{+\infty} dE''\, f(E'')\, R_{\text{abs}}(E-E'') \int_{\max(E,E'')}^{+\infty} dE' \frac{e^{-\int_E^{E'} de \frac{L}{P_{\text{em}}(T(e))}}}{P_{\text{em}}(T(E))} \quad (163)$$

This is again an eigenfunction equation for an integral operator. However, we can see that the kernel of this operator is lower triangular (because $R_{\rm abs}(E - E'') = 0$ if $E'' > E$). When discretizing the problem, we are left with the diagonalization of a triangular matrix, which is much faster than a general matrix.

We will not use this approximation here, but it is used in the DustEM code to which we compare our results in Sect. 6.4.2.

6.4 DUST EMISSIVITY

The most direct use of the temperature PDF of dust grains is the computation of the dust emissivity.

6.4.1 *Computation of the dust emissivity*

As noted in Sect. 5.1.2, one grain of size a and temperature T emits a power per unit photon energy:

$$P_{\rm em}(U, T; a) = 4\pi^2 a^2 Q_{\rm abs}(U; a) B_U(U, T) \tag{164}$$

where we explicitly expressed the dependency in a. This has units energy $\cdot$ time^{-1} $\cdot$ energy^{-1}.

For a grain whose temperature fluctuates with PDF $f_T(T)$, the average emitted power is thus:

$$P_{\rm em}^{\rm (mean)}(U; a) = \int_0^{+\infty} dT\, f_T(T)\, P_{\rm em}(U, T; a) \tag{165}$$

with the same units as previously.

The total dust emissivity per steradian per unit volume of gas (in units energy.time^{-1}.energy^{-1}.steradian^{-1}.length^{-3}) is thus:

$$\epsilon_U(U) = \sum_{i \in \text{components}} \int da\, \frac{dn^{(i)}}{da}\, \frac{P_{\rm em}^{\rm (mean)(i)}(U; a)}{4\,\pi} \tag{166}$$

where the first sum is over the different dust components (carbon grains, silicate grains, PAHs,...).

This is the emissivity per unit photon energy, rather than per unit wavelength or frequency. In order to have an easily convertible quantity, we will rather give $U\,\epsilon_U(U)$, as $U\,\epsilon_U(U) = \nu\,\epsilon_\nu(\nu) = \lambda\,\epsilon_\lambda(\lambda)$.

Fig. 42 shows the resulting average power emitted by individual amorphous carbon grains. For big grains the emission computed from the equilibrium temperature using Eq. 164 with T_{eq} computed as described in Sect. 5.1.4 (dashed lines) is a very accurate approximation of the true average emission (Eq. 165). For smaller grains, the peak of the emission is shifted towards

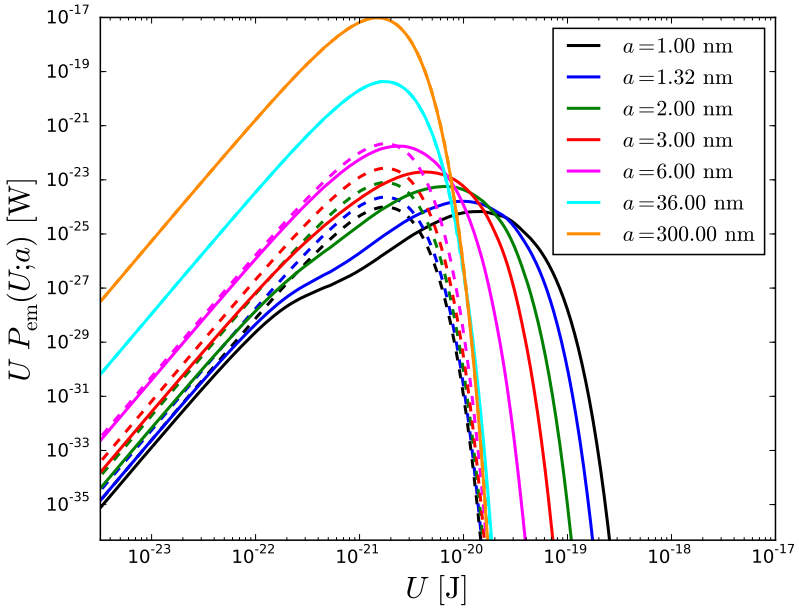

Figure 42: Power spectra emitted by individual dust grains (amorphous carbon), as function of the photon energy, under an external radiation field with $\chi = 1$. The solid lines show the average emission from fluctuating grains, while the dashed lines show the result of the equilibrium temperature approximation.

higher energies than predicted by the equilibrium temperature, as a high temperature tail develops in the PDF and becomes the dominant contribution to the emission (see Fig. 35).

The same comparison is shown on Fig. 43 for PAHs. The importance of fluctuations is obvious, and the well-known IR features only appear in the spectra when taking those fluctuations into account.

The overall emissivity of dust then results from the integration over the dust size distribution and populations. We will show this result using a realistic dust population when comparing our results with those of the `DustEM` code in the next subsection.

6.4.2 *Comparison with `DustEM`*

`DustEM` is a numerical tool[1] computing the extinction and emission by dust for any specified dust population (Compiègne et al. 2011). The emission is computed taking the temperature fluctuations into account by using the previously presented continuous cooling approximation (Sect. 6.3.2) and a low resolution to allow very fast computation. It can take into account more complex dust physics, such as temperature-dependent absorption cross section,

1 http://www.ias.u-psud.fr/DUSTEM/

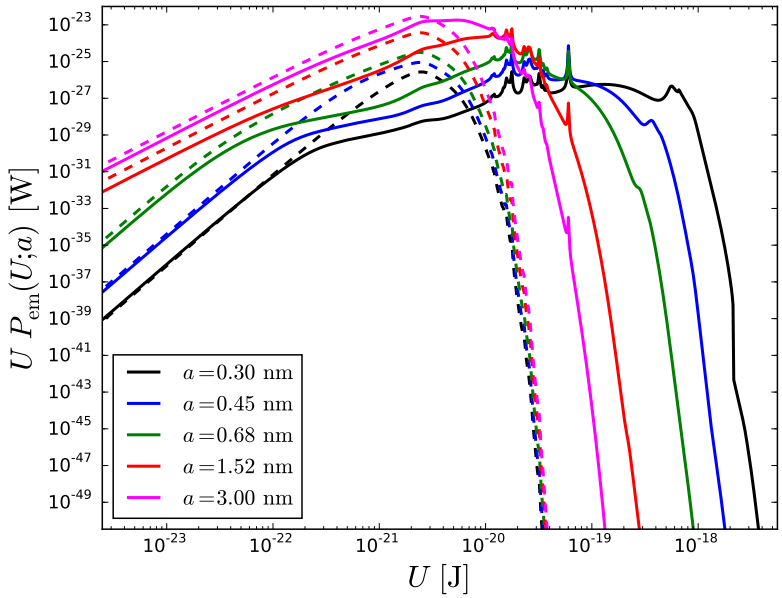

Figure 43: Same as Fig. 42 for PAHs.

and can also compute the charge of dust grains. We use it here to validate the results of our computation. However, we expect to find some differences due to the use of the continuous cooling approximation in DustEM, especially in the low temperature part of the temperature PDF.

Fig. 44 and 45 shows the comparison of the dust emissivity that we compute (black and gray) with the result of the `DustEM` code (red and orange). The thick lines show the total emissivity, while the other lines show the contributions from the different dust components (PAHs, amorphous carbon grains, silicate grains). Our results are in very good agreement with those of `DustEM`. Small discrepancies are visible, especially on the contribution of PAHs.

The actual comparison of the temperature PDF for PAHs and small grains show much bigger differences, as seen on Fig. 46. The high temperature tails are in good agreement, which explain the good agreement seen on the emission spectra (most of the PAH emission comes from the high temperature spikes). But the low temperature parts of the PDFs are strongly different.

Two kind of differences appear. First, the asymptotic behavior at low temperature is different. Our result goes to zero as a power-law. It comes from the plateau of the thermal energy, which was expected from analytical arguments (see the end of Sect. 6.1.3). The results of DustEM show a much faster decrease. This difference is expected from the use of the continuous cooling approximation in DustEM. With this approximation, a cooling grain will see its temperature decrease continuously until it absorbs another photon. But as the cooling speed decreases with the temperature, it slows down towards low temperature, until its characteristic time to move further to low tempera-

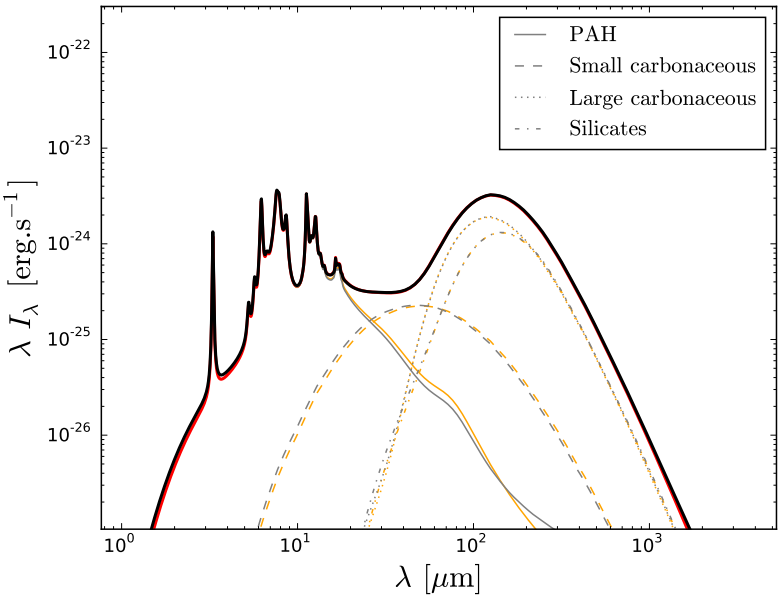

Figure 44: Emission spectra of dust, comparing our computation (black and grey lines) to the `DustEM` code (red and orange lines). The thin lines represents the emission of the different dust components, while the thick lines show the total emission. The emission is given per hydrogen gas atom, for a dust population following the DustEM dust model (Compiègne et al. 2011, see Sect. 5.3.3) irradiated by an external radiation field with $\chi = 1$.

ture becomes much bigger than the characteristic time of photon absorption. There is thus a region of low temperatures that the grain can effectively never reach, because the cooling becomes to slow, and this results in a low temperature cut-off in the PDF. On the contrary, when taking discrete cooling into account, a grain can at any time emit almost all of its thermal energy in a single photon and reach arbitrarily low temperatures. This explains the low energy plateau in the thermal energy PDF, and thus the power law behavior in the temperature PDF (because the heat capacity is a power law at low temperatures). This first difference is thus expected.

The second difference is the elbow, or change of slope, that appears in our results between the peak of the PDF and the high temperature tail. On the contrary, `DustEM` results show a roughly constant slope. The slope change actually comes from the fact that a grain cannot emit photons that would contain more energy than the thermal energy content of the grain. Small and cold dust grains thus have a reduced cooling capacity, resulting in this change of slope in the PDF. I implemented this emission cut-off for dust cooling in `DustEM`. The results are shown on Fig. 47 and are in better agreement. The same change of slope is present in both our results and DustEM results, and the remaining differences come from the continuous cooling approximation.

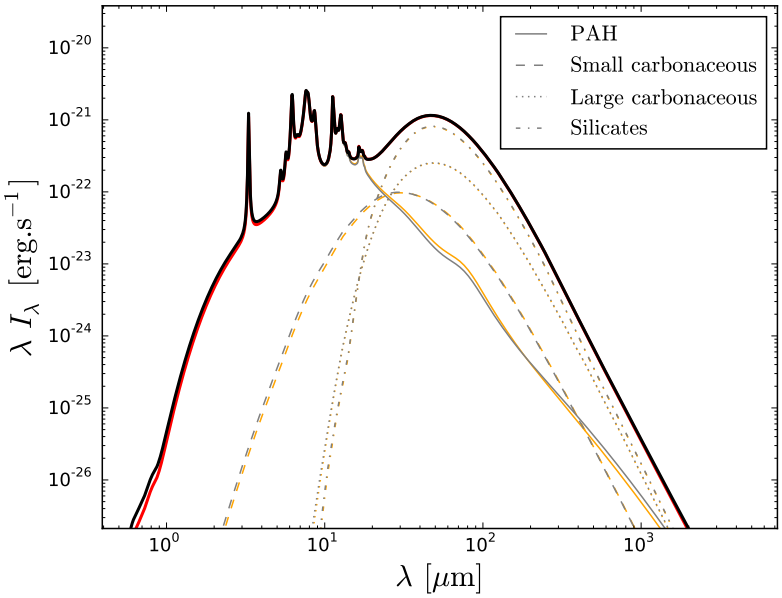

Figure 45: Same as Fig. 44 for an external radiation field with $\chi = 1000$.

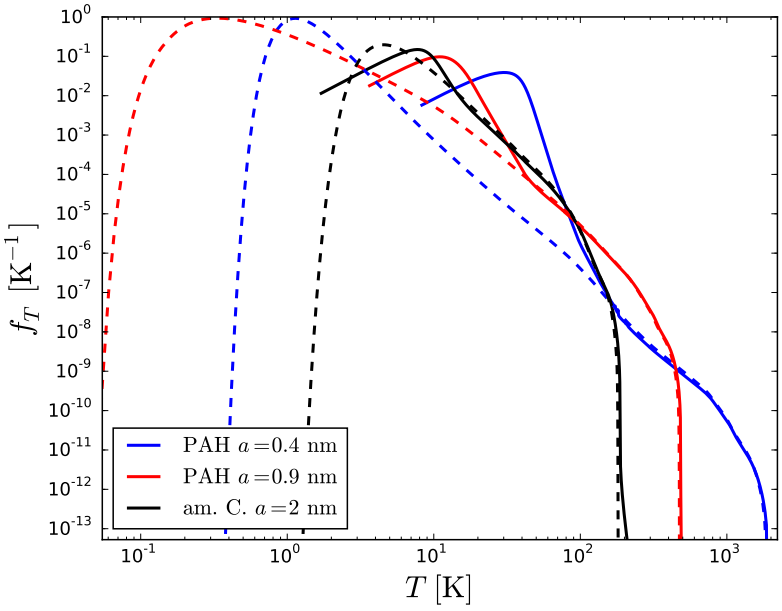

Figure 46: Temperature PDF for PAHs and small grains, comparing our results (solid lines) to those of `DustEM` (dashed lines), for $\chi = 1$.

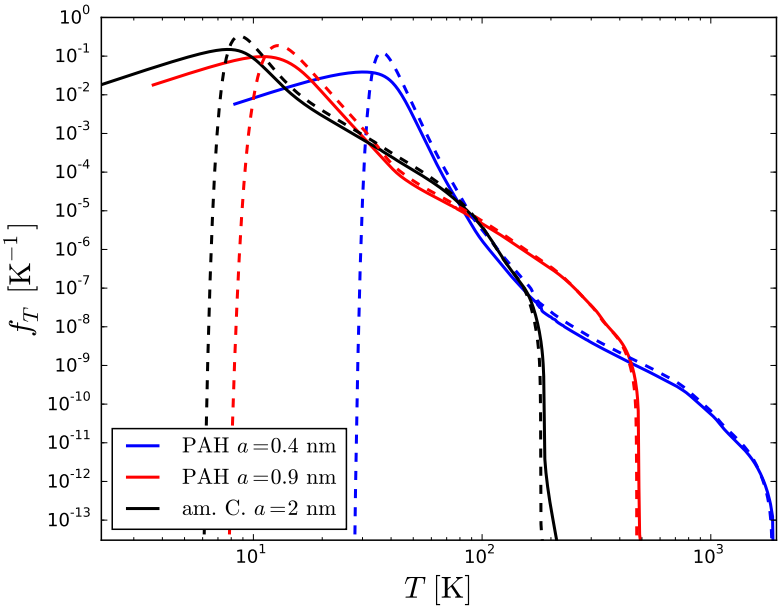

Figure 47: Same as Fig. 46, but comparing to a corrected version of `DustEM`, where the emission cut-off is properly implemented.

6.5 A FAST TREATMENT OF DUST EMISSIVITY

As a side project and a consequence of the previous work, I worked on an efficient method for computing the dust emissivity. Such a computation is indeed needed in interstellar cloud simulations. But the computation of the temperature PDF of dust grains, even when using the simplifying continuous cooling approximation and a low numerical resolution, still requires a few seconds per grain size. To compute the full SED, one need to integrate over the full dust size distribution, and thus to perform the computation for a sufficiently sampled grid of grain sizes. The resulting computation time is of the order of one minute.

In a full simulation of cloud, this computation needs to be repeated a large number of time. More specifically, our goal was to implement a computation of dust emissivity in the `Meudon PDR Code`. As the computation of the dust emissivity is required at each point in the cloud (several hundreds of points), and the whole computation is repeated iteratively (20 iterations), the repeated computation of the dust emissivity would take around one hundred hours, in addition to the other computations performed by the `Meudon PDR Code`.

I thus developed an approximation allowing a fast computation of dust emissivity, and this approximation was implemented in the `Meudon PDR Code` in collaboration with Benjamin Godard.

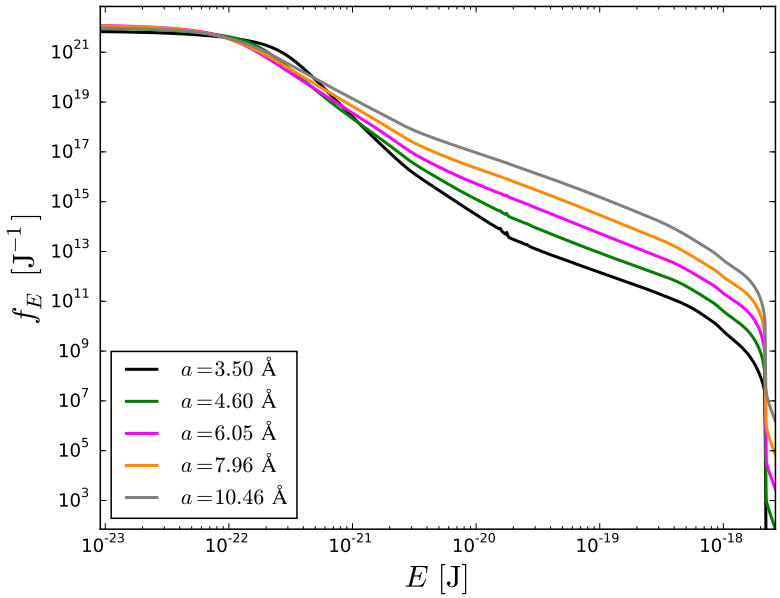

Figure 48: Thermal energy PDF of PAHs, under a radiation field with $\chi = 1$.

6.5.1 *Single photon approximation for small grains*

As shown on Fig. 48, the typical shape of the internal energy PDF f_E for PAHs is strongly asymmetrical, with most of the probability in the low energies and a long tail of low probability at high energy.

We construct an approximation based on this expected PDF shape for small grains. Our goal is to compute the emissivity and reproduce the part due to the stochastic heating of small grains. For fluctuating small grains, the emission will be dominated by the high temperature tail of the distribution. We are thus only interested in the high energy tail of the energy PDF. Therefore, we only approximate this high energy tail.

A small grain spends most of its time at low energy, and when absorbing a photon, it undergoes a cycle consisting in a jump to high energy, following by a cooling phase. At high energies, the cooling can be approximated as continuous, as the energy of one emitted photon is negligible compared to the internal energy of the grain.

We consider a small interval $[E, E + dE]$ in the high energy part, and try to evaluate the probability $P([E, E + dE])$ to find the grain in this interval. This probability is simply the ratio between the time τ_{stay} that the grain spends in the interval when it reaches it, over the characteristic time τ_{cycle} of the cycles that manage to reach our interval.

Under the approximation of continuous cooling, any cycle reaching an energy higher than E will pass through our interval while cooling down. Such cycles therefore happen each time the grain absorbs a photon of energy

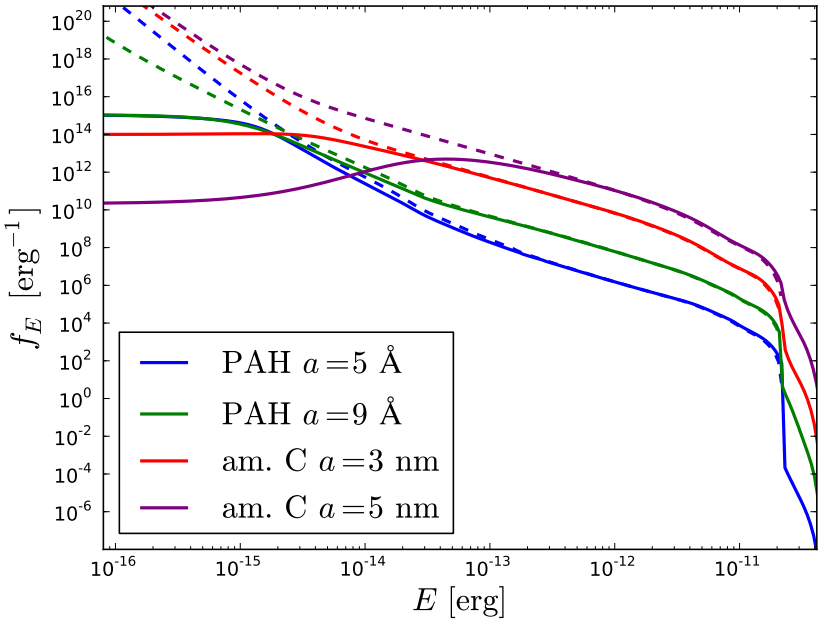

Figure 49: Thermal energy PDFs of PAHs and small grains, comparing the full computation (solid lines) to the approximation given by Eq. 170 (dashed lines).

higher than E (the initial energy before the absorption event is supposed very small and negligible compared to E). Their characteristic time is thus:

$$\tau_{\text{cycle}} = \frac{1}{\int_E^{+\infty} dU\, R_{\text{abs}}(U)} \tag{167}$$

Once reaching the interval, the grain cools down continuously with speed $\frac{dE}{dt} = P_{em}^{tot}(T)$. The time spent inside the interval (the crossing time) is:

$$\tau_{\text{stay}} = \frac{dE}{P_{em}^{tot}(T(E))} \tag{168}$$

The probability to find the grain in the interval is thus:

$$P([E, E+dE]) = \frac{\tau_{\text{stay}}}{\tau_{\text{cycle}}} = \frac{dE \int_E^{+\infty} dU\, R_{\text{abs}}(U)}{P_{em}^{tot}(T(E))} \tag{169}$$

Dividing by dE, we get the energy PDF:

$$f_E^{approx}(E) = \frac{\int_E^{+\infty} dU\, R_{\text{abs}}(U)}{P_{em}^{tot}(T(E))} \tag{170}$$

This formula is only valid for the high energy tail of the distribution. The results of the approximation for small grains are shown on Fig. 49. We obtain very good agreement on the high energy tail, with relative errors of the order of 10% or less. We note that this approximation always gives zero above the Lyman limit as the numerator of Eq. 170 is 0 in this case. This is due to

the fact that we neglect here multi-photon absorptions (i.e. absorption of a second photon while already being in the high-energy tail). Multi-photon absorptions can only be neglected for small grains. For big grains, this will not be a problem as a single grain temperature efficiently explains the emission spectra. This could be a problem for intermediate sizes.

We note that a similar expression was found by Guhathakurta and Draine 1989 (their Eq. 2.19, where $A_{k,i}$ should be $A_{k,f}$), who note a mathematical limit of the distribution (although problematic as given because not normalizable), but they do not actually use it. We independently reach the same expression for the high energy tail on the basis of physical arguments.

The idea is that the high energy part of the PDF, which is well reproduced by our approximation, is sufficient to explain the part of the emission spectra due to stochastic heating, and that the rest of the dust SED is caused by grains big enough so that their temperature fluctuations are negligible. This can be seen on Fig. 44 and 45, where the dominating contribution appear to be PAHs (below 1 nm) and big grains (above 5 nm), while the contribution of intermediate sizes (the "small amorphous carbon population") is very limited. We will thus use this approximation for the high energy tail of very small grains, and represent the remaining part by a single cold temperature. Moreover, our approximation will smoothly transition towards a single temperature equilibrium treatment for big grains.

We first need to construct a limit E_{lim} separating the tail over which the approximation is valid from the cold part. We start by noticing that when the approximation starts diverging from the exact curve, it does so very fast (typically as a power law) and becomes much higher.

The true PDF must be normalized: $\int_0^{+\infty} dE\, f_E(E) = 1$. Thus, when integrating the approximated PDF starting from the high energy end, the result will be close to the true integral as long as the approximation is valid, and then become much bigger and soon go above 1. Thus the energy E_{norm} defined by:

$$\int_{E_{\text{norm}}}^{+\infty} dE\, f_E^{approx}(E) = 1 \tag{171}$$

is a limit below which our approximation is certainly not valid anymore. Moreover, it can be expected to be close from the point at which the approximation actually starts to diverge, due to the fast divergence. We will thus take this limit multiplied by a safety factor of 3 (determined empirically by comparison with the true solution on final emission spectra):

$$E_{\text{lim}} = 3\, E_{\text{norm}} \tag{172}$$

The resulting approximated tails are represented on Fig. 50 for various grain sizes and two different radiation field strengths. We see that the choice of E_{lim} allows us to keep only the range in which the approximation is adequate. The approximate curve for the 5 nm amorphous carbon grain under a

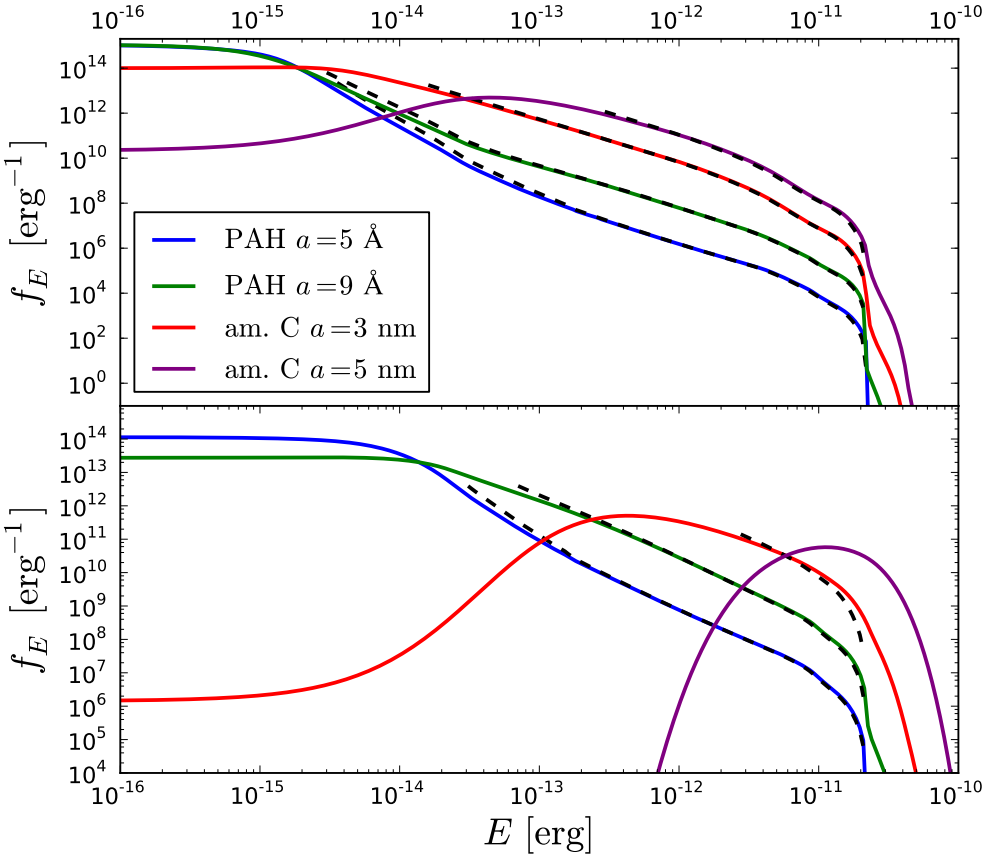

Figure 50: Comparison between the true PDFs (solid lines) and the approximated PDFs (dashed lines, computed from Eq. 170) plotted above E_{lim} only. The top panel show the results for a weak radiation field ($\chi = 1$) and the bottom panel for a strong radiation field ($\chi = 1000$).

$\chi = 1000$ radiation field does not appear on the graph as the range between the corresponding E_{lim} and the Lyman limit above which our approximation gives 0 is too small to appear on the graph. Therefore, the high energy tail will in this case be negligible, and the grain emission will be described by the big grain treatment. We start to see how the small grain treatment will smoothly transition toward the big grain treatment.

6.5.2 *A complete emissivity approximation*

The power emitted by the tail at photon energy U by a single grain (per unit photon energy) is then:

$$P_{\text{em}}^{(\text{tail})}(U) = \int_{\max(E_{\text{lim}},U)}^{+\infty} dE\, f_E(E)\, P_{\text{em}}(T(E), U) \tag{173}$$

where the max in the lower bound of the integral comes from the fact that we only consider the tail ($E > E_{\rm lim}$) and that grains with less thermal energy than U cannot emit at U. The total power emitted by the tail is then:

$$P_{\rm em}^{\rm tot\,(tail)} = \int_0^{+\infty} dU\, P_{\rm em}^{\rm (tail)}(U) \tag{174}$$

This only represents the contribution from the transient high temperature spikes. The total probability to be in this high energy tail is :

$$p_{\rm tail} = \int_{E_{\rm lim}}^{+\infty} dE\, f_E^{\rm approx}(E) \tag{175}$$

As the remaining fraction (low temperatures) contributes a negligible fraction of the emission, we simply represent the remaining part of the distribution by one single temperature $T_{\rm cold}$. The probability for this temperature is then:

$$p_{\rm cold} = 1 - p_{\rm tail} \tag{176}$$

As the grain must on average emit as much power as it absorbs, we choose $T_{\rm cold}$ so that the global energy balance for the grain is enforced. $T_{\rm cold}$ is therefore defined by:

$$p_{\rm cold}\, P_{\rm em}^{\rm tot}(T_{\rm cold}) + P_{\rm em}^{\rm tot\,(tail)} = P_{\rm abs}^{\rm tot} \tag{177}$$

The resulting power emitted by the grain at photon energy U (per unit photon energy) is then:

$$P_{\rm em}^{\rm (approx)}(U) = P_{\rm em}^{\rm (tail)}(U) + p_{\rm cold}\, P_{\rm em}(T_{\rm cold}, U) \tag{178}$$

As seen on Fig. 50, the extension of the tail decreases for big grains until completely vanishing, so that more and more of the probability will be affected to $T_{\rm cold}$ until $p_{\rm cold} = 1$ in which case $T_{\rm cold}$ becomes equal to the usual equilibrium temperature (see Sect. 5.1.4). Our approximation thus transitions smoothly to the usual equilibrium temperature approximation for big grains.

The resulting spectra computed using this approximation are shown on Fig. 51 and 52 for two different radiation field intensities. Despite some small discrepancies visible on specific dust components (especially PAHs and small carbonaceous grains), the agreement is excellent on the overall spectrum. The small problems for intermediate grain sizes are thus completely masked by the contribution of either very small grains, dominated by the single-photon temperature tail modeled by the approximation, or of big grains for which the equilibrium temperature approximation is enough.

Such an approximation is thus sufficient to compute the emission spectrum of dust, and it is much faster than the true computation of the temperature PDF (even with the continuous cooling approximation).

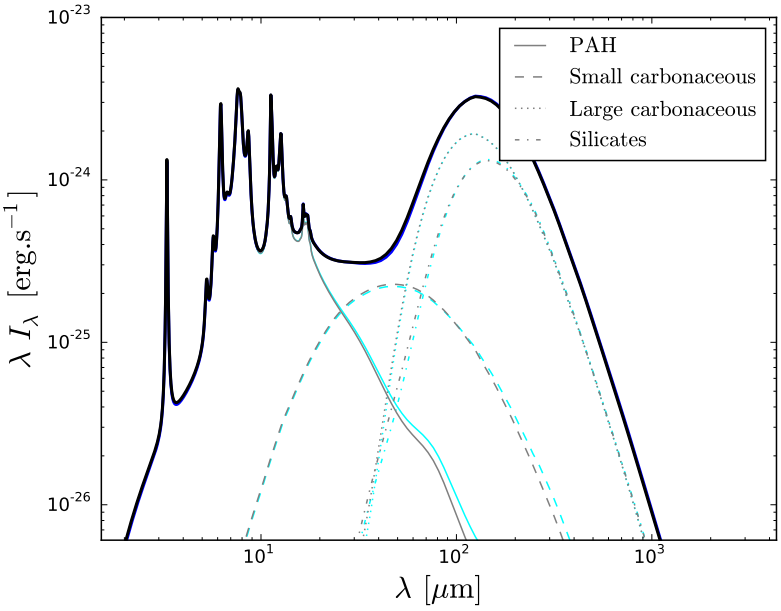

Figure 51: Comparison between the full dust emission spectrum (black and gray) and the result of the approximation (dark and light blue). The dust population corresponds to the DustEM dust model, and the contributions from the different dust components are shown by the thin lines, while the total spectra are shown by thick lines. The radiation field is $\chi = 1$.

6.5.3 *Implementation in the Meudon PDR Code*

In order to have a relevant computation of dust emissivity in the `Meudon PDR Code`, it was first necessary to add a PAH component to the dust population in order to correctly reproduce the near IR part of the spectrum. As described in Chapter B, the Meudon PDR Code included only a single power law distribution from 1 nm to 300 nm, with properties representing a mix of graphite and silicates. I added a second dust component corresponding to PAHs. The importance of this component is fixed by the parameter q_{PAH}, which represents the fraction of the total dust mass that is in this PAH component. For simplicity and clarity, we will call "PAH" this component, and "grains" (abbreviated as Gr) the component representing the other grains.

For the PAHs, we take a lognormal distribution similar to that of the `DustEM` dust model:

$$f_{\mathrm{PAH}}(a) = \frac{1}{a\,\sigma\sqrt{2\,\pi}} e^{-\left(\frac{\ln(a/a_0)}{\sqrt{2}\sigma}\right)^2} \tag{179}$$

with $a_0 = 6.4$Å and $\sigma = 0.1$.

As the lognormal distribution quickly goes to zero in the tails, we do not set a minimal and maximal size and we suppose the distribution to extend from 0 to $+\infty$. We will see that a 5-point Gauss-Hermite integration on this

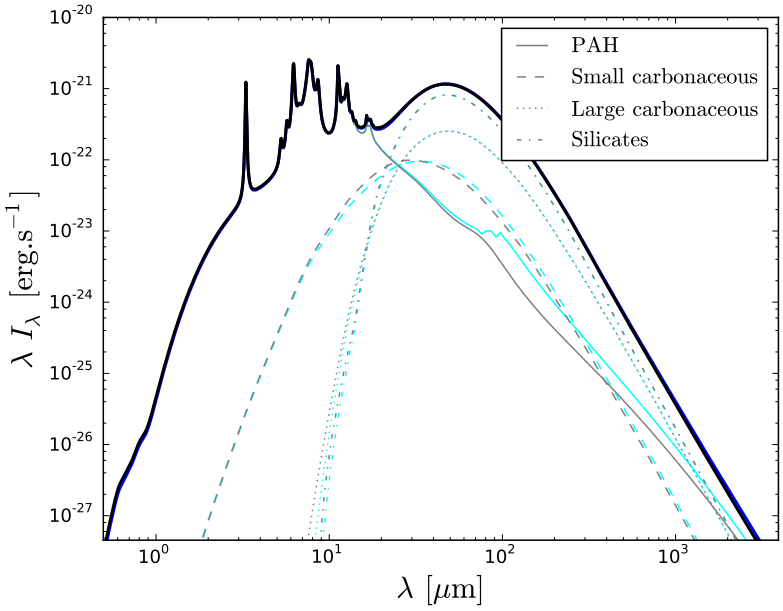

Figure 52: Same as Fig. 51 for a radiation field with $\chi = 1000$.

distribution gives abscissas in the range $\left[4.8\,\text{Å}, 8.5\,\text{Å}\right]$, so that we do not need to evaluate anything out of the range of sizes for which we have data.

The parameters a_0 and σ are fixed in the code, and only the total mass fraction of PAHs q_{PAH} is accessible to the user in the `pdr.in` file.

This distribution is normalized to 1, the number of PAH grains of size a per unit volume being given by:

$$dn_{PAH}(a) = n_H A_{PAH} f_{PAH}(a)\, da \tag{180}$$

where A_{PAH} will be determined below.

For the second component, we keep the power law distribution from $a_{min} = 1\,\text{nm}$ to $a_{max} = 300\,\text{nm}$ with exponent $\alpha = -3.5$:

$$f_{Gr}(a) = \begin{cases} a^{-3.5} & \text{if} \quad a \in [a_{min}, a_{max}] \\ 0 & else \end{cases} \tag{181}$$

We did not normalize this expression as it will make the later expressions simpler.

The exponent $\alpha = -3.5$ is fixed in the code, but a_{min} and a_{max} are accessible to the user in the `pdr.in` file.

This distribution is not normalized, and the number of grains of size a per unit volume is:

$$dn_{Gr}(a) = n_H A_{Gr} f_{Gr}(a)\, da \tag{182}$$

where A_{Gr} will be determined below.

We use PAHs data (absorption coefficient $Q_{\rm abs}$ and heat capacity C) from `DustEM` up to $a = 1\,$nm. We do a mixing of the properties of neutral PAHs and singly charged PAHs, taking 60% of the properties of the neutrals and 40% of the properties of PAH ions. The Q_{abs} are extended to low wavelengths by taking the graphite properties with a scaling factor ensuring continuity (from Li and Draine [2001], we see that $Q_{abs}^{(PAH)}(a) = Q_{abs}^{(gra)}(a)$ at low wavelengths). Above 3 nm, we use as before a mix of the properties of silicates and graphite, with 30% of silicates and 70% of graphites. The Q_{abs} and Q_{sca} are unchanged. The heat capacities C are taken from `DustEM` for silicates and graphites and mixed together similarly to the Q_{abs}. Finally, between 1 nm and 3 nm, the properties are interpolated between the PAHs and the "grains" properties, in order to have a smooth transition.

Finally, the normalization factors of the size distributions are constrained by two parameters: the total dust-to-gas mass ratio G, and the PAH fraction of the total dust mass $q_{\rm PAH}$. Both are accessible to the user in the `pdr.in` file.

The gas mass per unit volume is:

$$M_{gas} = 1.4\, m_H\, n_H \tag{183}$$

where the factor 1.4 accounts for helium, m_H is the hydrogen mass, and n_H the gas density.

The PAH total mass is:

$$M_{PAH} = n_H A_{PAH} \int_0^{+\infty} da\, f_{PAH}(a)\, \frac{4}{3}\pi a^3 \rho_{PAH} \tag{184}$$

where A_{PAH} is a normalization factor. We recall that for PAHs, the size a is defined as the radius of a sphere of same mass, so that taking a sphere formula for the mass is correct. By injecting Eq. 179 and doing the variable change $u = \frac{1}{\sqrt{2}\sigma}\log(\frac{a}{a_0})$, we then get:

$$M_{PAH} = n_H A_{PAH} \rho_{PAH} e^{\frac{9}{2}\sigma^2} \frac{4\pi}{3} a_0^3 \tag{185}$$

The total mass of the "grain" component is:

$$\begin{aligned} M_{Gr} &= n_H A_{Gr} \int_{a_{min}}^{a_{max}} da\, f_{Gr}(a)\, \frac{4}{3}\pi a^3 \rho_{Gr} \\ &= n_H A_{Gr} \frac{8}{3}\pi \rho_{Gr} (\sqrt{a_{max}} - \sqrt{a_{min}}) \end{aligned} \tag{186}$$

where ρ_{Gr} is taken a mix of ρ_{gra} and ρ_{sil} with the same weights as for the Q_{abs}.

Our constraints on A_{PAH} and A_{Gr} are thus:

$$\begin{cases} M_{PAH} + M_{Gr} = G\, M_{gas} \\ \frac{M_{PAH}}{M_{PAH}+M_{Gr}} = q_{PAH} \end{cases} \tag{187}$$

The second equation gives us:

$$A_{PAH} = q_{PAH} e^{-\frac{9}{2}\sigma^2} G \frac{1.4 m_H}{\frac{4\pi}{3} a_0^3 \rho_{PAH}} \tag{188}$$

The first equation then gives:

$$A_{Gr} = (1 - q_{PAH}) G \frac{1.4\, m_H}{\frac{8}{3}\pi \rho_{BG} (\sqrt{a_{max}} - \sqrt{a_{min}})} \tag{189}$$

We will need to perform numerical integrations over this dust population, for instance when computing the dust emissivity or surface chemistry. We will need to compute integrals of the form:

$$I = \int da \, \frac{dn}{da} \, g(a) \tag{190}$$

where g is a function that will have to be evaluated numerically, while $\frac{dn}{da}$ is known analytically according to the previous section.

We start by separating the PAH and "grain" parts of the integral, but we show later that the computation can be reunited for the actual implementation.

$$I = \int_0^{+\infty} da \, A_{PAH} n_H \, f_{PAH}(a) \, g(a) + \int_{a_{min}}^{a_{max}} da \, A_{Gr} n_H \, f_{Gr}(a) \, g(a) \tag{191}$$

The second integral corresponds to what was already implemented in the code. It is computed by Gauss integration, giving a family $(a_i^{(2)})$ of abscissas with the corresponding weights $w_i^{(2)}$ (we use the superscript index 2 for the "grain" component, and 1 for the PAH component). The second integral is then computed as:

$$n_H A_{Gr} \sum_i w_i^{(2)} g(a_i^{(2)}) \tag{192}$$

We will now transform the first integral so that we can use the classical case of Gauss-Hermite, for which the orthogonal polynomials are known, and the abscissas and weights easily found tabulated:

$$\int_0^{+\infty} da \, A_{PAH} n_H \, f_{PAH}(a) \, g(a) = \frac{A_{PAH} n_H}{\sigma \sqrt{2\,\pi}} \int_0^{+\infty} da \, \frac{1}{a} e^{-\left(\frac{ln(\frac{a}{a_0})}{\sqrt{2}\sigma}\right)^2} g(a) \tag{193}$$

We do the variable change $x = \frac{\ln(\frac{a}{a_0})}{\sqrt{2}\sigma}$, giving $a = a_0 e^{\sqrt{2}\sigma\, x}$ and $\frac{da}{a} = \sqrt{2}\sigma \, dx$:

$$\int_0^{+\infty} da \, A_{PAH} n_H \, f_{PAH}(a) \, g(a) = \frac{A_{PAH} n_H}{\sqrt{\pi}} \int_{-\infty}^{+\infty} dx \, e^{-x^2} \, g(a_0 e^{\sqrt{2}\sigma x}) \tag{194}$$

$x_i^{(1)}$	$a_i^{(1)}$ [nm]	$w_i^{(1)}$
−2.02018287046	0.480953780458491	0.019953242059
−0.958572464614	0.5588636682547928	0.393619323152
0.	0.64	0.945308720483
0.958572464614	0.732915777615478	0.393619323152
2.02018287046	0.8516410861965369	0.019953242059

Table 4: Abscissas and weights for the Gauss-Hermite integration over the PAH size distribution.

This integral is now a classical case of Gauss-Hermite integration (this is the reason why we keep the PAH size distribution from 0 to $+\infty$). We will take 5 size point in the Gauss-Hermite integration, the abscissas and weight are then given in Table 4. The abscissas $x_i^{(1)}$ are converted into sizes $a_i^{(1)}$ according to our variable change $a = a_0 e^{\sqrt{2}\sigma x}$.

We see that our abscissas stay in the range of sizes where our data are defined ($a > 3$Å). We could go up to a 19 points integration and still stay in the range. More points would result in the lowest abscissa to go below 3Å.

The first integral will therefore be computed as:

$$\int_0^{+\infty} da\, A_{PAH} n_H\, f_{PAH}(a)\, g(a) = \frac{A_{PAH} n_H}{\sqrt{\pi}} \sum_i w_i^{(1)} g(a_i^1) \tag{195}$$

We then define a final family of abscissas and weight as:

$$a_i = \begin{cases} a_i^{(1)} & \text{if} \quad 0 \leq i \leq 4 \\ a_{i+5}^{(2)} & \text{else} \end{cases} \tag{196}$$

and:

$$w_i = \begin{cases} \frac{A_{PAH}}{\sqrt{\pi}} w_i^{(1)} & \text{if} \quad 0 \leq i \leq 4 \\ A_{Gr} w_{i+5}^{(2)} & \text{else} \end{cases} \tag{197}$$

And we finally simply have:

$$I = n_H \sum_i w_i\, g(a_i) \tag{198}$$

The computation of the dust emissivity is then implemented following the method described in Sect. 6.5.1 and 6.5.2. The computation is performed at each position in the cloud, and is repeated for each global iteration of the code. The steps are computed in the following order:

1. We compute the approximated PDF using Eq. 170.

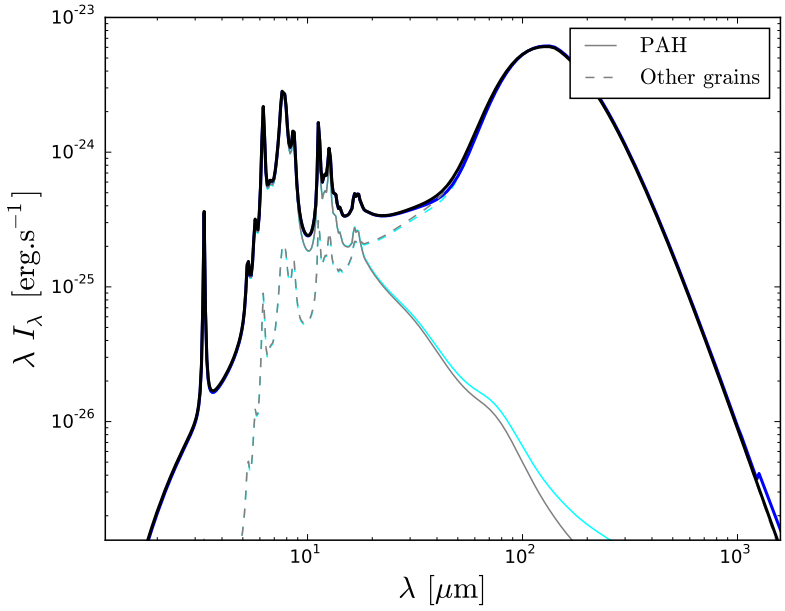

Figure 53: Same as Fig. 51 for a dust population corresponding to the improved PDR dust model. Radiation field: $\chi = 1$, PAH mass fraction: $q_{\mathrm{PAH}} = 4.6\%$.

2. The validity limit E_{lim} is computed from Eq. 171 and 172, by integrating the previously found PDF starting from the high energy end and successively adding intervals until the integral is 1.

3. We then compute p_{tail} and p_{cold} from Eq. 175 and 176. For this we perform again the integration of the PDF, this time knowing the validity limit.

4. We compute the total power emitted by the high temperature tail (Eq. 173 and 174)

5. The "cold" equilibrium temperature is then computed by dichotomy to balance the residual absorbed power (total absorbed power minus total power emitted by the tail) and the power emitted by the "cold" part of the distribution (Eq. 177)

6. Finally, the total emissivity spectrum of the grain is computed summing both the contribution of the high temperature tail, and that of the cold part (Eq. 178)

Fig. 53 and 54 show a final verification of the agreement between the full computation of the dust emission spectrum and the approximation, but this time for the dust population actually used in the `Meudon PDR Code` and described above. The agreement is again very good.

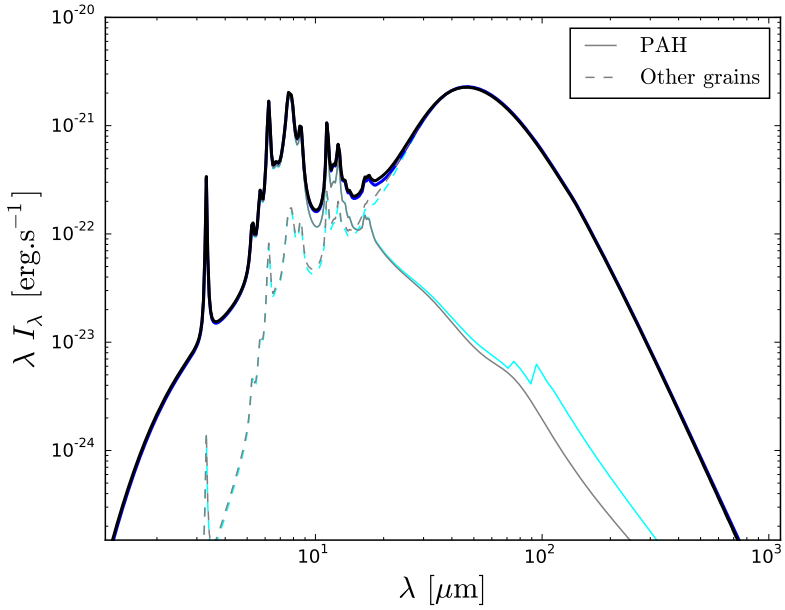

Figure 54: Same as Fig. 51 for a dust population corresponding to the improved PDR dust model. Radiation field: $\chi = 1000$, PAH mass fraction: $q_{\mathrm{PAH}} = 4.6\%$.

7

CHEMISTRY ON FLUCTUATING DUST GRAINS: THE CASE OF H_2

The temperature fluctuations investigated in the previous chapter do not only affect dust emissivity. Surface reactions are very sensitive to the grain temperature and are very likely to be affected by temperature fluctuations. We will focus on H_2 formation as it is the only surface reaction to occur in UV-rich environments such as PDRs or diffuse molecular clouds where fluctuations are large and frequent.

In this chapter, we generalize the Master Equation approach presented in the previous chapter to the case of coupled fluctuations of the grain temperature and the surface chemical state. For H_2 formation, the surface state is simply the number of adsorbed H atoms on the surface. The state of the grain is thus defined by those two variables.

We first present the general form of this Master equation, before applying it successively to the Langmuir-Hinshelwood and Eley-Rideal formation mechanisms. We then discuss the numerical resolution of these equations. Finally, we develop accurate approximations to compute the formation rate at a lower computational cost.

The results of the application of this method are then presented in the paper reproduced in Chap. 8.

7.1 A MASTER EQUATION APPROACH

We now consider a grain whose state is defined by its thermal energy content E and its number of adsorbed H atoms (or surface population) n. As previously, photon absorption and emission occur as Poisson processes, and are memoryless random events (i.e. they depend only on the present state). We make the same assumption for the chemical events affecting the surface population. This is exact for adsorption and desorption events, and for Eley-Rideal direct reaction, but is only an approximation for Langmuir-Hinshelwood-like processes which involve meeting between surface atoms, because n does not describe the state sufficiently accurately. A complete description would require giving the position of each surface atom. Such a level of detail would lead to intractable calculations, and this simpler description is sufficient for our purpose. We can thus approximate the evolution of the grain state by a pure jump Markov process, and try to compute the stationary PDF of the state $f(E, n)$.

7.1.1 *General Master Equation*

We now establish the general Master equation for this two-variables system.

Noting $W(E', n' \,|E, n)$ the transition rate from state E, n to state E', n', the general expression of the stationary Master equation (see Sect. 4.2.5):

$$\int dE' \sum_{n'=0}^{N_s} W(E, n \,|E', n')\, f(E', n') = f(E, n) \int dE' \sum_{n'=0}^{N_s} W(E', n' \,|E, n) \quad (199)$$

We will separate the transitions caused by photon interactions (absorption and emission) and the transition caused by chemical events on the surface. We note the transition rate for photon events W_{phot} and the transition rate for chemical events W_{chem}. The transition rate W_{phot} is the same as the one used in the previous chapter for the computation of the dust temperature PDF (Eq. 117). It does not depend on the surface population, neither do these transitions affect the surface population. We can thus simply note $W_{\text{phot}}(E' \,|E)$, and its expression is :

$$W_{\text{phot}}(E' \,|E) = \begin{cases} R_{\text{abs}}(E' - E) & \text{if} \quad E' > E \\ R_{\text{em}}(E - E', T(E)) & \text{if} \quad 0 < E' < E \\ 0 & \text{if} \quad E' < 0 \end{cases} \quad (200)$$

The chemical transitions depend on the mechanism we consider, we will thus keep a general expression for now. Those events in general depend on both the surface population and the grain thermal energy (through the grain temperature). Among those events, H_2 formation reactions leave a fraction of the formation energy in the grain. This energy is not well known, it has been estimated that an Eley-Rideal direct reaction on a chemisorbed atom leaves 1 eV into the grain (Sizun et al. [2010]), and reactions involving physisorbed atoms probably leave a smaller fraction because of the weaker interaction with the grain. We verified that this heating contribution is on average negligible compared to the heating by the radiation field, and discuss it in an appendix of the paper reproduced in Chap. 8. We will thus neglect this heating term, so that chemical transitions only affect the surface population of the grain. We then note the chemical transition rate $W_{\text{chem}}(n' \,|n\,; E)$.

We thus have photon transitions which only affect the thermal energy E, and chemical transitions which only affect the surface population n. We can rewrite Eq. 199, separating the two kind of transitions:

$$\int dE'\, W_{\text{phot}}(E\,|E')\, f(E',n) + \sum_{n'} W_{\text{chem}}(n\,|n'\,;E)\, f(E,n') = f(E,n)\left[\int dE'\, W_{\text{phot}}(E'\,|E) + \sum_{n'} W_{\text{chem}}(n'\,|n\,;E)\right] \tag{201}$$

We define a total loss rate:

$$L(E,n) = \int dE'\, W_{\text{phot}}(E'\,|E) + \sum_{n'} W_{\text{chem}}(n'\,|n\,;E) \tag{202}$$

We can then rewrite Eq. 201 as:

$$\boxed{\int dE'\, \frac{W_{\text{phot}}(E\,|E')}{L(E,n)}\, f(E',n) + \sum_{n'} \frac{W_{\text{chem}}(n\,|n'\,;E)}{L(E,n)}\, f(E,n') = f(E,n)} \tag{203}$$

This is an eigenfunction equation for the linear operator defined by the left-hand side for the eigenvalue 1, similarly to the Master equation of the previous chapter. We call $\mathcal{H}$ this operator.

Here again, it is easy to see that 1 is indeed in the spectrum of the operator. Let us consider the scalar product defined as:

$$\langle f, g\rangle = \int dE \sum_n f(E,n)\, g(E,n)$$

We can compute the adjoint operator of $\mathcal{H}$:

$$\begin{aligned}
\langle f, \mathcal{H}[g]\rangle &= \int dE \sum_n f(E,n) \left[\int dE' \frac{W_{\text{phot}}(E\,|E')}{L(E,n)}\, g(E',n) + \sum_{n'} \frac{W_{\text{chem}}(n\,|n'\,;E)}{L(E,n)}\, g(E,n')\right] \\
&= \int dE' \sum_n g(E',n) \int dE \frac{W_{\text{phot}}(E\,|E')}{L(E,n)}\, f(E,n) + \int dE \sum_{n'} g(E,n') \sum_n \frac{W_{\text{chem}}(n\,|n'\,;E)}{L(E,n)}\, f(E,n) \\
&= \int dE \sum_n g(E,n) \left[\int dE' \frac{W_{\text{phot}}(E'\,|E)}{L(E',n)}\, f(E',n) + \sum_{n'} \frac{W_{\text{chem}}(n'\,|n\,;E)}{L(E,n')}\, f(E,n')\right] \\
&= \langle \mathcal{H}^*[f], g\rangle
\end{aligned}$$

where $\mathcal{H}^*$ is the adjoint of $\mathcal{H}$. $\mathcal{H}^*$ is thus defined by:

$$\mathcal{H}^*[f](E,n) = \int dE' \frac{W_{\text{phot}}(E'|E)}{L(E',n)} f(E',n) + \sum_{n'} \frac{W_{\text{chem}}(n'|n;E)}{L(E,n')} f(E,n') \tag{204}$$

Then:

$$\begin{aligned} \mathcal{H}^*[L](E,n) &= \int dE' W_{\text{phot}}(E'|E) + \sum_{n'} W_{\text{chem}}(n'|n;E) \\ &= L(E,n) \end{aligned}$$

The adjoint operator thus has the eigenvalue 1, and 1 is therefore in the spectrum of $\mathcal{H}$. I don't have for this case a formal proof as in the previous Chapter, showing that 1 is the leading eigenvalue and is simple (the space is more complex, and we need to prove the compactness of this operator to proceed as previously). However, it is most probable that a similar result holds, as numerical results seem to evidence. (see Sect. 7.2).

We will now consider separately the two formation mechanisms described in Sect. 5.2, and write Eq. 203 explicitly for each mechanism.

7.1.2 *Langmuir-Hinshelwood: general resolution method*

We first consider the physisorption-based Langmuir-Hinshelwood mechanism (see Sect. 5.2.3), and apply our Master equation Eq. 203 to this case.

Chemical transitions can change the surface population by either ± 1 (adsorption, desorption, or Eley-Rideal reaction), or by -2 (Langmuir-Hinshelwood reaction). The chemical transition rate is:

$$W_{\text{chem}}(n'|n;E) = \begin{cases} k_{\text{coll}}\, s(T_{\text{gas}}) \left(1 - \dfrac{n}{N_s}\right) & \text{if} \quad n' - n = 1 \\ n\, k_{\text{des}}(T(E)) + k_{\text{coll}} \dfrac{n}{N_s} & \text{if} \quad n' - n = -1 \\ k_{\text{migr}}(T(E)) \dfrac{n\,(n-1)}{N_s} & \text{if} \quad n' - n = -2 \end{cases} \tag{205}$$

We can then explicitly expand the expressions. Eq. 202 becomes:

$$\begin{aligned} L(E,n) &= \int_0^E dU\, R_{\text{em}}(U, T(E)) + \int_0^{+\infty} dU\, R_{\text{abs}}(U) \\ &+ k_{\text{coll}}\, s(T_{\text{gas}}) \left(1 - \frac{n}{N_s}\right) + n\, k_{\text{des}}(T(E)) + k_{\text{coll}} \frac{n}{N_s} + k_{\text{migr}}(T(E)) \frac{n\,(n-1)}{N_s} \end{aligned} \tag{206}$$

and the Master Equation Eq. 203 becomes:

$$
\begin{aligned}
f(E,n) = \frac{1}{L(E,n)} \Bigg[& \int_0^E dE'\, R_{\text{abs}}(E-E')\, f(E',n) \\
& + \int_E^{+\infty} dE'\, R_{\text{em}}(E'-E, T(E'))\, f(E',n) \\
& + k_{\text{coll}}\, s(T_{\text{gas}}) \left(1 - \frac{n-1}{N_{\text{s}}}\right) f(E,n-1) \\
& + \left((n+1)\, k_{\text{des}}(T(E)) + k_{\text{coll}}\, \frac{n+1}{N_{\text{s}}}\right) f(E,n+1) \\
& + k_{\text{migr}}(T(E))\, \frac{(n+2)\,(n+1)}{N_{\text{s}}}\, f(E,n+2) \Bigg]
\end{aligned}
\tag{207}
$$

where, as limit conditions, the terms involving the expressions $n-1$, $n+1$ and $n+2$ are replaced with zero when those expressions become < 0 or $> N_{\text{s}}$.

The right-hand side defines the expression of the operator $\mathcal{H}$:

$$
\begin{aligned}
\mathcal{H}[g](E,n) = \frac{1}{L(E,n)} \Bigg[& \int_0^E dE'\, R_{\text{abs}}(E-E')\, g(E',n) \\
& + \int_E^{+\infty} dE'\, R_{\text{em}}(E'-E, T(E'))\, g(E',n) \\
& + k_{\text{coll}}\, s(T_{\text{gas}}) \left(1 - \frac{n-1}{N_{\text{s}}}\right) g(E,n-1) \\
& + \left((n+1)\, k_{\text{des}}(T(E)) + k_{\text{coll}}\, \frac{n+1}{N_{\text{s}}}\right) g(E,n+1) \\
& + k_{\text{migr}}(T(E))\, \frac{(n+2)\,(n+1)}{N_{\text{s}}}\, g(E,n+2) \Bigg] .
\end{aligned}
\tag{208}
$$

Diagonalizing this operator would not be numerically simple. Once discretized, the PDF will be represented by a matrix, and the operator should be a tensor of third order. This tensor would then need to be diagonalized. It can also be represented by a matrix if we "flatten" the PDF matrix into a vector by concatenating the vectors $f(E_i, n)$ for each value of n. However, this tensor or matrix would be of extremely large dimension (if the energy grid has 100 points, and the grain 100 sites, the PDF is represented by 10^4 numbers, and the operator by 10^8 numbers) and extremely sparse, as the expression of the operator for a function f at E, n only involves function values at E', n or E, n', where E' explores the whole energy range, while n' only explores $n-1$, $n+1$ and $n+2$.

As discussed in the previous section, we expect that a result similar to the one obtained in the previous chapter still holds in this case, so that an iterative method is possible. This method consists in iterating the application of the operator $\mathcal{H}$ to some initial guess. The application of the operator can

be computed directly by using Eq. 207, thus taking advantage of the sparsity of the operator.

We thus use this iterative method, whose numerical implementation will be discussed in Sect. 7.2.1, and will verify its justification by checking its convergence (which implies both that 1 is an eigenvalue, and that it is also the spectral radius).

The average H_2 formation rate can then be computed as:

$$\langle r_{H_2} \rangle = \int_0^{+\infty} dE \sum_{n=0}^{N_s} f(E,n) \left[k_{coll} \frac{n}{N_s} + k_{migr}(T(E)) \frac{n(n-1)}{N_s} \right] \tag{209}$$

The maximum possible formation rate is given by one half of the rate k_{coll} of collision with gas H atoms . We can thus define a formation efficiency by comparing the formation rate to this maximal rate. The average efficiency is thus:

$$\eta = \frac{2 \langle r_{H_2} \rangle}{k_{coll}} \tag{210}$$

7.1.3 *Eley-Rideal: a simplified equation*

We now similarly derive the Master equation for the Eley-Rideal mechanism (see Sect. 5.2.4). We will further prove that a significant analytical simplification can be made due to the linearity of the equations in this case.

The only processes are now adsorption ($\Delta n = +1$), desorption ($\Delta n = -1$), and Eley-Rideal reaction ($\Delta n = -1$). The transition rate is thus:

$$W_{chem}(n' \,|n\,; E) = \begin{cases} k_{coll}\, s(T_{gas}) \left(1 - \dfrac{n}{N_s}\right) & \text{if} \quad n' - n = 1 \\ n\, k_{des}(T(E)) + k_{coll} \dfrac{n}{N_s} & \text{if} \quad n' - n = -1 \end{cases} \tag{211}$$

The loss rate becomes:

$$\begin{aligned} L(E,n) = \int_0^E dU\, R_{em}(U, T(E)) + \int_0^{+\infty} dU\, R_{abs}(U) \\ + k_{coll}\, s(T_{gas}) \left(1 - \frac{n}{N_s}\right) + n\, k_{des}(T(E)) + k_{coll} \frac{n}{N_s} \end{aligned} \tag{212}$$

and the Master Equation becomes:

$$\begin{aligned} L(E,n)\, f(E,n) = \int_0^E dE'\, R_{abs}(E - E')\, f(E',n) \\ + \int_E^{+\infty} dE'\, R_{em}(E' - E, T(E'))\, f(E',n) \\ + k_{coll}\, s(T_{gas}) \left(1 - \frac{n-1}{N_s}\right) f(E, n-1) \\ + \left((n+1)\, k_{des}(T(E)) + k_{coll} \frac{n+1}{N_s} \right) f(E, n+1) \end{aligned} \tag{213}$$

where, as previously, terms in $n-1$ and $n+1$ become zero if these expressions become < 0 or $> N_s$.

In this case, the equation is completely linear in n. This allows us to significantly simplify the problem.

We are indeed only interested in the average H_2 formation rate, which is defined as:

$$\langle r_{H_2} \rangle = \int_0^{+\infty} dE \sum_{n=0}^{N_s} f(E,n)\, k_{coll} \frac{n}{N_s} \tag{214}$$

We can transform this expression. We recall that (see Appendix A) the marginal PDF of the thermal energy is defined as:

$$f_E(E) = \sum_{n=0}^{N_s} f(E,n) \tag{215}$$

and the conditional average surface population (conditional on the thermal energy of the grain) is defined:

$$\langle n \,|E\rangle = \sum_{n=0}^{N_s} n \frac{f(E,n)}{f_E(E)} \tag{216}$$

This quantity represents the average surface population of grains when they are at thermal energy E.

We can then reformulate Eq. 214 as:

$$\langle r_{H_2} \rangle = \int_0^{+\infty} dE\, f_E(E)\, k_{coll} \frac{\langle n \,|E\rangle}{N_s} \tag{217}$$

This shows that the knowledge of the full PDF $f(E,n)$ is not necessary to compute the formation rate, and the knowledge of the two single-variable functions $f_E(E)$ and $\langle n \,|E\rangle$ is enough.

We will now derive two separate equations governing $f_E(E)$ and $\langle n \,|E\rangle$. Those equations will be of lower dimension than the full Master equation, and thus simpler to solve numerically.

Let us first consider the equation for $f_E(E)$.

As the chemical processes do not affect the thermal energy and the photon events have rates that do not depend on the surface population, the thermal energy PDF $f(E)$ can be computed completely independently as described

in Chapter 6. This can be seen analytically by summing Eq. 213 over all n values. We get:

$$\begin{aligned}
&\sum_{n=0}^{N_s} k_{coll}\, s(T_{gas}) \left(1-\frac{n}{N_s}\right) f(E,n) + \sum_{n=0}^{N_s}\left[n\, k_{des}(T(E)) + k_{coll}\,\frac{n}{N_s}\right] f(E,n) \\
&\qquad + \sum_{n=0}^{N_s}\int_0^E dU\, R_{em}(U,T(E))\, f(E,n) + \sum_{n=0}^{N_s}\int_0^{+\infty} dU\, R_{abs}(U)\, f(E,n) \\
&= \sum_{n=0}^{N_s}\int_0^E dE'\, R_{abs}(E-E')\, f(E',n) + \sum_{n=0}^{N_s}\int_E^{+\infty} dE'\, R_{em}(E'-E,T(E'))\, f(E',n) \\
&\qquad + \sum_{n=1}^{N_s} k_{coll} s(T_{gas}) \left(1-\frac{n-1}{N_s}\right) f(E,n-1) \\
&\qquad + \sum_{n=0}^{N_s-1}\left((n+1)\, k_{des}(T(E)) + k_{coll}\,\frac{n+1}{N_s}\right) f(E,n+1) \qquad (218)
\end{aligned}$$

We recognize the expression of the marginal PDF $f_E(E)$ at several places, and we can also renumber the last three sums of the right-hand side:

$$\begin{aligned}
&\sum_{n=0}^{N_s} k_{coll}\, s(T_{gas}) \left(1-\frac{n}{N_s}\right) f(E,n) + \sum_{n=0}^{N_s}\left[n\, k_{des}(T(E)) + k_{coll}\,\frac{n}{N_s}\right] f(E,n) \\
&\qquad + \int_0^E dU\, R_{em}(U,T(E))\, f_E(E) + \int_0^{+\infty} dU\, R_{abs}(U)\, f_E(E) \\
&= \int_0^E dE'\, R_{abs}(E-E')\, f_E(E') + \int_E^{+\infty} dE'\, R_{em}(E'-E,T(E'))\, f_E(E') \\
&+ \sum_{n=0}^{N_s-1} k_{coll}\, s(T_{gas}) \left(1-\frac{n}{N_s}\right) f(E,n) + \sum_{n=1}^{N_s}\left(n\, k_{des}(T(E)) + k_{coll}\frac{n}{N_s}\right) f(E,n)
\end{aligned} \qquad (219)$$

Finally, the remaining sums on the right-hand side cancel the sums on the left-hand side, as the few terms not directly cancelled are zero by themselves. What remains is then:

$$\begin{aligned}
&\left[\int_0^E dU\, R_{em}(U,T(E)) + \int_0^{+\infty} dU\, R_{abs}(U)\right] f_E(E) = \\
&\qquad \int_0^E dE'\, R_{abs}(E-E')\, f_E(E') + \int_E^{+\infty} dE'\, R_{em}(E'-E,T(E'))\, f_E(E') \qquad (220)
\end{aligned}$$

We recognize the Master Equation derived in the case where we considered only the temperature fluctuations without taking surface chemistry into account (Chap. 6, Eq. 122). We thus know how to compute $f_E(E)$.

We now need to compute $\langle n\,|E\rangle$. For this purpose, we multiply Eq. 213 by n, and then sum the resulting equation over all values of n:

$$\begin{aligned}
&\sum_{n=0}^{N_s} k_{coll}\, s(T_{gas}) \left(1-\frac{n}{N_s}\right) n\, f(E,n) + \sum_{n=0}^{N_s} \left(n\, k_{des}(T(E)) + k_{coll}\frac{n}{N_s}\right) n\, f(E,n) \\
&\quad + \sum_{n=0}^{N_s} \int_0^E dU\, R_{em}(U,T(E))\, n\, f(E,n) + \sum_{n=0}^{N_s} \int_0^{+\infty} dU\, R_{abs}(U)\, n\, f(E,n) \\
&= \sum_{n=0}^{N_s} \int_0^E dE'\, R_{abs}(E-E')\, n\, f(E',n) + \sum_{n=0}^{N_s} \int_E^{+\infty} dE'\, R_{em}(E'-E,T(E'))\, n\, f(E',n) \\
&\qquad + \sum_{n=1}^{N_s} k_{coll}\, s(T_{gas}) \left(1-\frac{n-1}{N_s}\right) n\, f(E,n-1) \\
&\qquad + \sum_{n=0}^{N_s-1} \left((n+1)\, k_{des}(T(E)) + k_{coll}\frac{n+1}{N_s}\right) n\, f(E,n+1) \qquad (221)
\end{aligned}$$

We use the fact that $\sum_{n=0}^{N_s} n\, f(E,n) = \langle n\,|E\rangle\; f_E(E)$, and renumber the last two sums of the right-hand side:

$$\begin{aligned}
&\sum_{n=0}^{N_s} k_{coll}\, s(T_{gas}) \left(1-\frac{n}{N_s}\right) n\, f(E,n) + \sum_{n=0}^{N_s} \left(n\, k_{des}(T(E)) + k_{coll}\frac{n}{N_s}\right) n\, f(E,n) \\
&\quad + \int_0^E dU\, R_{em}(U,T(E))\; \langle n\,|E\rangle\; f_E(E) + \int_0^{+\infty} dU\, R_{abs}(U)\; \langle n\,|E\rangle\; f_E(E) \\
&\qquad = \int_0^E dE'\, R_{abs}(E-E')\; \langle n\,|E'\rangle\; f_E(E') \\
&\qquad + \int_E^{+\infty} dE'\, R_{em}(E'-E,T(E'))\; \langle n\,|E'\rangle\; f_E(E') \\
&\qquad + \sum_{n=0}^{N_s-1} k_{coll}\, s(T_{gas}) \left(1-\frac{n}{N_s}\right) (n+1)\, f(E,n) \\
&\qquad\quad + \sum_{n=1}^{N_s} \left(n\, k_{des}(T(E)) + k_{coll}\frac{n}{N_s}\right) (n-1)\; f(E,n) \qquad (222)
\end{aligned}$$

In the last two sums of the right-hand side, we can expand the factors $(n+1)$ in the first and $(n-1)$ in the second, giving each time two contributions, the first of which cancels the corresponding sum in the left-hand side (again, it

cancels almost all terms and the remaining term is zero by itself). So that what remains is:

$$\int_0^E dU\, R_{\rm em}(U, T(E))\ \langle n\,|E\rangle\ f_E(E) + \int_0^{+\infty} dU\, R_{\rm abs}(U)\ \langle n\,|E\rangle\ f_E(E) = \int_0^E dE'\, R_{\rm abs}(E-E')\ \langle n\,|E'\rangle\ f_E(E') + \int_E^{+\infty} dE'\, R_{\rm em}(E'-E, T(E'))\ \langle n\,|E'\rangle\ f_E(E') + \sum_{n=0}^{N_s} k_{\rm coll}\, s(T_{\rm gas})\ \left(1-\frac{n}{N_s}\right)\ f(E,n) - \sum_{n=0}^{N_s}\left(n\, k_{\rm des}(T(E)) + k_{\rm coll}\frac{n}{N_s}\right) f(E,n) \tag{223}$$

We can finally use again the fact that $\sum_{n=0}^{N_s} n\, f(E,n) = \langle n\,|E\rangle\ f_E(E)$:

$$\left[\int_0^E dU\, R_{\rm em}(U, T(E)) + \int_0^{+\infty} dU\, R_{\rm abs}(U)\right]\ \langle n\,|E\rangle\ f_E(E) = \int_0^E dE'\, R_{\rm abs}(E-E')\ \langle n\,|E'\rangle\ f_E(E') + \int_E^{+\infty} dE'\, R_{\rm em}(E'-E, T(E'))\ \langle n\,|E'\rangle\ f_E(E') + k_{\rm coll}\, s(T_{\rm gas})\ \left(1-\frac{\langle n\,|E\rangle}{N_s}\right)\ f_E(E) - \left(\langle n\,|E\rangle\ k_{\rm des}(T(E)) + k_{\rm coll}\frac{\langle n\,|E\rangle}{N_s}\right) f_E(E) \tag{224}$$

We reorganize the terms and get:

$$\begin{aligned} k_{\rm coll} s(T_{\rm gas})\, f_E(E) = M(E)\ \langle n\,|E\rangle\ f_E(E) \\ - \int_0^E dE'\, R_{\rm abs}(E-E')\, f_E(E')\ \langle n\,|E'\rangle \\ - \int_E^{+\infty} dE'\, R_{\rm em}(E'-E, T(E'))\, f_E(E')\ \langle n\,|E'\rangle \end{aligned} \tag{225}$$

where:

$$\begin{aligned} M(E) = \int_0^E dU\, R_{\rm em}(U, T(E)) + \int_0^{+\infty} dU\, R_{\rm abs}(U) \\ + \frac{k_{\rm coll}\left(1+s(T_{\rm gas})\right)}{N_s} + k_{\rm des}(T(E)) \end{aligned} \tag{226}$$

We thus have an integral equation governing $\langle n\,|E\rangle$. It is a Fredholm equation of the second kind. We have thus a way to avoid the costly resolution of a functional equation for functions of two variables (the full Master equation), and solve instead two successive equations for functions of one variable only: Eq. 220 to compute $f_E(E)$, and Eq. 225 to compute $\langle n\,|E\rangle$. The formation rate can then be obtained by use of Eq. 217. Such a simplification was not possible in the case of the Langmuir-Hinshelwood mechanism (Sect. 7.1.2), because one of the rates is quadratic in n. Eq. 220 can also be derived by the same method, but when deriving an equivalent to Eq. 225, a term in

$\langle n^2 | E \rangle$ appears. An equation for this conditional moment can be derived by multiplying Eq. 213 by n^2 and summing over all n values, but the resulting equation involves $\langle n^3 | E \rangle$. We thus have a closure problem, and cannot use this simplification for the Langmuir-Hinshelwood.

We take advantage of this simplification for the Eley-Rideal mechanism. When discretized over an energy grid, Eq. 225 becomes a linear system. However, the implementation of this method has shown that this system, despite not being formally singular, converges (exponentially fast) towards a singular system when the grain size increases. Numerical errors thus quickly cause problems.

In order to avoid such numerical troubles, a transformation of Eq. 225 is possible. Integrating Eq. 225 over E gives:

$$\begin{aligned}\int_0^{+\infty} dE\, k_{\text{coll}}\, s(T_{\text{gas}})\, f_E(E) &= \int_0^{+\infty} dE \int_0^{E} dE'\, R_{\text{em}}(E-E', T(E))\ \langle n | E \rangle\ f_E(E) \\ &+ \int_0^{+\infty} dE \int_E^{+\infty} dE'\, R_{\text{abs}}(E'-E)\ \langle n | E \rangle\ f_E(E) \\ + \int_0^{+\infty} dE\, \frac{k_{\text{coll}}\left(1+s(T_{\text{gas}})\right)}{N_{\text{s}}}\ \langle n | E \rangle\ f_E(E) &+ \int_0^{+\infty} dE\, k_{\text{des}}(T(E))\ \langle n | E \rangle\ f_E(E) \\ &- \int_0^{+\infty} dE \int_0^{E} dE'\, R_{\text{abs}}(E-E')\, f_E(E')\ \langle n | E' \rangle \\ &- \int_0^{+\infty} dE \int_E^{+\infty} dE'\, R_{\text{em}}(E'-E, T(E'))\, f_E(E')\ \langle n | E' \rangle \end{aligned} \quad (227)$$

In the first term of the right-hand side, we can permute the integrals :

$$\begin{aligned}\int_0^{+\infty} dE \int_0^{E} dE'\, R_{\text{em}}(E-E', T(E))\ \langle n | E \rangle\ f_E(E) = \\ \int_0^{+\infty} dE' \int_{E'}^{+\infty} dE\, R_{\text{em}}(E-E', T(E))\ \langle n | E \rangle\ f_E(E)\end{aligned} \quad (228)$$

so that this term cancels the second to last term of the right-hand side.

Similarly, we can permute the integrals in the second term:

$$\begin{aligned}\int_0^{+\infty} dE \int_E^{+\infty} dE'\, R_{\text{abs}}(E'-E)\ \langle n | E \rangle\ f_E(E) = \\ \int_0^{+\infty} dE' \int_0^{E} dE\, R_{\text{abs}}(E'-E)\ \langle n | E \rangle\ f_E(E)\end{aligned} \quad (229)$$

and this term thus cancels the last term of the right-hand side. What remains is:

$$\begin{aligned}\int_0^{+\infty} dE\, k_{\text{coll}} s(T_{\text{gas}})\, f_E(E) = \\ \int_0^{+\infty} dE \left[\frac{k_{\text{coll}}\left(1+s(T_{\text{gas}})\right)}{N_{\text{s}}} + k_{\text{des}}(T(E))\right] \langle n | E \rangle\ f_E(E)\end{aligned} \quad (230)$$

Finally, the integral of the marginal PDF $f_E(E)$ is 1 so that the first term simplifies:

$$k_{\rm coll} s(T_{\rm gas}) = \int_0^{+\infty} dE' \left[\frac{k_{\rm coll}\left(1+s(T_{\rm gas})\right)}{N_{\rm s}} + k_{\rm des}(T(E')) \right] \langle n \,|E'\rangle \, f_E(E') \tag{231}$$

We keep this equation aside for now, come back to Eq. 225 and divide it by $f_E(E)$, getting:

$$\begin{aligned} k_{\rm coll}\, s(T_{\rm gas}) = M(E)\, \langle n\,|E\rangle \\ - \int_0^{E} dE' \, \frac{R_{\rm abs}(E-E')\, f_E(E')}{f_E(E)} \, \langle n\,|E'\rangle \\ - \int_E^{+\infty} dE' \, \frac{R_{\rm em}(E'-E, T(E'))\, f_E(E')}{f_E(E)} \, \langle n\,|E'\rangle \end{aligned} \tag{232}$$

Finally, we subtract Eq. 231 from Eq. 232, and after dividing by $M(E)$, we get:

$$\begin{aligned} \langle n\,|E\rangle = \int_0^{E} dE' \, \frac{R_{\rm abs}(E-E')\, f_E(E')}{M(E)\, f_E(E)} \, \langle n\,|E'\rangle \\ + \int_E^{+\infty} dE' \, \frac{R_{\rm em}(E'-E, T(E'))\, f_E(E')}{M(E)\, f_E(E)} \, \langle n\,|E'\rangle \\ + \int_0^{+\infty} dE' \left[\frac{k_{\rm coll}\left(1+s(T_{\rm gas})\right)}{N_{\rm s}} + k_{\rm des}(T(E')) \right] \frac{f_E(E')}{M(E)} \, \langle n\,|E'\rangle \end{aligned} \tag{233}$$

We return to an eigenfunction equation for the eigenvalue 1 for the integral operator defined by the right-hand side. Let us call $\mathcal{K}$ this operator:

$$\begin{aligned} \mathcal{K}[g](E) = \int_0^{E} dE' \, \frac{R_{\rm abs}(E-E')\, f_E(E')}{M(E)\, f_E(E)} \, g(E') \\ + \int_E^{+\infty} dE' \, \frac{R_{\rm em}(E'-E, T(E'))\, f_E(E')}{M(E)\, f_E(E)} \, g(E') \\ + \int_0^{+\infty} dE' \left[\frac{k_{\rm coll}\left(1+s(T_{\rm gas})\right)}{N_{\rm s}} + k_{\rm des}(T(E')) \right] \frac{f_E(E')}{M(E)} \, g(E') \end{aligned} \tag{234}$$

We can again show that 1 is indeed in the spectrum of $\mathcal{K}$. Indeed, the adjoint of the operator $\mathcal{K}$ is $\mathcal{K}^*$ defined by:

$$\begin{aligned} \mathcal{K}^*[g](E) = \int_E^{+\infty} dE' \, \frac{R_{\rm abs}(E'-E)\, f_E(E)}{M(E')\, f_E(E')} \, g(E') \\ + \int_0^{E} dE' \, \frac{R_{\rm em}(E-E', T(E))\, f_E(E)}{M(E')\, f_E(E')} \, g(E') \\ + \int_0^{+\infty} dE' \left[\frac{k_{\rm coll}\left(1+s(T_{\rm gas})\right)}{N_{\rm s}} + k_{\rm des}(T(E)) \right] \frac{f_E(E)}{M(E')} \, g(E') \end{aligned} \tag{235}$$

So that:

$$\begin{aligned}\mathcal{K}^*[M \times f_E](E) = &\int_E^{+\infty} dE'\, R_{\text{abs}}(E' - E)\, f_E(E) \\ &+ \int_0^{E} dE'\, R_{\text{em}}(E - E', T(E))\, f_E(E) \\ &+ \int_0^{+\infty} dE' \left[\frac{k_{\text{coll}}\left(1 + s(T_{\text{gas}})\right)}{N_{\text{s}}} + k_{\text{des}}(T(E))\right] f_E(E')\, f_E(E)\end{aligned} \tag{236}$$

and thus:

$$\mathcal{K}^*[M \times f_E](E) = M(E)\, f_E(E) \tag{237}$$

The demonstration given in Sect. 6.1.2 still holds for Eq. 233. Therefore, the solution exists and is unique, and iterating the application of the operator $\mathcal{K}$ on an initial guess is equivalent to the projection on the eigenfunction. We can thus also use this iterative resolution method to solve this equation.

Once f_E and $\langle n\,|E\rangle$ have been computed, the average formation rate is computed using Eq. 217. Again, the efficiency is defined as:

$$\eta = \frac{2\,\langle r_{\text{H}_2}\rangle}{k_{\text{coll}}} \tag{238}$$

7.2 NUMERICAL RESOLUTION

The resolution methods described in the previous sections are then implemented numerically. We describe here the detail of the numerical resolution method, and test the convergence of the results. We start with the Langmuir-Hinshelwood mechanism, before describing the resolution for the Eley-Rideal mechanism.

7.2.1 *Langmuir-Hinshelwood*

The discretization of the thermal energy grid is the same as when considering temperature fluctuations alone in the previous chapter (Sect. 6.2.1), with N grid points. The PDF is thus represented by a 2-dimensional array $\{f(E_i, n)\}_{\substack{i\in[[1,N]]\\ n\in[[0,N_{\text{s}}]]}}$.

As explained is Sect. 7.1.2, we use the iterative method to compute the solution. Rather than computing the application of the operator $\mathcal{H}$ as a full tensor-matrix multiplication, we take advantage of its sparsity by applying its different components separately. We can rewrite its definition as

$$\mathcal{H}[g](E, n) = \frac{1}{L(E, n)}\,\left[\mathcal{G}[g](E, n) + \mathcal{J}[E, n]\right] \tag{239}$$

where

$$\mathcal{G}[g](E,n) = \int_0^E dE'\, R_{\text{abs}}(E-E')\, g(E',n) + \int_E^{+\infty} dE'\, R_{\text{em}}(E'-E, T(E'))\, g(E',n) \quad (240)$$

and

$$\mathcal{J}[g](E,n) = k_{\text{coll}}\, s(T_{\text{gas}}) \left(1 - \frac{n-1}{N_s}\right) g(E,n-1) + \left((n+1)\, k_{\text{des}}(T(E)) + k_{\text{coll}} \frac{n+1}{N_s}\right) g(E,n+1) + k_{\text{migr}}(T(E)) \frac{(n+2)\,(n+1)}{N_s}\, g(E,n+2) \quad (241)$$

If we look at $f(E,n)$ as a family of single-variable functions for each value of n, the application of the operator $\mathcal{G}$ is actually equivalent to the application of operator $\mathcal{L}$ (Eq. 124, without the division by $L(E)$) to each member of the family. We can thus compute the application of the operator $\mathcal{G}$ for each value of n, which amounts to one matrix-vector multiplication for each value of n. This operation is actually equivalent to multiplying the matrix representing $\mathcal{G}$ by the matrix representing the PDF $f(E,n)$, and we use this latter method. The computation cost is of order $O(N^2 N_s)$. We can re-use the discretized matrix M_{ij} built in Sect. 6.2.1, and avoid re-computing the integral slices. The application of the operator $\mathcal{G}$ to a piecewise linear function is then:

$$\mathcal{G}[g](E_i,n) = \sum_j M_{ij}\, g(E_j,n) \quad (242)$$

The application of operator $\mathcal{J}$ can simply be computed element by element, in one single pass over the PDF matrix (order $O(NN_s)$):

$$\mathcal{J}[g](E_i,n) = k_{\text{coll}}\, s(T_{\text{gas}}) \left(1 - \frac{n-1}{N_s}\right) g(E_i,n-1) + \left((n+1)\, k_{\text{des}}(T(E_i)) + k_{\text{coll}} \frac{n+1}{N_s}\right) g(E_i,n+1) + k_{\text{migr}}(T(E_i)) \frac{(n+2)\,(n+1)}{N_s}\, g(E_i,n+2) \quad (243)$$

Our resolution algorithm is thus the repeated application of this operations:

- Computation of $\mathcal{G}[f](E,n)$
- Computation of $\mathcal{J}[f](E,n)$
- Sum of the two contributions and division by $L(E,n)$

- Renormalize the PDF
- Compute the relative distance of the displacement of the PDF caused by the iteration, using a L_2 norm defined as

$$\|f(E,n)\| = \int_0^{+\infty} dE \sum_{n=0}^{+\infty} f(E,n)^2.$$

This is repeated until the relative distance of the displacement caused by one iteration goes below a chosen threshold (10^{-7} was used).

The resulting computation time is thus dominated by the first part, and the time per iteration is exactly N_s times the time per iteration for the computation of f_E alone in Chapter 6. The total computation time is determined by this time per iteration and by the total number of iterations necessary to converge. As $f_E(E) = \sum_n f(E,n)$, we cannot expect the computation of $f(E,n)$ to converge faster than the computation of f_E. We thus already see the problem that we will face. We remember from Sect. 6.2.2 that the number of iteration increased with grain size (roughly as a^2). As N_s also increases with grain size (as a^2), the computation time per iteration also increases. The total computation time will thus increase very fast with grain size, and make the computation intractable for big grains. We will come back to this problem in Sect. 7.2.3 and 7.3.

As initial guess, we use a PDF proportional to the marginal thermal energy PDF f_E and independent of n. This ensures that it is compatible with the marginal PDF f_E which has already been computed, but gives the same probability to all values of the surface population.

7.2.2 *Eley-Rideal*

We now describe the numerical resolution for the Eley-Rideal mechanism.

In this case, we simply need to choose a grid of thermal energy values. We then search for the two solution functions $f_E(E)$ and $\langle n\,|E\rangle$ as piecewise linear functions on this grid. These functions can thus be simply described as the 1D arrays of their values at the grid points: $\{f_E(E_i)\}_{i\in[1..N]}$ and $\{\langle n\,|E_i\rangle\}_{i\in[1..N]}$. We take the same energy grid as previously (Eq. 130 and 131) with N grid points. The thermal energy PDF f_E is solution of Eq. 220, while the conditional average $\langle n\,|E\rangle$ is solution of Eq. 233 (for which we need the knowledge of f_E). We thus need to solve successively these two equations for piecewise linear functions.

The resolution method for Eq. 220 has already been described in Chapter 6. We use the implementation described there to solve the first equation. Once $f_E(E)$ is known, we need to compute $\langle n\,|E\rangle$ using Eq. 233.

As noticed before, Eq. 233 is formally similar to the equation for f_E, and it can thus be solved using the same methods. The implementation is thus very

similar, and we use again both the diagonalization and iterative methods and discuss their advantages in Sect. 7.2.3.

The application of the integral operator $\mathcal{K}$ (defined by Eq. 234) on a piecewise linear function can again be reduced to a matrix form. We note $G(E, E')$ the kernel of this operator:

$$G(E,E') = \frac{R_{\text{abs}}(E-E')\, f_E(E')}{M(E)\, f_E(E)} + \left[\frac{k_{\text{coll}}\left(1+s(T_{\text{gas}})\right)}{N_{\text{s}}} + k_{\text{des}}(T(E'))\right] \frac{f_E(E')}{M(E)} \quad \text{if} \quad E' < E$$

$$G(E,E') = \frac{R_{\text{em}}(E'-E, T(E'))\, f_E(E')}{M(E)\, f_E(E)} + \left[\frac{k_{\text{coll}}\left(1+s(T_{\text{gas}})\right)}{N_{\text{s}}} + k_{\text{des}}(T(E'))\right] \frac{f_E(E')}{M(E)} \quad \text{if} \quad E' > E \tag{244}$$

Then,

$$\mathcal{G}[g](E) = \int_0^{+\infty} dE'\, G(E,E')\, g(E') \tag{245}$$

And for piecewise linear function of the grid $\{E_i\}_{i\in[1..N]}$, it takes the matrix form:

$$\mathcal{G}[g](E_i) = \sum_j G_{ij} g(E_j) \tag{246}$$

with

$$K_{ij} = \int_{E_j}^{E_{j+1}} dE'\, G(E_i,E')\, \frac{E_{j+1}-E'}{E_{j+1}-E_j} + \int_{E_{j-1}}^{E_j} dE'\, G(E_i,E')\, \frac{E'-E_{j-1}}{E_j-E_{j-1}} \tag{247}$$

for $j \in [2, N-1]$, and

$$K_{i1} = \int_{E_1}^{E_2} dE'\, G(E_i,E')\, \frac{E_2-E'}{E_2-E_1} \tag{248}$$

and:

$$K_{iN} = \int_{E_{N-1}}^{E_N} dE'\, G(E_i,E')\, \frac{E'-E_{N-1}}{E_N-E_{N-1}} \tag{249}$$

This discretization is completely similar to what was done for the operator $\mathcal{L}$ in Sect. 6.2.1, and here again, the integral slices are computed by numerical integration using the grid on which the data (Q_{abs}, J,...) are known. As f_E has been computed by assuming that it was piecewise linear, we naturally interpolate it linearly on this finer grid when needed.

We then compute the solution, either by diagonalizing the matrix K_{ij} and looking for the eigenvector associated with the eigenvalue 1, or by the iterative method (iteratively multiplying an initial guess by the matrix K_{ij} until we reach the stationary point). In this second method, we use again a stationarity threshold of 10^{-7}, and a constant function as initial guess.

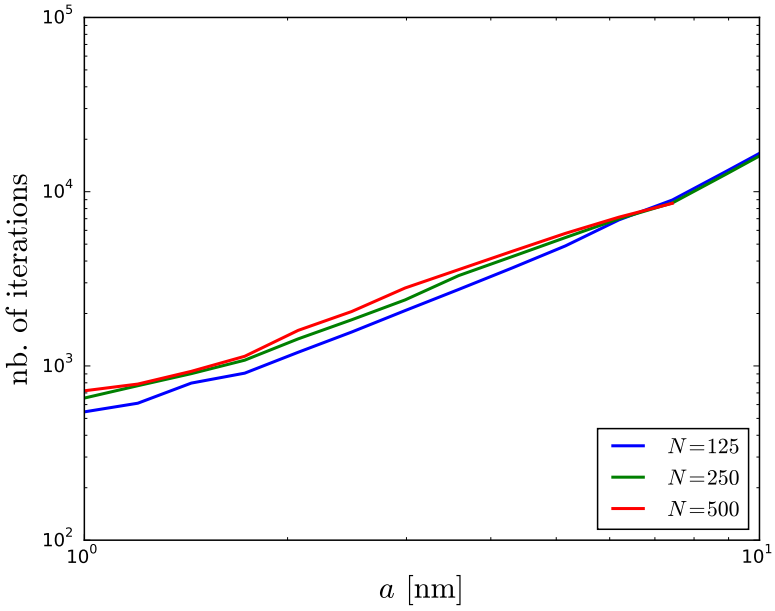

Figure 55: Number of iterations necessary to reach convergence in the computation of $f(E,n)$ for the Langmuir-Hinshelwood mechanism, for different values of the numerical resolution N.

7.2.3 *Numerical tests*

We now verify the convergence of the results obtained by these resolution methods.

LANGMUIR-HINSHELWOOD

As described in Sect. 7.2.1, we use the iterative method to solve the problem for the Langmuir-Hinshelwood mechanism. Figure 55 shows the number of iterations required to reach convergence in the computation of $f(E,n)$. This number seems roughly independent of the numerical resolution, which is expected as the speed of the convergence mainly depends on the properties of the operator $\mathcal{H}$ itself. It also increases with grain size, similarly to the case of the computation of $f_E(E)$ (see Sect. 6.2.2). As the number of sites N_s also grows with a (as a^2), the computation time quickly increases with size. We have stopped the computation at 10 nm as the computation time then becomes problematic (more than one day for one single grain size). This makes the computation unusable for grains bigger than $\sim$ 10 nm, and prompted us to develop an approximation. We come back to this problem later, and overcome it by the use of a much faster approximation presented in Sect. 7.3.

The two-variables PDF $f(E,n)$ is shown on Fig. 56 for a 1 nm grain. The PDF is presented as several functions of E, one for each value of n. Only the first few values of n are presented, and the sum of the remaining values is shown to represent the states $n > 4$. The bare state ($n = 0$) appears as the

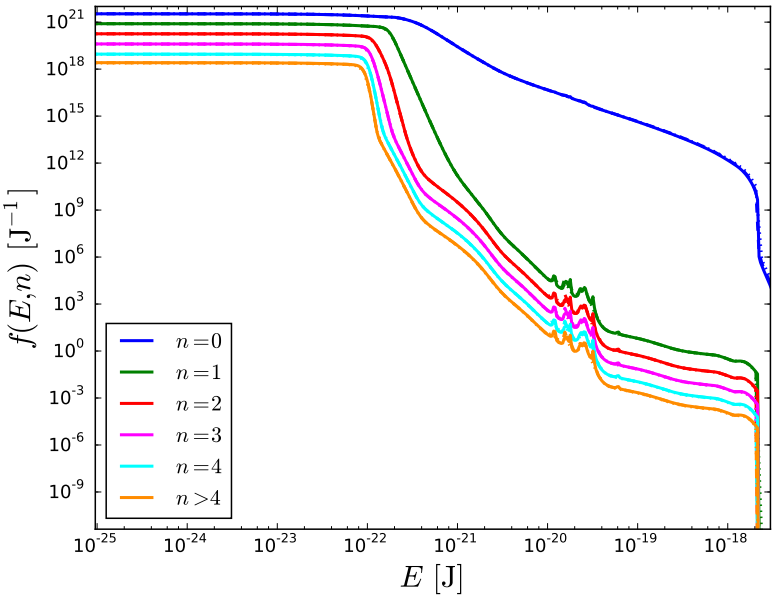

Figure 56: Two-variable PDF $f(E,n)$ of a 1 nm grain for the Langmuir-Hinshelwood mechanism, presented as one individual curve for each value of n as functions of E for the first few values of n, plus one corresponding to $n > 4$. The solid lines present the results at a resolution of $N = 500$, while the dotted line are for $N = 125$, but those curves are almost undistinguishable as the convergence is already almost complete for $N = 125$.

most probable at all energies. But while at low energy, the probabilities of the states $n > 0$ are close to each other and to $n = 0$, the probability to find a non-bare grain at high energies becomes completely negligible. We also recognize the shape of f_E for small grains (see Sect. 6.2.3), as $f_E(E) = \sum_n f(E,n)$. Figure 56 also shows the result computed at different values of the numerical resolution N. The results are undistinguishable, except at high energies for the $n = 0$ curve.

Figure 57 shows the PDF $f(E,n)$ for a 10 nm grain. The $n = 1$ state becomes as probable as the $n = 0$ state at low energies, as more adsorption sites are present on the grain (18590 sites at 10 nm, and 186 at 1 nm). Here again, the comparison of the results at $N = 125$ and $N = 250$ shows that the results are numerically converged. We will thus use a resolution of $N = 250$ in the following for the Langmuir-Hinshelwood mechanism.

Figure 58 shows the resulting formation efficiency as a function of the grain size, compared to the computation without fluctuations (rate equation at the equilibrium temperature, see Sect. 5.1.4 and 5.2.3). The numerical convergence is very good (we only see very small discrepancies at $N = 125$). We see that the results of the full computation of the PDF (taking the temperature fluctuations into account) are several orders of magnitude higher than the rate equation result at the equilibrium temperature (which neglects the effect

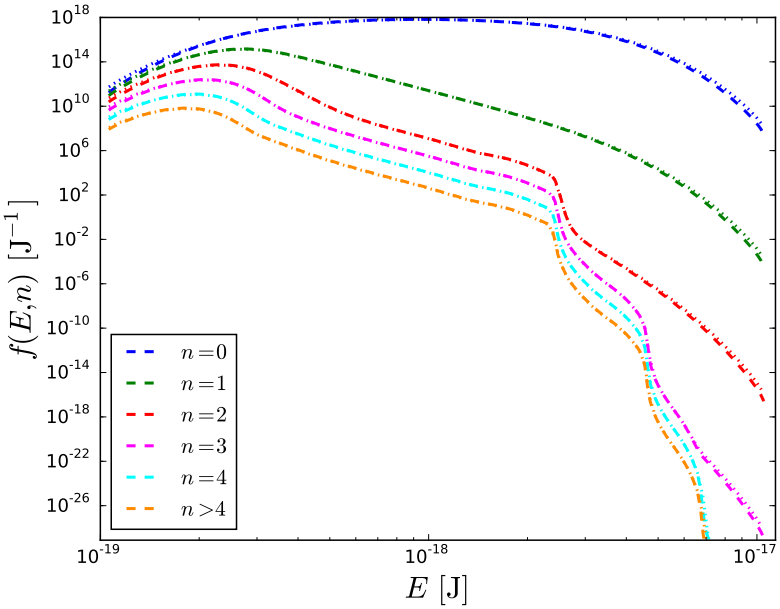

Figure 57: Two-variable PDF $f(E,n)$ of a 10 nm grain for the Langmuir-Hinshelwood mechanism, presented as one individual curve for each value of n as functions of E for the first few values of n, plus one corresponding to $n > 4$. The dashed lines present the results at a resolution of $N = 250$, while the dotted line are for $N = 125$.

of fluctuations). This effect will be presented and discussed in more details in Chapter 8, which reproduces the article Bron et al. [2014].

ELEY-RIDEAL

We start with the diagonalization method. The matrix K_{ij} is diagonalized, we find the eigenvalue that is closest to one, and take the corresponding eigenvector as the solution. The precision on the eigenvalue is shown on Fig. 59, as a function of grain size and for different values of the numerical resolution N. We observe a behavior that is very similar to what appeared for the computation of f_E (Fig. 29), with a better precision for larger sizes, and a very good overall precision, which remains even at low resolution.

However we noted in Sect. 6.2.2, that the precision of this eigenvalue was actually not a good indicator of the numerical precision of the result, as it was actually for big grains that the higher resolution was required. This is again true here. Figure 60 shows the resulting conditional average population $\langle n \,|T\rangle$ for small grains, computed at different numerical resolutions. We see a clear convergence and a numerical resolution of 500 appears to be sufficient. We clearly see the effect of the temperature fluctuations, keeping the surface chemistry out of equilibrium (the black curve shows the equilibrium result). For small grains, the frequent excursions in the high temperature domain (where desorption dominates) empty the grain surface, and they are frequent

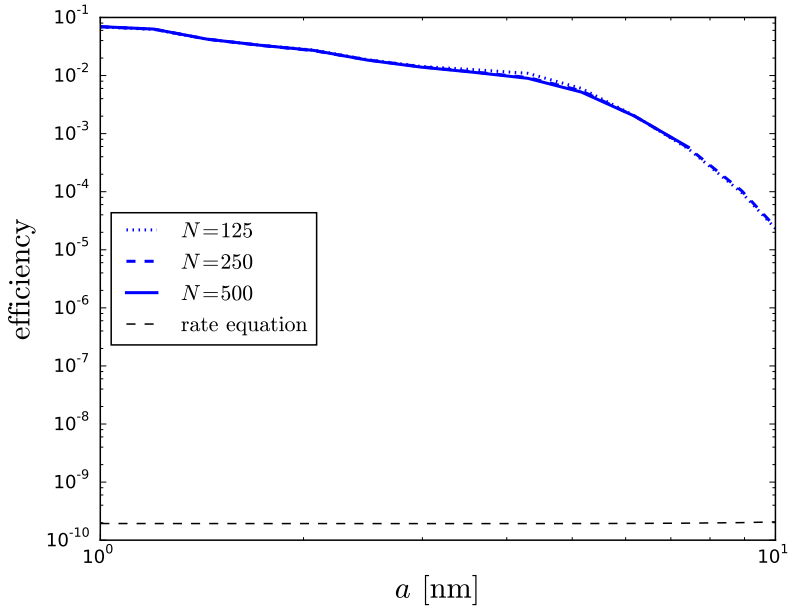

Figure 58: Formation efficiency of the Langmuir-Hinshelwood mechanism as a function of grain size and for different numerical resolutions. The black dashed line shows the equilibrium rate equation result at the equilibrium temperature.

enough so that the grain does not have enough time to repopulate completely between two temperature spikes. As a result, their average population when they are at low temperature is strongly reduced, i.e., they remain bare all the time. But this effect is limited to very small grains, as 2.2 nm grains are already very close to equilibrium. More discussion of this effect can be found in the article (Chap. 8).

For big grains, the convergence is not as good. Figure 61 shows this conditional average population computed for a bigger grain ($a = 51\,\mathrm{nm}$) for different values of the numerical resolution N. For such a size, we expect the fluctuations to be negligible and the result to be equal to the equilibrium result, as the results of lower sizes have already converged to the equilibrium result as shown in Fig. 60. However, as we increase the resolution, the discrepancies increase. The problem comes from the fact that as the grain size increases, the other eigenvalues of the operator $\mathcal{K}$ grow and approach 1. For very close eigenvalues, the numerical diagonalization results in a mixture of the corresponding eigenfunctions. Moreover, when we use a higher numerical resolution, the discretized representation of the operator possesses more eigenvalues, and it seems that it results in more eigenvalues in the vicinity of 1.

However, the temperature PDF f_T is already very peaked around 60 K, while the result for $\langle n \,|T\rangle$ is mostly distorted at the edges of the temperature grid, as is also shown on Fig. 61. This makes this problem unimportant, as

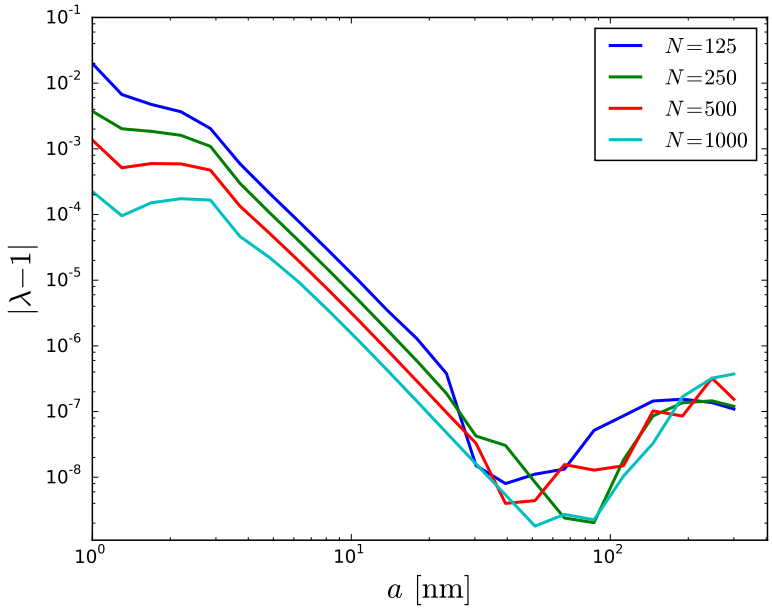

Figure 59: Difference between the leading eigenvalue of the operator $\mathcal{K}$ (1) and the leading eigenvalue of the matrix representation of this operator after discretization, as a function of grain size for different numerical resolutions.

the average formation rate (which results from the integration of $f_T(T)\,\langle n\,|T\rangle$) will be unaffected.

The average formation efficiency is shown on Fig. 62 as a function of grain size, compared to the result of equilibrium rate equation at the equilibrium temperature (black dashed line). The curves at different numerical resolutions show a clear convergence, and $N = 250$ appears sufficient. The problem described above for big grains does not appear at all. The formation efficiency is strongly reduced for small sizes compared to the equilibrium result because of the effect described previously. For small grains, the fluctuations are large enough to reach the regime where the chemisorbed atoms start to desorb, and frequent enough to keep the surface population low all the time (grains do not have enough time between fluctuations to regain their surface population). The range of affected sizes is very small ($a < 2-3\,\mathrm{nm}$).

To obtain the final formation rate in the gas, we must integrate over the dust size distribution. As it favors small grains in term of surface, the small range of affected sizes results in a significant decrease of the formation rate (see the results in the article reproduced in Chapter 8).

We can also perform the computation using the iterative method. The number of iterations necessary to reach convergence is shown on Fig. 63 for different numerical resolutions. For big grains, we have seen in Fig. 60 that $\langle n\,|T\rangle$ becomes a simple constant on the range of temperatures where the temperature PDF f_T is not completely negligible. As we start the itera-

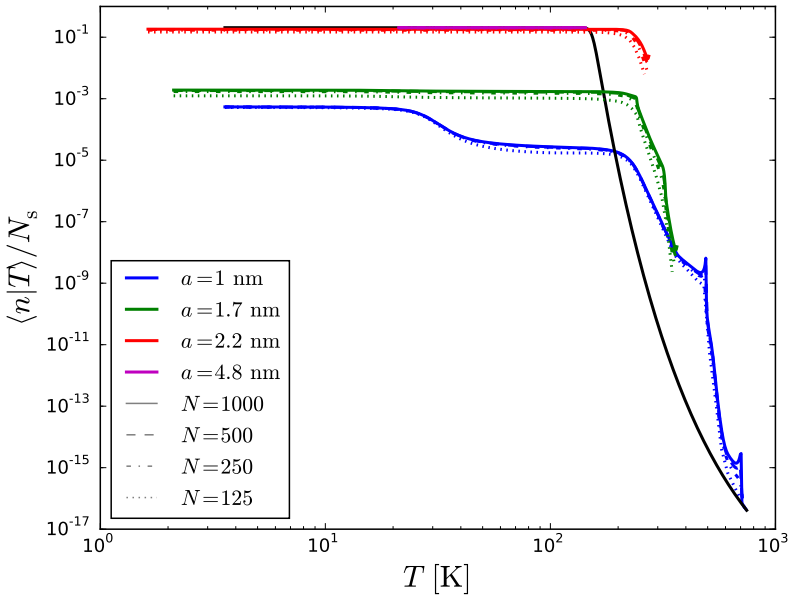

Figure 60: Conditional average of the surface population as a function of grain temperature computed by diagonalization, for different grain sizes (marked by the colors) and different numerical resolution N (marked by the line styles). The black line shows the equilibrium rate equation result at each temperature (for which the surface coverage fraction is independent of grain size in this range).

tive procedure with a constant function, the iterative procedure only needs to properly normalize the function, which is counted as 2 iterations on Fig. 63. We have this expected behavior at low resolution, but we see that at high resolution the big grains require on the contrary a larger number of iterations. This is caused by the mixing of several eigenfunctions because several eigenvalues are close to one. The number of iterations depends on two things: how close the initial guess is from the true eigenvector, and how close the second largest eigenvalue is to the leading eigenvalue. Here, the initial guess for big grains is indeed extremely close to the true eigenfunction, but, as seen previously (Fig. 61), the eigenvector of the discretized representation of the operator differs from the true eigenfunction (and more so when the numerical resolution is increased). The increase of the number of iterations necessary to reach convergence is an indication that some other eigenvalues are becoming very close to the leading eigenvalue.

The result of the iteration method presents the same big grain problem described above for the diagonalization method (Fig. 61). However, we have seen in Fig. 62, that the resulting formation rate converges to the equilibrium result as soon as $a = 2 - 3\,\mathrm{nm}$, far before the problematic size range. To reduce the computation time and avoid potentially unstable computations, we stop the full computation as soon as all quantities of interest have converged

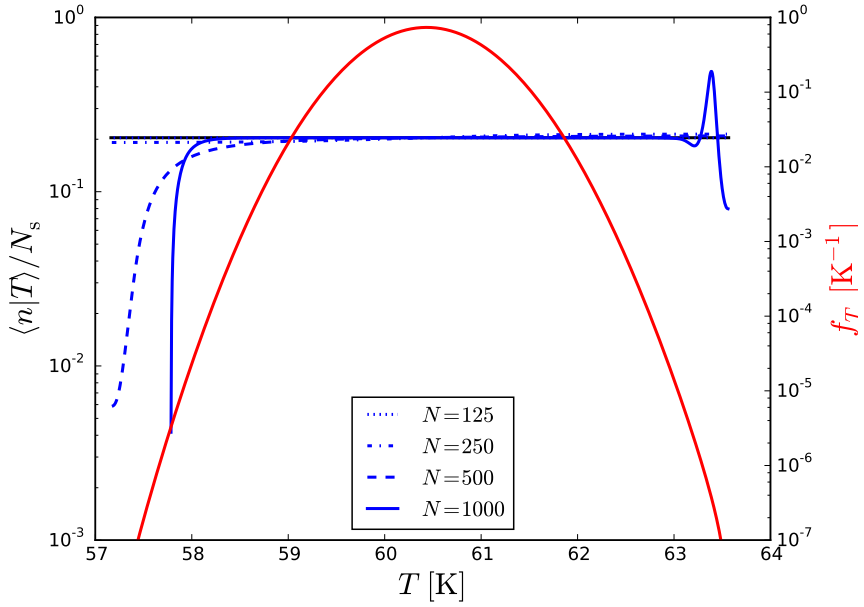

Figure 61: Evolution of the conditional average of the surface population as the numerical resolution varies (in blue, computed by diagonalization), for a grain of size $a = 51\,\text{nm}$. The equilibrium result of the rate equation approach is shown in black. For comparison, the temperature PDF f_T of the same grain is superimposed in red.

to their equilibrium values (with a precision of 1%). For larger sizes, we use the equilibrium temperature and the result of the equilibrium rate equation (see Sect. 5.1.4 and 5.2.4). As the iterative method is numerically efficient for small sizes, we use it as long as the results have not converged to the equilibrium result.

7.3 APPROXIMATIONS OF THE FORMATION RATE

As described in Sect. 7.2.3, the numerical computation of the Langmuir-Hinshelwood formation rate becomes intractable for big grains (larger than $10 - 20\,\text{nm}$). This range is not sufficient to see the complete convergence of the exact result towards the equilibrium rate equation result (which neglects the fluctuations). We cannot simply use the rate equation treatment when the exact resolution becomes too time-consuming. We thus need a more detailed approximation, complex enough to take into account the effects of the fluctuations, but simple enough to reduce to a fast computation.

We present in this section such an approximation, and show its general applicability to both the Langmuir-Hinshelwood and the Eley-Rideal mechanism. We perform a detailed comparison of the results of this approximation to the exact results to validate the approximation.

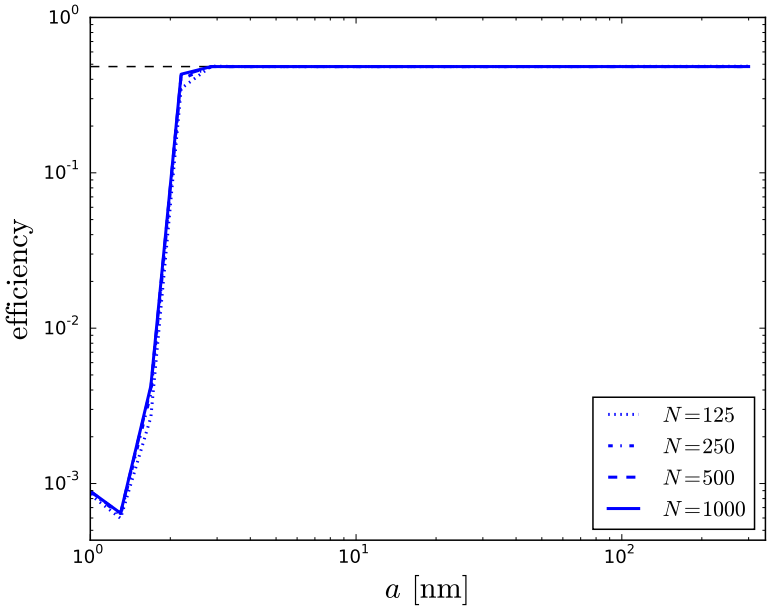

Figure 62: Average formation efficiency of the Eley-Rideal mechanism as a function of grain size (computed by diagonalization), for different numerical resolutions. The result of the equilibrium rate equation at the equilibrium temperature is shown as a black dashed line.

7.3.1 *Langmuir-Hinshelwood*

As the computation of f_E can be done efficiently (as described in Chapter 6), we take advantage of this characterization of the temperature fluctuations. In the Eley-Rideal case, we remember that a simplification was possible by deriving an equation for $\langle n \,|T\rangle$. We will try to do the same in this case, and use an approximation to close the resulting equation.

We will try to express a simplified equation for the conditional average $\langle n \,|T\rangle$ (the average of the surface population conditional on the grain temperature). Such an equation can be obtained through two different arguments: one based on a simple physical reasoning, the other based on the analysis of the equation for $\langle n \,|T\rangle$. The first approach is described in Bron et al. [2014], which is reproduced in Chapter 8. We present here the other approach.

We follow a derivation similar to what was done in the case of the Eley-Rideal mechanism (see Sect. 7.1.3). Of course, we know that in this case the result will not be in closed form because of the non-linear term, but we then make use of approximations to proceed further.

In order to derive this new equation, we start from the full Master Equation (Eq. 207), we re-multiply by $L(E,n)$), and multiply the equation by n before summing over all possible values of n:

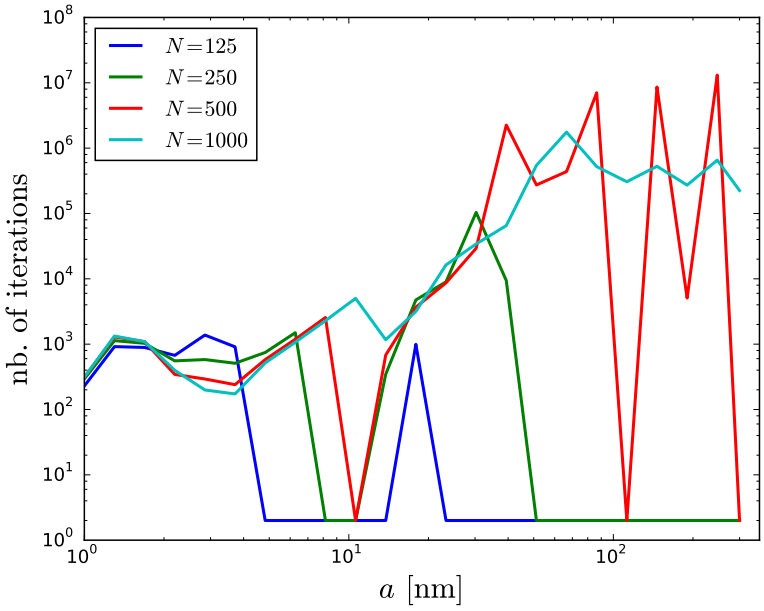

Figure 63: Number of iterations necessary to reach convergence for the computation of the conditional average population $\langle n\,|E\rangle$ by the iterative method, as a function of of grain size and for different numerical resolutions N.

$$
\begin{aligned}
&\sum_{n=0}^{N_s}\left(\int_0^E dU\,R_{\mathrm{em}}(U,T(E))+\int_0^{+\infty} dU\,R_{\mathrm{abs}}(U)\right)\,n\,f(E,n)\\
&\quad+\sum_{n=0}^{N_s} k_{\mathrm{coll}}\,s(T_{\mathrm{gas}})\,\left(1-\frac{n}{N_s}\right)\,n\,f(E,n)+\sum_{n=0}^{N_s} n\,k_{\mathrm{des}}(T(E))\,n\,f(E,n)\\
&\quad+\sum_{n=0}^{N_s} k_{\mathrm{coll}}\,\frac{n}{N_s}\,n\,f(E,n)+\sum_{n=0}^{N_s} k_{\mathrm{migr}}(T(E))\,\frac{n(n-1)}{N_s}\,n\,f(E,n)\\
&=\sum_{n=0}^{N_s}\int_0^E dE'\,R_{\mathrm{abs}}(E-E')\,n\,f(E',n)+\sum_{n=0}^{N_s}\int_E^{+\infty} dE'\,R_{\mathrm{em}}(E'-E,T(E'))\,n\,f(E',n)\\
&\quad+\sum_{n=1}^{N_s} k_{\mathrm{coll}}\,s(T_{\mathrm{gas}})\,\left(1-\frac{n-1}{N_s}\right)\,n\,f(E,n-1)\\
&\quad+\sum_{n=0}^{N_s-1}\left((n+1)\,k_{\mathrm{des}}(T(E))+k_{\mathrm{coll}}\,\frac{n+1}{N_s}\right)\,n\,f(E,n+1)\\
&\quad+\sum_{n=0}^{N_s-2} k_{\mathrm{migr}}(T(E))\,\frac{(n+2)\,(n+1)}{N_s}\,n\,f(E,n+2)
\end{aligned}
\tag{250}
$$

We use $\sum_{n=0}^{N_s} n\, f(E,n) = \langle n\,|E\rangle\; f_E(E)$, and we re-number the last three sums on the right-hand side:

$$\begin{aligned}
&\left(\int_0^E dU\, R_{\rm em}(U,T(E)) + \int_0^{+\infty} dU\, R_{\rm abs}(U)\right)\; \langle n\,|E\rangle\; f_E(E) \\
&\quad + \sum_{n=0}^{N_s} k_{\rm coll}\, s(T_{\rm gas})\; \left(1-\frac{n}{N_s}\right) n\, f(E,n) + \sum_{n=0}^{N_s} n\, k_{\rm des}(T(E))\, n\, f(E,n) \\
&\quad + \sum_{n=0}^{N_s} k_{\rm coll}\, \frac{n}{N_s}\, n\, f(E,n) + \sum_{n=0}^{N_s} k_{\rm migr}(T(E))\, \frac{n(n-1)}{N_s}\, n\, f(E,n) \\
&\qquad = \int_0^E dE'\, R_{\rm abs}(E-E')\, f_E(E')\; \left\langle n\,\middle|E'\right\rangle \\
&\qquad + \int_E^{+\infty} dE'\, R_{\rm em}(E'-E,T(E'))\, f_E(E')\; \left\langle n\,\middle|E'\right\rangle \\
&\qquad + \sum_{n=0}^{N_s-1} k_{\rm coll}\, s(T_{\rm gas})\; \left(1-\frac{n}{N_s}\right)\; (n+1)\, f(E,n) \\
&\qquad + \sum_{n=1}^{N_s} \left(n\, k_{\rm des}(T(E)) + k_{\rm coll}\, \frac{n}{N_s}\right)\; (n-1)\, f(E,n) \\
&\qquad\qquad + \sum_{n=2}^{N_s} k_{\rm migr}(T(E))\, \frac{n\,(n-1)}{N_s}\, (n-2)\, f(E,n) \qquad (251)
\end{aligned}$$

We then subtract the sums of the left-hand side form those of the right-hand side:

$$\begin{aligned}
&\left(\int_0^E dU\, R_{\rm em}(U,T(E)) + \int_0^{+\infty} dU\, R_{\rm abs}(U)\right)\; \langle n\,|E\rangle\; f_E(E) \\
&\qquad = \int_0^E dE'\, R_{\rm abs}(E-E')\, f_E(E')\; \left\langle n\,\middle|E'\right\rangle \\
&\qquad + \int_E^{+\infty} dE'\, R_{\rm em}(E'-E,T(E'))\, f_E(E')\; \left\langle n\,\middle|E'\right\rangle \\
&\qquad\quad + \sum_{n=0}^{N_s} k_{\rm coll}\, s(T_{\rm gas})\; \left(1-\frac{n}{N_s}\right)\; f(E,n) \\
&\qquad\quad - \sum_{n=0}^{N_s} \left(n\, k_{\rm des}(T(E)) + k_{\rm coll}\, \frac{n}{N_s}\right)\; f(E,n) \\
&\qquad\qquad - 2\, \sum_{n=0}^{N_s} k_{\rm migr}(T(E))\, \frac{n^2-n}{N_s}\, f(E,n) \qquad (252)
\end{aligned}$$

Finally, using the definition of the second order conditional moment:

$$\left\langle n^2\,|E\right\rangle\; f_E(E) = \sum_{n=0}^{N_s} n^2\, f(E,n),$$

we get:

$$\begin{aligned}
&\int_0^E dE'\, R_{\text{abs}}(E-E')\, f_E(E')\, \langle n \,|E'\rangle \\
&\qquad + \int_E^{+\infty} dE'\, R_{\text{em}}(E'-E, T(E'))\, f_E(E')\, \langle n \,|E'\rangle \\
&\qquad - \left(\int_0^E dU\, R_{\text{em}}(U, T(E)) + \int_0^{+\infty} dU\, R_{\text{abs}}(U) \right) \langle n \,|E\rangle \; f_E(E) \\
&+ k_{\text{coll}}\, s(T_{\text{gas}}) \left(1 - \frac{\langle n \,|E\rangle}{N_s}\right) f_E(E) - \left(\langle n \,|E\rangle \; k_{\text{des}}(T(E)) + k_{\text{coll}} \frac{\langle n \,|E\rangle}{N_s} \right) f_E(E) \\
&\qquad - 2\, k_{\text{migr}}(T(E)) \frac{\langle n^2 \,|E\rangle - \langle n \,|E\rangle}{N_s} f_E(E) = 0 \quad (253)
\end{aligned}$$

This equation can be interpreted as a rate equation for grains that are at thermal energy E at a given instant. The equation expresses the balance between the rates of gain and loss of surface atoms. In addition to the chemical terms (gain by adsorption and loss by desorption, Eley-Rideal reaction, and Langmuir-Hinshelwood reaction), which appear in the last two lines, the grains at energy E can gain or lose atoms (on average) due to grains leaving this thermal energy E or arriving in this state. As we are at statistical equilibrium, the rate of arrival in state E equals the rate at which grains leave this state. But if grains arriving have on average a lower surface population than the grains that leave, it results in an average loss of atoms for the grains at energy E. This contribution is expressed by the imbalance of the first two lines.

Defining $\left\langle n^{(\text{arrival})} \,|E \right\rangle$, the average surface population of the grains that arrive in state E, the first line becomes:

$$\begin{aligned}
&\left(\int_0^E dE'\, R_{\text{abs}}(E-E')\, f_E(E') + \int_E^{+\infty} dE'\, R_{\text{em}}(E'-E, T(E'))\, f_E(E') \right) \\
&\qquad \times \left\langle n^{(\text{arrival})} \,|E \right\rangle \quad (254)
\end{aligned}$$

Moreover, we already know (from Eq. 220) that

$$\begin{aligned}
&\int_0^E dE'\, R_{\text{abs}}(E-E')\, f_E(E') + \int_E^{+\infty} dE'\, R_{\text{em}}(E'-E, T(E'))\, f_E(E') = \\
&\qquad \left(\int_0^E dU\, R_{\text{em}}(U, T(E)) + \int_0^{+\infty} dU\, R_{\text{abs}}(U) \right) f_E(E) \quad (255)
\end{aligned}$$

so that the first two lines become

$$\left(\int_0^E dU\, R_{\text{em}}(U, T(E)) + \int_0^{+\infty} dU\, R_{\text{abs}}(U) \right) f_E(E) \left[\left\langle n^{(\text{arrival})} \,|E \right\rangle - \langle n \,|E\rangle \right] \quad (256)$$

For simplicity, we will now rewrite the equation in terms of temperature T instead of thermal energy E. We first note that

$$\langle n\,|T\rangle\; f_T(T) = \sum_n n\, f(T,n) = \sum_n n\, f(E,n)\, C(E) = \langle n\,|E\rangle\; f_E(E)\, C(E) \quad (257)$$

We thus multiply Eq. 253 by $C(E)$ and then divide by $f_T(T)$, and get

$$\begin{aligned}\left(\int_0^{E(T)} dU\, R_{\rm em}(U,T(E)) + \int_0^{+\infty} dU\, R_{\rm abs}(U)\right) \\ \times \left[\left\langle n^{(\rm arrival)}\,|T\right\rangle - \langle n\,|T\rangle\right] \\ + k_{\rm coll}\, s(T_{\rm gas}) \left(1 - \frac{\langle n\,|T\rangle}{N_{\rm s}}\right) - \left(\langle n\,|T\rangle\; k_{\rm des}(T) + k_{\rm coll}\,\frac{\langle n\,|T\rangle}{N_{\rm s}}\right) \\ - 2\,k_{\rm migr}(T)\,\frac{\langle n^2\,|T\rangle - \langle n\,|T\rangle}{N_{\rm s}} = 0 \quad (258)\end{aligned}$$

Up to now, the equation is exact. But two problems remain: the last term contains $\langle n^2\,|T\rangle$ so that the equation is not in closed form, and the full expression of the first term (see previous expressions) involves an integral operator, which makes the resolution more complex. We start by proposing an approximation to the first term. From now on, we simplify the notation of the sticking coefficient by noting s for $s(T_{\rm gas})$.

Our approximation is based on a few expectations:

- Physisorption-based formation occurs mainly when the grain is at low temperature (due to the low binding energy). We thus only need our approximation of $\langle n|\,T\rangle$ to be precise in the low temperature domain where desorption is not the dominating process.
- In this temperature domain of interest, absorption of photons dominates over emission. In other words, grains leaving this temperature mainly do so by absorbing a photon and going to higher temperatures. We also assume that grains arriving at these temperatures mainly come from higher temperatures. This is true if the temperatures of interest are low enough, which is the case for physisorption.
- Fluctuations which don't leave this low temperature domain do not matter much on the chemistry (as they do not trigger desorption). We will thus neglect those fluctuations and only consider fluctuations reaching at least the temperature T_{lim} where desorption starts dominating over adsorption (i.e. above which $\langle n|\,T\rangle$ is expected to decrease very rapidly and become negligible). This limit temperature is given by

$$T_{\rm lim} = \frac{T_{\rm phys}}{\ln(\frac{\nu_0}{k_{\rm coll} s})} \quad (259)$$

We thus do the following crude assumption: grains that undergo a fluctuation that does not go above T_{lim} come back with the same population, while grains going above T_{lim} come back completely bare. As a result, we have a net loss rate caused by fluctuations that can be expressed as

$$\left(\int_{\max(E(T_{\text{lim}})-E(T),0)}^{+\infty} dU\, R_{\text{abs}}(U) \right) \langle n \,|T\rangle \tag{260}$$

We define $k_{\text{phot}}(T)$ the rate of the fluctuations that go above T_{lim}:

$$k_{\text{phot}}(T) = \int_{\max(E(T_{\text{lim}})-E(T),0)}^{+\infty} dU\, R_{\text{abs}}(U) \tag{261}$$

and Eq. 258 becomes

$$\begin{aligned} & k_{\text{coll}}\, s \left(1 - \frac{\langle n \,|T\rangle}{N_{\text{s}}}\right) - k_{\text{coll}} \frac{\langle n \,|T\rangle}{N_{\text{s}}} \\ & \quad - 2\, k_{\text{migr}}(T) \frac{\langle n^2 \,|T\rangle - \langle n \,|T\rangle}{N_{\text{s}}} - \left(k_{\text{des}}(T) + k_{\text{phot}}(T)\right) \langle n \,|T\rangle = 0 \end{aligned} \tag{262}$$

We see that we have grouped this term with the desorption rate so as to obtain an effective desorption rate $k_{\text{des}}(T) + k_{\text{phot}}(T)$, which takes both the desorptions at T and the desorptions during the fluctuations into account.

We now need an approximation of the third term of this equation, in order to avoid the second order moment $\langle n^2 \,|T\rangle$. This third term represents the rate at which grains at temperature T lose surface atoms because of Langmuir-Hinshelwood reactions (two surface atoms meet while migrating). We distinguish two cases: $\langle n \,|T\rangle > 1$ and $\langle n \,|T\rangle < 1$.

When $\langle n \,|T\rangle > 1$, we assume that the discrete nature of the surface population is negligible, so that the fluctuations of n caused by jumps from n to $n+1$ (or $n-1$) can be neglected. Moreover, we expect that when the surface population is high, the formation will be dominated by direct Eley-Rideal reaction, and it is not necessary to have an accurate approximation of the Langmuir-Hinshelwood formation rate. We can then use the simple approximation $\langle n^2 \,|T\rangle = \langle n \,|T\rangle^2$. We then use for the Langmuir-Hinshelwood formation rate $k_{\text{migr}}(T) \frac{\langle n|T\rangle^2}{N_{\text{s}}}$. The resulting equation for $\langle n \,|T\rangle$ is then

$$\begin{aligned} & k_{\text{coll}}\, s \left(1 - \frac{\langle n \,|T\rangle}{N_{\text{s}}}\right) - k_{\text{coll}} \frac{\langle n \,|T\rangle}{N_{\text{s}}} \\ & \quad - 2\, k_{\text{migr}}(T) \frac{\langle n \,|T\rangle^2}{N_{\text{s}}} - \left(k_{\text{des}}(T) + k_{\text{phot}}(T)\right) \langle n \,|T\rangle = 0 \end{aligned} \tag{263}$$

The solution of this equation is

$$\langle n \,|T\rangle = \frac{1+s}{4}\,\frac{k_{\rm coll}}{k_{\rm migr}(T)}\left(1+\frac{N_{\rm s}(k_{\rm des}(T)+k_{\rm phot}(T))}{k_{\rm coll}(1+s)}\right) \times\left[\sqrt{1+\frac{8s}{(1+s)^2}\,\frac{k_{\rm migr}(T)}{k_{\rm coll}}\,\frac{N_{\rm s}}{\left(1+\frac{N_{\rm s}(k_{\rm des}(T)+k_{\rm phot}(T))}{k_{\rm coll}(1+s)}\right)^2}}-1\right]. \quad (264)$$

When this solution becomes lower than 1, we switch to the second regime.

In the second regime where $\langle n \,|T\rangle < 1$, we use an approximation inspired by the reasoning used in Garrod [2008]. As the Langmuir-Hinshelwood formation mechanism requires two atoms to be present on grain surface, the discrete nature of the surface population is very important in this regime. The idea of the approximation is that the population is most of the time 1 or 0 when $\langle n \,|T\rangle \ll 1$, so that

$$\langle n \,|T\rangle \simeq p(n=1\,|T) \quad (265)$$

where $p(n=1\,|T)$ is the conditional probability to have one atom on the grain surface, knowing that the grain temperature is T.

A Langmuir-Hinshelwood reaction occurs only when an atom of the gas is adsorbed while another atom was already present on the surface, and these two atoms meet before any other event removes one of the atoms (desorption or Eley-Rideal reaction). The rate at which adsorption happens on a grain which already has one surface atom is

$$k_{\rm coll}\,s\left(1-\frac{1}{N_{\rm s}}\right)p(n=1\,|T) \simeq k_{\rm coll}\,s\left(1-\frac{1}{N_{\rm s}}\right)\langle n \,|T\rangle \quad (266)$$

where we have used Eq. 265. The probability that the two atoms meet before anything else happen is

$$\frac{\frac{2k_{\rm migr}(T)}{N_{\rm s}}}{\frac{2k_{\rm migr}(T)}{N_{\rm s}}+\frac{2k_{\rm coll}}{N_{\rm s}}+2(k_{\rm des}(T)+k_{\rm phot}(T))} \quad (267)$$

so that the Langmuir-Hinshelwood formation rate can be approximated as

$$\frac{k_{\rm coll}\,s\left(1-\frac{1}{N_{\rm s}}\right)}{1+\frac{k_{\rm coll}}{k_{\rm migr}(T)}+N_{\rm s}\,\frac{k_{\rm des}(T)+k_{\rm phot}(T)}{k_{\rm migr}(T)}}\,\langle n \,|T\rangle \quad (268)$$

Equation 262 becomes

$$k_{\text{coll}}\, s \left(1 - \frac{\langle n\,|T\rangle}{N_s}\right) - k_{\text{coll}}\, \frac{\langle n\,|T\rangle}{N_s} - 2\, \frac{k_{\text{coll}}\, s \left(1 - \frac{1}{N_s}\right)}{1 + \frac{k_{\text{coll}}}{k_{\text{migr}}(T)} + N_s\, \frac{k_{\text{des}}(T)+k_{\text{phot}}(T)}{k_{\text{migr}}(T)}}\, \langle n\,|T\rangle - \left(k_{\text{des}}(T) + k_{\text{phot}}(T)\right)\, \langle n\,|T\rangle = 0 \tag{269}$$

The solution is

$$\boxed{\langle n|\, T\rangle = \frac{N_s}{N_s\, \frac{(k_{\text{des}}(T)+k_{\text{phot}}(T))}{k_{\text{coll}} s} + \frac{1+s}{s} + \frac{2(N_s-1)}{1+\frac{k_{\text{coll}}}{k_{\text{migr}}(T)} + N_s\, \frac{k_{\text{des}}(T)+k_{\text{phot}}(T)}{k_{\text{migr}}(T)}}}}. \tag{270}$$

Finally, we use Eq. 264 and 270 to compute $\langle n|\, T\rangle$. The total average formation rate is then computed as:

$$\langle r_{H_2}\rangle = \int_0^{T_{\text{switch}}} dT\, f(T) \left(\frac{k_{\text{coll}}}{N_s}\, \langle n|\, T\rangle + \frac{k_{\text{migr}}(T)}{N_s}\, \langle n|\, T\rangle^2\right) + \int_{T_{\text{switch}}}^{+\infty} dT\, f(T) \left(\frac{k_{\text{coll}}}{N_s}\, \langle n|\, T\rangle + \frac{k_{\text{coll}}\, s(1 - \frac{1}{N_s})}{1 + \frac{k_{\text{coll}}}{k_{\text{migr}}(T)} + \frac{N_s(k_{\text{des}}(T)+k_{\text{phot}}(T))}{k_{\text{migr}}(T)}}\, \langle n|\, T\rangle\right), \tag{271}$$

where T_{switch} is the temperature at which $\langle n|\, T\rangle$ becomes < 1 ($\langle n|\, T\rangle > 1$ for $T < T_{switch}$, and $\langle n|\, T\rangle < 1$ for $T > T_{switch}$).

We show the comparison of the results of this approximation to the results of the full resolution in Sect. 7.3.3.

7.3.2 *Eley-Rideal*

For completeness, we apply the same approximation idea to the Eley-Rideal mechanism.

In the case of the chemisorption-based Eley-Rideal mechanism, the equation for $\langle n|\, E\rangle$ has already been derived previously (Eq. 225). The corresponding equation for $\langle n|\, T\rangle$ is

$$\left(\int_0^{E(T)} dU\, R_{\text{em}}(U, T(E)) + \int_0^{+\infty} dU\, R_{\text{abs}}(U)\right) \left[\left\langle n^{(\text{arrival})}\,|T\right\rangle - \langle n\,|T\rangle\right] + k_{\text{coll}}\, s \left(1 - \frac{\langle n\,|T\rangle}{N_s}\right) - \frac{k_{\text{coll}}\, \langle n\,|T\rangle}{N_s} - k_{\text{des}}(T)\, \langle n\,|T\rangle = 0 \tag{272}$$

There is no quadratic term in this case, and we simply need to approximate the first term. This makes the approximation much simpler.

We use the same approximation as in the Langmuir-Hinshelwood case for the losses caused by fluctuations. We consider that only the grains that undergo fluctuations reaching the regime where desorption dominates, lose their population. We define the frontier of this regime as

$$T_{\text{lim}} = \frac{T_{\text{chem}}}{\ln(\frac{\nu_0}{k_{\text{coll}} s})} \tag{273}$$

and the net loss rate caused by fluctuations is

$$k_{\text{phot}}(T) \langle n | T \rangle \tag{274}$$

with

$$k_{\text{phot}}(T) = \int_{\max(E(T_{\text{lim}})-E(T),0)}^{+\infty} dU\, R_{\text{abs}}(U) \tag{275}$$

Equation 272 becomes

$$k_{\text{coll}}\, s \left(1 - \frac{\langle n | T \rangle}{N_s}\right) - \frac{k_{\text{coll}} \langle n | T \rangle}{N_s} - \left(k_{\text{des}}(T) + k_{\text{phot}}(T)\right) \langle n | T \rangle = 0 \tag{276}$$

The solution is

$$\boxed{\langle n | T \rangle = \frac{s}{1+s} \frac{N_s}{1 + \frac{N_s\left(k_{\text{des}}(T)+k_{\text{phot}}(T)\right)}{(1+s)\, k_{\text{coll}}}}} \tag{277}$$

The average formation rate can then be computed as

$$\langle r_{H_2} \rangle = \int_0^{+\infty} dT\, f(T) \frac{k_{\text{coll}}}{N_s} \langle n | T \rangle \tag{278}$$

We compare this approximation to the full resolution in the next section. This approximation is mostly given here for completeness, as the full resolution method described previously is sufficiently fast, in contrast to the Langmuir-Hinshelwood mechanism for which an approximation is necessary to keep an acceptable computation time.

7.3.3 *Accuracy assessment*

We now compare the results of these approximations to those of the full resolution methods presented in Sect. 7.2. All effects result from a competition between the timescale of the fluctuations and the timescale of the chemistry, which is controlled by the frequency of H atom adsorption from the gas. We thus explore the parameter space by varying the two parameters n_{H} the gas density (we assume here that the gas is atomic), and χ the radiation field scaling parameter.

We present the comparison on five models spanning the range of relevant parameters:

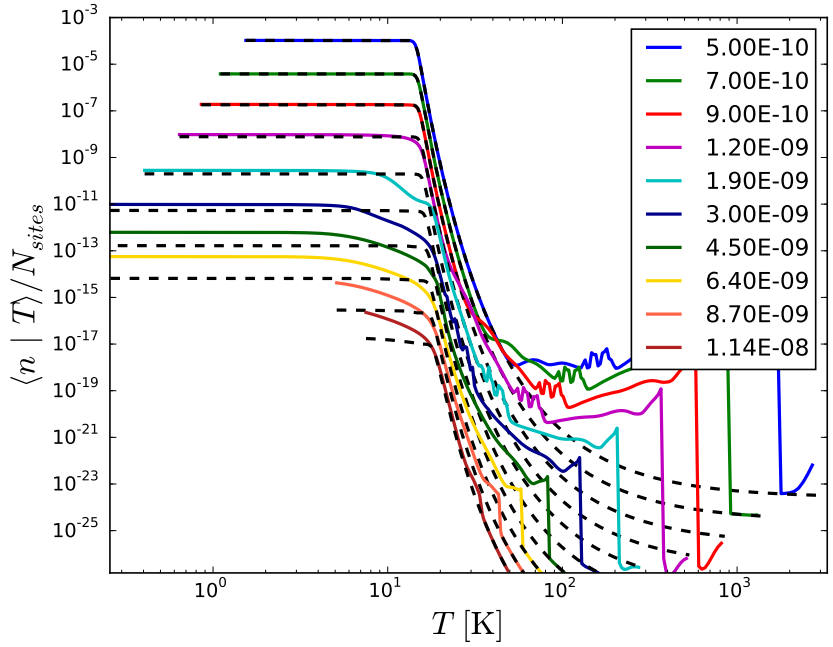

Figure 64: Conditional average $\langle n \,|T\rangle$ computed by the full resolution (solid lines) and by the approximation (dashed lines) for various grain sizes for the Langmuir-Hinshelwood mechanism. Each successive curve has been shifted down by a factor 10 for a better readability. Conditions: $n_{\mathrm{H}} = 1\,\mathrm{cm}^{-3}$ and $\chi = 1$.

- $n_{\mathrm{H}} = 1\,\mathrm{cm}^{-3}$, $\chi = 1$
- $n_{\mathrm{H}} = 1\,\mathrm{cm}^{-3}$, $\chi = 3160$
- $n_{\mathrm{H}} = 10^{6}\,\mathrm{cm}^{-3}$, $\chi = 1$
- $n_{\mathrm{H}} = 10^{6}\,\mathrm{cm}^{-3}$, $\chi = 3160$
- $n_{\mathrm{H}} = 10^{3}\,\mathrm{cm}^{-3}$, $\chi = 31.6$

LANGMUIR-HINSHELWOOD

We first perform this comparison for the Langmuir-Hinshelwood mechanism, as it is the case for which the exact computation is not practically usable due to its long computation time. We compare the results of the approximation to the exact results up to $a = 10\,\mathrm{nm}$. As the computation of the exact method becomes too long for larger sizes, we then compare to the equilibrium rate equation results and verify that the approximation converges to this equilibrium (no fluctuations) result for large grains.

As the approximation consists in computing $\langle n \,|T\rangle$, we first show the comparison on this quantity for individual sizes in the range $0.5\,\mathrm{nm} - 10\,\mathrm{nm}$. The comparison on the model $n_{\mathrm{H}} = 1\,\mathrm{cm}^{-3}$, $\chi = 1$ is shown on Fig. 64. The

conditional average of the surface coverage fraction $\langle n \,|T\rangle \,/N_s$ is shown for each grain size, shifted down by a factor 10 for each successive curve.

As explained previously, the average formation rate is dominated by the regime where the surface coverage is high (low temperatures), and we have focused our approximation on this regime. The large discrepancies that appear at high temperatures are thus expected and without consequences on the total formation rate. They come from the fact that we have only considered the negative impact of fluctuations of the surface populations: grains come back from the fluctuations with less surface atoms than initially. While this is correct at low temperatures, where grains mostly leave to go to higher temperatures where desorption is faster, the opposite is true at high temperatures. Grains leaving a high temperature state mostly do so by cooling to a lower temperature, while grains arriving mostly come from the low temperature domain where the surface population is higher. The net effect is thus a gain in surface population due to fluctuations. Moreover, we see the shape of the absorption coefficient and of the external radiation field re-appear in the resulting curve as some IR features (coming from the external radiation field here), and a clear cut corresponding to the Lyman limit. Indeed, the corresponding temperature states are more likely to be reached by a grain coming from the low temperature regime and thus having a high surface population.

On the low temperature part, the match between the approximation and the exact results is excellent for small grains, but a growing discrepancy appears for larger grains. However, two effects reduce the importance of this problem. First, the dust size distribution (see Sect. 5.3.3) gives more weight to the smallest sizes. Second, what matters for the average formation rate on one given grain is the product of $\langle n \,|T\rangle$ and f_T. As the peak of f_T shifts towards higher temperature as a grows in the range $1\,\mathrm{nm} - 10\,\mathrm{nm}$ (see Fig. 35), the importance of the low temperature plateau of $\langle n \,|T\rangle$ decreases.

The other test models are shown on Fig. 65, 66, 67 and 68. Very similar trends are seen. Overall, the approximation seems to work better for high radiation field models.

As what really matters is the average formation rate computed from this conditional average population, we show on Fig. 69 the comparison of the formation efficiencies obtained by the exact computation (solid lines), the approximation (dashed lines), and the equilibrium rate equation (dotted line) as functions of the grain size a. The approximation appears to be very accurate on the whole size range over which the comparison is made, with only small discrepancies around 10 nm. For the reasons explained above, the few problems visible when comparing the results for $\langle n \,|T\rangle$ have had very little impact on the average formation rate.

Finally, we are interested in the resulting formation rate in the gas, obtained by integration over the dust size distribution. The accuracy of the approximation on this final formation rate is given in Table 5, for two dust size distributions, both power-laws with exponent -3.5, but one starting at

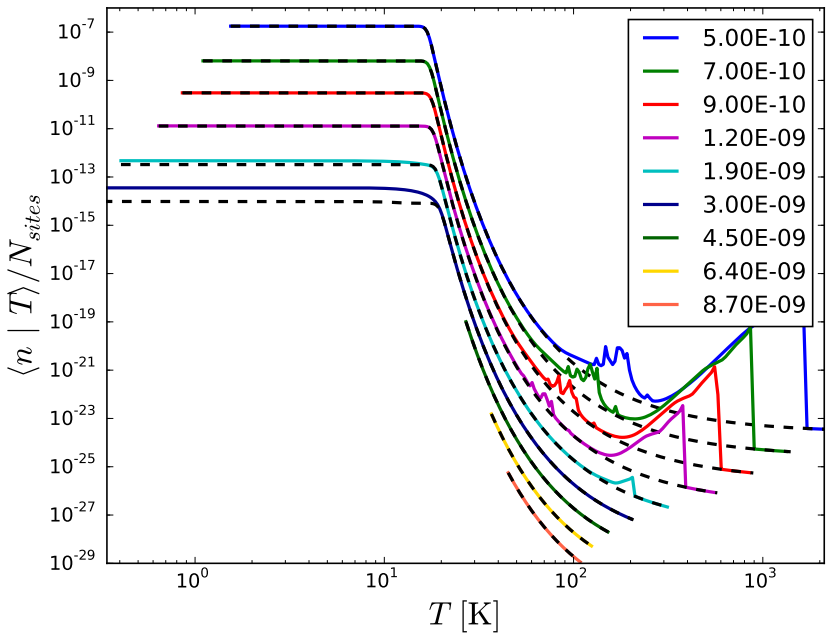

Figure 65: Same as Fig. 64 for $n_{\mathrm{H}} = 1\,\mathrm{cm}^{-3}$ and $\chi = 3160$.

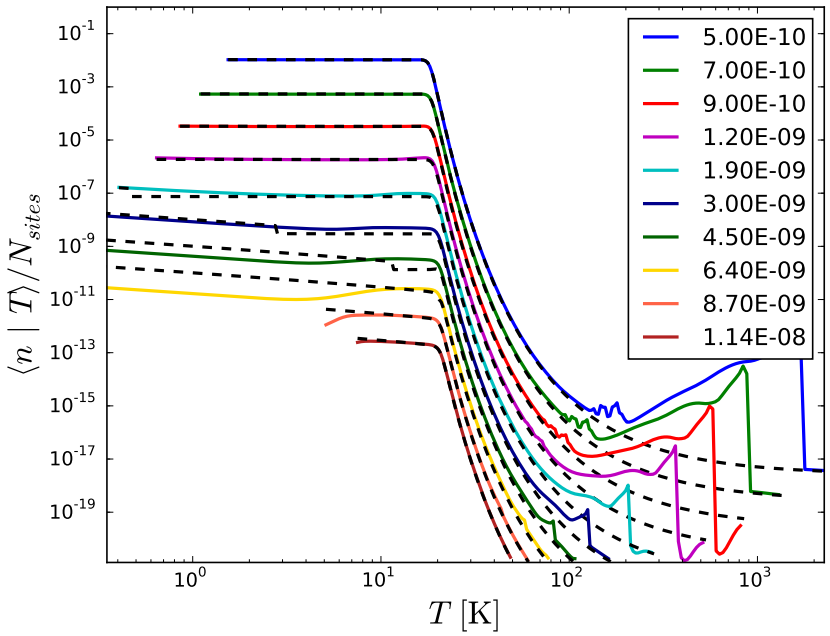

Figure 66: Same as Fig. 64 for $n_{\mathrm{H}} = 10^6\,\mathrm{cm}^{-3}$ and $\chi = 1$.

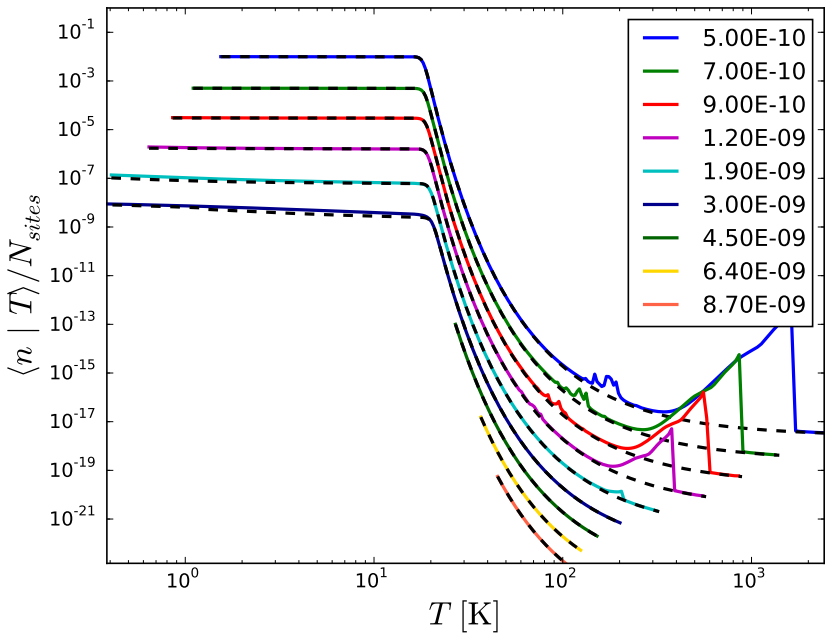

Figure 67: Same as Fig. 64 for $n_{\mathrm{H}} = 10^6\,\mathrm{cm}^{-3}$ and $\chi = 3160$.

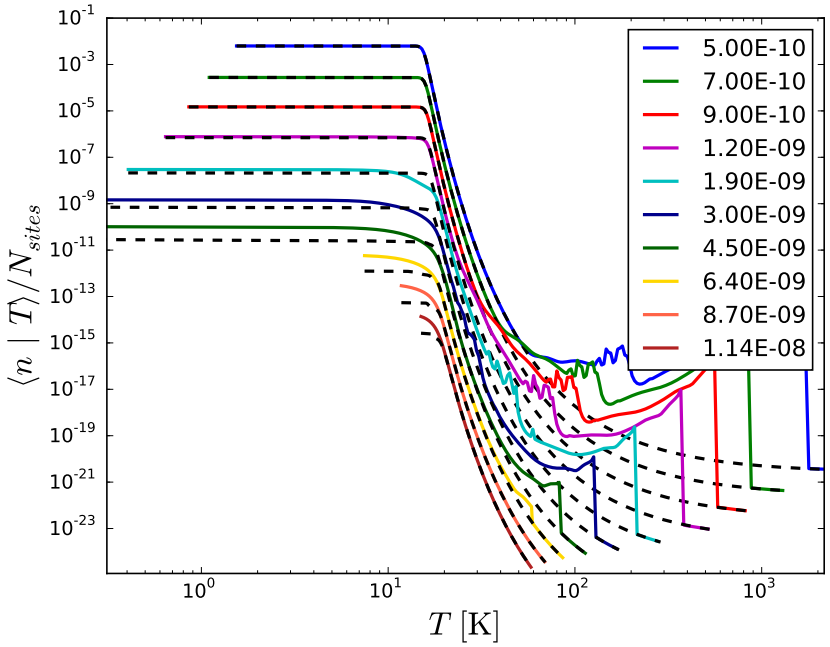

Figure 68: Same as Fig. 64 for $n_{\mathrm{H}} = 10^3\,\mathrm{cm}^{-3}$ and $\chi = 31.6$.

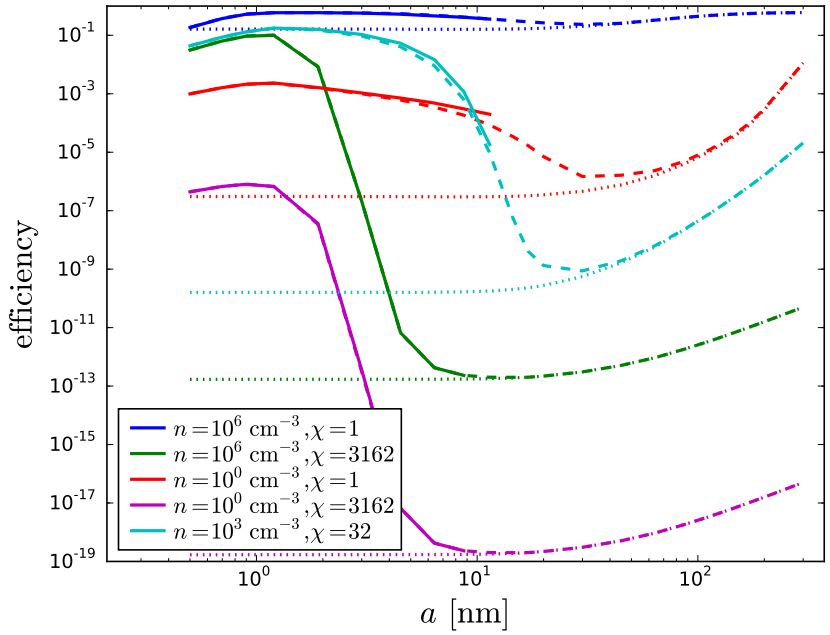

Figure 69: Formation efficiency as a function of grain size (Langmuir-Hinshelwood mechanism). Exact result: solid lines; approximation: dashed lines; equilibrium rate equation: dotted lines.

Table 5: Approximation error on the final formation rate integrated over the full size distribution for the Langmuir-Hinshelwood mechanism.

$a_{\min} =$	0.5 nm	1 nm
Model:		
$n = 1\,\mathrm{cm}^{-3}$, $\chi = 1$	2.95%	4.44%
$n = 1\,\mathrm{cm}^{-3}$, $\chi = 3160$	0.32%	0.02%
$n = 1 \times 10^6\,\mathrm{cm}^{-3}$, $\chi = 1$	1.18%	1.13%
$n = 1 \times 10^6\,\mathrm{cm}^{-3}$, $\chi = 3160$	1.52%	1.85%
$n = 1 \times 10^3\,\mathrm{cm}^{-3}$, $\chi = 31.6$	3.68%	4.95%

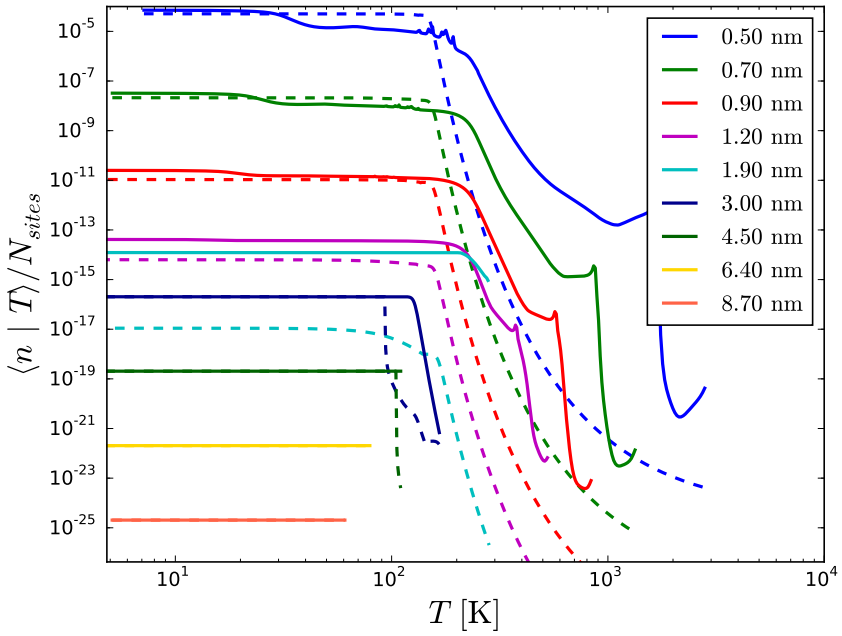

Figure 70: Conditional average $\langle n \,|\, T \rangle$ computed by the exact method (solid lines) and by the approximation (dashed lines) for various grain sizes for the Eley-Rideal mechanism. Each successive curve has been shifted down by a factor of 1000 for a better readability. Conditions: $n_{\mathrm{H}} = 1\,\mathrm{cm}^{-3}$ and $\chi = 1$.

5 Å and the other starting at 1 nm. The error is at worse of 5%. Our approximation is thus very accurate, while being much faster than the true computation. We thus use this approximation as the default way of computing the Langmuir-Hinshelwood formation rate.

ELEY-RIDEAL

We now perform the comparison for the Eley-Rideal mechanism, using the same five models. Again, we start by comparing the results for $\langle n \,|\, T \rangle$. The comparison is shown on Fig. 70, 71, 72, 73, and 74.

The agreement between the approximation and the exact result is not as good as in the case of the Langmuir-Hinshelwood. For the smallest grain sizes ($a < 1.5\,\mathrm{nm}$), the approximation gives a good estimate of the low temperature plateau (remember that f_T peaks at a few tens of K at most at these sizes). The approximation then strongly underestimate the surface population for grain of size $a = 1.5 - 2.5\,\mathrm{nm}$, before reaching a very good agreement for bigger grains.

The problems come from the fact that the limit temperature T_{lim} (see Sect. 7.3.2) in the case of the Eley-Rideal mechanism is as high as $100 - 200\,\mathrm{K}$ (due to the larger binding energy for chemisorption), so that our approximation

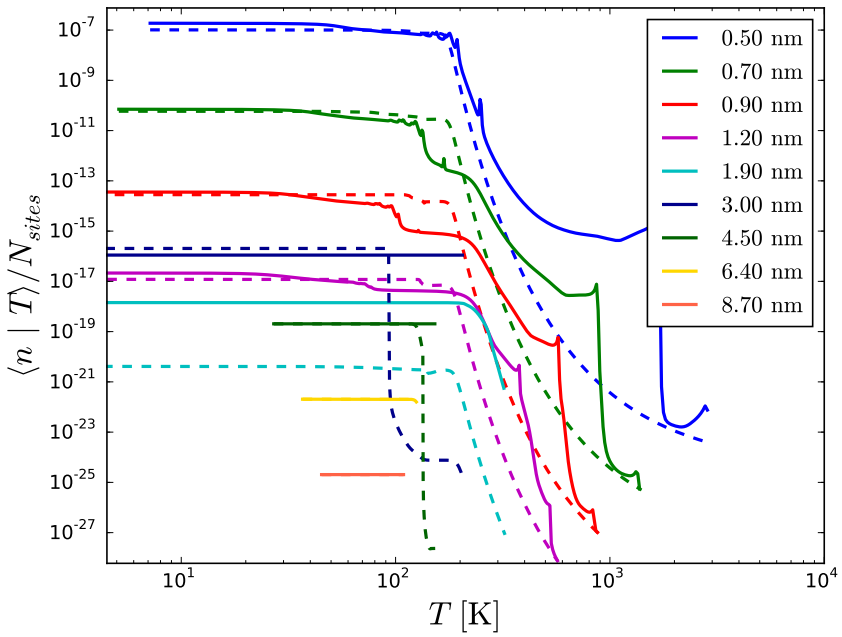

Figure 71: Same as Fig. 70 for $n_{\mathrm{H}} = 1\,\mathrm{cm}^{-3}$ and $\chi = 3160$.

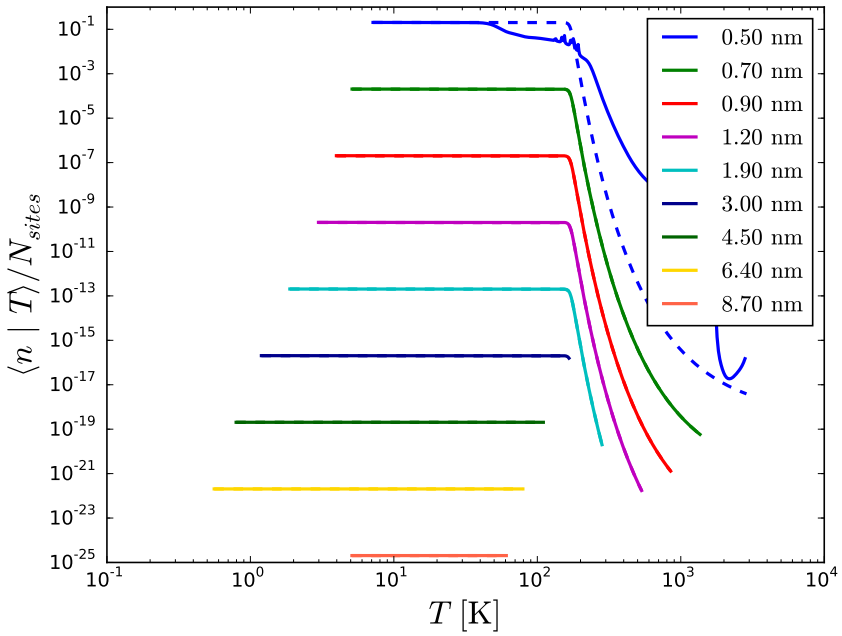

Figure 72: Same as Fig. 70 for $n_{\mathrm{H}} = 10^6\,\mathrm{cm}^{-3}$ and $\chi = 1$.

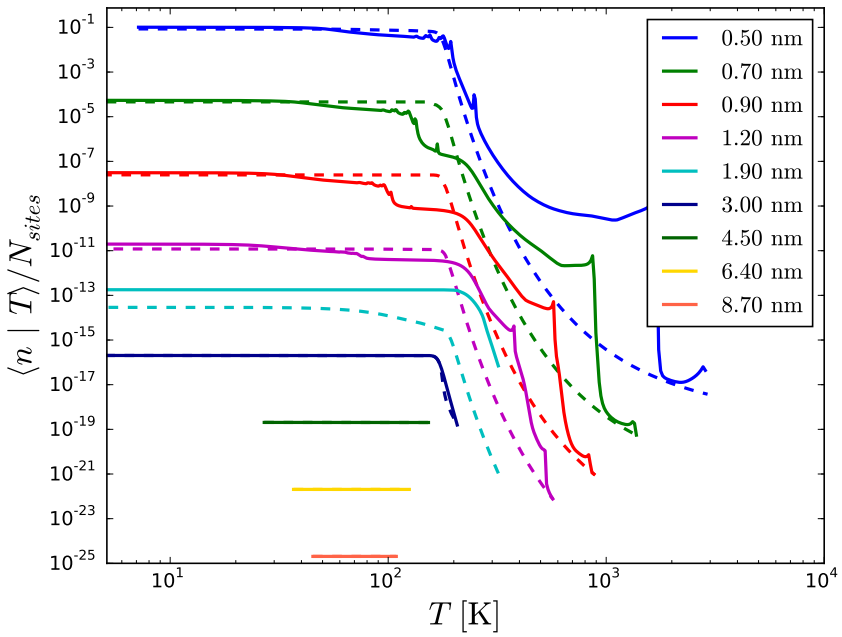

Figure 73: Same as Fig. 70 for $n_{\mathrm{H}} = 10^6\,\mathrm{cm}^{-3}$ and $\chi = 3160$.

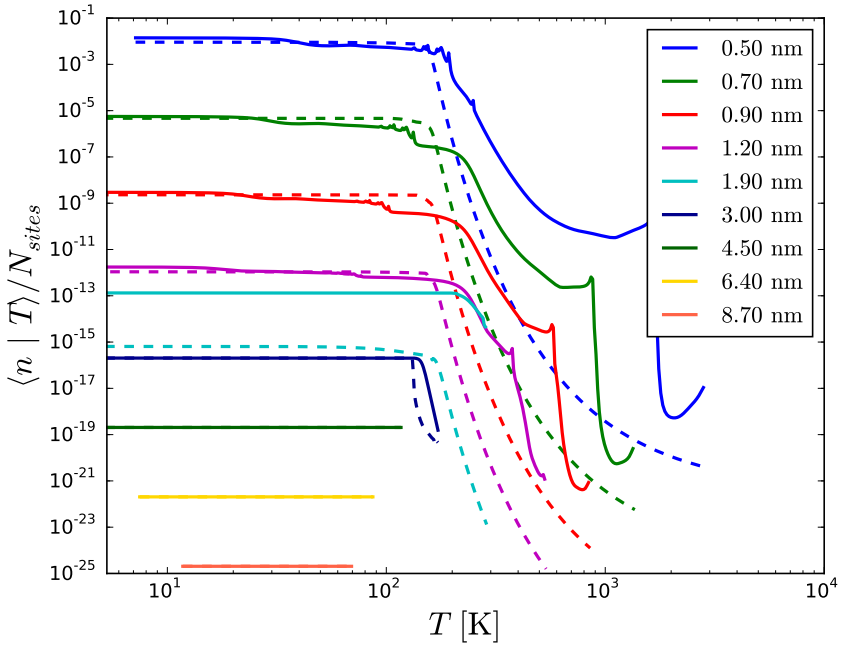

Figure 74: Same as Fig. 70 for $n_{\mathrm{H}} = 10^3\,\mathrm{cm}^{-3}$ and $\chi = 31.6$.

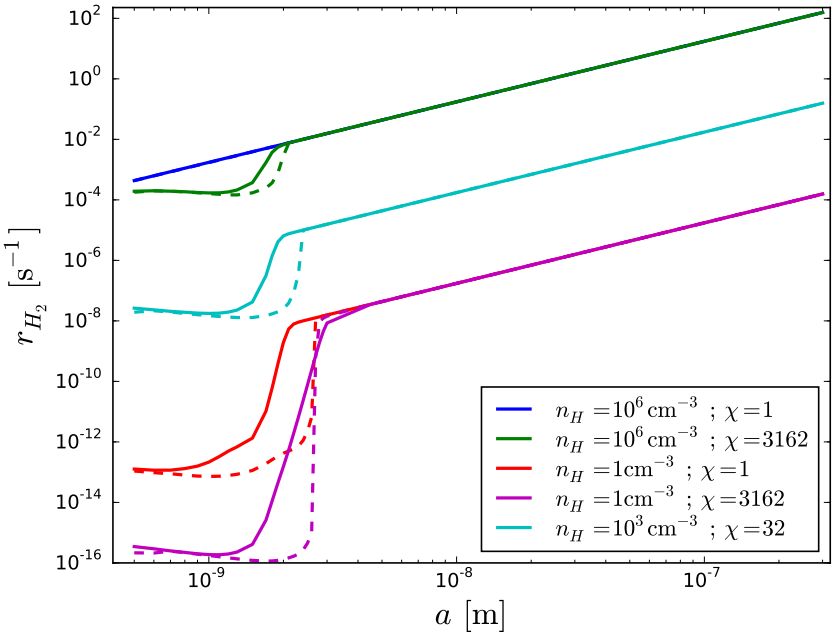

Figure 75: Formation efficiency as a function of grain size (Eley-Rideal mechanism). Exact result: solid lines; approximation: dashed lines; equilibrium rate equation: dotted lines.

that fluctuations occur mainly by photon absorption doesn't hold very well anymore, as photon emissions in this regime are not negligible.

The resulting formation rate as a function of grain size is shown in Fig. 75. The approximation thus tends to overestimate the size up to which fluctuations reduce the formation efficiency, which explains the large differences on $\langle n \,|T\rangle$ observed only for a very limited range of sizes.

However, the final formation rate in the gas (computed by integration over the dust size distribution) computed by the approximation remains a good estimate of the true results, as shown in Table 6. The error reaches 12% at worst.

We will not use this approximation for any application, as the exact method is fast enough to be practically usable. This test however shows that the ideas behind these approximations are solid enough to be applied with success to very different situations.

CONCLUSIONS

These resolution methods have been implemented in a stand-alone code called Fredholm. In addition, we developed a coupling between this code and the Meudon PDR Code, which allows the results of this detailed computation of the H_2 formation rate to be used in full cloud simulations. The

Table 6: Approximation error on the final formation rate integrated over the full size distribution for the Eley-Rideal mechanism.

$a_{\min}$ =	0.5 nm	1 nm
Model:		
$n = 1\,\mathrm{cm}^{-3}$, $\chi = 1$	0.0028%	0%
$n = 1\,\mathrm{cm}^{-3}$, $\chi = 3160$	8.19%	8.73%
$n = 1 \times 10^6\,\mathrm{cm}^{-3}$, $\chi = 1$	12.08%	12.08%
$n = 1 \times 10^6\,\mathrm{cm}^{-3}$, $\chi = 3160$	10.22%	10.22%
$n = 1 \times 10^3\,\mathrm{cm}^{-3}$, $\chi = 31.6$	6.26%	6.15%

Fredholm code and its coupling to the Meudon PDR Code are described in Appendix C.

The results obtained from this computation of the H_2 formation rate are now presented in the next chapter, which reproduces the article Bron et al. [2014].

8

RESULTS : BRON ET AL. 2014

The results of this new computation of the H_2 formation rate on dust grains were published in Bron et al. [2014]. We reproduce this article here.

After a description of the physical model of dust grains and surface chemistry, a brief explanation of the resolution method, and a presentation of the approximations, the results are presented. First, we present results on individual grains exposed to various radiation fields corresponding to unshielded conditions (such as the edge of clouds and PDRs), and investigate the effect of fluctuations and its dependance on the radiation field and the collision rate with gas H atoms. Second, we present full cloud simulations integrating this new computation of the H_2 formation rate, using the `Meudon PDR Code` and the coupling with `Fredholm` described in Chap. C, and describe the effects on cloud structure, exploring the parameter space of gas densities and radiation field strengths. The effects on molecular lines intensities are also discussed.

This article was a first application of the method, giving an overview of the effects on a large range of astrophysical conditions. This work will later be further developed in two directions :

- Exploring in more details the influence of the details of the microphysical processes of surface chemistry. The chemisorption-based Eley-Rideal mechanism still lacks precise constraints from theoretical and experimental studies. In particular, we assumed that surface defects would induce a strongly reduced chemisorption barrier. What is the surface density of such "open" sites ? We also assumed that all atoms reaching the surface fall onto a site, but chemisorption sites might have a smaller adsorption cross section. All those effects could significantly reduce the importance of the Eley-Rideal mechanism. A more detailed treatment of the excitation of the formed molecules could also lead to more precise observational signatures allowing to distinguish between the two formation mechanisms.

- Exploring in more details the observational consequences in specific astrophysical conditions. These are discussed in more depth in the conclusion of this chapter and include the residual atomic fraction in molecular gas when taking into account fluctuations caused by NIR photons and secondary UV photons (with application to cloud cores, for instance Li and Goldsmith [2003], and to the molecular fraction in diffuse clouds), a more detailed exploration of the observational consequences of the shift of the H/H_2 transitions on edge-on PDRs, or the research of observational signatures allowing to distinguish between the

two formation mechanisms (e.g., caused by differences in the excitation at formation).

8.1 THE ARTICLE

A&A 569, A100 (2014)
DOI: 10.1051/0004-6361/201322101

Astronomy & Astrophysics

Surface chemistry in the interstellar medium

II. H_2 formation on dust with random temperature fluctuations

Emeric Bron[1,2], Jacques Le Bourlot[1,2], and Franck Le Petit[1]

[1] LERMA, Observatoire de Paris & CNRS, 5 place Jules Janssen, 92190 Meudon, France
[2] Université Paris Diderot; 5 rue Thomas Mann, 75205 Paris, France
e-mail: jacques.lebourlot@obspm.fr

Received 18 June 2013 / Accepted 3 June 2014

ABSTRACT

Context. The H_2 formation on grains is known to be sensitive to dust temperature, which is also known to fluctuate for small grain sizes due to photon absorption.
Aims. We aim at exploring the consequences of simultaneous fluctuations of the dust temperature and the adsorbed H-atom population on the H_2 formation rate under the full range of astrophysically relevant UV intensities and gas conditions.
Methods. The master equation approach is generalized to coupled fluctuations in both the grain's temperature and its surface population and solved numerically. The resolution can be simplified in the case of the Eley-Rideal mechanism, allowing a fast computation. For the Langmuir-Hinshelwood mechanism, it remains computationally expensive, and accurate approximations are constructed.
Results. We find the Langmuir-Hinshelwood mechanism to become an efficient formation mechanism in unshielded photon dominated region edge conditions when taking those fluctuations into account, despite hot average dust temperatures. It reaches an importance comparable to the Eley-Rideal mechanism. However, we show that a simpler rate equation treatment gives qualitatively correct observable results in full cloud simulations under the most astrophysically relevant conditions. Typical differences are a factor of 2−3 on the intensities of the H_2 $v = 0$ lines. We also find that rare fluctuations in cloud cores are sufficient to significantly reduce the formation efficiency.
Conclusions. Our detailed analysis confirms that the usual approximations used in numerical models are adequate when interpreting observations, but a more sophisticated statistical analysis is required if one is interested in the details of surface processes.

Key words. astrochemistry – molecular processes – ISM: molecules – dust, extinction

1. Introduction

H_2 is the most abundant molecule in the interstellar medium. It is found in a wide variety of astrophysical environments in which it often plays a leading role in the physics and evolution of objects (see the book by Combes & Pineau des Forets 2001, for a review). As an efficient coolant of hot gas, it controls for instance through thermal balance the collapse of interstellar clouds leading ultimately to star formation. Furthermore, its formation is the first step of a long sequence of reactions leading to the great chemical complexity found in dense clouds. In addition to its physical importance, H_2 is also of great observational usefulness as a diagnostic probe for many different processes in various environments.

The detailed mechanism of its formation is thus a key part of the understanding and modeling of the interstellar medium. Direct gas phase formation is very inefficient and cannot explain the observed abundances. The ion-neutral reaction $H + H^-$ is more efficient, but the low H^- abundance does not allow sufficient H_2 formation this way. The H_2 molecule is thus thought to form mainly on the surface of dust grains (Gould & Salpeter 1963; Hollenbach & Salpeter 1971). Grains act as catalysts. They provide a surface on which adsorbed H atoms can meet and react, and they absorb that excess energy released by the formation that prevented the gas phase formation of a stable molecule.

This process is usually modeled using the Langmuir-Hinshelwood (LH) mechanism in which weakly bound adsorbed atoms migrate randomly on the surface, and one H_2 molecule is formed each time two atoms meet. This mechanism has been studied in detail using the master equation approach (Biham & Lipshtat 2002), the moment equation approach (Lipshtat & Biham 2003; Le Petit et al. 2009) and Monte Carlo simulations (Chang et al. 2005; Cuppen & Herbst 2005; Chang et al. 2006). Laboratory experiments have also been conduced and their results modeled (Pirronello et al. 1997a,b, 1999; Katz et al. 1999). It is found to be efficient over a limited range of grain temperatures of about 5−15 K for flat surfaces. However, observations of dense photon dominated regions (PDRs) found efficient formation despite higher grain temperatures (Habart et al. 2004, 2011). Various modifications of the mechanism have been proposed to extend the range of efficient formation. Some authors introduced sites of higher binding energies due to surface irregularities (Chang et al. 2005; Cuppen & Herbst 2005). Some introduced a reaction between chemisorbed atoms and atoms migrating from a physisorption site (Cazaux & Tielens 2004; Iqbal et al. 2012). Others proposed that the Eley-Rideal (ER) mechanism for chemisorbed atoms is a relevant formation process at the edge of PDRs (Duley 1996; Habart et al. 2004; Bachellerie et al. 2009; Le Bourlot et al. 2012). In this mechanism, chemisorbed H atoms, which are attached to the surface by a chemical bond, stay fixed on the surface until another atom of the gas falls into the same site, forming a H_2 molecule.

The grain temperatures in illuminated environments are not only higher but also strongly fluctuating. Small grains have small heat capacities, and each UV-photon absorption makes their temperature fluctuate widely. This effect has received much attention because some components of dust emission are produced during these transient temperature spikes (Desert et al. 1986; Draine & Li 2001; Li & Draine 2001; Compiègne et al. 2011). Those fluctuations are stronger in strong radiation field environments

like PDRs. Moreover, usual dust size distributions favor small grains so that they contribute the most to the total dust surface, making the small grains dominant for surface reactions. Those fluctuations can thus have an important effect on H_2 formation, especially in strongly illuminated environments, as temperature spikes are likely to cause massive desorption. This effect has so far only been studied by Cuppen et al. (2006) using Monte Carlo simulations for the LH mechanism, computing the H_2 formation rate in one single specific diffuse cloud condition under a standard interstellar radiation field. The dependance on the astrophysical parameters was not investigated. Very recently, similar models using the same Monte Carlo method were presented in Iqbal et al. (2014) for silicate surfaces. Those models also included the ER mechanism. The authors remain limited by the prohibitive computation time (several weeks) required by the kinetic Monte Carlo method when including temperature fluctuations. We study here this problem for both ER and LH in a wider range of environments, including PDRs and their high radiation fields, and study the effect induced on cloud structure and observable line intensities by introducing the computation of the fluctuation effect into full cloud simulations.

We propose an analytical approach of the joint fluctuations problem (temperature and surface coverage) based on the master equation, which takes the form of an integral equation. Its numerical resolution incurs a high computational cost, which grows with grain size. In the case of the ER mechanism, the absence of non-linear term in the chemistry allows a decomposition of the two-dimensional full master equation into two one-dimensional equations : a marginal master equation for the temperature fluctuations and an equation on the conditional average population (conditional on T). This makes the numerical computation much more tractable. In the case of the LH mechanism, such simplification is not possible. The computationally heavy full resolution is used to build and verify a fast and accurate approximation of the solution. The final method proposed here allows computation of the total formation rate with a computation time of the order of one minute.

In Sect. 2, we introduce the simple physical model that we use and the exact resolution method. In Sect. 3, approximations of the solution are constructed for both mechanisms. Section 4 presents the results of the numerical computation of the H_2 formation rate using the full method for ER and the approximation for LH. Section 5 then shows how this computed effect affects the structure of the cloud in PDR simulations. Section 6 is our conclusion.

2. The model

2.1. Physical description

We use a simple physical model of H_2 formation on grains to be able to solve the problem of the coupled fluctuations and to obtain an estimate of the importance of dust temperature fluctuations for H_2 formation.

Our system is a spherical grain of radius a, density $\rho_{\rm gr}$, mass $m = \frac{4}{3}\pi a^3 \rho$, and heat capacity $C(T)$. Its thermal state can be equivalently described by its temperature T or by its thermal energy $E = \int_0^T \mathrm{d}T'\, C(T')$ [1]. For polycyclic aromatic hydrocarbons (PAHs), we define the size a as the equivalent size of a sphere of the same mass (see Compiègne et al. 2011).

[1] We neglect energy discretization for the lower states, and adopt the normalization $E = 0$ for $T = 0$. See Li & Draine (2001) for a detailed state-by-state treatment.

We consider two groups of phenomena:

- Interaction with the radiation field through photon absorption and emission, which are both described as discrete events.
- Adsorption of H atoms of the gas onto the surface of the grain and H_2 formation on the surface (physisorption and chemisorption are considered separately, as are the two corresponding H_2 formation mechanisms).

2.1.1. Photon absorption and emission

Under an ambient isotropic radiation field of specific intensity $I_U(U)$ in $\mathrm{W\,m^{-2}\,J^{-1}\,sr^{-1}}$ (in this article, U always denotes a photon energy), the power received by the grain at a certain photon energy U is $P_{\rm abs}(U) = 4\pi^2 a^2 Q_{\rm abs}(U) I_U(U)$, where $Q_{\rm abs}(U)$ is the absorption efficiency coefficient of the grain at energy U. In later parts of the paper, we are interested in transition rates between states of the grain. The rate of photon absorptions at this energy U is simply

$$R_{\rm abs}(U) = \frac{P_{\rm abs}(U)}{U}.$$

We postulate that the grain emits according to a modified black body law with a specific intensity $Q_{\rm abs}(U)\, B_U(U,T)$, where $B_U(U,T)$ is the usual black body specific intensity. The power emitted at energy U is $P_{\rm em}(U,T) = 4\pi^2 a^2\, Q_{\rm abs}(U)\, B_U(U,T)$ and the photon emission rate is

$$R_{\rm em}(U,T) = \frac{P_{\rm em}(U,T)}{U}.$$

These events, which are supposed to occur as Poisson processes, cause fluctuations of the temperature. We treat these fluctuations exactly in Sect. 2.2.

When neglecting these fluctuations, the equilibrium temperature $T_{\rm eq}$ of the grain is defined as balancing the instantaneous emitted and absorbed powers

$$\int_0^{+\infty} \mathrm{d}U\, P_{\rm abs}(U) = \int_0^{E_{\rm grain}} \mathrm{d}U\, P_{\rm em}(U, T_{\rm eq}), \tag{1}$$

where the upper bound on the right hand side accounts for the finite total energy of a grain. This upper cutoff of emission frequencies can become very important for small cold grains, effectively stopping their cooling.

In the following, we use a standard interstellar radiation field (Mathis et al. 1983) and apply a scaling factor χ to the UV component of the field. We measure the UV intensity of those fields using the usual $G_0 = \frac{1}{u_{\rm Habing}} \int_{912\ \text{Å}}^{2400\ \text{Å}} \mathrm{d}\lambda\, u_\lambda(\lambda)$, where $u_{\rm Habing} = 5.3 \times 10^{-15}\,\mathrm{J\,m^{-3}}$.

The dust properties ($C(T)$, $Q_{\rm abs}(U)$ and ρ) are taken from Compiègne et al. (2011). We consider PAHs, amorphous carbon grains, and silicates dust populations and use the properties used in this reference (see references therein, in their Appendix A) for each of those populations.

2.1.2. Surface chemistry via Langmuir-Hinshelwood mechanism

We first consider the physisorption-based LH mechanism. In this mechanism, atoms bind to the grain surface due to Van der Waals interactions, leading to the so-called physisorption. These weakly bound atoms are able to migrate from site

to site. Formation can then occur when two such migrating atoms meet.

Real grain surfaces are irregular, and binding properties vary from site to site due to surface defects. To keep the model simple enough to allow a detailed modeling of temperature fluctuations, we assume identical binding sites uniformly distributed on the grain surface. The number of sites is $N_s = \frac{4\pi a^2}{d_s^2}$, where d_s is the typical distance between sites. We take $d_s = 0.26$ nm as in Le Bourlot et al. (2012). We assume the physisorption sites to be simple potential wells of depth E_{phys} without barrier.

Atoms from a gas at temperature T_{gas} collide with the grain at a rate $k_{coll} = \pi a^2 n(H) v_{th}$, where $v_{th} = \sqrt{\frac{8k T_{gas}}{\pi m_H}}$ is the thermal velocity. We call $s(T_{gas})$ the sticking probability and discuss later our choice for this function. The probability to land on an empty site is $1 - \frac{n}{N_s}$ and the physisorption rate is thus

$$R_{phys} = k_{coll}\, s(T_{gas}) \left(1 - \frac{n}{N_s}\right).$$

We assume that gas atoms falling on an occupied site are never rejected and react with the adsorbed atom to form a H_2 molecule, which is immediately desorbed by the formation energy. This assumption of Eley-Rideal-like reaction for physisorbed atoms is similarly made in the model of Cuppen et al. (2006) with the difference that they do not consider desorption at the formation of the new molecule. This direct Eley-Rideal process is expected to have a large cross section at temperatures relevant to the interstellar medium (Martinazzo & Tantardini 2006), and it is thus a reasonable assumption to assume that it dominates over rejection. To estimate the influence of this assumption on our results, we computed the contribution of this direct ER-like reaction process to the total mean formation rate through physisorption and found it to be a negligible fraction (always less than 1% of the total average formation rate). Despite the very small contribution of this Eley-Rideal-like process to the physisorption-based formation rate in our model, we keep calling the physisorption-based mechanism LH mechanism to distinguish it from the chemisorption-based ER mechanism.

Surface atoms can then evaporate. The adsorbed atoms are assumed to be thermalized at the grain temperature and must overcome the well energy E_{phys}. We take this desorption rate for one atom to be of the form $k_{des}(T) = \nu_0 \exp\left(-\frac{T_{phys}}{T}\right)$, where T is the grain temperature, $T_{phys} = E_{phys}/k$, and ν_0 is a typical vibration frequency taken as $\nu_0 = \frac{1}{\pi}\sqrt{\frac{2E_{phys}}{d_0^2 m_H}}$ with a typical size $d_0 = 0.1$ nm (Hasegawa et al. 1992). The total desorption rate on the grain is then

$$R_{des}(T) = n\, k_{des}(T).$$

To migrate from site to site, an atom must cross a barrier of height E_{migr}. It can do so by thermal hopping or by tunneling for which we use the formula from Le Bourlot et al. (2012). The migration rate for one physisorbed atom is thus

$$k_{migr}(T) = \nu_0 \exp\left(-\frac{T_{migr}}{T}\right) + \frac{\nu_0}{1 + \frac{T_{migr}^2 \sinh^2\left(d_s\sqrt{2m_H k(T_{migr}-T)}/\hbar\right)}{4T(T_{migr}-T)}},$$

where $T_{migr} = E_{migr}/k$.

The main formation process is the meeting of two physisorbed atoms during a migration event. In a simple approximation (see Lohmar & Krug 2006; Lohmar et al. 2009, for a more detailed treatment of the sweeping rate), we take this formation rate to be

$$R_{form}^{(1)}(T) = k_{migr}(T)\,\frac{n^2}{N_s}.$$

We also take direct reaction of a physisorbed atom with a gas atom in an ER-like mechanism into account, with a rate

$$R_{form}^{(2)}(T) = k_{coll}\,\frac{n}{N_s}.$$

This term is only significant for very low dust temperatures (a few K, depending on the collision rate with gas atoms).

We assume immediate desorption of the newly formed molecule because of the high formation energy compared to the binding energy, thus making a similar assumption to recent models (Iqbal et al. 2012; Le Bourlot et al. 2012). Experimental results indicate that a small fraction of the formed molecules may stay on the surface at formation (Katz et al. 1999; Perets et al. 2007). Theoretical studies (Morisset et al. 2004a, 2005) suggest that even when the formed molecule does not desorb immediately at formation, it desorbs after a few picoseconds by interacting with the surface due to its high internal energy. It is thus equivalent to immediate desorption compared to the timescales of the other events.

If the temperature fluctuations are neglected, an equilibrium surface population can be computed using the equilibrium rate equation $R_{phys} - R_{des}(T) - 2R_{form}^{(1)}(T) - R_{form}^{(2)}(T) = 0$ (the factor of 2 comes from the fact that one formation through migration event reduces the population by two). We find

$$n_{eq}(T) = \frac{\left(1 + s(T_{gas})\right)k_{coll}}{4\,k_{mig}(T)}\left(1 + \frac{N_s\, k_{des}(T)}{k_{coll}(1 + s(T_{gas}))}\right) \times \left[\sqrt{1 + \frac{8N_s\, k_{mig}(T)\, s(T_{gas})}{k_{coll}(1 + s(T_{gas}))^2}\,\frac{1}{\left(1 + \frac{N_s\, k_{des}(T)}{k_{coll}(1+s(T_{gas}))}\right)^2}} - 1\right], \quad (2)$$

and the corresponding equilibrium formation rate on one grain at temperature T is

$$r_{H_2}^{eq}(T) = k_{migr}(T)\frac{[n_{eq}(T)]^2}{N_s} + k_{coll}\frac{n_{eq}(T)}{N_s}. \quad (3)$$

Once again this expression is not valid for a fluctuating temperature and the full calculation is described in the next Sect. 2.2.

For the binding and migration energies, we use the values given in Table 1 associated to different substrates.

Many different expressions of the sticking coefficient have been given in the literature. For simplicity, we use the same

Table 1. Model parameters for physisorption.

Dust component	T_{phys} (K)	T_{migr} (K)	References	d_s (nm)
Amorphous carbon	658.0	510.6	1	0.26
Amorphous silicate	510.0	406.0	2	0.26
Ices	350.0	100.0	3	0.26

Notes. T_{phys} is the physisorption binding energy and T_{migr} the migration barrier. d_s is the distance between sites.

References. (1) Katz et al. (1999); (2) Perets et al. (2007); (3) Hasegawa et al. (1992).

sticking probability for the physisorption-based LH mechanism and the chemisorption-based ER mechanism, except for the additional presence of a barrier in the ER case. We use the expression from Le Bourlot et al. (2012):

$$s(T_{\rm gas}) = \frac{1}{1+\left(\frac{T_{\rm gas}}{T_2}\right)^{\beta}}$$

using $T_2 = 464$ K and $\beta = 1.5$, which gives results close to the expression of Sternberg & Dalgarno (1995).

We also simply assume an equipartition of the formation energy among the kinetic energy of the newly formed molecule, its excitation energy, and the heating of the grain.

The total volumic H_2 formation rate is often parametrized as $R_{H_2} = R_f\, n_H\, n(H)$ to factor out the dependency to the atomic H abundance n(H) and to the dust abundance, which is proportional to the total proton density n_H, coming from the collision rate between gas H atoms and dust grains. The standard value of R_f is 3×10^{-17}cm^3 s^{-1}. We also use the formation efficiency defined for one grain as $\frac{2\,r_{H_2}}{k_{\rm coll}}$, which represents the fraction of the H atoms colliding with the grain that are turned into H_2.

2.1.3. Surface chemistry via Eley-Rideal mechanism

We also consider the chemisorption-based ER mechanism. The H atoms of the gas phase that hit the grain can bind to the surface by a covalent bond after overcoming a repulsive barrier. This process is called chemisorption (see for instance Jeloaica & Sidis 1999). Once chemisorbed, the atoms either evaporate and return to the gas phase, or react if another gas H atom lands on the same adsorption site.

We assume the chemisorption sites to be similarly distributed with the same inter-site distance $d_s = 0.26$ nm. Each site is a potential well of depth $E_{\rm chem}$ and is separated from the free state by a potential barrier of height $E_{\rm barr}$.

The collision rate $k_{\rm coll}$ is the same as in the LH case. However, we have to take the presence of the chemisorption barrier into acount in the sticking coefficient. Following Le Bourlot et al. (2012), we use a sticking probability $s(T_{\rm gas}) = \exp\left(-\frac{E_{\rm barr}}{k\,T_{\rm gas}}\right)\left(1+\left(\frac{T_{\rm gas}}{T_2}\right)^{\beta}\right)^{-1}$, where the second term accounts for rebound of high energy atoms without sticking with $T_{\rm barr} = E_{\rm barr}/k = 300$ K, $T_2 = 464$ K, and $\beta = 1.5$. The energy barrier for chemisorption on perfect graphitic surfaces has been found to be of the order of 0.15−0.2 eV (but adsorption in para-dimer configuration has a much lower barrier of 0.04 eV) (Sha & Jackson 2002; Kerwin & Jackson 2008). As discussed in Le Bourlot et al. (2012), the choice made here of a lower barrier for chemisorption is based on the idea that real grain surfaces are not perfect flat surfaces like graphite, but present a large number of defects. Surface defects are expected to induce a strongly reduced barrier for chemisorption (Ivanovskaya et al. 2010; Casolo et al. 2013). Edge sites on PAHs behave in a similar way (Bonfanti et al. 2011). Moreover, Mennella (2008) found that chemisorption in aliphatic $CH_{2,3}$ groups could also lead to efficient Eley-Rideal formation with a very low chemisorption barrier.

Finally, only atoms arriving on an empty adsorption site stick, corresponding to a probability $1 - \frac{n}{N_s}$, where n is the number of chemisorbed atoms.

The chemisorption rate is thus

$$R_{\rm chem} = k_{\rm coll}\, s(T_{\rm gas}) \left(1 - \frac{n}{N_s}\right).$$

Table 2. Model parameters for chemisorption.

$T_{\rm chem}$ (K)	$T_{\rm barr}$ (K)	d_s (nm)
7000	300	0.26

Notes. $T_{\rm chem}$ is the chemisorption binding energy and $T_{\rm barr}$ the chemisorption barrier. d_s is the distance between sites. See references in the text.

Atoms hitting an occupied site react with the adsorbed atom to form a H_2 molecule. Some theoretical studies show a very small activation barrier of 9.2 meV (Morisset et al. 2004b) for this reaction, but the existence of this barrier is under debate (Rougeau et al. 2011). To stay consistent with the model of Le Bourlot et al. (2012) to which we compare our results in Sect. 5, we neglect this barrier compared to the stronger adsorption barrier. We found that including it in the model reduces the formation efficiency by less than 10% in the range of gas temperatures where the ER mechanism is important compared to the physisorption-based LH mechanism.

As the formation reaction releases 4.5 eV, which is much more than the binding energy, we assume that the new molecule is immediately released in the gas. The formation rate is then

$$R_{\rm form} = k_{\rm coll}\,\frac{n}{N_s}.$$

Last, chemisorbed atoms can evaporate. This effect is usually negligible at typical grain temperatures, but the fluctuating temperatures of small grains can easily make excursions into the domain where evaporation is significant. The adsorbed atoms are supposed to be thermalized at the grain temperature, and must overcome the well energy $E_{\rm chem}$. The desorption process is similar to the LH case, and we take again $k_{\rm des}(T) = \nu_0\, \exp\left(-\frac{T_{\rm chem}}{T}\right)$, where $T_{\rm chem} = E_{\rm chem}/k$, and $\nu_0 = \frac{1}{\pi}\sqrt{\frac{2\,E_{\rm chem}}{d_0^2\, m_H}}$ (with $d_0 = 0.1$ nm). The total desorption rate on the grain is then

$$R_{\rm des}(T) = n\, k_{\rm des}(T).$$

Theoretical studies find the chemisorption energy on graphene to be in the range 0.67−0.9 eV (Sha & Jackson 2002; Lehtinen et al. 2004; Casolo et al. 2009). On small PAHs, Bonfanti et al. (2011) find binding energies in the range 1−3 eV for edge sites and in the range 0.5−1 eV for non edge sites. In this overall range 5800 −35 000 K, we choose a low value of 7000 K to estimate the maximum effect of temperature fluctuations on the ER mechanism.

We sum up the model parameters in Table 2.

When neglecting the fluctuations of the grain temperature, we can calculate the equilibrium surface population $n_{\rm eq}$ using the equilibrium rate equation $R_{\rm chem} - R_{\rm form} - R_{\rm des}(T) = 0$, which gives

$$n_{\rm eq}(T) = N_s\,\frac{s(T_{\rm gas})}{1 + s(T_{\rm gas}) + \frac{N_s\, k_{\rm des}(T)}{k_{\rm coll}}}, \tag{4}$$

and the corresponding equilibrium formation rate on one grain at temperature T is

$$r_{H_2}^{\rm eq}(T) = k_{\rm coll}\,\frac{n_{\rm eq}(T)}{N_s}. \tag{5}$$

However, when temperature fluctuations are taken into account, this equilibrium situation is not valid. The method we use to calculate this effect is described in Sect. 2.2.

The energy liberated from the formation reaction is split between the excitation and kinetic energy of the molecule and the heating of the grain. As in Le Bourlot et al. (2012), we take the results of Sizun et al. (2010) for the ER mechanism : 2.7 eV goes into the excitation energy of the molecule, 0.6 eV into its kinetic energy, and 1 eV is given to the grain.

We must note that the part of the formation energy given to the grain creates another coupling between surface population and grain temperature. This fraction of the formation energy (1 eV) is not completely negligible compared to photon energies. This additional retro-coupling between surface chemistry and temperature is ignored in the statistical calculation presented in this article. However, its effect on the equilibrium situation when neglecting fluctuations is evaluated in Appendix A. It is found to be negligible as the power given to the grain is usually much smaller that the radiative power it receives.

We can again define the formation parameter R_f as $R_{\mathrm{H}_2} = R_\mathrm{f}\, n_\mathrm{H}\, n(\mathrm{H})$ and the formation efficiency for one grain as $\frac{2\, r_{\mathrm{H}_2}}{k_\mathrm{coll}}$.

2.2. Method

To take into account temperature fluctuations, we adopt a statistical point of view, and we describe the statistical properties of the fluctuating variables.

The necessary statistical information on our system is contained in the probability density function (PDF) $f(X)$, giving the probability to find the system in the state X that is defined by the two variables E, the thermal energy of the grain (equivalent to its temperature T), and n, the number of adsorbed H atoms on its surface. The function f is thus the joint PDF in the two variables. As we treat our two formation mechanisms independently, n counts chemisorbed *or* physisorbed atoms depending on which mechanism we are discussing.

The time evolution of this PDF is governed by the master equation:

$$\frac{\mathrm{d}f(X)}{\mathrm{d}t} = \int_\mathrm{states} \mathrm{d}Y\, p_{Y\to X}\, f(Y) - \int_\mathrm{states} \mathrm{d}Y\, p_{X\to Y}\, f(X),$$

where $p_{X\to Y}$ is the transition rate from state X to Y. This equation expresses that the probability of being in a given state varies in time due to the imbalance between the rate of arrivals and the rate of departures. In a stationary situation, the two rates, which we call as the gain and loss rates respectively, must compensate each other.

We are thus looking for a solution to the equation

$$\int_\mathrm{states} \mathrm{d}Y\, p_{Y\to X}\, f(Y) - f(X) \int_\mathrm{states} \mathrm{d}Y\, p_{X\to Y} = 0.$$

Two different kinds of transitions occur: the emission or absorption of a photon, which changes only the thermal energy E of the grain, and the adsorption, desorption, or reaction of hydrogen atoms, which changes only the surface population n. The two variables are only coupled by the transition rates for the chemical events, which depend on the grain temperature. The population fluctuations are thus entirely driven by the temperature fluctuations with no retroactions (as mentioned before we neglect grain heating by the formation process).

As the transition mechanisms modify only one variable at a time, we split each of the gain and loss terms into two parts, respectively for photon processes (affecting only E) and for surface chemical processes (affecting only n),

$$G_E(E,n) + G_n(E,n) - L_E(E,n) - L_n(E,n) = 0, \tag{6}$$

with

$$G_E(E,n) = \int_0^{+\infty} \mathrm{d}E'\, p_{E'\to E}\, f(E',n)$$

$$G_n(E,n) = \sum_{n'=0}^{N_s} p_{n'\to n}(E)\, f(E,n')$$

$$L_E(E,n) = f(E,n) \int_0^{+\infty} \mathrm{d}E'\, p_{E\to E'}$$

$$L_n(E,n) = f(E,n) \sum_{n'=0}^{N_s} p_{n\to n'}(E),$$

where we have simplified the notations for the transition rates as transitions only affect one variable at a time and the transitions affecting E (photon absorptions or emissions) have rates that are independent of n.

We now first show how the thermal energy marginal PDF $f_E(E)$ (or the equivalent temperature PDF $f_T(T)$) can be derived from our formalism, which reduces to equations similar to previous works (Desert et al. 1986; Draine & Li 2001). We then show how the formation rates in the LH case and in the ER case can be derived.

2.2.1. Thermal energy PDF

Summing Eq. (6) over all n values, we obtain

$$f_E(E) \int_{-\infty}^{+\infty} \mathrm{d}E'\, p_{E\to E'} = \int_{-\infty}^{+\infty} \mathrm{d}E'\, p_{E'\to E}\, f_E(E'), \tag{7}$$

where $f_E(E) = \sum_n f(E,n)$ is the marginal PDF for the single variable E. The marginal PDF f_E can easily be converted into a grain temperature PDF f_T through the relationship

$$f_T(T) = f_E(E)\, C(T).$$

We thus obtain an independent master equation for the temperature fluctuations.

Detailing the transition rates in Eq. (7), we can rewrite it as

$$f_E(E) = \frac{\int_0^E \mathrm{d}E' R_\mathrm{abs}(E-E') f_E(E') + \int_E^{+\infty} \mathrm{d}E' R_\mathrm{em}(E'-E, T(E')) f_E(E')}{\int_E^{+\infty} \mathrm{d}E' R_\mathrm{abs}(E'-E) + \int_0^E \mathrm{d}E' R_\mathrm{em}(E-E', T(E))}. \tag{8}$$

This equation is an eigenvector equation for the linear integral operator defined by the right-hand side: $f_E(E) = \mathcal{L}[f_E](E)$. A stationary PDF for the grain thermal energy is a positive and normalized eigenvector of this operator for the eigenvalue 1. The existence and unicity of this eigenvector is proven in Appendix B. Moreover, the other eigenvalues all have real parts that are lower than 1 (see Appendix B). We can thus converge toward the solution by building a sequence $\mathcal{L}^n[f_E]$ (the exponent refers to operator composition) from an initial guess. We solve this equation numerically by choosing an energy grid $\{E_i\}$ and solving for piecewise linear functions on this grid.

2.2.2. Eley-Rideal mechanism

We first present the method for the ER mechanism as the linearity of the chemical rates in n simplifies the problem significantly. We can avoid directly solving the full master equation for the joint PDF in two variables (Eq. (6)).

We are interested in the average ER formation rate

$$\langle R_{\rm form}\rangle = \int_0^{+\infty} {\rm d}E \sum_{n=0}^{N_{\rm s}} f(E,n)\, k_{\rm coll}\, \frac{n}{N_{\rm s}}.$$

Knowing $f_E(E)$, we can rewrite it as:

$$\langle R_{\rm form}\rangle = \int_0^{+\infty} {\rm d}E\, f_E(E)\, k_{\rm coll}\, \frac{\langle n \mid E\rangle}{N_{\rm s}},$$

where $\langle n \mid E\rangle = \sum_{n=0}^{N_{\rm s}} n \frac{f(E,n)}{f_E(E)}$ is the conditional expectation of the surface population at thermal energy E. It is by definition the expected value (or ensemble average) of the surface population of a grain, *knowing that* this grain has thermal energy E. Multiplying Eq. (6) by n and summing over all n values gives the equation governing this quantity $\langle n \mid E\rangle$,

$$\frac{k_{\rm coll}\, s}{M(E)} = \langle n \mid E\rangle - \int_0^{+\infty} {\rm d}E'\, \langle n \mid E'\rangle\, K(E,E'), \tag{9}$$

where

$$M(E) = \int_E^{+\infty} {\rm d}E'\, R_{\rm abs}(E'-E) + \int_0^E {\rm d}E'\, R_{\rm em}(E-E') + \frac{k_{\rm coll}(1+s)}{N_s} + k_{\rm des}(E)$$

and

$$K(E,E') = \begin{cases} \dfrac{f_E(E')\, R_{\rm abs}(E-E')}{f_E(E)\, M(E)} & \text{if} \quad E' \in [0,E] \\ \dfrac{f_E(E')\, R_{\rm em}(E'-E, T(E'))}{f_E(E)\, M(E)} & \text{if} \quad E' > E. \end{cases}$$

After a similar discretization, this is a linear system of equations. However, while being nonsingular, it converges exponentially fast toward a singular system as the grain size a grows, making standard numerical procedures unusable.

To avoid this problem, we rewrite this equation. Multiplying by $M(E) f_E(E)$ and integrating it over E yields

$$k_{\rm coll}\, s = \int_0^{+\infty} {\rm d}E' \left[\frac{k_{\rm coll}(1+s)}{N_s} + k_{\rm des}(E')\right] f_E(E')\, \langle n \mid E'\rangle\,. \tag{10}$$

Dividing again by $M(E)$ and subtracting it from the initial equation gives

$$0 = \langle n \mid E\rangle - \int_0^{+\infty} {\rm d}E'\, \langle n \mid E'\rangle\, K'(E,E'), \tag{11}$$

where $K'(E,E') = K(E,E') + \frac{k_{\rm coll}(1+s)+N_{\rm s}\, k_{\rm des}(E')}{N_{\rm s}\, M(E)}\, f_E(E')$. This is again an eigenvector equation for the eigenvalue 1 of a linear integral operator. After discretization, we numerically compute this eigenvector and use Eq. (10) as a normalization condition. This procedure proved to work on the entire range of relevant grain sizes.

2.2.3. Langmuir-Hinshelwood mechanism

For the LH mechanism, the formation rate contains a quadratic term. When trying to apply a similar method to the LH mechanism, the equivalent of Eq. (11) is then an infinite system of equations on the conditional moments of the population $\langle n \mid E\rangle$, $\left\langle n^2 \mid E\right\rangle$, $\left\langle n^3 \mid E\right\rangle$... We thus directly solve the main master equation (Eq. (6)), despite the computational burden.

Writing explicitly the transition rates in Eq. (6), we get

$$\begin{aligned} 0 = &\int_0^E {\rm d}E'\, R_{\rm abs}(E-E')\, f(E',n) \\ &+ \int_E^{+\infty} {\rm d}E'\, R_{\rm em}(E'-E, T(E'))\, f(E',n) \\ &+ f(E,n-1) k_{\rm coll} s(T_{\rm gas}) \left(1 - \frac{n-1}{N_{\rm s}}\right) \\ &+ f(E,n+1) \left[(n+1)\, k_{\rm des}(T) + k_{\rm coll} \frac{n+1}{N_{\rm s}}\right] \\ &+ f(E,n+2) k_{\rm mig}(T) \frac{(n+2)(n+1)}{N_{\rm s}} \\ &- \left[\int_E^{+\infty} {\rm d}E'\, R_{\rm abs}(E'-E) + \int_0^E {\rm d}E'\, R_{\rm em}(E-E')\right] f(E,n) \\ &- f(E,n) \left[k_{\rm coll} s(T_{\rm gas}) \left(1 - \frac{n}{N_{\rm s}}\right) + n\, k_{\rm des}(T) + k_{\rm coll} \frac{n}{N_{\rm s}} \right. \\ &\left. + k_{\rm mig}(T) \frac{n(n-1)}{N_{\rm s}}\right], \end{aligned} \tag{12}$$

where, as boundary conditions, all expressions $n-1$, $n+1$ and $n+2$ are implicitly taken to be 0 if they become negative or greater than $N_{\rm s}$.

We define the total loss rate as

$$\begin{aligned} Q(E,n) = &\int_E^{+\infty} {\rm d}E'\, R_{\rm abs}(E'-E) + \int_0^E {\rm d}E'\, R_{\rm em}(E-E') \\ &+ k_{\rm coll} s(T_{\rm gas}) \left(1 - \frac{n}{N_{\rm s}}\right) + n\, k_{\rm des}(T) + k_{\rm coll} \frac{n}{N_{\rm s}} \\ &+ k_{\rm mig}(T) \frac{n(n-1)}{N_{\rm s}}, \end{aligned}$$

the integral operator (for photon induced transitions) as

$$\begin{aligned} \mathcal{G}[f](E,n) = &\int_0^E {\rm d}E'\, R_{\rm abs}(E-E')\, f(E',n) \\ &+ \int_E^{+\infty} {\rm d}E'\, R_{\rm em}(E'-E, T(E'))\, f(E',n), \end{aligned}$$

and the discrete jump operator (for chemical transitions) as

$$\begin{aligned} \mathcal{J}[f](E,n) = &f(E,n-1) k_{\rm coll} s(T_{\rm gas}) \left(1 - \frac{n-1}{N_{\rm s}}\right) \\ &+ f(E,n+1) \left[(n+1)\, k_{\rm des}(T) + k_{\rm coll} \frac{n+1}{N_{\rm s}}\right] \\ &+ f(E,n+2) k_{\rm mig}(T) \frac{(n+2)(n+1)}{N_{\rm s}}. \end{aligned}$$

We can then rewrite Eq. (12) in a simplified form as

$$f(E,n) = \frac{1}{Q(E,n)} \left[\mathcal{G}[f](E,n) + \mathcal{J}[f](E,n)\right]. \tag{13}$$

This is an eigenvector equation for the eigenvalue 1, which is formally similar to Eq. (8). For the same reasons as previously, we expect the operator defined by the right hand side to have all its eigenvalues with real parts that are strictly lower than 1, except the eigenvalue 1, which is simple. We can thus find the solution by iterating the application of the operator from an initial guess.

The equation is solved numerically using this iterative procedure. The computation time is found to explode when increasing the grain size a. In addition to the number of possible values of n increasing as a^2, the number of iterations necessary to converge toward the stationary solution is also found to quickly increase with a. Grouping the values of n in bins to reduce the matrix size does not solve the problem, as the reduction of the computation time due to the smaller matrices is found to be balanced by a roughly equivalent increase in the number of iterations necessary to converge to a given stationarity threshold.

We can thus only use this method up to moderate grain sizes (~20 nm with 2 days of computation). In later sections, we see, however, that this is sufficient to observe the range of sizes for which the temperature fluctuations significantly impact the chemistry. In addition, a much quicker yet sufficiently accurate approximation is presented in Sect. 3.

3. Approximations

In this section, we construct fast approximations of the formation rate based on simple physical arguments and compare their results with those of the exact method presented in Sect. 2.2. An approximation is especially necessary for the LH mechanism to avoid the prohibitive computational cost of the exact method. A similar approximation is given for completeness for the ER mechanism. Those methods assume the temperature PDF $f_T(T)$ to be known. It can be computed, for instance, by the method described in Sect. 2.2.1.

3.1. Approximation of the Langmuir-Hinshelwood formation rate

We build our method around an approximation of $\langle n|\,T\rangle$, the average population on the grains that are at a given temperature T. We first write a balance equation for this average population, taking into account both chemical processes (changing only the grain's population), and grains leaving or reaching this temperature T.

We first consider the chemical processes. Those are described in Sect. 2.1.2:

- The grain can gain atoms through adsorption (average rate $k_{\rm ads} = k_{\rm coll} s(T_{\rm gas})\left(1 - \frac{\langle n|T\rangle}{N_{\rm sites}}\right)$).
- The grain can lose atoms through desorption (rate $\langle n|\,T\rangle\, k_{\rm des}(T)$).
- The grain can lose atoms through LH reaction, a term we express later. For now, let us write it as $\left\langle r_{\rm H_2}^{\rm LH}\middle|\,T\right\rangle$. We discuss this term in depth below.
- The grain can lose atoms through direct ER reaction (rate $k_{\rm coll}\frac{\langle n|T\rangle}{N_{\rm sites}}$).

On the other hand, the grain can also leave the temperature T. At equilibrium, the rate at which grains leave the state T is exactly balanced by the rate of arrivals from other states. The net effect on the conditional average $\langle n|\,T\rangle$ can be a loss or a gain depending on whether the average population of the grains arriving from other states is higher or lower than $\langle n|\,T\rangle$. In general, noting $k_{\rm leave}(T)$, the rate at which grains leave the state T, and $\langle n_{\rm arrivals}|\,T\rangle$, the average population on grains arriving in state T, the net gain rate is $k_{\rm leave}(T)\left(\langle n_{\rm arrivals}|\,T\rangle - \langle n|\,T\rangle\right)$.

Up to now, no approximation has been made.

As we expected high temperatures states, where desorption dominates all other processes, to have negligible formation and extremely low average population, we focus our approximation on a low temperature regime.

We want to estimate what fraction of the grains leaving state T will come back bare (or with a negligible population compared to $\langle n|\,T\rangle$). We make the following approximation: grains leaving T to reach the regime where desorption dominates, come back with no population. Fluctuations that do not reach the desorption regime leave the surface population unchanged. We define the temperature $T_{\rm lim}$ that delimits these regimes as the temperature at which the desorption rate for one atom becomes equal to the adsorption rate for the grain (we call $E_{\rm lim}$ the corresponding thermal energy):

$$T_{\rm lim} = \frac{T_{\rm phys}}{\ln\left(\frac{\nu_0}{k_{\rm coll}\, s(T_{\rm gas})}\right)}.$$

We thus define

$$k_{\rm phot}(T) = \int_{\max(E_{\rm lim}-E(T),0)}^{+\infty} {\rm d}U\, R_{\rm abs}(U), \tag{14}$$

the rate at which grains leave state T to reach a temperature above the limit. The net loss rate due to fluctuations is then $k_{\rm phot}(T)\,\langle n|\,T\rangle$.

We have thus obtained a rate equation for the conditional average population at temperature T:

$$k_{\rm coll} s(T_{\rm gas})\left(1 - \frac{\langle n|\,T\rangle}{N_{\rm sites}}\right) = \left(k_{\rm des}(T) + k_{\rm phot}(T)\right)\langle n|\,T\rangle + k_{\rm coll}\frac{\langle n|\,T\rangle}{N_{\rm sites}} + 2\left\langle r_{\rm H_2}^{\rm LH}\middle|\,T\right\rangle. \tag{15}$$

This equation is in closed form if we can express $\left\langle r_{\rm H_2}^{\rm LH}\middle|\,T\right\rangle$ as a function of $\langle n|\,T\rangle$ only. We distinguish the two regimes $\langle n|\,T\rangle > 1$ and $\langle n|\,T\rangle < 1$. From now on, we simplify the notations by noting $s = s(T_{\rm gas})$.

3.1.1. Regime with $\langle n|\,T\rangle > 1$

In this regime, we assume that the discrete nature of the number of surface atoms is negligible and treat this variable as continuous. We then have $\left\langle r_{\rm H_2}^{\rm LH}\middle|\,T\right\rangle = k_{\rm mig}(T)\frac{\langle n^2|T\rangle}{N_{\rm sites}}$. We also know that when $\langle n|\,T\rangle \gg 1$, direct ER reaction is likely to dominate so that a precise determination of the LH reaction rate is not necessary. We thus make the simple approximation $\left\langle n^2\middle|\,T\right\rangle = \langle n|\,T\rangle^2$. Using this approximation in Eq. (15), we then get

$$\langle n|\,T\rangle = \frac{1+s}{4}\frac{k_{\rm coll}}{k_{\rm mig}(T)}\left(1 + \frac{N_{\rm sites}(k_{\rm des}(T)+k_{\rm phot}(T))}{k_{\rm coll}(1+s)}\right) \times\left[\sqrt{1+\frac{8s}{(1+s)^2}\frac{k_{\rm mig}(T)}{k_{\rm coll}}\frac{N_{\rm sites}}{\left(1+\frac{N_{\rm sites}(k_{\rm des}(T)+k_{\rm phot}(T))}{k_{\rm coll}(1+s)}\right)^2}} - 1\right]. \tag{16}$$

If this results becomes smaller than 1, we switch to the other regime.

3.1.2. Regime with $\langle n|\,T\rangle < 1$

In this regime, discretisation effects are very important. Formation is dominated by LH reaction, which can only happen if two atoms are present on the grain at the same time. We use

reasoning that is similar to the modified rate equation approach developed by Garrod (2008).

As the average population is low, we can make the approximation $\langle n|T\rangle \simeq p(n=1\,|\,T)$, where the right hand side is the conditional probability of having one surface atom knowing that the temperature is T. The LH formation rate can then be computed the following way. The formation rate is the rate at which gas atoms fall on a grain that already had one adsorbed atom AND reaction occurs before any other process removes one of the atoms. The first part of the sentence gives a rate

$$k_{\rm coll}\, s\left(1-\frac{1}{N_{\rm sites}}\right) p(n=1\,|\,T) \simeq k_{\rm coll}\, s\left(1-\frac{1}{N_{\rm sites}}\right)\langle n|T\rangle$$

using the previous approximation. Once we have two atoms on the grain, the probability that they react before anything else removes one atom is

$$P=\frac{\frac{2k_{\rm mig}(T)}{N_{\rm sites}}}{\frac{2k_{\rm mig}(T)}{N_{\rm sites}}+\frac{2k_{\rm coll}}{N_{\rm sites}}+2(k_{\rm des}(T)+k_{\rm phot}(T))}.$$

This gives

$$\left\langle r_{\rm H_2}^{\rm LH}\middle|T\right\rangle = \frac{k_{\rm coll}\, s(1-\frac{1}{N_{\rm sites}})}{1+\frac{k_{\rm coll}}{k_{\rm mig}(T)}+\frac{N_{\rm sites}(k_{\rm des}(T)+k_{\rm phot}(T))}{k_{\rm mig}(T)}}\,\langle n|T\rangle\,.$$

We inject this expression in Eq. (15) and finally find the solution for this regime:

$$\langle n|T\rangle = \frac{N_{\rm sites}}{N_{\rm sites}\frac{(k_{\rm des}(T)+k_{\rm phot}(T))}{k_{\rm coll}s}+\frac{1+s}{s}+\frac{2(N_{\rm sites}-1)}{1+\frac{k_{\rm coll}}{k_{\rm mig}(T)}+N_{\rm sites}\frac{k_{\rm des}(T)+k_{\rm phot}(T)}{k_{mig(T)}}}}. \quad (17)$$

3.1.3. Total formation rate

The total formation rate is then computed by integrating over the temperature PDF $f(T)$ and distinguishing the two regimes:

$$\langle r_{\rm H_2}\rangle = \int_0^{T_{\rm switch}} {\rm d}T\, f(T)\left(\frac{k_{\rm coll}}{N_{\rm sites}}\langle n|T\rangle+\frac{k_{\rm mig}(T)}{N_{\rm sites}}\langle n|T\rangle^2\right) + \int_{T_{\rm switch}}^{+\infty}{\rm d}T\, f(T)\,\langle n|T\rangle\left(\frac{k_{\rm coll}}{N_{\rm sites}}+\frac{k_{\rm coll}\, s(1-\frac{1}{N_{\rm sites}})}{1+\frac{k_{\rm coll}+N_{\rm sites}(k_{\rm des}(T)+k_{\rm phot}(T))}{k_{\rm mig}(T)}}\right), \quad (18)$$

where $T_{\rm switch}$ is the temperature at which $\langle n|T\rangle$ becomes <1 ($\langle n|T\rangle > 1$ for $T < T_{\rm switch}$, and $\langle n|T\rangle < 1$ for $T > T_{\rm switch}$).

This approximation is compared to the exact method of Sect. 2.2.3 in Appendix C. It is found to give a very accurate estimate of the total average formation rate (within at most 6%). This approximation is used in all results shown in the following sections as the exact method is not practically usable.

3.2. Approximation of the Eley-Rideal formation rate

A similar approximation can be constructed in the case of the ER mechanism. We again write a rate equation for the conditional average $\langle n|T\rangle$, including a fluctuation loss term. We use the same approximation for this loss term with the limiting temperature being

$$T_{\rm lim}=\frac{T_{\rm chim}}{\ln\left(\frac{\nu_0}{k_{\rm coll}\, s(T_{\rm gas})}\right)},$$

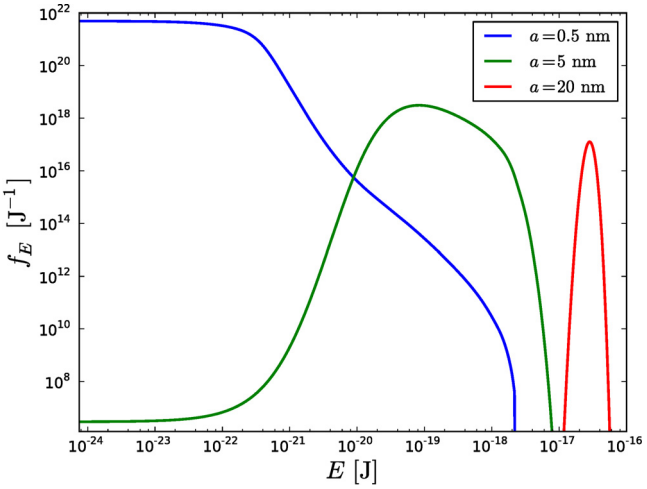

Fig. 1. Dust thermal energy PDFs for three grain sizes (amorphous carbon grains under a radiation field with $G_0 = 120$).

and the loss rate being $k_{\rm phot}(T)\langle n|T\rangle$ with $k_{\rm phot}(T)$ as defined as previously by Eq. (14). The resulting rate equation is then directly obtained in closed form:

$$k_{\rm coll}s(T_{\rm gas})\left(1-\frac{\langle n|T\rangle}{N_{\rm sites}}\right)=\left(k_{\rm des}(T)+k_{\rm phot}(T)\right)\langle n|T\rangle+k_{\rm coll}\frac{\langle n|T\rangle}{N_{\rm sites}},$$

and no further approximation is needed. The solution is

$$\langle n|T\rangle = \frac{s}{1+s}N_{\rm sites}\frac{1}{1+\frac{N_{\rm sites}}{1+s}\left(\frac{k_{\rm des}(T)+k_{\rm phot}(T)}{k_{\rm coll}}\right)},$$

and the average H_2 formation rate can then be computed as

$$\langle r_{\rm H_2}\rangle = \int_0^{+\infty}{\rm d}T\, f(T)\,\frac{k_{\rm coll}}{N_{\rm sites}}\,\langle n|T\rangle\,.$$

A comparison of this method with the exact result is also performed in Appendix C. However, as the exact method is easily tractable, the approximation is not used in the results presented in the rest of this article.

4. Results

The method described in the previous two sections was implemented as a stand alone code called `Fredholm`. The temperature PDF is computed using the exact method of Sect. 2.2.1 and the ER formation rate using the exact method of Sect. 2.2.2, while we use the approximation presented in Sect. 3 for the LH formation rate. This code is now used to study the effect of the temperature fluctuations on the formation rate and the influence of the external conditions (gas conditions and radiation field). We first present a few results on the temperature PDFs before presenting the results on H_2 formation by the ER and LH mechanisms.

4.1. Dust temperature probability density functions and grain emission

The thermal energy PDFs that we compute are shown in Fig. 1, which highlights the change of shape as we go from small grains to bigger grains. For small sizes, most of the grains are in the lowest energy states (the non-zero limit at zero energy can be easily derived from the master equation), while the high energy tail extends very far (the abrupt cut around 2×10^{-18} J is due

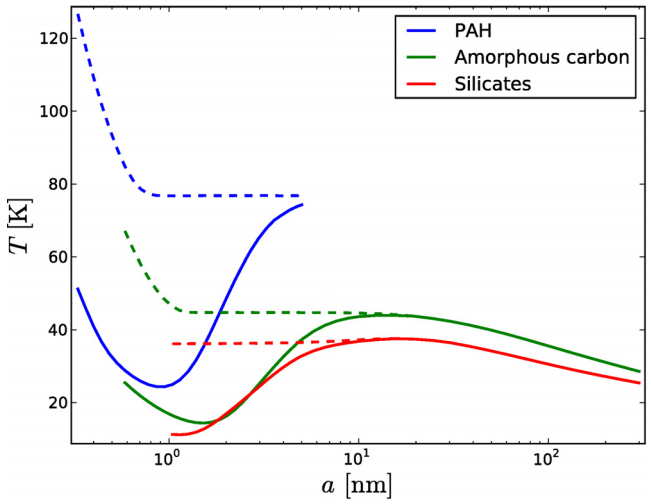

Fig. 2. Equilibrium temperature (dashed line) and actual average temperature (solid line), as a function of the grain size for the three types of grains (radiation field $G_0 = 120$).

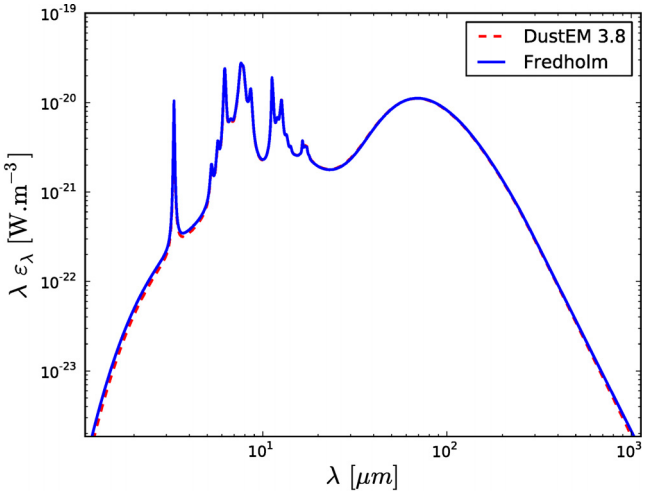

Fig. 3. Local dust emissivity (emitted power per unit of volume) as a function of wavelength for a dust population corresponding to Compiègne et al. (2011) under a radiation field with $G_0 = 100$. We compare our code, Fredholm, with DustEM.

to the Lyman cutoff present in the radiation field). As we go to bigger grains, the fraction of grains in the low energy plateau decreases, and the PDF takes a more peaked form but keeps a clear asymmetry. For the bigger sizes, the PDF becomes very sharp around its maximum and its relative width decreases towards zero, but the shape remains asymmetrical and could be asymptotically log-normal.

As expected, the average temperature converges toward the usual equilibrium temperature at large grain sizes but is significantly lower at small sizes, as shown in Fig. 2. High temperature grains have a much higher contribution to the average energy balance through their high emissivity. Thus, a very low fraction of high temperature grains is sufficient to lower the average temperature of the PDF compared to the equilibrium temperature. The temperature increase at very low grain sizes, which we can see on both the equilibrium and average temperatures, is due to the property that the smallest sizes have decreased cooling efficiency (as they cannot emit photons with higher energies than their own internal energy, their emission spectrum is reduced).

This part of the computation has been done before (Desert et al. 1986; Draine & Li 2001) and especially in the `DustEM` code (see Compiègne et al. 2011) to compute the infrared emission of dust. We checked the results of our code, which is named `Fredholm`, by comparing both the temperature PDFs, and the derived grain emissivity to the public `DustEM` code. We found a good agreement between the results, and despite small differences in the temperature PDFs (due mainly to the continuous cooling approximation in `DustEM`), the final emissivities are extremely close. Figure 3 shows the final comparison on a dust population corresponding to Compiègne et al. (2011) with PAHs, small carbonaceous grains, large carbonaceous grains, and large silicate grains.

4.2. H_2 formation rate: LH mechanism

We apply the approximation method described in Sect. 3 to compute the H_2 formation rate on physisorption sites. The results presented here concern unshielded gas in which the equilibrium rate equation method gives very inefficient LH formation rate due to high dust temperatures (i.e., PDR edges). For results in a more shielded gas, see Sect. 5 describing the coupling with full cloud simulations.

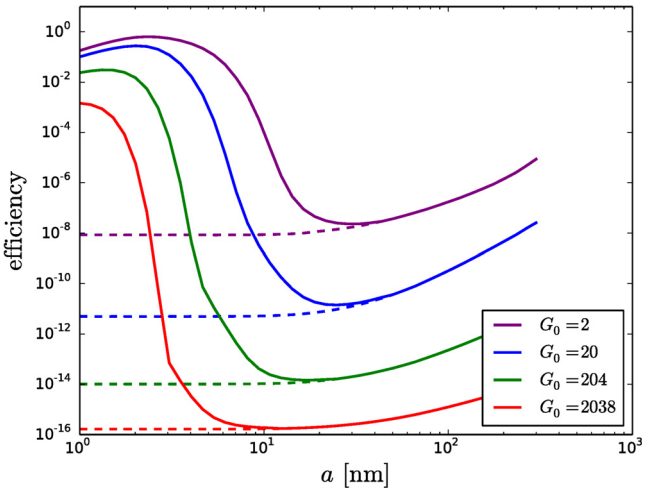

Fig. 4. Formation efficiency (LH mechanism) on one grain (carbonaceous) as a function of size for different radiation field intensities (in a gas at $n_H = 10^4\,cm^{-3}$, $T = 100\,K$). Solid lines: full computation. Dashed line: equilibrium rate equation results. The binding and barrier energies correspond to ices.

The results shown in this section use binding and barrier energies corresponding to either ices or amorphous carbon surfaces (see Table 1) as specified for each figure. Silicates have intermediate values and are thus not shown here. On the other hand, the optical and thermal properties of the grains are those of amorphous carbon grains.

We first show results for ice surfaces. Figure 4 shows the formation efficiency on one carbonaceous grain as a function of the grain size under various radiation field intensities and compares the equilibrium rate equation method with our estimation of the fluctuation effects. The results for small grains are different by several orders of magnitude; the method presented here giving a much more efficient formation. For large grains, the two methods converge as expected.

To understand those differences, we show how the temperature of a 3 nm dust grain is distributed compared to the formation efficiency domain in Fig. 5. We show both the efficiency curve that would be obtained from an equilibrium computation without

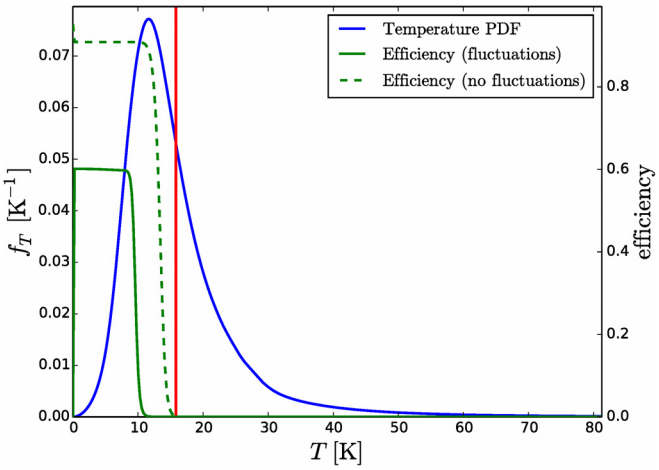

Fig. 5. Temperature PDF (blue line, left axis) for a 3 nm carbonaceous dust grain, as compared to the formation efficiency (LH mechanism) as a function of temperature (green lines, right axis). The red vertical line marks the mean temperature of the blue PDF. The grain receives a G_0 = 20 radiation field and is surrounded by a 100 K gas with $n_{\rm H} = 10^4$ cm^{-3}. The energy values correspond to ices.

fluctuations (dashed line) and the true conditional mean efficiency $\frac{2\langle r_{\rm H_2}|T\rangle}{k_{\rm coll}}$(solid line), for fluctuating grains when they are at the given temperature T. We see two different effects caused by the fluctuations. First, the efficiency domain is reduced in both range and maximum value. This occurs because grains do not stay in the low temperature regime but undergo frequent fluctuations going to the high temperature domain where their surface population evaporates quickly before cooling down. Their average coverage when they are at low temperatures is thus decreased. The amplitude of this effect depends on the competition between the fluctuation timescale and the adsorption timescale.

The other effect comes from the spread of the temperature PDF. While the average temperature of the PDF falls in the low efficiency domain (and the equilibrium temperature, being higher, is even worse), a significant part of the temperature PDF actually falls in the high efficiency domain, resulting in a quite efficient formation as seen in Fig. 4. The grain spends most of its time in the cold states and makes quick excursions into the high temperatures that shift the average toward high temperatures. The resulting formation rate is thus determined by the fraction of the time spent in the high efficiency domain and not by the equilibrium or average temperature of the grain. As described in Sect. 4.1, the smaller the grain, the more asymmetric the temperature PDF with most of the PDF below its average and a long high temperature tail. The smallest grains are thus the most affected, and we see (Fig. 4) that formation on the very small grains is significantly improved even for the highest radiation field intensities. As the radiation field intensity is decreased, larger grains are affected and become efficient. Grains up to 20 nm are affected. We note here that Cuppen et al. (2006) do not consider grains smaller than 5 nm and thus do not include part of the affected range; they, however, find a similar effect from 5 nm to ∼10 nm on their flat surface model.

To evaluate the importance of this effect on the global formation rate, we integrate our formation rate on a MRN-like power law distribution (Mathis et al. 1977) of carbonaceous grains with an extended size range that goes from 1 nm to 0.3 μm (see Table 3) and obtain a volumic formation rate $R_{\rm H_2}$.

Table 3. Parameters of the dust population.

$a_{\rm min}$ (nm)	$a_{\rm max}$ (nm)	β	Dust type
1	300	−3.5	amorphous carbon

Notes. The distribution is a MRN-like power law with exponent β, with grain sizes going from $a_{\rm min}$ to $a_{\rm max}$.

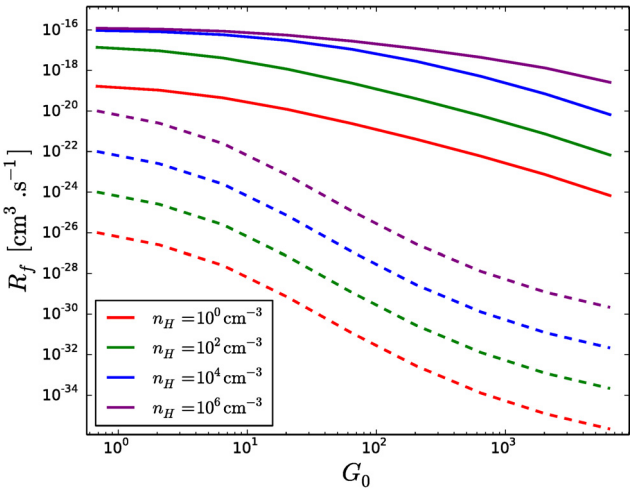

Fig. 6. Integrated formation rate parameter $R_{\rm f}$ (LH mechanism) for a carbonaceous dust population (see Table 3) as a function of the radiation field intensity G_0 for different gas densities (the gas temperature is fixed at 100 K). Solid lines: full computation. Dashed lines: equilibrium rate equation results. Binding and barrier energies corresponding to ices.

As this distribution strongly favors small grains in term of surface, this integrated rate is strongly affected by the effect on small grains. Figure 6 shows this total formation rate as a function of the radiation field intensity for various gas densities (still using ice energy values). We obtain very efficient formation from the LH mechanism in unshielded PDR edge conditions for high gas densities. In all cases, the formation rate is increased by several orders of magnitude compared to the equilibrium computation. As the smallest grains remain efficient even for strong radiation fields, the total formation rate decreases more slowly when increasing the radiation field.

Moreover, we note a difference in the dependency to the gas density. The gas density dependency that comes from the collision rate is already factored out in the definition of the $R_{\rm f}$ parameter shown on this graph. The equilibrium rate equation result is in the low efficiency regime, where the efficiency is determined by the competition between the adsorption rate (proportional to $n_{\rm H}$) and the desorption rate, and is thus proportional to the gas density. The result from the method presented here is mainly determined by the fraction of the time spend in the high efficiency regime. This fraction is fully determined by the photon absorption and emission processes and is independent of the gas density. The final result for high gas densities ($n_{\rm H} > 10^3$ cm^{-3}) is thus largely independent of the gas density. For low densities, the reduction of the conditional average efficiency curve (noted in Fig. 5) becomes dominant. As this effect results from the competition between the fluctuation rate (due to photons) and the adsorption rate (proportional to $n_{\rm H}$), the resulting formation parameter $R_{\rm f}$ becomes proportional again to the gas density for low densities ($n_{\rm H} < 10^3$ cm^{-3}). This change of behavior corresponds to the point where the fluctuation timescale becomes significantly smaller than the adsorption timescale.

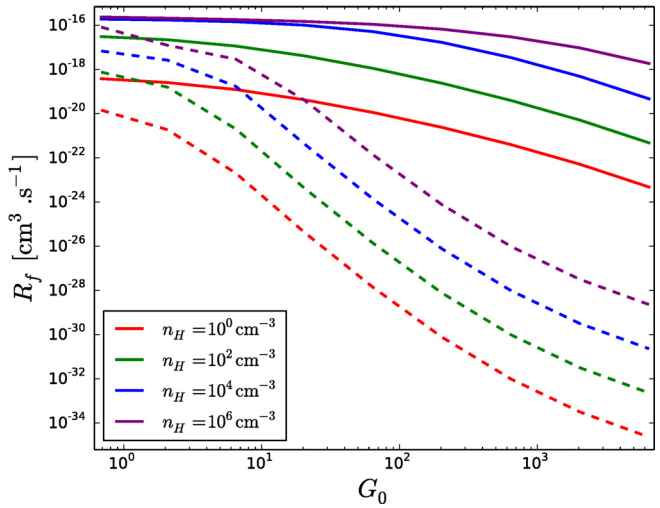

Fig. 7. Same as Fig. 6 with binding and barrier energies corresponding to amorphous carbon surfaces.

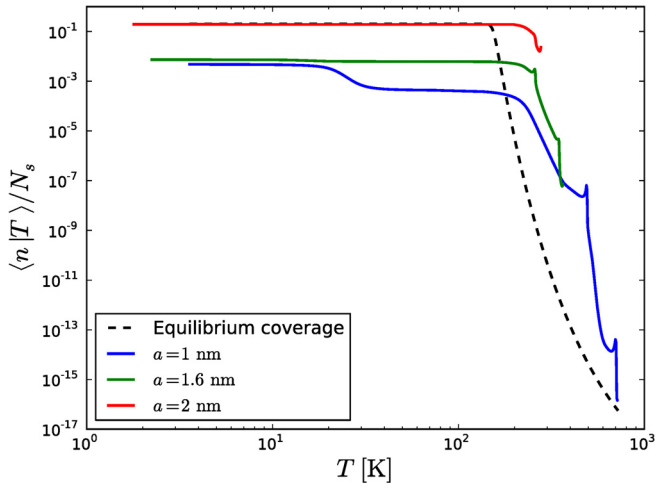

Fig. 8. Conditional mean of the surface coverage (chemisorption only) as a function of grain temperature for three sizes of amorphous carbon grains (solid lines) and equilibrium coverage (dashed line). The grain is surrounded by gas at density $n_{\rm H} = 10^4$ cm^{-3} and temperature $T = 350$ K under a radiation field with $G_0 = 120$.

Figure 7 shows the same result when using binding and barrier energies corresponding to amorphous carbon surfaces. As a consequence of the higher binding energy for amorphous carbon surface, the equilibrium result yields higher formation rates. The increase caused by the fluctuations is thus less dramatic but remains very large for strong radiation fields.

We can already note here that the formation rates obtained in those unshielded PDR edge conditions are comparable to the typical value of 3×10^{-17} cm^3 s^{-1}. The LH and the ER mechanisms thus become of comparable importance in PDR edges for high densities, as seen in the results of full cloud simulations shown in Sect. 5.

4.3. H_2 formation rate: ER mechanism

The first step in our computation of the formation rate is the conditional mean of the surface population knowing the grain temperature. We show this quantity (as a fraction of the total number of sites) in Fig. 8, as compared to the coverage fraction for a grain at equilibrium at constant temperature (this equilibrium coverage fraction is independent of the grain size). As expected, the equilibrium coverage shows a plateau as long as the desorption rate is negligible compared to the adsorption rate. This plateau is lower than unity as the sticking is less than unity. Then the equilibrium coverage decreases as desorption becomes dominant. The dynamical effect of the temperature fluctuations has a consequence that the actual average populations are not at equilibrium. The grains undergoing a fluctuation to high temperature arrive in their new state with their previous population and then go through a transient desorption phase, which lasts a certain time, thus increasing the average population at the high temperatures compared to the equilibrium. When cooling down back to the low temperature states, re-accretion of their population takes some time, and this effect lowers the average population at low temperatures. Because this lowering effect is important, as seen in Fig. 8, it means that the characteristic time between two temperature spikes is sufficiently short compared to the adsorption timescale. The mechanism at play is thus that grains that go to high temperatures lose their population but then cool down faster than they re-adsorb their surface population and do not spend enough time in the low temperature state before the next fluctuation to have regained their equilibrium population. Of course, as the fluctuations are less dramatic for bigger grains (as a given photon energy makes a smaller temperature change: a Lyman photon at 912 Å brings a 1 nm grain to ~500 K but a 2 nm grain to only ~200 K), the effect disappears for larger grains, as seen in Fig. 8.

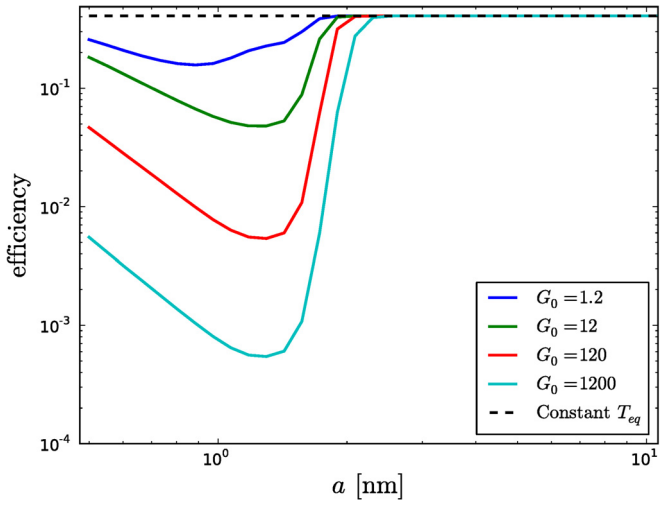

Fig. 9. H_2 formation efficiency (ER mechanism) as a function of grain size for various radiation fields (carbonaceous grains in a gas at $n_{\rm H} = 10^4$ cm^{-3} and $T = 350$ K).

The formation rate on one grain is then simply $r_{\rm H_2} = \int_0^{+\infty} {\rm d}T\, f_T(T)\, k_{\rm coll} \frac{\langle n|T\rangle}{N_s}$. The resulting formation efficiency on one grain is shown in Fig. 9 as a function of grain size.

As explained above, the smaller grains have a lower coverage than equilibrium due to temperature fluctuations and, thus, a decreased formation rate. Only grains below 2 nm are affected, as the same photon absorption causes a smaller temperature fluctuation for bigger grains. For stronger radiation fields, fluctuations occur with a shorter timescale, leaving less time for the surface population to reach equilibrium. The effect is then stronger and extends to higher sizes.

The affected range seems very small, but we have to remember that usual dust size distributions are such that the small grains represent most of the surface (e.g., the MRN

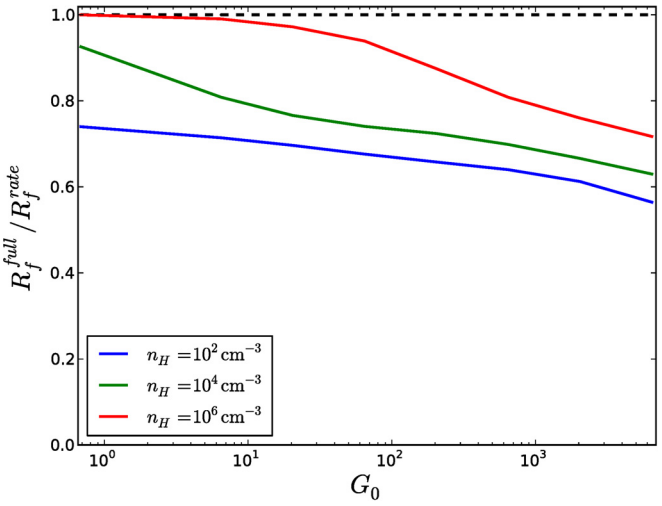

Fig. 10. Integrated formation rate R_f (ER mechanism) over a full dust size distribution (see Table 3) as a fraction of the equilibrium rate equation result. The result is shown for three different gas densities (thus changing the collision rate) as a function of the radiation field intensity.

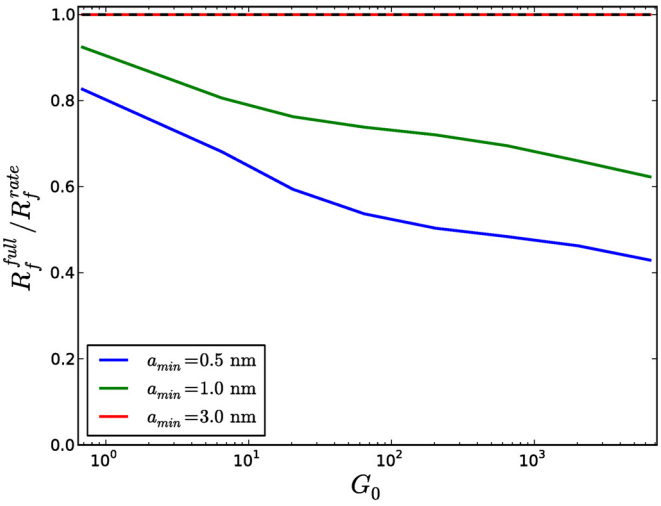

Fig. 11. Integrated formation rate ratio (ER mechanism) over a full dust size distribution, as a function of the radiation field intensity when changing the inferior limit of the grain size distribution ($n_\mathrm{H} = 10^4\,\mathrm{cm}^{-3}$).

distribution). Thus, the contribution from the smallest grain sizes dominates the global formation rate. By integrating over the dust size distribution (same as in Sect. 4.2), we obtain the volumic formation rate in the gas, which we can express as $R_{\mathrm{H}_2} = R_\mathrm{f}\, n(H)\, n_\mathrm{H}$ defining R_f. In the following, we compare the integrated formation rate that we obtain to the one obtained with the rate equation at constant temperature as used in Le Bourlot et al. (2012) and plot our results as a fraction of this reference formation rate.

The two main parameters are the radiation field intensity and the H atom collision rate (and the sticking coefficient, which modifies the effective collision rate). We use standard interstellar radiation fields with a scaling factor as explained in Sect. 2.1.1.

Figure 10 shows the effect of these two parameters. We show the formation rate as a function of the radiation field intensity for different gas densities to probe the effect of the collision rate. Note that the reference rate equation result at constant temperature does not depend on either of these parameters: the density dependency (from the collision rate) is eliminated in the definition of R_f, and the radiation field has no effect when the fluctuations are neglected (the equilibrium temperature is too low to trigger desorption). The effect we show is thus fully the effect of grain temperature fluctuations. As expected, the formation rate decreases when either the radiation intensity is increased or the collision rate is decreased, as the effect results from a competition between the fluctuation rate and the collision rate. The observed reduction remains limited and reaches a ~40% reduction or lower in the range of parameters that we explore. The result that an effect affecting only a tiny fraction of the range of grain sizes can have a significant effect on the integrated formation rate illustrates how the smallest sizes dominate the chemistry in the usual MRN size distribution.

The choice of the lower limit of this size distribution is thus of crucial importance. The lower this minimal size, the larger the usual equilibrium rate equation formation rate will be, as the total dust surface is increased for a constant total dust mass. However, as we lower this limit, we extend the range affected by the fluctuations, and thus obtain a stronger decrease compared to the rate equation result, as shown in Fig. 11. We observe no effect if the size distribution starts above the affected size (e.g., for $a_\mathrm{min} = 3$ nm), while a lower limit causes a stronger effect (up to ~60% with $a_\mathrm{min} = 0.5$ nm).

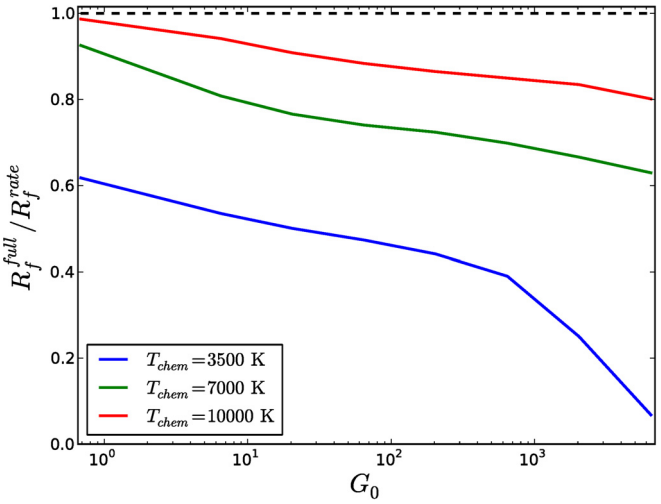

Fig. 12. Integrated formation rate ratio (ER mechanism) over a full dust size distribution, as a function of the radiation field intensity for different chemisorption binding energies ($n_\mathrm{H} = 10^4\,\mathrm{cm}^{-3}$).

Last, as noted in Sect. 2.1.3, the microphysical parameters of the adsorption process are not well known. The adsorption barrier affects the sticking and changes the effective collision rate (see Fig. 10 for the effect of the collision rate). The vibration frequency ν_0 has a negligible effect in the range of reasonable values. The most important microphysical parameter is the chemisorption energy T_chem. Figure 12 shows the strong influence of this parameter on the result. A lower chemisorption energy allows for smaller fluctuations to trigger desorption. Bigger grains are thus affected, resulting in a much lower formation rate (e.g., a reduction of more than 90% for $T_\mathrm{chem} = 3500$ K).

5. Integration into the Meudon PDR code

We now investigate the effects of the changes in the formation rate found in the previous section on the overall structure and chemistry of an interstellar cloud with special attention to the observable line intensities.

Our code `Fredholm`, which computes the H_2 formation rate from the LH and ER mechanisms as described in Sects. 2 and 3, has been coupled to the Meudon PDR code described in Le Petit et al. (2006).

The Meudon PDR code models stationary interstellar clouds in a 1D geometry with a full treatment of the radiative transfer (including absorption and emission by both gas and dust), thermal balance, and chemical equilibrium done in a self-consistent way. In its standard settings, the formation of H_2 on dust grains is treated using rate equations and including both the LH and ER mechanism, as described in Le Bourlot et al. (2012). We have now enabled the possibility to compute the H_2 formation rate using our code `Fredholm` from the gas conditions and the radiation field sent by the PDR code at each position in the cloud, thus taking temperature fluctuations into account. We compare the results of those coupled runs with the simpler rate equation treatment. The dust population in the PDR models presented here is a single component following a MRN-like power-law distribution from 1 nm to 0.3 μm with an exponent of −3.5, using properties corresponding to a 70−30% mix of graphites and silicates above 3 nm and a progressive transition to PAH properties from 3 nm to 1 nm.

A direct comparison between the rate equation approximation and a full account of stochastic effects is thus possible. In addition to the radiation field illuminating the front side of the cloud, whose strength is indicated for each model, the back side of the cloud is always illuminated by a standard interstellar radiation field ($G_0 = 1$) in the following models.

5.1. Detailed analysis

5.1.1. Effects on PDR edges

We focus first on the effects on PDR edges, as the main effects of a change in formation rate come from the shift of the H/H_2 transition that is induced. We have seen in Sect. 4 that the full treatment of fluctuations reduces the efficiency of the ER mechanism while strongly increasing the efficiency of the LH mechanism (compared to a rate equation treatment). The resulting effect in full cloud models depends on the relative importance of the two mechanisms.

For low radiation field models, the full treatment increases the LH mechanism at the edge to a level comparable or even higher than the ER mechanism, as shown in Fig. 13. The LH formation rate is increased by more than one order of magnitude and becomes higher than the ER rate, while it was one order of magnitude below in the standard rate equation model. The net result is an increase of the total formation rate by a factor of 4. While we were expecting the ER mechanism to be slightly decreased by the full treatment, we can note that it is slightly increased here. This is due to the gas temperature sensitivity of the ER mechanism. In this low radiation field model, the heating of the gas due to H_2 formation is not negligible compared to the usually dominant photoelectric effect. A higher total H_2 formation rate increases the heating of the gas resulting in a higher temperature at the edge (see Fig. 14). The ER mechanism is thus made slightly more efficient.

The main effect is a shift of the H/H_2 transition from $A_V = 4{\times}10^{-2}$ to $A_V = 8{\times}10^{-3}$, as shown of Fig. 15. As a result, the column density of excited H_2 is increased, as shown in Table 4. As we are in low excitation conditions, the effect is mainly visible on the levels $v = 0$, $J = 2$ and $v = 0$, $J = 3$.

We also note a significant increase of the H_2 abundance before the transition, which results in increased CH^+ formation at

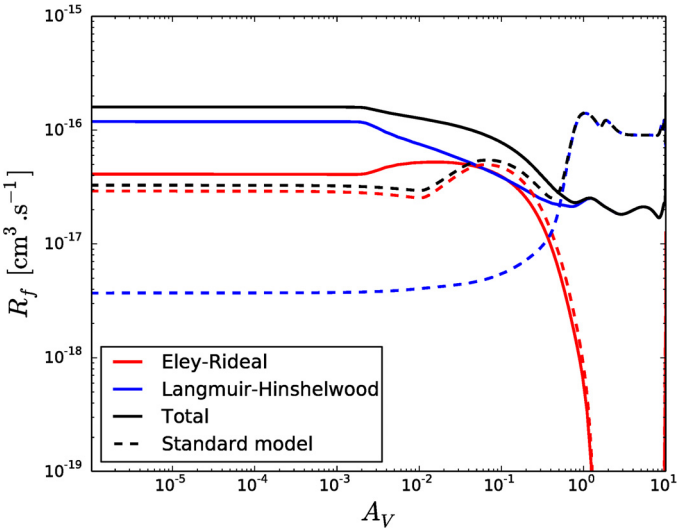

Fig. 13. H_2 formation parameter R_f (full treatment: solid lines, standard treatment: dashed lines) for the two processes in a cloud with $n_H = 10^3$ cm^{-3} and $G_0 = 10$.

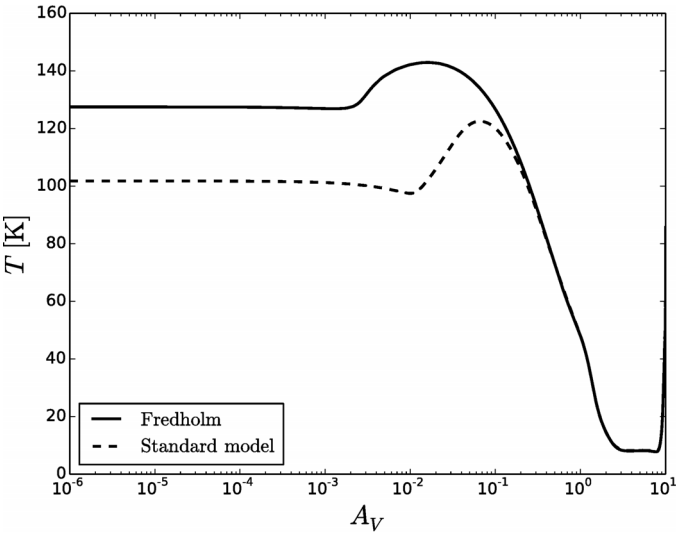

Fig. 14. Gas temperature (same cloud as Fig. 13).

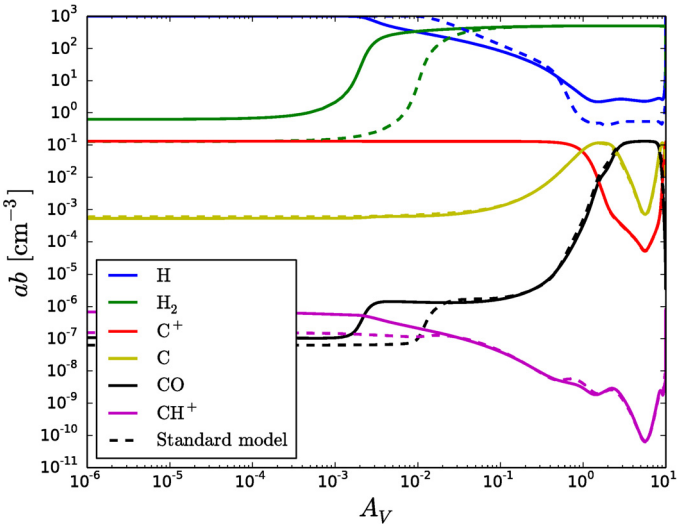

Fig. 15. Abundances of the species of interest in the same cloud as Fig. 13.

Table 4. H_2 intensities in the same cloud as Fig. 13.

	Integrated intensity W m^{-2} sr^{-1}	
H_2 line	Standard model	Full treatment
(0−0) S(0)	8.14×10^{-10}	1.06×10^{-9}
(0−0) S(1)	6.40×10^{-11}	1.56×10^{-10}
(0−0) S(2)	3.74×10^{-11}	4.37×10^{-11}
(0−0) S(3)	3.53×10^{-11}	4.21×10^{-11}
(0−0) S(4)	1.88×10^{-11}	2.15×10^{-11}
(0−0) S(5)	3.28×10^{-11}	3.72×10^{-11}
(1−0) S(1)	4.40×10^{-11}	5.72×10^{-11}

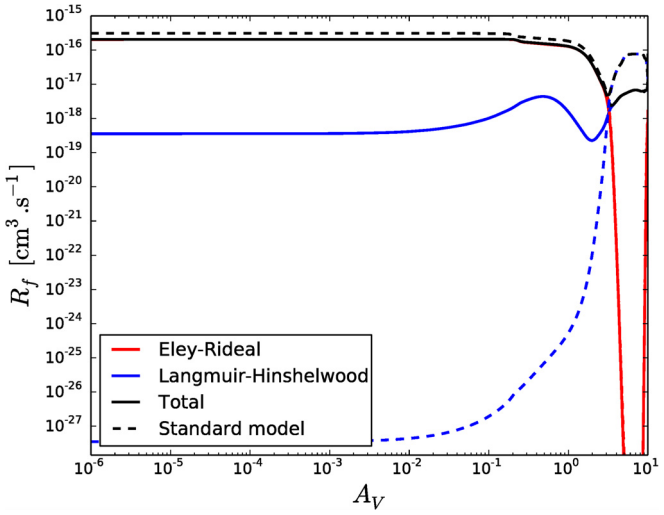

Fig. 16. Same as Fig. 13 for a cloud with $n_H = 10^3$ cm^{-3} and $G_0 = 10^3$.

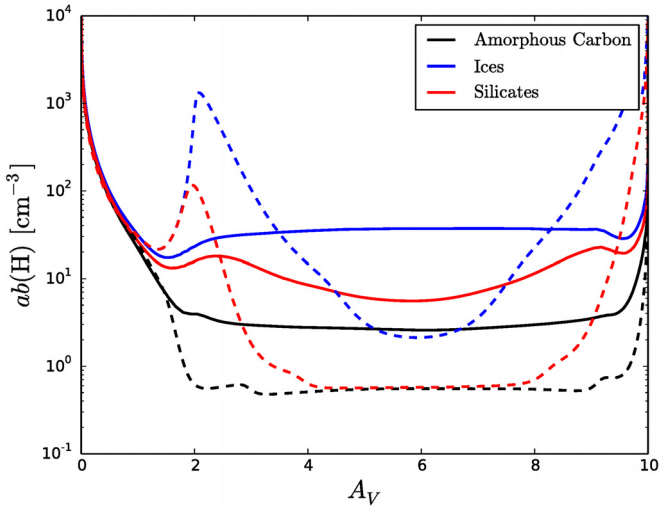

Fig. 17. Atomic H abundance in a cloud with $n_H = 10^4$ cm^{-3} and $G_0 = 10^2$. Comparison of rate equations results (dashed lines) with our full treatment (solid lines).

the edge. This effect and the higher temperature at the edge result in stronger excited lines of CH^+ with differences of a factor of 2 on line (4−3). The excitation temperature computed from the observed intensities above (4−3) closely follow the change in gas temperature at the edge. The increase in intensity thus becomes larger as we go to larger levels, but those intensities remain most probably unobservable in this case.

The situation is different for high radiation field PDRs. The increase in the efficiency of the LH mechanism at the edge is not

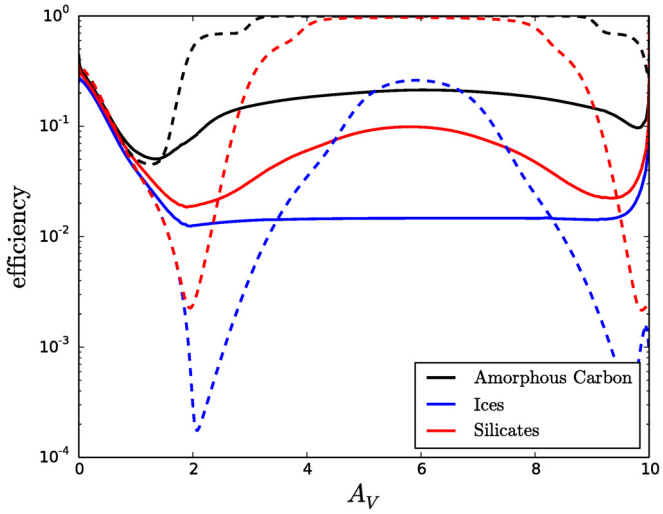

Fig. 18. H_2 formation efficiency. Same case as Fig. 17.

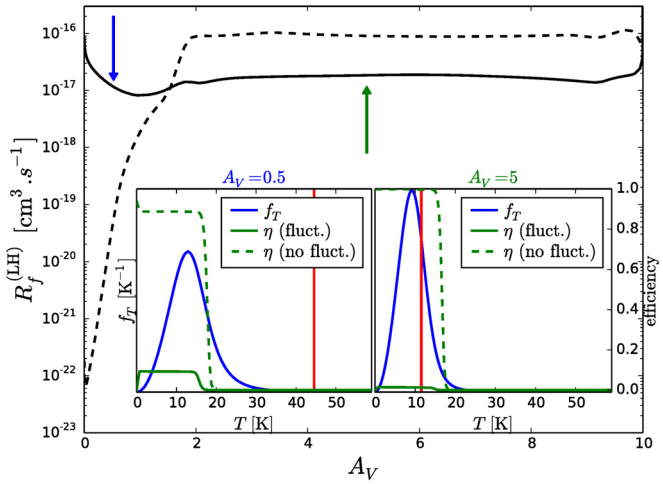

Fig. 19. Same cloud as Fig. 17, with formation parameter R_f for the LH mechanism, comparing standard (dashed black) and coupled (solid black) models. The *insets* show the effect of fluctuations on a 1 nm grain at the two positions in the cloud marked by the arrows. Blue: temperature PDF, red: equilibrium temperature, dashed green: equilibrium efficiency, and solid green: conditional efficiency with fluctuations. See the text for more details.

sufficient to make it comparable to the ER mechanism and the net result is a decrease of the total formation rate as the ER efficiency is reduced (see Fig. 16). This results in inverse effects with the H/H_2 transition slightly shifted away from the edge, but of smaller amplitude as the formation rate difference is much smaller.

We present a wider investigation of the effects on observable intensities in Sect. 5.2, covering a large domain of cloud conditions.

5.1.2. Effects on cloud cores

Unexpectedly, temperature fluctuations of small dust grains are found to have an effect on H_2 formation even in cloud cores where the UV field has been fully extinguished. As an example, Fig. 17 shows the atomic hydrogen abundance in a specific cloud ($n_H = 10^4$ cm^{-3}, $\chi = 100$, total $A_V = 10$) and compares the standard models to the coupled models with full treatment of the fluctuations for the different binding energy

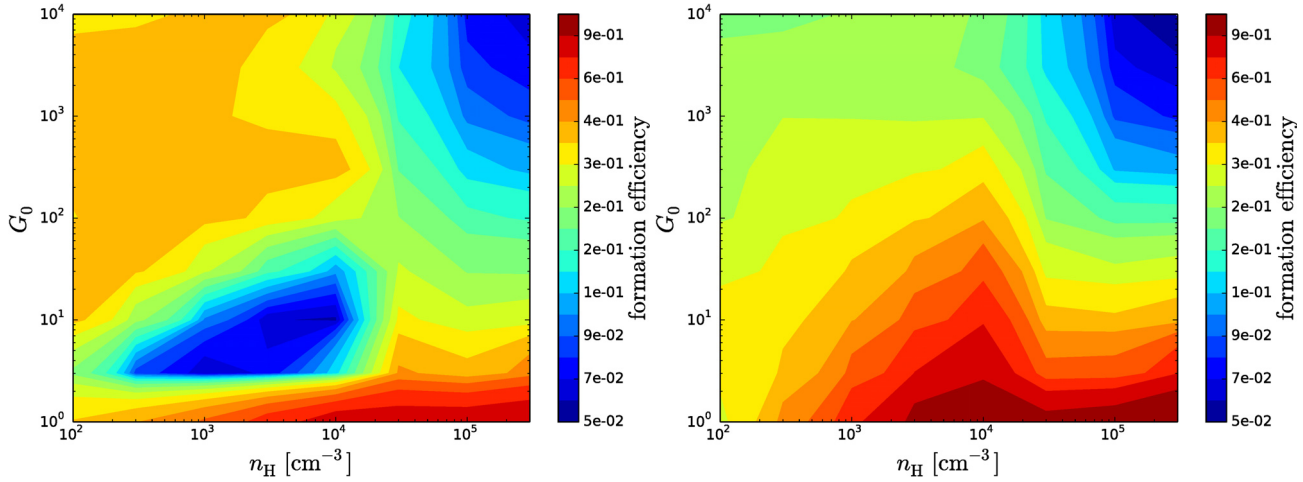

Fig. 20. H_2 formation efficiency at the edge of the cloud as a function of the gas density $n_{\rm H}$ and the radiation field intensity G_0. The standard models (*left*) are compared with the full coupled models (*right*).

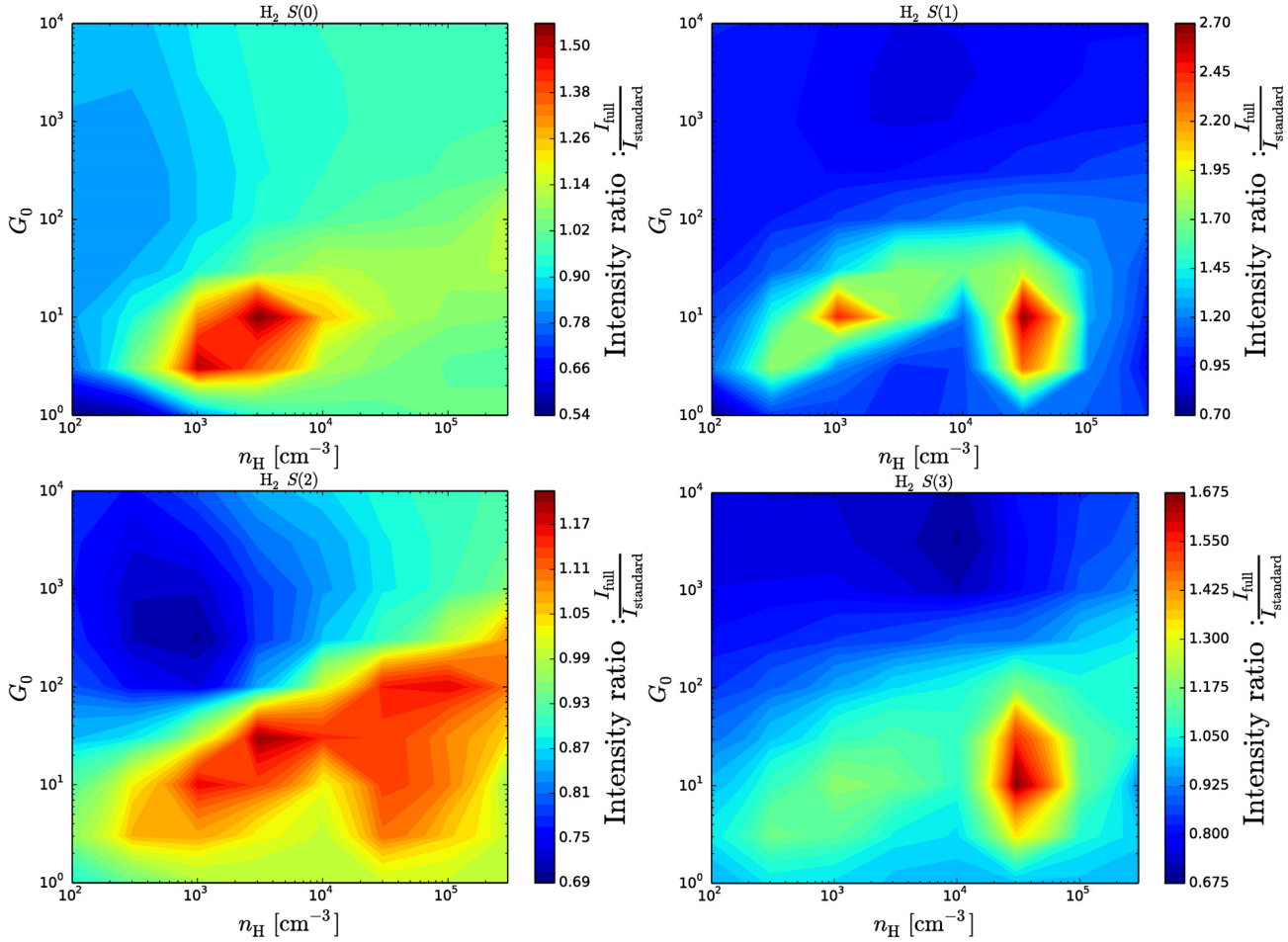

Fig. 21. Effect on H_2 rotational lines intensities $S(0)$ to $S(3)$, shown as a comparison between the full computation result and the standard PDR result (neglecting dust temperature fluctuations). Parameters are the gas density $n_{\rm H}$ and the scaling factor of the radiation field G_0.

values of Table 1. The residual atomic H abundance in the core is found to be systematically higher when taking the fluctuations into account, which is a direct consequence of a lower formation efficiency (the efficiencies are shown for the same models in Fig. 18). We recall that the formation efficiency is defined as the ratio between the formation rate and half the collision rate between H atoms and grains (whose expression is $k_{\rm max} = \frac{1}{2} v_{\rm th}({\rm H}) \frac{S_{\rm gr} n_{\rm H}}{4} n({\rm H})$), as this rate is the maximum formation rate that would occur if one molecule was formed every two collisions. We also notice that standard models tend to show a strong variability of the formation efficiency (and consequently of the H abundance) with a gap around $A_V = 2$ with very low efficiency, where neither the ER mechanism (the gas is not warm enough) nor the LH mechanism (the grains are too warm) are efficient. This variability disappears in the coupled models as fluctuations make the LH mechanism much less dependent

on the grain equilibrium temperature (see Sect. 4.2), and the efficiency stays of the order of 10% (for amorphous carbon surfaces) across the cloud.

The formation efficiency at the center of the cloud is decreased by almost one order of magnitude when including the fluctuations. This unexpected effect is detailed in Fig. 19 for amorphous carbon surfaces: the formation parameter R_f for the LH mechanism is shown for the standard model (black dashed line) and the coupled model (black solid line), and two inset plots show the effect of fluctuations on a 1 nm grain at two positions ($A_V = 0.5$ and $A_V = 5$, marked, respectively, by the blue and green vertical arrows on the main plot). Each inset contains a plot similar to Fig. 5, displaying the temperature PDF (blue line), the equilibrium temperature (red line), the equilibrium efficiency curve (dashed green line), and the effective conditional efficiency curve when taking fluctuations into account (solid green line).

Close to the edge of the cloud (at $A_V = 0.5$), the situation is similar to the discussion of Fig. 5 (see Sect. 4.2). The main effect occurs because the temperature PDF has an important part inside the efficiency domain, while the equilibrium temperature is out of this domain. It results in increased efficiency. The dangers of using the equilibrium temperature are strikingly emphasized on this figure: when allowing fluctuations, a very small fraction of high temperature grains is sufficient to radiate away all the absorbed energy and most of the grains can be cold, while the grains must all be warm enough to balance the absorbed energy if we force them all to have a single temperature.

Deeper in the cloud (at $A_V = 5$), the situation is different: the equilibrium temperature now falls close to the actual peak of the PDF and inside the efficiency domain, so that the actual position and spread of the PDF does not change the result much. The dominant effect is now that the conditional efficiency with fluctuations is strongly reduced compared to the equilibrium efficiency. As discussed in Sect. 4.2, this reduction comes from the competition between the fluctuation timescale and the adsorption timescale. At this optical depth, the grains are mainly heated by IR photons emitted by the hot dust at the edge, and for 1 nm grains, the IR photons are sufficient to bring the grains temporarily out of the efficiency domain (above 18 K here) where they lose their surface population. On the other hand, adsorption of H atoms are extremely rare, as the gas is almost completely molecular. As a result, the grain rarely manages to have two atoms on its surface, and the formation efficiency is thus reduced.

The effect described here concern very small grains, and one might question the presence of such very small grains and PAHs deep in the cloud core (the grain population is independent of position in our model). However, secondary UV photons, which were not considered for grain heating in these models, could induce a similar effect for much bigger grains, and further reduce the formation efficiency at high optical depth inside the cloud. This mechanism tends to increase the residual atomic H fraction in the core and could be relevant in explaining the slightly higher than expected atomic H abundances deduced from observations of HI self-absorption in dark clouds (e.g., Li & Goldsmith 2003).

No detectable effects on intensities were found in these models but the inclusion of secondary UV photons may induce stronger effects.

5.2. Grid of models

A grid of constant density PDR models was run to check the effect on observable intensities over a wider parameter range. We explore gas densities from $n_H = 10^2$ cm^{-3} to $n_H = 3 \times 10^5$ cm^{-3} and scaling factors on the standard ISRF (Mathis et al. 1983) from 1 to 10^4 (as explained previously, the scaling factor only affects the UV part of the radiation field).

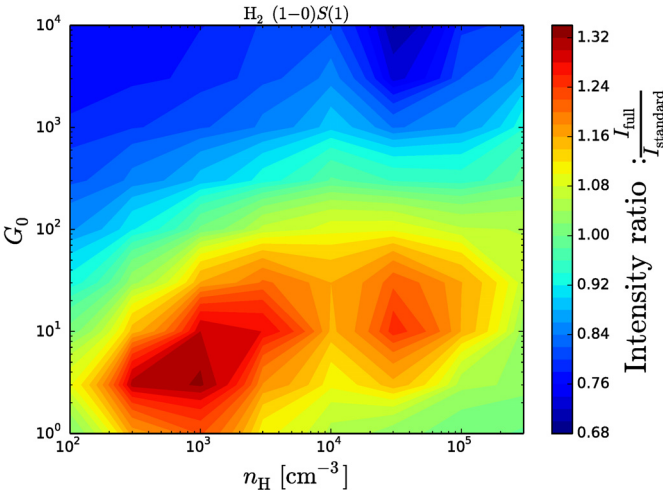

Fig. 22. Effect on H_2 ro-vibrational line intensity $(1-0)S(1)$, shown as a comparison between the full computation result and the standard PDR result (neglecting dust temperature fluctuations). Parameters are the gas density n_H and the scaling factor of the radiation field G_0.

The effects of the fluctuations are mostly found on tracers of the PDR edges. The formation efficiency at the edge of the cloud is shown as a color map in Fig. 20, which compares the standard models with the full models including fluctuations. In the upper part of the map, the ER formation is decreased, and the LH mechanism remains negligible, resulting in an overall (small) decrease in efficiency. In the lower part, the LH mechanism is not negligible anymore, and its strong increase due to fluctuations results in an overall increase in efficiency. The region around $G_0 = 10$ and $n_H = 10^3$–10^4cm^{-3} is strikingly affected. In this region, the ER mechanism stops being efficient due to the low gas temperature at the edge. In standard models, the equilibrium temperature of the dust at the edge is still too high for the LH mechanism to work, giving a very low total formation efficiency. When taking into account fluctuations, the LH mechanism works efficiently, assuring a high formation efficiency. The effect is further amplified as gas heating by H_2 formation is dominant in this region. The efficient LH formation heats up the gas, thus keeping ER formation efficient as well.

Figure 21 shows the modification of the H_2 lower rotational intensities as the ratio between the result of the full computation, which includes dust temperature fluctuations, and the result of a standard PDR model. Higher rotational lines are affected very similarly to the $S(3)$ line. Figure 22 shows the effect on the ro-vibrationnal line $(1-0)S(1)$ in the same way. As expected from our discussion of Fig. 20, we see increased intensities for low radiation fields (roughly $G_0 < 200$), especially in regions where the gas temperature is highly sensitive on H_2 formation heating and where LH formation can further trigger an amplification of ER formation. For higher radiation fields, the intensities are slightly decreased. The effect remains small, the increase for low radiation field models is at most a factor of 2.7 (on the $S(1)$ line), and the decrease on the high radiation field models is at most 30%.

Another species affected by the more efficient formation of H_2 at the edge is CH^+. It is formed by the reaction of $C^+ + H_2$, which is allowed by the high gas temperature at the edge of the PDR and by the internal energy of the H_2 molecule, as described

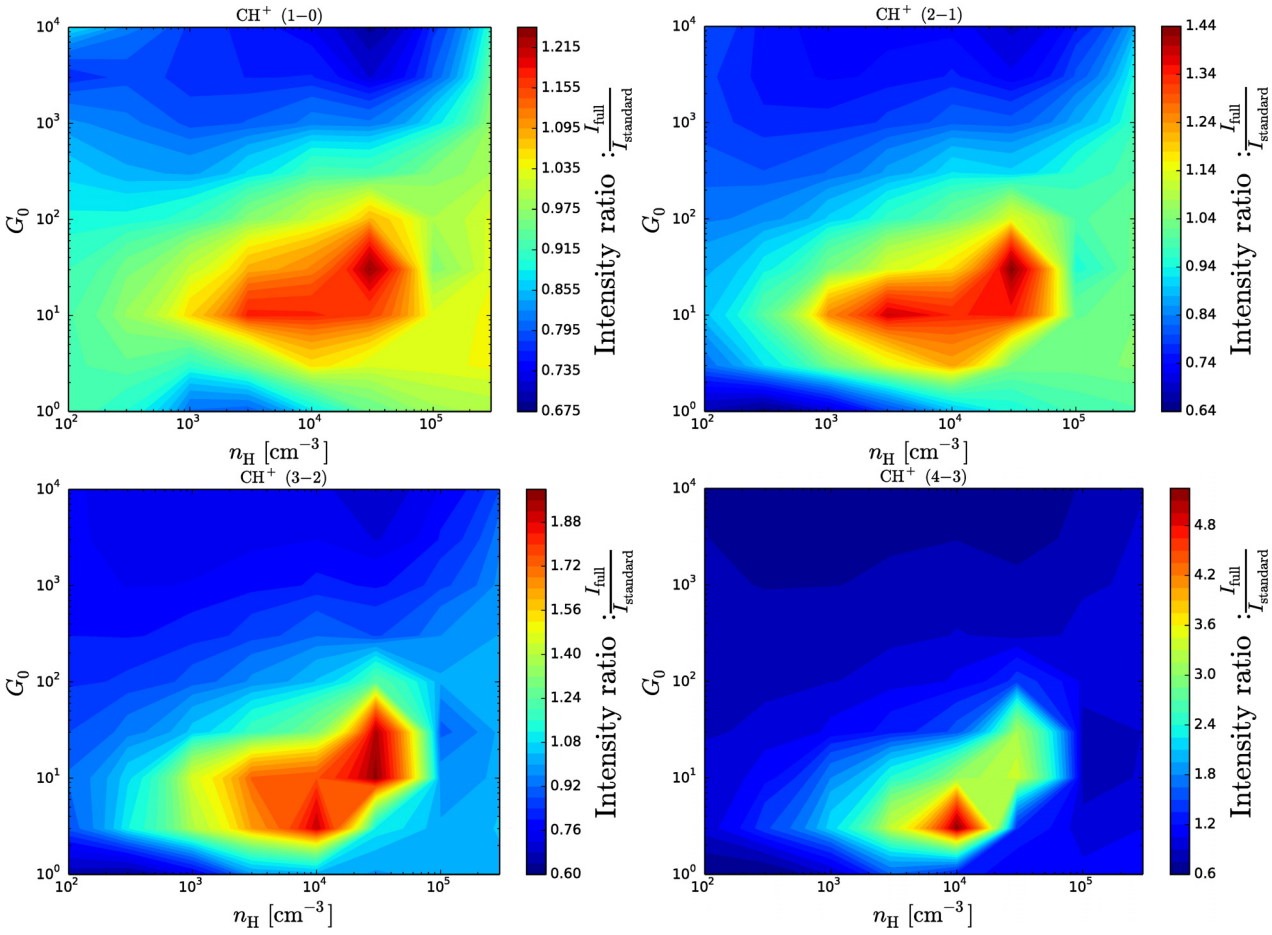

Fig. 23. Effect on CH^+ line intensities, shown as a comparison between the full computation result and the standard PDR result (neglecting dust temperature fluctuations). Parameters are the gas density n_H and the scaling factor of the radiation field G_0.

in Agúndez et al. (2010) (pumped by UV photons and by its formation process). A higher H_2 formation rate at the edge induces a higher H_2 fraction before the transition, which leads to a higher CH^+ formation rate. Gas heating by H_2 formation can further enhance its formation. Figure 23 shows the effect on CH^+ intensities. We again observe increased emission in the domain where the H_2 formation efficiency is enhanced, due to both higher abundances of CH^+ and higher gas temperatures. The domain of strong enhancement is quite similar to the one for H_2 rotational lines, corresponding to the domain where gas heating is dominated by H_2 formation heating. This temperature effect is visible on all high excitation lines emitted before the H/H_2 transition (e.g., the most excited lines of HCO^+, CS, HCN, ...).

6. Conclusion and perspectives

We presented a method to compute H_2 formation on dust grains taking fully the fluctuating temperature of the grain for both the ER and the LH mechanism into account.

As a side result of this work, we revisited the computation of dust temperature fluctuations. We confirm that the continuous cooling approximation (e.g., used in DustEM) is sufficient for an accurate computation of the mid- and near-infrared spectrum. However, the detailed treatment of surface processes requires a better estimation of the low temperature part of the dust temperature PDF, which is done in this paper by including the discrete nature of photon emission.

The coupled fluctuations problem was solved exactly for both the ER and the LH mechanisms. A numerically efficient way of computing the ER formation rate was found. The effect on the ER formation rate is limited to a factor of 2, and the effect on full cloud simulations is limited. The standard rate equation treatment of this ER mechanism is thus a good treatment for the purpose of complete PDR simulations.

With the exact solution for the LH mechanism being numerically intractable for big grains, we constructed an approximation based on simple physical arguments to compute the fluctuation effect on the LH mechanism and checked for small grains that the approximation yields accurate results. The effect is strong as fluctuating grains spend a significant part of their time in the low temperature range, in which formation is efficient, even when their average temperature is out of the rate equation efficiency domain. This results in a strong increase in LH formation efficiency in unshielded environments where the average dust temperature is high and only fluctuations can allow LH formation.

The LH mechanism is found to become of comparable importance with the ER mechanism at the edge of PDRs, except for strong radiation fields. The resulting increase of H_2 formation rate at the edge induces a shift in the H/H_2 transition toward the edge of the PDR. The resulting effect on observable lines emitted in this region remains limited and does not reach one order of magnitude in the strongest cases.

On the contrary, fluctuations of the smallest grains caused by IR photons reduce the formation efficiency by almost one order of magnitude in the core of the clouds, as collisions with H atoms in a completely molecular gas are much rarer than absorption of

IR photons heating temporarily the grain above 18 K. No significant effects are found on intensities, but including secondary UV photons could induce stronger effects.

Overall, the variations induced in observational intensities are comparable to what can be expected from many other poorly known parameters. The interpretation of observations with standard PDR codes, thus, need not use the detailed treatment analyzed here and a simple rate coefficient approximation can be used most of the time. However, this cannot be blindly extended to any arbitrary process and must be checked in each specific case. In particular, the existence of temperature fluctuations of the smallest grains deep inside the cloud should be taken into account for other surface chemical processes. Possible consequences on the abundance of light organic molecules are currently being investigated.

Acknowledgements. This work was funded by grant ANR-09-BLAN-0231-01 from the French Agence Nationale de la Recherche as part of the SCHISM project. We thank Laurent Verstraete for fruitful discussions on dust properties, and Evelyne Roueff for many discussions. We thank our referee for his useful comments.

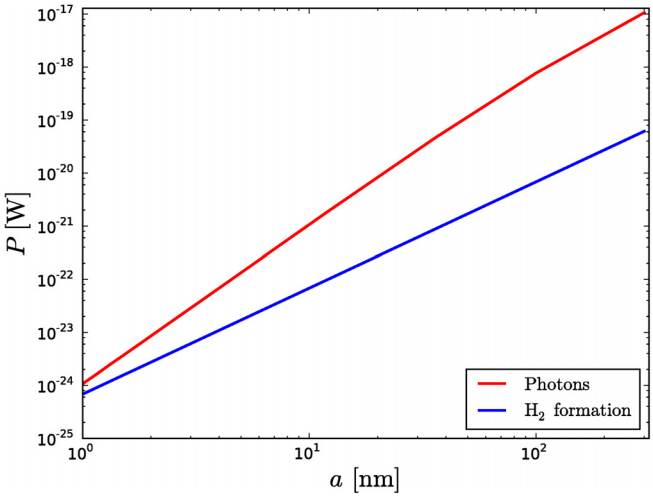

Fig. A.1. Heating power received by a grain as a function of grain size. Power received from photons in red and H_2 formation in blue.

Appendix A: Effect of H_2 formation energy on the equilibrium rate equation calculation

We first consider the heating of the grain by the Eley-Rideal mechanism. Each formation reaction gives 1 eV to the grain.

The liberation of energy left in the grain by each formation reaction creates an additional coupling between the surface population and the grain temperature. The method described in Sect. 2.2.2, which was based on a one-way coupling between the two variables, is thus not possible here.

To evaluate this effect, we use the standard equilibrium temperature equation and chemical rate equation with a coupling term representing the heating of the grain by the formation reaction. We assume that each formation reaction gives an energy $E_{f_{H_2}} = 1$ eV to the grain, which is instantly converted into thermal energy.

For ER formation on chemisorption sites, we thus have the system of equations:

$$n_{eq}(T_{eq}) = N_s \frac{s(T_{gas})}{1 + s(T_{gas}) + \frac{N_s\, k_{des}(T_{eq})}{k_{coll}}},$$

$$\int_0^{+\infty} \mathrm{d}U\, P_{abs}(U) + E_{f_{H_2}}\, k_{coll}\, \frac{n_{eq}(T_{eq})}{N} = \int_0^{E_{grain}} \mathrm{d}U\, P_{em}(U, T_{eq}),$$

which can be easily solved. However, we find that the effect of this average heating of the grain by formation reactions is completely negligible in the range of realistic values of parameters, resulting in a change of the grain temperature by less than 1%.

Independently of the detail of the formation mechanism, we can put an upper limit on the heating term caused by H_2 formation by assuming that all H atoms hitting the grain are turned into H_2. In this case, the formation rate is simply $\frac{1}{2}k_{coll}$, and the heating power is $\frac{1}{2}k_{coll}E_{f_{H_2}}$. We can then compare this term to the absorbed power coming from photons.

The result is shown here in Fig. A.1 in an extreme case with a low radiation field ($G_0 = 1$) and a high collision rate (atomic gas with $n = 10^3\,\mathrm{cm}^{-3}$ and $T = 350\,\mathrm{K}$). Despite assuming a total formation efficiency in a low radiation field, high collision rate environment, we can see that the heating term due to H_2 formation becomes barely significant only for the smallest grain sizes. We can thus safely neglect the grain heating coming from H_2 formation (through the ER mechanism, and all the more for the LH mechanism as the $E_{f_{H_2}}$ is probably much lower as physisorbed atoms are much more weakly bound) in most usual conditions. Moreover, under a radiation field with $G_0 = 1$, the gas would not be as warm as we assumed here and the ER efficiency would be very low.

Appendix B: Eigenvalues of the integral operator for the thermal energy PDF

The operator $\mathcal{L}$ defined in equation 8 can be rewritten as

$$\mathcal{L}[f](E) = \int_0^{+\infty} \mathrm{d}E'\, A(E, E')\, f(E')$$

with

$$A(E, E') = \begin{cases} \dfrac{R_{abs}(E - E')}{P(E)} & \text{if} \quad E' < E \\ \dfrac{R_{em}(E' - E, T(E'))}{P(E)} & \text{if} \quad E' \geq E, \end{cases}$$

where

$$P(E) = \int_0^{E} \mathrm{d}E'\, R_{em}(E - E', T(E)) + \int_E^{+\infty} \mathrm{d}E'\, R_{abs}(E' - E)\cdot$$

The existence of a solution to our problem is equivalent to the existence of a positive eigenfunction associated with the eigenvalue 1.

This operator is continuous, compact, and strongly positive. The Krein-Rutman theorem (see Du 2006, Chap. 1) tells us that its spectral radius is a simple eigenvalue associated with a positive eigenfunction and that this eigenfunction is the only positive eigenfunction.

We first show that 1 is an eigenvalue of the adjoint operator $\mathcal{L}^*[f](E) = \int_0^{+\infty} \mathrm{d}E'\, A(E', E)\, f(E')$ and that it is associated with a positive eigenfunction. We can easily find such a positive

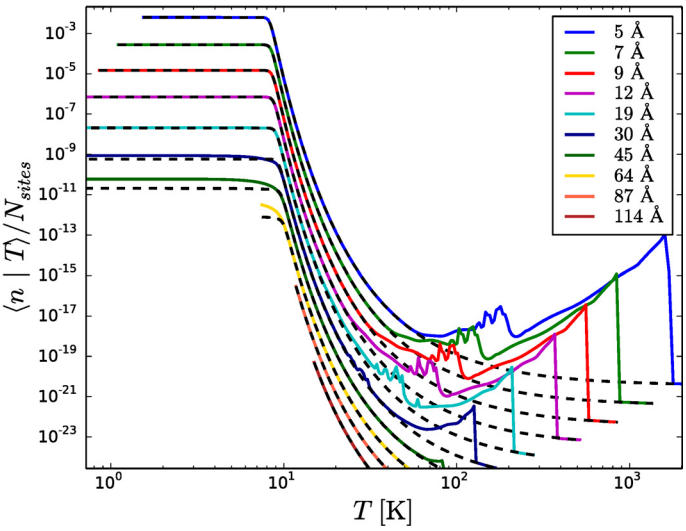

Fig. C.1. Approximated $\langle n|T\rangle$ (dashed lines) for the LH mechanism compared to the exact results (solid lines). Model with gas density $n = 10^3$ cm^{-3} and $G_0 = 20$ with barrier and binding energies for ices. For clarity, each successive curve has been shifted by a factor of ten.

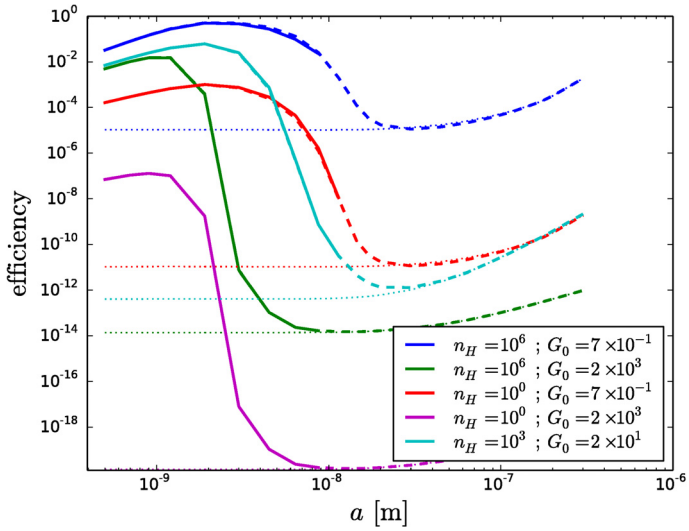

Fig. C.2. Approximated LH formation efficiency for one grain (dashed lines) compared to the exact results (solid lines). The formation efficiencies at the constant equilibrium temperatures are shown in dotted lines. The densities are given in cm^{-3}. The binding and barrier energies correspond to ices.

eigenfunction with the eigenvalue 1 for this adjoint operator:

$$\begin{aligned}\mathcal{L}^*[\mathrm{P}](\mathrm{E}) &= \int_0^{+\infty} \mathrm{d}E'\, A(E',E)\, P(E') \\ &= \int_0^{E} \mathrm{d}E' \frac{R_{\mathrm{em}}(E-E',T(E))}{P(E')} P(E') \\ &+ \int_E^{+\infty} \mathrm{d}E' \frac{R_{\mathrm{abs}}(E'-E)}{P(E')} P(E') \\ &= P(E),\end{aligned}$$

and P(E) is a positive function. Thus, 1 is the spectral radius of $\mathcal{L}^*$ and hence of $\mathcal{L}$. This proves the existence and the unicity of the solution to our problem. Moreover, it proves that all the other eigenvalues λ are such that $|\lambda| \leq 1$ and thus $Re(\lambda) < 1$. We can therefore iterate the application of the operator to an initial function and converge toward the solution, assuming that the initial function is not orthogonal to the solution. Starting with a positive initial function is sufficient.

Appendix C: Verification of the approximations

In this appendix, we evaluate the accuracy of our approximations by comparing their results to those of the exact methods presented in Sect. 2.2.

C.1. LH mechanism

For the LH mechanism, the exact method (cf. Sect. 2.2.3) is only tractable for a limited range of grain sizes. We compare the approximation (cf. Sect. 3.1) with it on this range and verify that the approximation joins the equilibrium result for bigger grains.

Figure C.1 shows the resulting curves for $\langle n|T\rangle$ for different grain sizes and compares the approximation to the exact result. The binding and barrier energies are taken for ice surfaces in Table 1. We see a very good match for small grains in the low temperature domain. Large discrepancies appear at high temperature but do not matter for the average formation rate on the grain as the contribution of this regime is negligible. For bigger grains, the approximation of the low temperature regime starts to be less accurate. However, we know that total formation rate is mostly influenced by the smallest grain sizes due to the −3.5 exponent of the size distribution.

Table C.1. Approximation error on the final formation rate integrated over the full size distribution for the LH mechanism.

Surface type :	Ices		amC	
$a_{\min}$ =	0.5 nm	1 nm	0.5 nm	1 nm
Model :				
$n = 1$, $G_0 = 0.7$	1.64%	2.10%	2.95%	4.44%
$n = 1$, $G_0 = 2 \times 10^3$	0.53%	0.45%	0.32%	0.02%
$n = 1 \times 10^6$, $G_0 = 0.7$	6.09%	6.65%	1.18%	1.13%
$n = 1 \times 10^6$, $G_0 = 2 \times 10^3$	1.46%	1.82%	1.52%	1.85%
$n = 1 \times 10^3$, $G_0 = 2 \times 10^1$	0.35%	0.50%	3.68%	4.95%

The resulting formation rate per grain is shown in Fig. C.2 as a function of grain size for 5 models spanning the parameter domain. We again assumed here an ice surface. The match is very good on the domain on which the exact computation could be performed, and the approximation smoothly joins with the equilibrium result neglecting fluctuations for big grains. The relative errors on the final formation rate integrated over the size distribution are given for each model in the first part of Table C.1. The results are given for two size distributions. Both are MRN-like power-law distributions with exponent −3.5, but one starts at 5 Å and the other at 1 nm. Both go up to 0.3 μm. We find extremely accurate results for the approximation in most case with a relative error at most around 5%.

When using the energy values corresponding to an amorphous carbon surface (see Table 1), the same levels of accuracy are achieved. The formation rate as a function of grain size is shown in Fig. C.3. When integrated over the size distribution, the formation rate obtained from the approximation is again within 5% from exact result (see second part of Table C.1).

C.2. ER mechanism

We now perform the same verification for the ER mechanism. The approximation of Sect. 3.2 is compared to the exact method

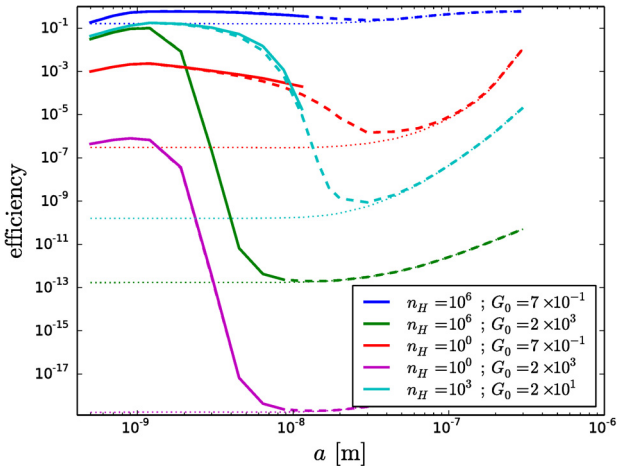

Fig. C.3. Same as Fig. C.2 for binding and barrier energies corresponding to amorphous carbon grains.

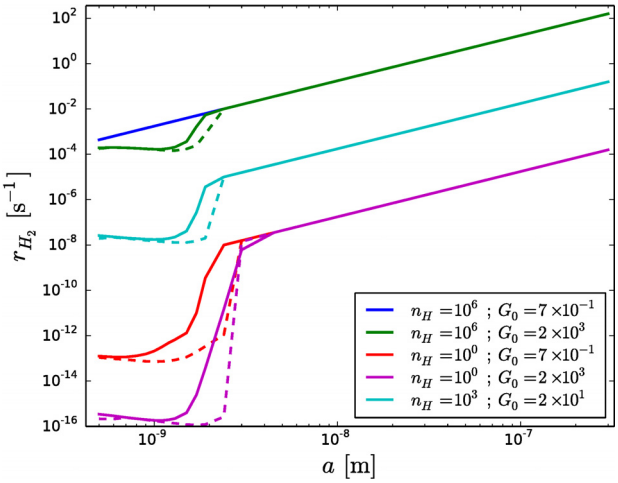

Fig. C.4. Approximated ER formation rate for one grain (dashed lines) compared to the exact results (solid lines). The densities are given in cm^{-3}.

Table C.2. Approximation error on the final formation rate integrated over the full size distribution for the ER mechanism.

$a_{\min}$ =	0.5 nm	1 nm
Model :		
$n = 1$, $G_0 = 0.7$	0.0028%	0%
$n = 1$, $G_0 = 2 \times 10^3$	8.19%	8.73%
$n = 1 \times 10^6$, $G_0 = 0.7$	12.08%	12.08%
$n = 1 \times 10^6$, $G_0 = 2 \times 10^3$	10.22%	10.22%
$n = 1 \times 10^3$, $G_0 = 2 \times 10^1$	6.26%	6.15%

of Sect. 2.2.2. Figure C.4 shows the formation rate as a function of grain size. The qualitative effect is captured by the approximation, but large discrepancies appear locally for some sizes, due to a shifted transition from a low efficiency regime to a high efficiency one. However, the results when integrating over the dust size distribution remain reasonably accurate, as shown in Table C.2. We recall that this approximation is not used in this paper as the exact method is numerically efficient.

References

Agúndez, M., Goicoechea, J. R., Cernicharo, J., Faure, A., & Roueff, E. 2010, ApJ, 713, 662
Bachellerie, D., Sizun, M., Aguillon, F., et al. 2009, Phys. Chem. Chem. Phys., 11, 2715
Biham, O., & Lipshtat, A. 2002, Phys. Rev. E, 66, 056103
Bonfanti, M., Casolo, S., Tantardini, G. F., Ponti, A., & Martinazzo, R. 2011, J. Chem. Phys., 135, 164701
Casolo, S., Løvvik, O. M., Martinazzo, R., & Tantardini, G. F. 2009, J. Chem. Phys., 130, 054704
Casolo, S., Tantardini, G. F., & Martinazzo, R. 2013, Proc. Nat. Acad. Sci., 110, 6674
Cazaux, S., & Tielens, A. G. G. M. 2004, ApJ, 604, 222
Chang, Q., Cuppen, H. M., & Herbst, E. 2005, A&A, 434, 599
Chang, Q., Cuppen, H. M., & Herbst, E. 2006, A&A, 458, 497
Combes, F., & Pineau des Forets, G., 2001, Molecular Hydrogen in Space (Cambridge, UK: Cambridge University Press)
Compiègne, M., Verstraete, L., Jones, A., et al. 2011, A&A, 525, A103
Cuppen, H. M., & Herbst, E. 2005, MNRAS, 361, 565
Cuppen, H. M., Morata, O., & Herbst, E. 2006, MNRAS, 367, 1757
Desert, F. X., Boulanger, F., & Shore, S. N. 1986, A&A, 160, 295
Draine, B. T., & Li, A. 2001, ApJ, 551, 807
Du, Y. 2006, Order Structure and Topological Methods In Nonlinear partial Differential Equations., Vol. 1: Maximum Principles and Applications (World Scientific)
Duley, W. W. 1996, MNRAS, 279, 591
Garrod, R. T. 2008, A&A, 491, 239
Gould, R. J., & Salpeter, E. E. 1963, ApJ, 138, 393
Habart, E., Boulanger, F., Verstraete, L., Walmsley, C. M., & Pineau des Forêts, G. 2004, A&A, 414, 531
Habart, E., Abergel, A., Boulanger, F., et al. 2011, A&A, 527, A122
Hasegawa, T. I., Herbst, E., & Leung, C. M. 1992, ApJS, 82, 167
Hollenbach, D., & Salpeter, E. E. 1971, ApJ, 163, 155
Iqbal, W., Acharyya, K., & Herbst, E. 2012, ApJ, 751, 58
Iqbal, W., Acharyya, K., & Herbst, E. 2014, ApJ, 784, 139
Ivanovskaya, V. V., Zobelli, A., Teillet-Billy, D., et al. 2010, Phys. Rev. B, 82, 245407
Jeloaica, L., & Sidis, V. 1999, Chem. Phys. Lett., 300, 157
Katz, N., Furman, I., Biham, O., Pirronello, V., & Vidali, G. 1999, ApJ, 522, 305
Kerwin, J., & Jackson, B. 2008, J. Chem. Phys., 128, 084702
Le Bourlot, J., Le Petit, F., Pinto, C., Roueff, E., & Roy, F. 2012, A&A, 541, A76
Le Petit, F., Nehmé, C., Le Bourlot, J., & Roueff, E. 2006, ApJS, 164, 506
Le Petit, F., Barzel, B., Biham, O., Roueff, E., & Le Bourlot, J. 2009, A&A, 505, 1153
Lehtinen, P. O., Foster, A. S., Ma, Y., Krasheninnikov, A. V., & Nieminen, R. M. 2004, Phys. Rev. Lett., 93, 187202
Li, A., & Draine, B. T. 2001, ApJ, 554, 778
Li, D., & Goldsmith, P. F. 2003, ApJ, 585, 823
Lipshtat, A., & Biham, O. 2003, A&A, 400, 585
Lohmar, I., & Krug, J. 2006, MNRAS, 370, 1025
Lohmar, I., Krug, J., & Biham, O. 2009, A&A, 504, L5
Martinazzo, R., & Tantardini, G. F. 2006, J. Chem. Phys., 124, 124703
Mathis, J. S., Rumpl, W., & Nordsieck, K. H. 1977, ApJ, 217, 425
Mathis, J. S., Mezger, P. G., & Panagia, N. 1983, A&A, 128, 212
Mennella, V. 2008, ApJ, 684, L25
Morisset, S., Aguillon, F., Sizun, M., & Sidis, V. 2004a, J. Chem. Phys., 121, 6493
Morisset, S., Aguillon, F., Sizun, M., & Sidis, V. 2004b, J. Phys. Chem. A, 108, 8571
Morisset, S., Aguillon, F., Sizun, M., & Sidis, V. 2005, J. Chem. Phys., 122, 194702
Perets, H. B., Lederhendler, A., Biham, O., et al. 2007, ApJ, 661, L163
Pirronello, V., Liu, C., Roser, J. E., & Vidali, G. 1999, A&A, 344, 681
Pirronello, V., Biham, O., Liu, C., Shen, L., & Vidali, G. 1997a, ApJ, 483, L131
Pirronello, V., Liu, C., Shen, L., & Vidali, G. 1997b, ApJ, 475, L69
Rougeau, N., Teillet-Billy, D., & Sidis, V. 2011, Phys. Chem. Chem. Phys., 13, 17579
Sha, X., & Jackson, B. 2002, Surface Science, 496, 318
Sizun, M., Bachellerie, D., Aguillon, F., & Sidis, V. 2010, Chem. Phys. Lett., 498, 32
Sternberg, A., & Dalgarno, A. 1995, ApJS, 99, 565

8.2 CONCLUSIONS AND PERSPECTIVES

The main result of this article is the spectacular increase in the efficiency of the Langmuir-Hinshelwood mechanism in UV-rich environments. As explained in Chapter 2, the contradiction between the experimental results showing that the Langmuir-Hinshelwood only worked below $15 - 20\,\mathrm{K}$ (surface temperature) and the observations of PDRs showing efficient H_2 formation despite much higher dust temperatures is still an open problem for H_2 formation, for which several explanations have been proposed. We show here that this problem actually only exists for extreme PDRs ($G_0 \gtrsim 1000$). Indeed, experiments cannot reproduce the fluctuating temperatures that characterize small dust grains, and those fluctuations allow the grains to spend a large fraction of their time at low temperatures where the formation is efficient. Grains cannot be characterized by a single temperature and the detailed properties of the temperature fluctuations have to be taken into account in order to properly compute the formation rate. As a result, physisorption-based Langmuir-Hinshelwood formation can explain H_2 formation in all unshielded environments with moderate UV fields (G_0 up to a few hundreds). This makes the Eley-Rideal mechanism, which had been proposed in order to explain formation in unshielded conditions, much less necessary. In particular, in order to explain formation in PDRs before fluctuations were taken into account, the chemisorption barrier had to be set very low (see Le Bourlot et al. 2012) compared to theoretical estimates. This should now be re-evaluated and a more realistic value would probably be sufficient to explain formation in extreme PDRs where the gas is above $1000\,\mathrm{K}$.

Another important conclusion is that temperature fluctuations cannot be neglected for the computation of surface reactions in general. Taking a single representative temperature can lead to errors by several orders of magnitude on the average reaction rate. Studies of more complex surface chemical networks as occur deeper in the clouds should thus take possible fluctuation effects into account. As soon as surface processes involve barriers at temperatures that are frequently crossed by the temperature fluctuations, the effects can be expected to be important. Moreover, the effects depend on a competition between the chemistry timescale, which is mostly controlled by the rate of arrival of new atoms from the gas, and the timescale of the fluctuations. Thus, rare fluctuations can still have a strong effect if the adsorption of reactive species is even rarer. Reactions involving rarer reactive species (rare elements such as C, N, O,...) are more sensitive to fluctuations than H_2 formation. In cloud cores, secondary UV photons could be an important source of fluctuations for moderate size grains. Cosmic rays could also directly cause fluctuations for big grains.

The fluctuations of grain temperatures in cloud cores and shielded molecular gas might also be relevant to explain the atomic hydrogen fraction in molecular gas. Observations of HI self-absorption in dark cloud (Li and Gold-

smith 2003) have shown a slightly higher atomic fraction than expected from current models. Our results show that fluctuations of the smallest grains deep in the cloud (caused by NIR photons) are sufficient to increase the atomic fraction by almost one order of magnitude. This is again due to the competition between the fluctuation timescale and the adsorption timescale. As the gas becomes molecular, the adsorption timescale (for atomic H atoms) decreases and the formation efficiency becomes more sensitive to fluctuations. The result is a self-limitation of the molecular fraction. This should be investigated further taking the secondary UV photons into account. It could also be relevant to correctly predict the molecular fraction in diffuse clouds.

Part III

TURBULENCE-DRIVEN CHEMISTRY IN THE DIFFUSE ISM

9

A STOCHASTIC MODEL FOR TURBULENT CHEMISTRY

As shown in Chap. 3, consistent observational features suggest a view in which turbulence is ubiquitous in the interstellar medium. In the CNM, where chemical complexification occurs, the chemistry can be affected by the presence of turbulence at two levels: by the mixing effect of turbulence that can transport material across boundaries (e.g., between molecular and atomic gas regions), and by the kinetic energy it carries and dissipates into heat (by viscous or magnetic dissipation processes at the atomic level). It is this last effect that will be the focus of this chapter and the next, although the tools that will be developed here will also prove potentially useful for the study of turbulent mixing.

The average rate at which kinetic energy is turned into heat by turbulence is usually small compared to the dominant heating sources (e.g., the photoelectric heating mechanism). However, this dissipation does not occur homogeneously. As discussed in Chap. 3, intermittency is one of the characteristics of turbulence, and dissipation is concentrated in very small regions. During those bursts, the heating rate due to turbulent dissipation can become orders of magnitude higher than the other heating sources, and create temporarily hot spots in the gas. This will suddenly open endothermic chemical pathways, such as the formation of CH^+ ($C^+ + H_2 \rightarrow CH^+ + H$, with an endothermicity of 4640 K), and could explain the omnipresence of CH^+ and SH^+, as well as the observed abundances of CO (as the formation of CH^+ opens a new pathway towards CO), in the diffuse CNM. Moreover, the excited H_2 contained in such hot spots could be observable. This was discussed in Sect. 3.3.

In addition to heating the gas, the strong dissipation process in those dissipation regions could also directly transmit energy to the chemistry by causing suprathermal collisions. This can be caused by ion-neutral drift if the dominant dissipation mechanism is ambipolar diffusion, but suprathermal collisions are also expected in shocks and in regions of high shear. This kind of direct transmission of energy to chemistry represents only a negligible fraction compared to the energy dissipated into heat, but can be the dominant effect for chemistry. It was proposed to be the dominant mechanism (through ambipolar diffusion) enabling CH^+ formation in the diffuse ISM by Godard et al. [2009] (see Sect. 3.3.2 for a detailed discussion).

This problem concerns once again a situation in which fluctuations activate the chemistry. In contrast to the case of H_2 formation on dust, where the substrate temperature was the fluctuating variable with a simple and known statistics (Poisson), the gas temperature is here an intermediate vari-

able, and the heating rate is fluctuating, with statistics that remain to clarify. The goal of this chapter is to propose a formalism adapted to this problem. This formalism is applied to a simplified problem (the excitation of H_2 by the dissipation bursts) in the next chapter.

9.1 MOMENT APPROACHES AND TURBULENT CHEMISTRY

Turbulence is characterized by the fact that it is only statistically reproducible: for a given experiment with identical conditions, the details of the flow change for each repetition, but its statistical properties remain the same. The goal of turbulence models is thus to make statistical predictions, and it is natural to formulate the models in statistical terms. For instance, one may seek to predict the average quantities (in the ensemble meaning) of the flow at each position and time. This leads naturally to the question of writing equations governing those average quantities, and gave rise to a family of models that we can call the moment approaches, as they are centered around building systems of equations governing a particular set of moments of the quantities of the flow.

9.1.1 *The moment approaches*

Let us start with a simple example, and consider a constant density and constant temperature reactive fluid. We note $\overrightarrow{U}$ the fluid velocity and n_α the abundances of the chemical species. In this chapter, we use roman indices (i, j) for the spatial coordinates of vectors, and greek indices for the different chemical species. We also use the implicit summation rule for repeated indices.

The evolution of these quantities is governed by three conservation equations. The mass conservation gives

$$\frac{\partial U_i}{\partial x_i} = 0, \tag{279}$$

the conservation of momentum gives

$$\frac{DU_i}{Dt} = \nu \triangle U_i - \frac{1}{\rho}\frac{\partial p}{\partial x_i} \tag{280}$$

where ν is the kinematic viscosity, ρ the fluid density, p the pressure, and $\frac{D}{Dt}$ denotes the Lagrangian derivative ($\frac{D}{Dt} = \frac{\partial}{\partial t} + U_i\partial_i$). Finally, conservation of the chemical abundances gives

$$\frac{Dn_\alpha}{Dt} = w_\alpha + D \triangle n_\alpha \tag{281}$$

where w_α is the net formation rate for species α and D the molecular diffusivity.

If we try to derive the corresponding equations for the mean quantities, we get:

$$\frac{\partial \langle U_i \rangle}{\partial x_i} = 0, \tag{282}$$

$$\frac{\partial \langle U_i \rangle}{\partial t} + \partial_j \langle U_i U_j \rangle = \nu \triangle \langle U_i \rangle - \frac{1}{\rho} \frac{\partial \langle p \rangle}{\partial x_i} \tag{283}$$

$$\frac{\partial \langle n_\alpha \rangle}{\partial t} + \partial_j \langle U_j n_\alpha \rangle = \langle w_\alpha \rangle + D \triangle \langle n_\alpha \rangle \tag{284}$$

We have taken advantage of the fact that derivatives commute with the average. The resulting system is not closed as additional variables appear ($\langle U_i U_j \rangle$, $\langle w_\alpha \rangle$, $\langle U_j n_\alpha \rangle$) that cannot be deduced from the average quantities ($\langle U_i \rangle$, $\langle n_\alpha \rangle$). All non linear terms in the initial equations result in unclosed terms[1] in the average equations.

The usual approach is to separate the quantities into averages and fluctuations: $U_i = \langle U_i \rangle + u_i$, $n_\alpha = \langle n_\alpha \rangle + n'_\alpha$ so that the covariance terms can separate into a contribution from the averages and a contribution from the fluctuations (e.g., $\langle U_i U_j \rangle = \langle U_i \rangle \langle U_j \rangle + \langle u_i u_j \rangle$). One can then try to write additional equations for the moments of the fluctuations. New higher order moments arise from any such tentative, so that the system of equation cannot be exactly closed. This is the closure problem of turbulence. The moment approaches usually build the system of equations up to some order, and add some approximations of the higher order terms to close the system.

9.1.2 *Strengths and limitations*

In all such approaches, non-linear terms cannot be treated exactly. Simple non-linearity such as products of variables give rise to higher order moments for which additional equation can easily be found and meaningful approximations can be constructed. However, chemical formation rate involve stronger non-linearities with threshold effects (e.g. reaction rates in $\exp(-\frac{T_{\text{act}}}{T_{\text{gas}}})$). For the resulting formation terms $\langle k_{\alpha\beta}(T_{\text{gas}}) n_\alpha n_\beta \rangle$, evolution equations become more complex (and many new terms appear in them), and approximations less meaningful.

This weakness of moment approaches is thus particularly problematic for the study of turbulent chemistry as neither reaction terms nor turbulent transport terms (which are the two mechanisms of interest) can be treated exactly.

1 When trying to derive a set of equations governing a set of variables, we call unclosed terms the terms that cannot be expressed as explicit functions of the variables and the other known parameters, and thus increase the number of variables in the system.

On the other hand, these methods treat exactly all derivative terms, such as the molecular diffusivity and viscosity, or the pressure gradient. But those processes are of lesser interest for turbulent chemistry.

9.2 A PDF METHOD FOR TURBULENCE-DRIVEN CHEMISTRY

Another family of statistical methods is centered around the probability density functions (PDF) of the quantities. Those methods are thus called PDF methods. The PDF methods originated in the work of Lundgren [1967, 1969] on the PDF formulation of a statistical theory of turbulence. It was soon recognized as a powerful approach to turbulent reacting flows (see for instance Dopazo and O'Brien 1974). This approach was then developed into a complete computational method by S. B. Pope and coworkers in the field of turbulent combustion. A very detailed presentation and demonstration of the method is given in Pope [1985], and an introduction to the approach is also given in the corresponding chapter of the book by Pope [2000]. Reviews of the recent advances are given in Pope [1994, 1997], Van Slooten and Jayesh [1998], Pope [2004, 2011].

Our problem differs from the typical problem of turbulent combustion where the temperature fluctuations are caused by very exothermic reactions. In our case, the gas is sufficiently cold for the dissipation of the kinetic energy of turbulence to become the dominant heating mechanism during fluctuations. We thus adapt the velocity-dissipation-composition PDF method to our problem (Pope and Chen 1990).

In the first part of this chapter, we develop the general formalism of this method. We then limit ourselves to the stationary homogeneous case in which significant simplifications of the formalism occur, and our application presented in the next chapter only use the stationary homogeneous case. In this simplified case, the concept of the method becomes simpler. However, we start by presenting the complete formalism in order to show the generality of the method and its potential for more complex models (especially to study the problem of turbulent mixing).

We develop the formalism in the context of incompressible turbulence for simplicity, as it does not affect the stationary homogeneous simplified formalism. PDF methods can be generalized to compressible turbulence (e.g., Delarue and Pope 1997), and the general formalism presented here would need to be adapted for general application to interstellar turbulent flows. In our limited case of homogeneous turbulence, this is not necessary as will be discussed later.

We consider a turbulent flow comprising N reactive species, and follow the fluid velocity, the abundances of the species and the thermal energy of the gas (equivalent to its temperature). In astrophysical fluids, the excitation of

atoms and molecules is usually not at thermal equilibrium, while the kinetic energy of the particles is. We thus define the gas temperature with respect to the (volumic) kinetic energy e only:

$$e = \frac{3}{2} n \, k_B \, T_{\text{gas}}, \tag{285}$$

where n is the total number density ($n = \sum_{\alpha=1}^{N} n_\alpha$), and k_B the Boltzmann constant. In an exact formalism, our variables are thus the three U_i, n_α ($\alpha = 1, \ldots, N$) and the thermal energy e. We will see at some point in the demonstration that, in order to build a closure approximation, we will need to add the local and instantaneous dissipation rate

$$\epsilon = \frac{1}{2} \nu \left(\frac{\partial u_i}{\partial x_j} + \frac{\partial u_j}{\partial x_i} \right) \left(\frac{\partial u_i}{\partial x_j} + \frac{\partial u_j}{\partial x_i} \right) \tag{286}$$

as a variable. We will note spatial vectors with arrows, for instance the velocity $\overrightarrow{U} = (U_x, U_y, U_z)$, and the abundance vector in bold font, $\mathbf{n} = (n_1, n_2, \ldots, n_N)$.

The equations governing our variables are the previously given mass, momentum, and chemical abundances conservation equations:

$$\frac{\partial U_i}{\partial x_i} = 0, \tag{287}$$

$$\frac{D U_i}{D t} = \nu \triangle U_i - \frac{1}{\rho} \frac{\partial p}{\partial x_i} \tag{288}$$

$$\frac{D n_\alpha}{D t} = w_\alpha(T_{\text{gas}}, \mathbf{n}) + D \triangle n_\alpha \tag{289}$$

where we have explicitly written the dependency of the net formation rates on the abundance vector and the gas temperature (which is related to e by Eq. 285), and the energy conservation equation

$$\frac{D e}{D t} = \epsilon + B_{chem}(T_{\text{gas}}, \mathbf{n}) + \frac{\partial}{\partial x_i} \left(\lambda \frac{\partial T_{\text{gas}}}{\partial x_i} \right) \tag{290}$$

where λ is the heat conductivity of the gas, ϵ is the dissipation rate defined above, and B_{chem} is the net heating rate due to chemical reactions. As e only includes the thermal kinetic energy of the gas, collisional excitations and de-excitations have to be counted here as chemical reactions and their contributions included in B_{chem}.

Of course, as we consider an incompressible flow, we neglect the relation between the pressure and the temperature. This should be refined later by considering the general case of compressible turbulence.

In order to simplify the notation in later expressions, we group the thermal energy and the chemical abundance in a thermo-chemical state vector. We

can rewrite Eq. 289 and 290 in a similar form by defining the generalized chemical variables

$$Y_\beta = \begin{cases} e & \text{if} \quad \beta = 0 \\ n_\beta & \text{else} \end{cases}. \tag{291}$$

We again note the corresponding vector in bold fonts: $\mathbf{Y}$. We then have the general conservation equation

$$\frac{DY_\beta}{Dt} = -\frac{\partial J_i^{(\beta)}}{\partial x_i} + S^{(\beta)} \tag{292}$$

with

$$S^{(\beta)} = \begin{cases} \epsilon + B_{chem}(\mathbf{Y}) & \text{if} \quad \beta = 0 \\ w_\beta(\mathbf{Y}) & \text{else} \end{cases}, \tag{293}$$

and

$$J_i^{(\beta)} = \begin{cases} -\lambda \frac{\partial T}{\partial x_i} & \text{if} \quad \beta = 0 \\ -D \frac{\partial n_\beta}{\partial x_i} & \text{else} \end{cases}, \tag{294}$$

For clarity, we will always index those generalized chemical variables by β, while α will be used to index the original chemical abundances. Thus, $0 \leq \beta \leq N$ and $1 \leq \alpha \leq N$.

9.2.1 *The one-point PDF transport equation*

The principle of PDF methods is to derive a transport equation for the joint PDF of the variables describing the system, and to then close the equation by proposing models for the unclosed terms.

We now derive a transport equation for the one-point joint PDF of our variables. When using PDFs, we will always distinguish the physical variables $(\vec{U}, \mathbf{Y})$ from the sample space variables $(\vec{u}, \mathbf{y})$.

The PDF $f_{\vec{U}\mathbf{Y}}(\vec{u}, \mathbf{y}; \vec{x}, t)$ gives the density of probability of having $\vec{U} = \vec{u}$, $\mathbf{Y} = \mathbf{y}$, at the position $\vec{x}$ and time t.

We adopt here the derivation method used in Pope 2000 (which was also used initially by Lundgren 1967). An alternative derivation is used in Pope 1985.

For one single realization of the flow, which gives $(\vec{U}, \mathbf{Y})$ at position $\overrightarrow{x}, t$, it is possible to define a one-realization PDF as a Dirac function:

$$f'(\vec{u}, \mathbf{y}; \vec{x}, t) = \delta^3(\vec{U}(\vec{x}, t) - \vec{u})\delta^{N+1}(\mathbf{Y}(\vec{x}, t) - \mathbf{y}) \tag{295}$$

where δ^n denotes a product of n δ functions applied to each component of the vector argument. Note that there is one different one-realization PDF associated to each possible outcome $(\vec{U}, \mathbf{Y})$.

As the result of the experiment is known, this one-realization PDF is zero everywhere except on the result. The true PDF is then the ensemble average of the one-realization PDF over all possible realization of the flow

$$f_{\vec{U}\mathbf{Y}} = \left\langle f' \right\rangle \tag{296}$$

This equation is tautological, as can be seen by expanding the average in term of its integral expression over the PDF.

A less obvious relation is that for any quantity of the flow $Q(\overrightarrow{x}, t)$,

$$\left\langle Q(\vec{x},t)\, f'(\vec{u},\mathbf{y};\vec{x},t) \right\rangle = \left\langle Q(\vec{x},t) \,\middle|\, \vec{U}(\vec{x},t) = \vec{u}, \mathbf{Y}(\vec{x},t) = \mathbf{y} \right\rangle f_{\vec{U}\mathbf{Y}}(\vec{u},\mathbf{y};\vec{x},t). \tag{297}$$

where the term appearing on the right-hand side is the conditional average of $Q(\overrightarrow{x}, t)$ knowing the values of $\overrightarrow{U}(\overrightarrow{x}, t)$ and $\mathbf{Y}(\overrightarrow{x}, t)$.

This result will be useful soon, and is derived by considering the joint PDF $f_{\vec{U}\mathbf{Y}Q}$ of Q and our variables (we note q the sample space variable corresponding to Q, and $\mathbf{z}$ that of $\mathbf{y}$):

$$\begin{aligned}
\left\langle Q(\vec{x},t)\, f'(\vec{u},\mathbf{y};\vec{x},t) \right\rangle &= \int d^3\vec{v}\, d^{N+1}\mathbf{z}\, dq\, q\, \delta^3(\vec{v}-\vec{u})\delta^{N+1}(\mathbf{z}-\mathbf{y})\, f_{\vec{U}\mathbf{Y}Q}(\vec{v},\mathbf{z},q;\vec{x},t) \\
&= \int dq\, q\, f_{\vec{U}\mathbf{Y}Q}(\vec{u},\mathbf{y},q;\vec{x},t) \\
&= f_{\vec{U}\mathbf{Y}}(\vec{u},\mathbf{y};\vec{x},t) \int dq\, q\, f_{Q|\vec{U}\mathbf{Y}}(q;\vec{x},t \,|\, \vec{U}=\vec{u}, \mathbf{Y}=\mathbf{y}) \\
&= f_{\vec{U}\mathbf{Y}}(\vec{u},\mathbf{y};\vec{x},t) \left\langle Q(\vec{x},t) \,\middle|\, \vec{U}(\vec{x},t) = \vec{u}, \mathbf{Y}(\vec{x},t) = \mathbf{y} \right\rangle
\end{aligned}$$

The idea is now to derive a transport equation for the one-realization PDF, before averaging it in order to get the transport equation for the true PDF.

We note $\delta^{(1)}$ the first derivative of the Dirac function δ.

$$\begin{aligned}
\frac{\partial f'(\vec{u},\mathbf{y};\vec{x},t)}{\partial t} &= \frac{\partial}{\partial t}\left(\delta^3(\vec{U}(\vec{x},t)-\vec{u})\delta^{N+1}(\mathbf{Y}(\vec{x},t)-\mathbf{y})\right) \\
&= \sum_i \frac{\partial U_i}{\partial t}\delta^{(1)}(U_i(\vec{x},t)-u_i)\prod_{j\neq i}\delta(U_j(\vec{x},t)-u_j)\prod_\beta \delta(Y_\beta(\vec{x},t)-y_\beta) \\
&+ \sum_\beta \frac{\partial Y_\beta}{\partial t}\delta^{(1)}(Y_\beta(\vec{x},t)-y_\beta)\prod_{\gamma\neq\beta}\delta(Y_\gamma(\vec{x},t)-y_\gamma)\prod_i \delta(U_i(\vec{x},t)-u_i) \\
&= -\frac{\partial U_i}{\partial t}\frac{\partial f'(\vec{u},\mathbf{y};\vec{x},t)}{\partial u_i} - \frac{\partial Y_\beta}{\partial t}\frac{\partial f'(\vec{u},\mathbf{y};\vec{x},t)}{\partial y_\beta}
\end{aligned} \tag{298}$$

By a similar derivation, we can show that:

$$\frac{\partial f'(\vec{u},\mathbf{y};\vec{x},t)}{\partial x_j} = -\frac{\partial U_k}{\partial x_j}\frac{\partial f'(\vec{u},\mathbf{y};\vec{x},t)}{\partial u_k} - \frac{\partial Y_\beta}{\partial x_j}\frac{\partial f'(\vec{u},\mathbf{y};\vec{x},t)}{\partial y_\beta} \tag{299}$$

We thus have:

$$\begin{aligned}\frac{Df'(\vec{u},\mathbf{y};\vec{x},t)}{Dt} &= \frac{\partial f'(\vec{u},\mathbf{y};\vec{x},t)}{\partial t} + U_j\frac{\partial f'(\vec{u},\mathbf{y};\vec{x},t)}{\partial x_j} \\ &= -\frac{DU_k}{Dt}\frac{\partial f'(\vec{u},\mathbf{y};\vec{x},t)}{\partial u_k} - \frac{DY_\beta}{Dt}\frac{\partial f'(\vec{u},\mathbf{y};\vec{x},t)}{\partial y_\beta} \\ &= -\frac{\partial}{\partial u_k}\left[\frac{DU_k}{Dt}f'(\vec{u},\mathbf{y};\vec{x},t)\right] - \frac{\partial}{\partial y_\beta}\left[\frac{DY_\beta}{Dt}f'(\vec{u},\mathbf{y};\vec{x},t)\right] \end{aligned} \quad (300)$$

which is the transport equation for the one-realization PDF.

By taking the statistical average of Eq. 300 and using the relation of Eq. 297, we can then deduce the true PDF transport equation:

$$\begin{aligned}&\frac{\partial f_{\vec{U}\mathbf{Y}}(\vec{u},\mathbf{y};\vec{x},t)}{\partial t} + u_j\frac{\partial f_{\vec{U}\mathbf{Y}}(\vec{u},\mathbf{y};\vec{x},t)}{\partial x_j} = \\ &\quad -\frac{\partial}{\partial u_k}\left[\left\langle \frac{DU_k}{Dt}\middle|\, \vec{U}(\vec{x},t)=\vec{u},\mathbf{Y}(\vec{x},t)=\mathbf{y}\right\rangle f_{\vec{U}\mathbf{Y}}(\vec{u},\mathbf{y};\vec{x},t)\right] \\ &\quad -\frac{\partial}{\partial y_\beta}\left[\left\langle \frac{DY_\beta}{Dt}\middle|\, \vec{U}(\vec{x},t)=\vec{u},\mathbf{Y}(\vec{x},t)=\mathbf{y}\right\rangle f_{\vec{U}\mathbf{Y}}(\vec{u},\mathbf{y};\vec{x},t)\right] \end{aligned} \quad (301)$$

Up to now, this equation contains no physics and is only a consequence of the definition of a PDF. We note that if we were considering an additional variable Z (with sample variable z), and writing the transport equation for the PDF $f_{\vec{U}\mathbf{Y}Z}(\vec{u},\mathbf{y},z;\vec{x},t)$, it would simply result in an additional term on the right-hand side

$$-\frac{\partial}{\partial z}\left[\left\langle \frac{DZ}{Dt}\middle|\, \vec{U}(\vec{x},t)=\vec{u},\mathbf{Y}(\vec{x},t)=\mathbf{y},Z(\vec{x},t)=z\right\rangle f_{\vec{U}\mathbf{Y}Z}(\vec{u},\mathbf{y},z;\vec{x},t)\right] \quad (302)$$

and in the inclusion of the new variable in the other terms.

The physics comes in when injecting the conservation equations (Eq. 288 and 292) to replace the terms $\frac{DU_k}{Dt}$ and $\frac{DY_\beta}{Dt}$. From now on, we drop the arguments of the PDF to simplify the notations, and also drop $\vec{x}$ and t from the arguments of all functions. The PDF and the physical variables ($\vec{U}$, $\mathbf{Y}$,...) thus implicitly depend on $\vec{x}$ and t. We then get:

$$\frac{\partial f_{\vec{U}\mathbf{Y}}}{\partial t} + u_j \frac{\partial f_{\vec{U}\mathbf{Y}}}{\partial x_j} = - \frac{\partial}{\partial u_k}\left[\left\langle \nu \triangle U_k \middle| \vec{U} = \vec{u}, \mathbf{Y} = \mathbf{y} \right\rangle f_{\vec{U}\mathbf{Y}}\right] + \frac{\partial}{\partial u_k}\left[\left\langle \frac{1}{\rho}\frac{\partial p}{\partial x_k} \middle| \vec{U} = \vec{u}, \mathbf{Y} = \mathbf{y} \right\rangle f_{\vec{U}\mathbf{Y}}\right] + \frac{\partial}{\partial y_\beta}\left[\left\langle \frac{\partial J_i^{(\beta)}}{\partial x_i} \middle| \vec{U} = \vec{u}, \mathbf{Y} = \mathbf{y} \right\rangle f_{\vec{U}\mathbf{Y}}\right] - \frac{\partial}{\partial y_\beta}\left[\left\langle S^{(\beta)} \middle| \vec{U} = \vec{u}, \mathbf{Y} = \mathbf{y} \right\rangle f_{\vec{U}\mathbf{Y}}\right] \quad (303)$$

We will now consider the conditional average terms appearing on the right-hand side.

9.2.2 *Closed and unclosed terms*

As such, this equation is not closed because of the four conditional average terms appearing on the right-hand side. Some can be exactly expressed in closed form, while other cannot and will need to be modeled.

Before trying to express those terms, we note that the advection term in the left-hand side naturally appears in closed form. Turbulent transport needs no approximation in the PDF method, which is the first of its strength for turbulent combustion modeling, but could also be useful in astrophysical contexts for turbulence in chemically stratified clouds (e.g., PDRs).

We must note, however, that, while in moment approaches the turbulent mixing term often "replaces" molecular diffusion, in PDF approaches turbulent mixing and molecular diffusion have very distinct effects. Consider for example homogeneous turbulence where, as initial condition, the left half of space possesses some concentration c of an inert scalar tracer, while none is present in the right half. Initially, the PDF of the tracer concentration is a Dirac at c in the left half and a Dirac at 0 in the right half. The effect of turbulent mixing will be to homogenize spatially the PDF, so that after a sufficiently long time, the PDF is the same at every position. But in the absence of molecular diffusion, this final PDF will remain composed of two Diracs. Fluid elements coming from both sides have been statistically mixed, in the sense that at any given position, we are as likely to find an element coming from the left than from the right. But each fluid element has maintained its initial concentration. The action of molecular diffusion will be to progressively populate all intermediate values between 0 and c, before concentrating the final PDF in a new intermediate Dirac when the concentration

has become completely homogeneous. The term corresponding to molecular diffusion is one of the right-hand-side terms that we will now discuss.

The simplest of the conditional average terms is the chemical source term $S^{(\beta)}$ for $\beta > 0$. It is then $w_\beta(\mathbf{Y})$, the net formation rate. If we know the abundance vector $\mathbf{Y}(\overrightarrow{x}, t) = \mathbf{y}$, this quantity is completely determined, so that the conditional average is simply $w_\beta(\mathbf{y})$. However non-linear the chemical rates are, they appear in closed form in the PDF transport equation and need no approximation. This is the second strength of PDF methods for turbulent chemistry, and the one that interests us most.

For $\beta = 0$, $S^{(\beta)} = \epsilon + B_{chem}(\mathbf{Y})$. The second term, the net chemical heating rate is again completely determined by the knowledge of $\mathbf{Y}(\overrightarrow{x}, t) = \mathbf{y}$. The first term, the instantaneous turbulent-dissipation heating rate, however, is related to the derivatives of $\overrightarrow{U}$ (Eq. 286). The knowledge of the local values of $\overrightarrow{U}$ and $\mathbf{Y}$ alone is not sufficient to determine it, and the one-point PDF contains no information on spatial derivatives. This is the main drawback of one-point PDF methods.

The exact expression of derivative terms would involve the two-points PDF. Similarly, writing the transport equation for the two-points PDF would involve terms that can only be expressed in term of the three-points PDF. For the velocity PDF, the derivation of the full hierarchy of equations for the n-point PDFs is presented in Lundgren 1967, who find it to be formally identical to the BBGKY hierarchy (Bogoliubov-Born-Green-Kirkwood-Yvon hierarchy, Bogoliubov 1946) of statistical physics. PDF methods thus do not avoid the closure problem of turbulence. But when compared to moment approaches, they allow a new choice of which terms are exactly treated, that is more adapted to the modeling of turbulent chemistry.

The three remaining terms (the viscous term for velocity, the pressure gradient term and the molecular diffusion term for heat and chemical abundances) are all derivatives, and thus suffer from the same problem.

A one-point PDF approach already treats exactly the reaction rates and the turbulent transport term, while the unclosed terms have clear physical meaning, which helps for building approximations. A higher order (e.g. two-points PDF) approach would not close the problem, and would result in more complex unclosed terms with unclear physical meaning, for which proposing an approximation would be difficult.

We will thus limit ourselves to a one-point PDF model. The terms that need modeling are thus:

- The instantaneous dissipation rate term $\left\langle \epsilon \middle| \vec{U} = \vec{u}, \mathbf{Y} = \mathbf{y} \right\rangle$
- The molecular diffusion terms for the chemical concentrations and the kinetic thermal energy $\left\langle \frac{\partial J_i^{(\beta)}}{\partial x_i} \middle| \vec{U} = \vec{u}, \mathbf{Y} = \mathbf{y} \right\rangle$

- The pressure gradient term $\left\langle \frac{1}{\rho}\frac{\partial p}{\partial x_k} \middle| \vec{U} = \vec{u}, \mathbf{Y} = \mathbf{y} \right\rangle$
- The viscosity term $\left\langle \nu \triangle U_k \middle| \vec{U} = \vec{u}, \mathbf{Y} = \mathbf{y} \right\rangle$

As turbulent-dissipation heating is the source of the effect we wish to investigate (creation of hotspots), we have to be especially careful with the way we treat the first term. In order to model this effect as well as possible, we do not try to relate it to the other variables (as we lack all informations about derivatives). Instead, we consider the PDF not only of $\overrightarrow{U}$ and $\mathbf{Y}$, but the joint PDF of the three variables $\overrightarrow{U}$, $\mathbf{Y}$, ϵ, PDF $f_{\overrightarrow{U}\mathbf{Y}\epsilon}(\overrightarrow{u}, \mathbf{y}, \varepsilon; \overrightarrow{x}, t)$, and write the transport equation for this new PDF (see Eq. 302 for the effect of adding a variable to the PDF). Adding this variable, and expressing the terms for $S^{(\alpha)}$, the PDF transport equation becomes:

$$\begin{aligned}
\frac{\partial f_{\vec{U}\mathbf{Y}\epsilon}}{\partial t} + u_j \frac{\partial f_{\vec{U}\mathbf{Y}\epsilon}}{\partial x_j} + \frac{\partial}{\partial y_\alpha}\left[w_\alpha(\mathbf{y})\, f_{\vec{U}\mathbf{Y}\epsilon}\right]\Big|_{\alpha>0} + \frac{\partial}{\partial e}\left[\left(B_{\text{chem}}(\mathbf{y}) + \varepsilon\right) f_{\vec{U}\mathbf{Y}\epsilon}\right] = \\
- \frac{\partial}{\partial u_k}\left[\left\langle \nu \triangle U_k \middle| \vec{U} = \vec{u}, \mathbf{Y} = \mathbf{y}, \epsilon = \varepsilon \right\rangle f_{\vec{U}\mathbf{Y}\epsilon}\right] \\
+ \frac{\partial}{\partial u_k}\left[\left\langle \frac{1}{\rho}\frac{\partial p}{\partial x_k} \middle| \vec{U} = \vec{u}, \mathbf{Y} = \mathbf{y}, \epsilon = \varepsilon \right\rangle f_{\vec{U}\mathbf{Y}\epsilon}\right] \\
+ \frac{\partial}{\partial y_\beta}\left[\left\langle \frac{\partial J_i^{(\beta)}}{\partial x_i} \middle| \vec{U} = \vec{u}, \mathbf{Y} = \mathbf{y}, \epsilon = \varepsilon \right\rangle f_{\vec{U}\mathbf{Y}\epsilon}\right] \\
- \frac{\partial}{\partial \varepsilon}\left[\left\langle \frac{D\epsilon}{Dt} \middle| \vec{U} = \vec{u}, \mathbf{Y} = \mathbf{y}, \epsilon = \varepsilon \right\rangle f_{\vec{U}\mathbf{Y}\epsilon}\right] \qquad (304)
\end{aligned}$$

where the exactly expressed terms have been moved to the left-hand side. Those include turbulent transport, chemical reactions, chemical heating and turbulent heating (thanks to our newly added variable). The idea of adding ϵ to the PDF has been used by Pope and Chen [1990] for a different purpose: it provides a local timescale for better modeling of the evolution of the Lagrangian velocity.

But this modification added a new unclosed term on the right-hand side (the conditional average of $\frac{D\epsilon}{Dt}$). As the true expression of $\frac{D\epsilon}{Dt}$ could not be expressed in terms of $\overrightarrow{U}$, $\mathbf{Y}$ and ϵ only (it would involve derivatives), we will construct a model of the Lagrangian evolution of ϵ experienced by a fluid element.

Before describing this model, we consider the other remaining terms. Molecular diffusion of heat and chemical abundances will be neglected in a first approach, considering that the disturbances of the thermo-chemical state of the gas induced by the fluctuating heating will return to their initial state by cooling and chemical reactions rather than by diffusive mixing with undisturbed gas. This approximation will need to be revised in later developments of this

work. Indeed, we can estimate the timescales corresponding to radiative and diffusive cooling for a hot parcel of gas with $n_{\mathrm{H}} = 100\,\mathrm{cm}^{-3}$, $T = 1000\,\mathrm{K}$. We take a $\mathrm{H} - \mathrm{H}$ collision cross section of $\sigma_{\mathrm{H-H}} = 5.7 \times 10^{-15}\,\mathrm{cm}^2$ (Spitzer 1978) to estimate the thermal conductivity of the gas, and assume that for such hot spot the temperature variation scale is of the order of or larger than the Kolmogorov scale so that $\frac{\partial^2 T}{\partial x_i^2} \simeq T/\eta^2$, which is an upper estimate. An estimation of η and the cooling rate for atomic gas are given in the next chapter (Eq. 357 and 369). We then find a lower bound on the diffusive cooling time scale to be of the order of 10^9 s, while the radiative cooling timescale is of the order of 10^{11} s. Diffusion will thus need to be later added to the model. Numerous models have been proposed for the molecular diffusion terms, which all have shortcomings in some aspect (see Pope 2000, Chap. 12.7.4, who reviews some of them). The simplest consists in replacing the conditional average $\left\langle \frac{\partial J_i^{(\beta)}}{\partial x_i} \middle| \vec{U} = \vec{u}, \mathbf{Y} = \mathbf{y}, \epsilon = \varepsilon \right\rangle$ by a term of the form $K\left(y_\beta - \langle y_\beta \rangle\right)$, an approximation named IEM (Interaction by Exchange with the Mean). This correctly contracts the chemical composition PDF towards its mean, but incorrectly leaves the shape of the PDF invariant during the contraction (the shape should tend towards a gaussian under the effect of molecular diffusion). The resulting term is closed as $\langle y_\beta \rangle$ can be derived from the PDF.

We will not enter into the details of modeling the pressure gradient and the viscous terms as, from Sect. 9.3 on, we will consider homogeneous turbulence in which those terms disappear. Various models based on the construction of a stochastic model for the Lagrangian evolution of a fluid element have been proposed, as for instance the refined Langevin model presented in Pope and Chen 1990, which makes use of the dissipation rate variable ϵ to provide a timescale to the model. A complete application of this formalism to a non homogeneous case would require using one of those models.

9.2.3 *A stochastic Lagrangian model of turbulent dissipation*

If one adopts the Lagrangian point of view of a fluid element, turbulence is characterized by a fluctuating and seemingly random evolution. As we do not want to involve any two-point statistics (or derivatives) in our model for the evolution of the dissipation rate, we do not have access to any information about the surroundings of the fluid element, which could give a deterministic insight into the future of the evolution. We can thus only model this evolution as a continuous stochastic process. We will assume that the evolution of ϵ only depends on the current value of ϵ in the fluid element, and not on its velocity $\overrightarrow{U}$ or its composition $\mathbf{Y}$. We use a similar stochastic model for the dissipation rate as the one used by Pope and Chen [1990], except that we add a more precise constraint on the variance of the dissipation.

We have constraints about the statistical properties of the dissipation rate. We will adopt the refined self-similarity hypotheses (Kolmogorov 1962) and the associated log-normal model of intermittency (see Sect. 3.1.3). Despite some shortcomings, this model predicts the exponents of the structure functions reasonably well. It thus accounts for the intermittency of dissipation. We note that a similar model could be constructed for other assumptions on the statistics of the dissipation. We adopt the log-normal model in a first approach.

Our constraints are then:

- The PDF of the dissipation rate ϵ is log-normal
- The scaling of its variance is given by

$$\frac{\langle \epsilon^2 \rangle}{\langle \epsilon \rangle^2} \propto \left(\frac{L}{\eta}\right)^{\mu} \propto \mathrm{Re}^{\frac{3}{4}\mu} \tag{305}$$

  where η is the Kolmogorov dissipation length scale, Re the large-scale Reynolds number, and μ a constant for which experiments indicate a value of $\sim \frac{1}{4}$.
- In addition, the Lagrangian autocorrelation function of dissipation is roughly exponential, with characteristic time $\tau_\epsilon \sim 0.5\, T_L$ where T_L is the large-scale timescale of turbulence (Yeung and Pope 1989).

We now build a diffusion stochastic process satisfying those three constraints.

If ϵ is to be log-normally distributed, $X = \ln(\frac{\epsilon}{\langle \epsilon \rangle})$ needs to be normally distributed. A simple way to construct a normally-distributed diffusion process is to use an Ornstein-Uhlenbeck process (see Sect. 4.2.6). Such a model is characterized by three parameters μ, k and D, and is defined as having $A(x) = -k(x-\mu)$ and $B(x) = D$. It can thus be written as the stochastic differential equation (see Sect. 4.3.4):

$$dX = -k(X-\mu)\,dt + \sqrt{D}\,dW_t \tag{306}$$

For reasons that will be clear soon, we prefer to reparameterize this process as:

$$dX = -(X-\mu)\,\frac{dt}{T} + \sqrt{\frac{2\,\sigma^2}{T}}\,dW_t \tag{307}$$

It is then easily verified (see Eq. 57 in Chap. 4) that the stationary distribution of this process is:

$$f_X(x) = \frac{1}{\sqrt{2\pi}\sigma}\, e^{-\frac{(x-\mu)^2}{2\sigma^2}} \tag{308}$$

From the definition of X, we want $\langle e^X \rangle = 1$. From the PDF (Eq. 308), it can be easily shown that

$$\left\langle e^X \right\rangle = e^{\mu + \frac{\sigma^2}{2}} \tag{309}$$

We deduce that we need

$$\mu = -\frac{\sigma^2}{2} \tag{310}$$

Our stochastic diffusion process is now defined as

$$dX = -(X + \frac{\sigma^2}{2})\,\frac{dt}{T} + \sqrt{\frac{2\,\sigma^2}{T}}\,dW_t \tag{311}$$

The corresponding equation for the dissipation process $\epsilon = \langle\epsilon\rangle \exp(X)$ is (we use Itō's lemma, see Sect. 4.3.3, Eq. 65):

$$d\epsilon = \left[\frac{d\,\langle\epsilon\rangle}{dt}\,\frac{\epsilon}{\langle\epsilon\rangle} - \frac{\epsilon}{T}\left(\ln\left(\frac{\epsilon}{\langle\epsilon\rangle}\right) - \frac{\sigma^2}{2}\right)\right]\,dt \,+\, \epsilon\,\sqrt{\frac{2\sigma^2}{T}}\,dW_t \tag{312}$$

Where the first time derivative term is for general inhomogeneous flow where the intensity of the turbulence can be different at different positions in the flow, or vary in time (e.g., decay). In both cases, the Lagrangian particle will experience a change in the ensemble average of the dissipation rate. If necessary, this time derivative can be modeled using the usual equation from the $k-\epsilon$ model (Jones and Launder 1972), but we will neglect it here in view of our stationary homogeneous turbulence application. Our process is thus

$$d\epsilon = -\left[\frac{\epsilon}{T}\left(\ln\left(\frac{\epsilon}{\langle\epsilon\rangle}\right) - \frac{\sigma^2}{2}\right)\right]\,dt \,+\, \epsilon\,\sqrt{\frac{2\sigma^2}{T}}\,dW_t \tag{313}$$

where $\langle\epsilon\rangle$, σ and T are constants. $\langle\epsilon\rangle$ is a parameter of the turbulence and will thus be a parameter of our model. It is usually expressed in terms of the other parameters, such as $\langle\epsilon\rangle = \frac{U^3}{L}$ where U and L are the large-scale velocity and length scale. But as estimation of $\langle\epsilon\rangle$ in the ISM are available, we will use it as one of the control parameters of the turbulence. On the other hand, σ and T remain to be expressed.

The PDF $f_\epsilon(\varepsilon)$ of the stochastic process ϵ defined by Eq. 313 is

$$f_\epsilon(\varepsilon) = \frac{1}{\varepsilon\,\sigma\,\sqrt{2\pi}}\,\exp\left(-\frac{\left(\ln(\frac{\varepsilon}{\langle\epsilon\rangle}) + \frac{\sigma^2}{2}\right)^2}{2\,\sigma^2}\right) \tag{314}$$

This can be derived as the stationary solution of the Fokker-Planck equation associated to Eq. 313 (see Sect. 4.3.4), or in a simpler way from the PDF of X (Eq. 308) and the variable change $X = \ln(\frac{\epsilon}{\langle\epsilon\rangle})$.

We now try to relate the remaining parameters σ and T to physical parameters of the turbulence.

We first use our second constraint:

$$\frac{\langle\epsilon^2\rangle}{\langle\epsilon\rangle^2} \propto \left(\frac{L}{\eta}\right)^\mu \propto \mathrm{Re}^{\frac{3}{4}\mu} \propto \left(\frac{u_{\mathrm{rms}}^4}{\nu\,\langle\epsilon\rangle}\right)^{\frac{3}{4}\mu} \tag{315}$$

The last parametrization is in terms of the final quantities of our models. Indeed, $\langle\epsilon\rangle$ and $u_{\rm rms} = \sqrt{\langle u^2\rangle}$ have been estimated in the ISM, and ν can be be estimated for the ISM gas.

We thus compute $\left\langle \epsilon^2 \right\rangle$:

$$\begin{aligned}\left\langle \epsilon^2 \right\rangle &= \int_0^{+\infty} d\varepsilon\, \varepsilon^2\, f_\epsilon(\varepsilon) \\ &= \langle\epsilon\rangle^2\, e^{\sigma^2}\end{aligned} \tag{316}$$

We can thus relate σ to our parameters:

$$\sigma^2 = c_0 + \frac{3}{4}\mu\, \ln\left(\frac{u_{\rm rms}^4}{\nu\,\langle\epsilon\rangle}\right) \tag{317}$$

where c_0 is a constant. Numerical simulations suggest the relationship (Yeung and Pope 1989)

$$\sigma^2 = 0.29\, \ln\left(\mathrm{Re}_\lambda\right) - 0.36 \tag{318}$$

where Re_λ is the Taylor-scale Reynolds number. Given the relationship $\mathrm{Re}_\lambda = (\frac{20}{3}\mathrm{Re})^{\frac{1}{2}}$, this translates into

$$\sigma^2 = 0.145\, \ln\left(\mathrm{Re}\right) - 0.085 = 0.145\, \ln\left(\frac{u_{\rm rms}^4}{\nu\,\langle\epsilon\rangle}\right) - 0.085 \tag{319}$$

We note that a more recent study by the same authors (Yeung et al. [2006]) gives a new estimate of this relationship as $\sigma^2 = 0.375\, \ln(\mathrm{Re}_\lambda) - 0.863$, obtained on a much larger range of Reynolds numbers. This better relationship was not implemented in the models presented here, but will be used in future developments of this work.

We finally need to constraint T, which plays the role of a characteristic timescale in Eq. 313, and, as expected for a timescale of the stochastic process, does not appear in the stationary PDF (Eq. 314).

Our last constraint is that the autocorrelation function of the Lagrangian dissipation is roughly exponential, with timescale $\sim 0.5\, T_L$. We now compute the autocorrelation function for the process ϵ defined by Eq. 313. Let us consider the (stationary) autocovariance function of ϵ:

$$R_\epsilon(\tau) = \left\langle \left(\epsilon(t+\tau) - \langle\epsilon\rangle\right)\left(\epsilon(t) - \langle\epsilon\rangle\right)\right\rangle \tag{320}$$

which does not depend on t from stationarity. We then have

$$R_\epsilon(\tau) = \langle\epsilon\rangle^2 \left[\frac{\langle\epsilon(t)\,\epsilon(t+\tau)\rangle}{\langle\epsilon\rangle^2} - 1\right] \tag{321}$$

As $\epsilon = \langle\epsilon\rangle\, e^X$, this can be written as

$$R_\epsilon(\tau) = \langle\epsilon\rangle^2 \left[\left\langle e^{X(t)+X(t+\tau)}\right\rangle - 1\right] \tag{322}$$

As the joint PDF of the stationary Ornstein-Uhlenbeck process at two times is gaussian (see Eq. 56 and 57), $X(t) + X(t+\tau)$ is itself a gaussian variable, and we can use the fact that for a gaussian variable y,

$$\langle e^y \rangle = e^{\langle y \rangle + \frac{\mathrm{Var}(y)}{2}} \tag{323}$$

We have

$$\langle X(t) + X(t+\tau) \rangle = 2 \langle X \rangle = -\sigma^2 \tag{324}$$

and

$$\begin{aligned} \mathrm{Var}\left(X(t) + X(t+\tau)\right) &= \left\langle \left(X(t) + X(t+\tau)\right)^2 \right\rangle - 4 \langle X \rangle^2 \\ &= 2\,\mathrm{Var}(X) + 2\,R_X(\tau) \end{aligned} \tag{325}$$

where $R_X(\tau)$ is the autocovariance function of the stochastic process X.

We compute it in the following way:

$$\begin{aligned} &\langle X(t+\tau)\, X(t) \rangle = \\ &\quad \left\langle \left(X(t) - \int_t^{t+\tau} (X(t') + \frac{\sigma^2}{2}) \frac{dt'}{T} + \int_t^{t+\tau} \sqrt{\frac{2\sigma^2}{T}}\, dW_{t'} \right) X(t) \right\rangle \\ &\qquad = \left\langle X^2 \right\rangle - \left\langle \int_t^{t+\tau} X(t) \left(X(t') + \frac{\sigma^2}{2} \right) \frac{dt'}{T} \right\rangle \\ &\qquad\qquad + \left\langle \int_t^{t+\tau} X(t) \sqrt{\frac{2\sigma^2}{T}}\, dW_{t'} \right\rangle \end{aligned} \tag{326}$$

As $X(t)\sqrt{\frac{2\sigma^2}{T}}$ is independent of $dW_{t'}$ for $t' > t$, the last term is zero (see Sect. 4.3.2).

We now consider

$$\begin{aligned} \frac{d\,\langle X(t+\tau)\, X(t) \rangle}{d\tau} &= -\left\langle X(t) \left(X(t+\tau) + \frac{\sigma^2}{2} \right) \frac{1}{T} \right\rangle \\ &= -\frac{1}{T} \langle X(t+\tau)\, X(t) \rangle - \frac{\sigma^2}{2} \frac{\langle X \rangle}{T} \end{aligned} \tag{327}$$

Consequently,

$$\langle X(t+\tau)\, X(t) \rangle = -\frac{\sigma^2}{2} \langle X \rangle + \left(\left\langle X^2 \right\rangle + \frac{\sigma^2}{2} \langle X \rangle \right) e^{-\frac{\tau}{T}} \tag{328}$$

We recall that $\langle X \rangle = -\frac{\sigma^2}{2}$ and $\langle X^2 \rangle = \sigma^2 + \frac{\sigma^4}{4}$, so that

$$\langle X(t+\tau)\, X(t) \rangle = \frac{\sigma^4}{4} + \sigma^2\, e^{-\frac{\tau}{T}}, \tag{329}$$

and the autocovariance function is

$$\begin{aligned} R_X(\tau) &= \langle X(t+\tau)\, X(t) \rangle - \langle X \rangle^2 \\ &= \sigma^2\, e^{-\frac{\tau}{T}} \end{aligned} \tag{330}$$

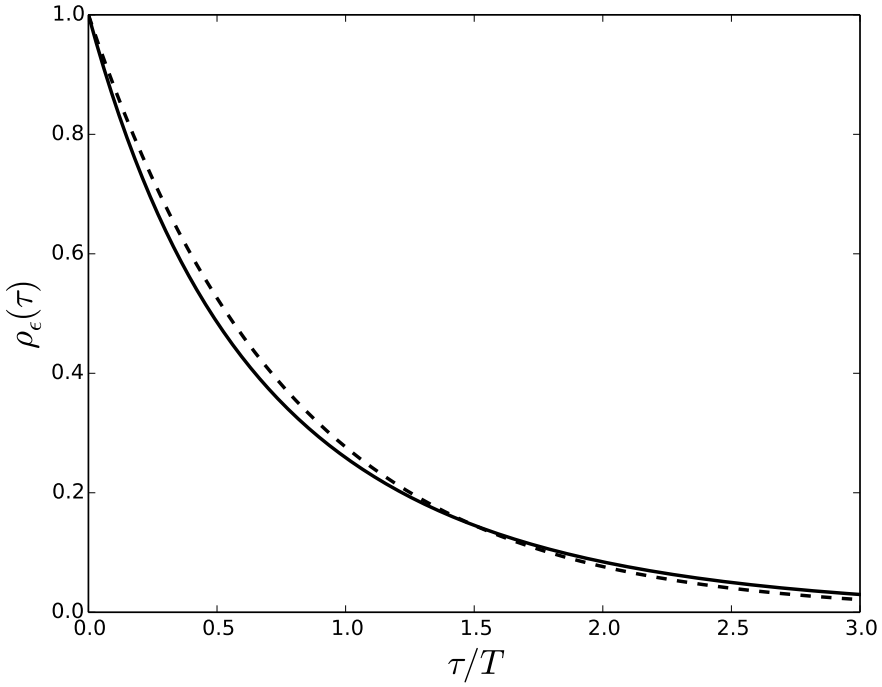

Figure 76: True autocorrelation of the process ϵ (solid line), compared to an exponential autocorrelation function with correlation time $\frac{7}{9}T$ (dashed line).

Coming back to Eq. 325,

$$\mathrm{Var}\left(X(t) + X(t+\tau)\right) = 2\sigma^2\left(1 + e^{-\frac{\tau}{T}}\right) \tag{331}$$

and (from Eq. 323)

$$\left\langle e^{X(t)+X(t+\tau)} \right\rangle = e^{\sigma^2 e^{-\frac{\tau}{T}}} \tag{332}$$

Finally,

$$R_\epsilon(\tau) = \langle\epsilon\rangle^2 \left[e^{\sigma^2 e^{-\frac{\tau}{T}}} - 1\right] \tag{333}$$

and the autocorrelation function $\rho_\epsilon(\tau) = \frac{R_\epsilon(\tau)}{\mathrm{Var}(\epsilon)}$ is

$$\begin{aligned} \rho_\epsilon(\tau) &= \frac{\langle\epsilon\rangle^2}{\langle\epsilon^2\rangle - \langle\epsilon\rangle^2}\left[e^{\sigma^2 e^{-\frac{\tau}{T}}} - 1\right] \\ &= \frac{1}{e^{\sigma^2} - 1}\left[e^{\sigma^2 e^{-\frac{\tau}{T}}} - 1\right] \end{aligned} \tag{334}$$

This converges towards $e^{-\frac{\tau}{T}}$ as $\sigma \to 0$. For $\sigma \sim 1$, this function is still close to a decreasing exponential with characteristic time $\sim \frac{7}{9}\,T$, as is shown on Fig. 76. We will thus consider this process as satisfactory, remembering that the autocorrelation function in real turbulence is only approximately exponential. We thus set $\frac{7}{9}\,T = \frac{1}{2}\,T_L$, or

$$T = \frac{9}{14}\,T_L \tag{335}$$

and T_L is taken by dimensional considerations as

$$T_L = \frac{u_{rms}^2}{\langle \epsilon \rangle} \tag{336}$$

Our stochastic model for diffusion is thus fully specified by its stochastic differential equation (Eq. 313), and by the expressions of its parameters in terms of the physical parameters of turbulence (Eq. 319 and 335). In order to re-inject this into the main PDF equation, we would need Lagrangian models (stochastic or deterministic) for the other unclosed terms. We will here demonstrate this for homogeneous turbulence.

9.3 APPLICATION TO HOMOGENEOUS TURBULENCE IN THE INTERSTELLAR MEDIUM

We call homogeneous turbulence a turbulence in which all statistical properties of the flow are independent of the position. Similarly turbulence is called stationary if all statistical quantities are independent of time. In the following, we will consider stationary homogeneous turbulence. If we take the example of the turbulence in the diffuse CNM, this is probably a good first approximation, excepted for the chemical stratification caused by the progressive extinction of the radiation field. We do not take this into consideration in the models presented in the next chapter, but this point will have to be refined in future developments.

We now show how the PDF formalism is simplified in a homogeneous case.

9.3.1 *Marginal PDF in the chemical composition-dissipation space only*

In a first step, we derive the general transport equation for the composition-dissipation PDF $f_{\mathbf{Y}\epsilon}$ (without the velocity). Indeed, we are ultimately only interested in the statistics of the thermo-chemical state of the fluid (e.g., what total column densities will we observe ?), it is thus natural to try to express the problem in terms of only the variables in which we are interested. We will see that in the general case, this results in more unclosed terms that need to be modeled, while in the homogeneous case, it can be done without loss of exactitude.

In order to eliminate the velocity variables from the PDF, we integrate Eq. 304 over the velocity space. We will treat each term separately. We have:

$$\int d^3\vec{u}\, \frac{\partial f_{\vec{U}\mathbf{Y}\epsilon}}{\partial t} = \frac{\partial}{\partial t}\left[\int d^3\vec{u}\, f_{\vec{U}\mathbf{Y}\epsilon}\right] = \frac{\partial f_{\mathbf{Y}\epsilon}}{\partial t} \tag{337}$$

$$\int d^3\vec{u}\, u_j \frac{\partial f_{\vec{U}\mathbf{Y}\epsilon}}{\partial x_j} = \frac{\partial}{\partial x_j}\left[\int d^3\vec{u}\, u_j\, f_{\vec{U}\mathbf{Y}\epsilon}\right] = \frac{\partial \left[\left\langle U_j \middle| \mathbf{Y} = \mathbf{y}, \epsilon = \varepsilon \right\rangle f_{\mathbf{Y}\epsilon}\right]}{\partial x_j} \tag{338}$$

For any quantity of the flow taking the form of a vector in the tridimensional space $\overrightarrow{Q}$,

$$\int d^3\vec{u}\,\frac{\partial}{\partial u_k}\left[\left\langle Q_k|\,\vec{U}=\vec{u},\mathbf{Y}=\mathbf{y},\epsilon=\varepsilon\right\rangle f_{\vec{U}\mathbf{Y}\epsilon}\right]=0 \tag{339}$$

For any quantity of the flow taking the form of a vector in the chemical space $\mathbf{Q}$,

$$\begin{aligned}\int d^3\vec{u}\,\frac{\partial}{\partial y_\beta}&\left[\left\langle Q_\beta|\,\vec{U}=\vec{u},\mathbf{Y}=\mathbf{y},\epsilon=\varepsilon\right\rangle f_{\vec{U}\mathbf{Y}\epsilon}\right]\\ &=\frac{\partial}{\partial y_\beta}\left[\int d^3\vec{u}\,\left\langle Q_k|\,\vec{U}=\vec{u},\mathbf{Y}=\mathbf{y},\epsilon=\varepsilon\right\rangle f_{\vec{U}\mathbf{Y}\epsilon}\right]\\ &=\frac{\partial}{\partial y_\beta}\left[\int d^3\vec{u}\,dq_k\,q_k\,f_{\vec{U}\mathbf{Y}Q\epsilon}\right]\\ &=\frac{\partial}{\partial y_\beta}\left[\langle Q_k|\,\mathbf{Y}=\mathbf{y},\epsilon=\varepsilon\rangle\,f_{\mathbf{Y}\epsilon}\right]\end{aligned} \tag{340}$$

And for any scalar quantity Q,

$$\begin{aligned}\int d^3\vec{u}\,\frac{\partial}{\partial \varepsilon}&\left[\left\langle Q|\,\vec{U}=\vec{u},\mathbf{Y}=\mathbf{y},\epsilon=\varepsilon\right\rangle f_{\vec{U}\mathbf{Y}\epsilon}\right]\\ &=\frac{\partial}{\partial \varepsilon}\left[\int d^3\vec{u}\,\left\langle Q|\,\vec{U}=\vec{u},\mathbf{Y}=\mathbf{y},\epsilon=\varepsilon\right\rangle f_{\vec{U}\mathbf{Y}\epsilon}\right]\\ &=\frac{\partial}{\partial \varepsilon}\left[\int d^3\vec{u}\,dq_k\,q_k\,f_{\vec{U}\mathbf{Y}Q\epsilon}\right]\\ &=\frac{\partial}{\partial \varepsilon}\left[\langle Q|\,\mathbf{Y}=\mathbf{y},\epsilon=\varepsilon\rangle\,f_{\mathbf{Y}\epsilon}\right]\end{aligned} \tag{341}$$

Using Eq. 337, 338, 339, 340, and 341, we can now write a transport equation for the marginal PDF $f_{\mathbf{Y}\epsilon}$:

$$\begin{aligned}\frac{\partial f_{\mathbf{Y}\epsilon}}{\partial t}+\frac{\partial\left[\langle U_j|\,\mathbf{Y}=\mathbf{y},\epsilon=\varepsilon\rangle\,f_{\mathbf{Y}\epsilon}\right]}{\partial x_j}=&\\ \frac{\partial}{\partial y_\beta}&\left[\left\langle\frac{\partial J_i^{(\beta)}}{\partial x_i}\middle|\,\mathbf{Y}=\mathbf{y},\epsilon=\varepsilon\right\rangle f_{\mathbf{Y}\epsilon}\right]\\ -\frac{\partial}{\partial y_\beta}&\left[\left\langle S^{(\beta)}\middle|\,\mathbf{Y}=\mathbf{y},\epsilon=\varepsilon\right\rangle f_{\mathbf{Y}}\right]\\ -\frac{\partial}{\partial \varepsilon}&\left[\left\langle\frac{D\epsilon}{Dt}\middle|\,\mathbf{Y}=\mathbf{y},\epsilon=\varepsilon\right\rangle f_{\mathbf{Y}\epsilon}\right]\end{aligned} \tag{342}$$

We see that in the general case, the equation for the PDF without the velocity results in an unclosed term for the turbulent transport, which then

need to be modeled. The chemical reaction rates remains exactly treated (the conditional average of $S^{(\beta)}$ is simply $S^{(\beta)}(\epsilon, \mathbf{y})$).

But for the homogeneous case, the turbulent transport term disappears (the PDF is already spatially constant) as we will now see.

9.3.2 *Simplification for homogeneous turbulence*

The only term in Eq. 342 involving the velocity fields – and that is now in unclosed form – is the turbulent advection term on the left-hand-side. In homogeneous turbulence, the statistical properties are independent of the position, and the turbulent advection term thus disappears:

$$\begin{aligned}\frac{\partial f_{\mathbf{Y}\epsilon}}{\partial t} = \frac{\partial}{\partial y_\beta}\left[\left\langle \frac{\partial J_i^{(\beta)}}{\partial x_i}\middle| \mathbf{Y}=\mathbf{y}, \epsilon=\varepsilon\right\rangle f_{\mathbf{Y}\epsilon}\right] \\ - \frac{\partial}{\partial y_\beta}\left[\left\langle S^{(\beta)}\middle| \mathbf{Y}=\mathbf{y}, \epsilon=\varepsilon\right\rangle f_{\mathbf{Y}\epsilon}\right] \\ - \frac{\partial}{\partial \varepsilon}\left[\left\langle \frac{D\epsilon}{Dt}\middle| \mathbf{Y}=\mathbf{y}, \epsilon=\varepsilon\right\rangle f_{\mathbf{Y}\epsilon}\right] \end{aligned} \quad (343)$$

First, the source terms for heat and chemical abundances only depends on the thermo-chemical state $\mathbf{Y}$ and the dissipation rate ϵ, so that

$$\left\langle S^{(\beta)}\middle| \mathbf{Y}=\mathbf{y}, \epsilon=\varepsilon\right\rangle = S^{(\beta)}(\mathbf{y}, \varepsilon) \quad (344)$$

So that our equation, after writing in exact form all terms that can be, becomes

$$\begin{aligned}\frac{\partial f_{\mathbf{Y}\epsilon}}{\partial t} = \frac{\partial}{\partial y_\beta}\left[\left\langle \frac{\partial J_i^{(\beta)}}{\partial x_i}\middle| \mathbf{Y}=\mathbf{y}, \epsilon=\varepsilon\right\rangle f_{\mathbf{Y}\epsilon}\right] \\ - \frac{\partial}{\partial y_\beta}\left[S^{(\beta)}(\mathbf{y}, \varepsilon) f_{\mathbf{Y}\epsilon}\right] \\ - \frac{\partial}{\partial \varepsilon}\left[\left\langle \frac{D\epsilon}{Dt}\middle| \mathbf{Y}=\mathbf{y}, \epsilon=\varepsilon\right\rangle f_{\mathbf{Y}\epsilon}\right] \end{aligned} \quad (345)$$

We will now plug in our stochastic model of dissipation. For simplicity, we neglect the molecular diffusion term. The Lagrangian evolution of the thermo-chemical state $\mathbf{Y}$ is then simply

$$d\mathbf{Y} = \mathbf{S}(\mathbf{Y}, \epsilon)\, dt$$

Including our model for dissipation, the Lagrangian evolution of the full state of a fluid element ($\mathbf{Y}$ and ϵ) is governed by the system of stochastic differential equations

$$\begin{cases} d\mathbf{Y} = \mathbf{S}(\mathbf{Y}, \epsilon)\, dt \\ d\epsilon = -\left[\frac{\epsilon}{T}\left(\ln\left(\frac{\epsilon}{\langle\epsilon\rangle}\right) - \frac{\sigma^2}{2}\right)\right] dt + \epsilon\sqrt{\frac{2\sigma^2}{T}} dW_t \end{cases} \tag{346}$$

Here, all the physics and chemistry of the gas apart from turbulence is contained in the generalized source term $\mathbf{S}$.

The Fokker-Planck equation associated to the multi-variate stochastic process is then (see Sect. 4.3.4)

$$\frac{\partial f_{\epsilon\mathbf{Y}}}{\partial t} = -\frac{\partial}{\partial y_\beta}\left[S_\beta(\epsilon, \mathbf{y})\, f_{\epsilon\mathbf{Y}}\right] + \frac{\partial}{\partial \varepsilon}\left[\frac{\varepsilon}{T}(\ln(\frac{\varepsilon}{\langle\epsilon\rangle}) - \frac{\sigma^2}{2})\, f_{\epsilon\mathbf{Y}}\right] + \frac{\partial^2}{\partial \varepsilon^2}\left[\varepsilon^2 \frac{\sigma^2}{T} f_{\epsilon\mathbf{Y}}\right] \tag{347}$$

which gives us back our PDF equation with the unclosed term replaced according to our stochastic model. We see that the result of using a stochastic model is the apparition of a second derivative in the equation, that breaks the conservation of volume in phase space. This represents the progressive loss of information in a chaotic system. If our closure model had been purely deterministic, the equation would have remained a first order partial differential equation.

For a non-trivial chemical network, the dimension of this equation is high, making usual numerical methods unusable. We will thus present a Monte Carlo method of solution.

9.4 A LAGRANGIAN MONTE CARLO METHOD

As the final PDF equation describes a multivariate stochastic process, the idea proposed by Pope [1985] is to perform direct Monte Carlo simulation of the underlying process. For the stationary solution of Eq. 347, the computation of a single long enough trajectory is sufficient.

We simulate the process using the Euler-Maruyama algorithm (which is the simplest simulation algorithm for continuous stochastic processes). This method follows the idea of the Euler method: at each time step, an increment is computed for all variables, using a first order approximation and using the stochastic differential equation defining the process. The increment of the Wiener process is computed by taking advantage of the fact that $W(t_2) - W(t_1)$ is independent of $W(t)$ for $t \leq t_1$ and is a gaussian variable of mean 0 and variance $t_2 - t_1$.

If we have the simple stochastic differential equation

$$dx = a(x)\, dt + b\, dW \tag{348}$$

and want to compute one timestep of length Δt starting from the initial condition $x(0)$, we generate a gaussian random variable θ with mean 0 and variance Δt, and compute

$$x(\Delta t) = x(0) + a(x(0))\,\Delta t + b\,\theta \tag{349}$$

This procedure is applied to our process defined by Eq. 346, and a trajectory is computed until the statistical quantity of interest have converged.

CONCLUSIONS

This resolution method is applied in the next chapter to two simple models of the diffuse CNM, with the goal to compute the distribution of gas temperatures in this medium, and the average excitation of H_2. The results are compared to FUSE observations of H_2.

Before proceeding to these applications, two comments on the possibility of generalization for this model are necessary:

- We considered here that the only effect of the dissipation rate is to heat the gas. Previous models of dissipative structures (see Sect. 3.3.2) have found that non-thermal effects such as ion-neutral drift can be important. This can be integrated in this formalism by either relating the drift velocity to the instantaneous dissipation rate ϵ (if we assume that ambipolar diffusion occurs in the same structures as viscous dissipation, as is done in Godard et al. 2009), or by having a second stochastic process for the ambipolar diffusion dissipation rate. This second case requires statistical constraints on the Lagrangian evolution of the different dissipation terms (especially their correlation). Such statistics could be obtained from numerical simulations.

- The general case presented in the first part of this chapter would allow to treat in a same model the chemistry triggered by turbulent dissipation, and the turbulent transport of species across UV-induced chemical frontiers (such as the H/H_2 transition). This will be done in a future development of this work.

10

APPLICATION TO THE EXCITATION OF H2 IN THE INTERSTELLAR MEDIUM

In this chapter, we apply the PDF method presented in the last chapter to two simple models. For those first applications, we do not consider the chemical effects of the dissipation fluctuations, but only follow the thermal state of the gas and the excitation of H_2. We are interested in diffuse CNM, either atomic or diffuse molecular (in the sense that only hydrogen is in molecular form).

As the stochastic diffusion process is independent of the other variables, we first describe the implementation of its simulation and show numerical verifications of the properties of the process (Sect. 10.1). We then present two models: one concerning the diffuse atomic CNM, with the physics taken from Pan and Padoan [2009] and Wolfire et al. [2003] (see Sect. 10.2), and one concerning diffuse molecular gas to investigate the effect of H_2 cooling during dissipation bursts, as well as the signature that those bursts leave on the observable H_2 excitation (Sect. 10.3).

10.1 SIMULATION AND TEST OF THE STOCHASTIC DIFFUSION PROCESS

The method consists in simulating the evolution of a multivariate stochastic process, defined by the system of stochastic differential equations Eq. 346. However, as the stochastic equation for the dissipation rate ϵ is independent from the other variables, it is possible to compute it separately. We show here the results of this computation and verify that the expected properties of the process are indeed observed.

10.1.1 *Physics and algorithm*

The stochastic dissipation process is

$$d\epsilon = -\left[\frac{\epsilon}{T}\left(\ln\left(\frac{\epsilon}{\langle\epsilon\rangle}\right) - \frac{\sigma^2}{2}\right)\right]dt + \epsilon\sqrt{\frac{2\sigma^2}{T}}\,dW_t \tag{350}$$

We need to relate the parameters of this process to observed properties of ISM turbulence. We assume a cloud size of the order of 1 pc. The observed velocity dispersion σ_V at scale 1 pc is usually in the range $1-3\,\mathrm{km.s^{-1}}$ (Heiles and Troland 2005). We thus take σ_V as the one-dimensional rms velocity of

the turbulence in the diffuse cloud. The full rms velocity is thus $u_{rms} = \sqrt{3}\,\sigma_V$. Dimensionally, the average dissipation rate is then

$$\begin{aligned}
\langle\epsilon\rangle &= \frac{u_{rms}^3}{L} \\
&= 3\sqrt{3}\,\frac{\left(1\,\mathrm{km.s^{-1}}\right)^3}{1\,\mathrm{pc}}\left(\frac{\sigma_V}{1\,\mathrm{km.s^{-1}}}\right)^3 \\
&= \frac{3\sqrt{3}}{3.087}\,10^{-3}\left(\frac{\sigma_V}{1\,\mathrm{km.s^{-1}}}\right)^3 \mathrm{cm^2.s^{-3}} \\
&= 1.68\times10^{-3}\left(\frac{\sigma_V}{1\,\mathrm{km.s^{-1}}}\right)^3 \mathrm{erg.s^{-1}.g^{-1}} \qquad (351)
\end{aligned}$$

We note that this is equivalent to

$$\rho\,\langle\epsilon\rangle = 3.43\times10^{-27}\left(\frac{\sigma_V}{1\,\mathrm{km.s^{-1}}}\right)^3 n_\mathrm{H}\,\mathrm{erg.s^{-1}.cm^{-3}}, \qquad (352)$$

for atomic gas, which, for typical densities in the range $30-100\,\mathrm{cm^{-3}}$, is very close to the value used in the models of Godard et al. [2009] of $2\times10^{-25}\,\mathrm{erg.s^{-1}.cm^{-3}}$.

All parameters of our model of dissipation thus only depend on σ_V and ν:

$$\langle\epsilon\rangle = 1.68\times10^{-3}\left(\frac{\sigma_V}{1\,\mathrm{km.s^{-1}}}\right)^3 \mathrm{erg.s^{-1}.g^{-1}} \qquad (353)$$

$$\sigma^2 = 0.145\,\ln\left(\frac{9\,\sigma_V^4}{\nu\,\langle\epsilon\rangle}\right) - 0.085 \qquad (354)$$

$$T = 1.9\,\frac{\sigma_V^2}{\langle\epsilon\rangle}\,\mathrm{s} \qquad (355)$$

The real viscosity of a gas depends on its temperature. For atomic hydrogen, Kay and Laby [1966] give for the dynamic viscosity $\rho\nu = 6\times10^{-6}\,T^{\frac{1}{2}}\,\mathrm{g.cm^{-1}.s^{-1}}$. While in usual laboratory turbulence, the temperature and heat capacity of the fluid are such that the effect of the bursts of turbulent dissipation heating is week or negligible, interstellar turbulence has the specificity that it occurs in a very low temperature (below 100 K) and very low density ($\sim 100\,\mathrm{cm^{-3}}$) gas, in which, as we will see soon, the intermittent bursts of dissipation can heat up the gas to several hundreds of Kelvins. This will lead to an increase of the viscosity in the dissipative structures. This is not accounted for by usual models of turbulence, which were designed for the usual laboratory flows. In a first approach, we will neglect this effect, and as the viscosity only enters our model through a logarithm, we will assume a constant value, taking the value at 100 K.

We thus take $\nu = 2.58\times10^{19}\left(\frac{1\,\mathrm{cm^{-3}}}{n_H}\right)\,\mathrm{cm^2.s^{-1}}$, so that our model of turbulent dissipation is only parametrized by σ_V, and the gas by its density

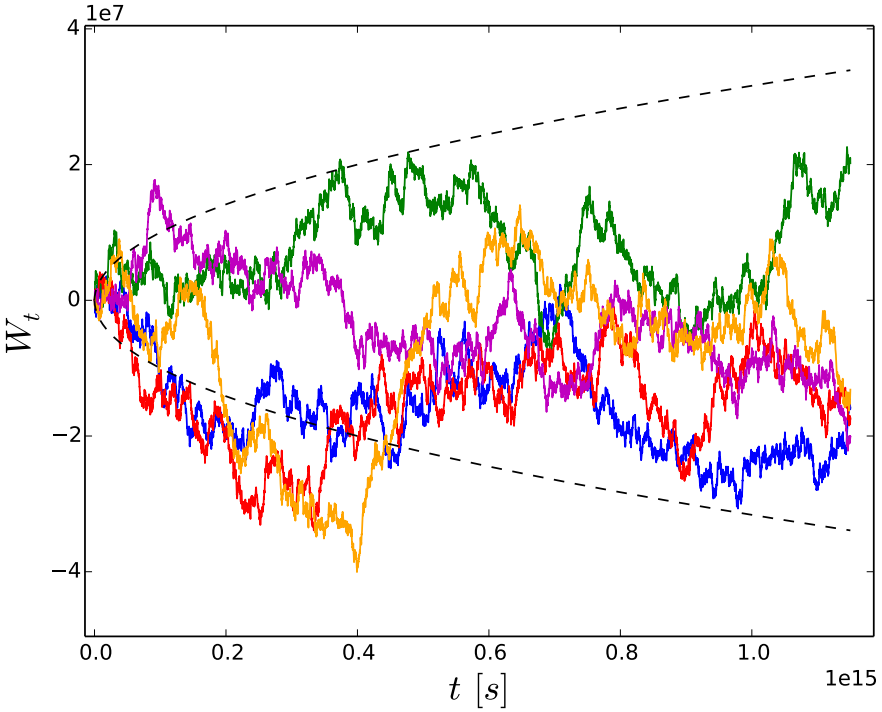

Figure 77: Five simulated trajectories of a standard Wiener process, starting at 0. The dashed lines show the expected evolution of the one-standard-deviation interval.

n_H. This gives a Reynolds number of Re $\sim 2 \times 10^6$ for $\sigma_V = 1\,\mathrm{km.s^{-1}}$ and $n_\mathrm{H} = 100\,\mathrm{cm^{-3}}$. The corresponding Kolmogorov length scale and timescale are $\eta = 3.79\,\mathrm{AU}$ and $\tau_\eta = 392\,\mathrm{yr}$ (see Chap. 3 for the scaling relations).

More generally,

$$\mathrm{Re} = 2.1 \times 10^4 \left(\frac{n_\mathrm{H}}{1\,\mathrm{cm^{-3}}}\right)\left(\frac{\sigma_V}{1\,\mathrm{km.s^{-1}}}\right) \tag{356}$$

$$\eta = 1.20 \times 10^2 \left(\frac{1\,\mathrm{cm^{-3}}}{n_H}\frac{1\,\mathrm{km.s^{-1}}}{\sigma_V}\right)^{\frac{3}{4}}\ \mathrm{AU} \tag{357}$$

$$\tau_\eta = 3.92 \times 10^3 \left(\frac{1\,\mathrm{cm^{-3}}}{n_H}\right)^{\frac{1}{2}}\left(\frac{1\,\mathrm{km.s^{-1}}}{\sigma_V}\right)^{\frac{3}{2}}\ \mathrm{yr} \tag{358}$$

We can here verify the validity of the fluid approximation, using a $\mathrm{H}-\mathrm{H}$ collison cross section $\sigma_{\mathrm{H}-\mathrm{H}} = 5.5 \times 10^{-15}\mathrm{cm}^2$, we find a mean free path of the order of $10^{-1}\,\mathrm{AU}$, so that we can consider a fluid element smaller than the Kolmogorov dissipative scale, but larger than the mean free path. The small separation between the scales indicate that the fluid description is only barely correct at the scale of interest. This should be investigated in more details later.

We can now rewrite our model parameters as functions of σ_V and n_{H} only:

$$\langle \epsilon \rangle = 1.68 \times 10^{-3} \left(\frac{\sigma_V}{1\,\mathrm{km.s^{-1}}} \right)^3 \mathrm{erg.s^{-1}.g^{-1}} \tag{359}$$

$$\sigma^2 = 1.36 + 0.145 \ln \left(\frac{n_{\mathrm{H}}}{1\,\mathrm{cm^{-3}}} \frac{\sigma_V}{1\,\mathrm{km.s^{-1}}} \right) \tag{360}$$

$$T = 1.15 \times 10^{13} \left(\frac{1\,\mathrm{km.s^{-1}}}{\sigma_V} \right) \mathrm{s} \tag{361}$$

In order to perform the computations on a dimensionless quantity with limited variations, we actually follow $X = \ln\left(\frac{\epsilon}{\langle\epsilon\rangle}\right)$. We recall that this quantity follows the stochastic process

$$dX = -(X + \frac{\sigma^2}{2}) \frac{dt}{T} + \sqrt{\frac{2\,\sigma^2}{T}}\, dW_t \tag{362}$$

As described in Sect. 9.4, we simulate the evolution of this process over a period of time long enough to give its stationary statistical properties. For each time step of size Δt, we compute $X(t + \Delta t)$ according to the Euler-Maruyama method as

$$X(t + \Delta t) = X(t) - (X + \frac{\sigma^2}{2}) \frac{\Delta t}{T} + \sqrt{\frac{2\,\sigma^2}{T}}\, \theta$$

where θ is a random gaussian variable with mean zero and variance Δt. θ is generated using the Ziggurat method of Marsaglia and Tsang [2000] and the fast implementation given by the authors.

Finally, the choice of the time step is not straightforward. Smoothness conditions are not usable as a diffusion process is not differentiable anywhere. In a first approach, we relate it to the characteristic time of the process T, and take $\Delta t = T/100$.

Note that the Euler-Maruyama method has a precision which is generally of the order of $\Delta t^{\frac{1}{2}}$, but that for a process where the diffusion coefficient is constant (the coefficient of the dW_t term in the stochastic differential equation), its precision becomes of the order of Δt. Indeed, the Milstein method, which is of order Δt, reduces to the Euler-Maruyama method for such processes. This is why we simulate the process X rather than ϵ.

As a simple illustration of the method, Fig. 77 shows the simulated trajectories of a standard Wiener process (also called Brownian motion).

10.1.2 *Numerical test*

We now study the properties of the simulated process for ϵ and verify that they correspond to the expected theoretical properties described in the previous chapter.

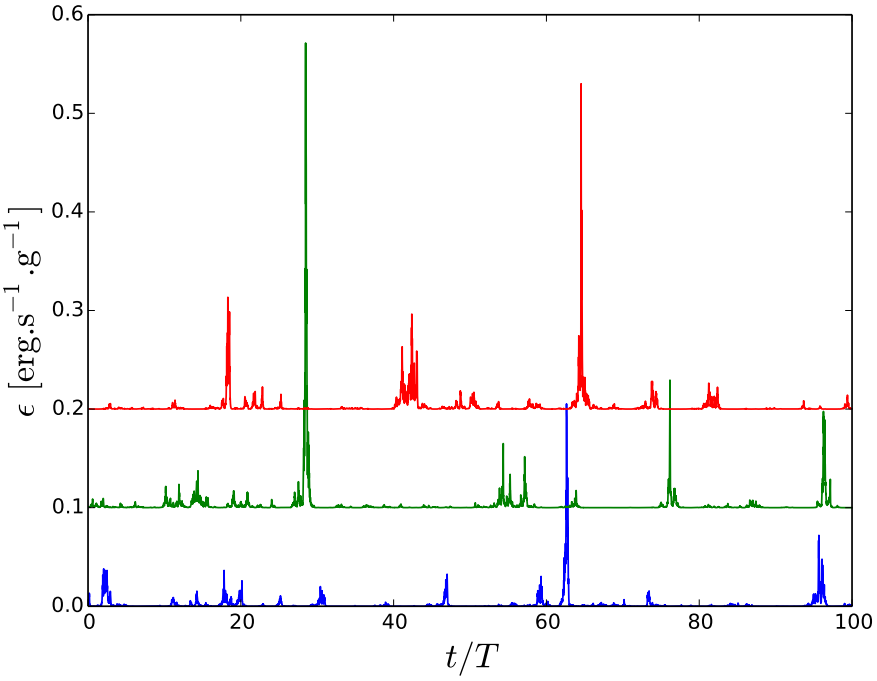

Figure 78: Three simulated trajectories of the stochastic dissipation process. The curves have been shifted from each other for a better visibility.

Fig. 78 shows a few simulated trajectories of the process. We see the strong intermittency with rare strong bursts of dissipation.

According to our model process, the PDF of ϵ during our simulated trajectories is expected to be:

$$f_\epsilon(\varepsilon) = \frac{1}{\varepsilon\,\sigma\,\sqrt{2\pi}}\,\exp\left(-\frac{\left(\ln(\frac{\varepsilon}{\langle\epsilon\rangle}) + \frac{\sigma^2}{2}\right)^2}{2\,\sigma^2}\right)$$

We show the simulated PDF after different numbers of time steps N (colored solid lines), with the true expected PDF (black dashed line) on Fig. 79. We see a quick convergence for the central part ($N = 10^5$ is enough), while longer simulation times allow to sample more extreme events. $N = 10^7$ allows to sample correctly events with dissipation rates up to $\epsilon \gtrsim 10^3\,\langle\epsilon\rangle$.

Fig. 80 shows the convergence of the mean and the variance of the process towards their theoretical values. As the process is strongly intermittent with rare extreme events, the variance converges slower than the mean (higher order moments are more sensitive to extreme events).

These properties are only one-time statistics and thus do not give any information about the temporal behavior of our process. The last quantity we need to verify is the time autocorrelation function $\rho_\epsilon(\tau)$. The theoretical prediction is given by Eq. 334. Fig. 81 shows the convergence of the autocorrelation function towards the theoretical prediction as the length of the simulation is increased.

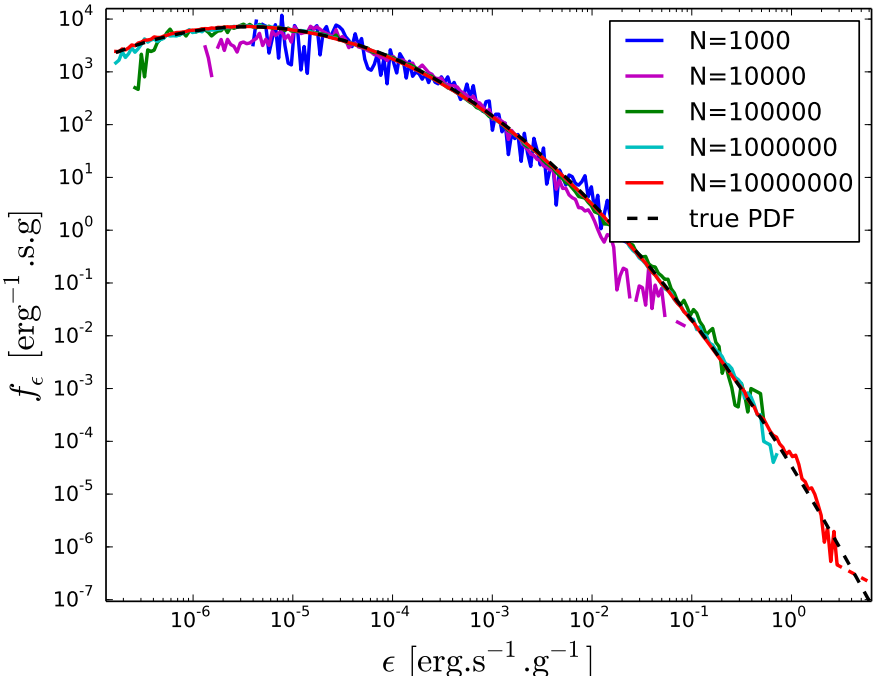

Figure 79: PDFs of the dissipation rate, computed by simulating the stochastic process for N time steps (colored solid lines), compared with the theoretical PDF (black dashed line).

Our simulation of the dissipation process thus fulfills all of our statistical constraints as expected.

10.2 DIFFUSE ATOMIC ISM: TEMPERATURE DISTRIBUTION

As a test case and a first application, we start with a model of the diffuse atomic ISM. As not much chemistry occurs in this medium, we only follow the thermal state of the gas given by its temperature T_{gas} or kinetic thermal energy e (volumic energy density). For this type of medium, we use the physics described in Wolfire et al. [2003] and the analytical approximate expressions given in this reference, as described below.

10.2.1 *The model*

We assume that the cooling properties are represented by known (volumic) cooling and heating functions ($\Lambda(T_{\text{gas}})$ and $\Gamma(T_{\text{gas}})$, where T_{gas} is the gas temperature) representing all processes apart from turbulent dissipation. So that the conservation equation for the gas thermal energy $e(\overrightarrow{x}, t)$ is:

$$\frac{De}{Dt} = \rho\,\epsilon + \Gamma(T_{\text{gas}}) - \Lambda(T_{\text{gas}}) \tag{363}$$

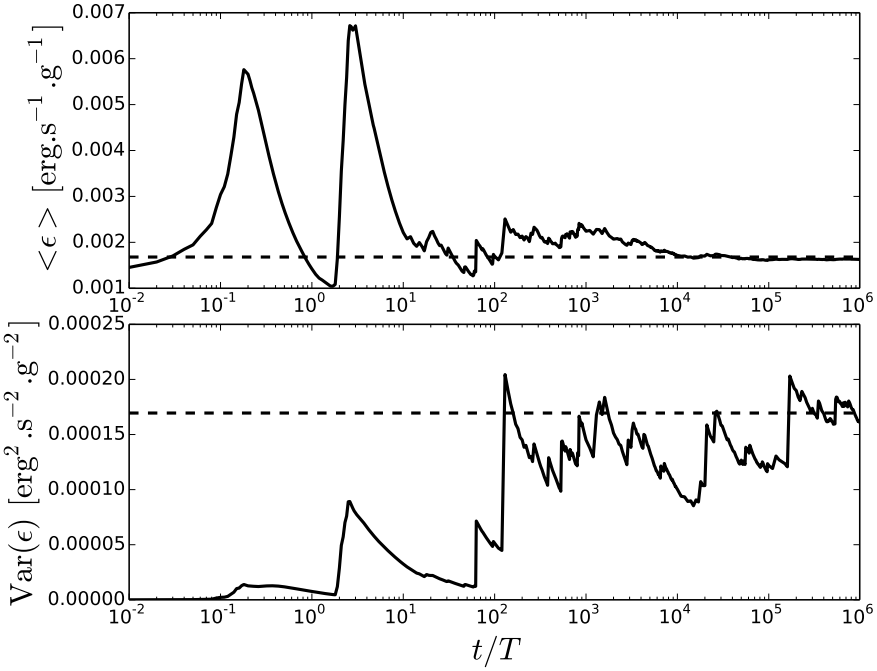

Figure 80: Convergence of the mean and the variance of the dissipation rate ϵ in a simulation. The dashed lines show the theoretical values.

where ϵ is the local dissipation rate of the turbulence (per unit mass) and $\rho = n_{\mathrm{H}}\,\mu\,m_{\mathrm{H}}$ is the gas mass density (n_{H} is the number density of H nuclei, and $\mu = 1.4$ the mean mass per H nucleus, taking into account the additional presence of helium).

We note $C(T_{\mathrm{gas}}) = \Lambda(T_{\mathrm{gas}}) - \Gamma(T_{\mathrm{gas}})$ the net cooling function. As the relation between e and T_{gas} is known (see below), we will write $C(e)$ instead of $C(T_{\mathrm{gas}})$. Our conservation equation is thus:

$$\frac{De}{Dt} = \rho\,\epsilon - C(e) \tag{364}$$

We have neglected molecular diffusion, as we expect the cooling to be dominated by radiative processes. We recall that this equation models the Lagrangian evolution for a fluid element in homogeneous and stationary turbulence. In the absence of fluctuations of the turbulent heating rate, everything remains constant.

10.2.2 *Net cooling function*

10.2.2.1 *Heating processes*

We take into account photoelectric heating and cosmic rays heating, although the first mechanism is expected to be dominant in our situation.

The cosmic ray heating rate per unit volume is taken to be:

$$\Gamma_{cr} = 0.8 \cdot 10^{-27}\, n_{\mathrm{H}}\ \mathrm{erg.cm^{-3}}.s^{-1} \tag{365}$$

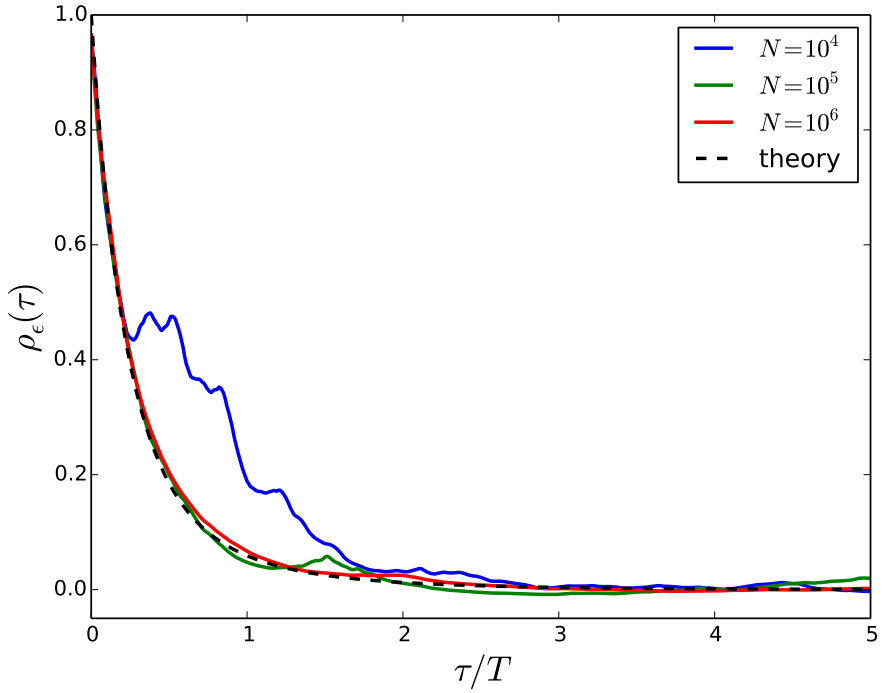

Figure 81: Autocorrelation functions for the simulated trajectory of the dissipation process for three different numbers of time step N (colored solid lines), compared with the theoretical prediction (black dashed line).

following Pan and Padoan [2009].

For the photoelectric heating rate per unit volume, we use the expression from Wolfire et al. [2003]:

$$\Gamma_{pe} = 1.3 \times 10^{-24}\, n_{\rm H}\, G_0\, \epsilon_{pe} - 4.65 \times 10^{-30}\, T_{\rm gas}^{0.94} \left(\frac{G_0 T_{\rm gas}^{1/2}}{n_e \phi_{PAH}}\right)^{\frac{0.74}{T^{0.068}}} n_e\, \phi_{PAH}\, n_{\rm H} \ \text{erg.cm}^{-3}.s^{-1}, \quad (366)$$

with

$$\epsilon_{pe} = \frac{4.9 \times 10^{-2}}{1 + 4 \times 10^{-3}\, (G_0\, T_{\rm gas}^{1/2} / n_e\, \phi_{PAH})^{0.73}} + \frac{3.7 \times 10^{-2}\, (T_{\rm gas}/10^4)^{0.7}}{1 + 2 \times 10^{-4}\, (G_0\, T_{\rm gas}^{1/2} / n_e\, \phi_{PAH})}, \quad (367)$$

$\phi_{PAH} = 0.5$ (efficiency parameter for recombination with PAHs), and

$$n_e = 2.4 \times 10^{-3} \left(\frac{T_{\rm gas}}{100\ \text{K}}\right)^{1/4} \left(\frac{G_0}{1.7}\right)^{1/2} {\phi_{PAH}}^{-1}\ \text{cm}^{-3}. \quad (368)$$

We use $G_0 = 1.7$ for our standard model (in Habing units; the value 1.7 is the standard ISM value according to Draine 1978).

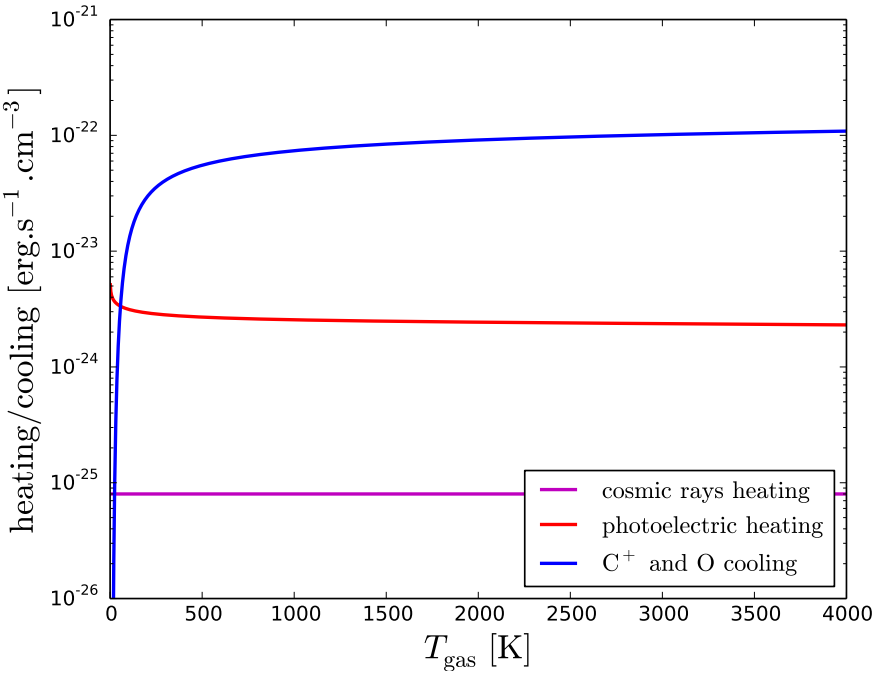

Figure 82: Heating and cooling curves for an atomic gas with density $n_{\rm H} = 100\,{\rm cm}^{-3}$.

The instantaneous turbulent heating rate is computed following the stochastic process model described above, so that it fluctuates over time with strong intermittency.

10.2.2.2 *Cooling processes*

In an atomic gas, the cooling is dominated by C^+ and O lines, for which we use the formula given by Wolfire et al. [2003]. The cooling rate per unit volume is then:

$$\Lambda_{C^+ + O} = 5.4 \times 10^{-27} \left(\frac{T_{\rm gas}}{100\,{\rm K}}\right)^{0.2} e^{-1.5\left(\frac{100\,{\rm K}}{T_{\rm gas}}\right)} n_H^2 \ {\rm erg.cm^{-3}}.s^{-1} \tag{369}$$

Fig. 82 summarizes the variations of the heating and cooling rates with temperature. Note that the cooling function is very flat at high temperatures. The heating from turbulent dissipation is not included as it is stochastic and intermittent, but its average values for $\sigma_V = 1\,{\rm km.s^{-1}}$ is $3.43 \times 10^{-25}\,{\rm erg.s^{-1}.cm^{-3}}$, which is negligible in comparison with photoelectric heating.

10.2.3 *Gas heat capacity*

As we define e as being only the kinetic thermal energy, it is simply related to the number density of particle n through the heat capacity:

$$c = \frac{3}{2} n\, k \tag{370}$$

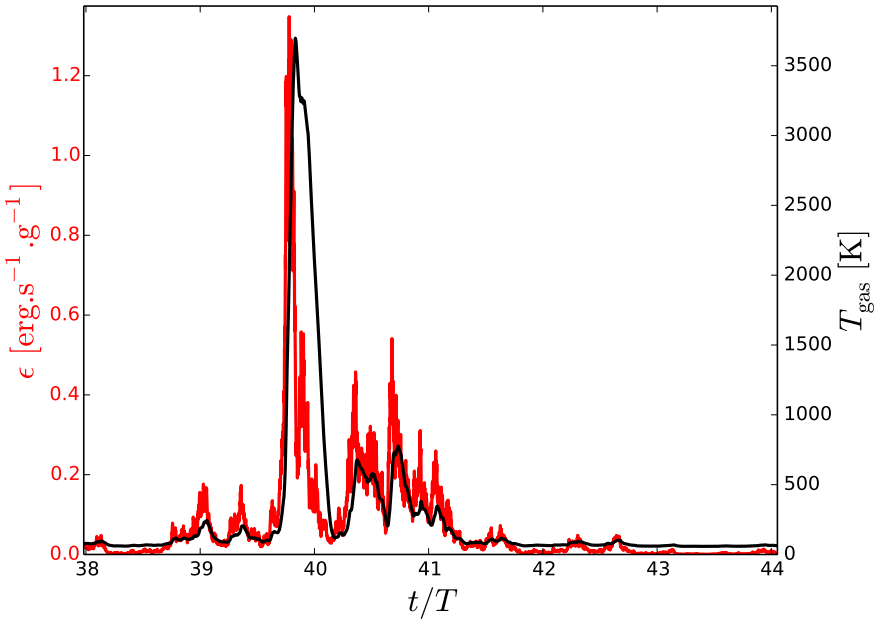

Figure 83: Simultaneous evolution of the dissipation rate (red) and the gas temperature (black) during an extreme dissipation event. Model with $n_{\rm H} = 100\,{\rm cm}^{-3}$ and $\sigma_V = 2\,{\rm km.s}^{-1}$.

The relation between the gas temperature and the thermal energy per unit volume is thus:

$$e = \frac{3}{2} n\, k\, T_{\rm gas} \quad \text{and} \quad T_{\rm gas} = \frac{2\,e}{3\,n\,k} \tag{371}$$

For our atomic gas, $n = 1.1\, n_{\rm H}$, to account for helium.

10.2.4 *Results*

We now present the results of this model. The simultaneous evolution of the dissipation rate ϵ and the gas temperature $T_{\rm gas}$ are computed, and the statistics are computed along the trajectory.

Fig. 83 shows the evolution of the two variables during an extreme dissipation event. The thermal state of the gas is kept out of equilibrium during this event, as is shown by the fact that the temperature peak is delayed compared to the dissipation peak (which means that the temperature does not have time to reach its equilibrium value at the peak dissipation rate), and by the fact that the cool down phase is slower than the fall of the dissipation rate after the peak. The delay of the peak is of the order of a few tenth of the dissipation peak duration, while the duration of the temperature peak is of the order of a few times the duration of the dissipation peak. The goal of this model is to capture this kind of out-of-equilibrium effects, while if equilibrium were assumed all statistics could be immediately derived from the dissipation PDF as done in Pan and Padoan [2009].

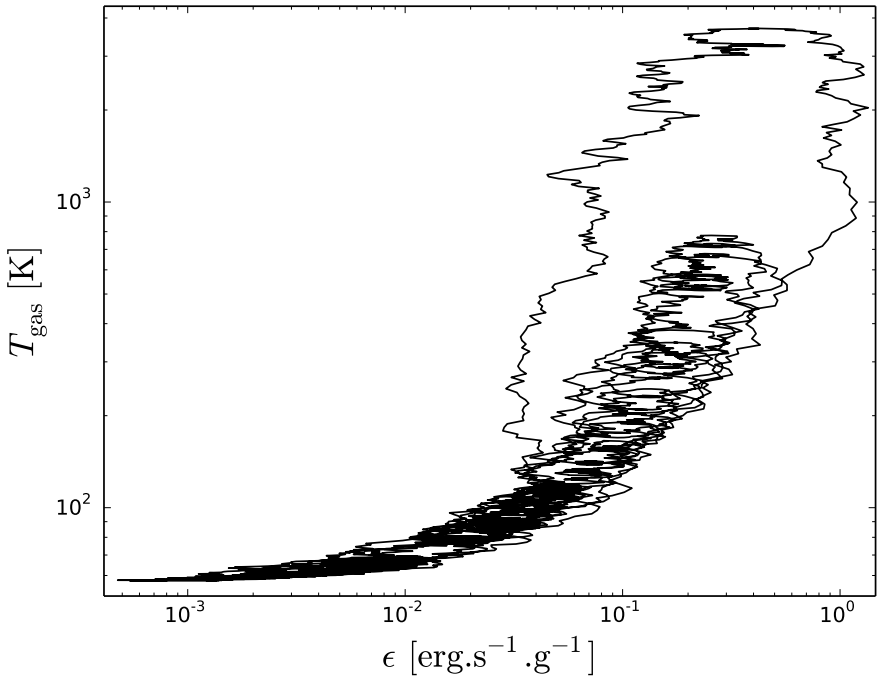

Figure 84: A short segment of trajectory drawn in the state space and including the extreme dissipation event visible on Fig. 83.

However, as the duration of the temperature peak remains of the same order as the dissipation peak, we can expect that these out-of-equilibrium effects will not result in differences larger than a factor of a few. As seen on Fig. 83, the duration of extreme dissipation peaks is of the order of $10^{-1}\,T$, and T is of the order of the large-scale timescale of the turbulence T_L. Those extreme events correspond to the fluid element going through a dissipative structure. Their duration should thus correspond to the time spent by the fluid element inside the dissipative structure. In incompressible hydrodynamic turbulence, it has been shown that particles are trapped in the vortices for about ten periods (Biferale et al. 2005, 2006), or about $10\,\tau_\eta$ where τ_η is the Kolmogorov-scale timescale. The usual scalings give $\tau_\eta \sim \mathrm{Re}^{-1/2}\,T_L$. For a Reynolds number of 10^7, this gives $\tau_\eta \sim 10^{-4}\,T_L$, so that strong dissipation events should last of the order of $10^{-3}\,T_L$. Our stochastic Lagrangian model of the dissipation process thus does not account properly for the timescales of the intermittency. This means that the time autocorrelation function of the dissipation rate is not a sufficient constraint as it does not reflect the time properties of strong dissipation events. It will need to be refined, by extracting Lagrangian trajectories of the dissipation rate from numerical simulations of turbulence and using their statistics as constraints for our stochastic model. In addition, this could be done for more general turbulence (supersonic and/or magnetized). A better stochastic model would probably result in stronger out-of-equilibrium effects, as the dissipation bursts would have shorter timescales.

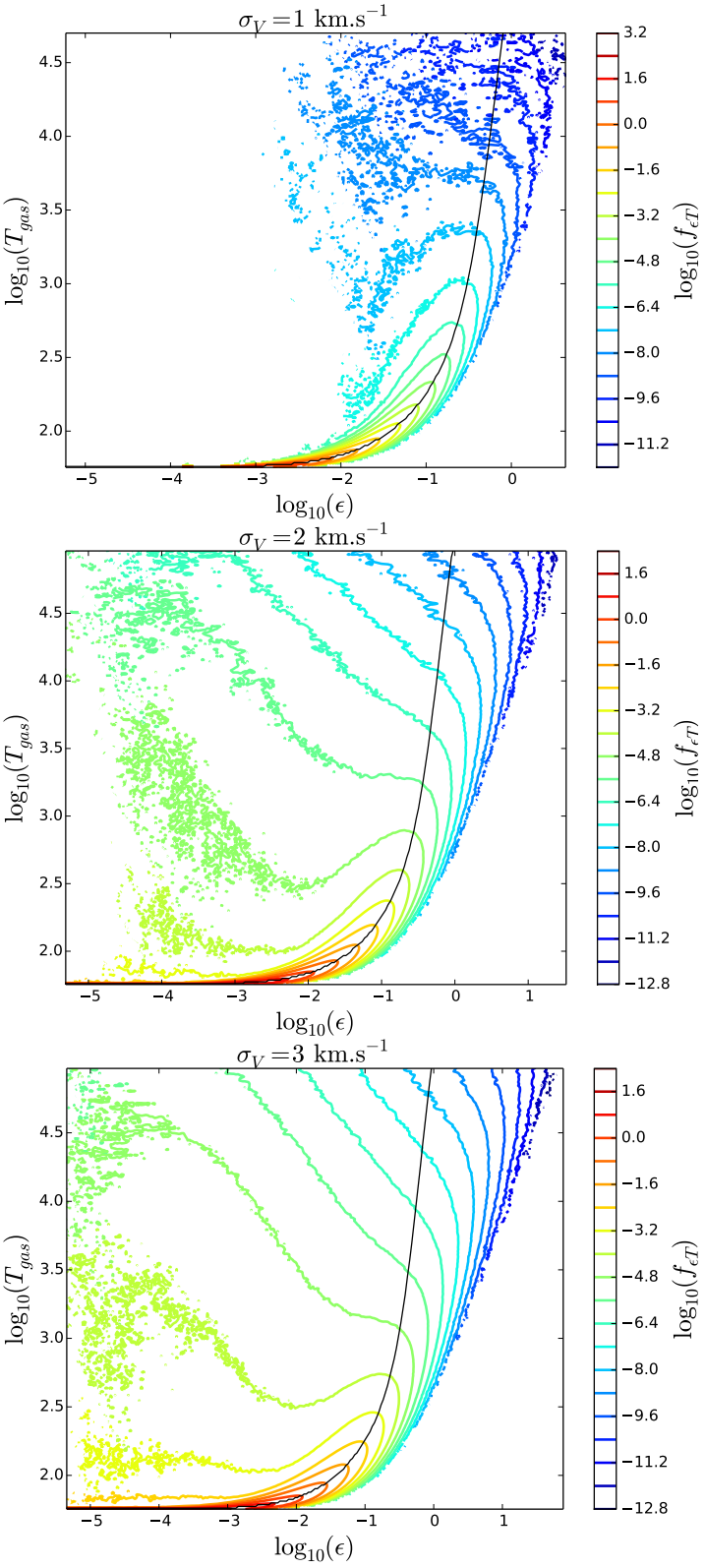

Figure 85: Contour plots of the joint PDF of ϵ and T_{gas} for three different turbulence intensities (controlled by σ_V), for gas at $n_H = 100\,\text{cm}^{-3}$. The solid black line shows the equilibrium temperature at constant turbulent dissipation rate ϵ.

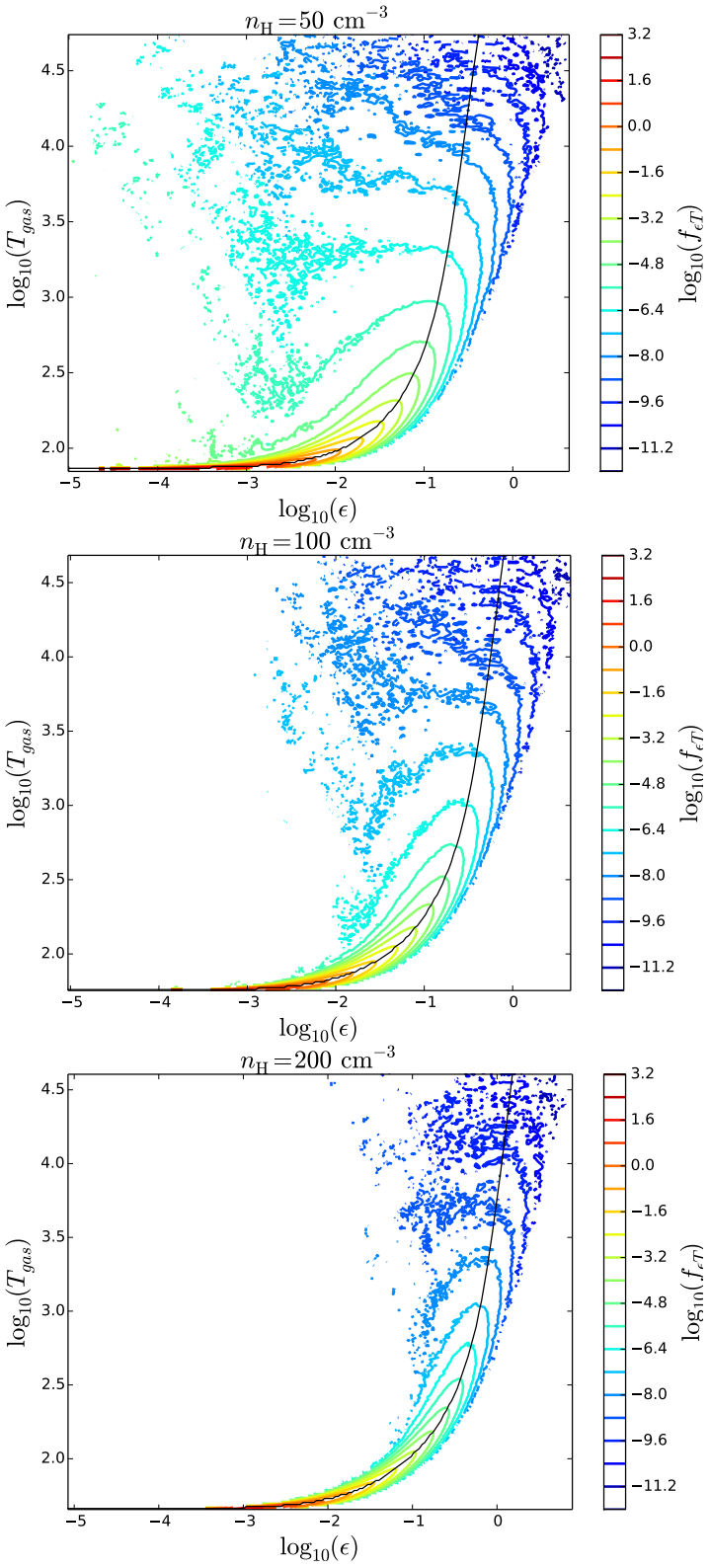

Figure 86: Contour plots of the joint PDF of ϵ and $T_{\rm gas}$ for three different gas densities, for a turbulent velocity dispersion $\sigma_V = 1\,{\rm km.s}^{-1}$. The solid black line shows the equilibrium temperature at constant turbulent dissipation rate ϵ.

The trajectories can be plotted in the 2D state space ($\epsilon - T_{\rm gas}$), as shown on Fig. 84. Strong dissipation events appear as counter-clockwise loops as the temperature evolution lags behind the dissipation rate evolution. The fluid element is thus below its equilibrium temperature during the first part of the burst, and above it during the second phase. The accumulation of the trajectory in some regions gives an idea of the joint-PDF of the two variables, and we expect it to be very peaked around the equilibrium temperature for low temperatures as this region correspond to relatively quiescent parts of the trajectory devoid of any strong dissipation events, and we expect it to become more spread out in the high temperature region, which is populated by the short bursts of dissipation.

Those joint-PDF of the dissipation rate ϵ and the gas temperature $T_{\rm gas}$ computed from the simulations are displayed of Fig. 85 and 86 as contour plots. Figure 85 shows the influence of the turbulent velocity dispersion σ_V on the PDF for a constant gas density $n_{\rm H} = 100\,{\rm cm}^{-3}$, while Fig. 86 shows the influence of the gas density for $\sigma_V = 1\,{\rm km.s}^{-1}$. The equilibrium temperature curve is shown on each plot as a black line.

Increasing the velocity dispersion simultaneously increases the average dissipation rate, increases its variance (thus increasing the strength of the extreme dissipation events even more), and decreases the timescale T of the process, making the bursts shorter and thus increasing the out-of-equilibrium effects. The combination of these effects result in an increased population of the low-ϵ high-T region, corresponding to cooling gas from a past dissipation burst. As seen on Fig. 85, the extension of the PDF towards the upper left region indeed increases with σ_V. At the same time, the PDF spreads along the equilibrium curve towards the high-ϵ high-T region as the strong dissipation events become both more intense and more frequent when σ_V increases.

The main impact of the gas density $n_{\rm H}$ is to increase the cooling efficiency. Indeed, the cooling efficiency varies as $\propto n_{\rm H}^2$, while the heating efficiency only varies as $\propto n_{\rm H}$. Increasing the gas density thus mainly results in a tightening of the PDF around the equilibrium curve as the thermal equilibration timescale is shortened. The equilibrium temperature at each dissipation rate is of course also reduced. Those effects appear clearly on Fig. 86.

From this 2D joint PDF, we can easily derive the marginal temperature PDF. The temperature PDFs are shown on Fig. 87 (varying σ_V) and Fig. 88 (varying $n_{\rm H}$). We noted before that except during strong dissipation events, the dissipation heating is negligible compared to the photoelectric heating. Thus, the temperature stays at a constant value (the thermal equilibrium value in the absence of dissipation heating, which we will note $T_{\rm eq}^{\rm (nt)}$) during the quiescent phases of the trajectories, and increases when dissipation events occur. As a result, the temperature can only be above $T_{\rm eq}^{\rm (nt)}$. Moreover, the gas spends a large fraction of the time at this temperature, and a small fraction at extreme temperatures. The temperature PDF is thus strictly decreasing, starting with

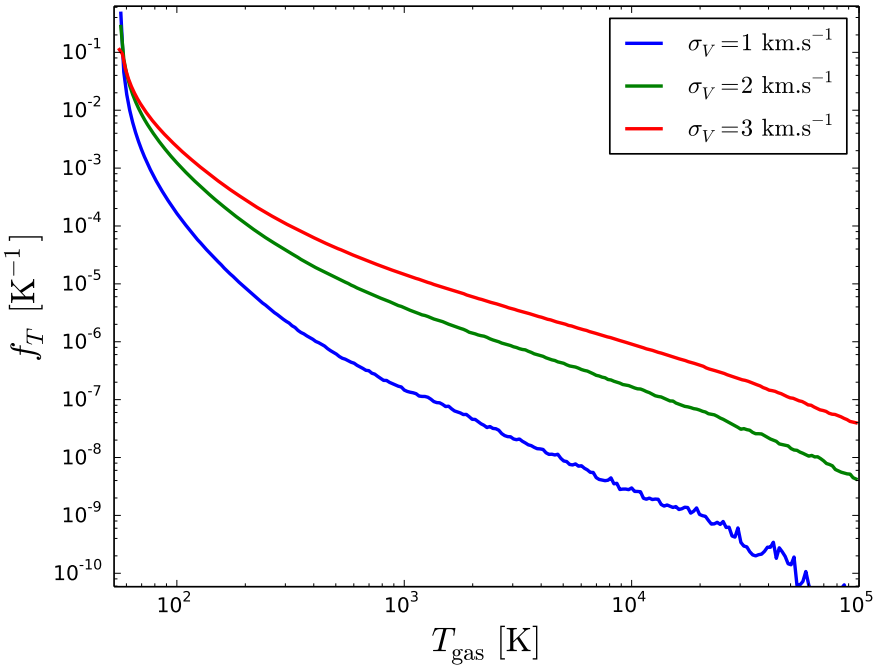

Figure 87: Resulting temperature marginal PDFs in the gas for three different turbulence intensities (controlled by σ_V), for a gas at density $n_{\rm H} = 100\,{\rm cm}^{-3}$.

a peak at $T_{\rm eq}^{\rm (nt)}$ (the PDF is zero below this temperature) and a long tail at low probabilities.

When varying σ_V at constant $n_{\rm H}$, $T_{\rm eq}^{\rm (nt)}$ remains unchanged but the probability residing in the high temperature tail increases with σ_V , as shown on Fig. 87. As an increase in σ_V not only increases the average of the dissipation rate but also makes the extreme events more intense and frequent, the tail decays slower for larger σ_V. We note that this tail is extremely extended, with a quasi-power-law behavior over more than one order of magnitude. It is the result of the extremely flat cooling curve (cf. Fig. 82). However, for temperature $\gtrsim 10^4\,{\rm K}$, other cooling mechanisms should start to dominate (e.g., H α) significantly increasing the cooling efficiency. This would result in a sharper cut-off above $10^4\,{\rm K}$ (see also next section).

When varying the gas density at constant σ_V, the properties of the turbulence remain unchanged but the cooling efficiency is changed. For a lower density $n_{\rm H}$, the cooling efficiency is reduced and this results both in an increased $T_{\rm eq}^{\rm (nt)}$, and in more probability in the tail, as shown on Fig. 88. However as the distribution of the dissipation events does not change, the exponent of the power law tail remains unchanged.

From these distributions, one can compare a few interesting statistics. In Table 7, we give for each model: the equilibrium temperature in the absence of turbulence $T_{\rm eq}^{(nt)}$, the equilibrium temperature $T_{\rm eq}^{\rm (t)}$ assuming a constant dissipation rate $\langle\epsilon\rangle$, the average temperature $T_{\rm mean}$, the median temperature $T_{\rm median}$, the probability $P(T_{\rm gas} > 1000\,{\rm K})$ of having $T_{\rm gas} > 1000\,{\rm K}$ (which can

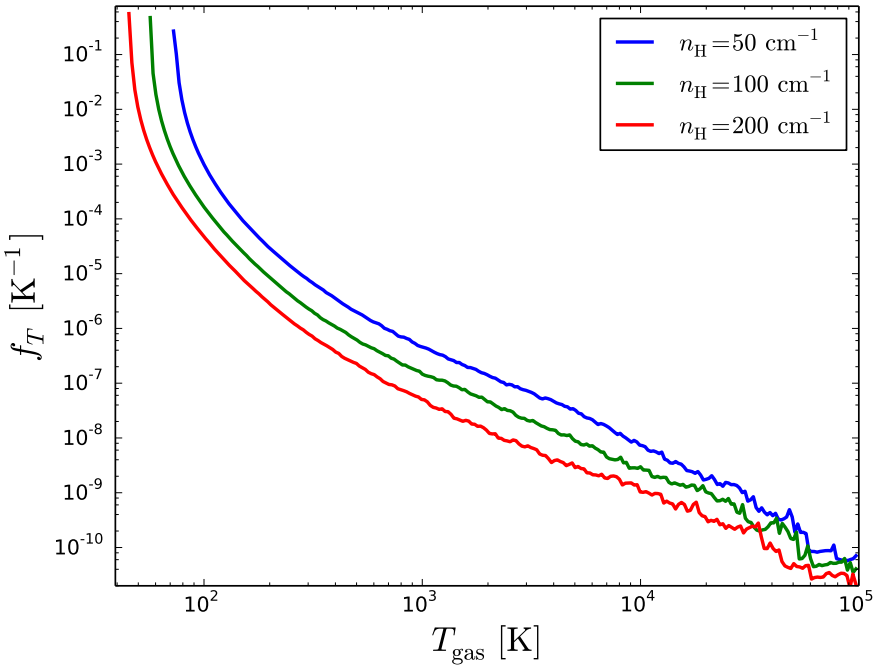

Figure 88: Resulting temperature marginal PDFs in the gas for three different gas densities n_{H}, for a turbulent velocity dispersion $\sigma_V = 1\,\mathrm{km.s}^{-1}$.

be interpreted as the fraction of gas above 1000 K in a sufficiently large volume of gas), and the standard deviation of the temperature $\mathrm{std}(T_{\mathrm{gas}})$. However, this last quantity is actually not well defined here. Indeed, the temperature PDFs show a power law decay for more than one decade before showing the beginning of a faster decay. On the power law part, the exponent is less than 3, so that the estimation of the variance will only converge when the faster decay part of the high temperature end has been sufficiently sampled, which is not the case here. For $\sigma_V = 3\,\mathrm{km.s}^{-1}$, the exponent becomes close to 2, so that even the convergence of the mean is problematic. Of course, all of this results from the very flat cooling curve at high temperature and our lack of the relevant cooling mechanism for those temperatures. T_{median} and $P(T_{\mathrm{gas}} > 1000\,\mathrm{K})$ are unaffected by these problems as they do not depend on the high temperature end of the tail of the PDF.

We see that the median temperature remains very close to the equilibrium temperature in the absence of turbulence, which means that most of the gas is unaffected by the turbulence. The average temperature departs from this value when the turbulence intensity is increased because of the rare extreme events only. For $\sigma_V = 3\,\mathrm{km.s}^{-1}$, a few percents of the gas are above 1000 K.

The convergence problem is illustrated on Fig. 89. While the mean appears to converge (slowly), the standard deviation clearly does not converge (note the logarithmic y-axis) as short phases that seem to converge are separated by brutal jumps of up to one order of magnitude caused by rare extreme events. If the PDF had a true T_{gas}^{-2} tail, this behavior would continue indefinitely and

n_H $[cm^{-3}]$	σ_V $[km.s^{-1}]$	$T_{eq}^{(nt)}$ [K]	$T_{eq}^{(t)}$ [K]	T_{mean} [K]	T_{median} [K]	$P(T_{gas} > 1000\,K)$	$std(T_{gas})$ [K]
50	1	74	78	80	75	6.0×10^{-4}	274
100	1	58	59	60	58	2.1×10^{-4}	180
200	1	46	47	48	47	6.6×10^{-5}	125
100	2	58	73	161	60	8.3×10^{-3}	1800
100	3	58	107	677	63	4.1×10^{-2}	4858

Table 7: Statistics of the temperature for models with different gas densities n_H and turbulent velocity dispersions σ_V. $std(T_{gas})$ is the standard deviation of the temperature (see the text for a discussion of the reliability of this quantity).

the measured standard deviation would diverge. Here we expect that if we wait long enough to sample the final drop of the PDF correctly, convergence would finally occur. But as discussed previously, this behavior is mainly due to the lack of a high temperature coolant in the model.

Finally, we compare our results to the models of Pan and Padoan [2009], who studied the temperature distribution of the atomic CNM. Their model differs from ours in two respects:

- They use a log-Poisson model (She and Leveque 1994, which is the best theory of intermittency so far in terms of reproducing the exponents of the structure functions) for the PDF of the dissipation rate, fitted to direct numerical simulations of supersonic turbulence (which is more realistic than incompressible turbulence for the ISM).

- However, their statistical treatment of the temperature is much more crude than the one presented here, as they assume that the temperature is always at equilibrium with the instantaneous dissipation rate, based on the argument that the cooling timescale is shorter than the overall dynamical timescale of the clouds (which is *not* the timescale of the dissipation fluctuations).

After adapting all our parameters to the values adopted by Pan and Padoan 2009, we compare our results to the values they quote. For $n_H = 50\,K$, and $\sigma_V = 2\,km.s^{-1}$, they find that the equilibrium temperature in the absence of turbulence $T_{eq}^{(nt)}$ is 53 K, the equilibrium temperature $T_{eq}^{(t)}$ for a constant dissipation rate at $\langle\epsilon\rangle$ is 63 K, and the average temperature T_{mean} is 100 K. For this model, we find $T_{eq}^{(nt)} = 55\,K$, $T_{eq}^{(t)} = 69\,K$ and $T_{mean} = 95\,K$. They also estimate the fraction of gas above 1000 K, for $\sigma = 1$, 2 and $3\,km.s^{-1}$, they find respectively 3.6×10^{-5}, 3×10^{-3}, and 1.9×10^{-2}, while we find 7.4×10^{-5}, 5.0×10^{-3}, and 2.9×10^{-2}. We are thus in good agreement with their result, which is not surprising as our too long dissipation events (see discussion

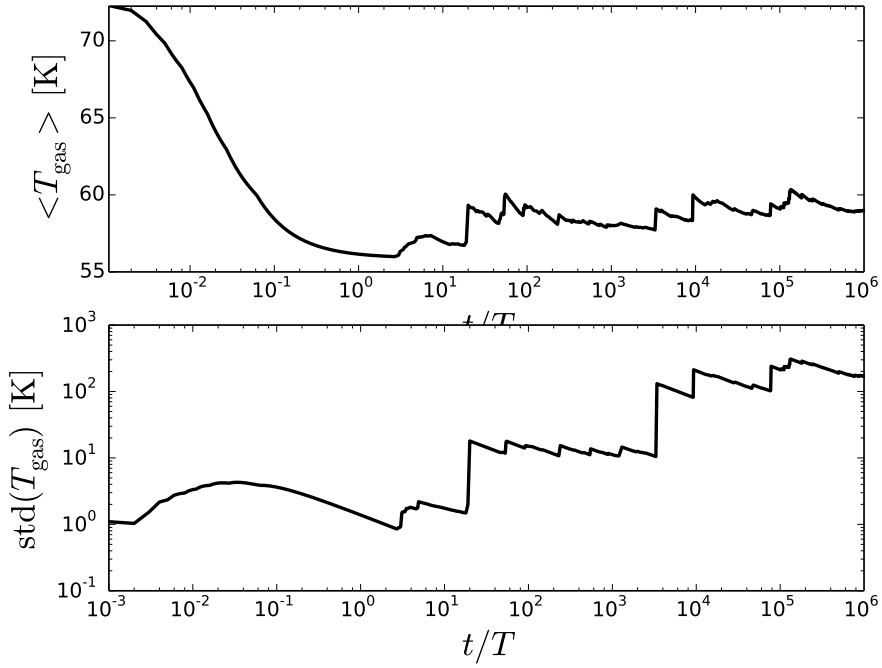

Figure 89: Convergence of the mean and the standard deviation of the gas temperature for a model with $n_H = 100\,\mathrm{cm}^{-3}$ and $\sigma_V = 1\,\mathrm{km.s}^{-1}$. Note that the y-axis of the lower plot is in logarithmic scale, emphasizing the absence of convergence.

at the beginning of this section) makes their thermal equilibrium assumption almost correct. A more correct model of the duration of the dissipation events would probably give much more differing results.

10.3 DIFFUSE MOLECULAR GAS: H_2 EXCITATION

Some diffuse lines of sight show a fraction of their hydrogen in molecular form (while carbon is not yet molecular). As discussed in Chap. 1 (Sect. 1.2.2), such medium is called diffuse molecular.

In such medium, observations have found a suprathermal contribution to H_2 excitation that can not be explained by the effect of the UV radiation field (e.g. Gry et al. 2002). It has been proposed that this contribution could come from hot gas in the dissipative structures of the turbulence, which are mixed along the line of sight with large low dissipation regions (see discussion in Sect. 3.3). We try here a simple application of our stochastic model to this problem. This section presents a very preliminary version of this model.

We do not follow yet the evolution of the chemical state of the gas, but it remains one of the goals of the development of this model to be able to compute the resulting average abundances of such species as CH^+, which are believed to be formed due to the energy dissipated by turbulence.

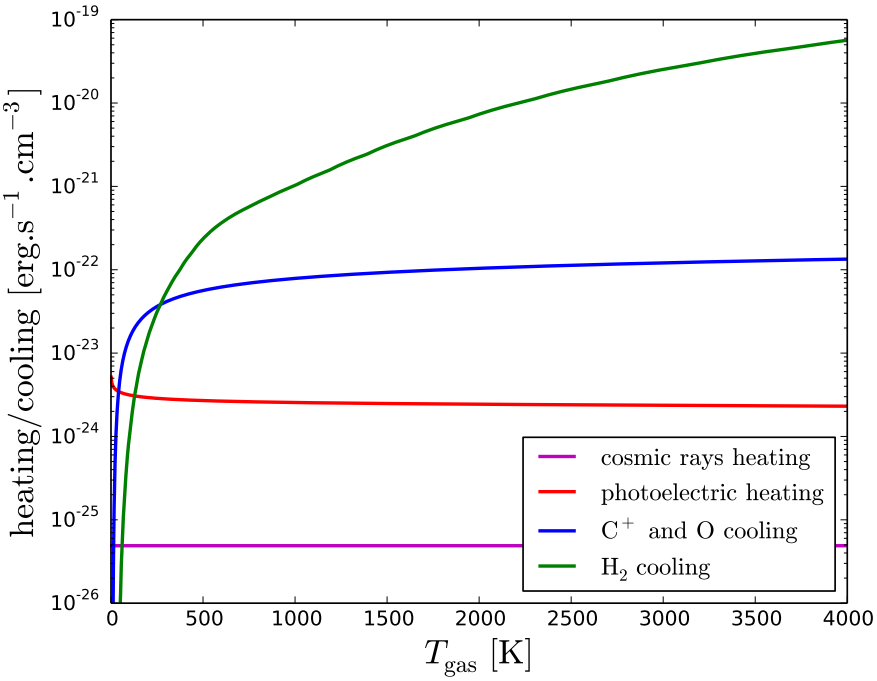

Figure 90: Heating and cooling rates for a gas with $n_H = 100\,cm^{-3}$, $G_0 = 1.7$ and $A_V = 0.2$.

10.3.1 *The model*

We use the same model as previously, but add the contribution of H_2 to the cooling. In a first approach, we assume that the excitation of H_2 remains at equilibrium at all time. Indeed, we are mainly interested in levels $J = 3 - 4$ (where the problematic contributions appear), for which the radiative lifetimes are $2.1\,10^9$ s and $3.6\,10^8$ s seconds, or 66 yr and 11 yr. As shown before (see Sect. 10.1.2), this is short compared to the duration of the dissipation bursts in our process.

We also assume the formation-destruction balance of H_2 to stay at steady-state as it is not much affected by the temperature fluctuations.

For simplicity, we use tabulated values of the H_2 fraction, H_2 level populations and H_2 cooling rate as functions of the gas temperature. These have been computed using the Meudon PDR Code, for different gas densities and at different shieldings A_V from the UV radiation field. For our standard model we consider gas at $A_V = 0.2$, for which the molecular fraction is ~ 0.98.

The number density of particles is now $n = n(H) + n(H_2) + 0.1\,n_H$ where the last term accounts for helium. This is used in the heat capacity of the gas (Eq. 370).

Fig. 90 compares the heating and cooling terms (excepted the turbulent heating which fluctuates widely). The cooling by H_2 becomes dominant above 250 K in those conditions. Moreover, the cooling rate by H_2 keeps in-

creasing steadily at high temperature, contrary to cooling by C^+ and O which becomes very flat. We can thus expect that the high temperature tail of the PDF will be strongly reduced due to the efficient cooling by H_2. This will limit the convergence problems experienced previously in the pure atomic gas.

As the cooling timescale can become very short at high temperature, we adopted a variable time step taking the minimum value of $T/100$ and $T_{\rm cooling}/10$, where the cooling timescale is defined as

$$T_{\rm cooling} = \frac{e}{C(e)} \tag{372}$$

10.3.2 *Results*

The resulting joint PDF of the dissipation rate ϵ and the gas temperature $T_{\rm gas}$ are shown on Fig. 91 for models with $n_{\rm H} = 40\,{\rm cm}^{-3}$ and different turbulent velocity dispersions. The efficiency of the cooling by H_2 appears clearly in the fact that the PDFs are very narrow around the equilibrium curve, and especially so at high temperatures. This indicates that cooling is fast enough to keep the gas at thermal equilibrium at all time, even for the strongest turbulence intensity σ_V tested here. Once again, more realistic time statistics for the dissipation bursts would result in the extreme events being much shorter, and could thus widen these PDFs. A more intense turbulence simply results in higher temperatures being reached, following the equilibrium curve.

The marginal temperature PDFs are shown on Fig. 92 for the same models. They have a similar shape to previously, but the tails are less extended and decay faster than power laws (which avoids the convergence problems experienced previously) as a result of the efficient cooling by H_2. The gas temperature without turbulence is 65 K and all three PDFs peak at this temperature, while the average temperatures are respectively 68, 86, and 115 K for $\sigma_V = 1$, 2, and $3\,{\rm km.s}^{-1}$. The corresponding standard deviations are 12, 50, and 101 K. The large probability represented by the initial peak of the distribution ensures that the lowest levels of H_2 will show a rotational temperature of ~ 65 K as observed, independently of the true average temperature of the gas.

The goal of this model is of course to deduce the average excitation of H_2 and compare it to observations of the diffuse CNM. The fractional abundances in the rotational levels are also tabulated, and averaged over the temperature PDF to get the mean fractional abundance of each level (we recall our assumption that H_2 excitation is always at equilibrium). If a line of sight is long enough, it will sample gas in different states and the resulting observed excitation will converge towards the statistical average for long lines of sight.

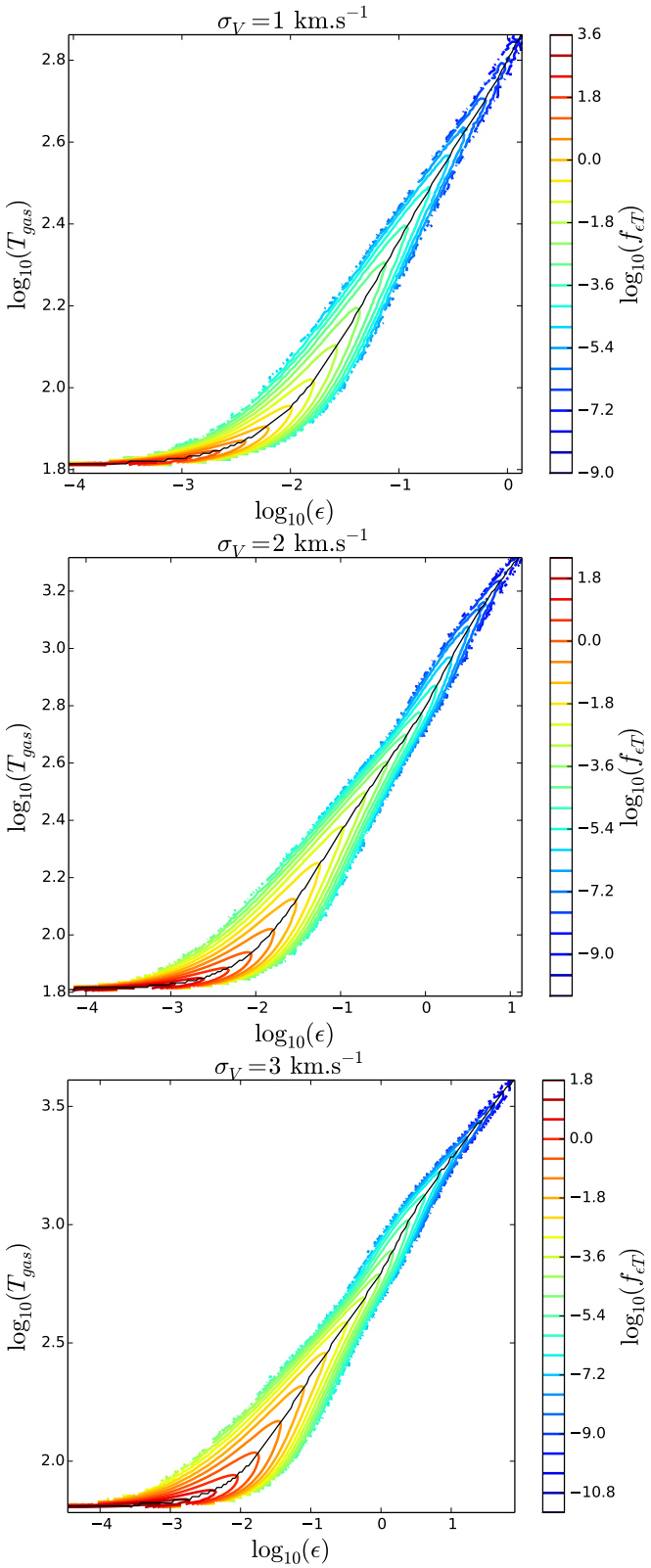

Figure 91: Contour plots of the joint PDF of ϵ and $T_{\rm gas}$ for three different turbulence intensities (controlled by σ_V), for gas at $n_H = 40\,{\rm cm}^{-3}$.

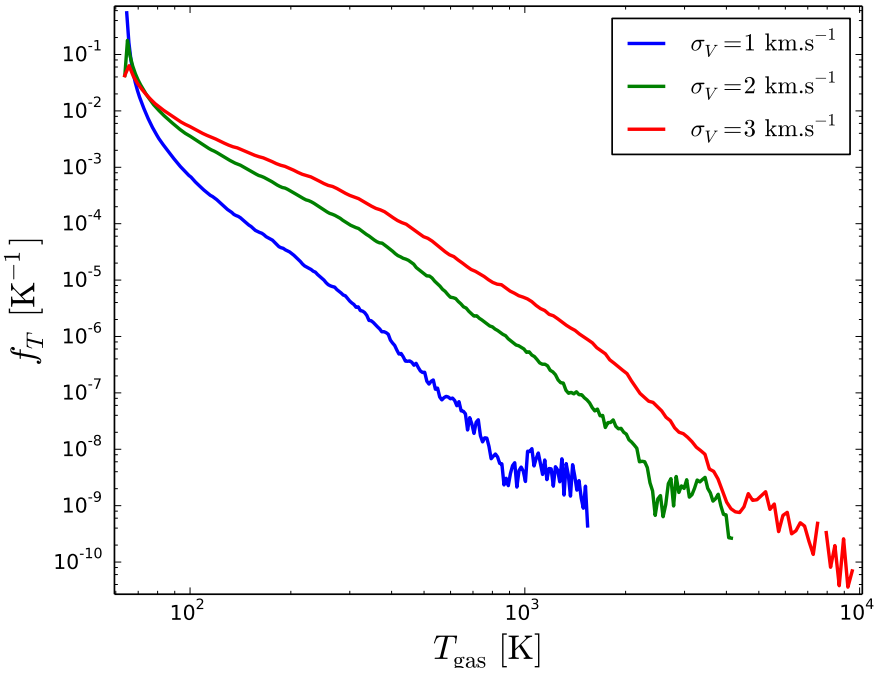

Figure 92: Resulting temperature marginal PDFs for three different turbulence intensities (controlled by σ_V), for a gas at density $n_{\rm H} = 40\,{\rm cm}^{-3}$.

We show on Fig. 93 the excitation diagrams obtained for $n_{\rm H} = 40\,{\rm cm}^{-3}$ and different values of the turbulent velocity dispersion σ_V. We also show FUSE observations of a compilation of 7 diffuse lines of sight with a significant molecular fraction taken from Gry et al. [2002] (HD102065, HD 108927, and HD 96675) and Lacour et al. [2005] (HD73882, HD192639, HD206267, and HD207538). The excitation diagrams are plotted in terms of the fractional abundances $x_i = N(H_2, J = i)/N(H_2)$, and thus independent of the total column density. The model curve in the absence of turbulence is also shown for comparison. Turbulence is seen to increase significantly the populations of levels $J > 2$, while the first two levels are unaffected. Moreover, the increased populations are compatible with the observations for realistic values of the velocity dispersion.

Figure 94 shows the influence of gas density on the models for $\sigma_V = 2.5\,{\rm km.s}^{-1}$. The density mainly affects the ratio of the first two levels. This ratio is often used to compute the excitation temperature T_{01}, which is used as a proxy for the gas temperature. As most of the gas is unaffected by the turbulence, this temperature corresponds to the temperature of the gas when the dissipation rate is negligible compared to the other mechanisms. The excited lines that are affected by the turbulence appear to be independent of the gas density.

Finally, we show on Fig. 95 a tentative fit for two specific lines of sight with our two-parameters model. The gas density is constrained by the first two levels and is here $n_{\rm H} = 40\,{\rm cm}^{-3}$, while the higher levels are adjusted

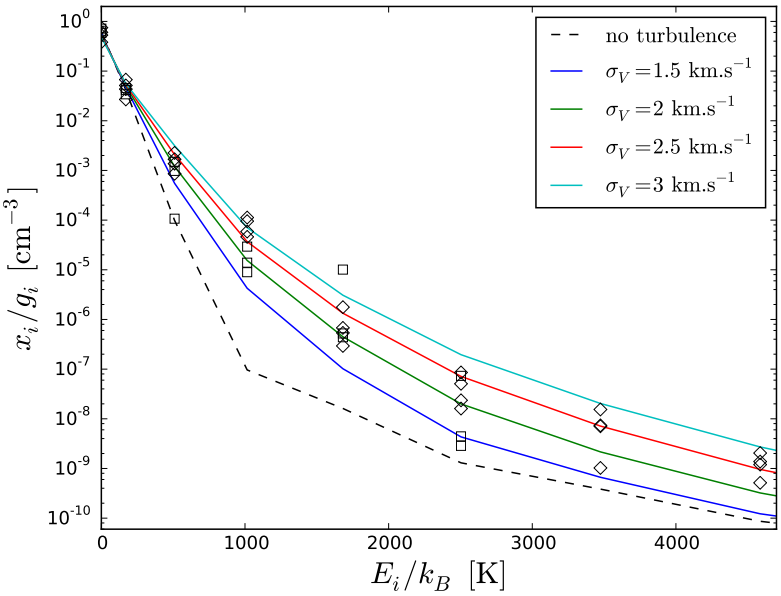

Figure 93: Excitation diagrams of H_2 for models with $n_H = 40\,cm^{-3}$ and different values of the turbulent velocity dispersion σ_V (colored solid lines), and for a similar model without turbulence (black dashed lines). The observations of three lines of sight by Gry et al. [2002] are shown as open squares, and the four lines of sight of Lacour et al. [2005] as open diamonds. The excitation diagram is plotted in terms of fractional abundances, in order to be independent of the total column density and molecular fraction of the lines of sight.

by varying the turbulence intensity. A good fit is obtained, but we seem to slightly underestimate the level $J = 4$. This remains to be investigated further.

10.4 CONCLUSIONS AND PERSPECTIVES

These two simple applications give a first demonstration of the practical usability of the method. They remain very rudimentary toy models, in which several aspects need to be refined. Despite their limitations, those models already give accurate predictions for the FUSE observations of H_2 excitation in the diffuse CNM. Several separate paths of improvement of the method can be envisioned.

First, we have seen that the time statistics of our process were not completely satisfactory, as the extreme dissipation events have a longer duration than expected. This shows that the Lagrangian autocorrelation function is not a sufficient constraint for the time behavior of the process. Indeed, the rare extreme events do not contribute enough to this statistic, and more complex

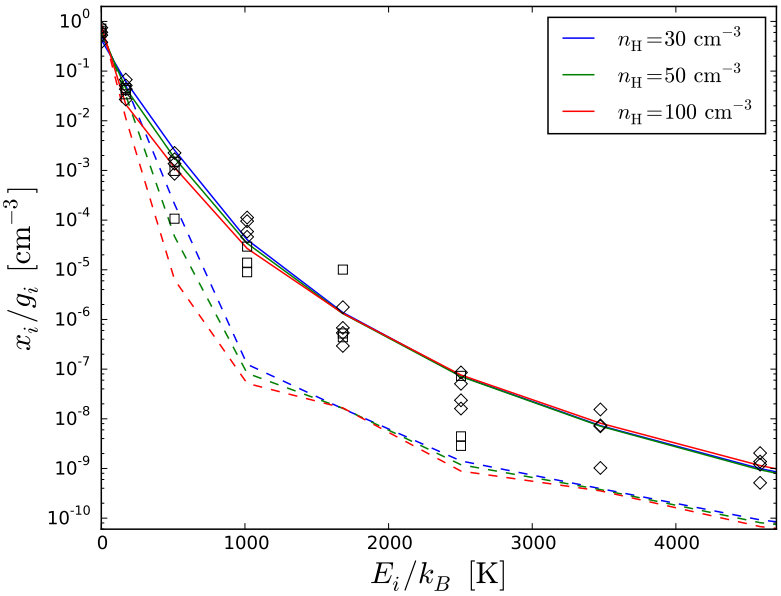

Figure 94: Excitation diagrams of H_2 for models with $\sigma_V = 2.5\,\mathrm{km.s}^{-1}$ and different values of the gas density $n_{\rm H}$ (solid lines), compared to the same models in the absence of turbulence (dashed lines). The observations are the same as on Fig. 93.

quantities would be needed, such as the conditional autocorrelation functions (conditional on the initial value), or the average times of flight above different dissipation levels. The constraints on such statistics could be taken from direct numerical simulations.

In addition, our log-normal model of intermittency (that we use to constrain the PDF of the dissipation rate) could be replaced by the prediction of the log-Poisson model (She and Leveque 1994, Dubrulle 1994, She and Waymire 1995).

Second, we experienced convergence problems for some quantities. Those were due to an incomplete physical model (we lack high temperature cooling mechanism). But even for non-problematic quantities, the convergence times are long. We typically need of the order of $\gtrsim 10^6$ times the autocorrelation timescale T of the process. This can be understood from the fact that the effects of turbulence in our system come from the rare extreme dissipation events. We thus need sufficient sampling of those rare events and this requires long simulation times. With the current physical model, the computation time remains of the order of a few minutes, but this would increase when including a chemical network, at least proportionally to the total number of variables (if the convergence time is not affected). Optimization of the sampling would be useful.

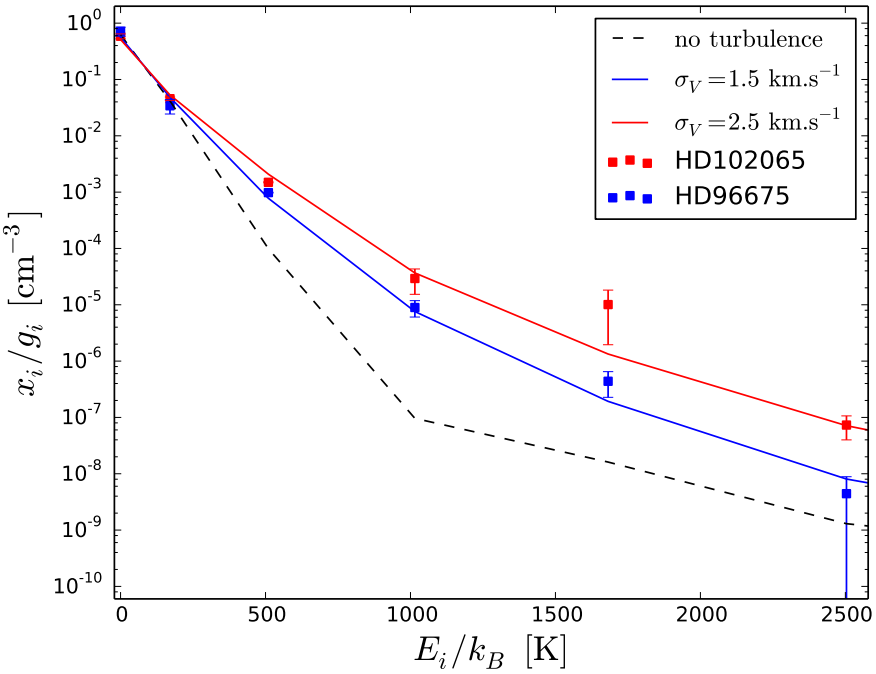

Figure 95: Models with $n_{\mathrm{H}} = 40\,\mathrm{cm}^{-3}$ fitting two specific lines of sights from Gry et al. [2002].

We would need a way to sample the rare events more often, without biasing the dynamical evolution of the trajectory. This is possible by using several parallel trajectories (which, in addition, makes parallelization easier) and a splitting/merging procedure with varying weights. This method, called Weighted Ensemble method, was proposed by Huber and Kim [1996] for Monte-Carlo simulation of protein reactions. The idea is to associate weights (used to compute the statistics) to the different trajectories (initially the same weight), and to avoid oversampling some uninteresting regions by merging trajectories that are in this region (taking two trajectories, stopping one at the current time, and continuing the other one with the sum of the two weights), while simultaneously splitting the trajectories that lie in under-sampled interesting regions (starting a new trajectory at the current position of the existing trajectory, with both trajectory taking one half of the initial weight). This procedure brings more trajectories with low weights to the interesting regions, which gives better sampling of those regions without biasing the statistics, while the uninteresting but more probable regions are sampled by less trajectories with higher weights. Such a sampling method will thus be developed for our model.

A third point is that when adding a chemical network to our problem, the resulting system of stochastic differential equations will become stiff (because of the simultaneous presence of very slow and very fast mechanisms). Usual methods for stiff differential equations cannot be directly applied to stiff stochastic differential equations, and specialized methods will have to be

used, such as the S-ROCK method of Abdulle and Li [2008].

Finally, as discussed in Chap. 3 (Sect. 3.3.2), previous attempts to study the abundances of CH^+ in terms of the dissipative structures of turbulence have found that a purely thermal effect would produce too much OH when adjusted to produce the required quantity of CH^+. It was shown that ion-neutral drift in the dissipative structures of magnetized turbulence (ambipolar diffusion or magnetized shocks) could produce the required enhancement of CH^+ without overproducing OH. Such effects can be taken into account in our model by relating the ion-neutral drift velocity to the instantaneous dissipation rate. The question is of course to know if the dissipation by ambipolar diffusion occurs in the same structures as viscous dissipation (such as hypothesized in Godard et al. 2009), or in separate structures. The general case can be treated by having one dissipation rate variable for each dissipation process, with a stochastic process model giving the correct correlation or non-correlation between the variables. Here again the detailed statistics of the mechanism-specific dissipation rates and their correlations will need to be taken from numerical simulations.

Later developments could include the addition of a spatial dimension to study the effect of turbulent mixing in chemically stratified objects such as PDRs. In this case, we simply add the position to the variables defining the state of the fluid element. We then need to use the general PDF formalism (presented in Chap. 9, Eq. 304), for which a stochastic model for the Lagrangian evolution of the velocity (in addition to the dissipation rate) would be needed. Several such models have been developed, such as the velocity-dissipation model (Pope and Chen 1990). The method could also be transposed to the more general compressible case.

Part IV

SIMULATIONS OF THE NGC7023 NORTH-WEST PDR

11

MODELS OF THE NGC7023 NORTH-WEST PDR

In bright but spatially unresolved PDRs such as the Orion Bar or M17 SW, the attempts to model the observations have repeatedly reached the conclusion that uniform models were insufficient, and that dense components embedded in lower density gas at scales that cannot be resolved by the observations were necessary (Stutzki et al. 1988, Stutzki and Guesten 1990, Jaffe et al. 1990, Howe et al. 1991). In particular, the high-J rotational lines of CO seem to arise in dense small scale structures, while the C^+ emission is dominated by the lower density surrounding medium.

PDRs in which the spatial structure can be resolved can thus be used to verify this hypothesis. The idea of this project (in collaboration with C. Joblin) was to test the PDR models on such a resolved PDR, NGC7023 NW, in order to gain insight to better understand other PDRs in which the spatial structure is not resolved (e.g. the Orion Bar). This work is based on observations from the Herschel key-program WADI.

11.1 THE OBJECT

11.1.1 *Characteristics*

Located in the Cepheus constellation, NGC7023 (also known as the Iris Nebula) is a bright reflection nebula. It surrounds the star HD200775 (RA(2000) = 21h01m36.9s , Dec(2000) = +68°09′47.8″), a triple system which consists of a massive spectroscopic binary (of pre-main sequence stars, type B3Ve+B5) and a third farther component.

The orbital parameters of this system have been recently re-estimated in Benisty et al. [2013], from which a distance of 320 ± 51 pc was deduced. In comparison, the parallax measurement by Hipparcos gave 430^{+160}_{-90} pc in the 1997 catalogue (van den Ancker et al. 1997), while the new reduction by van Leeuwen [2007] gives 520 ± 150 pc.

This star occupies the center of a cavity in the surrounding molecular cloud. The cavity has a biconical shape suggesting a past bipolar outflow that carved the current walls of the cavity (Fuente et al. 1998). Several PDRs are located at the walls of the cavity, where the walls are closest to the star. The brightest is located $\sim 45''$ to the northwest (taking the position of the H_2 peak, its position is RA(2000) = 21h01m32.4s , Dec(2000) = +68°10′25.0″), and is usually called the Northwest (NW) PDR. Here, we will focus on this PDR. Two other

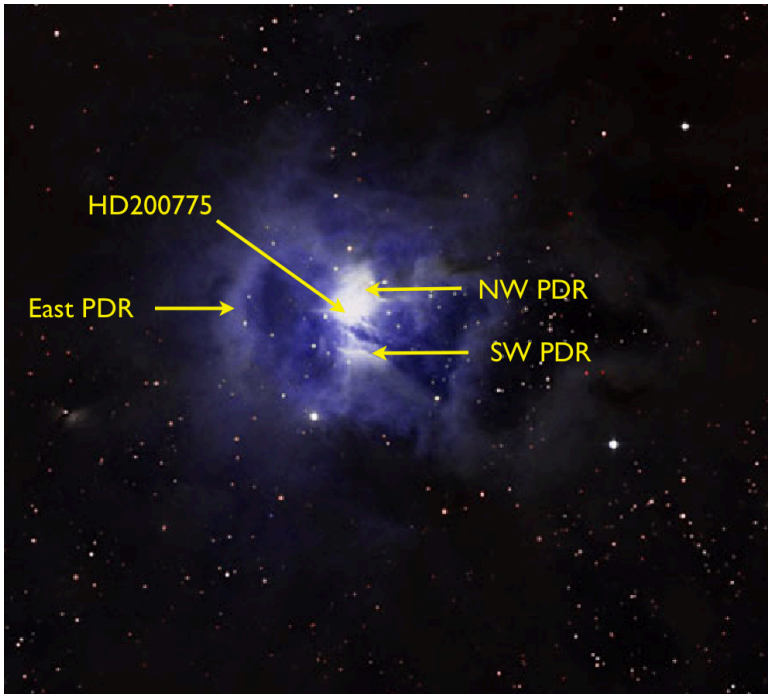

Figure 96: DDS2 image of the Iris Nebula (NGC7023), with approximative positions of the three PDRs and the main illuminating star. Credit: John Corban & the ESA/ESO/NASA Photoshop FITS Liberator.

dimmer PDRs are located to the southwest and to the east. The configuration is shown on Fig. 96.

11.1.2 *Previous works*

NGC7023 being one of the brightest reflection nebulae, it has been observed for a long time. Chokshi et al. [1988] were the first to identify the NW PDR from observations of the cooling lines of C^+ and O, deducing a gas density of $n \sim 4 \times 10^3\,\mathrm{cm}^{-3}$ for a dense region embedded in $n \sim 500\,\mathrm{cm}^{-3}$ gas. Other atomic and molecular observations of this PDR quickly followed. Fuente et al. [1992] observed the molecular gas with CO and ^{13}CO, and later with a larger number of molecular tracers (Fuente et al. 1993, CO, HCO^+, HCN, HNC, N_2H^+, CS, CN, C_2H, and isotopomers), deducing a density of $n \sim 1 \times 10^5\,\mathrm{cm}^{-3}$ in the dense parts. Rogers et al. [1995] also observed the HI filling the cavity delineated by CO.

The density contrasts needed to explain different tracers led to the conclusion that small high density structures were present. Filamentary structures in the PDR were indeed resolved first in dust observations (Sellgren et al. 1992), then by observations of vibrationaly excited H_2 (Lemaire et al. 1996, shown in Fig. 97), and HCO^+ observations (Fuente et al. 1996). This last article found densities peaking at $n = 1 \times 10^5 - 1 \times 10^6\,\mathrm{cm}^{-3}$ in the filament,

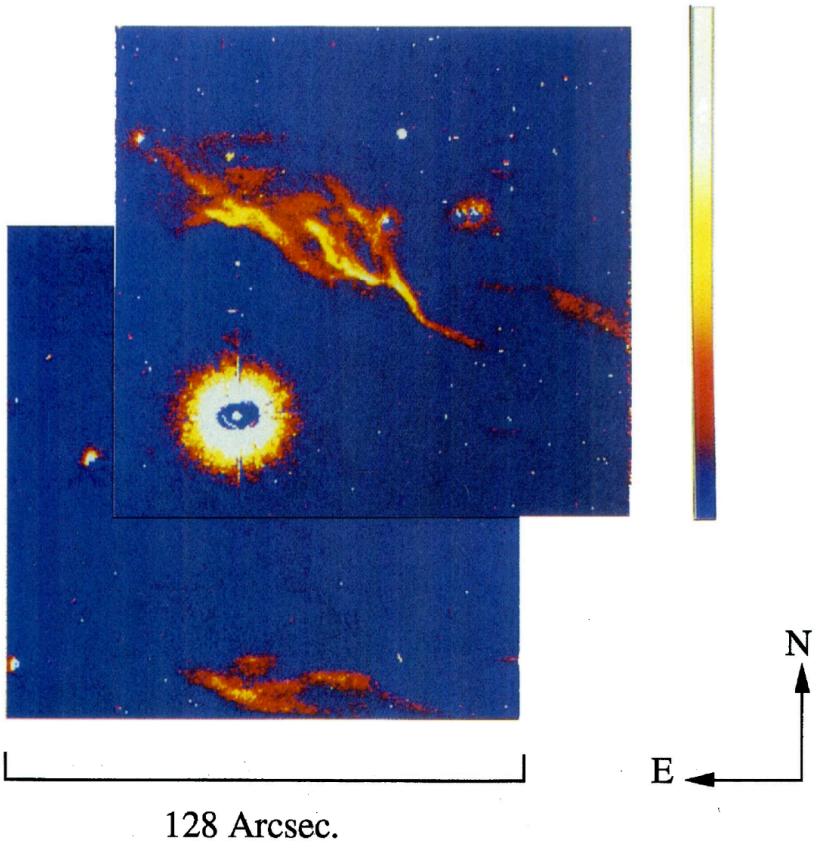

Figure 97: Map of NGC7023 in H_2 emission at 2.121 μm obtained with the Canada-France-Hawaii Telescope by Lemaire et al. [1996]. Figure taken from Lemaire et al. [1996].

and argued that limb brightening in the cavity walls seen edge-on was not sufficient and that a density enhancement in the structures was necessary.

Such high densities were confirmed by observations of vibrationaly excited H_2 (Martini et al. 1997, finding $n = 1 \times 10^5 - 1 \times 10^6\,\mathrm{cm}^{-3}$, and Lemaire et al. 1999, finding a pressure $P = 1 - 5 \times 10^8\,\mathrm{K.cm}^{-3}$). Lemaire et al. [1999] also evidenced a velocity gradient from the PDR to the molecular cloud, perhaps indicative of a photo-evaporation front.

Further observations confirmed this picture of dense filaments ($n \sim 10^6\,\mathrm{cm}^{-3}$) in less dense gas at $n \sim 10^4\,\mathrm{cm}^{-3}$ (Fuente and Martín-Pintado 1997, Fuente et al. 1998, Gerin et al. 1998, Fuente et al. 1999, 2000). Recent Herschel observations have been presented in Joblin et al. [2010], in which C^+ observations were presented, with a deduced density of $n = 7 \times 10^3\,\mathrm{cm}^{-3}$ corresponding to the low density medium. More recently, Köhler et al. [2014] presented observations of CO (up to $J = 13$) and ^{13}CO (up to $J = 10$), from which a density of $n \sim 10^6\,\mathrm{cm}^{-3}$ was deduced for the dense component. Both of those observations will be used to constrain our models, supplemented by higher J CO lines (up to J=19). See Sect. 11.2 for more detail on the observations that we will use.

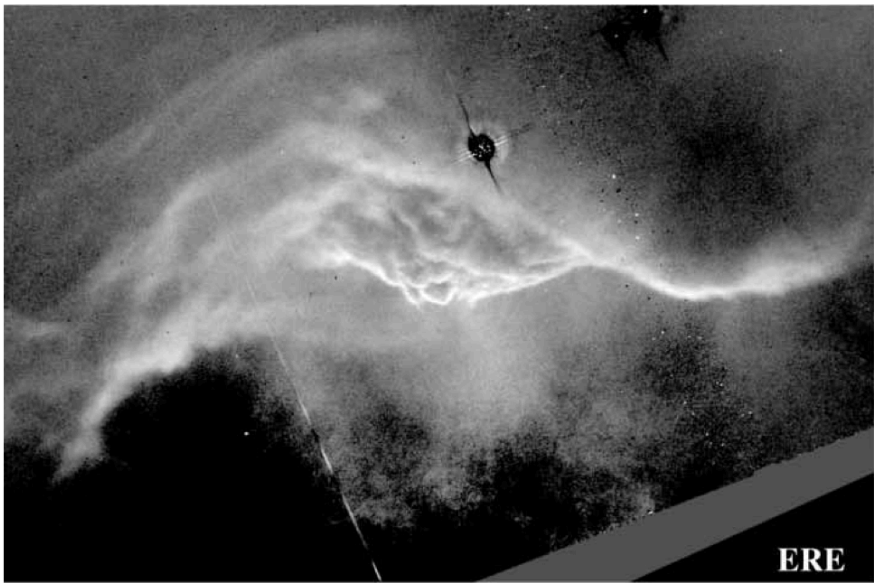

Figure 98: Extended red emission map of NGC7023NW obtained with the Hubble Space Telescope by Witt et al. [2006]. Figure taken from Witt et al. [2006].

The NGC7023 NW PDR has then been used to study PAH formation and destruction (Rapacioli et al. 2006), PAH and VSG properties (Berné et al. 2007, Pilleri et al. 2012), or the photoelectric heating efficiency (Okada et al. 2013).

11.1.3 *Constraining the model from the literature*

Depending on the distance to the star that we adopt, the angular separation between the star and the PDR (45″) gives a lower limit on the distance between the star and the PDR. From the value of van den Ancker et al. [1997], we get $d_{\mathrm{min}} = 9.4^{+3.5}_{-2.0} \times 10^{-2}$ pc, from the value of van Leeuwen [2007] we get $d_{\mathrm{min}} = 7.0 \pm 1.1 \times 10^{-2}$ pc, and from the value of Benisty et al. [2013] we get $d_{\mathrm{min}} = 1.1 \pm 0.33 \times 10^{-1}$ pc.

In our models, we will assume that the PDR front is illuminated by the radiation field proposed by Pilleri et al. [2012], consisting of the Kurucz spectrum corresponding to the spectral type of the binary star with a geometric dilution corresponding to $d = 1.43 \times 10^{-1}$ pc. This results in a UV intensity $G_0 = 2.6 \times 10^3$ in Habing units at the PDR front, as deduced by Chokshi et al. [1988] from C^+ and O observations.

In addition, Witt et al. [2006] give an estimate of the intensity of the scattered light at 475 nm in the nebula and find it to be 4% of the radiation field from the star. We use an extrapolation of this value, and take $G_0 = 100$ on the side of the cloud opposite to the star.

Witt et al. [2006] also determined the R_V value in the PDR front by comparing fluorescent H_2 emission to scattered light to probe the penetration of the UV field in the cloud. They found $R_V = 5.62^{+0.61}_{-0.48}$, which is consistent

with the values usually found in molecular gas. We thus adopt this value. In addition, we take the extinction curve measured towards HD38087, a line of sight probing molecular gas.

Finally, the observations show that the PDR is seen nearly edge-on. As our models assume a plane parallel geometry, we cannot use angles close to 90°. We thus adopted a viewing angle of 60°. In addition, the observed line profiles of the low-J CO lines show significant reabsorption (up to $J = 10$), which might be interpreted as the PDR front being seen from behind. We thus assume that the PDR is viewed from behind with a 60° viewing angle.

The "filamentary" structure can be better understood from the image obtained in the extended red emission by Witt et al. [2006], and shown on Fig. 98. It seems that the bright filamentary regions arise from limb brightening at the edge of the cloud, on the part of the very irregular surface that are seen edge-on. A better representation of the object's geometry would involve estimating the local radius of curvature (e.g. assuming identical curvatures perpendicular to and along the line of sight), and computing the line intensities with a spherical geometry.

However, only the vibrational H_2 observations seem to be spatially resolved. For the other observations, the observed intensities result from the dilution of the true intensities in the beam of the instrument. The intensities of the model thus need to be diluted by an unknown dilution factor, which we will constrain from the observations along with the physical parameters. In first approximation, a simple geometrical estimation from the dimension of the structure seen in vibrational H_2 indicates that a reasonable value for this dilution factor should not be more than a factor of a few.

11.2 THE OBSERVATIONS

The observations we will use are mainly Hershel observations obtained during the WADI key-program, supplemented by data taken from the literature. We summarize here the available data.

Hershel gives access to a much larger number of rotational lines of CO than previously accessible, up to the $(J = 23 \rightarrow 22)$ transition in bright PDRs such as the Orion Bar. The low-mid J transitions (up to $(13 - 12)$) are provided by the SPIRE and HIFI instruments, while the PACS instrument detects the higher J lines. In NGC7023 NW, the lower rotational lines of CO detected by SPIRE have been presented in Köhler et al. [2014]. Additional data from HIFI and PACS have been provided by C. Joblin and collaborators (Joblin et al. in prep.). Those data are presented in Table 8. Such high rotational lines of CO trace the most illuminated parts of the PDR, close to the H/H_2 transition, and are thus excellent constraints for PDR models.

transition	SPIRE	SPIRE (alt. pos.)	HIFI	PACS
$(4-3)$	$7.6 \pm 2.3 \times 10^{-10}$	$9.3 \pm 2.8 \times 10^{-10}$	-	-
$(5-4)$	$2.0 \pm 0.6 \times 10^{-9}$	$2.5 \pm 0.8 \times 10^{-9}$	-	-
$(6-5)$	$5.3 \pm 1.6 \times 10^{-9}$	$7.6 \pm 2.3 \times 10^{-9}$	$7.4 \pm 0.7 \times 10^{-9}$	-
$(7-6)$	$1.1 \pm 0.3 \times 10^{-8}$	$2.2 \pm 0.7 \times 10^{-8}$	-	-
$(8-7)$	$1.1 \pm 0.3 \times 10^{-8}$	$3.4 \pm 1.0 \times 10^{-8}$	$2.5 \pm 0.3 \times 10^{-8}$	-
$(9-8)$	$1.8 \pm 0.5 \times 10^{-8}$	$3.9 \pm 1.2 \times 10^{-8}$	$4.1 \pm 0.4 \times 10^{-8}$	-
$(10-9)$	$1.9 \pm 0.6 \times 10^{-8}$	$4.6 \pm 1.4 \times 10^{-8}$	$3.3 \pm 0.4 \times 10^{-8}$	-
$(11-10)$	$2.8 \pm 0.8 \times 10^{-8}$	$5.6 \pm 1.7 \times 10^{-8}$	-	-
$(12-11)$	$2.5 \pm 0.7 \times 10^{-8}$	$3.6 \pm 1.1 \times 10^{-8}$	-	-
$(13-12)$	$2.5 \pm 0.7 \times 10^{-8}$	$3.6 \pm 1.1 \times 10^{-8}$	$3.8 \pm 0.5 \times 10^{-8}$	-
$(14-13)$	-	-	-	-
$(15-14)$	-	-	-	$3.4 \pm 0.7 \times 10^{-8}$
$(16-15)$	-	-	-	$2.0 \pm 0.4 \times 10^{-8}$
$(17-16)$	-	-	-	$1.2 \pm 0.3 \times 10^{-8}$
$(18-17)$	-	-	-	$7.3 \pm 1.7 \times 10^{-9}$
$(19-18)$	-	-	-	$4.3 \pm 2.5 \times 10^{-9}$

Table 8: Observational data: intensities of the rotational ^{12}CO lines. The intensities are given in W.m^{-2}.sr^{-1}. The column noted "alt. pos." corresponds to the SPIRE observations at another close position (RA(2000) = 21h01m29.4s , Dec(2000) = +68°10′29.0″).

Similar rotational lines (but up to $J = 10$ only) are also available for ^{13}CO. See again Köhler et al. [2014] for the SPIRE data. Those data are presented in Table 9.

H_2 emission is also expected to trace the conditions of the excited edge of the PDR. We thus use the available data from the literature. ISO data have been presented by Fuente et al. [1999], and additional observations of vibrationaly excited H_2 are taken from Lemaire et al. [1996]. The Spitzer data were taken from the Spitzer archive.

Finally, we supplement those constraints with observations of other tracers. The C^+ observation of Joblin et al. [2010] (Herschel) gives access to the energy budget of the gas in the hot part of the PDR. Additional Herschel observations of $C^{18}O$, CH^+, HCO^+, O, C and HD are also used, the $(1-0)$ line of HCO^+ is taken from Fuente et al. [1996], and an additional measurement of the O 63 μm transition is taken from Okada et al. [2013]. Those data are presented in Table 11.

transition	SPIRE	SPIRE (alt. pos.)	HIFI
$(5-4)$	$1.0 \pm 0.3 \times 10^{-9}$	$1.4 \pm 0.4 \times 10^{-9}$	$1.7 \pm 0.2 \times 10^{-9}$
$(6-5)$	$1.1 \pm 0.3 \times 10^{-9}$	$3.1 \pm 0.9 \times 10^{-9}$	-
$(7-6)$	$1.8 \pm 0.5 \times 10^{-9}$	$3.8 \pm 1.1 \times 10^{-9}$	-
$(8-7)$	$2.3 \pm 0.7 \times 10^{-9}$	$4.9 \pm 1.5 \times 10^{-9}$	$4.1 \pm 0.4 \times 10^{-9}$
$(9-8)$	$3.8 \pm 1.1 \times 10^{-9}$	$5.3 \pm 1.6 \times 10^{-9}$	-
$(10-9)$	$3.1 \pm 0.9 \times 10^{-9}$	$5.0 \pm 1.5 \times 10^{-9}$	$4.8 \pm 0.5 \times 10^{-9}$

Table 9: Observational data: intensities of the rotational ^{13}CO lines. The intensities are given in W.m^{-2}.sr^{-1}. The column noted "alt. pos." corresponds to the SPIRE observations at another close position (RA(2000) = 21h01m29.4s , Dec$(2000) = +68°10'29.0''$).

transition	ISO	Spitzer	Lemaire et al. [1996]
$S(0)$	3.5×10^{-8}	-	-
$S(1)$	2.1×10^{-7}	$2.0^{+0.6}_{-0.3} \times 10^{-7}$	-
$S(2)$	2.4×10^{-7}	$5.5^{+2.0}_{-1.7} \times 10^{-7}$	-
$S(3)$	4.1×10^{-7}	$6.9^{+3.1}_{-1.5} \times 10^{-7}$	-
$S(4)$	1.5×10^{-7}	-	-
$S(5)$	2.6×10^{-7}	$4.6 \pm 1.4 \times 10^{-7}$	-
$(1-0)S(1)$	-	-	$2.1 \pm 0.21 \times 10^{-7}$
$(1-0)S(2)$	-	-	$7.6 \pm 1.7 \times 10^{-7}$

Table 10: Observational data: intensities of the ro-vibrational H_2 lines. The intensities are given in W.m^{-2}.sr^{-1}.

species/transition	SPIRE	HIFI	PACS1	PACS2	other
$C^{18}O\,(5-4)$	-	$2.9 \pm 0.3 \times 10^{-10}$	-	-	-
$C^{18}O\,(9-8)$	-	$2.6 \pm 0.3 \times 10^{-10}$	-	-	-
$CH^+\,(1-0)$	-	$1.0 \pm 0.1 \times 10^{-9}$	-	-	-
$CH^+\,(2-1)$	-	$5.5 \pm 0.8 \times 10^{-10}$	$6.6 \pm 2.5 \times 10^{-9}$	-	-
$CH^+\,(3-2)$	-	-	$5.6 \pm 2.1 \times 10^{-9}$	-	-
$HCO^+\,(1-0)$	-	-	-	-	$4.5 \pm 1.3 \times 10^{-12}$
$HCO^+\,(6-5)$	-	$8.2 \pm 0.7 \times 10^{-11}$	-	-	-
$C^+\,(158\,\mu m)$	-	$7.6 \pm 1.1 \times 10^{-7}$	$7.3 \pm 1.5 \times 10^{-7}$	$9.9 \pm 2.0 \times 10^{-7}$	-
$C\,(609\,\mu m)$	2.75×10^{-10}	-	-	-	-
$C\,(370\,\mu m)$	5.89×10^{-9}	-	-	-	-
$O\,(145\,\mu m)$	-	-	$4.0 \pm 0.8 \times 10^{-7}$	$3.8 \pm 0.8 \times 10^{-7}$	-
$O\,(63\,\mu m)$	-	-	-	$1.9 \pm 0.4 \times 10^{-6}$	$2.3 \pm 0.5 \times 10^{-6}$
$HD\,(1-0)$	-	-	$2.7 \pm 2.2 \times 10^{-9}$	-	-

Table 11: Observational data: intensities of other tracers. The intensities are given in $W.m^{-2}.sr^{-1}$. See the text for references for the non-Herschel observations.

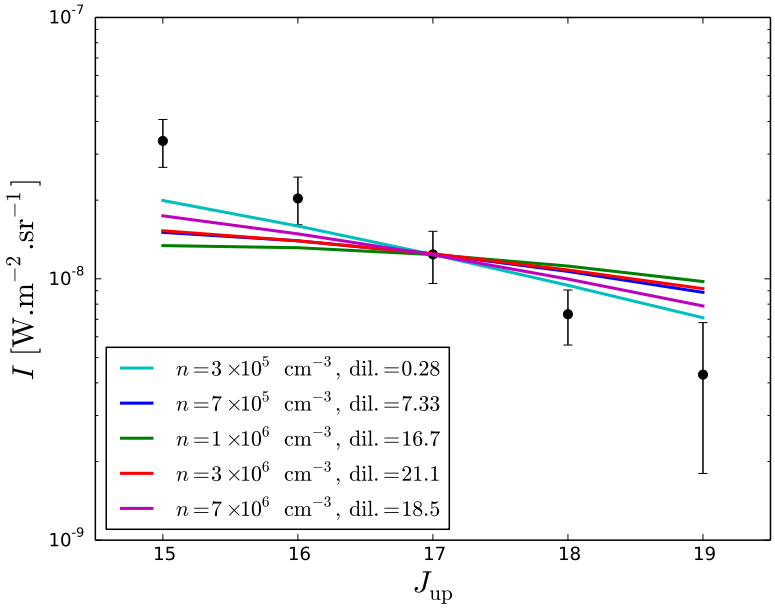

Figure 99: Comparison of constant density models with the observations of the high-J CO lines. The model intensities have been diluted by a factor indicated in the legend.

11.3 THE MODELS

We now present the comparison of models with those observational constraints. The models were run using the Meudon PDR Code (Le Petit et al. 2006). The large number of constraints, with various tracers probing different parts of the PDR, allows us to test the capabilities of the models in depth. This work was done in parallel with a similar comparison performed for the Orion Bar PDR with similar constraints, and will be published with it in a forthcoming paper (Joblin et al. in prep.).

11.3.1 *Constant density vs. constant pressures*

As said before, the observations of high-J CO lines allow us to probe in detail the very edge of the PDR, close to the H/H_2 transition where the UV radiation field is being quickly extinguished. The structure of this edge in terms of the spatial variations of the gas density and temperature can thus be explored. The gas temperature is computed by the Meudon PDR Code in a self-consistent way and will thus be a result of our models. The density can either be assumed constant, provided as a given spatial profile, or be computed from a constant pressure constraint. We thus tested these different possibilities against our observational constraints tracing the edge of the PDR.

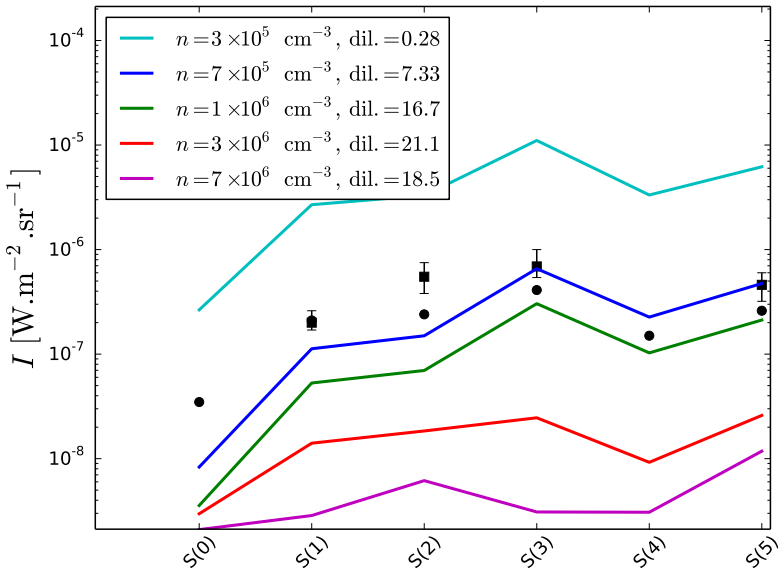

Figure 100: Comparison of the constant density models presented in Fig. 99 (with the same dilution factors) with the observations of the rotational H_2 lines. The squares are the SPITZER observations and the circles are the ISO observations.

Fig. 99 shows the comparison of constant density models with the PACS observations of the high-J CO lines. For each model, the best dilution factor has been adjusted to the observations. The models all have a total depth $A_V = 5$, as these lines are only emitted at the edge of the PDR and are optically thin, so they are unaffected by the total depth of the gas layer.

We see that none of the models presented is able to reproduce the observed slope of the intensities. Moreover, unrealistic dilution factors excludes low density models with $n \leq 3 \times 10^5\,\mathrm{cm}^{-3}$ (which need dilution factors lower than 1), and very high density models with $n \geq 1 \times 10^6\,\mathrm{cm}^{-3}$. The model with the most realistic dilution factor is $n = 7 \times 10^5\,\mathrm{cm}^{-3}$ but clearly does not fit the slope of the intensities.

The rotational lines of H_2 also trace the H/H_2 transition region. Fig. 100 shows the prediction of the same models as in Fig. 99 (with the dilution factors adjusted for the CO intensities) for the rotational lines, compared to the ISO and SPITZER observations.

We see that for most models, the dilution factor adjusted from the CO clearly does not fit the H_2 observation. The only model for which the dilution factor works reasonably well is the model with $n = 7 \times 10^5\,\mathrm{cm}^{-3}$ (with significant discrepancies on the first three lines). This shows that models with lower densities emit too much in H_2 compared to their high-J CO emission, while higher density models emit to much high-J CO relative to H_2. Thus, selecting based solely on the reasonableness of the dilution factor adjusted on

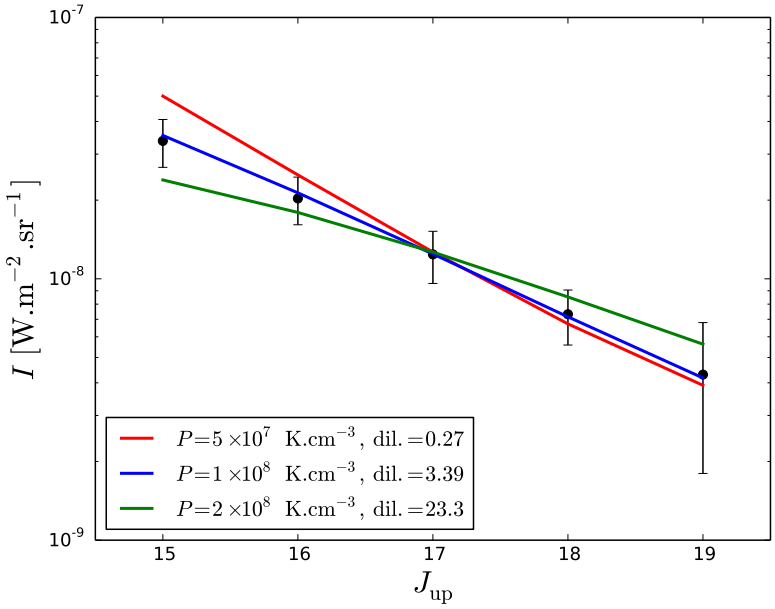

Figure 101: Comparison of constant pressure models with the observations of the high-J CO lines. The model intensities have been diluted by a factor indicated in the legend.

CO observations, or based on the simultaneous agreement with both CO and H_2 observations, results in a similar best model. However, this best model has significant discrepancies with the observations.

We thus investigated non-constant density profiles, and found that profiles with a density gradient (density increasing with depth) gives a better agreement (especially on the slope of the high-J CO intensities). The best fit was obtained for constant pressure models (which give the right gradient as gas temperature naturally decreases from the edge to the core).

Fig. 101 shows the comparison of constant pressure models with the observations for the high-J CO lines. The total A_V is again 5, and the best dilution factor has been adjusted. We see that the model with $P = 1 \times 10^8$ K.cm^{-3} fits the intensity slope perfectly, and that this slope is sensitive to the pressure value so that it effectively constrains the pressure. Moreover, this model also has the most reasonable dilution factor.

The comparison of those same models (with the same dilution factors) with the H_2 observations is shown on Fig. 102. We see that the only model for which the CO-adjusted dilution factor gives a good fit of the H_2 observations is again the model with $P = 1 \times 10^8$ K.cm^{-3}. Models with lower pressure emit to much in H_2 relative to high-J CO, while the higher pressure models emit to much high-J CO relative to H_2.

All the constraints investigated so far indicate that the density profile at the edge of the PDR (around the H/H_2 transition region) is close to pressure

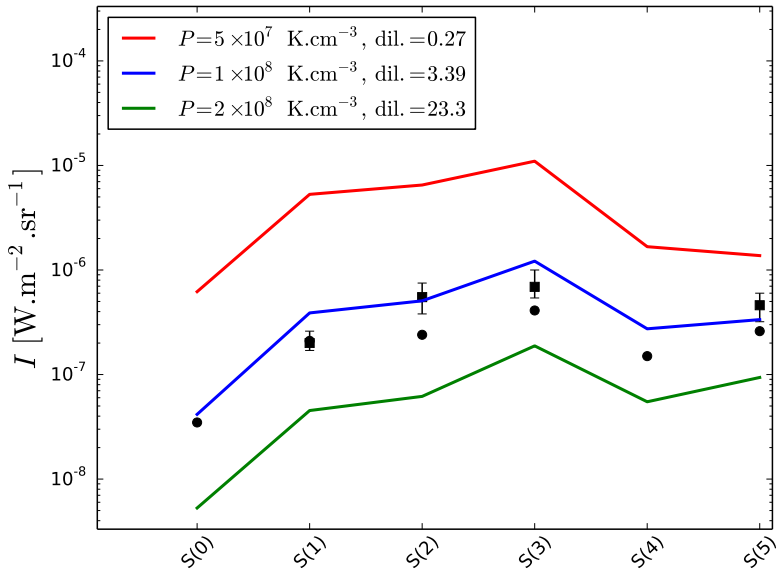

Figure 102: Comparison of the constant pressure models presented in Fig. 101 (with the same dilution factors) with the observations of the rotational H_2 lines. The squares are the SPITZER observations and the circles are the ISO observations.

equilibrium. We will now discuss the other constraints, keeping a constant pressure model.

11.3.2 *Best model*

The model with $P = 1 \times 10^8$ K.cm^{-3} turns out to be the best fitting model for most of the other observations. A total A_V of 5 was adopted based on the observations ^{13}CO. The dilution factor was slightly modified to 4 for better agreement. The parameters of this model are summarized in Table 12.

Fig. 103 shows the comparison for H_2 in the form of an excitation diagram. For the model, the excitation diagram is computed from the intensities, as is done for the observations (the column densities represented are thus the true column densities only for optically thin lines). An additional lower pressure model is shown for comparison with an adjusted dilution factor. As the vibrationaly excited lines were observed with higher resolution (enough to resolve the spatial structure), their intensities in the model are not diluted by the dilution factor (all other lines are).

We see that our model is in good agreement with the rotational lines, while it underestimates the vibrationaly excited lines by a factor of ~ 2. The comparison between the ISO and SPITZER observations show that independent measurements of the same lines with different instrument typically differ by

Parameter	Value
Density profile	Isobaric
Pressure	1×10^8 K.cm^{-3}
Total A_V	5
Observer position	back side
Observing angle	60°
Frontside radiation field	Kurucz spectrum with $G_0 \approx 2600$
Backside radiation field	$G_0 = 100$
R_V	5.62
$N_H/E(B-V)$	1.05×10^{22} cm^{-2}
Dust/gas mass ratio	0.01
Dust size distribution	Power law (-3.5)
Min. dust size	3×10^{-9} m
Max. dust size	3×10^{-7} m

Table 12: Parameters of the best model.

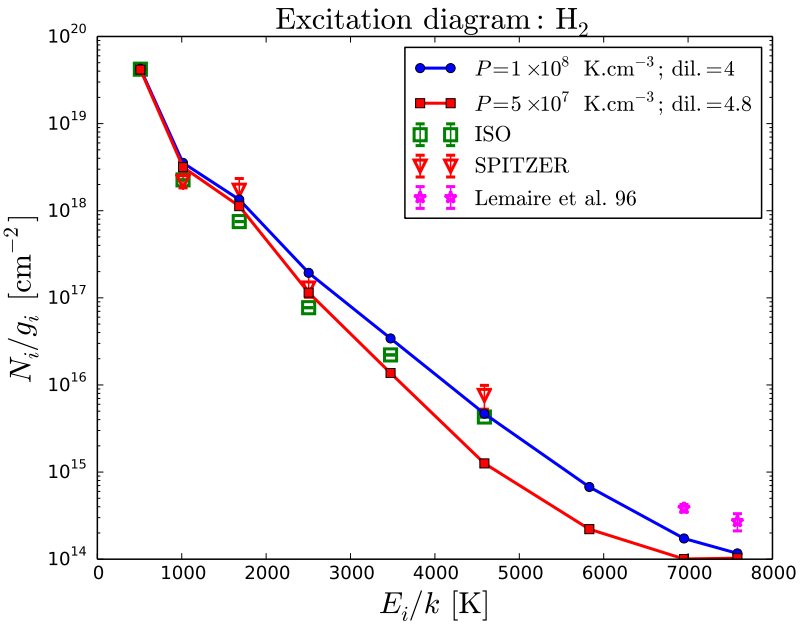

Figure 103: Observable excitation diagram of H_2 for the best model (blue, $P = 1 \times 10^8$ K.cm^{-3}, $A_V = 5$), compared to a lower pressure model, and to our observational constraints.

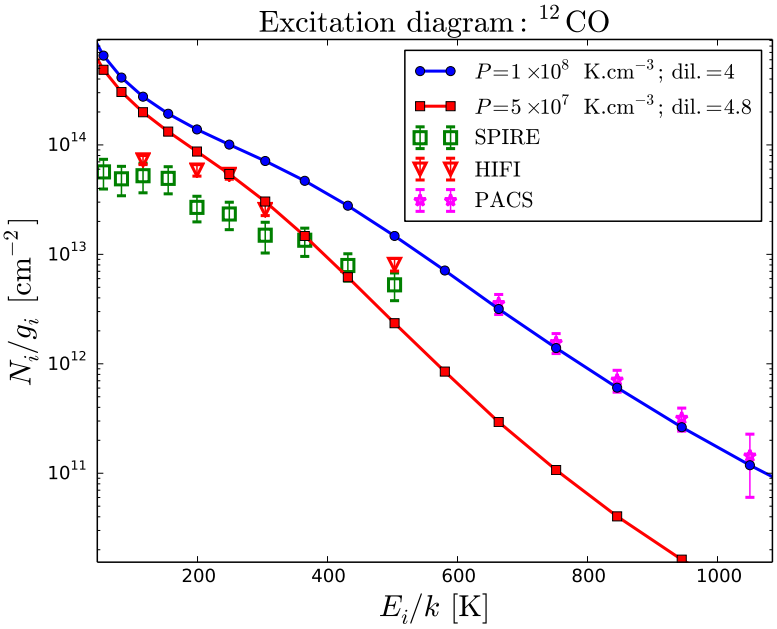

Figure 104: Observable excitation diagram of ^{12}CO for the best model (blue, $P = 1 \times 10^8$ K.cm^{-3}, $A_V = 5$), compared to a lower pressure model, and to our observational constraints.

a factor of 2 (may be due to calibration errors). Our error thus remains acceptable.

Fig. 104 shows the comparison of the model with the observations of ^{12}CO. As found in the previous section, our model fits perfectly the high-J CO lines. However, we overestimate the low-J CO lines. The first few rotational lines could be reabsorbed by intervening gas on the line of sight (the observed line profile show strong re-absorption). But higher J ($5 < J < 14$), are also all overestimated by a factor between 4 and 2. A lower pressure model is shown for comparison: lowering the pressure can only make thing worse as the overall slope becomes steeper. A higher pressure model would have a better general shape but would require a very high dilution factor (in addition to having the wrong slope for the high J, as shown before). We will discuss a plausible explanation of the discrepancies on the low-J CO lines in the next section.

Fig. 105 shows the same comparison for ^{13}CO. Our model is in reasonable agreement with the observation but slightly overestimate some of the lines (be a factor < 2). A lower pressure gives a less adequate slope.

For CH^+, the comparison is shown on Fig. 106. The agreement is very good except for the $(1-0)$ line. The observed line profile for this line shows strong re-absorption, so that the discrepancy could be due to re-absorption by intervening gas on the line of sight.

Fig. 107 shows the same comparison for HCO^+. As the observation of the $(1-0)$ line with the Plateau-de-Bures Interferometer has sufficient spatial

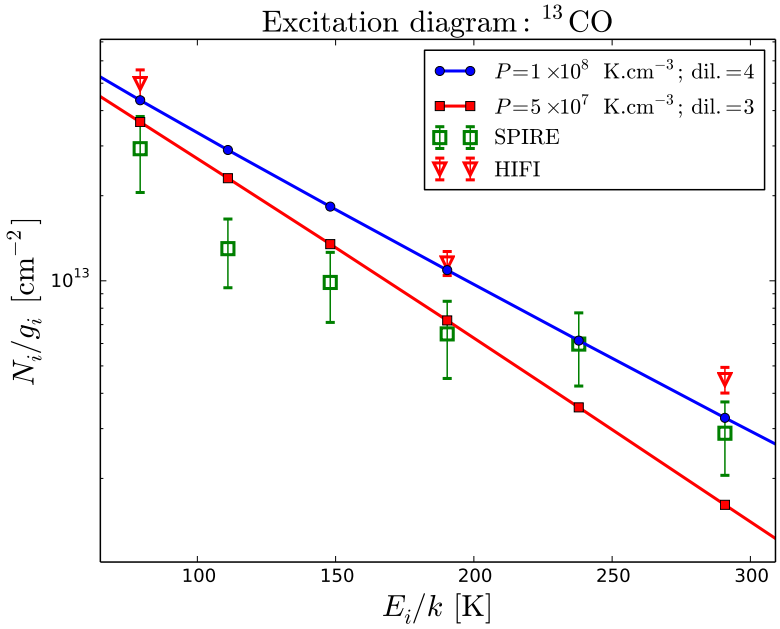

Figure 105: Observable excitation diagram of ^{13}CO for the best model (blue, $P = 1 \times 10^8$ K.cm^{-3}, $A_V = 5$), compared to a lower pressure model, and to our observational constraints.

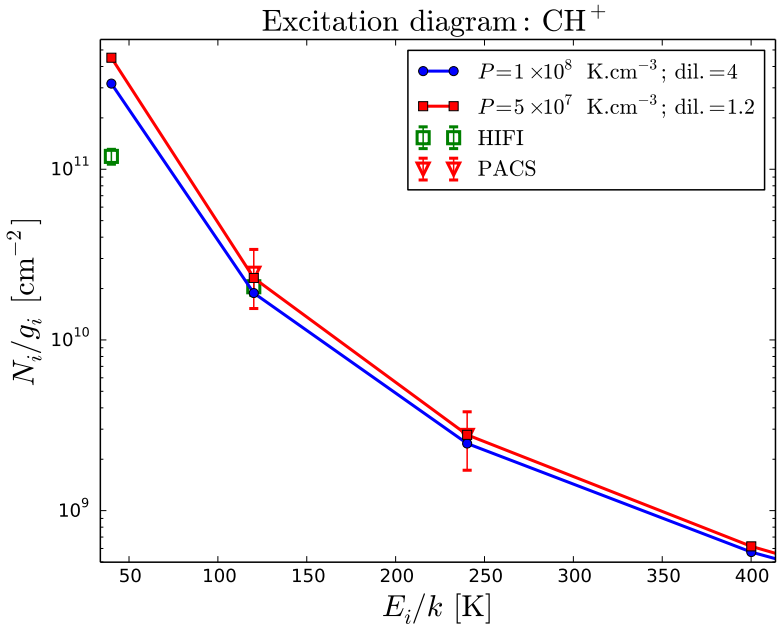

Figure 106: Observable excitation diagram of CH$^+$ for the best model (blue, $P = 1 \times 10^8$ K.cm^{-3}, $A_V = 5$), compared to a lower pressure model, and to our observational constraints.

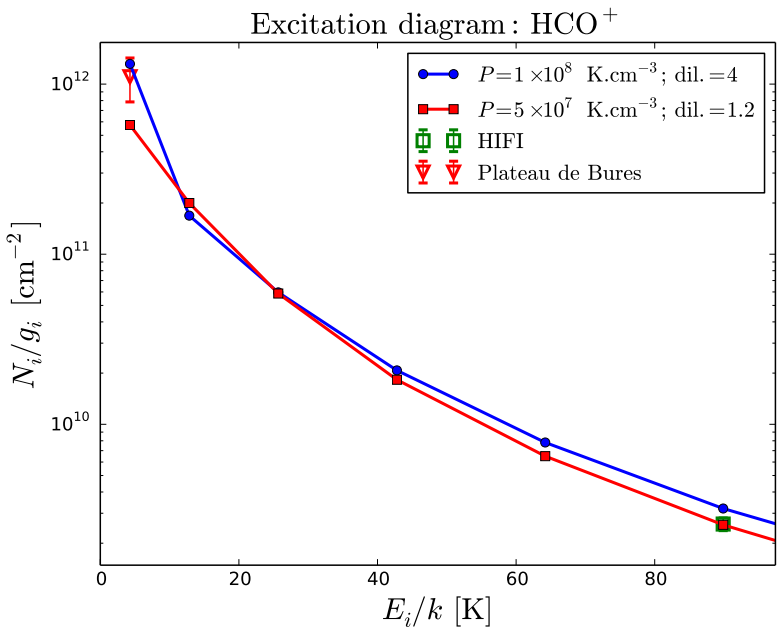

Figure 107: Observable excitation diagram of HCO^+ for the best model (blue, $P = 1 \times 10^8$ K.cm^{-3}, $A_V = 5$), compared to a lower pressure model, and to our observational constraints.

resolution to resolve the filament (3.3″ × 2.4″), we do not apply the dilution factor to this line in our model (all other lines are diluted). The agreement is excellent for both the $(1-0)$ line and the $(6-5)$ line.

Finally, Fig. 108 shows the comparison for $C^{18}O$. Large discrepancies appear (a factor of 19 on the first line). A possible explanation will be discussed in the next section.

The full comparison is given in Table 13 with observations of additional species. A good agreement is found for the first rotational line of HD and the two observed fine-structure lines of O. The C fine-structure lines tend to be overestimated by our model (especially the 609 μm line), this will be discussed in conjunction with the discrepancies on $C^{18}O$ in the next section. Finally the C^+ intensity is also slightly underestimated.

Finally, the physical structure of our model is presented on Fig. 109 (hydrogen density and temperature profiles) and 110 (density profiles for the main chemical species). We first see that in our model the gas layer has the thickness of $\sim 4 \times 10^{-3}$ pc, which gives an angular size between 1.59″ and 2.59″ depending on the distance estimate that we use.

The density goes up to $n_H =$ a few 10^6 cm^{-3} in the coldest part ($T_{\rm gas} \approx 60$ K), while it is around a few 10^5 in the region of the H/H_2 transition with a temperature of several 10^2 K, and a few 10^4 in the atomic region with $T_{\rm gas} \approx 2000$ K. We also see that most of the thickness is gas with hydrogen in molecular form, while carbon is ionized. The molecular carbon region only occupies a small fraction of the layer (the densest part).

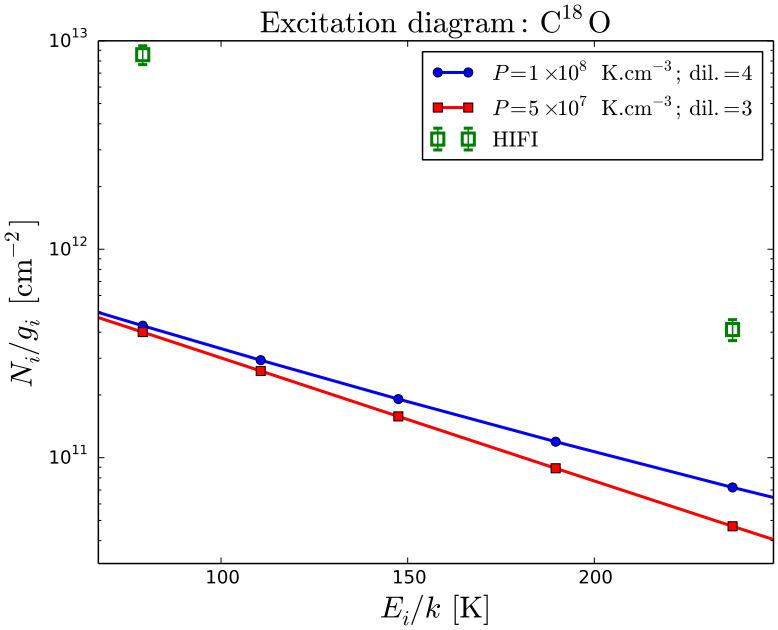

Figure 108: Observable excitation diagram of $C^{18}O$ for the best model (blue, $P = 1 \times 10^8$ K.cm^{-3}, $A_V = 5$), compared to a lower pressure model, and to our observational constraints.

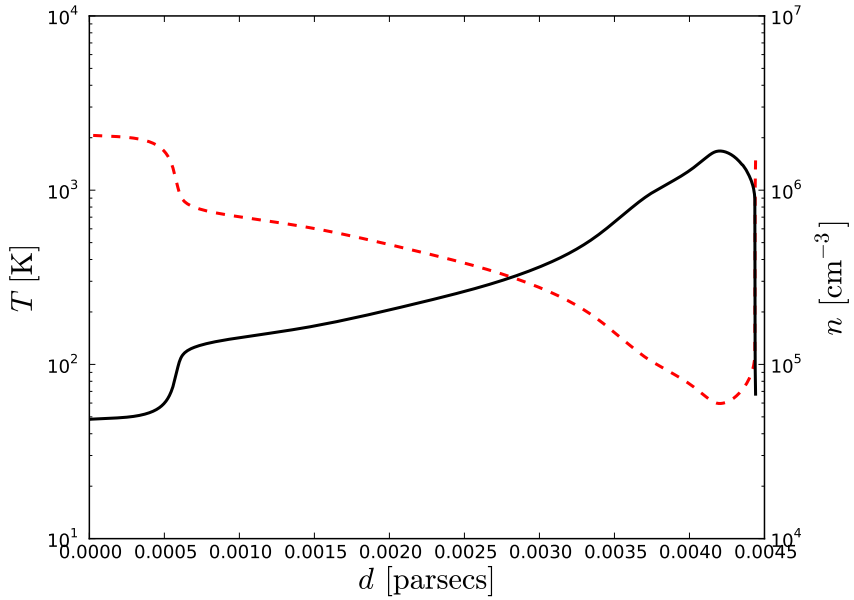

Figure 109: Density (black) and temperature (red) profiles for the best model (constant pressure, $P = 1 \times 10^8$ K.cm^{-3}, $A_V = 5$).

Species	Line	Observations					Models		
		SPIRE	HIFI	PACS1	PACS2	Other	Intensities	Error factor	Col. den.
^{12}CO									[cm^{-2}]
	(4 – 3)	$7.6 \pm 2.3(-10)$	-	-	-	-	8.8(−9)	11.6(+)	1.1(17)
	(5 – 4)	$2.0 \pm 0.6(-9)$	-	-	-	-	1.7(−8)	8.5(+)	9.8(16)
	(6 – 5)	$5.3 \pm 1.6(-9)$	$7.4 \pm 0.7(-9)$	-	-	-	2.8(−8)	3.8(+)	6.7(16)
	(7 – 6)	$1.1 \pm 0.3(-8)$	-	-	-	-	4.2(−8)	3.8(+)	5.6(16)
	(8 – 7)	$1.1 \pm 0.3(-8)$	$2.5 \pm 0.3(-8)$	-	-	-	5.9(−8)	2.4(+)	3.7(16)
	(9 – 8)	$1.8 \pm 0.5(-8)$	$4.1 \pm 0.4(-8)$	-	-	-	7.7(−8)		2.4(16)
	(10 – 9)	$1.9 \pm 0.6(-8)$	$3.3 \pm 0.4(-8)$	-	-	-	9.1(−8)	2.8(+)	1.4(16)
	(11 – 10)	$2.8 \pm 0.8(-8)$	-	-	-	-	9.7(−8)	3.5(+)	7.6(15)
	(12 – 11)	$2.5 \pm 0.7(-8)$	-	-	-	-	8.8(−8)	3.5(+)	3.9(15)
	(13 – 12)	$2.5 \pm 0.7(-8)$	$3.8 \pm 0.5(-8)$	-	-	-	6.9(−8)		1.9(15)
	(15 – 14)	-	-	$3.4 \pm 0.7(-8)$	-	-	3.0(−8)		4.1(14)
	(16 – 15)	-	-	$2.0 \pm 0.4(-8)$	-	-	1.8(−8)		1.9(14)
	(17 – 16)	-	-	$1.2 \pm 0.3(-8)$	-	-	1.1(−8)		8.6(13)
	(18 – 17)	-	-	$7.3 \pm 1.7(-9)$	-	-	6.1(−9)		3.9(13)
	(19 – 18)	-	-	$4.3 \pm 2.5(-9)$	-	-	3.5(−9)		1.8(13)
^{13}CO									
	(5 – 4)	$1.0 \pm 0.3(-9)$	$1.7 \pm 0.2(-9)$	-	-	-	1.5(−9)		
	(6 – 5)	$1.1 \pm 0.3(-9)$	-	-	-	-	2.5(−9)		
	(7 – 6)	$1.8 \pm 0.5(-9)$	-	-	-	-	3.3(−9)		
	(8 – 7)	$2.3 \pm 0.7(-9)$	$4.1 \pm 0.4(-9)$	-	-	-	3.9(−9)		
	(9 – 8)	$3.8 \pm 1.1(-9)$	-	-	-	-	3.9(−9)		
	(10 – 9)	$3.1 \pm 0.9(-9)$	$4.8 \pm 0.5(-9)$	-	-	-	3.5(−9)		
C^{18}O									
	(5 – 4)	-	$2.9 \pm 0.3(-10)$	-	-	-	1.5(−11)	19(−)	
	(9 – 8)	-	$2.6 \pm 0.3(-10)$	-	-	-	4.5(−11)	5.8(−)	
CH$^+$									
	(1 – 0)	-	$1.0 \pm 0.1(-9)$	-	-	-	2.7(−9)	2.7(+)	
	(2 – 1)	-	$5.5 \pm 0.8(-10)$	$6.6 \pm 2.5(-9)$	-	-	5.1(−9)		
	(3 – 2)	-	-	$5.6 \pm 2.1(-9)$	-	-	5.0(−9)		
HCO$^+$									
	(1 – 0)	-	-	-	-	$4.5 \pm 1.3(-12)$	5.2(−12)		
	(6 – 5)	-	$8.2 \pm 0.7(-11)$	-	-	-	1.0(−10)		
C$^+$									
	158 μm	-	$7.6 \pm 1.1(-7)$	$7.3 \pm 1.5(-7)$	$9.9 \pm 2.0(-7)$	-	2.3(−7)	3.2(−)	
C									
	609 μm	2.7(−10)	-	-	-	-	1.8(−9)	6.7(+)	
	370 μm	5.9(−9)	-	-	-	-	1.0(−8)		
O									
	145 μm	-	-	$4.0 \pm 0.8(-7)$	$3.8 \pm 0.8(-7)$	-	5.0(−7)		
	63 μm	-	-	-	$1.9 \pm 0.4(-6)$	$2.3 \pm 0.5(-6)$	3.5(−6)		
HD									
	(1 – 0)	-	-	$2.7 \pm 2.2(-9)$	-	-	9.2(−10)		
H_2		ISO	SPITZER	Lemaire et al. [1996]					
	$S(0)$	3.5(−8)	-	-			3.5(−8)		
	$S(1)$	2.1(−7)	$2.0^{+0.6}_{-0.3}(-7)$	-			3.3(−7)		
	$S(2)$	2.4(−7)	$5.5^{+2.0}_{-1.7}(-7)$	-			4.3(−7)		
	$S(3)$	4.1(−7)	$6.9^{+3.1}_{-1.5}(-7)$	-			1.0(−6)		
	$S(4)$	1.5(−7)	-	-			2.3(−7)		
	$S(5)$	2.6(−7)	$4.6 \pm 1.4(-7)$	-			2.8(−7)		
	(1 – 0)$S(1)$	-	-	$2.1 \pm 0.21(-7)$			9.4(−8)		
	(1 – 0)$S(2)$	-	-	$7.6 \pm 1.7(-8)$			3.3(−8)	2.3(−)	

Table 13: Comparison of the observations at the H_2 peak position with our best model (constant pressure $P = 1 \times 10^8$ K.cm^{-3}, $A_V = 5$). Green: the models are within the error bars; blue: within a factor of 2; red: otherwise, with the error factor given (plus sign: model intensities are larger that the observation; minus sign: smaller). The intensities are given in W.m^{-2}.sr^{-1}.

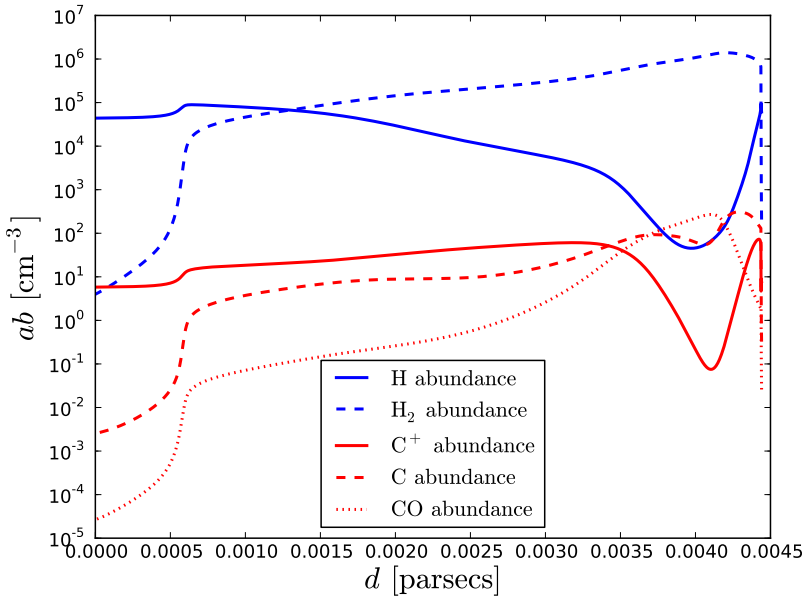

Figure 110: Abundance profiles of the main chemical species for the best model (constant pressure, $P = 1 \times 10^8$ K.cm^{-3}, $A_V = 5$).

Our model reproduces most of the observations satisfactorily (roughly two-third of the constraints), while some observations are mispredicted by a factor greater than 2. We will now see that some of these discrepancies can be explained, while plausible explanations can be proposed for the others.

11.3.3 *Additional aspects*

We now discuss possible explanations for the discrepancies noticed in the previous section.

11.3.3.1 *Low-J* ^{12}CO *and* ^{13}CO *lines*

As the PDR is seen almost edge-on, it is expected that the emission of species that emit at differing depths in the PDR will peak at different angular positions. In particular, the lines tracing the edge of the PDR (H_2 and high-J CO lines) should appear slightly closer to the star than the lines tracing the deeper colder layer (low-J CO and ^{13}CO). As the SPIRE data come from a map, we have access to the intensities at other positions. We took the position RA(2000) = 21h01m29.4s , Dec(2000) = +68°10′29.0″, slightly behind the H_2 emission peak position (at which the other observations have been taken) and corresponding to the peak of the 250 μm dust emission. Those data were presented in Tables 8 and 9.

Fig. 111 shows the comparison between the SPIRE observations of ^{12}CO at the two positions and our best model. We see that the observations at the back

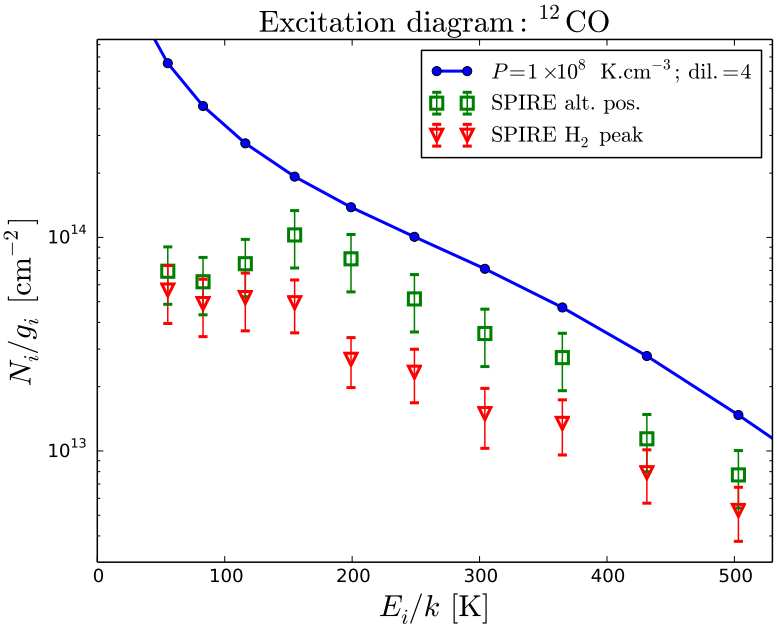

Figure 111: Comparison of the best model (constant pressure $P = 1 \times 10^8$ K.cm^{-3}, $A_V = 5$) with the SPIRE ^{12}CO data at the position of the H_2 peak (red triangles) and at the position of the 250 μm emission peak (green squares).

position are significantly closer to the predictions of the model so that most of the lines are now within a factor of 2 of the model predictions. The same comparison for ^{13}CO is shown on Fig. 112. Here again, the observations at the new position are closer to the predictions of the model. All the predictions fall within the error bars of these new observations.

The global comparison is shown on Table 14. We now have a perfect agreement with all ^{13}CO lines, and a good agreement on most of the low-J CO lines.

11.3.3.2 *Mutual shielding between* H_2, ^{12}CO, ^{13}CO *and* C^{18}O

Our model so far computes the radiative transfer using the usual FGK approximation for self-shielding (Federman, Glassgold, and Kwan 1979) which ignores possible effects of mutual shielding between the dissociation lines of different species, or between different lines of the same species. As the properties of ^{12}CO, ^{13}CO and C^{18}O are very close, mutual shielding effects can be important between these species, especially for the rarer isotopes whose column densities are not enough for significant self-shielding. Moreover, at depth greater than the H/H_2 transition, the dissociation lines of H_2 are very saturated with large tails and absorb a significant fraction of the total UV flux in regions where the dissociation lines of CO (and its isotopomers) are also located. We can thus also expect H_2 to protect CO from photodissociation.

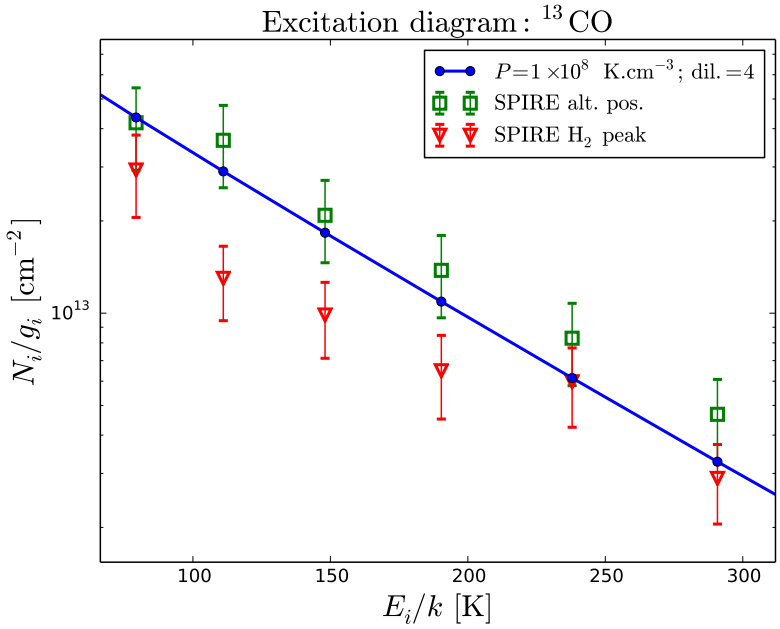

Figure 112: Comparison of the best model (constant pressure $P = 1 \times 10^8$ K.cm^{-3}, $A_V = 5$) with the SPIRE ^{13}CO data at the position of the H_2 peak (red triangles) and at the position of the 250 μm emission peak (green squares).

We investigated this effect as a possible explanation for the high observed intensities of C^{18}O.

As the Meudon PDR Code allows the exact computation of radiative transfer for a given set of absorption lines, we compared our best model with and without the exact transfer in the main dissociation lines of H_2, ^{12}CO, ^{13}CO and C^{18}O. Fig. 113 show the comparison of the chemical structures of the two models (solid line: FGK approximation as before, dashed line: full transfer). A first effect is that the H/H_2 transition is shifted slightly towards the edge of the cloud. This occurs because of overlapping between different H_2 dissociation lines. A much larger effect appears for CO: because of the shielding of CO by H_2, CO appears significantly closer to the edge, and a direct transition from C^+ to CO is observed, without the neutral C region. This disappearance of the C abundance peak when taking mutual shielding into account could explain our previously overestimated C (609 μm) line.

Fig. 114 shows the profiles of the abundances of the different isotopomers of CO. The strongest effect appears to be for C^{18}O, which sees its total column density increased by one order of magnitude. The abundance profiles for ^{12}CO and ^{13}CO remain similar because the two species are strongly coupled through the exchange reaction $^{12}\mathrm{CO} + {}^{13}\mathrm{C}^+ \rightleftharpoons {}^{13}\mathrm{CO} + {}^{12}\mathrm{C}^+$ (there is no enrichment as the gas temperature is ~ 100 K), so that ^{13}CO is not very sensitive to changes of its photodissociation rate. The formation of C^{18}O is

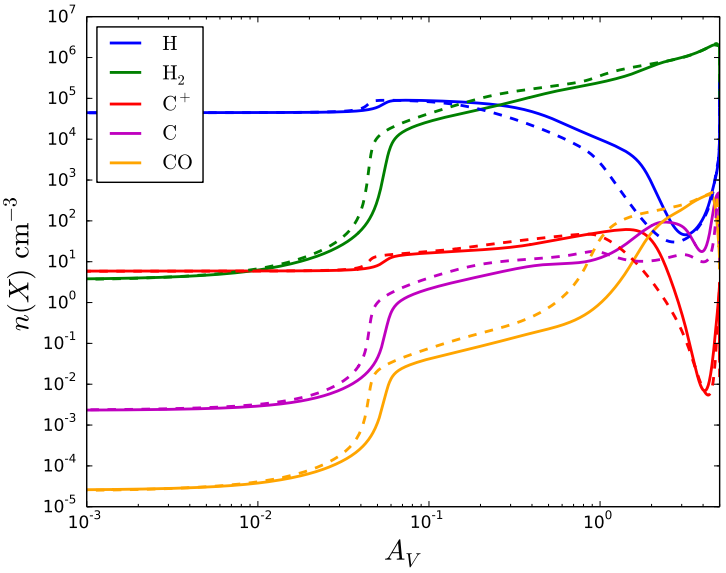

Figure 113: Comparison of the chemical structure of our standard best model ($P = 1 \times 10^8$ K.cm^{-3}, $A_V = 5$, solid lines) with an identical model with the full computation of the radiative transfer (dashed line, taking into account mutual shielding effects).

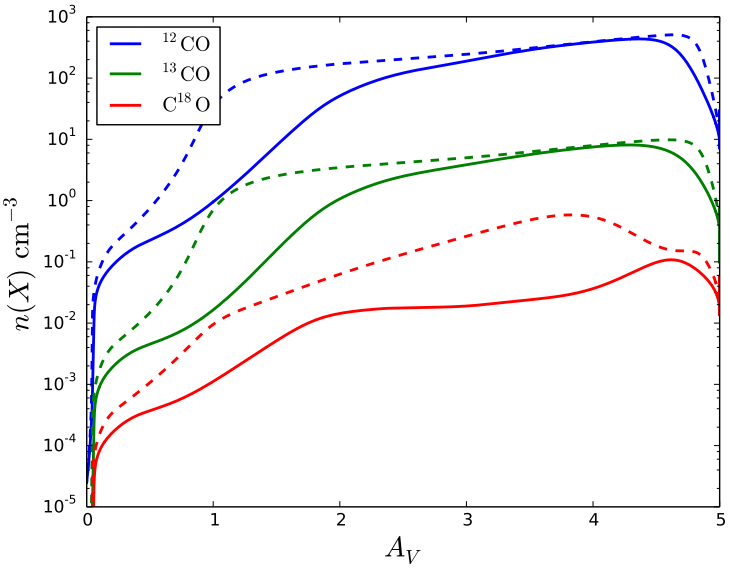

Figure 114: Comparison of the abundance profiles of the isotopomers of CO between our standard best model ($P = 1 \times 10^8$ K.cm^{-3}, $A_V = 5$, solid lines) and an identical model with the full computation of the radiative transfer (dashed line, taking into account mutual shielding effects).

Species	Line	SPIRE (alt. pos.)	Model	
^{12}CO			Intensity	Error factor
	$(4-3)$	$9.3 \pm 2.8 \times 10^{-10}$	8.8(−9)	9.5(+)
	$(5-4)$	$2.5 \pm 0.8 \times 10^{-9}$	1.7(−8)	6.8(+)
	$(6-5)$	$7.6 \pm 2.3 \times 10^{-9}$	2.8(−8)	3.7(+)
	$(7-6)$	$2.2 \pm 0.7 \times 10^{-8}$	4.2(−8)	
	$(8-7)$	$3.4 \pm 1.0 \times 10^{-8}$	5.9(−8)	
	$(9-8)$	$3.9 \pm 1.2 \times 10^{-8}$	7.7(−8)	
	$(10-9)$	$4.6 \pm 1.4 \times 10^{-8}$	9.1(−8)	
	$(11-10)$	$5.6 \pm 1.7 \times 10^{-8}$	9.7(−8)	
	$(12-11)$	$3.6 \pm 1.1 \times 10^{-8}$	8.8(−8)	2.4(+)
	$(13-12)$	$3.6 \pm 1.1 \times 10^{-8}$	6.9(−8)	
^{13}CO				
	$(5-4)$	$1.4 \pm 0.4 \times 10^{-9}$	1.5(−9)	
	$(6-5)$	$3.1 \pm 0.9 \times 10^{-9}$	2.5(−9)	
	$(7-6)$	$3.8 \pm 1.1 \times 10^{-9}$	3.3(−9)	
	$(8-7)$	$4.9 \pm 1.5 \times 10^{-9}$	3.9(−9)	
	$(9-8)$	$5.3 \pm 1.6 \times 10^{-9}$	3.9(−9)	
	$(10-9)$	$5.0 \pm 1.5 \times 10^{-9}$	3.5(−9)	

Table 14: Comparison of the SPIRE observations at the 250 μm emission peak position with our best model (constant pressure $P = 1 \times 10^8$ K.cm^{-3}, $A_V = 5$). The model intensities are colored in green if they are within the error bars of an observation, in blue if they are within a factor of 2 of an observation, and in red otherwise, in which case the error factor is given (a plus sign indicates that the model intensities is larger that the observation, a minus sign that it is smaller). The intensities are given in W.m^{-2}.sr^{-1}.

dominated by the reactions of CH, CH_2 and C_2H with ^{18}O, and it is thus more directly affected by the reduced photodissociaton rate.

For the rotational lines of interest ($(5-4)$ and $(9-8)$), the ^{12}CO lines are almost unaffected (factors of 1.1 and 1.5 respectively), the ^{13}CO lines are slightly increased (factors of 1.6 and 2.3 respectively), while the C^{18}O lines are strongly enhanced (factors of 8.2 and 6.8 respectively). A new best model would need to be adjusted as the intensities of the high-J CO and H_2 lines have been modified, but the relative variation of those three species (for the low-J lines) are consistent with the discrepancies of our current best model (^{12}CO slightly overestimated, ^{13}CO perfectly reproduced, and C^{18}O strongly underestimated). Moreover, the disappearance of the neutral C region could also resolve our overestimation of the C line.

Constant pressure models with full transfer computation are currently very unstable (they have to be carefully initialized to properly converge), so that running large grids of models to adjust a new best model was not practical. These results should be investigated again when the numerical difficulties will have been solved to check that the effects are not only "in the right direction", but also quantitatively reproduce the observations.

For now, mutual shielding effects are a plausible explanation for our discrepancies on the $C^{18}O$ and C lines.

11.3.3.3 C^+ *intensity*

The intensity of the C^+ 158 μm line in the models shows very little variation with pressure (decreasing the pressure to 3×10^6 K.cm^{-3} only increases the intensity by a factor of 1.8). Any gas surrounding the PDR (possibly at lower pressure) and filling the beam of the observation would thus explain the observed intensity. This discrepancy could thus be explained by geometry effects.

CONCLUSIONS

In this work, a very large number of observational constraints were available for a single object, allowing an in-depth modeling of the PDR. We had 42 observational constraints which we fitted with a 3-parameters model (pressure, total A_V, dilution factor. All other parameters were fixed *a priori*). This gives good hopes that the good results of the model imply that the relevant physics is correctly included.

Of these constraints, 24 corresponds to tracers of the PDR edge (defined broadly as the region between the H/H_2 transition and the C^+/CO transition). 20 of those were well reproduced by the model. This gives us a good confidence that a constant pressure is a good approximation in this region, and the value of the pressure at $P = 1 \times 10^8$ K.cm^{-3} is well constrained. There is a degeneracy for the dilution factor and the viewing angle as the edge tracers are all optically thin lines. Fixing a somewhat arbitrary value for the viewing angle resulted in a well constrained dilution factor.

The remaining 18 observations tracing the deeper parts of the PDR are not as well reproduced by our model (only 8 are well reproduced), which may indicate that some aspects of the physics or the geometry of this region are not well described. We saw that including mutual shielding effects could allow 3 more constraints to be reproduced. In addition, nearly edge-on viewing could result in some species having their emission peak shifted. A tentative correction for this effect resulted in 4 more reproduced constraints.

Finally, the derived value for the pressure and the density values in the different regions are in good agreement with previously deduced values in the literature (see Sect. 11.1.2).

Part V

CONCLUSIONS AND PERSPECTIVES

CONCLUSIONS

The work presented in this thesis focused on two seemingly unrelated subjects. On the one hand, we studied the influence of the fluctuations of the dust temperature on the chemistry that occurs on grain surfaces, and more specifically on the formation of H_2. The goal was to set an exact formalism to treat the problem of the coupled fluctuations of the grain temperature and the population of adsorbed atoms on the grain surface. Indeed, the grain temperature fluctuates each time a UV photon is absorbed by the grain, and these fluctuations perturbate the chemical equilibrium on the grain surface and drive fluctuations of the chemical populations. This results in fluctuations of the H_2 formation efficiency, and the goal was to derive the resulting average formation rate.

On the other hand, we tackled the question of how the dissipation of turbulence at the smallest scales affects the chemical and thermal state of the diffuse CNM, and whether these mechanisms could explain the observed excitation of H_2 and the observed abundances of CH^+ and other chemical tracers. The goal was here again to propose a formalism in which the problem of the thermo-chemical evolution of a gas submitted to a fluctuating heating rate caused by turbulence could be treated, and which could give access to the average values of the observables (and possibly higher order statistics).

Thus, these two problems turn out to be similar, and could be more generally expressed as problems of the stationary state of a chemical system submitted to (large) fluctuations of its parameters. They were thus naturally expressed in the framework of stochastic processes.

We expressed the problem of surface chemistry on grains with temperature fluctuations in a fully consistent formalism based on (pure jump) stochastic processes and their associated master equation, which is completely independent of any discretization procedure.

This formalism allowed us to revisit the statistics of the temperature fluctuations, for which we verified the agreement of our results with previously published works. We also derived an analytical approximation for big grains, and a second physically-based approximation that allows a very fast computation of the dust emissivity, and was implemented in the Meudon PDR Code.

More generally, the framework presented can be applied to any surface reaction on grains subject to temperature fluctuations, in the limits of the computational possibilities.

This framework was applied to two different mechanisms for H_2 formation: the Langmuir-Hinshelwood mechanism (reaction between surface atoms) on

physisorption sites, and the Eley-Rideal mechanism (reaction between a surface atom and a gas atom) on chemisorption sites. It was shown that the master equation can be significantly simplified for linear reactions such as the Eley-Rideal mechanism. A numerical resolution method was proposed for both cases, based on the properties of the eigenvalues of the integral operators appearing in the equations.

The most surprising result of this computation is that the Langmuir-Hinshelwood mechanism can be efficient even in a gas that is not shielded from the UV radiation field for UV intensities G_0 up to a few hundreds. A long standing problem for the Langmuir-Hinshelwood mechanism was that experiments and models predict a very restricted range of efficiency in terms of grain temperatures ($T < 20\,\mathrm{K}$), while the grain temperatures in regions exposed to the UV radiation field have been estimated to be hotter than that. As we know that H_2 formation occurs also efficiently in these regions, it results in a paradox for which various solutions have been proposed (such as other mechanisms supplementing the Langmuir-Hinshelwood mechanism in these regions).

However, as temperature fluctuates, most of the energy absorbed by the grain is radiated away during short temperature spikes following photon-absorption events, and most of the time is actually spent in very low temperature states. Thus H_2 formation can be efficient during a large fraction of the time. This behavior only occurs for grains small enough to have significant temperature fluctuations. For the Langmuir-Hinshelwood mechanism, it is found that grains up to 20 nm are affected by this effect. As a result, the Langmuir-Hinshelwood mechanism is efficient in a wide range of astronomical environments, including moderate PDRs (G_0 up to a few hundreds).

The Eley-Rideal mechanism is only slightly affected by the fluctuations, with a small reduction of its efficiency, caused by the fact the grain does not have enough time between fluctuations (that evaporate its surface population) to recover its equilibrium surface population. This effect results from a competition between the timescale of the fluctuations and the timescale of adsorption of atoms from the gas.

This effect becomes important also for the Langmuir-Hinshelwood mechanism deeper inside the cloud, after the H/H_2 transition. Indeed, in a molecular gas, the abundance of atomic hydrogen is very low, so that the adsorption timescale becomes very long, and even rare fluctuations caused by IR photons that can penetrate at this depth inside the cloud become sufficient keep the grain permanently out of equilibrium, resulting in reduced formation efficiency. This can be seen as a self-limitation mechanism: the gas cannot become completely molecular as when the atomic abundance declines, fluctuations starts to reduce the efficiency. Inside dense molecular clouds, such fluctuations could be caused by secondary UV photons and by cosmic rays, while in diffuse clouds rare visible-NIR photons would be sufficient (the grains are smaller). This limitation mechanism could be relevant to explain

the atomic fraction inside molecular clouds, as observed through HI narrow self-absorption, or the molecular fraction in diffuse clouds.

To tackle the problem of turbulent chemistry in the interstellar medium, we proposed an adaptation of the PDF methods that have been developed in the field of turbulent combustion. These methods consist in modeling the unclosed terms of the one-point PDF transport equation by the use of Lagrangian stochastic models. The direct Monte Carlo simulation of the stochastic processes is then used to solve for the PDF.

In the simplest case of stationary homogeneous turbulence, this reduces to modeling the Lagrangian evolution of the dissipation rate as a stochastic process, and coupling the dynamical evolution of the thermo-chemical state of the fluid element to this stochastic process. We proposed here a simple model for the dissipation stochastic process that gives the correct PDF and time autocorrelation function according to the log-normal model of intermittency. However, the time statistics of the most extreme events appear to be incorrect when compared to the usual turbulence scaling laws, resulting in extreme events that are not short enough.

We applied this framework to a simple model of the diffuse CNM aimed at computing the temperature PDF and average H_2 excitation in diffuse molecular clouds. In this preliminary version, the chemical evolution was not followed and only the thermal state of the gas was dynamically computed. The resulting model predicts the average excitation of H_2 observed by FUSE in absorption with a good accuracy.

The framework of the PDF method presented naturally treats turbulent transport and mixing when the hypothesis of spatial homogeneity is released. Similar methods have also proved very efficient as sub-grid models for LES simulations of turbulent reacting flows.

PERSPECTIVES

From the current state of these two projects, several lines of development are possible to extend, improve, and test the models.

An unexpected result of our models of H_2 formation on dust grains is the reduction of the formation efficiency in the molecular part of the clouds. Li and Goldsmith [2003], Goldsmith and Li [2005] have presented observations of HI narrow self-absorption that trace the atomic fraction present in dense molecular cores. These observations provide the first constraint on H_2 formation efficiency in the cold regions of dense clouds, and our prediction for a self-limitation of the formation efficiency could be tested against these observations.

Our present models show that this self-limitation effect increases when the density is decreased. For a gas density of $n = 100\,\mathrm{cm}^{-3}$, the atomic fraction in the core remains above 10%. This could help to explain the observed molecular fractions in the diffuse ISM. Previous PDR models tend to predict sharp transitions to almost fully molecular gas above some total column density, while the observations show a wide range of fractions. We will thus study further the predictions of our model in terms of molecular fraction in the diffuse ISM.

Moreover, our microphysical model of the formation mechanisms mostly followed that of a previous paper by Le Bourlot et al. [2012]. This model could be updated to incorporate more recent experimental and theoretical constraints, especially concerning the Eley-Rideal mechanism, for which the adopted parameters were mostly guestimates. Theoretical predictions of the excitation state of the newly formed molecule should also be integrated more precisely (we currently only use the constraint on the average internal energy, but assume a Boltzmann distribution). We could then look for possible signatures of the precise formation mechanism taking place in the different regions of the ISM (e.g. the Langmuir-Hinshelwood mechanism is expected to form molecules in a higher rotational state due to the geometry of the reaction). Finally, our formalism could be applied to more complex formation mechanisms, for instance by taking into account transitions between physisorption and chemisorption sites.

A later development will be the application of our formalism to other surface reactions. As discussed in the conclusion of Chap. 8, reactions involving rarer reactive species (C, O,...) should be more sensitive to the effects of fluctuations (because of the longer adsorption timescale), if those reactions involve barriers that can be crossed by the fluctuations. In the conditions where those reactions take place (UV radiation field completely absorbed), the fluctuations caused by secondary UV photons, secondary electrons, and cosmic rays should be considered. Such a precise statistical treatment might be useful to understand the return to the gas phase of the species formed in the ice layer.

Our models of the effects of turbulent dissipation in the diffuse ISM could first be further compared to the observations of FUSE [Gry et al., 2002, Lacour et al., 2005, Jensen et al., 2010], and we should especially derive predictions on the line widths to compare to the observed increase of the line width for higher J [Lacour et al., 2005]. The temperature PDF could also be tested by comparing our model to C^+ observations in the diffuse ISM. Langer et al. [2010] indeed found higher than expected C^+ emission that could be associated with the warm H_2 component.

The natural next step in the development of this model is to simultaneously follow the dynamical evolution of a simple chemical network containing the molecules of interest (CH^+, HCO^+, CO, ...). The model could then be tested

by comparison to these observations. Note that also following the dynamical evolution of the excitation of H_2 (it is currently assumed at statistical equilibrium), could lead to interesting effects. Short dissipation events could keep the excitation out of equilibrium and affect the cooling function. If the extreme events are frequent enough, it could affect the average ortho-para ratio as ortho-para conversion is slow.

Our stochastic model of the dissipation process also needs to be improved for more accurate time statistics of the extreme dissipation events. This could be done by comparison with numerical simulations. Moreover, previous models [Flower and Pineau des Forets, 1998, Godard et al., 2009] have shown that taking the ion-neutral drift in the dissipation structures into account is probably necessary to reproduce the observations. This can be done in several ways: if we assume that ambipolar diffusion occurs in the same structures as viscous dissipation (as is done in the previous models), we can simply relate the ion-neutral drift to the dissipation rate variable, otherwise a multivariate stochastic process representing the various dissipative processes would be needed. Here again, the precise statistics (correlations, or absence thereof, between the different dissipation processes) should be studied from numerical simulations of turbulence.

Our model will then be easily extended to include a spatial dimension and to study turbulent transport in chemically stratified clouds. In our formalism, adding a spatial dimension is not more computationally expansive than adding one chemical species. A simple treatment of radiative transfer can easily be implemented by using the average properties at each positions, but more careful modeling will be needed for a real statistical treatment of radiative transfer taking into account fluctuations and spatial correlations. This would result in the first complete model of the diffuse medium, which is controlled by turbulence-driven formation reactions and UV-driven photodissociation reactions.

In parallel, the possibility to couple similar PDF methods to numerical simulations of interstellar turbulence should be explored. Indeed, resolving the dissipative scales in simulations of interstellar turbulence at realistic Reynolds number is not yet possible, and adding a chemical network would further reduce the resolution (for computation time constraints). PDF methods have been successfully used as sub-grid models in RANS simulation (Reynolds-averaged Navier Stokes simulations, such as $k-\epsilon$ models), and such methods have also been adapted for Large Eddy Simulations (LES). The idea would be to simulate only the largest scales of the turbulent cascade (the principle of LES), while modeling the influence of the smaller scales by a PDF method (called in this case FDF methods, for filtered density functions, see Sheikhi et al., 2009).

The complexity of the ISM revealed by modern instruments calls for a more statistical approach to modeling in astrophysics. The understanding

that is gained from a model can be gauged by how much it simplifies reality while still correctly predicting the observables. A good model keeps only the important effects and ignores the complexity of the unimportant details. It has become obvious that interstellar clouds have highly complex structures with individual details shaped by chance events, and the universal laws that govern these objects regardless of the individual details of their shapes and histories can only be statistical in nature. The prediction and formulation of such laws require a stochastic modeling framework. Examples of such problems include the phase transition between CNM and WNM in a turbulent medium, or radiative transfer across density heterogeneities resulting from compressible turbulence, i.e., how far can dissociative UV radiation penetrate in such a medium ?

This thesis gathered and experimented with a few mathematical modeling tools that could be useful in such an endeavor.

Part VI

APPENDIX

A

TOOLS AND NOTATIONS IN PROBABILITY

This appendix defines a few tools, sets the notations for chapter 4, and gives some useful classical results (without proof). We stay at an intuitive level of the concept of probability, and do not venture into measure-theoretic probability theory. Our presentation of the definitions is mainly restricted to random variables and not as general as they could be.

A.1 SINGLE-VARIABLE CASE

A.1.1 *Random variables and probabilities*

At an intuitive level, a random variable is a variable whose value changes randomly each time an experiment is repeated. We will mostly consider here real variables, but the definitions can be adapted for integer variables as well.

An event is a set of outcomes of the experiment. For instance if we call our variable X, $\{X = 3\}$, $\{X < 5\}$ or $\{X \in [0;1]\}$ are events. To any event A is associated a probability $P(A)$ which must verify the following conditions:

- $P(A)$ is a positive real number
- $P(X \in \mathbb{R}) = 1$, i.e. the probability that the variable takes any of its possible values is 1.
- For any countable family of events A_i that are mutually exclusive, the probability that at least one of the event is realized is $\sum_i P(A_i)$

This probability can be interpreted either as the frequency of realization of the event if the experiment is realized infinitely many times, or as a measure of our expectation (or belief) that an event will realize (it can be shown that any consistent system of belief must verify those three axioms of probability).

The three conditions above can be shown to imply the other usual rules of probability:

- $P(X \in \emptyset) = 0$
- If $A \subset B$ (A implies B), $P(A) > P(B)$
- for any event $P(A) \in [0;1]$
- $P(A \cup B) = P(A) + P(B) - P(A \cap B)$ ($A \cup B$ is the event that at least one of A and B is realized, and $A \cap B$ the event that both A and B are realized)

A.1.2 *Cumulative distribution functions and probability distribution functions*

A particular class of events that are particularly useful consists in the events of the form $\{X < x\}$. Note the distinct notations for the random variable X and the particular value x that defines the event. The variable defining the event is usually called the sample space variable, and a distinct notation must be kept to avoid dangerous ambiguities later.

The probabilities of these specific events are used to define an important function characterizing the random variable, the *cumulative distribution function:*

$$F_X(x) = P(X < x) \tag{373}$$

This function obviously verifies $F_X(x) \in [0;1]$, $F_X(-\infty) = 0$ and $F_X(+\infty) = 1$ and is an increasing function.

From this function, a second more practical characterizing function can be defined, the *probability distribution function* (PDF):

$$f_X(x) = \frac{dF_X(x)}{dx} \tag{374}$$

This definition can be generalized if F_X is not differentiable, or even discontinuous at some points by the use of the Dirac δ function.

The properties of the PDF f_X are that $f_X(x) \geq 0$, and

$$\int_{-\infty}^{+\infty} dx\, f_X(x) = 1. \tag{375}$$

This function gives the relative probability of the neighborhood of the value x. Note that our notation explicitly refers to a random variable X, so that we can handle several random variables.

If we define a second random variable Y related to X by $Y = g(X)$, the PDF of Y is related to that of X by the relation

$$f_Y(y) = \sum_k f_X(x_k) \frac{1}{\left|\frac{dg}{dx}(x_k)\right|} \tag{376}$$

where the x_k are the solutions to the equation $y = g(x)$. If g is bijective, this simplifies to the usual formula:

$$f_Y(y) = f_X(x) \frac{1}{\left|\frac{dg}{dx}(x)\right|} \tag{377}$$

A.1.3 *Mean and moments*

The mean, or expected value, of the variable X is defined as

$$\langle X \rangle = \int_{-\infty}^{+\infty} dx\, x\, f_X(x) \tag{378}$$

if this integral converges absolutely. In pathological cases, where the PDF f_X is not defined, the correct definition is in term of the Stieltjes integral:

$$\langle X \rangle = \int_{-\infty}^{+\infty} x \, dF_X(x) \tag{379}$$

(we recall that the Stieltjes integral with respect to a function f is defined as $\int_a^b g(x)\, df(x) = \lim_{h \to 0} \sum_{i=0}^{n-1} g(c_i)(f(x_i) - f(x_{i+1}))$, where the x_i are so that $a = x_0 < x_1 < \ldots < x_{n-1} = b$ with $x_{i+1} - x_i = h$, and $c_i \in [x_i, x_{i+1}]$). Note that the expected value behaves as a linear operator.

The variable change for the PDF (Eq. 377) ensures that for $Y = g(X)$,

$$\langle Y \rangle = \int_{-\infty}^{+\infty} dy \, y \, f_Y(y) = \int_{-\infty}^{+\infty} dx \, g(x) \, f_X(x) \tag{380}$$

so that the computation of the average of any function of X does not require to explicitly compute the corresponding PDF, and $\langle Y \rangle$ can be noted $\langle g(X) \rangle$.

More generally the moment of order n of the random variable is defined as

$$\langle X^n \rangle = \int_{-\infty}^{+\infty} dx \, x^n \, f_X(x) \tag{381}$$

if this integral converges absolutely.

A random variable can have no mean, or no moment of order n. If it does not have a moment of order n, then it does not have any moment of order $m > n$ either.

It is usual to define the central moment of order n as

$$M_n(X) = \langle (X - \langle X \rangle)^n \rangle = \int_{-\infty}^{+\infty} dx \; (x - \langle X \rangle)^n \; f_X(x) \tag{382}$$

Commonly used quantities derived from these central moments include the variance

$$\mathrm{Var}(X) = M_2(X), \tag{383}$$

the standard deviation

$$\mathrm{std}(X) = \sqrt{\mathrm{Var}(X)}, \tag{384}$$

the skewness

$$S(X) = \frac{M_3(X)}{(\mathrm{std}(X))^3}, \tag{385}$$

and the kurtosis

$$K(X) = \frac{M_4(X)}{(\mathrm{Var}(X))^2} - 3. \tag{386}$$

The standard deviation gives the average absolute deviation from the mean, the skewness measures the asymmetry of the PDF around the mean, and the kurtosis gives an idea (for unimodal distributions) of wether probability lies in the peak and the tails, or in the shoulders in between. For a normal distribution, both the skewness and the kurtosis are zero.

A.2 MULTI-VARIABLE CASE

A.2.1 *Independence*

Two events A and B are said to be independent if

$$P(A \cap B) = P(A)P(B) \tag{387}$$

For more than two events, this definition must be made more specific.

A family $\{A_i\}$ of events are said to be pairwise independent if any two events A_i and A_j are independent as defined by Eq. 387.

A family $\{A_i\}$ is said to be mutually independent if for any subset $\{A_j\}$,

$$P(\bigcap_j A_j) = \prod_j P(A_j) \tag{388}$$

A.2.2 *Probability density function and moments*

If we consider several random variables $X_0, \ldots, X_n$, the cumulative distribution function is defined as

$$F_{X_0 \ldots X_n}(x_0, \ldots, x_n) = P(\{X_0 < x_0\} \cup \{X_1 < x_1\} \cup \ldots \cup \{X_n < x_n\}) \tag{389}$$

and the PDF as

$$f_{X_0 \ldots X_n}(x_0, \ldots, x_n) = \frac{d^n F_{X_0 \ldots X_n}}{dx_0\, dx_1 \ldots dx_n}(x_0, \ldots, x_n) \tag{390}$$

Two random variables are said to be independent if

$$f_{XY}(x, y) = f_X(x)\, f_Y(y) \tag{391}$$

The moment of order $(m_0, \ldots, m_1)$ is defined as

$$\left\langle X_0^{m_0}, \ldots, X_n^{m_n} \right\rangle = \int dx_0 \ldots dx_n\, x_0^{m_0} \ldots x_n^{m_n}\, f_{X_0 \ldots X_n}(x_0, \ldots, x_n) \tag{392}$$

One commonly used quantity is the correlation coefficient defined as

$$\rho_{X_i X_j} = \frac{\left\langle \left(X_i - \langle X_i \rangle\right)\, \left(X_j - \left\langle X_j \right\rangle\right) \right\rangle}{\mathrm{std}(X_i)\, \mathrm{std}(X_j)} \tag{393}$$

This coefficient takes values between -1 and 1. It is exactly -1 or 1 if $X_j = aX_i + b$ (-1 if $a < 0$, $+1$ if $a > 0$). Otherwise it measures how close to linearly dependent the variables are. If 0, the variables are said uncorrelated, which does not imply that they are independent, as seen for $X_j = X_i^2$.

For a variable change

$$\begin{cases} Y_0 = g_0(X_0) \\ \vdots \\ Y_n = g_n(X_n) \end{cases} \tag{394}$$

the PDF of the new variables is related to that of the old ones by

$$f_{Y_0 \dots Y_n}(y_0, \dots, y_n) = \sum_k f_{X_0 \dots X_n}(x_0^{(k)}, \dots, x_n^{(k)}) \frac{1}{\left| \text{Det} \left(\frac{\partial g_i}{\partial x_j}(x_0^{(k)}, \dots, x_n^{(k)}) \right) \right|} \tag{395}$$

where the families $(x_0^{(k)}, \dots, x_n^{(k)})$ are the solutions to the system of equations

$$\begin{cases} y_0 = g_0(x_0) \\ \vdots \\ y_n = g_n(x_n) \end{cases} \tag{396}$$

and the denominator is the determinant of the Jacobian matrix of the variable change. Note that this formula can be used simply when $m < n$ new variables are considered by completing with the old variables.

A.2.3 *Marginal PDF*

One can decide to consider only a subgroup of j of our n variables (we take the first j variables for simplicity of notations). It follows from the definitions that

$$F_{X_0 \dots X_j}(x_0, \dots, x_j) = F_{X_0 \dots X_n}(x_0, \dots, x_j, +\infty, \dots, +\infty) \tag{397}$$

and

$$f_{X_0 \dots X_j}(x_0, \dots, x_j) = \int dx_{j+1} \dots dx_n \, f_{X_0 \dots X_n}(x_0, \dots, x_n) \tag{398}$$

In particular, for a single variable X_0, the cumulative distribution function and the PDF are called *marginal* in this case. The *marginal* cumulative distribution function is

$$F_{X_0}(x_0) = F_{X_0 \dots X_n}(x_0, +\infty, \dots, +\infty) \tag{399}$$

and the marginal PDF is

$$f_{X_0}(x_0) = \int dx_1 \dots dx_n \, f_{X_0 \dots X_n}(x_0, \dots, x_n) \tag{400}$$

A.2.4 *Conditional PDF and moments*

Given and event B, it is possible to define a new measure of probability

$$P_B(A) = \frac{P(A \cap B)}{P(B)} \tag{401}$$

If $P(B) \neq 0$, this new measure of probability verifies the three necessary properties (see Sect. A.1.1). This new measure represents the probability of event A knowing that event B is realized. It is called the conditional probability and usually noted $P(A\,|B\,)$.

The Bayes formula is a direct consequence of this definition:

$$P(B\,|A\,) = \frac{P(A\,|B\,)P(B)}{P(A)}$$

Coming back to our several random variables $X_0, \ldots, X_n$, we might want to define a conditional cumulative distribution function

$$F_{X_0 \ldots X_i | X_{i+1} \ldots X_n}(x_0, \ldots, x_i\,|x_{i+1}, \ldots, x_n) = P(X_0 < x_0, \ldots, X_i < x_i\,|X_{i+1} = x_{i+1}, \ldots, X_n = x_n\,) \tag{402}$$

which is conditioned on the other variables having precise values. However, we saw previously that we can only define a conditional probability with respect to an event whose probability is not zero. The conditioning event that we need here has most likely zero probability. We can properly define this quantity in the following way.

For simplicity, let us consider two variables X and Y, and for a given Δy, let us define the (well defined) conditional cumulative distribution function

$$\begin{aligned} F(x\,|y < Y \leq y + \Delta y\,) &= P(X < x\,|y < Y \leq y + \Delta y\,) \\ &= \frac{P(\{X < x\} \cup \{y < Y \leq y + \Delta y\})}{P(y < Y \leq y + \Delta y)} \\ &= \frac{F_{XY}(x, y + \Delta y) - F_{XY}(x, y)}{F_Y(y + \Delta y) - F_Y(y)} \end{aligned} \tag{403}$$

We then define $F(x\,|Y = y\,)$ as the limit of this quantity when Δy goes to zero. This gives the relation

$$F_{X|Y}(x\,|Y = y\,) = \frac{\frac{\partial}{\partial y} F_{XY}(x, y)}{f_Y(y)} \tag{404}$$

It follows that the relation for the conditional PDF $f_{X|Y}(x\,|Y = y)$ is

$$f_{X|Y}(x\,|Y = y) = \frac{f_{XY}(x, y)}{f_Y(y)} \tag{405}$$

which, as expected, is similar to the definition of the conditional probability Eq. 401. For simplicity, and when the notation for the sample space variables are clear enough, we often simply write the conditional PDF as $f_{X|Y}(x|y)$.

We see that the independence of X and Y is equivalent to

$$f_{X|Y}(x|y) = f_X(x) \tag{406}$$

As expected, knowing a variable that is independent of X does not give any information on the outcome of X.

We can then define the conditional moment of X knowing Y of order n as

$$\langle X^n | Y = y \rangle = \int_{-\infty}^{+\infty} dx\, x^n\, f_{X|Y}(x|y) \tag{407}$$

These definitions can easily be generalized to many variables for the conditional PDF:

$$f_{X_0 \dots X_j | X_{j+1} \dots X_n}(x_0, \dots, x_j | x_{j+1}, \dots, x_n) = \frac{f_{X_0 \dots X_n}(x_0, \dots, x_n)}{f_{X_{j+1} \dots X_n}(x_{j+1}, \dots, x_n)} \tag{408}$$

and the conditional moments of $X_0 \dots X_j$ knowing $X_{j+1} \dots X_n$ of order $(m_0, \dots, m_j)$:

$$\left\langle X_0^{m_0} \dots X_j^{m_j} | X_{j+1} = x_{j+1}, \dots, X_n = x_n \right\rangle = \int dx_0 \dots dx_j\, x_0^{m_0} \dots x_j^{m_j}\, f_{X_0 \dots X_j | X_{j+1} \dots X_n}(x_0, \dots, x_j | x_{j+1}, \dots, x_n) \tag{409}$$

A.3 STOCHASTIC PROCESSES AND FIELDS

A.3.1 *Definitions*

A stochastic process is a family of random variables indexed by a variable called "time" (which we will note t), which can be continuous. The random process is thus noted X_t. When no ambiguity is possible, we may simply note X. A stochastic process is called stationary if all its one-time statistics are independent of time, and if all its multi-time statistics only depend on time differences.

This notion can be generalized to a multidimensional indexing variable, in which case it is called a stochastic field, the indexing variable representing the spatial coordinates. In this case, we may write it $S_{(x,y,z)}$. A stochastic field is called homogeneous if all its one-point statistics are independent of position, and if all its multi-points statistics only depend on position differences.

A.3.2 *Probability density functions*

The one time PDF of a stochastic process X is simply a function of t, which returns the PDF of the random variable X_t. We note it

$$f_{X_t}(x; t) \tag{410}$$

We use a semi colon to separate the sample variable, with respect to which this function is a PDF, from the time parameter.

We can define the multi-time joint PDF for any number of times as the PDF of the corresponding set of random variables. We note it

$$f_{X_{t_0}\dots X_{t_n}}(x_0, \dots, x_n; t_0, \dots, t_n) \tag{411}$$

Note again the use of the semi-colon.

We can define the same quantities for a stochastic field. For any set of positions $(\overrightarrow{x_0}, \dots, \overrightarrow{x_n})$, the multi-point PDF is the PDF of the corresponding set of random variables, which we note

$$f_{S_{\overrightarrow{x_0}}\dots S_{\overrightarrow{x_n}}}(s_0, \dots, s_n; \overrightarrow{x_0}, \dots, \overrightarrow{x_n}) \tag{412}$$

When no ambiguity is possible, the n-points PDF of the stochastic field S can be noted $f_S^{(n)}$. Similarly the n-times PDF of the stochastic process can be noted $f_X^{(n)}$.

A.3.3 *Autocorrelation function*

Finally, one useful tool to characterize the dependency between the values of the process at different times, or the values of the field at different positions, is the autocorrelation function. For a stochastic process X, it is

$$\rho_X(\tau, t) = \frac{\langle (X_{t+\tau} - \langle X_{t+\tau} \rangle)\ (X_t - \langle X_t \rangle) \rangle}{\operatorname{std}(X_{t+\tau}) \operatorname{std}(X_t)} \tag{413}$$

For a stationary process, the autocorrelation function only depends on τ.

Similarly, for a stochastic field S, the autocorrelation function is

$$\rho_S(\overrightarrow{r}, \overrightarrow{x}) = \frac{\left\langle \left(X_{\overrightarrow{x}+\overrightarrow{r}} - \left\langle X_{\overrightarrow{x}+\overrightarrow{r}} \right\rangle\right)\ (X_{\overrightarrow{x}} - \langle X_{\overrightarrow{x}} \rangle) \right\rangle}{\operatorname{std}(X_{\overrightarrow{x}+\overrightarrow{r}}) \operatorname{std}(X_{\overrightarrow{x}})} \tag{414}$$

For an homogeneous field, the autocorrelation function depends only on $\overrightarrow{r}$.

B

INTERSTELLAR CLOUD MODELS: THE MEUDON PDR CODE

Several numerical tools have been developed to study PDR regions. As the physics and chemistry of these regions is controlled by the progressive extinction of the UV field, such codes must compute simultaneously the radiative transfer across the cloud and the physics and chemistry of the gas. They usually assume simple geometries (such as 1D plane-parallel) in order to make the computation of radiative transfer more tractable. An inventory of the most developed PDR codes and a detailed comparison of their results can be found in Röllig et al. [2007].

Among these codes, we give here a short overview of the Meudon PDR Code (Le Petit et al. 2006). This code was developed over the years by the team in which my thesis was done (Le Bourlot et al. 1993), and was used at several points in the work of this thesis. The computation of H_2 formation rate developed in Chap. 7 was coupled to this code to study the effects of this new computation on the cloud chemical structure and observable intensities (see the article in Chap. 8). It was also used to interpret a large set of observations of the PDR NGC7023 NW in Chap. 11.

We give here a quick overview of this model, discussing its hypotheses, describing briefly the resolution method, and describing the physics and chemistry included in the model. A more detailed description can be found in Le Petit et al. [2006], although some aspects of the physics have been significantly improved since this article (e.g. see Goicoechea and Le Bourlot 2007 and Gonzalez Garcia et al. 2008 for the radiative transfer, and Le Bourlot et al. 2012 for the implementation of H_2 formation).

B.1 OVERVIEW

B.1.1 *Principle and hypotheses*

This model considers a slab of gas illuminated from both sides, and computes its stationary state. The geometry is one-dimensional as the slab is infinite in two directions (plane-parallel geometry). The stationary state is obtained by simultaneously resolving the global radiative transfer, and solving at each position in the cloud the statistical equilibrium equations for the excitation of a selected set of species (we do not assume local thermal equilibrium), the set of chemical equations, the thermal balance equation, and the thermal and charge balance equations for dust grains. No gas dynamics is taken into

account, except for line broadening (a turbulent rms velocity is included). The state variables of the gas at each position are thus only coupled through the radiative transfer.

The model thus stands on two simplifying assumptions:

- the 1D plane-parallel geometry ignores the complex geometry of real objects. This can affect the intensity of scattered light received at a given position, or the effective depth of penetration of the UV field (e.g., for a spherical cloud under an isotropic external radiation field, the UV field should penetrate deeper than in our approximation).

- the stationary state computation assumes that the cloud has had enough time to reach the equilibrium without having its external conditions significantly changed. This implies that the timescales of all physical and chemical processes in the cloud must be smaller than that of the changes in the external conditions, and of the gas dynamics.

In addition, different assumptions are possible for the density profile of the cloud. The model can either assume constant density (which often results in large pressure gradients as the temperature varies strongly around the H/H_2 transition region), a fixed density profile given by the user, or a constant pressure. This last case is the most consistent with the hypothesis of stationarity of the model. However, constant density models are often used as the physics is easier to interpret in such models.

Finally, the physics of this model only deals with neutral gas (in the sense that the hydrogen is in atomic or molecular form). It thus assumes that all radiation below 912 Å has been absorbed prior to entering the part of the cloud that is described by the model. The most recent version (still in development) adds the X-rays domain, but the EUV part of the field is still assumed to have been completely extinguished.

B.1.2 *Model parameters*

The user controls:

- The density profile, by either giving a density value for constant density models, providing a tabulated density profile, or giving a pressure value for constant pressure models.

- The total thickness of the model, given in term of the total visible extinction A_V. For constant density models (or fixed density profiles), the extinction is easily translated into a physical distance from the values of R_V and of the ratio $N_H/E(B-V)$ (which are also user-specified parameters of the model). For constant pressure models, the physical size cannot be known beforehand.

- The external radiation field. This can be an isotropic radiation field using either the Mathis et al. [1983] or the Draine [1978] prescription for the standard ISRF, with a scaling factor for the UV part of the field (cf. Fig. 18 in Sect. 5.1.2). One scaling factor is given for each side of the cloud. In addition, a stellar radiation field can be used, by providing a tabulated spectrum. This unidirectional radiation field is then added to the isotropic field after geometric dilution according to the distance to the star specified by the user.

Those three parameters are the main parameters. The other parameters have default standard values that can be left unchanged unless specifically needed. These other parameters include:

- The dust properties, through several parameters:
  - the dust size distribution is necessarily a power-law distribution, but the user can specify the exponent, and the minimum and maximum sizes.
  - the gas-to-dust mass ratio.
  - the extinction properties. A specific extinction curve can be selected among a given set found in the file data/Astrodata/line_of_sight.data (a new extinction curve can easily be added by the coefficients of its Fintzpatrick&Massa fit). The R_V parameter can be chosen independently of the extinction curve, but the two should be consistent (as all the other coefficients of the fit are usually strongly correlated with R_V). The $N_{\mathrm{H}}/E(B-V)$ ratio can also be chosen by the user.
- The cosmic ray ionization rate, in terms of number of ionizations of H_2 per second.
- The turbulent velocity for line broadening.

The user can also modify a few numerical parameters such as the number of iterations. All those parameters are grouped in an input file (the pdr.in file). In addition, the user can choose the list of species for which the excitation distribution is computed (and the number of levels included) in a separate file (data/spectre.flag). The chemistry is also specified by the user in a chemistry input files containing the list of species, the elemental abundances and the list of reactions (see below in Sect. B.2.2).

B.1.3 *Code structure*

As said before, each position in the cloud is coupled to all other positions through radiative transfer effects, so that the thermo-chemical state cannot be solved independently at each position. The solution adopted in the Meudon

PDR Code consists in alternatively solving the global radiative transfer at fixed local state at each position, and then solve the local state (chemistry, temperature, and excitation) at each position at fixed radiation field. The alternation is iterated for 20 iterations (or more if the user wants) and convergence can be verified by comparing the last two iterations.

In addition, the local state of the gas is solved using an hybrid method were the chemical balance, the thermal balance and the excitation are alternatively solved using standard methods (Newton-Raphson and dichotomy), instead of solving jointly for all three. This simplifies the implementation but can induce numerical oscillations and instabilities in some cases.

The simplified structure of the code can be summarized as follow:

- Global loop:
  - Local loop over positions:
    - Loop for local state convergence:
      - Excitation statistical equilibrium.
      - Chemical balance (Newton-Raphson).
      - Thermal balance (dichotomy).
  - Global radiative transfer computation.

Convergence is checked in the inner loop for local state computation, and the number of iterations is automatically adjusted. In addition, the position grid is automatically refined during the loop over positions: if steep spatial variations are detected, additional intermediate positions are added.

B.2 PHYSICO-CHEMISTRY

We now give a quick overview of the physics and chemistry that is included in the Meudon PDR Code.

B.2.1 *Radiative transfer and excitation of species*

The continuum radiative transfer is solved using a Legendre polynomial decomposition method (Roberge 1983, Goicoechea and Le Bourlot 2007). For this part of the transfer, we only take into account:

- The extinction by dust, using the user-specified extinction curve.
- The scattering by dust, using a Henyey-Greestein approximation (Henyey and Greenstein 1941) for the phase function and dust properties from Laor and Draine [1993].

- The emission by dust. In earlier versions of the code, each dust size emits according to its temperature. In the latest version (still in development), temperature fluctuations of the small grains are taken into account by using the approximation of the dust temperature PDF described in Sect. 6.5.

- Gas absorption from the ionization of atomic species (C, S,...).

- In addition, gas absorption in the dissociation lines of some species can be optionally taken into account in the continuum transfer at a high computational cost. H_2 lines up to a level chosen by the user are then taken into account. The pre-dissociation lines of CO and its isotopomers can also be included. See below for the approximation used for the other lines.

Different approximations are used for line transfer in lines than are not included below. For absorption by dissociation lines that are not included in the full continuum transfer, the FGK approximation for self-shielding is used (Federman, Glassgold, and Kwan 1979). For emission lines, the escape probability approximation of de Jong et al. [1980] is used, so that the emitted photons are either absorbed on the spot or leave the cloud.

The species for which the detailed excitation can be solved are H_2, HD, CO and its isotopomers, C, N, O, O_2, S, Si, CS, HCN, OH, H_2O, C^+, N^+, O^+, S^+, Si^+, H_3^+, HCO^+, CH^+, OH^+, SH^+. In the latest versions, H, C^{2+}, N^{2+}, O^{2+}, S^{2+}, Ne^+ and Ne^{2+} have been added to the list. For each species, the user chooses the number of levels that are taken into account. For H_2 and CO, the cascade approximation (Black and Dalgarno 1976) is used to only explicitly compute the ro-vibrational levels of the ground electronic state while still accounting for transitory passage through the electronic excited states.

B.2.2 *Chemistry*

The chemistry included can be completely chosen by the user by providing the list of species and reactions to include. Only species formed from H, C, N, O, He, D, ^{13}C, ^{15}N, ^{18}O, Li, F, Na, Mg, Al, Si, Ne, S, Cl, Ca and Fe can be included. For each species, the composition in terms of element, the formation enthalpy and the initial abundance must be specified. The formation enthalpies are used to compute the endothermicity/exothermicity of reactions.

The list of reactions is also chosen by the user, who must give for each reaction the list of reactants and products, the reaction type (among a list of possible types), and the reaction parameters (the meaning of which depend on the reaction type). This list of reactions can include:

- photodissociation and photoionization reactions, whose rate are computed by integrating the local radiation field over the cross-sections when available.
- two-body and three-body reactions.
- Surface reactions are treated by considering adsorbed species as separate species from their gas counterpart. Reactions between adsorbed species, and between adsorbed and gas species on one hand, and adsorption and desorption reactions on the other hand, are thus allowed. Adsorbed species on different grain sizes are counted separately. Rate equations are used, except if the coupling with Fredholm is activated for H_2 formation.

Complete chemistry files are included with the code, with $\sim$ 150 species and $\sim$ 3000 reactions.

B.2.3 *Thermal balance*

The gas temperature at each position is computed by balancing the heating and cooling contributions. For heating, the code includes:

- The photo-electric heating on dust grains (UV photons eject energetic electrons from grains, and the electrons then thermalize with the gas, thus heating the gas). The older versions of the code use the formula from Bakes and Tielens [1994], while the latest version uses the more detailed treatment from Weingartner and Draine [2001b,c], Weingartner et al. [2006]. This rate is computed simultaneously to the computation of the grain charge discussed in the next section. This heating contribution usually dominates from the very edge of the cloud to the $C^+/C/CO$ transition.
- Heating by photodissociation and photo-ionization reactions. The products of the reaction are formed with typically a few eV of kinetic energy which they then transmit to the gas. Cosmic rays ionization induces a similar heating term.
- Exothermic reactions give energy to their products. The distribution of this energy between the kinetic and internal energies of the products is often not well known, and simple approximations are then used. For the formation reaction of H_2, the distribution computed theoretically by Sizun et al. [2010] is used, and the resulting heating contribution can become important close to the H/H_2 transition region. Endorthermic reactions are counted as a cooling term.

The cooling comes mainly from the emission of atomic and molecular species. The cooling contributions of all the species whose excitation is computed are

taken into account. The cooling is usually dominated by C^+ and O at the edge of the PDR, and by CO and its isotopomers in the core of the cloud.

In this radiative cooling process, the energy is transformed from kinetic to excitation energy by collisions and then radiated away. But the inverse process can sometimes take place. This is the case for H_2: the molecule can be excited to an electronic excited state by a UV photon, then transition back to a high ro-vibrational state of the ground electronic state, and cascade down by radiative de-excitation until collisional de-excitation becomes dominant, at which point a small fraction of the initial energy of the UV photon is given to the gas as kinetic energy.

Finally, the contribution of gas-grain collisions is taken into account, according to the computation of Burke and Hollenbach [1983]. This can be a heating or a cooling term depending on the temperature difference between the gas and the grains of different sizes. It is usually an important contribution only in the core of dense clouds.

B.2.4 *Dust physics*

The code takes into account a full dust size distribution. A power-law size distribution with exponent α and minimum and maximum sizes a_{min} and a_{max} (standard values $\alpha = -3.5$, $a_{min} = 3\,nm$ and $a_{max} = 300\,nm$) is considered, with properties corresponding to a mix of graphite and silicates, as described in Sect. 5.3.2. In the latest version, the dust population has been completed by a log-normal PAH distribution, as discussed in Sect. 6.5.3. The dust temperature and charge distribution are computed as functions of dust size.

The dust temperature is computed from radiative balance only (collisions with the gas are neglected), using the equilibrium temperature (see Sect. 5.1.4). In the latest version, the approximation of the temperature PDF described in Sect. 6.5 has been added. A temperature PDF is thus computed for each dust size.

The dust charge distribution is computed for each size, taking into account the photo-electric effect, photo-detachment, attachment, recombination, and charge exchange with ions. The implementation follows Weingartner and Draine [2001b,c], Weingartner et al. [2006].

C

THE FREDHOLM CODE

C.1 DESCRIPTION OF THE FREDHOLM CODE

The method of computation of the temperature PDF and of the dust emissivity (as well as the corresponding approximation) described in Chapter 6, the computation of the H_2 formation rate by the Langmuir-Hinshelwood and Eley-Rideal mechanism (Sect. 7.1 and 7.2) and the corresponding approximations (Sect. 7.3), as well as the corresponding computations without fluctuations (equilibrium temperature as described in Sect. 5.1.4, and rate equation results described in Sect. 5.2.3 and 5.2.4) have all been implemented in a stand alone numerical code, named `Fredholm` because of the central place of several integral equations, whose mathematical study started with the work of Ivar Fredholm and which took his name, and developped in the language C.

In this section, we quickly describe the structure of this code, as well as its configuration and use, and the format of the data files that it requires.

C.1.1 *Code structure*

The code is organized at two different levels:

- different files regroup the definitions of functions related to the same theme (e.g., Eley-Rideal chemistry, or inputs and outputs).
- All computations that aim at the same goal and are performed together are grouped and called through high-level functions, which we call *master functions*. This allows to outline the algorithmic structure of the code.

This structure, in terms of master functions, is represented in Fig. 115. We describe each element succinctly below:

- `Initialize_code()`: Reads the configuration files, performs initializations for the loop on grain sizes, reads the data that are independent of grain size (external radiation field, λ grid for the $Q_{\rm abs}$), prepare the dust size distribution and computes the normalization factor, and prepare outputs files.
- `Initialize_size()`: Reads size-dependent data ($Q_{\rm abs}$), computes properties of the current grain sizes (e.g., number of sites), and prepare outputs files.

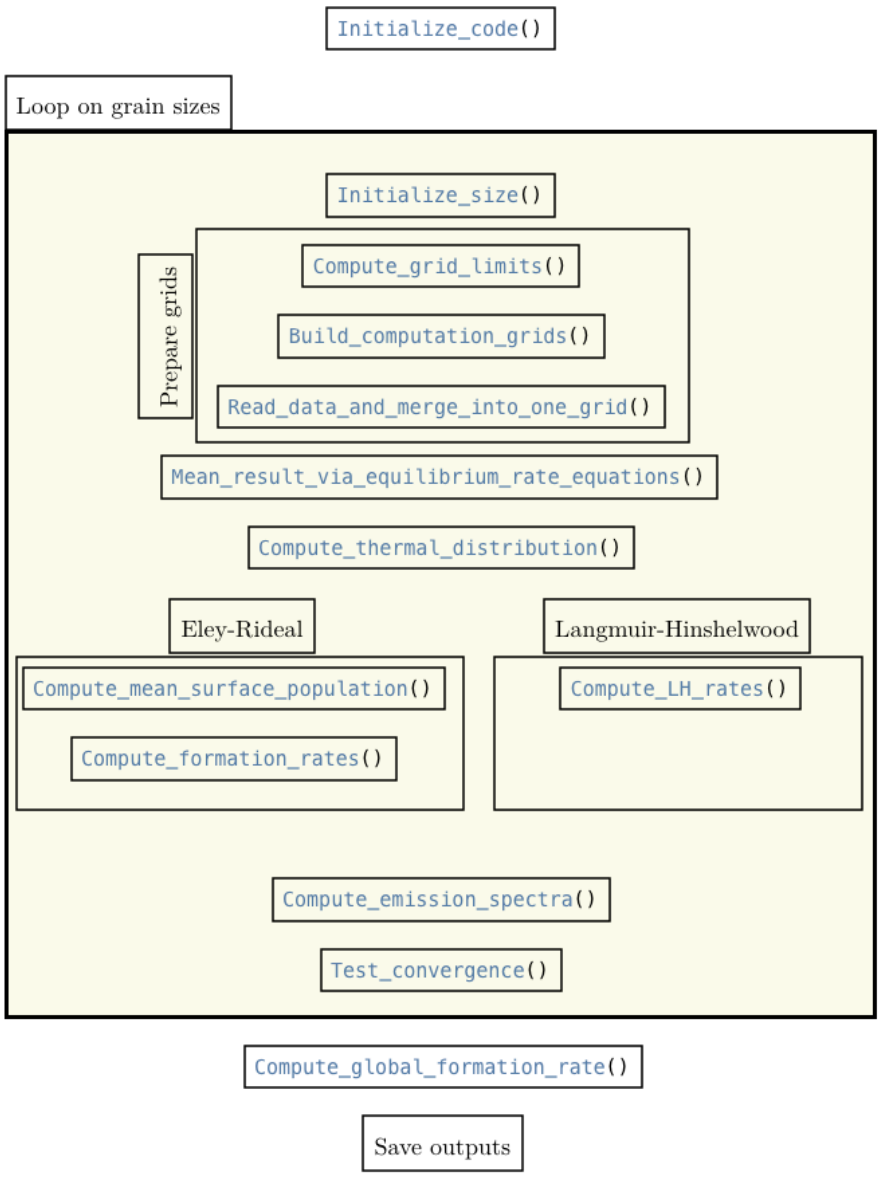

Figure 115: Overview of the structure of the code `Fredholm`. See the text for the description of the different elements.

- `Compute_grid_limits()`: Estimates the optimal bounds of the thermal energy grid from grain properties using empirical formula.
- `Build_computation_grids()`: Reads the heat capacity data, and build the thermal energy discretization grid and the corresponding temperature grid.
- `Read_data_and_merge_into_one_grid()`: Merge all the photon energy grids on which the data are given into one and interpolate all data on this grid.
- `Mean_result_via_equilibrium_rate_equations()`: Computes the equilibrium temperature (as described in Sect. 5.1.4), the formation rates obtained by use of the rate equation (as described in Sect. 5.2.3 and 5.2.4), and also performs a coupled computation of the equilibrium temperature and the rate equation formation rate when taking into account the heating of the grain by H_2 formation (see the article, Appendix A, in Chapter 8).
- `Compute_thermal_distribution()`: Computes the thermal energy PDF f_E of the grain using the method presented in Sect. 6.1.1 and 6.2, and the corresponding temperature PDF f_T, computes the resulting average and median temperatures, and computes the Kramers-Moyal approximation of the PDF f_E (described in Sect. 6.3.1).
- `Compute_mean_surface_population()`: Computes the conditional average population $\langle n \,|E\rangle$ for the Eley-Rideal mechanism using the method described in Sect. 7.1.3 and 7.2.2, and the corresponding equilibrium population $n^{(\mathrm{eq})}(T)$ (obtained by the rate equation) at each population for comparison.
- `Compute_formation_rates()`: Computes the Eley-Rideal formation rate on the grain from the conditional average population $\langle n \,|E\rangle$ and the thermal energy PDF f_E, also computes the equivalent result using the approximation described in Sect. 7.3.2.
- `Compute_LH_rates()`: Computes the Langmuir-Hinshelwood formation rate using the approximation described in Sect. 7.3.1 and the exact method described in Sect. 7.1.2 and 7.2.1.
- `Compute_emission_spectra()`: Computes the emission spectrum of the grain from the temperature PDF f_T as described in Sect. 6.4, and the approximation of the emission spectrum presented in Sect. 6.5.
- `Test_convergence()`: Disables the full computations of the different parts as soon as their result has converged to the equilibrium rate equation result.

- `Compute_global_formation_rate()`: Integrates the various estimates of the formation rate over the dust size distribution to yield the final formation rate per unit volume of gas.

This grouping is based on the algorithmic steps of the computations. On the other hand, we have grouped the low-level functions thematically into different files:

- `main.c`: Contains the main program, only calling the master functions, performing the loop on grain sizes and managing global allocations/deallocations.
- `master_functions.c`: Contains the master functions described above
- `global_variables.c`: Declaration of all global variables, containing both physical and numerical constants, and computational variables that need to be set as global because of their pervasive use in the code.
- `grids.c`: All functions related to reading the data and building the numerical grids (both the thermal energy discretization grid, and the photon energy integration grid).
- `E_distr.c`: All functions related to the computation of the thermal energy PDF f_E and various approximation of the grain temperature.
- `eley-rideal.c`: All function related to the computation of the Eley-Rideal formation rate and its various approximations.
- `langmuir-hinshelwood.c`: All function related to the computation of the Langmuir-Hinshelwood formation rate and its various approximations.
- `approximation.c`: All functions constituting the approximation of the dust emissivity presented in Sect. 6.5.
- `inputs_outputs.c`: Contains the function for reading the configuration files, and writing the output files.
- `physics.c`: Contains most of the physical expressions, so that minor changes of the physics can be made without affecting the rest of the code.
- `tools.c`: numerical and mathematical functions (norms and distances, interpolations, array search, Newton-Raphson, integration,...).

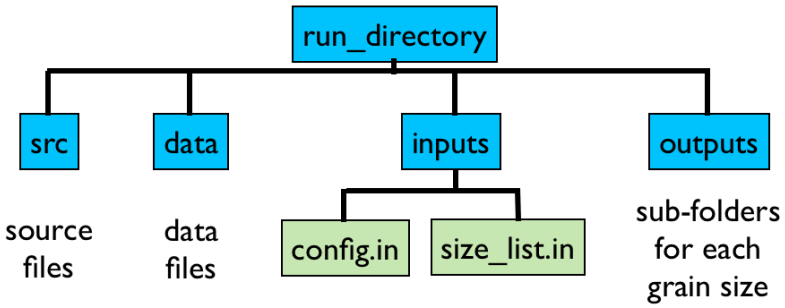

Figure 116: Structure of the run directory.

C.1.2 *Configuration and use*

The structure of the run directory is presented on Fig. 116. The configuration is mainly made through the config.in file, but a few more advanced options have to be activated directly in the code. In order to launch a run:

- Set the run configuration in the `config.in` file (see the meaning of the options below)
- Choose the list of grain sizes in the `size_list.in` file (the first and last sizes given must match the values given in the `config.in` file for `minimum grain size` and `maximum grain size`).
- Compile the code in the `src` directory.
- Launch the executable in the main run directory
- The results will be located in the `outputs` directory, with one sub-directory for each grain size, plus global result files.

Note that all physical quantities in Fredholm are in S.I. units.
The config.in file is shown on Listings 1, 2 and 3.
We describe the use of each option below:

DISCRETIZATION PARAMETERS

- `resolution`: Numerical resolution N, number of grid point in the thermal energy grid.
- grid type: Repartition of the grid points. Values: uniform or log

DUST PARAMETERS

- `data files (C,Qabs)`: Names of the two data files (heat capacity and absorption coefficient), separated by a space. The files must be located in the data subdirectory of the run directory.

Listing 1: `config.in`

```
_____________________________________
#####################################
PARAMETERS
_____________________________________
Discretisation parameters

resolution: 500
grid type: log
_____________________________________
Dust parameters

data files (C,Qabs): C_amCBEx.DAT Q_amCBEx.DAT
minimum grain size: 5E-10
maximum grain size: 3E-7
mass density (kg.m^-3): 2.31E3
grain/gas mass ratio: 0.01
chemisorption energy (K): 7000
dust distribution: powlaw
dust distribution parameters: -3.5
_____________________________________
Gas parameters

atomic hydrogen density (m^-3): 1.E6
proton density (m^-3): 1.E6
gas temperature (K): 350.
_____________________________________
Radiation field parameters
radiation field data file: Khi0.dat
_____________________________________
#####################################
OPTIONS
_____________________________________
General options

quiet: 1
PDR: 0
_____________________________________
Grid options

energy grid from file: 0
_____________________________________
Rate equation calculation

rate equation without desorption: 1
with H2 formation energy: 0
```

Listing 2: `config.in` (continued)

```
_____________________________________
Thermal energy distribution function

stage: 1
f_E from file: 0
_____________________________________
Average surface population

stage: 1
n from file: 0
compute equilibrium populations: 1
_____________________________________
Local emissivity

stage: 0
_____________________________________
Formation rate calculations

equilibrium population approximation: 0
mean desorption rate approximation: 0
final comparison with rate equation at mean temperature or without
    desorption: 0
_____________________________________
Caracteristic timescales

computation of caracteristic timescales: 0
_____________________________________
LH approximation

stage: 0
full resolution: 0
_____________________________________
#####################################
QUIET OUTPUTS

a: 1
T_eq: 1
R_h2_rate: 0
R_h2_rate_nodesorp: 0
T_eq_coupled: 0
R_h2_rate_coupled: 0
T_moy: 1
R_h2_full: 0
R_h2_n_eq: 0
R_h2_mean_des: 0
R_h2_rate_Tmoy: 0
```

Listing 3: `config.in` (continued)

```
_____________________________________
#####################################
FILES OUTPUTS

gridE: 1
gridT: 1
incrE: 0
C: 0
dE: 0
Q: 0
I: 0
P: 0
G: 0
L: 0
M: 0
K: 0
f_E: 1
f_T: 1
n(E): 1
```

- `minimum grain size`: Minimum size of the dust size distribution. Must match the first size given in size_list.in.
- `maximum grain size`: Minimum size of the dust size distribution. Must match the first size given in size_list.in.
- `mass density (kg.m^-3)`: Mass density of the dust grains.
- `grain/gas mass ratio`: Ratio dust mass over gas mass.
- `chemisorption energy (K)`: Chemisorption binding energy (in Kelvins).
- `dust distribution`: Functional form of the dust size distribution. Possible values: powlaw (simple power law, Eq. 106), lognorm (log-normal law, Eq. 112), or powlaw-expdec (power law with an exponential decay at large sizes, Eq. 114).
- `dust distribution parameters`: Parameters of the dust size distribution. The number of parameters depend of the previous choice. The parameters must be separated by spaces. powlaw: exponent α; lognorm: central size a_0 and width σ; powlaw-expdec: exponent α, cut-off size a_c, decay scale a_t, exponent of the decay γ.

GAS PARAMETERS

- `atomic hydrogen density (m^-3)`: Atomic hydrogen density.
- `proton density (m^-3)`: Proton density.
- `gas temperature (K)`: Gas temperature.

RADIATION FIELD PARAMETERS

- `radiation field data file`: Name of the data file of the external radiation field.

GENERAL OPTIONS

- `quiet`: If set to 0, displays many diagnostics and debugging prints; if set to 1, only the results activated in the section `QUIET OUTPUTS` below will be displayed for each size.
- `PDR`: For coupling with the `Meudon PDR Code`, see Sect. C.2.

GRID OPTIONS

- `energy grid from file`: Set to 1 to read the discretization grid (thermal energy E) from a file instead of building it. The file must then be named `gridE.in` and located in the subdirectory `inputs` of the run directory.

RATE EQUATION CALCULATION

- `rate equation without desorption`: not used anymore
- `with H2 formation energy`: To perform the coupled computation of the equilibrium temperature and the equilibrium rate equation result for the formation rate when including the retroaction of the heating of the grain by H_2 formation.

THERMAL ENERGY DISTRIBUTION FUNCTION

- `stage`: Set to 1, to activate the computation of the thermal energy PDF f_E. If set to 0, all result will be derived from the equilibrium temperature.
- `f_E from file`: Set to 1 to read the thermal energy PDF f_E from a file and use it for the other computation stages instead of computing it. The file must be named f_E.in and located in the subdirectory `inputs` of the run directory.

AVERAGE SURFACE POPULATION

- `stage`: Set to 1 to activate the computation of the conditional average surface population $\langle n|E \rangle$ for the Eley-Rideal mechanism.
- `n from file`: Set to 1 to read $\langle n|E \rangle$ from a file and use it for the other computation stages instead of computing it. The file must be named n_E.in and located in the subdirectory `inputs` of the run directory.
- `compute equilibrium populations`: Set to 1 to compute the equilibrium population (from the rate equation) at each temperature of the grid.

LOCAL EMISSIVITY

- `stage`: Set to 1 to activate the computation of of the dust emissivity (both the full computation and the approximation).

FORMATION RATE CALCULATIONS

- `equilibrium population approximation`: Set to 1 to compute as an approximation of the formation rate the average of the rate equation result over the temperature PDF (takes into account the distribution of grain temperatures but not the dynamical effect of the fluctuations).
- `mean desorption rate approximation`: Set to 1 to compute as an approximation of the formation rate the rate equation result by using the average desorption rate over the temperature PDF.
- `final comparison with rate equation at mean temperature or without desorption`: Set to 1 to display the final comparison of the total formation rate between the exact result and the rate equation result at the true average temperature, and 0 to compare to the rate equation result at the equilibrium temperature.

CHARACTERISTIC TIMESCALES

- `computation of characteristic timescales`: Not used anymore.

LH APPROXIMATION

- `stage`: Set to 1 to activate the computation of the Langmuir-Hinshelwood formation rate.
- `full resolution`: Set to 1 to use the full resolution method for the Langmuir-Hinshelwood mechanism instead of the approximation (very long computation time).

QUIET OUTPUTS (Choose which quantities are displayed for each size in quiet mode)

- `a`: Grain size.
- `T_eq`: Equilibrium temperature.
- `R_h2_rate`: Eley-Rideal formation rate computed using the rate equation approach at the equilibrium temperature.
- `R_h2_rate_nodesorp`: Eley-Rideal formation rate computed using the rate equation without desorption.
- `T_eq_coupled`: Equilibrium temperature when including the heating of the grain by H_2 formation (Eley-Rideal).
- `R_h2_rate_coupled`: Eley-Rideal formation rate computed using the rate equation approach at the equilibrium temperature when including the heating of the grain by H_2 formation.
- `T_moy`: Average temperature (computed from the temperature PDF).
- `R_h2_full`: Result of the full computation of the Eley-Rideal formation rate.
- `R_h2_n_eq`: Eley-Rideal formation rate computed by integrating the equilibrium rate equation result over the temperature PDF.
- `R_h2_mean_des`: Eley-Rideal formation rate computed form the rate equation using the average desorption rate over the temperature PDF.
- `R_h2_rate_Tmoy`: Eley-Rideal formation rate computed using the rate equation approach at the average temperature.

FILES OUTPUTS (Choose which quantities are written in output files for each sizes)

- `gridE`: Thermal energy grid.
- `gridT`: Temperature grid.
- `incrE`: Energy increment of the thermal energy grid (differences between successive points of the thermal energy grid).
- `C`: Heat capacity.
- `dE`: Photon energy grid.
- `Q`: Absorption coefficient.

- `I`: External radiation field.
- `P`: Loss term $L(E)$ defined by Eq. 121.
- `G`: Matrix M_{ij} defined by Eq. 134, 135 and 136.
- `L`: Write the matrix $M_{ij}/L(E_i)$.
- `M`: Loss term $M(E)$ defined by Eq. 226.
- `K`: Matrix K_{ij} defined by Eq. 247, 248 and 249.
- `f_E`: Thermal energy PDF f_E.
- `f_T`: Temperature energy PDF f_T.
- `n(E)`: Conditional average population $\langle n \,|E\rangle$ for the Eley-Rideal mechanism.

Other options or parameters can be changed directly in the code:

- The binding energy and migration energy for physisorption must be changed directly in `master_functions.c` at the beginning of the function `Compute_LH_rates()` (variables `T_physi_des` and `T_physi_mig`).
- The properties of the sticking function (see Eq. 84 and 85) and the chemisorption barrier must be changed in `global_variables.c` (variables `T1`, `T2` and `beta`).
- The distance between adsorption sites must be changed in `global_variables.c` (variable `d_s`).
- An activation barrier can be added for the Eley-Rideal reaction by modifying the variable `T_act_ER` in `global_variables.c`.
- Tunneling migration can be switched off by changing the variable `f_tunneling` to zero in `global_variables.c`.

The input file `size_list.in` must contain the dust size grid, with one size per line and in m.

Once the run is finished, the result files are located in the `outputs` subdirectory. The file `results_vs_sizes.out` gather the main results for each sizes. For each size, one subdirectory named `a_[size]` has been created in `outputs`. It contains the files chosen in the section `FILES OUTPUTS` of the `config.in` file. In addition, it can contain additional files depending on which options have been activated.

As we use the data files of the code `DustEM`, we have kept the format of those data files, and our code require the data files to be given according to this format.

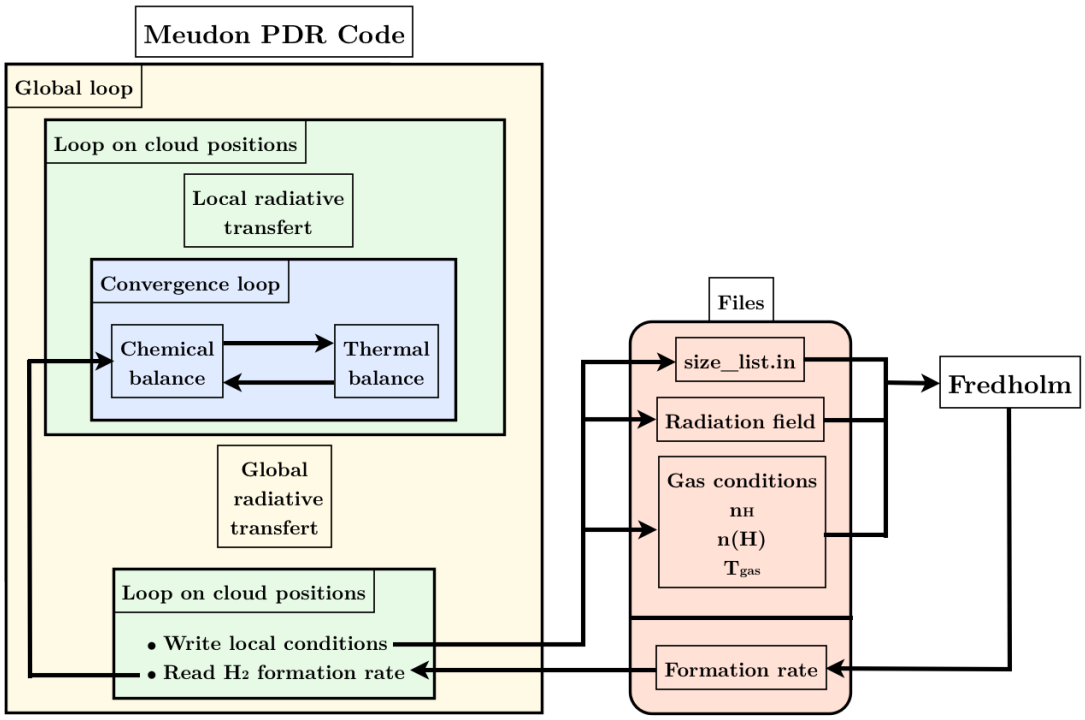

Figure 117: Description of the coupling between `Fredholm` and the `Meudon PDR Code`.

C.2 COUPLING BETWEEN FREDHOLM AND THE MEUDON PDR CODE

In order to use this new computation of the formation of H_2 on dust grains with temperature fluctuations in full cloud simulations, a coupling was developed with the `Meudon PDR Code` (described in Chapter B). The gas conditions are sent by the `Meudon PDR Code` to `Fredholm`, which then returns the formation rate to be used by the `Meudon PDR Code` in the computation of the chemical balance. We give here a short description of this coupling, and some explanations on its use.

C.2.1 *Implementation*

The coupling is described in Fig. 117. As described in Chapter B, the Meudon PDR Code is centered around three imbricated loops, which are represented on Fig. 117:

- The innermost loop alternates the chemical balance computation and the thermal balance computation at one position in the cloud until a stable result is found.

- This step is repeated at each position in the cloud, which constitutes the middle loop.

- This first part is alternated with the computation of the global radiative transfer through the cloud, and repeated until convergence. This constitutes the outermost loop.

The formation rates are needed in the innermost loop for the computation of the chemical balance. However, as the computation of the formation rate by `Fredholm` takes of the order of one minute and the innermost loop is repeated an extremely large number of times, we compute the formation rate of H_2 only once for all positions in one passage of the outermost loop. The formation rate is then kept constant during the convergence of the innermost loop. This is of course not fully consistent, as the density of atomic hydrogen and the gas temperature evolve during the convergence of the innermost loop. This result in reduced numerical stability, but does not affect the results if convergence is achieved, as at a stable point, the estimate of the formation rate becomes fully consistent.

As a result, we experienced oscillatory behaviors in the convergence of the outermost loop: for instance the density of atomic hydrogen alternating infinitely between two values because the estimate of the formation rate is always one step late.This was avoided by periodically (every three global iterations) taking the average of the last two estimates of the formation rate. Again, this does not affect the final results as it does not modify the position of the fixed point of the algorithm, and only affects its stability and the convergence properties. This procedure allowed convergence without problem in all cases.

As shown in Fig. 117, the communication between the two codes is done through files. The `Meudon PDR Codes` writes the current gas state (n_{H}, $n(\mathrm{H})$ and T_{gas}) in a file, replaces the current radiation field data file by the ambient radiation field at the current cloud positions, and writes the list of grain sizes it uses. It then calls a bash script which adapts the config.in file accordingly and launch `Fredholm`, which computes the formation rate and writes its results as usual. The formation rate is then read and used by the `Meudon PDR Code`. As the computation time of `Fredholm` is much longer than the access time to a file, a more sophisticated communication method was unnecessary.

C.2.2 *Configuration and use*

This coupling is included in the version 1.5.3 of the `Meudon PDR Code`. Fredholm is included as a subdirectory of the main run directory. In order to use the coupling, the steps are as follow:

- Compile both the `Meudon PDR Code` in `[run_directory]/src/` and `Fredholm` in `[run_directory]/fredholm/src/`

- Adapt the `pdr.in` file for the `Meudon PDR Code`. The chemistry file must be adapted to the coupling. It must contain as formation of H_2 on dust grains the following reactions:

```
ERFOR h h h2 1.00E+00 0.00 0.00 31
LHFOR h h h2 1.00E+00 0.00 0.00 32
```

  For instance, the file `ch1302_cnos_Fredholm_ERLH.chi` included in `[run_directory]/data/Chimie/` is appropriate. The presence of reactions labeled as type 31 and/or 32 will automatically activate the coupling with `Fredholm`.

- Choose the parameters of the run as usual for the `Meudon PDR Code` in the `pdr.in` file.

- Adapt the `config.in` file for `Fredholm` in `[run_directory]/fredholm/inputs/` as usual. The radiation field name MUST be `ISRF.DAT`, otherwise the radiation field from the `Meudon PDR Code` will not be used. Note that the gas conditions will be overwritten. The minimal and maximal grain sizes must be consistent with those indicated in the `pdr.in` file for the `Meudon PDR Code` (the units are different: cm for the `pdr.in` file, m for the `config.in` file).

In addition to the results of the `Meudon PDR Code`, detailed results on the computation of the formation rate for each grain size will be available in `[run_directory]/fredholm/outputs/`.

BIBLIOGRAPHY

A. Abdulle and T. Li. S-rock methods for stiff ito sdes. *Communications in Mathematical Sciences*, 6(4):845–868, 12 2008. URL http://projecteuclid.org/euclid.cms/1229619673. (Cited on page 280.)

W. S. Adams. Some Results with the COUDÉ Spectrograph of the Mount Wilson Observatory. ApJ, 93:11, January 1941. doi: 10.1086/144237. (Cited on page 39.)

A. Alexakis, P. D. Mininni, and A. Pouquet. Shell-to-shell energy transfer in magnetohydrodynamics. I. Steady state turbulence. Phys. Rev. E, 72 (4):046301, October 2005. doi: 10.1103/PhysRevE.72.046301. (Cited on page 68.)

J. W. Armstrong, B. J. Rickett, and S. R. Spangler. Electron density power spectrum in the local interstellar medium. ApJ, 443:209–221, April 1995. doi: 10.1086/175515. (Cited on page 70.)

E. L. O. Bakes and A. G. G. M. Tielens. The photoelectric heating mechanism for very small graphitic grains and polycyclic aromatic hydrocarbons. ApJ, 427:822–838, June 1994. doi: 10.1086/174188. (Cited on page 330.)

M. Benisty, K. Perraut, D. Mourard, P. Stee, G. H. R. A. Lima, J. B. Le Bouquin, M. Borges Fernandes, O. Chesneau, N. Nardetto, I. Tallon-Bosc, H. McAlister, T. Ten Brummelaar, S. Ridgway, J. Sturmann, L. Sturmann, N. Turner, C. Farrington, and P. J. Goldfinger. Enhanced H_{alpha} activity at periastron in the young and massive spectroscopic binary HD 200775. A&A, 555: A113, July 2013. doi: 10.1051/0004-6361/201219893. (Cited on pages 283 and 286.)

F. Bensch, J. Stutzki, and V. Ossenkopf. Quantification of molecular cloud structure using the Delta -variance. A&A, 366:636–650, February 2001. doi: 10.1051/0004-6361:20000292. (Cited on page 70.)

O. Berné, C. Joblin, Y. Deville, J. D. Smith, M. Rapacioli, J. P. Bernard, J. Thomas, W. Reach, and A. Abergel. Analysis of the emission of very small dust particles from Spitzer spectro-imagery data using blind signal separation methods. A&A, 469:575–586, July 2007. doi: 10.1051/0004-6361:20066282. (Cited on page 286.)

L. Biferale, G. Boffetta, A. Celani, A. Lanotte, and F. Toschi. Particle trapping in three-dimensional fully developed turbulence. *Physics of Fluids*, 17(2): 021701, February 2005. doi: 10.1063/1.1846771. (Cited on page 265.)

L. Biferale, G. Boffetta, A. Celani, A. Lanotte, and F. Toschi. Lagrangian statistics in fully developed turbulence. *Journal of Turbulence*, 7:6, January 2006. doi: 10.1080/14685240500460832. (Cited on page 265.)

O. Biham and A. Lipshtat. Exact results for hydrogen recombination on dust grain surfaces. Phys. Rev. E, 66(5):056103, November 2002. doi: 10.1103/PhysRevE.66.056103. (Cited on pages 114 and 123.)

O. Biham, I. Furman, N. Katz, V. Pirronello, and G. Vidali. H2 formation on interstellar grains in different physical regimes. MNRAS, 296:869–872, June 1998. doi: 10.1046/j.1365-8711.1998.01427.x. (Cited on page 107.)

D. Biskamp. *Magnetohydrodynamic Turbulence*. July 2003. (Cited on page 69.)

J. H. Black and A. Dalgarno. Interstellar H2 - The population of excited rotational states and the infrared response to ultraviolet radiation. ApJ, 203:132–142, January 1976. doi: 10.1086/154055. (Cited on page 329.)

P. Blasi. The origin of galactic cosmic rays. A&A Rev., 21:70, November 2013. doi: 10.1007/s00159-013-0070-7. (Cited on page 31.)

N. N. Bogoliubov. Kinetic Equations. *Journal of Physics USSR*, 10(3):265–274, 1946. (Cited on page 242.)

S. Boldyrev, Å. Nordlund, and P. Padoan. Supersonic Turbulence and Structure of Interstellar Molecular Clouds. *Physical Review Letters*, 89(3):031102, July 2002. doi: 10.1103/PhysRevLett.89.031102. (Cited on page 70.)

M. Bonfanti, S. Casolo, G. F. Tantardini, A. Ponti, and R. Martinazzo. A few simple rules governing hydrogenation of graphene dots. J. Chem. Phys., 135(16):164701, October 2011. doi: 10.1063/1.3650693. (Cited on pages 108 and 109.)

E. Bron, J. Le Bourlot, and F. Le Petit. Surface chemistry in the interstellar medium. II. H_2 formation on dust with random temperature fluctuations. A&A, 569:A100, September 2014. doi: 10.1051/0004-6361/201322101. (Cited on pages 183, 188, 206, and 207.)

J. R. Burke and D. J. Hollenbach. The gas-grain interaction in the interstellar medium - Thermal accommodation and trapping. ApJ, 265:223–234, February 1983. doi: 10.1086/160667. (Cited on pages 56 and 331.)

J. A. Cardelli, G. C. Clayton, and J. S. Mathis. The relationship between infrared, optical, and ultraviolet extinction. ApJ, 345:245–256, October 1989. doi: 10.1086/167900. (Cited on page 45.)

S. Casolo, O. M. Lovvik, R. Martinazzo, and G. F. Tantardini. Understanding adsorption of hydrogen atoms on graphene. J. Chem. Phys., 130(5):054704, February 2009. doi: 10.1063/1.3072333. (Cited on page 108.)

S. Casolo, G. F. Tantardini, and R. Martinazzo. Insights into H2 formation in space from ab initio molecular dynamics. *Proceedings of the National Academy of Science*, 110:6674–6677, April 2013. doi: 10.1073/pnas.1301433110. (Cited on page 109.)

S. Cazaux and A. G. G. M. Tielens. H_2 Formation on Grain Surfaces. ApJ, 604:222–237, March 2004. doi: 10.1086/381775. (Cited on page 95.)

Liang Chen, Alan C. Cooper, Guido P. Pez, and Hansong Cheng. Mechanistic study on hydrogen spillover onto graphitic carbon materials. *The Journal of Physical Chemistry C*, 111(51):18995–19000, 2007. doi: 10.1021/jp074920g. URL http://pubs.acs.org/doi/abs/10.1021/jp074920g. (Cited on page 108.)

A. Chokshi, A. G. G. M. Tielens, M. W. Werner, and M. W. Castelaz. C II 158 micron and O I 63 micron observations of NGC 7023 - A model for its photodissociation region. ApJ, 334:803–814, November 1988. doi: 10.1086/166878. (Cited on pages 284 and 286.)

L. Colangeli, V. Mennella, P. Palumbo, A. Rotundi, and E. Bussoletti. Mass extinction coefficients of various submicron amorphous carbon grains: Tabulated values from 40 NM to 2 mm. A&AS, 113:561, November 1995. (Cited on page 98.)

M. Compiègne, L. Verstraete, A. Jones, J.-P. Bernard, F. Boulanger, N. Flagey, J. Le Bourlot, D. Paradis, and N. Ysard. The global dust SED: tracing the nature and evolution of dust with DustEM. A&A, 525:A103, January 2011. doi: 10.1051/0004-6361/201015292. (Cited on pages 5, 55, 95, 96, 98, 101, 104, 105, 106, 117, 120, 123, 147, and 149.)

D. P. Cox. The Three-Phase Interstellar Medium Revisited. ARA&A, 43:337–385, September 2005. doi: 10.1146/annurev.astro.43.072103.150615. (Cited on pages 25, 34, 37, 38, and 39.)

P. A. Davidson. *Turbulence : an introduction for scientists and engineers*. 2004. (Cited on pages 61 and 63.)

T. de Jong, W. Boland, and A. Dalgarno. Hydrostatic models of molecular clouds. A&A, 91:68–84, November 1980. (Cited on page 329.)

B. J. Delarue and S. B. Pope. Application of PDF methods to compressible turbulent flows. *Physics of Fluids*, 9:2704–2715, September 1997. doi: 10.1063/1.869382. (Cited on page 236.)

F. X. Desert, F. Boulanger, and S. N. Shore. Grain temperature fluctuations - A key to infrared spectra. A&A, 160:295–300, May 1986. (Cited on pages 123 and 143.)

A. A. Deshpande, K. S. Dwarakanath, and W. M. Goss. Power Spectrum of the Density of Cold Atomic Gas in the Galaxy toward Cassiopeia A and Cygnus A. ApJ, 543:227–234, November 2000. doi: 10.1086/317104. (Cited on page 70.)

C. Dopazo and E. E. O'Brien. An approach to the autoignition of a turbulent mixture. *Acta Astronautica*, 1:1239–1266, 1974. doi: 10.1016/0094-5765(74)90050-2. (Cited on page 236.)

A. E. Douglas and G. Herzberg. Note on CH^{+} in Interstellar Space and in the Laboratory. ApJ, 94:381, September 1941. doi: 10.1086/144342. (Cited on page 39.)

B. T. Draine. Photoelectric heating of interstellar gas. ApJS, 36:595–619, April 1978. doi: 10.1086/190513. (Cited on pages 262 and 327.)

B. T. Draine. Interstellar shock waves with magnetic precursors. ApJ, 241:1021–1038, November 1980. doi: 10.1086/158416. (Cited on page 74.)

B. T. Draine. Magnetohydrodynamic shocks in diffuse clouds. III - The line of sight toward Zeta Ophiuchi. ApJ, 310:408–418, November 1986. doi: 10.1086/164694. (Cited on page 74.)

B. T. Draine. Scattering by Interstellar Dust Grains. I. Optical and Ultraviolet. ApJ, 598:1017–1025, December 2003a. doi: 10.1086/379118. (Cited on pages 47 and 98.)

B. T. Draine. Scattering by Interstellar Dust Grains. II. X-Rays. ApJ, 598:1026–1037, December 2003b. doi: 10.1086/379123. (Cited on page 47.)

B. T. Draine. Interstellar Dust Grains. ARA&A, 41:241–289, 2003c. doi: 10.1146/annurev.astro.41.011802.094840. (Cited on page 52.)

B. T. Draine. Interstellar Dust Models. In A. N. Witt, G. C. Clayton, and B. T. Draine, editors, *Astrophysics of Dust*, volume 309 of *Astronomical Society of the Pacific Conference Series*, page 691, May 2004a. (Cited on pages 52 and 53.)

B. T. Draine. *Astrophysics of Dust in Cold Clouds*, page 213. 2004b. doi: 10.1007/3-540-31636-13. (Cited on page 97.)

B. T. Draine and N. Katz. Magnetohydrodynamic shocks in diffuse clouds. I - Chemical processes. ApJ, 306:655–666, July 1986a. doi: 10.1086/164375. (Cited on page 74.)

B. T. Draine and N. Katz. Magnetohydrodynamic shocks in diffuse clouds. II - Production of CH(+), OH, CH, and other species. ApJ, 310:392–407, November 1986b. doi: 10.1086/164693. (Cited on page 74.)

B. T. Draine and A. Li. Infrared Emission from Interstellar Dust. I. Stochastic Heating of Small Grains. ApJ, 551:807–824, April 2001. doi: 10.1086/320227. (Cited on pages 50, 53, 54, 96, 104, 105, 119, 123, and 143.)

B. T. Draine and A. Li. Infrared Emission from Interstellar Dust. IV. The Silicate-Graphite-PAH Model in the Post-Spitzer Era. ApJ, 657:810–837, March 2007. doi: 10.1086/511055. (Cited on pages 53, 54, 98, 104, 105, 117, and 119.)

Y. Du. *"Order Structure and Topological Methods In Nonlinear partial Differential Equations."*, volume 1: "Maximum Principles and Applications", chapter 1: "Krein-Rutman Theorem and the Principal Eigenvalue". World Scientific, 2006. (Cited on page 126.)

B. Dubrulle. Intermittency in fully developed turbulence: Log-Poisson statistics and generalized scale covariance. *Physical Review Letters*, 73:959–962, August 1994. doi: 10.1103/PhysRevLett.73.959. (Cited on pages 68 and 278.)

E. J. Duplock, M. Scheffler, and P. J. Lindan. Hallmark of Perfect Graphene. *Physical Review Letters*, 92(22):225502, June 2004. doi: 10.1103/PhysRevLett.92.225502. (Cited on page 108.)

R. Durrer and A. Neronov. Cosmological magnetic fields: their generation, evolution and observation. A&A Rev., 21:62, June 2013. doi: 10.1007/s00159-013-0062-7. (Cited on page 30.)

E. Dwek, V. Zubko, R. G. Arendt, and R. K. Smith. Probing Interstellar Dust Models Through SAXS (Small Angle X-Ray Scattering). In A. N. Witt, G. C. Clayton, and B. T. Draine, editors, *Astrophysics of Dust*, volume 309 of *Astronomical Society of the Pacific Conference Series*, page 499, May 2004. (Cited on pages 47 and 55.)

A. Einstein. Über die von der molekularkinetischen Theorie der Wärme geforderte Bewegung von in ruhenden Flüssigkeiten suspendierten Teilchen. *Annalen der Physik*, 322:549–560, 1905. doi: 10.1002/andp.19053220806. (Cited on page 140.)

M. Elitzur and W. D. Watson. Formation of molecular CH/+/ in interstellar shocks. ApJ, 222:L141–L144, June 1978. doi: 10.1086/182711. (Cited on page 74.)

B. G. Elmegreen and J. Scalo. Interstellar Turbulence I: Observations and Processes. ARA&A, 42:211–273, September 2004. doi: 10.1146/annurev.astro.41.011802.094859. (Cited on pages 71 and 72.)

B. G. Elmegreen, S. Kim, and L. Staveley-Smith. A Fractal Analysis of the H I Emission from the Large Magellanic Cloud. ApJ, 548:749–769, February 2001. doi: 10.1086/319021. (Cited on pages 70 and 72.)

E. Falgarone, L. Verstraete, G. Pineau Des Forêts, and P. Hily-Blant. Warm gas in the cold diffuse interstellar medium: Spectral signatures in the H_2 pure rotational lines. A&A, 433:997–1006, April 2005. doi: 10.1051/0004-6361:20041893. (Cited on page 74.)

E. Falgarone, J. Pety, and P. Hily-Blant. Intermittency of interstellar turbulence: extreme velocity-shears and CO emission on milliparsec scale. A&A, 507:355–368, November 2009. doi: 10.1051/0004-6361/200810963. (Cited on page 71.)

S. R. Federman, A. E. Glassgold, and J. Kwan. Atomic to molecular hydrogen transition in interstellar clouds. ApJ, 227:466–473, January 1979. doi: 10.1086/156753. (Cited on pages 302 and 329.)

A. S. Ferrarotti and H.-P. Gail. Composition and quantities of dust produced by AGB-stars and returned to the interstellar medium. A&A, 447:553–576, February 2006. doi: 10.1051/0004-6361:20041198. (Cited on page 58.)

K. Ferrière. The Hot Gas Filling Factor in Our Galaxy. ApJ, 503:700–716, August 1998. doi: 10.1086/306003. (Cited on page 38.)

K. M. Ferrière. The interstellar environment of our galaxy. *Reviews of Modern Physics*, 73:1031–1066, October 2001. doi: 10.1103/RevModPhys.73.1031. (Cited on pages 25 and 32.)

Y. Ferro, F. Marinelli, and A. Allouche. Density functional theory investigation of H adsorption and H2 recombination on the basal plane and in the bulk of graphite: Connection between slab and cluster model. J. Chem. Phys., 116:8124–8131, May 2002. doi: 10.1063/1.1469600. (Cited on page 107.)

Y. Ferro, F. Marinelli, and A. Allouche. Density functional theory investigation of the diffusion and recombination of H on a graphite surface. *Chemical Physics Letters*, 368:609–615, January 2003. doi: 10.1016/S0009-2614(02)01908-5. (Cited on page 108.)

E. L. Fitzpatrick. Correcting for the Effects of Interstellar Extinction. PASP, 111:63–75, January 1999. doi: 10.1086/316293. (Cited on page 54.)

E. L. Fitzpatrick and D. Massa. An analysis on the shapes of ultraviolet extinction curves. I - The 2175 A bump. ApJ, 307:286–294, August 1986. doi: 10.1086/164415. (Cited on page 45.)

E. L. Fitzpatrick and D. Massa. An analysis of the shapes of ultraviolet extinction curves. II - The far-UV extinction. ApJ, 328:734–746, May 1988. doi: 10.1086/166332. (Cited on page 45.)

E. L. Fitzpatrick and D. Massa. An analysis of the shapes of ultraviolet extinction curves. III - an atlas of ultraviolet extinction curves. ApJS, 72:163–189, January 1990. doi: 10.1086/191413. (Cited on page 45.)

E. L. Fitzpatrick and D. Massa. An Analysis of the Shapes of Ultraviolet Extinction Curves. IV. Extinction without Standards. AJ, 130:1127–1140, September 2005. doi: 10.1086/431900. (Cited on page 45.)

E. L. Fitzpatrick and D. Massa. An Analysis of the Shapes of Interstellar Extinction Curves. V. The IR-through-UV Curve Morphology. ApJ, 663: 320–341, July 2007. doi: 10.1086/518158. (Cited on pages 44, 45, and 46.)

E. L. Fitzpatrick and D. Massa. An Analysis of the Shapes of Interstellar Extinction Curves. VI. The Near-IR Extinction Law. ApJ, 699:1209–1222, July 2009. doi: 10.1088/0004-637X/699/2/1209. (Cited on page 45.)

D. R. Flower and G. Pineau des Forets. C-type shocks in the interstellar medium: profiles of CHˆ+ and CH absorption lines. MNRAS, 297:1182–1188, July 1998. doi: 10.1046/j.1365-8711.1998.01574.x. (Cited on pages 74 and 313.)

U. Frisch. *Turbulence. The legacy of A. N. Kolmogorov.* 1995. (Cited on page 61.)

A. Fuente and J. Martín-Pintado. Detection of CO^+ toward the Reflection Nebula NGC 7023. ApJ, 477:L107–L109, March 1997. doi: 10.1086/310532. (Cited on page 285.)

A. Fuente, J. Martin-Pintado, J. Cernicharo, N. Brouillet, and G. Duvert. Physical conditions of the molecular gas and dust associated with the Herbig Ae/Be stars. A&A, 260:341–354, July 1992. (Cited on page 284.)

A. Fuente, J. Martin-Pintado, J. Cernicharo, and R. Bachiller. A chemical study of the photodissociation region NGC 7023. A&A, 276:473, September 1993. (Cited on page 284.)

A. Fuente, J. Martin-Pintado, R. Neri, C. Rogers, and G. Moriarty-Schieven. The filamentary structure of the interface between the atomic and the molecular phases in NGC 7023. A&A, 310:286–296, June 1996. (Cited on pages 284 and 288.)

A. Fuente, J. Martin-Pintado, A. Rodriguez-Franco, and G. D. Moriarty-Schieven. The biconical cavity associated with HD 200775: the formation of a cometary nebula. A&A, 339:575–586, November 1998. (Cited on pages 283 and 285.)

A. Fuente, J. Martín-Pintado, N. J. Rodríguez-Fernández, A. Rodríguez-Franco, P. de Vicente, and D. Kunze. Infrared Space Observatory Observations toward the Reflection Nebula NGC 7023: A Nonequilibrium Ortho-to-Para-H_2 Ratio. ApJ, 518:L45–L48, June 1999. doi: 10.1086/312063. (Cited on pages 285 and 288.)

A. Fuente, J. Martin-Pintado, N. J. Rodriguez-Fernández, J. Cernicharo, and M. Gerin. ISO SWS-LWS observations of the prototypical reflection nebula NGC 7023. A&A, 354:1053–1061, February 2000. (Cited on page 285.)

H.-P. Gail, S. Wetzel, A. Pucci, and A. Tamanai. Seed particle formation for silicate dust condensation by SiO nucleation. A&A, 555:A119, July 2013. doi: 10.1051/0004-6361/201321807. (Cited on page 58.)

C. W. Gardiner. *Handbook of stochastic methods for physics, chemistry and the natural sciences*, volume 13 of *Springer Series in Synergetics*. Springer-Verlag, third edition, 2004. ISBN 3-540-20882-8. (Cited on pages 77, 81, and 82.)

R. T. Garrod. A new modified-rate approach for gas-grain chemical simulations. A&A, 491:239–251, November 2008. doi: 10.1051/0004-6361:200810518. (Cited on pages 114 and 194.)

R. T. Garrod. A Three-phase Chemical Model of Hot Cores: The Formation of Glycine. ApJ, 765:60, March 2013. doi: 10.1088/0004-637X/765/1/60. (Cited on page 58.)

R. T. Garrod and T. Pauly. On the Formation of CO_2 and Other Interstellar Ices. ApJ, 735:15, July 2011. doi: 10.1088/0004-637X/735/1/15. (Cited on page 58.)

R. T. Garrod, S. L. W. Weaver, and E. Herbst. Complex Chemistry in Star-forming Regions: An Expanded Gas-Grain Warm-up Chemical Model. ApJ, 682:283–302, July 2008. doi: 10.1086/588035. (Cited on page 58.)

M. Gerin, T. G. Phillips, J. Keene, A. L. Betz, and R. T. Boreiko. CO, C i, and C II Observations of NGC 7023. ApJ, 500:329–341, June 1998. doi: 10.1086/305726. (Cited on page 285.)

E. L. Gibb, D. C. B. Whittet, A. C. A. Boogert, and A. G. G. M. Tielens. Interstellar Ice: The Infrared Space Observatory Legacy. ApJS, 151:35–73, March 2004. doi: 10.1086/381182. (Cited on page 58.)

Daniel T. Gillespie. *Markov processes : an introduction for physical scientists*. Academic Press, Boston, San Diego, New York, 1992. ISBN 0-12-283955-2. (Cited on pages 77 and 81.)

B. Godard, E. Falgarone, and G. Pineau Des Forêts. Models of turbulent dissipation regions in the diffuse interstellar medium. A&A, 495:847–867, March 2009. doi: 10.1051/0004-6361:200810803. (Cited on pages 74, 233, 254, 256, 280, and 313.)

B. Godard, E. Falgarone, M. Gerin, D. C. Lis, M. De Luca, J. H. Black, J. R. Goicoechea, J. Cernicharo, D. A. Neufeld, K. M. Menten, and M. Emprechtinger. Comparative study of CH+ and SH+ absorption lines observed towards distant star-forming regions. A&A, 540:A87, April 2012. doi: 10.1051/0004-6361/201117664. (Cited on page 73.)

J. R. Goicoechea and J. Le Bourlot. The penetration of Far-UV radiation into molecular clouds. A&A, 467:1–14, May 2007. doi: 10.1051/0004-6361:20066119. (Cited on pages 325 and 328.)

P. Goldreich and S. Sridhar. Magnetohydrodynamic Turbulence Revisited. ApJ, 485:680–688, August 1997. (Cited on page 69.)

P. F. Goldsmith and D. Li. H I Narrow Self-Absorption in Dark Clouds: Correlations with Molecular Gas and Implications for Cloud Evolution and Star Formation. ApJ, 622:938–958, April 2005. doi: 10.1086/428032. (Cited on page 311.)

M. Gonzalez Garcia, J. Le Bourlot, F. Le Petit, and E. Roueff. Radiative transfer revisited for emission lines in photon dominated regions. A&A, 485:127–136, July 2008. doi: 10.1051/0004-6361:200809440. (Cited on page 325.)

K. D. Gordon. Interstellar Dust Scattering Properties. In A. N. Witt, G. C. Clayton, and B. T. Draine, editors, *Astrophysics of Dust*, volume 309 of *Astronomical Society of the Pacific Conference Series*, page 77, May 2004. (Cited on pages 47 and 48.)

R. J. Gould and E. E. Salpeter. The Interstellar Abundance of the Hydrogen Molecule. I. Basic Processes. ApJ, 138:393, August 1963. doi: 10.1086/147654. (Cited on page 57.)

R. Gredel, G. Pineau des Forêts, and S. R. Federman. Interstellar CN toward CH^+-forming regions. A&A, 389:993–1014, July 2002. doi: 10.1051/0004-6361:20020543. (Cited on page 74.)

C. Gry, F. Boulanger, C. Nehmé, G. Pineau des Forêts, E. Habart, and E. Falgarone. H_2 formation and excitation in the diffuse interstellar medium. A&A, 391:675–680, August 2002. doi: 10.1051/0004-6361:20020691. (Cited on pages 73, 272, 276, 277, 279, and 312.)

P. Guhathakurta and B. T. Draine. Temperature fluctuations in interstellar grains. I - Computational method and sublimation of small grains. ApJ, 345:230–244, October 1989. doi: 10.1086/167899. (Cited on page 154.)

E. Habart, A. Abergel, F. Boulanger, C. Joblin, L. Verstraete, M. Compiègne, G. Pineau Des Forêts, and J. Le Bourlot. Excitation of H_2 in photodissociation regions as seen by Spitzer. A&A, 527:A122, March 2011. doi: 10.1051/0004-6361/20077327. (Cited on page 15.)

H. J. Habing. The interstellar radiation density between 912 A and 2400 A. Bull. Astron. Inst. Netherlands, 19:421, January 1968. (Cited on pages 15 and 101.)

L. M. Haffner, R.-J. Dettmar, J. E. Beckman, K. Wood, J. D. Slavin, C. Giammanco, G. J. Madsen, A. Zurita, and R. J. Reynolds. The warm ionized medium in spiral galaxies. *Reviews of Modern Physics*, 81:969–997, July 2009. doi: 10.1103/RevModPhys.81.969. (Cited on page 33.)

J. S. Hall. Observations of the Polarized Light from Stars. *Science*, 109:166–167, February 1949. doi: 10.1126/science.109.2825.166. (Cited on pages 47 and 97.)

T. I. Hasegawa, E. Herbst, and C. M. Leung. Models of gas-grain chemistry in dense interstellar clouds with complex organic molecules. ApJS, 82:167–195, September 1992. doi: 10.1086/191713. (Cited on page 111.)

C. Heiles and T. H. Troland. The Millennium Arecibo 21 Centimeter Absorption-Line Survey. IV. Statistics of Magnetic Field, Column Density, and Turbulence. ApJ, 624:773–793, May 2005. doi: 10.1086/428896. (Cited on page 255.)

P. Hennebelle and E. Falgarone. Turbulent molecular clouds. A&A Rev., 20:55, November 2012. doi: 10.1007/s00159-012-0055-y. (Cited on pages 71 and 72.)

L. G. Henyey and J. L. Greenstein. Diffuse radiation in the Galaxy. ApJ, 93:70–83, January 1941. doi: 10.1086/144246. (Cited on pages 47 and 328.)

E. Herbst and E. F. van Dishoeck. Complex Organic Interstellar Molecules. ARA&A, 47:427–480, September 2009. doi: 10.1146/annurev-astro-082708-101654. (Cited on page 58.)

M. H. Heyer and C. M. Brunt. The Universality of Turbulence in Galactic Molecular Clouds. ApJ, 615:L45–L48, November 2004. doi: 10.1086/425978. (Cited on page 70.)

P. Hily-Blant and E. Falgarone. Intermittency of interstellar turbulence: parsec-scale coherent structure of intense, velocity shear. A&A, 500:L29–L32, June 2009. doi: 10.1051/0004-6361/200912296. (Cited on page 70.)

P. Hily-Blant, E. Falgarone, and J. Pety. Dissipative structures of diffuse molecular gas. III. Small-scale intermittency of intense velocity-shears. A&A, 481:367–380, April 2008. doi: 10.1051/0004-6361:20078423. (Cited on page 70.)

D. Hollenbach and E. E. Salpeter. Surface Recombination of Hydrogen Molecules. ApJ, 163:155, January 1971. doi: 10.1086/150754. (Cited on page 57.)

H. Holweger. Photospheric abundances: Problems, updates, implications. In R. F. Wimmer-Schweingruber, editor, *Joint SOHO/ACE workshop "Solar and Galactic Composition"*, volume 598 of *American Institute of Physics Conference Series*, pages 23–30, November 2001. doi: 10.1063/1.1433974. (Cited on pages 51 and 52.)

L. Hornekær, E. Rauls, W. Xu, Ž. Šljivančanin, R. Otero, I. Stensgaard, E. Lægsgaard, B. Hammer, and F. Besenbacher. Clustering of Chemisorbed H(D) Atoms on the Graphite (0001) Surface due to Preferential Sticking. *Physical Review Letters*, 97(18):186102, November 2006. doi: 10.1103/PhysRevLett.97.186102. (Cited on pages 108 and 109.)

J. E. Howe, D. T. Jaffe, R. Genzel, and G. J. Stacey. Parsec-scale penetration of ultraviolet photons into molecular clouds - (C II) 158 micron mapping of W3, NGC 1977, and NGC 2023. ApJ, 373:158–168, May 1991. doi: 10.1086/170034. (Cited on page 283.)

G.A. Huber and S. Kim. Weighted-ensemble brownian dynamics simulations for protein association reactions. *Biophysical Journal*, 70(1):97 – 110, 1996. ISSN 0006-3495. doi: http://dx.doi.org/10.1016/S0006-3495(96)79552-8. URL http://www.sciencedirect.com/science/article/pii/S0006349596795528. (Cited on page 279.)

V. V. Ivanovskaya, A. Zobelli, D. Teillet-Billy, N. Rougeau, V. Sidis, and P. R. Briddon. Enhanced H_2 catalytic formation on specific topological defects in interstellar graphenic dust grain models. Phys. Rev. B, 82(24):245407, December 2010. doi: 10.1103/PhysRevB.82.245407. (Cited on page 109.)

D. T. Jaffe, R. Genzel, A. I. Harris, J. E. Howe, G. J. Stacey, and J. Stutzki. Warm dense gas in the reflection nebula NGC 2023. ApJ, 353:193–199, April 1990. doi: 10.1086/168606. (Cited on page 283.)

L. Jeloaica and V. Sidis. DFT investigation of the adsorption of atomic hydrogen on a cluster-model graphite surface. *Chemical Physics Letters*, 300:157–162, January 1999. doi: 10.1016/S0009-2614(98)01337-2. (Cited on pages 106, 107, and 108.)

E. B. Jenkins. A Unified Representation of Gas-Phase Element Depletions in the Interstellar Medium. ApJ, 700:1299–1348, August 2009. doi: 10.1088/0004-637X/700/2/1299. (Cited on page 52.)

A. G. Jensen, T. P. Snow, G. Sonneborn, and B. L. Rachford. Observational Properties of Rotationally Excited Molecular Hydrogen in Translucent Lines of Sight. ApJ, 711:1236–1256, March 2010. doi: 10.1088/0004-637X/711/2/1236. (Cited on page 312.)

C. Joblin, P. Pilleri, J. Montillaud, A. Fuente, M. Gerin, O. Berné, V. Ossenkopf, J. Le Bourlot, D. Teyssier, J. R. Goicoechea, F. Le Petit, M. Röllig, M. Akyilmaz, A. O. Benz, F. Boulanger, S. Bruderer, C. Dedes, K. France, R. Güsten, A. Harris, T. Klein, C. Kramer, S. D. Lord, P. G. Martin, J. Martin-Pintado, B. Mookerjea, Y. Okada, T. G. Phillips, J. R. Rizzo, R. Simon, J. Stutzki, F. van der Tak, H. W. Yorke, E. Steinmetz, C. Jarchow, P. Hartogh, C. E. Honingh, O. Siebertz, E. Caux, and B. Colin. Gas morphology and energetics at the surface of PDRs: New insights with Herschel observations of NGC 7023. A&A, 521:L25, October 2010. doi: 10.1051/0004-6361/201015129. (Cited on pages 285 and 288.)

C. Joblin, C. Pinto, E. Bron, M. Gerin, P. Pilleri, O. BernÃ©, E. Habart, F. Le Petit, J. Le Bourlot, M. KÃ¶hler, J. Montillaud, J.R. Goicoechea, A. Fuente, V. Ossenkopf, and E. Bergin. Gas morphology and energetics in bright photodissociation regions. in prep. (Cited on pages 287 and 291.)

A. P. Jones. Variations on a theme - the evolution of hydrocarbon solids. I. Compositional and spectral modelling - the eRCN and DG models. A&A, 540:A1, April 2012a. doi: 10.1051/0004-6361/201117623. (Cited on page 55.)

A. P. Jones. Variations on a theme - the evolution of hydrocarbon solids. II. Optical property modelling - the optEC$_{(s)}$ model. A&A, 540:A2, April 2012b. doi: 10.1051/0004-6361/201117624. (Cited on page 55.)

A. P. Jones. Variations on a theme - the evolution of hydrocarbon solids. III. Size-dependent properties - the optEC$_{(s)}$(a) model. A&A, 542:A98, June 2012c. doi: 10.1051/0004-6361/201118483. (Cited on page 55.)

A. P. Jones and J. A. Nuth. Dust destruction in the ISM: a re-evaluation of dust lifetimes. A&A, 530:A44, June 2011. doi: 10.1051/0004-6361/201014440. (Cited on page 59.)

A. P. Jones, L. Fanciullo, M. Köhler, L. Verstraete, V. Guillet, M. Bocchio, and N. Ysard. The evolution of amorphous hydrocarbons in the ISM: dust modelling from a new vantage point. A&A, 558:A62, October 2013. doi: 10.1051/0004-6361/201321686. (Cited on pages 5, 51, 55, and 59.)

W. P. Jones and B. E. Launder. The Prediction of Laminarization with a Two-Equation Model of Turbulence. *nternational Journal of Heat and Mass Transfer*, 15:301–314, 1972. doi: 10.1051/0004-6361/201321686. (Cited on page 246.)

K. Joulain, E. Falgarone, G. Pineau des Forets, and D. Flower. Non-equilibrium chemistry in the dissipative structures of interstellar turbulence. A&A, 340:241–256, December 1998. (Cited on page 74.)

N. Katz, I. Furman, O. Biham, V. Pirronello, and G. Vidali. Molecular Hydrogen Formation on Astrophysically Relevant Surfaces. ApJ, 522:305–312, September 1999. doi: 10.1086/307642. (Cited on pages 15, 107, 108, and 109.)

G. W. C. Kay and T. H. Laby. *Tables of physical and chemical constants*. Londres: Longmans, 1966. (Cited on page 256.)

Jay Kerwin and Bret Jackson. The sticking of h and d atoms on a graphite (0001) surface: The effects of coverage and energy dissipation. *The Journal of Chemical Physics*, 128(8):084702, 2008. doi: http://dx.doi.org/10.1063/1.2868771. URL http://scitation.aip.org/content/aip/journal/jcp/128/8/10.1063/1.2868771. (Cited on pages 108 and 109.)

R. S. Klessen and P. Hennebelle. Accretion-driven turbulence as universal process: galaxies, molecular clouds, and protostellar disks. A&A, 520:A17, September 2010. doi: 10.1051/0004-6361/200913780. (Cited on page 72.)

M. Köhler, E. Habart, H. Arab, J. Bernard-Salas, H. Ayasso, A. Abergel, A. Zavagno, E. Polehampton, M. H. D. van der Wiel, D. A. Naylor, G. Makiwa, K. Dassas, C. Joblin, P. Pilleri, O. Berné, A. Fuente, M. Gerin, J. R. Goicoechea, and D. Teyssier. Physical structure of the photodissociation regions in ngc 7023. A&A, 569:A109, 2014. doi: 10.1051/0004-6361/201322711. URL http://dx.doi.org/10.1051/0004-6361/201322711. (Cited on pages 285, 287, and 288.)

A. N. Kolmogorov. A refinement of previous hypotheses concerning the local structure of turbulence in a viscous incompressible fluid at high reynolds number. *Journal of Fluid Mechanics*, 13:82–85, 1962. doi: http://dx.doi.org/10.1017/S0022112062000518. (Cited on pages 67 and 245.)

R. H. Kraichnan. Inertial-Range Spectrum of Hydromagnetic Turbulence. *Physics of Fluids*, 8:1385–1387, July 1965. doi: 10.1063/1.1761412. (Cited on page 69.)

H. A. Kramers. Brownian motion in a field of force and the diffusion model of chemical reactions. *Physica*, 7:284–304, April 1940. doi: 10.1016/S0031-8914(40)90098-2. (Cited on page 140.)

J. Krelowski. Organic molecules and the diffuse interstellar bands. *Advances in Space Research*, 30:1395–1407, 2002. doi: 10.1016/S0273-1177(02)00503-3. (Cited on page 47.)

S. Lacour, V. Ziskin, G. Hébrard, C. Oliveira, M. K. André, R. Ferlet, and A. Vidal-Madjar. Velocity Dispersion of the High Rotational Levels of H_2. ApJ, 627:251–262, July 2005. doi: 10.1086/430291. (Cited on pages 73, 276, 277, and 312.)

W. D. Langer, T. Velusamy, J. L. Pineda, P. F. Goldsmith, D. Li, and H. W. Yorke. C^+ detection of warm dark gas in diffuse clouds. A&A, 521:L17, October 2010. doi: 10.1051/0004-6361/201015088. (Cited on page 312.)

A. Laor and B. T. Draine. Spectroscopic constraints on the properties of dust in active galactic nuclei. ApJ, 402:441–468, January 1993. doi: 10.1086/172149. (Cited on page 328.)

R. B. Larson. Turbulence and star formation in molecular clouds. MNRAS, 194:809–826, March 1981. (Cited on page 69.)

A. Lazarian. Magnetic Fields via Polarimetry: Progress of Grain Alignment Theory. J. Quant. Spec. Radiat. Transf., 79:881, 2003. doi: 10.1016/S0022-4073(02)00326-6. (Cited on page 49.)

A. Lazarian and D. Finkbeiner. Microwave emission from aligned dust. New A Rev., 47:1107–1116, December 2003. doi: 10.1016/j.newar.2003.09.037. (Cited on page 50.)

J. Le Bourlot, G. Pineau Des Forets, E. Roueff, and D. R. Flower. Infrared and submillimetric emission lines from the envelopes of dark clouds. A&A, 267:233–254, January 1993. (Cited on page 325.)

J. Le Bourlot, F. Le Petit, C. Pinto, E. Roueff, and F. Roy. Surface chemistry in the interstellar medium. I. H_2 formation by Langmuir-Hinshelwood and Eley-Rideal mechanisms. A&A, 541:A76, May 2012. doi: 10.1051/0004-6361/201118126. (Cited on pages 109, 110, 111, 112, 229, 312, and 325.)

F. Le Petit, C. Nehmé, J. Le Bourlot, and E. Roueff. A Model for Atomic and Molecular Interstellar Gas: The Meudon PDR Code. ApJS, 164:506–529, June 2006. doi: 10.1086/503252. (Cited on pages 291 and 325.)

A. Leger, M. Jura, and A. Omont. Desorption from interstellar grains. A&A, 144:147–160, March 1985. (Cited on page 96.)

P. O. Lehtinen, A. S. Foster, Y. Ma, A. V. Krasheninnikov, and R. M. Nieminen. Irradiation-Induced Magnetism in Graphite: A Density Functional Study. *Physical Review Letters*, 93(18):187202, October 2004. doi: 10.1103/PhysRevLett.93.187202. (Cited on page 108.)

J. L. Lemaire, D. Field, M. Gerin, S. Leach, G. Pineau des Forets, F. Rostas, and D. Rouan. High spatial resolution observations of H_2_ vibrational emission in NGC 7023. A&A, 308:895–907, April 1996. (Cited on pages 284, 285, 288, 289, and 300.)

J. L. Lemaire, D. Field, J. P. Maillard, G. Pineau des Forêts, E. Falgarone, F. P. Pijpers, M. Gerin, and F. Rostas. High resolution Fourier transform spectroscopy of H_2 IR emission in NGC 7023. A&A, 349:253–258, September 1999. (Cited on page 285.)

F. Levrier, F. Le Petit, P. Hennebelle, P. Lesaffre, M. Gerin, and E. Falgarone. UV-driven chemistry in simulations of the interstellar medium. I. Post-processed chemistry with the Meudon PDR code. A&A, 544:A22, August 2012. doi: 10.1051/0004-6361/201218865. (Cited on page 74.)

A. Li. Interaction of Nanoparticles with Radiation. In A. N. Witt, G. C. Clayton, and B. T. Draine, editors, *Astrophysics of Dust*, volume 309 of *Astronomical Society of the Pacific Conference Series*, page 417, May 2004. (Cited on page 50.)

A. Li and B. T. Draine. Infrared Emission from Interstellar Dust. II. The Diffuse Interstellar Medium. ApJ, 554:778–802, June 2001. doi: 10.1086/323147. (Cited on pages 51, 53, 54, 119, 123, and 159.)

A. Li and B. T. Draine. Infrared Emission from Interstellar Dust. III. The Small Magellanic Cloud. ApJ, 576:762–772, September 2002. doi: 10.1086/341796. (Cited on pages 53 and 119.)

D. Li and P. F. Goldsmith. H I Narrow Self-Absorption in Dark Clouds. ApJ, 585:823–839, March 2003. doi: 10.1086/346227. (Cited on pages 207, 229, and 311.)

A. Lipshtat and O. Biham. Moment equations for chemical reactions on interstellar dust grains. A&A, 400:585–593, March 2003. doi: 10.1051/0004-6361:20021902. (Cited on page 114.)

I. Lohmar and J. Krug. The sweeping rate in diffusion-mediated reactions on dust grain surfaces. MNRAS, 370:1025–1033, August 2006. doi: 10.1111/j.1365-2966.2006.10541.x. (Cited on page 113.)

I. Lohmar, J. Krug, and O. Biham. Accurate rate coefficients for models of interstellar gas-grain chemistry. A&A, 504:L5–L8, September 2009. doi: 10.1051/0004-6361/200912746. (Cited on page 113.)

T. S. Lundgren. Distribution Functions in the Statistical Theory of Turbulence. *Physics of Fluids*, 10:969–975, May 1967. doi: 10.1063/1.1762249. (Cited on pages 236, 238, and 242.)

T. S. Lundgren. Model Equation for Nonhomogeneous Turbulence. *Physics of Fluids*, 12:485–497, March 1969. doi: 10.1063/1.1692511. (Cited on page 236.)

George Marsaglia and Wai Wan Tsang. The ziggurat method for generating random variables. *Journal of Statistical Software*, 5(8):1–7, 10 2000. ISSN 1548-7660. URL http://www.jstatsoft.org/v05/i08. (Cited on page 258.)

P. G. Martin, G. C. Clayton, and M. J. Wolff. Ultraviolet Interstellar Linear Polarization. V. Analysis of the Final Data Set. ApJ, 510:905–914, January 1999. doi: 10.1086/306613. (Cited on page 49.)

R. Martinazzo and G. F. Tantardini. Quantum study of Eley-Rideal reaction and collision induced desorption of hydrogen atoms on a graphite surface. II. H-physisorbed case. J. Chem. Phys., 124(12):124703, March 2006. doi: 10.1063/1.2177655. (Cited on page 112.)

P. Martini, K. Sellgren, and J. L. Hora. Near-Infrared Spectroscopy of Molecular Filaments in the Reflection Nebula NGC 7023. ApJ, 484:296–303, July 1997. (Cited on page 285.)

J. S. Mathis, W. Rumpl, and K. H. Nordsieck. The size distribution of interstellar grains. ApJ, 217:425–433, October 1977. doi: 10.1086/155591. (Cited on pages 5, 53, 117, and 118.)

J. S. Mathis, P. G. Mezger, and N. Panagia. Interstellar radiation field and dust temperatures in the diffuse interstellar matter and in giant molecular clouds. A&A, 128:212–229, November 1983. (Cited on pages 101 and 327.)

C. F. McKee and E. C. Ostriker. Theory of Star Formation. ARA&A, 45:565–687, September 2007. doi: 10.1146/annurev.astro.45.051806.110602. (Cited on page 28.)

A. McKellar. Evidence for the Molecular Origin of Some Hitherto Unidentified Interstellar Lines. PASP, 52:187, June 1940. doi: 10.1086/125159. (Cited on page 39.)

A. McKellar. The Problems of Possible Molecular Identification for Interstellar Lines. PASP, 53:233–235, August 1941. doi: 10.1086/125323. (Cited on page 41.)

D. M. Meyer, J. A. Cardelli, and U. J. Sofia. The Abundance of Interstellar Nitrogen. ApJ, 490:L103–L106, November 1997. doi: 10.1086/311023. (Cited on page 28.)

D. M. Meyer, M. Jura, and J. A. Cardelli. The Definitive Abundance of Interstellar Oxygen. ApJ, 493:222–229, January 1998. doi: 10.1086/305128. (Cited on page 28.)

M.-A. Miville-Deschênes, G. Joncas, E. Falgarone, and F. Boulanger. High resolution 21 cm mapping of the Ursa Major Galactic cirrus: Power spectra of the high-latitude H I gas. A&A, 411:109–121, November 2003. doi: 10.1051/0004-6361:20031297. (Cited on page 70.)

M.-A. Miville-Deschênes, P. G. Martin, A. Abergel, J.-P. Bernard, F. Boulanger, G. Lagache, L. D. Anderson, P. André, H. Arab, J.-P. Baluteau, K. Blagrave, S. Bontemps, M. Cohen, M. Compiegne, P. Cox, E. Dartois, G. Davis, R. Emery, T. Fulton, C. Gry, E. Habart, M. Huang, C. Joblin, S. C. Jones, J. Kirk, T. Lim, S. Madden, G. Makiwa, A. Menshchikov, S. Molinari, H. Moseley, F. Motte, D. A. Naylor, K. Okumura, D. Pinheiro Gonçalves, E. Polehampton, J. A. Rodón, D. Russeil, P. Saraceno, N. Schneider, S. Sidher, L. Spencer, B. Swinyard, D. Ward-Thompson, G. J. White, and A. Zavagno. Herschel-SPIRE observations of the Polaris flare: Structure of the diffuse interstellar medium at the sub-parsec scale. A&A, 518:L104, July 2010. doi: 10.1051/0004-6361/201014678. (Cited on page 70.)

A. S. Monin and A. M. Yaglom. *Statistical fluid mechanics; mechanics of turbulence*. 1971. (Cited on page 61.)

A. S. Monin and A. M. Yaglom. *Statistical fluid mechanics: Mechanics of turbulence. Volume 2 /revised and enlarged edition/*. 1975. (Cited on page 61.)

S. Morisset, F. Aguillon, M. Sizun, and V. Sidis. Role of surface relaxation in the eley-rideal formation of h2 on a graphite surface. *The Journal of Physical Chemistry A*, 108(41):8571–8579, 2004. doi: 10.1021/jp049969q. URL http://pubs.acs.org/doi/abs/10.1021/jp049969q. (Cited on page 112.)

J. E. Moyal. *J. R. Stat. Soc. B*, 11(150), 1949. (Cited on page 140.)

K. Nomoto, C. Kobayashi, and N. Tominaga. Nucleosynthesis in Stars and the Chemical Enrichment of Galaxies. ARA&A, 51:457–509, August 2013. doi: 10.1146/annurev-astro-082812-140956. (Cited on page 27.)

A. M. Obukhov. Some Specific Features of Atmospheric Turbulence. J. Geophys. Res., 67:3011, July 1962. doi: 10.1029/JZ067i008p03011. (Cited on page 67.)

Y. Okada, P. Pilleri, O. Berné, V. Ossenkopf, A. Fuente, J. R. Goicoechea, C. Joblin, C. Kramer, M. Röllig, D. Teyssier, and F. F. S. van der Tak. Probing the role of polycyclic aromatic hydrocarbons in the photoelectric heating within photodissociation regions. A&A, 553:A2, May 2013. doi: 10.1051/0004-6361/201118450. (Cited on pages 286 and 288.)

L. Pan and P. Padoan. The Temperature of Interstellar Clouds from Turbulent Heating. ApJ, 692:594–607, February 2009. doi: 10.1088/0004-637X/692/1/594. (Cited on pages 255, 262, 264, and 271.)

H. B. Perets, O. Biham, G. Manicó, V. Pirronello, J. Roser, S. Swords, and G. Vidali. Molecular Hydrogen Formation on Ice Under Interstellar Conditions. ApJ, 627:850–860, July 2005. doi: 10.1086/430435. (Cited on pages 108 and 109.)

H. B. Perets, A. Lederhendler, O. Biham, G. Vidali, L. Li, S. Swords, E. Congiu, J. Roser, G. Manicó, J. R. Brucato, and V. Pirronello. Molecular Hydrogen Formation on Amorphous Silicates under Interstellar Conditions. ApJ, 661: L163–L166, June 2007. doi: 10.1086/518862. (Cited on pages 107 and 109.)

P. Pilleri, J. Montillaud, O. Berné, and C. Joblin. Evaporating very small grains as tracers of the UV radiation field in photo-dissociation regions. A&A, 542: A69, June 2012. doi: 10.1051/0004-6361/201015915. (Cited on page 286.)

V. Pirronello, O. Biham, C. Liu, L. Shen, and G. Vidali. Efficiency of Molecular Hydrogen Formation on Silicates. ApJ, 483:L131–L134, July 1997a. doi: 10.1086/310746. (Cited on page 107.)

V. Pirronello, C. Liu, L. Shen, and G. Vidali. Laboratory Synthesis of Molecular Hydrogen on Surfaces of Astrophysical Interest. ApJ, 475:L69–L72, January 1997b. doi: 10.1086/310464. (Cited on pages 106 and 107.)

V. Pirronello, C. Liu, J. E. Roser, and G. Vidali. Measurements of molecular hydrogen formation on carbonaceous grains. A&A, 344:681–686, April 1999. (Cited on page 108.)

S. B. Pope. PDF methods for turbulent reactive flows. *Progress in Energy and Combustion Science*, 11:119–192, 1985. (Cited on pages 16, 236, 238, and 253.)

S. B. Pope. Lagrangian pdf methods for turbulent flows. *Annual Review of Fluid Mechanics*, 26:23–63, 1994. doi: 10.1146/annurev.fl.26.010194.000323. (Cited on page 236.)

S. B. Pope. New developments in pdf modelling of nonreactive and reactive turbulent flows. *Turbulence, heat and mass transfer* 2, pages 35–45, 1997. (Cited on page 236.)

S. B. Pope. *Turbulent Flows*. August 2000. (Cited on pages 61, 236, 238, and 244.)

S. B. Pope. Advances in PDF methods for turbulent reactive flows. In H. I. Andersson and P.-A. Krogstad, editors, *Proceedings of the Tenth European Turbulence Conference*, Advances in Turbulence X, pages 529–536, 2004. (Cited on page 236.)

S. B. Pope. Simple models of turbulent flowsa). *Physics of Fluids*, 23(1):011301, January 2011. doi: 10.1063/1.3531744. (Cited on page 236.)

S. B. Pope and Y. L. Chen. The velocity-dissipation probability density function model for turbulent flows. *Physics of Fluids A: Fluid Dynamics, Volume 2, Issue 8, p.1437-1449*, 2:1437–1449, August 1990. doi: 10.1063/1.857592. (Cited on pages 236, 243, 244, and 280.)

D. Porter, A. Pouquet, and P. Woodward. Measures of intermittency in driven supersonic flows. Phys. Rev. E, 66(2):026301, August 2002. doi: 10.1103/PhysRevE.66.026301. (Cited on page 69.)

M. Rapacioli, F. Calvo, C. Joblin, P. Parneix, D. Toublanc, and F. Spiegelman. Formation and destruction of polycyclic aromatic hydrocarbon clusters in the interstellar medium. A&A, 460:519–531, December 2006. doi: 10.1051/0004-6361:20065412. (Cited on page 286.)

W. G. Roberge. The spherical harmonics solution for the radiation field in plane-parallel clouds with embedded sources. ApJ, 275:292–306, December 1983. doi: 10.1086/161533. (Cited on page 328.)

W. G. Roberge. Alignment of Interstellar Dust. In A. N. Witt, G. C. Clayton, and B. T. Draine, editors, *Astrophysics of Dust*, volume 309 of *Astronomical Society of the Pacific Conference Series*, page 467, May 2004. (Cited on page 49.)

C. Rogers, M. H. Heyer, and P. E. Dewdney. H I, CO, and IRAS observations of NGC 7023. ApJ, 442:694–713, April 1995. doi: 10.1086/175475. (Cited on page 284.)

M. Röllig, N. P. Abel, T. Bell, F. Bensch, J. Black, G. J. Ferland, B. Jonkheid, I. Kamp, M. J. Kaufman, J. Le Bourlot, F. Le Petit, R. Meijerink, O. Morata, V. Ossenkopf, E. Roueff, G. Shaw, M. Spaans, A. Sternberg, J. Stutzki, W.-F. Thi, E. F. van Dishoeck, P. A. M. van Hoof, S. Viti, and M. G. Wolfire. A photon dominated region code comparison study. A&A, 467:187–206, May 2007. doi: 10.1051/0004-6361:20065918. (Cited on page 325.)

Tanglaw Roman, Wilson Agerico Dino, Hiroshi Nakanishi, Hideaki Kasai, Tsuyoshi Sugimoto, and Kyouichi Tange. Hydrogen pairing on graphene. *Carbon*, 45(1):218 – 220, 2007. ISSN 0008-6223. doi: http://dx.doi.org/10.1016/j.carbon.2006.09.027. URL http://www.sciencedirect.com/science/article/pii/S0008622306004878. (Cited on page 108.)

N. Rougeau, D. Teillet-Billy, and V. Sidis. On the PES for the interaction of an H atom with an H chemisorbate on a graphenic platelet. *Physical Chemistry Chemical Physics (Incorporating Faraday Transactions)*, 13:17579, 2011. doi: 10.1039/c1cp22202c. (Cited on page 112.)

D. Ruelle. Non-equilibrium statistical mechanics of turbulence. *ArXiv e-prints*, May 2014. (Cited on page 68.)

D. P. Ruelle. Hydrodynamic turbulence as a problem in nonequilibrium statistical mechanics. *Proceedings of the National Academy of Science*, 109:20344–20346, December 2012. doi: 10.1073/pnas.1218747109. (Cited on page 68.)

B. D. Savage and K. R. Sembach. Interstellar Gas-Phase Abundances and Physical Conditions toward Two Distant High-Latitude Halo Stars. ApJ, 470:893, October 1996. doi: 10.1086/177919. (Cited on page 28.)

J. Scalo and B. G. Elmegreen. Interstellar Turbulence II: Implications and Effects. ARA&A, 42:275–316, September 2004. doi: 10.1146/annurev.astro.42.120403.143327. (Cited on page 72.)

K. Sellgren, M. W. Werner, and H. L. Dinerstein. Scattering of infrared radiation by dust in NGC 7023 and NGC 2023. ApJ, 400:238–247, November 1992. doi: 10.1086/171990. (Cited on page 284.)

L. Serra Díaz-Cano and A. P. Jones. Carbonaceous dust in interstellar shock waves: hydrogenated amorphous carbon (a-C:H) vs. graphite. A&A, 492:127–133, December 2008. doi: 10.1051/0004-6361:200810622. (Cited on page 55.)

X. Sha and B. Jackson. First-principles study of the structural and energetic properties of H atoms on a graphite (0 0 0 1) surface. *Surface Science*, 496:318–330, January 2002. doi: 10.1016/S0039-6028(01)01602-8. (Cited on pages 107, 108, and 109.)

Z.-S. She and E. Leveque. Universal scaling laws in fully developed turbulence. *Physical Review Letters*, 72:336–339, January 1994. doi: 10.1103/PhysRevLett.72.336. (Cited on pages 68, 70, 271, and 278.)

Z.-S. She and E. C. Waymire. Quantized Energy Cascade and Log-Poisson Statistics in Fully Developed Turbulence. *Physical Review Letters*, 74:262–265, January 1995. doi: 10.1103/PhysRevLett.74.262. (Cited on pages 68 and 278.)

M. R. H. Sheikhi, P. Givi, and S. B. Pope. Frequency-velocity-scalar filtered mass density function for large eddy simulation of turbulent flows. *Physics of Fluids*, 21(7):075102, July 2009. doi: 10.1063/1.3153907. (Cited on page 313.)

M. Sizun, D. Bachellerie, F. Aguillon, and V. Sidis. Investigation of ZPE and temperature effects on the Eley-Rideal recombination of hydrogen atoms on graphene using a multidimensional graphene-H-H potential. *Chemical Physics Letters*, 498:32–37, September 2010. doi: 10.1016/j.cplett.2010.08.039. (Cited on pages 166 and 330.)

J. D. Slavin. The Origins and Physical Properties of the Complex of Local Interstellar Clouds. Space Sci. Rev., 143:311–322, March 2009. doi: 10.1007/s11214-008-9342-3. (Cited on page 55.)

T. P. Snow and J. D. Destree. The Diffuse Interstellar Bands in History and in the UV. In C. Joblin and A. G. G. M. Tielens, editors, *EAS Publications Series*, volume 46 of *EAS Publications Series*, pages 341–347, March 2011. doi: 10.1051/eas/1146035. (Cited on page 47.)

T. P. Snow and B. J. McCall. Diffuse Atomic and Molecular Clouds. ARA&A, 44:367–414, September 2006. doi: 10.1146/annurev.astro.43.072103.150624. (Cited on pages 35, 37, and 39.)

U. J. Sofia and D. M. Meyer. Interstellar Abundance Standards Revisited. ApJ, 554:L221–L224, June 2001. doi: 10.1086/321715. (Cited on pages 51, 52, and 53.)

L. Spitzer. *Physical processes in the interstellar medium*. 1978. (Cited on page 244.)

S. W. Stahler and F. Palla. *The Formation of Stars*. 2005. (Cited on pages 28 and 32.)

J. Stutzki and R. Guesten. High spatial resolution isotopic CO and CS observations of M17 SW - The clumpy structure of the molecular cloud core. ApJ, 356:513–533, June 1990. doi: 10.1086/168859. (Cited on page 283.)

J. Stutzki, G. J. Stacey, R. Genzel, A. I. Harris, D. T. Jaffe, and J. B. Lugten. Submillimeter and far-infrared line observations of M17 SW - A clumpy molecular cloud penetrated by ultraviolet radiation. ApJ, 332:379–399, September 1988. doi: 10.1086/166663. (Cited on page 283.)

P. Thaddeus and J. F. Clauser. Cosmic Microwave Radiation at 2.63 mm from Observations of Interstellar CN. *Physical Review Letters*, 16:819–822, May 1966. doi: 10.1103/PhysRevLett.16.819. (Cited on page 41.)

A. G. G. M. Tielens. Interstellar Polycyclic Aromatic Hydrocarbon Molecules. ARA&A, 46:289–337, September 2008. doi: 10.1146/annurev.astro.46.060407.145211. (Cited on pages 50 and 57.)

R. J. Trumpler. Preliminary results on the distances, dimensions and space distribution of open star clusters. *Lick Observatory Bulletin*, 14:154–188, 1930a. (Cited on pages 29 and 43.)

R. J. Trumpler. Absorption of Light in the Galactic System. PASP, 42:214, August 1930b. doi: 10.1086/124039. (Cited on page 43.)

R. J. Trumpler. Spectrophotometric Measures of Interstellar Light Absorption. PASP, 42:267, October 1930c. doi: 10.1086/124051. (Cited on page 43.)

M. E. van den Ancker, P. S. The, H. R. E. Tjin A Djie, C. Catala, D. de Winter, P. F. C. Blondel, and L. B. F. M. Waters. HIPPARCOS data on Herbig Ae/Be stars: an evolutionary scenario. A&A, 324:L33–L36, August 1997. (Cited on pages 283 and 286.)

F. van Leeuwen, editor. *Hipparcos, the New Reduction of the Raw Data*, volume 350 of *Astrophysics and Space Science Library*, 2007. (Cited on pages 283 and 286.)

P. R. Van Slooten and P. Jayesh, S. B. Advances in PDF modeling for inhomogeneous turbulent flows. *Physics of Fluids*, 10:246–265, January 1998. doi: 10.1063/1.869564. (Cited on page 236.)

A. I. Vasyunin and E. Herbst. Reactive Desorption and Radiative Association as Possible Drivers of Complex Molecule Formation in the Cold Interstellar Medium. ApJ, 769:34, May 2013. doi: 10.1088/0004-637X/769/1/34. (Cited on page 58.)

E. Vázquez-Semadeni, A. Gazol, T. Passot, and et al. Thermal Instability and Magnetic Pressure in the Turbulent Interstellar Medium. In E. Falgarone and T. Passot, editors, *Turbulence and Magnetic Fields in Astrophysics*, volume 614 of *Lecture Notes in Physics, Berlin Springer Verlag*, pages 213–251, 2003. (Cited on page 34.)

C. F. von Weizsäcker. The Evolution of Galaxies and Stars. ApJ, 114:165, September 1951. doi: 10.1086/145462. (Cited on page 69.)

W. R. Webber. A New Estimate of the Local Interstellar Energy Density and Ionization Rate of Galactic Cosmic Cosmic Rays. ApJ, 506:329–334, October 1998. doi: 10.1086/306222. (Cited on page 30.)

J. C. Weingartner and B. T. Draine. Dust Grain-Size Distributions and Extinction in the Milky Way, Large Magellanic Cloud, and Small Magellanic Cloud. ApJ, 548:296–309, February 2001a. doi: 10.1086/318651. (Cited on pages 53, 54, and 119.)

J. C. Weingartner and B. T. Draine. Photoelectric Emission from Interstellar Dust: Grain Charging and Gas Heating. ApJS, 134:263–281, June 2001b. doi: 10.1086/320852. (Cited on pages 56, 330, and 331.)

J. C. Weingartner and B. T. Draine. Electron-Ion Recombination on Grains and Polycyclic Aromatic Hydrocarbons. ApJ, 563:842–852, December 2001c. doi: 10.1086/324035. (Cited on pages 56, 330, and 331.)

J. C. Weingartner, B. T. Draine, and D. K. Barr. Photoelectric Emission from Dust Grains Exposed to Extreme Ultraviolet and X-Ray Radiation. ApJ, 645:1188–1197, July 2006. doi: 10.1086/504420. (Cited on pages 56, 330, and 331.)

D. E. Welty, E. B. Jenkins, J. C. Raymond, C. Mallouris, and D. G. York. Intermediate- and High-Velocity Ionized Gas toward ζ Orionis. ApJ, 579: 304–326, November 2002. doi: 10.1086/342755. (Cited on page 55.)

D. C. B. Whittet. Polarization of Starlight. In A. N. Witt, G. C. Clayton, and B. T. Draine, editors, *Astrophysics of Dust*, volume 309 of *Astronomical Society of the Pacific Conference Series*, page 65, May 2004. (Cited on page 49.)

D. C. B. Whittet. Oxygen Depletion in the Interstellar Medium: Implications for Grain Models and the Distribution of Elemental Oxygen. ApJ, 710: 1009–1016, February 2010. doi: 10.1088/0004-637X/710/2/1009. (Cited on page 52.)

L. M. Widrow, D. Ryu, D. R. G. Schleicher, K. Subramanian, C. G. Tsagas, and R. A. Treumann. The First Magnetic Fields. Space Sci. Rev., 166:37–70, May 2012. doi: 10.1007/s11214-011-9833-5. (Cited on page 30.)

M. E. Wiedenbeck. Cosmic-Ray Energy Spectra and Time Variations in the Local Interstellar Medium: Constraints and Uncertainties. Space Sci. Rev., 176:35–46, June 2013. doi: 10.1007/s11214-011-9778-8. (Cited on page 31.)

A. N. Witt, K. D. Gordon, U. P. Vijh, P. H. Sell, T. L. Smith, and R.-H. Xie. The Excitation of Extended Red Emission: New Constraints on Its Carrier from Hubble Space Telescope Observations of NGC 7023. ApJ, 636:303–315, January 2006. doi: 10.1086/498052. (Cited on pages 286 and 287.)

M. G. Wolfire, C. F. McKee, D. Hollenbach, and A. G. G. M. Tielens. Neutral Atomic Phases of the Interstellar Medium in the Galaxy. ApJ, 587:278–311, April 2003. doi: 10.1086/368016. (Cited on pages 33, 34, 255, 260, 262, and 263.)

P. K. Yeung and S. B. Pope. Lagrangian statistics from direct numerical simulations of isotropic turbulence. *Journal of Fluid Mechanics*, 207:531–586, October 1989. doi: 10.1017/S0022112089002697. (Cited on pages 245 and 247.)

P. K. Yeung, S. B. Pope, A. G. Lamorgese, and D. A. Donzis. Acceleration and dissipation statistics of numerically simulated isotropic turbulence. *Physics of Fluids*, 18(6):065103, June 2006. doi: 10.1063/1.2204053. (Cited on page 247.)

N. Ysard, M. A. Miville-Deschênes, and L. Verstraete. Probing the origin of the microwave anomalous foreground. A&A, 509:L1, January 2010. doi: 10.1051/0004-6361/200912715. (Cited on page 50.)

T. Zecho, A. Guttler, X. Sha, B. Jackson, and J. Kuppers. Adsorption of hydrogen and deuterium atoms on the (0001) graphite surface. J. Chem. Phys., 117:8486–8492, November 2002. doi: 10.1063/1.1511729. (Cited on page 106.)

V. Zubko, E. Dwek, and R. G. Arendt. Interstellar Dust Models Consistent with Extinction, Emission, and Abundance Constraints. ApJS, 152:211–249, June 2004. doi: 10.1086/382351. (Cited on pages 5, 51, 53, and 54.)